Molecular Level Analysis of Atmospheric Organic Compounds

Zur Erlangung des akademischen Grades einer

DOKTORIN DER NATURWISSENSCHAFTEN (Dr. rer. nat.)

von der KIT-Fakultät für

Bauingenieur-, Geo- und Umweltwissenschaften

des Karlsruher Instituts für Technologie (KIT)

genehmigte

DISSERTATION

von

M. Eng. Wei Huang

aus

Jiangxi, China

Tag der mündlichen Prüfung: 05.07.2019

Referent: Prof. Dr. Stefan Norra

Korreferent: Prof. Dr. Thomas Leisner

Karlsruhe, den 08.07.2019

Erklärung

Hiermit erkläre ich, dass ich die vorliegende Dissertation, abgesehen von der Benutzung der angegebenen Hilfsmittel, selbständig verfasst habe.

Alle Stellen, die gemäß Wortlaut oder Inhalt aus anderen Arbeiten entnommen sind, wurden durch Angabe der Quelle als Entlehnungen kenntlich gemacht.

Diese Dissertation liegt in gleicher oder ähnlicher Form keiner anderen Prüfungsbehörde vor.

Karlsruhe, im Juli 2019

Wei Huang

Abstract

Atmospheric aerosols, tiny particles suspended in air, have important impacts on climate, visibility, and human health. Organic compounds make up a significant fraction of submicron particulate mass. The gas-phase oxidation of volatile organic compounds (VOC) by ozone (O_3), hydroxyl radicals (OH), or nitrate radicals (NO_3) form secondary organic aerosol (SOA). SOA dominates the global budget of organic aerosols (OA). Precursor VOC of SOA can stem from biogenic and/or anthropogenic source. However, ambient SOA contain thousands of compounds with a wide range of functionalities and physicochemical properties (e.g., volatility, viscosity), and its complexity hinders quantification and prediction of its impact on air quality and climate. Knowledge gaps still exist whether the molecular composition of SOA is correlated with its physicochemical properties and whether different organic compounds formed from different sources play different roles (e.g., new particle formation (NPF), particle growth, and ice nucleation).

Molecular composition of SOA particles formed from the ozonolysis of α-pinene, one of the most abundant biogenic SOA precursors, was firstly characterized at low temperature conditions (223 K) in the atmospheric simulation chambers at KIT simulating SOA formation in the upper troposphere or SOA in air parcels rising from the boundary layer. SOA formed directly at 223 K was found to be smaller particles (100–300 nm vacuum aerodynamic diameter, d_{va}) with higher mass fraction of oligomers (>40 %) compared to SOA formed at room temperature (296 K) and then transferred to 223 K (particle size: ~500 nm d_{va}; oligomer content: <35 %). SOA particles comprising of a higher oligomer content also evaporated slower. The results demonstrate that SOA particle evaporation is not only related to a compound's volatility, but also influenced by other factors, such as diffusion limitations within the particles (particle viscosity) and interactions between particles (particle matrix).

I used the knowledge of chemical composition and physicochemical properties obtained from the chamber studies, to identify SOA in field measurements which were performed at a rural site near Eggenstein-Leopoldshafen, an urban background site in Stuttgart, and a remote site near La Paz in Bolivia. Some organic tracer compounds identified in α-pinene SOA, toluene SOA, and biomass burning from my chamber studies were also found in the field, indicating contributions of different sources (e.g., forests, industry, and city) to OA measured in these measurement sites.

For the rural site near Eggenstein-Leopoldshafen, I identified anthropogenic contributions to OA mass loadings (5.0 ± 3.3 μg m^{-3}, average ± 1 standard deviation), with substantial fractions of highly functionalized organonitrates (ON, the products of the interaction between anthroposphere and biosphere) during the night in summer. The diel patterns of ON compounds with 5, 7, 10, 15 carbon atoms per molecule varied, indicating a corresponding behavior of their potential precursor VOC isoprene, toluene, monoterpenes, and sesquiterpenes, respectively. Good correlations were observed between the temporal behavior of ON and the number concentration of ultrafine particles after sunset, indicating a potential role of ON in night-time NPF which was regularly observed at this site. Organonitrates contributed 18–25 % to the mass increase of newly formed particles after sunset. The results reveal that these highly functionalized ON contribute to night-time SOA formation and particle growth. It is also one of the rare evidences yet, for night-time NPF events.

For the urban site influenced by more anthropogenic emissions (Stuttgart), the average OA were lower in summer (5.1 ± 3.2 μg m^{-3}) compared to winter (8.4 ± 5.6 μg m^{-3}), but larger mass contributions of OA were found in summer (69 %) than in winter (35 %). OA particles in summer were more influenced by biogenic emissions (similar to Eggenstein-Leopoldshafen), while biomass burning emissions (both primary and secondary) were an important source in winter. Winter OA particles were found to be less volatile, resulting from higher elemental oxygen-to-carbon (O:C) ratios and a higher oligomer content, which is consistent with the results from my chamber studies. It could also be inferred that differences in sources and/or chemistry between these two seasons are more important than partitioning. The results show the important contributions of non-fossil OA from biogenic and biomass burning emissions even in an urban area with high traffic emissions.

For the remote site in Bolivia, I identified organic tracer compounds from biogenic emissions (e.g., isoprene and monoterpenes) via e.g. regional transport of Amazon basin, as well as from anthropogenic pollution (e.g., toluene, black carbon) from the La Paz city. The results demonstrate the influences from regional transport and vertical mixing of SOA even at such a remote location.

This dissertation identifies the SOA molecular composition responsible for its physicochemical properties like particle viscosity and volatility, different organic compounds specific for anthropogenic and biogenic sources, as well as their interactions contributing to changing particle properties and to particle growth. It provides new insights on a molecular basis for the understanding of SOA, and its effects on air quality and climate.

Zusammenfassung

Atmosphärische Aerosole, winzige in der Luft schwebende Partikel, haben bedeutende Auswirkungen auf das Klima, die Sichtweite und die menschliche Gesundheit. Organische Verbindungen machen einen erheblichen Teil der Partikelmasse im Submikronbereich aus. Gasphasenoxidation von flüchtigen organischen Verbindungen (VOC) mit Ozon (O_3), Hydroxylradikalen (OH) oder Nitratradikalen (NO_3) bildet sekundäres organisches Aerosol (SOA). SOA dominiert das globale Budget des organischen Aerosols (OA). Die Vorläufer-VOC von SOA können biogenen und/oder anthropogenen Ursprungs sein. SOA kann tausende von Verbindungen mit einem breiten Spektrum an Funktionalitäten und physikalisch-chemischen Eigenschaften (z. B. Flüchtigkeit und Viskosität) enthalten. Diese Komplexität von SOA behindert Quantifizierung und Vorhersage der Auswirkungen von SOA auf Luftqualität und Klima. Es bestehen noch Wissenslücken, ob die molekulare Zusammensetzung der SOA mit ihren physikalisch-chemischen Eigenschaften korreliert ist und ob verschiedene organische Verbindungen aus verschiedenen Quellen unterschiedliche Rollen spielen (z. B. neue Partikelbildung, Partikelwachstum und Eiskeimbildung).

Die molekulare Zusammensetzung von SOA-Partikeln, die durch Ozonolyse von α-Pinen, einem der häufigsten biogenen SOA-Vorläufer, gebildet wurden, wurde bei Temperaturen um 223 K in Simulationskammern des KIT charakterisiert, um die SOA-Bildung in der oberen Troposphäre oder SOA-Transport von der Grenzschicht in die obere Troposphäre zu simulieren. Bei 223 K bildeten sich relativ kleine SOA Partikel (100–300 nm d_{va}) mit Oligomermassenanteilen über 40 %. SOA Partikel die bei 296 K erzeugt und dann auf 223 K abgekühlt wurden waren größer (~500 nm d_{va}) mit einem Oligomeranteil von unter 35 %. Die SOA Partikel mit höheren Oligomeranteilen verdampften langsamer. Diese Ergebnisse zeigen, dass die Verdampfung von SOA-Partikeln nicht nur mit der Flüchtigkeit einer Verbindung zusammenhängt, sondern auch durch andere Faktoren, wie Diffusionsbeschränkungen innerhalb der Partikel (Partikelviskosität) und Wechselwirkungen zwischen den Partikeln (Partikelmatrix), beeinflusst wird.

Mit den gewonnenen Erkenntnissen über die chemische Zusammensetzung und die physikalisch-chemischen Eigenschaften von SOA aus den Kammerstudien konnte ich SOA in Feldmessungen identifizieren. Diese Feldmessungen wurden auf dem Land nahe Eggenstein-Leopoldshafen, einem stätischen Hintergrund in Stuttgart und auf einer entlegenen Bergstation

nahe La Paz in Bolivien durchgeführt. Einige organische Marker-Verbindungen die ich bereits in Kammermessungen mit α-Pinen SOA, Toluol SOA und Verbrennung von Biomasse identifiziert hatte, konnte ich in den Feldmessungen nachweisen und verschiedenen Quellen des OA zuordnen (z.B. Wäldern, Industrie, Stadt).

Für den ländlichen Ort nahe Eggenstein-Leopoldshafen, konnte ich anthropogenen Beiträge zum OA (OA Mittelwert: 5.0 ± 3.3 μg m^{-3}) identifizieren mit erheblichen Anteilen hoch funktionalisierter organischer Nitrate (ON, Produkte der Wechselwirkung zwischen Anthroposphäre und Biosphäre) in warmen Sommernächten. Die Tagesgänge von ON-Verbindungen mit 5, 7, 10 und 15 Kohlenstoffatomen pro Molekül zeigten unterschiedliche Verläufe, was auf ein entsprechendes Verhalten ihrer potentiellen Vorläufer-VOC (z. B. Isopren, Toluol, Monoterpene, Sesquiterpene) hinweist. Das zeitliche Verhalten von ON nach Sonnenuntergang korrelierte auch mit der Anzahlkonzentration ultrafeiner Partikel, was auf eine mögliche Rolle von ON in nächtlicher Neupartikelbildung hinweist, die regelmäßig an dieser Stelle beobachtet werden. ON trug 18–25 % zur Massenzunahme der neu gebildeten Partikel nach Sonnenuntergang bei. Die Ergebnisse zeigen, dass diese hoch funktionalisierten ON, zu nächtlicher SOA-Bildung und Partikelwachstum beitragen. Dies ist eines der seltenen Nachweise für Neupartikelbildung in der Nacht.

Für den städtischen Standort in Stuttgart, der mehr von anthropogenen Emissionen beeinflusst ist, waren die mittleren OA Konzentrationen im Sommer geringer (5.1 ± 3.2 μg m^{-3}) als im Winter (8.4 ± 5.6 μg m^{-3}) wobei die Anteile des OA am Gesamtaerosol ($PM_{2.5}$) mit 69% im Sommer höher waren als im Winter mit 35%. OA-Partikel wurden im Sommer stärker von biogenen Emissionen beeinflusst (ähnlich wie nahe Eggenstein-Leopoldshafen), während die Verbrennung von Biomasse (sowohl primär als auch sekundär) eine wichtige Quelle im Winter war. OA-Partikel waren im Winter auch weniger flüchtig, möglicherweise aufgrund des höheren O:C-Verhältnisses (Verhältnis von Sauerstoff zu Kohlenstoff) sowie des höheren Oligomergehalts, was ebenfalls mit den Ergebnissen meiner Kammerstudien übereinstimmt. Der Unterschied in Emissionsquellen und/oder chemischer Prozesse zwischen diesen beiden Jahreszeiten spielt eine wichtigere Rolle als die Partitionierung. Die Ergebnisse zeigen die wichtigen Beiträge der nicht-fossilen OA aus biogenen Emissionen und der Verbrennung von Biomasse, selbst in einem Stadtgebiet mit hohen Verkehrsemissionen.

Für den entlegenen Standort in Bolivien identifizierte ich organische Marker-Verbindungen aus biogenen Emissionen (z. B. Isopren und Monoterpene) aus z. B. regionalem Transport vom Amazonasbecken sowie von anthropogenen Einflüssen (z. B. Toluol, Ruß) aus der Stadt La Paz. Die Ergebnisse zeigen die Einflüsse des regionalen Transports und der vertikalen Vermischung von SOA auch an einem solch entlegenen Standort.

Diese Arbeit identifiziert die molekulare Zusammensetzung von SOA, die für ihre physikalisch-chemischen Eigenschaften wie Partikelviskosität und -flüchtigkeit verantwortlich ist sowie verschiedene organische Verbindungen, die für anthropogene und biogene Quellen spezifisch sind, und deren Wechselwirkungen, die zur Veränderung der Partikeleigenschaften und des Partikelwachstums beitragen. Damit liefert sie auf molekularer Basis neue Erkenntnisse zum Verständnis der SOA und ihrer potenziellen Auswirkungen auf die Luftqualität und das Klima.

Contents

List of Figures

List of Tables

Abbreviations

ACSM	Aerosol Chemical Speciation Monitor
AIDA	Aerosol Interaction and Dynamics in the Atmosphere
AMS	Aerosol Mass Spectrometer
APC	Aerosol Preparation and Characterization
AVOC	Anthropogenic Volatile Organic Compounds
BSQ	Big Segmented Quadruple
BVOC	Biogenic Volatile Organic Compounds
CCN	Cloud Condensation Nuclei
CH_3I	methyliodide
CI	Chemical Ionization
CIs	Criegee Intermediates
CIMS	Chemical Ionization Mass Spectrometer
CO_2	carbon dioxide
C_{sat}	effective saturation mass concentrations
d_{va}	aerodynamic diameter
EESI-TOF	Extractive ElectroSpray Ionization Time-Of-Flight mass spectrometer
EI	Electron Ionization
ELVOC	Extremely Low Volatile Organic Compounds
eV	electronVolts
FEP	Fluorinated Ethylene Propylene
FIGAERO-HR-ToF-CIMS	Filter Inlet for Gases and AEROsols coupled to a High-Resolution Time-of-Flight Chemical Ionization Mass Spectrometer
GAW	Global Atmosphere Watch
GUI	Graphical User Interface
H:C	Hydrogen-to-Carbon ratio
H_2SO_4	sulfuric acid
HNO_3	nitric acid
HOM	Highly Oxygenated organic Molecules
HO_2	hydroperoxyl radical
HR-ToF	High-Resolution Time-of-Flight

HR-ToF-AMS	High-Resolution Time-of-Flight Aerosol Mass Spectrometer
I^-	iodide ion
IEPOX	Isoprene EPOXydiol
IMK	Institute of Meteorology and Climate Research
IMR	Ion Molecule Reaction
IN	Ice Nuclei
KIT	Karlsruhe Institute of Technology
LIDAR	LIght Detection and RAnging
LOD	Limit of Detection
LVOC	Low Volatile Organic Compounds
MCP	MultiChannel Plate
MS	Mass Spectrometry
m/z	mass-to-charge ratio
NO	nitric oxide
NO_2	nitrogen dioxide
NO_3	nitrate radicals
NO_x	nitrogen oxides
NPF	New Particle Formation
OA	Organic Aerosols
O_2	oxygen
O_3	ozone
O:C	Oxygen-to-Carbon ratio
OH	hydroxyl radicals
PB	Primary Beam
PBL	Planetary Boundary Layer
PIKA	Peak Integration by Key Analysis
PMF	Positive Matrix Factorization
POA	Primary Organic Aerosol
PSI	Paul Scherrer Institute
PSI-SCAC	Paul Scherrer Institute-the Simulation Chamber for Atmospheric Chemistry
PTFE	PolyTetraFluoroEthylene

PToF	Particle Time-of-Flight
RH	Relative Humidity
RO	alkoxy radical
RO_2	organic peroxy radical
$RONO_2$, ON	OrganoNitrate
ROOH	hydroxperoxide
$ROONO_2$	peroxynitrate
ROOR	organic peroxides
SALTENA	Southern hemisphere high ALTitude Experiment on particle Nucleation And growth
sCIs	stabilized Criegee Intermediates
SOA	Secondary Organic Aerosol
SQUIRREL	SeQUential Igor data RetRiEvaL
SSQ	Small Segmented Quadruple
SVOC	Semi-Volatile Organic Compounds
S/N	Signal-to-Noise ratio
T_{max}	Maximum desorption temperatures
ToF	Time of Flight
UHP	Ultra-High-Purity
VBS	Volatility Basis Sets
VOC	Volatile Organic Compounds

1 Context of this dissertation

Atmospheric aerosols, defined as suspension of particles in gas, are ubiquitous in the Earth's atmosphere and have significant impacts on climate (IPCC, 2013), visibility (Boers et al., 2015), and health (Nel, 2005; Rückerl et al., 2011). Organic aerosols (OA) make up a significant fraction (20–90 %) of submicron particulate mass (Murphy et al., 2006; Zhang et al., 2007; Jimenez et al., 2009; Ehn et al., 2014). The chemical composition and physicochemical properties (e.g., volatility, viscosity) of OA are of great research interest since they influence OA lifetime and with that air quality and climate effects. However, these issues are still not fully quantified or understood yet and thus prevent the accurate quantification and prediction of OA effects. In this context this dissertation aims to provide a substantial scientific contribution to OA molecular composition responsible for their physicochemical properties like particle viscosity and volatility, different organic compounds specific for anthropogenic and biogenic sources, as well as their interactions contributing to changing particle properties and to particle growth. This dissertation is based on the cumulation of nine scientific publications which are all research papers. For three of them (sections 2–4 and the corresponding supplement in Appendix A.1–A.3) I am the first author, and for the other six of them (sections Appendix B.1–B.6) I am a co-author. These research papers are all based on laboratory studies, field work, and/or modelling that were performed during my PhD study.

Organic aerosols will be detailed introduced in the following section 1.1. Basic knowledge about mass spectrometry will be introduced in section 1.2. Motivated by the knowledge gaps remaining in the aerosol research, the specific research objectives for my research work are in section 1.3. Within section 1.4, methodology used in my research work including two mass spectrometers, three atmospheric simulation chambers as well as the deployment of these two mass spectrometers in my chamber studies and field work will be introduced.

1.1 Organic aerosols

The atmospheric processing of OA is shown in Figure 1 (Shiraiwa et al., 2011). Atmospheric OA can be separated into primary organic aerosol (POA) and secondary organic aerosol (SOA). POA is directly emitted from sources such as fossil fuel combustion and forest fires; while SOA is formed via gas-phase oxidation of precursor volatile organic compounds (VOC). SOA dominates OA's global budget (Shrivastava et al., 2015). After OA are emitted or formed, they

will go through chemical and physical transformations during their lifetime in the atmosphere, and interact with water vapor to form clouds. In the following, the state-of-the-art knowledge of their emissions/formation, oxidation mechanisms, as well as chemical composition and physicochemical properties of the resulting oxidation products will be introduced.

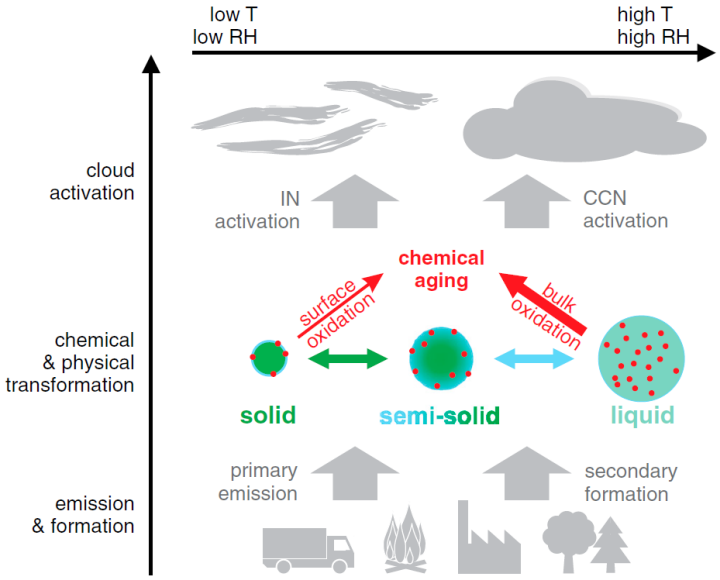

Figure 1. Life cycle of atmospheric organic aerosol particles from primary emissions or secondary formation (Shiraiwa et al., 2011). Green circles stand for particles and small red circles stand for oxidants and other trace gases.

1.1.1 Precursor volatile organic compounds

The gas-phase precursor VOC for SOA can stem from biogenic and/or anthropogenic source. Global estimates indicate that biogenic VOC (BVOC) emissions (539 Tg C a^{-1}) dominate over anthropogenic VOC (AVOC) emissions (aromatics: 16 Tg C a^{-1}), and that the global SOA production from BVOC (22.9 Tg C a^{-1}) outreaches that from AVOC (1.4 Tg C a^{-1}) as well (Heald et al., 2008). Despite the lower annual emissions and SOA formation from AVOC compared to that from BVOC, they have important effects on air quality and human health, particularly in urban locations.

1.1.1.1 Biogenic volatile organic compounds

The global BVOC emissions are dominated by isoprene (496 Tg C a^{-1}) and monoterpenes (43 Tg C a^{-1}; Heald et al., 2008).

Isoprene, with the molecular formula of C_5H_8 (Figure 2), is produced and emitted by many species of trees (e.g., oak trees, some legumes; Langford et al., 2017; Monson et al., 2013). Isoprene emission in plants is dependent on e.g. light and temperature (Guenther et al., 1995). It appears to be a mechanism that trees use to combat abiotic stresses, such as heat stress and reactive oxygen species (Sharkey et al., 2008; Sharkey and Yeh, 2001). The amount of isoprene released from isoprene-emitting plants depends on e.g. leaf temperature and light intensity (Sharkey et al., 2008; Sharkey and Yeh, 2001). Therefore, little isoprene is emitted from tree leaves during the night, while substantial isoprene is expected to be emitted from many oak species during the daytime of hot sunny days. Isoprene is also a byproduct of the thermal cracking of naphtha or oil, and a side product of ethylene production. About 95 % of isoprene production from industry is used to produce a synthetic version of natural rubber, cis-1,4-polyisoprene (Greve, 2000).

Monoterpenes, with the molecular formula of $C_{10}H_{16}$, are a class of terpenes with two isoprene units. Their molecular structure can be linear or contain rings. They are emitted by many plants (e.g., pine trees, citrus trees; Komenda and Koppmann, 2002; Fares et al., 2011). One of the most abundant monoterpenes is α-pinene (24.8 % mass contribution to global monoterpene emissions, Kanakidou et al., 2005; Figure 2). Different from isoprene, emissions of monoterpenes are reported to be mainly dependent on temperature (e.g., Juuti et al., 1990; Komenda and Koppmann, 2002). Climate warming are assumed to have an effect on monoterpene emissions (Constable et al., 1999). Trees emit monoterpenes in order to fight pests and diseases, attract natural enemies of pests, and warn neighboring plants for similar prevention (Kessler and Baldwin, 2001; Karban et al., 2006; Mofikoya et al., 2017). Monoterpenes are also related to the pharmaceutical, cosmetic, agricultural, and food industries (Breitmaier, 2006).

1.1.1.2 Anthropogenic volatile organic compounds

The global AVOC emissions are largely contributed by aromatic hydrocarbons (16 Tg C a^{-1}, Heald et al., 2008), while biomass burning emissions can be an important contributor particularly in winter (Canonaco et al., 2015; Daellenbach et al., 2019). Domestic heating (e.g., Xu et al., 2016; Hu et al., 2017) as well as cooking emissions can also be important sources in some regions (e.g., Mohr et al., 2012; Reyes-Villegas et al., 2018).

Toluene, with the molecular formula of C_7H_8 (Figure 2), is one of the most abundant anthropogenic aromatic hydrocarbons (6.9 Tg C a^{-1}; Henze et al., 2008). It is emitted when used as a solvent and also during its own production and/or the production of gasoline and of coke from

coal, but it is mainly emitted from anthropogenic emissions related to traffic or industrial activities (EPA, 1994).

Biomass burning is the burning of living and/or dead vegetation, which includes human-initiated burning for land clearing and land use/usage-change as well as natural, lightning-induced fires. Biomass containing 2000 to 5000 Tg C is burned annually (Crutzen and Andreae, 1990; van der Werf et al., 2006). During the biomass burning processes, apart from emissions of greenhouse gases, such as carbon dioxide (CO_2) which helps to warm the Earth, and soot particles which can serve as cloud condensation nuclei (CCN) and affect cloud properties, products from incomplete combustion are emitted as well. They play an important role in atmospheric chemistry and climate. Examples are hydrocarbons (e.g., alkanes, alkenes, aromatics), aldehydes, ketones, alcohols, phenols and substituted phenols, organic acids, and levoglucosan, etc. (Crutzen and Andreae, 1990; Schauer et al., 2001). Due to its source-specificity and abundance, levoglucosan (molecular formula of $C_6H_{10}O_5$, Figure 2, formed by the pyrolysis of cellulose and hemicellulose) is used as a tracer compound for biomass burning emissions (e.g., Simoneit et al., 1999; Saarnio et al., 2010).

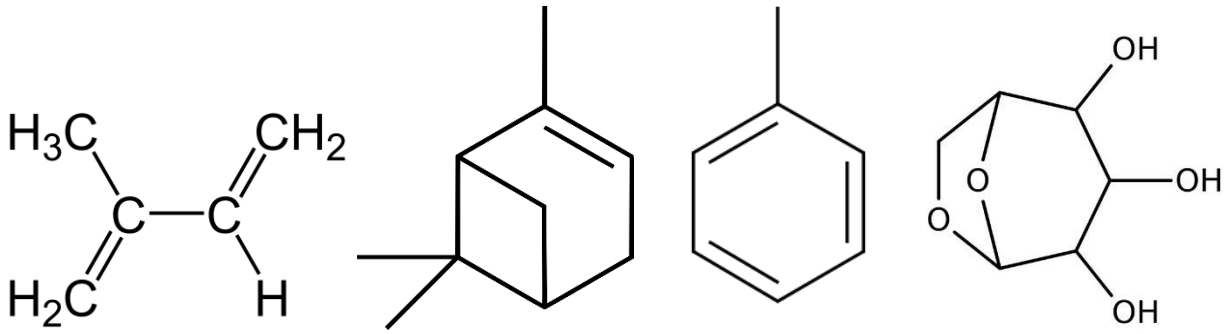

Isoprene α-Pinene Toluene Levoglucosan

Figure 2. Structural formulae of isoprene, α-pinene, toluene, and levoglucosan.

1.1.2 Secondary organic aerosol

In the atmosphere, the gas-phase precursor VOC are oxidized by ozone (O_3), hydroxyl radicals (OH), or nitrate radicals (NO_3) into semi-volatile, low volatile, and extremely low volatile organic compounds (SVOC, LVOC, and ELVOC, respectively). These compounds can partition into the particle phase and contribute to SOA particulate mass. Due to the abundant precursor VOC and formation mechanisms, SOA is very complex and can contain thousands of compounds with different functionalities and physicochemical properties (e.g., volatility, viscosity) in both gas phase and particle phase (Hallquist et al., 2009; Nozière et al., 2015). In the following, a simplified

summary of the atmospheric oxidation chemistry and the resulting oxidation products from the abovementioned BVOC (i.e., α-pinene and isoprene) and AVOC (i.e., toluene and biomass burning) will be discussed, and then the physicochemical properties (e.g., volatility, viscosity) that affect the chemical aging processes will also be introduced.

1.1.2.1 Oxidation mechanisms of volatile organic compounds

Despite the chemical complexity of the oxidation processes, there are several oxidation mechanisms which have already been identified in SOA formation (Atkinson and Arey, 2003; Kroll and Seinfeld, 2008). A simplified oxidation chemistry for VOC is shown in Figure 3 (Kroll and Seinfeld, 2008). General reactions in the gas phase include the initial attack of the oxidants (e.g., O_3, OH radicals and/or NO_3 radicals), organic peroxy (RO_2) radical reactions (e.g., autoxidation), and alkoxy (RO) radical reactions, etc. (Atkinson and Arey, 2003; Kroll and Seinfeld, 2008). Briefly, VOC can be attacked initially by the oxidants via radical-initiated oxidation (abstraction of a hydrogen atom or addition to a C–C double bond) or cleavage of a C–C double bond by O_3 (for alkenes; Kroll and Seinfeld, 2008). The cleavage of an alkene by O_3 lead to the formation of a carbonyl and an energetically excited carbonyl oxide, i.e., Criegee Intermediates (CIs), which can decompose to form OH and an alkyl radical, or stabilize to form stabilized Criegee Intermediates (sCIs) and then react with water or oxygenated organics to form a hydroxy-hydroperoxide or an ozonide (Atkinson and Arey, 2003; Kroll and Seinfeld, 2008). After the alkyl radicals are formed, they form RO_2 radicals rapidly, which then react with hydroperoxyl (HO_2) radicals to form a hydroxperoxide (ROOH, a major component in SOA; Docherty et al., 2005), or with NO or NO_2 to form RO radicals and an organonitrate ($RONO_2$), or a peroxynitrate ($ROONO_2$; Sobanski et al., 2017; Faxon et al., 2018). Most $ROONO_2$ are thermally unstable or photolabile, and can decompose back to NO_x (including NO and NO_2; Singh and Hanst, 1981; Sobanski et al., 2017). Under NO_x-free conditions, RO_2 radicals can also undergo self- and cross-reactions to form an organic peroxide (ROOR), and/or alcohol and a carbonyl. After the RO radicals are formed, they can dissociate, isomerize or react with O_2 to form a carbonyl, and/or an alkyl radical and HO_2 (Atkinson, 2007). Depending on the volatility of individual organic compounds, they can partition into the particle phase and continue chemical reactions including heterogeneous and multiphase reactions, which can be non-oxidative or oxidative (Kroll and Seinfeld, 2008). The non-oxidative reactions (the oxidation state of the total carbon is unchanged), or the so-called accretion reactions, form high molecular-weight oligomers (e.g., Surratt et al.,

2006; Sato et al., 2007; D'Ambro et al., 2017; Huang et al., 2018); whereas the oxidative reactions (the carbon is oxidized), or the so-called aerosol aging processes, are similar to the gas phase reactions shown in Figure 3 but with varying branching ratios among different pathways (Rudich et al., 2007). Chemistry can also continue over several generations in either gas phase or particle phase (Kroll and Seinfeld, 2008). Despite these abovementioned identified oxidation mechanisms, the underestimation and overestimation of SOA in modellings compared to ambient observations suggests unrevealed oxidation pathways for SOA formation in chamber experiments and/or insufficient oxidation pathways included in models, and incorrect oxidation pathways included in models, respectively (Kroll and Seinfeld, 2008).

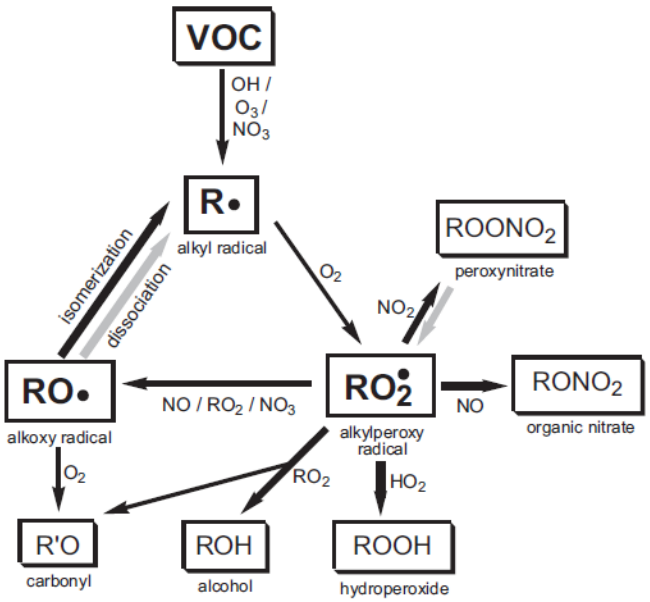

Figure 3. Simplified oxidation mechanisms of VOC. Thick black arrows stand for reactions that can decrease volatility; gray arrows stand for reactions that can increase volatility. Reprinted from Kroll and Seinfeld (2008), Copyright © 2008, with permission from Elsevier.

1.1.2.2 Molecular composition of secondary organic aerosol

As a result of the different sources and oxidation mechanisms, SOA can contain thousands of organic compounds with a wide range of functionalities and physicochemical properties (e.g., volatility, viscosity).

SOA formed from α-pinene oxidation reactions has been studied extensively in atmospheric simulation chambers (e.g., Kristensen et al., 2016; Denjean et al., 2015; McVay et al., 2016). The reactions of α-pinene with different oxidants (e.g., O_3, and OH and NO_3 radicals) lead to the formation of a lot of oxygenated products including e.g. aldehydes, oxy-aldehydes, carboxylic

acids, hydroxy-carboxylic acids, oxy-carboxylic acids, dicarboxylic acids, and organonitrates, etc. (Winterhalter et al., 2003; Kanakidou et al., 2005). Aerosol yields from α-pinene oxidations vary for different oxidants, and the most important oxidation in terms of SOA formation is its reaction with O_3 (Kanakidou et al., 2005). Therefore, a lot of oxidation experiments of α-pinene have been carried out with O_3 in the laboratory. The molecular composition of organic compounds accounting for ~58−72 % of SOA mass formed from the ozonolysis of α-pinene were characterized, and most of these organic compounds can be grouped into monomers (oxidation products from one α-pinene molecule) with molecular formulae of $C_{8-10}H_{12-16}O_{3-6}$, and dimers (oxidation products from two α-pinene molecules) with molecular formulae of $C_{14-19}H_{24-28}O_{5-9}$ (Zhang et al., 2015). Two major dimers, $C_{17}H_{26}O_8$ and $C_{19}H_{28}O_7$, have been elucidated as a cis-pinyl-diaterpenyl ester (Yasmeen et al., 2010) and a cis-pinyl-hydroxypinonyl ester (Müller et al., 2008), respectively. Autoxidation processes involving RO_2 radicals and multiple addition reactions of O_2 can form highly oxygenated organic molecules (HOM, elemental oxygen-to-carbon (O:C) ratios of 0.7−1.3, Ehn et al., 2012; Bianchi et al., 2019). Recently, the α-pinene HOM dimers were found to be suppressed by the product scavenging effects due to the presence of isoprene (McFiggans et al., 2019). Both HOM monomers and dimers have been shown to play an important role in atmospheric new particle formation (NPF; Kulmala et al., 2013; Ehn et al., 2014; Bianchi et al., 2016). However, the formation mechanisms for most less oxygenated dimers (e.g., esters and other accretion products), which are a large class of the major products in α-pinene SOA, are still not known yet. They have been proposed as crucial components in OA particle growth both in the laboratory and in the field (Kristensen et al., 2014; Kristensen et al., 2016; Tröstl et al., 2016; Zhang et al., 2015; Mohr et al., 2017).

Due to the minor SOA yields and volatile properties of key oxidation products from isoprene oxidation, it was believed that isoprene oxidation does not contribute to atmospheric SOA (Pandis et al., 1991). Only more than a decade ago results from field (e.g., Claeys et al., 2004) and laboratory studies (e.g., Kroll et al., 2005) indicated that owing to the large global emissions isoprene oxidation may indeed contribute to SOA formation in the atmosphere (Carlton et al., 2009). Since then, many laboratory studies have been performed for isoprene SOA formation. Isoprene SOA yields vary a lot, suggesting that they are quite sensitive to experimental and/or reaction conditions (Carlton et al., 2009). In the atmosphere, the primary removal mechanism for isoprene is by gas-phase reactions with OH radicals, NO_3 radicals, and, to a lesser extent, O_3

(Carlton et al., 2009; Nestorowicz et al., 2018). These oxidation processes result in the formation of gas- and particle-phase products including e.g. 2-methyltetrols, 2-methylglyceric acid, C_5-alkene triols, and organosulfates, etc. (Edney et al., 2005; Surratt et al., 2007; Riva et al., 2016; Spolnik et al., 2018). Highly oxygenated C_5 compounds such as compounds with molecular formulae of $C_5H_{8,10,12}O_{3–8}$ have been observed as major components (~50 %) for SOA formed from isoprene photochemical oxidation under high HO_2 and low NO conditions (D'Ambro et al., 2017). Oligomerization is found to be an important SOA formation pathway in the isoprene photooxidation SOA in the presence of NO_x, but the nature of the oligomers depends strongly on the NO_x level (Surratt et al., 2006). Acidic products (mainly polyesters accounting for ∼22−34 % of the SOA mass) are formed only under high NO_x conditions, while non-acidic organic peroxides (contributing ∼61 % of the SOA mass for nucleation experiments and ∼25−30 % in the presence of seed particles) are formed under low NO_x conditions (Surratt et al., 2006). Besides, acidic seeds have been shown to play an important role in isoprene oligomerization and thus to some extent compensating its oxidant- (OH radicals) and product scavenging effects for α-pinene SOA (McFiggans et al., 2019).

There are fewer studies on SOA formation from toluene compared to those from α-pinene and isoprene. The oxidation of toluene is initiated by the OH radicals (Perry et al., 1977), and the majority of the previous studies were focused on the SOA yields from toluene photooxidation, which were found to strongly depend on experimental conditions such as temperature and/or NO_x levels (Takekawa et al., 2003; Ng et al., 2007; Hildebrandt et al., 2009). Oxidation processes of toluene lead to the formation of many products including anhydrides (e.g., 2,5-furandione, 3-methyl-2,5-furandione, 3-ethyl-2,5-furandione), glyoxylic acid, methylglyoxylic acid, cresols, bezaldehyde, dihydroxymethybenzenes, and organonitrates, etc. (Forstner et al., 1997; Jang and Kamens, 2001; Ji et al., 2017; Gramlich, 2018). Monomers with 7 carbon atoms and dimers with 14 carbon atoms are found to dominate the peak abundances in toluene SOA (Hinks et al., 2018). HOM with molecular formulae of $C_7H_{8,10,12}O_{4–11}$ have been found in the gas-phase oxidation products of toluene, formed via autoxidation chain reactions (Molteni et al., 2018). Some of those HOM were also observed in particle-phase studies of toluene SOA (Sato et al., 2007;Hinks et al., 2018). Several major monomers have been elucidated as methyloxohexadienoic acids ($C_7H_8O_3$; Jang and Kamens, 2001), C_7 unsaturated oxacyclic ixocarboxylic acids and C_7 unsaturated oxacyclic dicarboxylic acids ($C_7H_8O_4$ and $C_7H_8O_5$; Sato et al., 2007). Sato et al. (2007) found that

hemiacetal and peroxy hemiacetal oligomers as well as low-molecular-weight dicarboxylic acids contribute significantly in terms of mass to the toluene photooxidation SOA in the presence of NO_x. However, a significant decrease in oligomer fraction has been observed for toluene low-NO_x SOA under high relative humidity (RH) conditions compared to that under dry conditions, possibly due to the oligomerization suppression caused by either water vapor or aerosol liquid water (Hinks et al., 2018).

Despite the high primary biomass burning emissions (Crutzen and Andreae, 1990; van der Werf et al., 2006), SOA can also be formed during the biomass burning processes. However, even fewer studies have been performed for SOA from biomass burning. Despite that levoglucosan is found to be abundant and stable in the atmosphere (Fraser and Lakshmanan, 2000; Simoneit et al., 2004), it is also subject to atmospheric loss, resulting in the formation of SOA mass (Zhao et al., 2014; Gilardoni et al., 2016; Enami et al., 2017). The OH-initiated oxidation of levoglucosan is one of the main eliminating mechanisms (Yang et al., 2009; Bai et al., 2013). Different oxidation processes of levoglucosan lead to the formation of organic compounds with different functional groups, such as small organic acids, poly-carbonyl intermediates, etc. (Zhao et al., 2014). The dominant oxidation products for aqueous-phase photooxidation of levoglucosan have been found to have molecular formulae of $C_{3–6}H_{2,4,6,8,10}O_{3–7}$, potentially resulting from the functionalization and bond scission mechanisms (Zhao et al., 2014). The formation of high molecular-weight (*m/z* up to 1000 Th) compounds (i.e., oligomers) were also found in levoglucosan SOA by Holmes and Petrucci (2006, 2007), suggesting that oligomerization is an important pathway for levoglucosan SOA formation in both Fenton (Holmes and Petrucci, 2007) and acid-catalyzed chemistry (Holmes and Petrucci, 2006). Besides, levoglucosan were also found to react with Criegee intermediates (CIs), such as the CIs formed from the ozonolysis of sesquiterpenes ($C_{15}H_{24}$, a class of terpenes that consist of three isoprene units), and lead to the formation of adducts (Enami et al., 2017).

1.1.2.3 Physicochemical properties of secondary organic aerosol

As a consequence of its highly dynamic reactions, SOA continually evolves in the atmosphere, becoming increasingly oxidized, less volatile, and more hygroscopic (Jimenez et al., 2009). SOA residence time (or lifetime) in the atmosphere is influenced by meteorological conditions (e.g., temperature, wind, precipitation, and solar radiation), physical processes (e.g., wet or dry deposition), chemical transformation (e.g., hydrolysis, oxidation), atmospheric dispersion, as well as its location and the topography (Baumbach and Vogt, 2003; D'Amato et al., 2014; Kinney, 2018;

Zare et al., 2018). SOA lifetime has a strong effect on physicochemical properties of SOA particles, and thus on air quality and climate (Tsigaridis et al., 2006; Jimenez et al., 2009; Shiraiwa et al., 2017). Vice versa, the changes in the physicochemical properties of SOA also affect the chemical aging processes. As illustrated in Figure 1, the chemical transformation and aging upon the interaction of particles with oxidants (e.g., O_3, OH and NO_3 radicals) and other trace gases proceeds relatively slow via surface oxidation on solid particles but relatively fast via bulk oxidation in liquid particles (Shiraiwa et al., 2011). It is therefore of great significance to investigate the physicochemical properties of SOA. State-of-the-art instruments, such as the linear trap quadrupole Orbitrap mass spectrometer (Daellenbach et al., 2019), the filter inlet for gases and aerosols coupled to a high-resolution time-of-flight chemical ionization mass spectrometer (FIGAERO-HR-ToF-CIMS; Huang et al., 2019), and the newly developed extractive electrospray ionization time-of-flight mass spectrometer (EESI-TOF; Qi et al., 2019), provide insights into the molecular composition of OA and enable the link between the molecular composition of SOA and its physicochemical properties. For example, using molecular information obtained from these instruments in volatility parameterizations, effective saturation mass concentrations (C_{sat}) of individual organic compounds can be calculated (Li et al., 2016; Donahue et al., 2011). Based on the C_{sat} value of each organic compound, one can group different organic compounds into different volatility classes (or bins), i.e., volatility basis sets (VBS; Donahue et al., 2006; 2011; 2012; Cappa and Jimenez, 2010).

Volatility is one of the most important physicochemical properties that determines whether an organic compound partitions into the particle phase and contributes to particulate mass. It influences the physicochemical transformation processes of SOA and thus SOA lifetime and air quality (Donahue et al., 2013; Ehn et al., 2014; Buchholz et al., 2019). As a result of the link between molecular formulae and structure of each organic compound obtained with the abovementioned state-of-the-art instruments and its volatility, different atmospheric OA types can be grouped into different volatility bins. The resulting volatility of different OA types can vary depending on different sources. For e.g. OA measured in the southeastern U.S., isoprene epoxydiol (IEPOX) derived SOA was observed to be the most volatile (Lopez-Hilfiker et al., 2016b). In addition, OA apparent volatility can also be influenced by diffusion limitations within the particles (particle viscosity), resulting from the amorphous phase state of SOA particles (Cappa and Wilson, 2011; Vaden et al., 2011; Roldin et al., 2014; Yli-Juuti et al., 2017).

Phase state (i.e., viscosity) is another important physicochemical property of SOA. The phase state of biogenic SOA particles in the atmosphere has been shown to range from liquid to amorphous (semi-)solid (Virtanen et al., 2010; Bateman et al., 2016; Shiraiwa et al., 2017). The phase state of SOA particles influence the gas uptake, gas-particle partitioning, diffusion, the particles' capability to act as CCN and/or ice nuclei (IN), as well as the particles' lifetime in the atmosphere (Shiraiwa et al., 2011;Price et al., 2015;Lienhard et al., 2015). As illustrated before, during the chemical transformation processes, organic compounds in solid particles react slower compared to liquid particles. Upon interactions with water vapor to form clouds, solid particles tend to be activated as IN to form ice crystals, while liquid particles favor to be activated as CCN to form water droplets (Figure 1; Shiraiwa et al., 2011). It is therefore of great significance to investigate the viscosity of SOA particles. The phase state and viscosity of atmospheric SOA particles can be affected by e.g. ambient temperature and RH (Figure 1; Shiraiwa et al., 2011). For example, at around room temperature, the viscosity of α-pinene SOA at dry conditions (Song et al., 2016;Renbaum-Wolff et al., 2013;Pajunoja et al., 2014) corresponds to a semisolid state (Shiraiwa et al., 2011), while its viscosity drops tremendously at 90 % RH conditions (Renbaum-Wolff et al., 2013). In general, higher viscosity can be expected for SOA at cool and dry conditions (e.g., Song et al., 2016; Järvinen et al., 2016; Shiraiwa et al., 2011; Wang et al., 2015; Kidd et al., 2014).

1.2 Mass spectrometry

Mass spectrometry (MS) has become an important tool in real-time detection and chemical analysis of aerosol particles (Sullivan and Prather, 2005; Nash et al., 2006). Mass spectrometry (MS) is an analytical technique that ionizes chemical species, sorts the ions based on their mass-to-charge ratio (*m/z*), and detects them qualitatively and quantitatively by their respective *m/z* and abundance (Gross, 2017).

Normally a mass spectrometer consists of three basic parts: an ion generator, a mass analyzer, and a detector (Figure 4A; Gross, 2017). In order to reduce the ion losses and maximize the transmission efficiency, these parts are operated under high vacuum conditions. The most important information derived from the mass spectrometer is the mass spectrum (Figure 4B), a two-dimensional representation of signal intensity versus its *m/z* (Gross, 2017). The signals for each ion is usually called a peak (or stick), and the intensity of the peak is related to the abundance of that ion, which can be obtained from the measured peak heights or peak areas (Gross, 2017).

The performance of a mass spectrometer can be evaluated by several parameters: sensitivity (a specified ion species reaching the detector per mass of analyte used), limit of detection (LOD; the lowest amount of analyte necessary to obtain a signal that can be distinguished from the background noise), and signal-to-noise ratio (S/N; a quantitative measure of a signal's quality by quantifying the ratio of the intensity of a signal relative to noise; Gross, 2017).

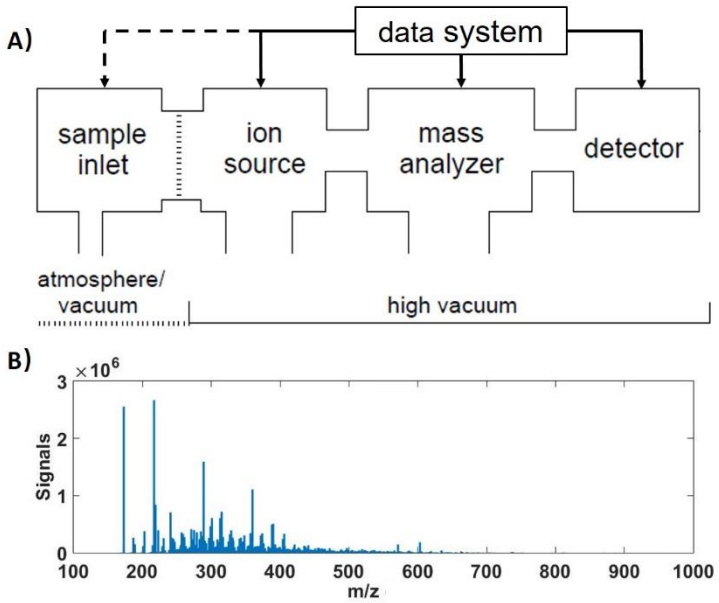

Figure 4. (A) General scheme of a mass spectrometer (modified from Gross, 2017); (B) example of a mass spectrum.

Mass spectrometers have been widely used in aerosol research. Many variations of aerosol mass spectrometers have been developed for organic and inorganic compound analysis, differing in sampling inlets, desorption/ionization methods, and/or mass analyzers (e.g., time of flight, ToF, which uses the velocity of an ion to determine its *m/z*) (Suess and Prather, 1999). In the following two commonly used ionization methods (electron ionization, chemical ionization) and examples of their corresponding mass spectrometers will be introduced.

1.2.1 Electron ionization and aerosol mass spectrometer

A classical ionization method used in MS is electron ionization (EI; e.g., Jayne et al., 2000; DeCarlo et al., 2006; Canagaratna et al., 2007) by forming ions via shooting energetic electrons at a gaseous neutral. After a neutral is hit by an energetic electron carrying several tens of electron-volts (eV) of kinetic energy, some of the energy is transferred from the electron to the neutral, resulting in the ejection (form positive ions, most desirable process) or addition (form negative

ions) of an electron out of or to the neutral (Gross, 2017). The ionization efficiency reaches maximum at electron energies around 70 eV, at which the EI mass spectra are always acquired (e.g., the aerosol mass spectrometer (AMS); Jayne et al., 2000; DeCarlo et al., 2006). However, the ionization energies of most molecules are in the range of 7–15 eV, and the extra electron energies will split the whole molecule and lead to the fragmentation of ions (Gross, 2017).

One example of MS utilizing EI is AMS. The instrumental development of the AMS, which is able to measure non-refractory particle composition and quantify OA time evolution and absolute mass concentrations at high time resolution (Jayne et al., 2000; DeCarlo et al., 2006; Canagaratna et al., 2007), was a major breakthrough after using offline high-volume filter measurements (Schauer et al., 1996; Zheng et al., 2002).

1.2.2 Chemical ionization and chemical ionization mass spectrometer

Different from the hard ionization method EI, another common ionization technique used in aerosol research is chemical ionization (CI; e.g., Caldwell et al., 1989; Munson, 2000; Zhao et al., 2014; Ehn et al., 2014; Lopez-Hilfiker et al., 2014; Mohr et al., 2017; Huang et al., 2018; Huang et al., 2019). CI is a highly selective, soft ionization method (Gross, 2017) that utilizes the reactivity of the analytes towards the reagent ion to ionize molecules via transfer of an electron, proton, or other ions such as iodide (e.g., Caldwell et al., 1989; Lee et al., 2014; Lopez-Hilfiker et al., 2016a). The molecular structure of the parental molecule is mostly kept intact, which facilitates conclusions on chemical reaction processes (Munson, 2000). The benefits of CIMS include that it measures online, in real-time with high time resolution, is highly reproducible and highly sensitive with some selectivity; whereas the general drawbacks of CIMS include that it cannot separate isomers and thus does not have structural information, and needs authentic standards to derive sensitivity (Lee et al., 2014; Lopez-Hilfiker et al., 2016a). CIMS is often used to detect atmospheric trace species such as inorganic acids (e.g., H_2SO_4, HNO_3), free radicals (e.g., HO, HO_2, RO_2), VOC, and complex organic aerosol components (e.g., Berresheim et al., 2000; Ammann et al., 2004; Ehn et al., 2014; Sanchez et al., 2016; Mohr et al., 2017; Huang et al., 2018; Huang et al., 2019).

Negative-ion CIMS represents one general approach capable of quantifying a variety of oxygenated organic compounds (Caldwell et al., 1989). Iodide (I^-) is a commonly used reagent ion in CIMS (Lee et al., 2014; Lopez-Hilfiker et al., 2016a), due to its significantly electronegative property (Lee et al., 2014). Fragmentation is minimal during the adduct formation since the adduct

formation is typically slightly exoergic. Electron transfer (except for e.g. NO_3 radicals) and proton abstraction (except for e.g. H_2SO_4) are also essentially negligible (Lee et al., 2014).

The state-of-the-art instruments such as AMS and CIMS provide important insights into oxidation mechanisms, chemical composition, and physicochemical properties of SOA from chamber studies and field measurements. By the deployment of them, I could investigate the chemical composition and physicochemical properties of SOA in gas and/or particle phases.

1.3 Research objectives

In order to quantify and predict the impacts of atmospheric SOA on air quality and climate, investigations on molecular composition and physicochemical properties of SOA from chamber studies, field work as well as modellings are needed. Despite the tremendous research work on SOA that has been done till now, a lot of scientific questions are still open to be answered. For example, the chemical composition and volatility of OA at a wide range of atmospherically relevant conditions, especially at low temperature conditions, which are representative of the upper troposphere where they can be transported to or formed in-situ, are rarely simulated in chamber studies, despite the potential significance for their cloud formation potential (Virtanen et al., 2010; Zhang et al., 2015). In addition, ambient observations contributing to the understanding of the role/influences of different organic compounds in the atmosphere (e.g., new particle formation, particle growth, ice nucleation), particularly organonitrates and organosulfates which are the products of interactions of anthroposphere and biosphere, are scarce. And the relationship between OA molecular composition and their physicochemical properties (e.g., volatility, viscosity) are also poorly understood. These existing knowledge gaps in the aerosol research lead to my following research objectives:

a) Identify and quantify organic compounds of OA formed in the atmospheric simulation chambers in order to assess and understand atmospheric aging processes of atmospheric aerosols from different sources. Study the influence of various temperatures (particularly at low temperatures), and the interaction of biogenic emissions and anthropogenic emissions on chemical composition and physicochemical properties of atmospheric OA;
b) Analysis of the chemical composition of OA in rural, urban, and remote locations. Measure concentration levels and chemical composition of OA compounds in both gas and particle phases in a rural site near Eggenstein-Leopoldshafen and an urban background site in

Stuttgart, respectively, in Germany (Northern Hemisphere), and a remote mountain site in Bolivia (Southern Hemisphere);

c) Derive sources, formation processes, and physicochemical properties (e.g., volatility and viscosity) of ambient OA using organic tracer compounds identified in the chambers. Investigate the relationship between OA molecular composition and their physicochemical properties, and whether this relationship is influenced by other factors (e.g., environmental conditions);

d) Investigate the role of different organic compounds in the atmosphere (e.g., new particle formation. particle growth, and ice nucleation ability) based on chamber studies and field measurements in Germany and Bolivia.

1.4 Methodology

Motivated by the research objectives and open scientific questions of OA, I used mainly two instruments in this dissertation: a high-resolution time-of-flight aerosol mass spectrometer (HR-ToF-AMS, Aerodyne Inc.) and a filter inlet for gases and aerosols coupled to a high-resolution time-of-flight chemical ionization mass spectrometer (FIGAERO-HR-ToF-CIMS, Aerodyne Inc.). HR-ToF-AMS and FIGAERO-HR-ToF-CIMS can provide real time quantification on chemical composition for gases and/or aerosol particles. Both instruments can be compared and compensated with each other (Table 1).

Table 1. Comparison between HR-TOF-AMS and FIGAERO-HR-ToF-CIMS

	HR-ToF-AMS	FIGAERO-HR-ToF-CIMS
Ionization method	Electron ionization	Chemical ionization
ToF-MS type	Measures fragment cations	Measures intact molecular ions
Aerosols measured	Only particle phase	Both gas phase and particle phase
Analysis of non-refractory species	Organic compounds, and most sulfate, nitrate, ammonium, and chloride salts	Organic compounds, inorganic acids, radicals, and some trace gases (e.g., O_3)
Quantification	Yes	Yes
Expectations	Total particle mass concentrations; Bulk O:C ratios; Chemical composition; Particle size (d_{va})	Gas and particle mass concentrations; Bulk O:C ratios; Molecular composition; Volatility

Laboratory studies utilizing these two mass spectrometers were mainly performed at three atmospheric simulation chambers, with two at Institute of Meteorology and Climate Research (IMK) of KIT and one at Paul Scherrer Institute (PSI) in Switzerland. In the following, the principal and data analysis procedures of the two abovementioned mass spectrometers as well as the three atmospheric simulation chambers used in my research work will be introduced.

1.4.1 Analytical methods

1.4.1.1 Aerosol mass spectrometer

HR-ToF-AMS (Figure 5; DeCarlo et al., 2006; hereafter AMS) is equipped with a high-pressure aerodynamic lens (Williams et al., 2013) and coupled to a high-resolution time-of-flight (HR-ToF) mass analyzer. It is capable of directly distinguishing the elemental composition of ions having the same nominal mass as a function of particle size (up to 2.5 μm particle aerodynamic diameter d_{va}). A schematic of the AMS by DeCarlo et al. (2006) is shown in Figure 5. The instrument includes several parts: sample introduction system, sizing region, and vaporization and ionization systems. Briefly, ambient air is sampled through a critical orifice into the aerodynamic lens, which focuses particles into a narrow beam. At the exit of the lens, a supersonic expansion accelerates the particles into the sizing region (particle time-of-flight, PToF), where particle size is determined by measuring particle flight time across a fixed distance. After the particles reach the thermal vaporization and ionization region, they are vaporized by impaction on a resistively heated tungsten surface (~600 °C) and ionized by EI. Then the ions travel to the ToF region and are separated based on their *m/z* values before reaching the multichannel plate (MCP) detector. Only non-refractory species are vaporized and detected by AMS. Therefore, it can detect organic species and most nitrate and sulfate salts, but cannot detect crustal material, sea salt, and black carbon (DeCarlo et al., 2006).

With AMS, there are two main pieces of information we can get from it: mass spectra with fragments of non-refractory species in the particle phase, and particle size. Due to fragmentation of organic molecules during the ionization process in the AMS, molecular information of OA cannot be provided. However, it is quantitative and can provide absolute mass concentrations of total OA and inorganic species for data comparison and complementation of instruments that are capable of molecular level analysis, such as the chemical ionization mass spectrometer (CIMS). More information about CIMS are given in section 1.2.2 and 1.4.1.2.

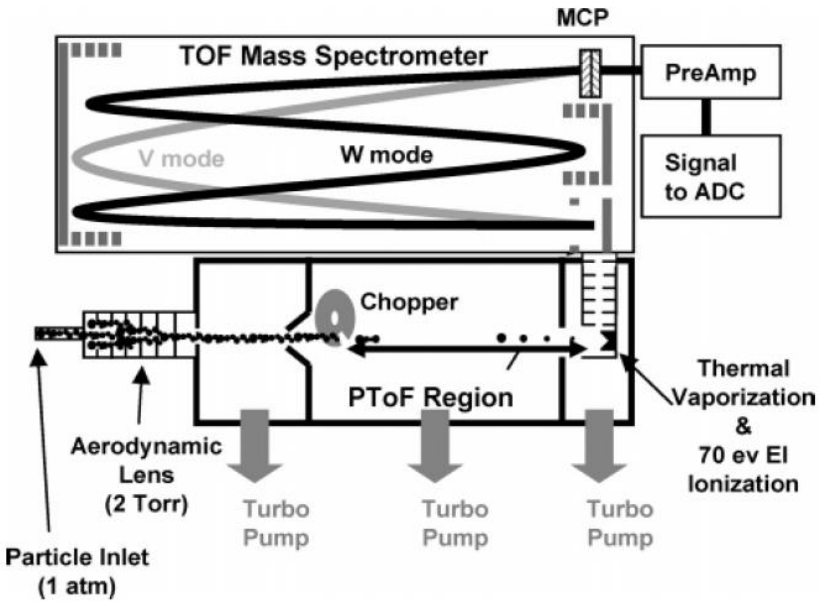

Figure 5. Schematic of the HR-ToF-AMS. Reprinted with the permission from DeCarlo et al. (2006). Copyright © 2006, American Chemical Society.

AMS data collected during my PhD study and discussed in this dissertation was analyzed by me with the AMS data analysis software packages SQUIRREL and PIKA (Canagaratna et al., 2015). Due to the fact that the AMS generates large amounts of data in short amounts of time, SQUIRREL (SeQUential Igor data RetRiEvaL) was developed with a standard user interface for the analysis of large datasets. Its development has been led by the University of Manchester, University of Colorado-Boulder, Max-Plank Institute (Mainz), and Aerodyne Research, Inc. SQUIRREL is an AMS unit resolution analysis software that yields total signals at every nominal mass. Due to the need for the speciation and quantification of HR-ToF-AMS data, PIKA (Peak Integration by Key Analysis) was developed by the Jimenez Group at the University of Colorado, Boulder as a high resolution analysis software for HR-ToF-AMS data. For the HR-ToF-AMS data analysis, I followed the steps listed on the Jimenez Research Group Wiki by the University of Colorado-Boulder (http://cires1.colorado.edu/jimenez-group/wiki/index.php/ToF-AMS_Analysis_Software) and briefly listed here:

a) load the raw data files into SQUIRREL;
b) *m/z* and baseline calibration for *m/z* from 12 until e.g. 210;
c) pre-process the raw data;
d) parameter corrections (e.g., flowrate, airbeam, particle size);
e) generate graphs with unit resolution data, e.g., time series and average mass spectra;

f) generate peak width parameters and peak shape for high resolution fitting in PIKA;

g) high resolution fitting for each nominal mass with several reasonable ions for *m/z* from 12 until e.g. 210 (Figure 6);

h) generate graphs of my choosing with high resolution data.

Within these steps, high resolution fitting, or the so-called peak fitting, is the most time-consuming step. The peak fitting process results in a peak list, which includes the fragment formula and mass of all detected fragment ions. Although PIKA has already listed the possible fragments for each nominal mass, the user needs to select the most reasonable fragment ions (e.g., ions with small fitting error, and the isotope peak needs to be fitted; Figure 6). Without taking into account the computer processing time for each step, the AMS high resolution fitting process alone took me several hours to one day for each experiment/campaign. For the chamber experiments and field measurements discussed in this dissertation, peak lists for AMS data were all created by me. Based on my scientific purposes, I also did further AMS data analysis, e.g., calculating the elemental O:C and hydrogen-to-carbon (H:C) ratios using the EALight_1_06 procedure in PIKA, or utilizing the data matrix analyzed with SQUIRREL/PIKA for source apportionment by positive matrix factorization (PMF; Ulbrich et al., 2009).

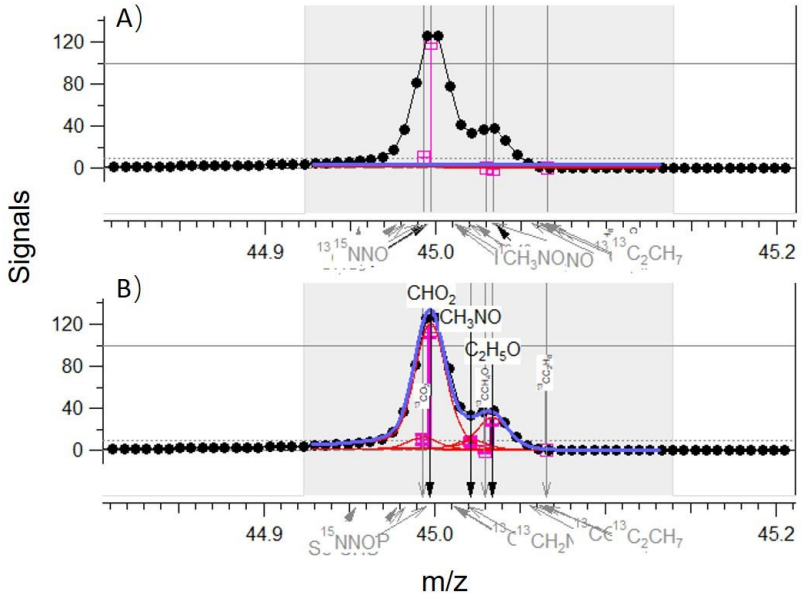

Figure 6. Example of *m/z* 45 before (A) and after (B) high resolution fitting for HR-ToF-AMS data. Gray region: high resolution fitting region; black dotted line: raw data; blue: fits with all selected compounds in the peaklist at this mass; thick red: fits of the baseline; pink: center of the individual ion with error bars; red: Gaussian distribution for the respective ion.

1.4.1.2 Chemical ionization mass spectrometer with a filter inlet for gases and aerosols (FIGAERO)

In recent years, in order to study the dynamic OA system on a molecular level, online instrumentations to analyze both gas- and particle-phase molecular composition in high time resolution have been developed. One of them is the filter inlet for gases and aerosols coupled to high-resolution time-of-flight CIMS (FIGAERO-HR-ToF-CIMS; hereafter FIGAERO-CIMS; Lopez-Hilfiker et al., 2014). The specialty of this instrument is the FIGAERO inlet (Figure 7A) designed by Lopez-Hilfiker et al. (2014). There are two modes for the FIGAERO inlet. During the first mode, compounds in the gas phase are directly measured by the instrument, while the particles are simultaneously collected on a Teflon (Polytetrafluoroethylene, PTFE) filter via a separate sampling port (Figure 7B). After certain time intervals (e.g., 30 min), the instrument can move to the next mode (Figure 7C): the gas phase is bypassed while the particles collected on the Teflon filter are thermally desorbed by a flow of ultra-high-purity (UHP) nitrogen heated from room temperature to 200 °C over the course of e.g. 35 min.

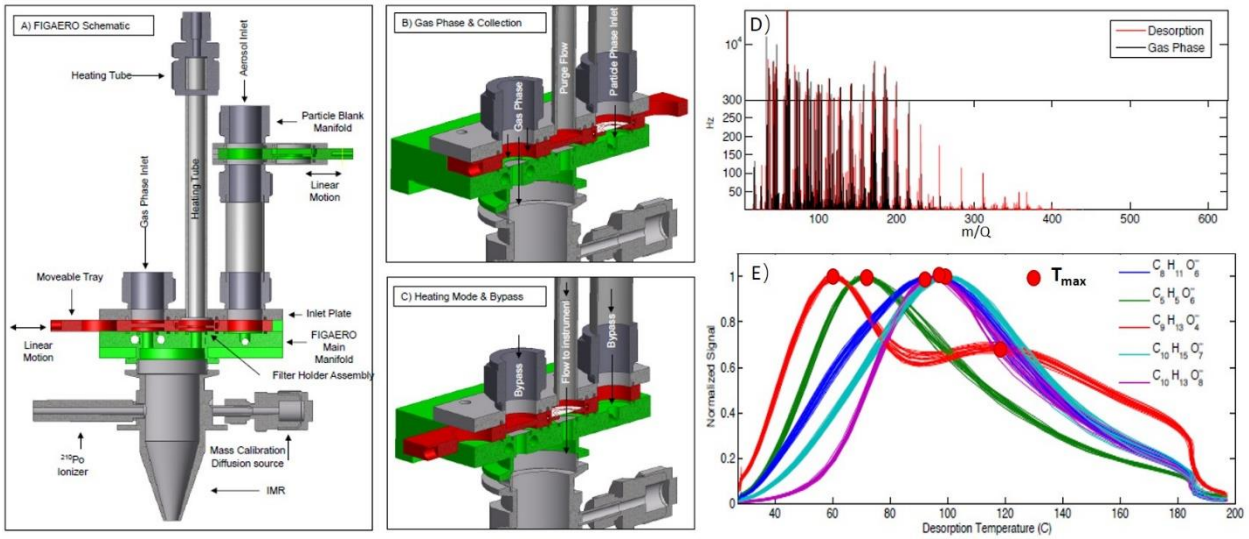

Figure 7. (A) Schematic of FIGAERO inlet; (B) FIGAERO in gas measurement and particle collection mode; (C) FIGAERO in particle analysis mode; (D) a mass spectra example for comparison of gas phase and particle phase; (E) an example of single-mode and multi-mode (in red line) thermograms (Lopez-Hilfiker et al., 2014).

After the compounds reach the ion molecule reaction (IMR) region of the HR-ToF-CIMS (Figure 8), they will react with the reagent ion, I^-, which is formed by flowing UHP nitrogen over a permeation tube with methyliodide (CH_3I) through a radioactive polonium-210 source, and form

the iodide-clustered ions. Then the ions travel to the ToF analyzer region through the small segmented quadruple (SSQ) region, big segmented quadruple (BSQ) region, and primary beam (PB) region, with increasing vacuum conditions (green numbers in Figure 8) in order to focus the ion beam. In the ToF analyzer region, the ions are separated based on their *m/z* values before reaching the MCP detector.

With the FIGAERO-CIMS, there are two main pieces of information we can get from it: mass spectra with molecular information for hundreds to thousands of compounds (organic compounds and inorganic acids) in both gas and particle phases (Figure 7D), and thermograms from the thermal desorptions which can be used to infer the volatility of individual compounds (Figure 7E; Lopez-Hilfiker et al., 2014). For individual compounds, signals that peak at distinct desorption temperatures (T_{max}) are related to their saturation vapor pressure (single-mode thermograms; Lopez-Hilfiker et al., 2015; Mohr et al., 2017) but interference from isomers with different vapor pressures or thermal decomposition of oligomers can lead to more complex multi-mode thermograms (Lopez-Hilfiker et al., 2015). Integration of thermograms of individual compounds yields their total particle-phase signal. Due to its advantages (e.g., capable of providing molecular information of OA for both gas phase and particle phase, highly reproducible, and low detection limit), it has quickly been commercialized by Aerodyne Research Inc., and become popular within the aerosol science community for aerosol research (e.g., Lopez-Hilfiker et al., 2016b; D'Ambro et al., 2017; Mohr et al., 2017; Huang et al., 2018; Huang et al., 2019).

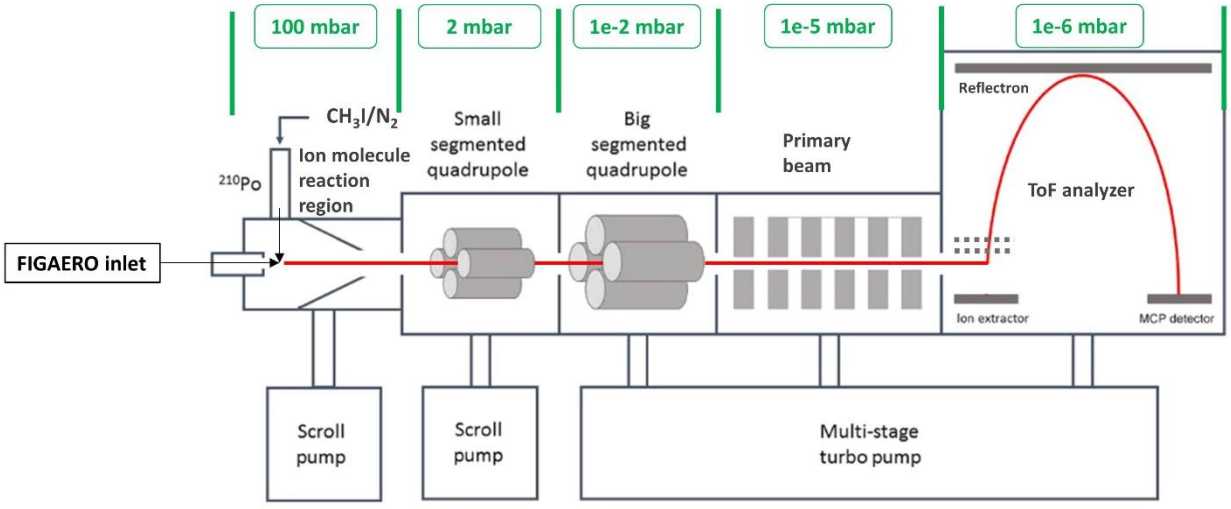

Figure 8. Schematic of HR-ToF-CIMS with a FIGAERO inlet (modified from Sanchez et al., 2016). Green numbers refer to the pressure for each region.

FIGAERO-CIMS data collected during my PhD study and discussed in this dissertation was analyzed by me with Matlab, using the toftools software package developed by the University of Helsinki (Junninen et al., 2010). Similar to AMS data analysis, the data analysis for FIGAERO-CIMS also includes unit resolution and high resolution analysis. Steps performed for FIGAERO-CIMS data are briefly listed below:

a) mass calibration, average the 1 s time resolution of the raw data to e.g. 30 s, and stick integration using the HR_FDL_Laptop.m procedure in toftools;
b) generate graphs for unit resolution time series and mass spectra;
c) generate resolution function (slope and intercept) and peak shape for high resolution fitting;
d) go to GUI (graphical user interface) window and redo mass calibration with several known ions which contain only one single peak, e.g., I^-, $I(H_2O)^-$, $I(CH_2O_2)^-$, $I(HNO_3)^-$, I_2^-, and I_3^-;
e) high resolution fitting for each nominal mass with several reasonable ions for *m/z* from 32 until e.g. 700 (Figure 9);
f) load FIGAERO data, and separate gas and particle phase data;
g) generate graphs for compounds in gas and particle phase with high resolution data.

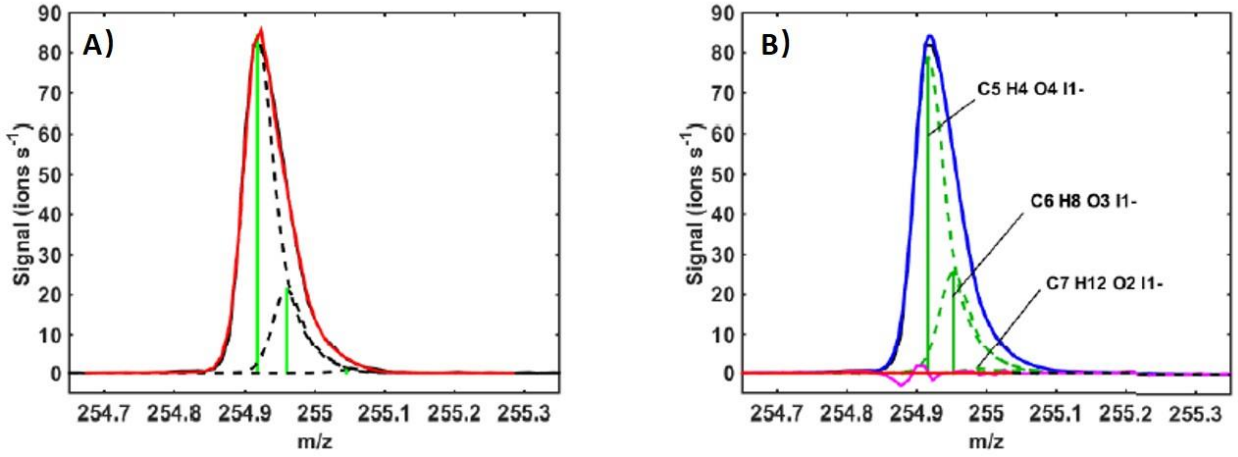

Figure 9. Example of m/z 255 before (A) and after (B) high resolution fitting for CIMS data in GUI window. Black: raw data; red: sum of all fits; blue: fits with all selected compounds in the peaklist at this mass; green solid: centre of the individual ion; green dashed: Gaussian distribution for the respective ion; pink: residual of the signal (Gramlich, 2018).

Similar to AMS data analysis, the most time-consuming process for FIGAERO-CIMS data analysis is also the high resolution fitting, or the so-called peak fitting (Figure 9). The peak fitting

process results in a peak list, which includes the molecular formula and the mass of all detected compounds either clustered with iodide, or deprotonated and without iodide. In order to do the peak fitting, the user has to select the most reasonable ion composition for all the peaks at each nominal mass, based on the suggested molecular compositions for each peak in the GUI. Slightly different from the high resolution fitting for AMS data, the user has more possibilities for the molecular composition since intact molecular ions are detected without hard fragmentation like EI in AMS. Therefore, in addition to the common criteria for peak fitting in AMS such as small fitting error, and the fitted isotope peak, the user also needs to e.g. select compounds with realistic chemical composition (e.g., $C_xH_{y\leq 2x+2}O_{z\leq 2x}$). Besides, due to the highly dynamic evolution of OA and/or different volatilities of each compound, several time points for gas and particle phases need to be considered in order to identify a reasonable amount of molecular ions at each nominal mass. Therefore, the peak fitting process for the entire peak list alone took me several weeks to months for each type of experiment/campaign. For the chamber experiments and field measurements discussed in this dissertation, peak lists for FIGAERO-CIMS data were all created by me. Based on the scientific questions, I also did further FIGAERO-CIMS data analysis, e.g., group different compounds into different categories and discuss their diurnal patterns, or compare the thermograms of different compounds to infer the volatility information and with that the link between molecular composition and physicochemical properties.

1.4.2 Atmospheric simulation chambers

There are three atmospheric simulation chambers in which I have performed the chamber studies: two at IMK of KIT: the Aerosol Interaction and Dynamics in the Atmosphere (AIDA) aerosol and cloud chamber (Figure 10A), and the Aerosol Preparation and Characterization (APC) chamber; and one at PSI: the Simulation Chamber for Atmospheric Chemistry (PSI-SCAC).

The AIDA aerosol and cloud chamber is an 84.3 m^3 sized aluminum vessel that can be operated under a wide range of atmospherically relevant temperatures (183–333 K), pressures (1–1000 hPa), RH (close to 0–200%), and at different warming and cooling rates (Schnaiter et al., 2016; Möhler et al., 2003; Saathoff et al., 2009). A light source has been installed recently in late 2018 on the top of the AIDA chamber to simulate OA photochemical reactions. The combination of its size, temperature range, and comprehensive trace gas, aerosol, and cloud instrumentation (Figure 10A) makes it a unique facility for air pollution, weather, and climate research.

The APC chamber is a 3.7 m^3 sized stainless steel vessel, situated next to AIDA and connected to it by a stainless steel tube (Huang et al., 2018). The APC chamber can only be operated at room temperature (296 K) and it is commonly used to prepare SOA particles in a reproducible manner (Wagner et al., 2017; Huang et al., 2018).

The PSI-SCAC chamber is a 27 m^3 sized Teflon fluorinated ethylene propylene (FEP) bag which is situated in an 80 m^3 sized temperature-controlled wooden enclosure and can be operated at a temperature range of 288–303 K (Paulsen et al., 2005). Xenon arc lamps are installed to simulate the solar light spectrum and to mimic photochemistry in the atmosphere. The walls and ceiling of the enclosure are covered with reflective aluminum foil to maximize the light intensity (Paulsen et al., 2005). The PSI-SCAC chamber is a very useful tool for the investigation of photochemical aging processes of aerosols.

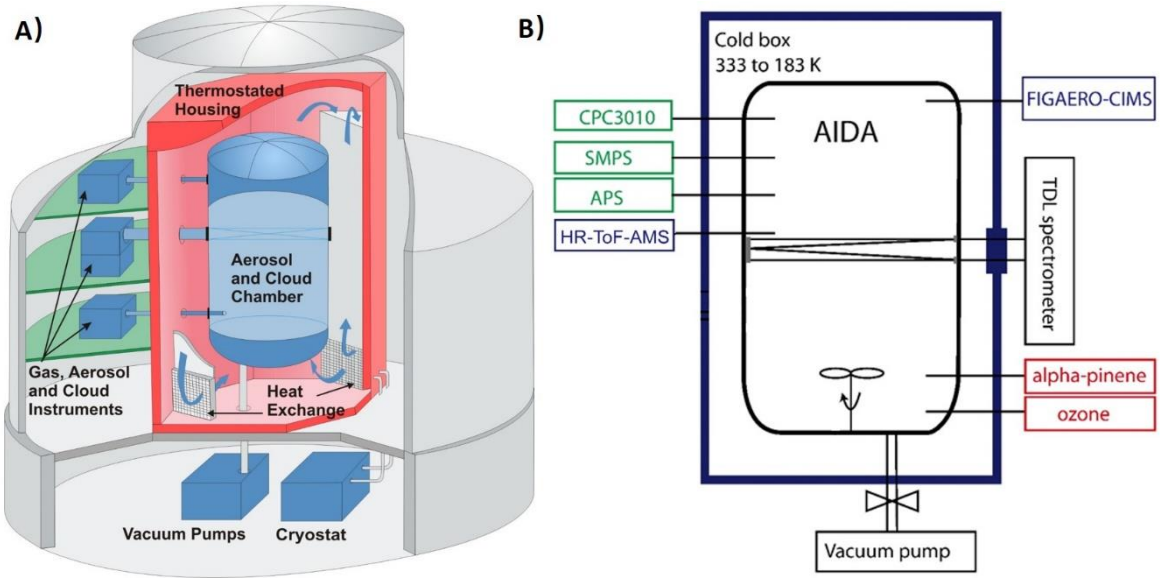

Figure 10. (A) Schematic of AIDA aerosol and cloud chamber (https://www.imk-aaf.kit.edu/73.php); (B) example of instrumental setup during the chamber experiments at AIDA (modified from Wagner et al., 2017; Huang et al., 2018).

1.4.3 Performed research work during the PhD study

Based on my research objectives, I have performed the chemical characterization of SOA from mainly five chamber studies and four field measurements by the deployment of FIGAERO-CIMS and AMS.

Figure 11 summarizes the major chamber studies and field work I have performed during my PhD study. Chamber experiments were performed every year for 1–2 months with different

experimental conditions at the atmospheric simulation chambers of IMK at KIT or of PSI. Field measurements were performed for 1–3 months at different environments (e.g., rural, urban, or mountain sites) in different locations in Germany (e.g., Eggenstein-Leopoldshafen, Stuttgart) and in another country (e.g., Mt. Chacaltaya (5240 m a.s.l.) in Bolivia). All of these measurements falls into my research objectives for the investigation of chemical composition, physicochemical properties, and roles of atmospheric OA at different experimental conditions and in the field. Different chamber studies are complementary with each other for the investigation of atmospheric OA formed at different experimental conditions and can be used for the identification of OA measured in the field.

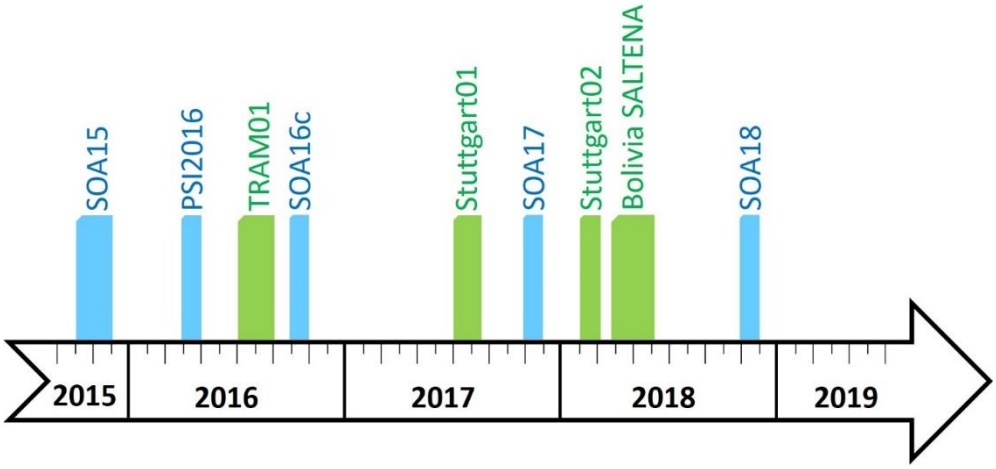

Figure 11. Timeline of the major campaigns I performed during my PhD study from October 2015 to July 2019. Chamber studies are colored in blue and field work are colored in green.

1.4.3.1 Chamber studies

With the chambers available at IMK of KIT and at PSI, I have mainly performed five chamber campaigns (SOA15, PSI2016, SOA16c, SOA17, SOA18; Figure 11) during my PhD study. SOA15 was a two-month measurement campaign performed in October and November 2015, which investigated yields, physical properties, and chemical composition of SOA generated from ozonolysis of only one biogenic precursor, α-pinene, with different precursor concentration, temperature and RH, as well as the SOA ice nucleation abilities. In addition, wall loss experiments were also performed to investigate the reactants' and products' losses to the AIDA chamber wall. PSI2016 was a five-week measurement campaign performed in April and early May 2016 at PSI in Switzerland. The purposes of this campaign were to investigate α-pinene SOA photochemistry, molecular composition by FIGAERO-CIMS, and to do a comparison with a newly developed

instrument (extractive electrospray ionization time-of-flight, EESI-TOF; Lopez-Hilfiker et al., 2019; section Appendix B.2). SOA16c was a three-week measurement campaign performed in November 2016, which aimed at the room-temperature formation and mixing processes of anthropogenic and biogenic SOA as well as the oxidation of levoglucosan with OH radicals. SOA17 was a three-week measurement campaign performed in November 2017. The focus of this campaign was the formation and mixing processes of anthropogenic and biogenic SOA as a function of temperature and RH so to help interpret the field data I obtained (section 1.4.3.2). SOA18 was a four-week measurement campaign performed in November 2018, which investigated the photochemical aging of anthropogenic and biogenic SOA after the installation of a light source in the AIDA chamber in 2018.

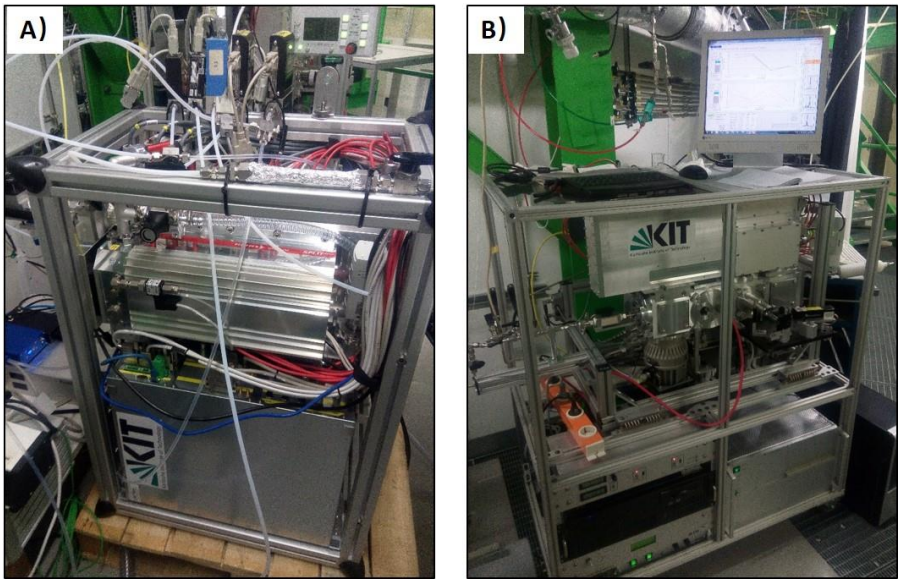

Figure 12. (A) FIGAERO-CIMS and (B) AMS connected to AIDA chamber. Photo: W. Huang, 11.2015.

During all of the five chamber campaigns, both FIGAERO-CIMS and AMS were used for the chemical characterization of SOA (Figure 10B and Figure 12). I was responsible for the AMS operation and calibrations (except for PSI2016), and FIGAERO-CIMS setup, operation and calibrations, as well as the AMS and FIGAERO-CIMS data analysis and/or interpretation. For the collected wall loss experiment samples, I was responsible to set up the experimental device to concentrate and pretreat the samples, and then analyze them with the FIGAERO-CIMS.

Besides, our FIGAERO-CIMS was also shipped to the University of Eastern Finland for a four-week laboratory campaign there in September 2016 (Kuopio2016 campaign). Although I

didn't participate in this campaign, I was involved in the FIGAERO-CIMS data analysis and interpretation.

Part of the SOA15 results have already been published by me in *Atmospheric Chemistry and Physics* (section 2 and Appendix A.1 of this dissertation). Some other aspects of the SOA15 results have also been published with me as a co-author in *Journal of Geophysical Research-Atmospheres* (Wagner et al., 2017; section Appendix B.1). Part of the PSI2016 and Kuopio2016 results are submitted to *Atmospheric Measurement Techniques* (Lopez-Hilfiker et al., 2019; section Appendix B.2) and *Science Advances* (Pospisilova et al., 2019), and published in *Atmospheric Chemistry and Physics* (Buchholz et al., 2019; section Appendix B.3), respectively, with me as a co-author. Part of the SOA16c, SOA17 results are involved in three of my co-authored research papers, with two published in *Atmospheric Measurement Techniques* (Shen et al., 2018; 2019b; section Appendix B.4 and B.5) and one under review in *Atmospheric Chemistry and Physics* (Shen et al., 2019a; section Appendix B.6). Data analysis for these campaigns as well as the SOA18 campaign is still ongoing.

1.4.3.2 Field measurements

During my PhD study, I have mainly performed four field campaigns in three different locations (Figure 11), three times in Germany (Eggenstein-Leopoldshafen and Stuttgart; Figure 13) and once in another country (Mt. Chacaltaya (5240 m a.s.l.) in Bolivia; Figure 14). Organic compounds identified from the chamber studies can be used in the interpretation of the ambient OA measured in these measurement sites. Field work performed at these three measurement sites represent atmospheric OA at rural, urban, or remote mountain sites. Therefore, by identifying and quantifying the organic compounds measured at different locations, a better understanding of atmospheric OA lifetime, fate, and climate effects can be achieved.

I participated in a field campaign in a rural site near Frankfurter street in Eggenstein-Leopoldshafen, Germany (TRAM01) from July 8th to September 1st, 2016 (Figure 13A). The research objective of this campaign was to study rural aerosols, with a focus on influences from nearby industrial emissions. In addition to particle and trace gas measurements, FIGAERO-CIMS and AMS were used for the atmospheric SOA characterization. I was responsible for the AMS operation and calibrations, and FIGAERO-CIMS setup, operation and calibrations, as well as the AMS and FIGAERO-CIMS data analysis and/or interpretation. Part of the TRAM01 results have already been published by me in *Environmental Science & Technology* (section 3 and Appendix

A.2 of this dissertation). Some other aspects of the TRAM01 results are included in three research papers with me as a co-author, with two already published in *Atmospheric Measurement Techniques* (Shen et al., 2018; 2019b; section Appendix B.4 and B.5) and one under review in *Atmospheric Chemistry and Physics* (Shen et al., 2019a; section Appendix B.6).

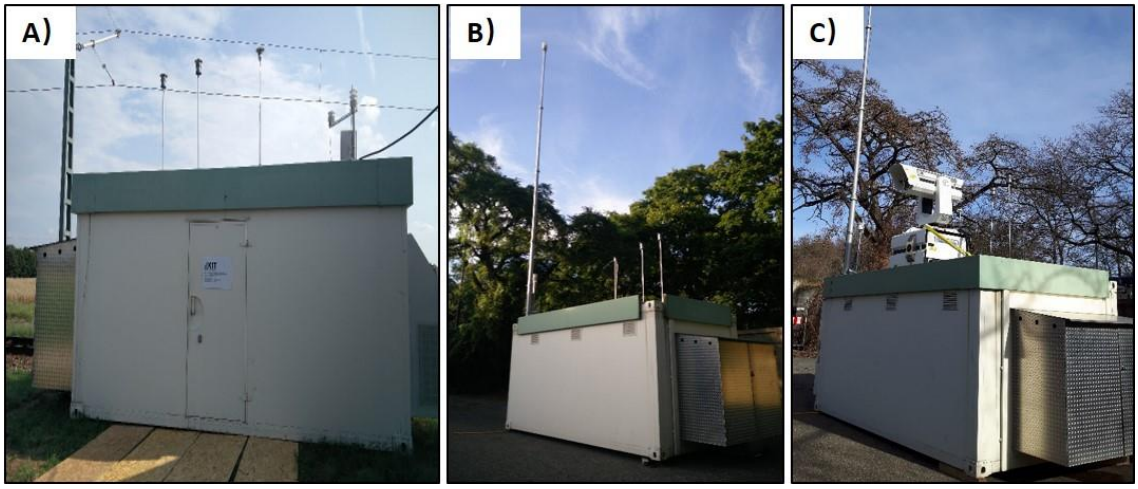

Figure 13. Measurement container during (A) TRAM01 (Photo: W. Huang, 07.2016), (B) Stuttgart01 (Photo: W. Huang, 07.2017), and (C) Stuttgart02 (Photo: X. Shen, 03.2018).

I also participated in two field campaigns in an urban background site in Schloßgarten, Stuttgart, Germany (Stuttgart01 and Stuttgart02), with one in summer (from July 5th to August 17th, 2017; Figure 13B) and the other one in winter (from February 5th to March 5th, 2018; Figure 13C). The research objective of these field campaigns was to study urban aerosols in Stuttgart in different seasons, validate new models for the evolution of urban aerosols and provide air quality predictions necessary for effective abatement activities by city administrators. In addition to the trace gas and AMS measurements, aerosol particles were collected on filters and analyzed with FIGAERO-CIMS in the laboratory. Besides, a LIght Detection and RAnging (LIDAR; on the top of the measurement container in Figure 13C) was also deployed in winter to obtain the planetary boundary layer (PBL) information. I was responsible for the AMS operation and calibrations, and FIGAERO-CIMS setup, operation and calibrations, as well as the AMS and FIGAERO-CIMS data analysis and/or interpretation. For the filter samples collected during the Stuttgart01 and Stuttgart02 campaigns, I was responsible for the filter sampling and analysis with FIGAERO-CIMS in the laboratory. Part of the Stuttgart01 and Stuttgart02 results have already been written by me in a manuscript and currently under review in *Atmospheric Chemistry and Physics* (section 4 of this dissertation).

Figure 14. Global Atmosphere Watch (GAW) high-altitude research station Chacaltaya (5240 m), La Paz, Bolivia, showing dramatic weather changes in one day. Photo: W. Huang, 03.2018.

I also participated in a field campaign (Southern hemisphere high ALTitude Experiment on particle Nucleation And growth; SALTENA), at the GAW (Global Atmosphere Watch) high-altitude research station Chacaltaya (5240 m) close to La Paz in Bolivia, from March 25th to June 5th, 2018 (Figure 14). This campaign was led by University of Helsinki and Stockholm University as well as in close collaboration with the Universidad Mayor de San Andres, La Paz. It aimed at understanding new particle formation (NPF) and growth and their implications for climate at this high altitude, as well as the effects of different emissions (from e.g. Amazon basin, La Paz city, the Pacific Ocean) and processes on air quality and climate there. A lot of instruments (including FIGAERO-CIMS from our institute, other CIMS and aerosol chemical speciation monitor (ACSM, similar to AMS) from many other institutions) were transported to Bolivia for the measurement there. We can therefore compare the data from different instruments and derive a more complete picture about the aerosols there. In addition to the online measurement with FIGAERO-CIMS on GAW station, aerosol particles were also collected on filters inside the La Paz city and analyzed with FIGAERO-CIMS in the laboratory for data comparison. Due to GAW station is one of the few monitoring sites of Essential Climate Variables (meteorological variables, aerosols and greenhouse gases) in the Southern Hemisphere, this dataset contributes to deepen our understanding of ambient SOA formation and evolution from different sources at this high altitude in the Southern Hemisphere. I was responsible for FIGAERO-CIMS setup, operation and calibrations, as well as the FIGAERO-CIMS data analysis and/or interpretation. I was also responsible for taking filter samples inside the La Paz city in Bolivia. Data analysis for the Bolivia

SALTENA campaign is still ongoing and only preliminary results are included in this dissertation. It would be of great interest to compare the OA measured in Germany (Northern Hemisphere) to OA measured in Bolivia (Southern Hemisphere).

2 α-Pinene secondary organic aerosol at low temperature

Publication title: α-Pinene secondary organic aerosol at low temperature: chemical composition and implications for particle viscosity

Authors: Wei Huang, Harald Saathoff, Aki Pajunoja, Xiaoli Shen, Karl-Heinz Naumann, Robert Wagner, Annele Virtanen, Thomas Leisner, and Claudia Mohr

In: Atmospheric Chemistry and Physics, 18, 2883–2898, 2018. DOI: 10.5194/acp-18-2883-2018.

Authorship statement

This peer-reviewed scientific journal article was written by me and is based on the chamber data from a two-month measurement campaign (SOA15) in October and November 2015 at simulation chambers at KIT, with a focus on the chemical composition and physicochemical properties of SOA from α-pinene ozonolysis with different precursor concentration, temperature, and RH. I was responsible for the setup, operation and calibrations of FIGAERO-CIMS and AMS, data analysis, interpretation, and the writing of this article.

The full article is reprinted from Copernicus Publications for the European Geosciences Union below and in Appendix A.1 (supplement).

This article is a highly cited paper on Web of Science (cited 10 times till the end of April 2019).

Atmos. Chem. Phys., 18, 2883–2898, 2018
https://doi.org/10.5194/acp-18-2883-2018

Atmospheric Chemistry and Physics Open Access EGU

α-Pinene secondary organic aerosol at low temperature: chemical composition and implications for particle viscosity

Wei Huang[1,2], Harald Saathoff[1], Aki Pajunoja[3], Xiaoli Shen[1,2], Karl-Heinz Naumann[1], Robert Wagner[1], Annele Virtanen[3], Thomas Leisner[1], and Claudia Mohr[1,4]

[1]Institute of Meteorology and Climate Research, Karlsruhe Institute of Technology, 76344 Eggenstein-Leopoldshafen, Germany
[2]Institute of Geography and Geoecology, Karlsruhe Institute of Technology, 76131 Karlsruhe, Germany
[3]Department of Applied Physics, University of Eastern Finland, Kuopio, 80101, Finland
[4]Department of Environmental Science and Analytical Chemistry, Stockholm University, Stockholm, 11418, Sweden

Correspondence: Claudia Mohr (claudia.mohr@aces.su.se)

Received: 23 August 2017 – Discussion started: 4 September 2017
Revised: 5 January 2018 – Accepted: 29 January 2018 – Published: 28 February 2018

Abstract. Chemical composition, size distributions, and degree of oligomerization of secondary organic aerosol (SOA) from α-pinene ($C_{10}H_{16}$) ozonolysis were investigated for low-temperature conditions (223 K). Two types of experiments were performed using two simulation chambers at the Karlsruhe Institute of Technology: the Aerosol Preparation and Characterization (APC) chamber, and the Aerosol Interaction and Dynamics in the Atmosphere (AIDA) chamber. Experiment type 1 simulated SOA formation at upper tropospheric conditions: SOA was generated in the AIDA chamber directly at 223 K at 61 % relative humidity (RH; experiment termed "cold humid", CH) and for comparison at 6 % RH (experiment termed "cold dry", CD) conditions. Experiment type 2 simulated SOA uplifting: SOA was formed in the APC chamber at room temperature (296 K) and < 1 % RH (experiment termed "warm dry", WD) or 21 % RH (experiment termed "warm humid", WH) conditions, and then partially transferred to the AIDA chamber kept at 223 K, and 61 % RH (WDtoCH) or 30 % RH (WHtoCH), respectively. Precursor concentrations varied between 0.7 and 2.2 ppm α-pinene, and between 2.3 and 1.8 ppm ozone for type 1 and type 2 experiments, respectively. Among other instrumentation, a chemical ionization mass spectrometer (CIMS) coupled to a filter inlet for gases and aerosols (FIGAERO), deploying I^- as reagent ion, was used for SOA chemical composition analysis.

For type 1 experiments with lower α-pinene concentrations and cold SOA formation temperature (223 K), smaller particles of 100–300 nm vacuum aerodynamic diameter (d_{va}) and higher mass fractions (> 40 %) of adducts (molecules with more than 10 carbon atoms) of α-pinene oxidation products were observed. For type 2 experiments with higher α-pinene concentrations and warm SOA formation temperature (296 K), larger particles (∼ 500 nm d_{va}) with smaller mass fractions of adducts (< 35 %) were produced.

We also observed differences (up to 20 °C) in maximum desorption temperature (T_{max}) of individual compounds desorbing from the particles deposited on the FIGAERO Teflon filter for different experiments, indicating that T_{max} is not purely a function of a compound's vapor pressure or volatility, but is also influenced by diffusion limitations within the particles (particle viscosity), interactions between particles deposited on the filter (particle matrix), and/or particle mass on the filter. Highest T_{max} were observed for SOA under dry conditions and with higher adduct mass fraction; lowest T_{max} were observed for SOA under humid conditions and with lower adduct mass fraction. The observations indicate that particle viscosity may be influenced by intra- and inter-molecular hydrogen bonding between oligomers, and particle water uptake, even under such low-temperature conditions.

Published by Copernicus Publications on behalf of the European Geosciences Union.

Our results suggest that particle physicochemical properties such as viscosity and oligomer content mutually influence each other, and that variation in T_{max} of particle desorptions may have implications for particle viscosity and particle matrix effects. The differences in particle physicochemical properties observed between our different experiments demonstrate the importance of taking experimental conditions into consideration when interpreting data from laboratory studies or using them as input in climate models.

1 Introduction

Atmospheric aerosols have adverse impacts on human health (Nel, 2005; Rückerl et al., 2011) and rank among the main drivers of anthropogenic climate change (IPCC, 2013). Organic compounds make up a large fraction (20–90 %) of submicron particulate mass (Zhang et al., 2007; Murphy et al., 2006; Jimenez et al., 2009; Ehn et al., 2014). Organic aerosol (OA) particles can be directly emitted into the atmosphere from sources such as fossil fuel combustion and forest fires (primary organic aerosol, POA), or be formed in the atmosphere from the oxidation of gas-phase precursors (secondary organic aerosol, SOA). Secondary organic aerosol dominates the global budget of OA (Shrivastava et al., 2015), and its gaseous precursors (volatile organic compounds, VOCs) can be of both biogenic and anthropogenic origin. In the atmosphere, VOCs are oxidized by the hydroxyl radical (OH), ozone (O_3), or the nitrate radical (NO_3) into semi-volatile, low-volatility, and/or extremely low-volatility organic compounds (SVOC, LVOC/ELVOC), which can partition into the particle phase and lead to the formation of SOA (Jimenez et al., 2009; Hallquist et al., 2009; Jokinen et al., 2015; Ehn et al., 2014). Due to the wealth of precursors and formation mechanisms in both the gas and particle phase, SOA is very complex and can contain thousands of compounds with a wide range of functionalities, volatilities, and other physicochemical properties (Hallquist et al., 2009; Nozière et al., 2015).

Global estimates indicate that biogenic VOC emissions ($539\,Tg\,C\,a^{-1}$) dominate over anthropogenic VOC emissions ($16\,Tg\,C\,a^{-1}$), and that the global SOA production from biogenic VOCs ($22.9\,Tg\,C\,a^{-1}$) outpaces that from anthropogenic VOCs ($1.4\,Tg\,C\,a^{-1}$) as well (Heald et al., 2008). An important class of biogenic VOCs is monoterpenes ($C_{10}H_{16}$), emitted in substantial amounts ($43\,Tg\,C\,a^{-1}$; Heald et al., 2008) by vegetation (e.g., many coniferous trees, notably pine). One of the most abundant monoterpenes is α-pinene (24.8 % mass contribution to global monoterpenes emissions; Kanakidou et al., 2005). Secondary organic aerosol from monoterpenes is very important in the boreal regions in summertime, and the fraction of total SOA mass from monoterpene oxidation products is estimated to be ∼ 15 % globally (Heald et al., 2008).

SOA formation from α-pinene has been studied extensively in smog chambers (e.g., Kristensen et al., 2016; Denjean et al., 2015; McVay et al., 2016), although studies covering a wide temperature range are rare (Saathoff et al., 2009; Donahue et al., 2012). The reactions of α-pinene with O_3 as well as radicals OH and NO_3 lead to a large suite of oxygenated reaction products including aldehydes, oxyaldehydes, carboxylic acids, oxy-carboxylic acids, hydroxycarboxylic acids, dicarboxylic acids, organic nitrates, etc. (Winterhalter et al., 2003; Kanakidou et al., 2005). Aerosol yields vary for the different oxidants, and the most important process with regard to aerosol mass formation from the oxidation of α-pinene is the reaction with O_3 (Kanakidou et al., 2005).

The molecular formulae of organic species accounting for ∼ 58–72 % of SOA mass from α-pinene ozonolysis have been identified, and can largely be grouped into monomers ($C_{8-10}H_{12-16}O_{3-6}$, oxidation products from one α-pinene molecule) and dimers ($C_{14-19}H_{24-28}O_{5-9}$, oxidation products from two α-pinene molecules; Zhang et al., 2015). Major dimers of the α-pinene SOA system have been structurally elucidated as a *cis*-pinyl-diaterpenyl ester ($C_{17}H_{26}O_8$; MW 358; Yasmeen et al., 2010) and a *cis*-pinyl-hydroxypinonyl ester ($C_{19}H_{28}O_7$; MW 368; Müller et al., 2008). Autoxidation processes can form highly oxidized molecules (HOM; elemental oxygen-to-carbon ratios of 0.7–1.3; Ehn et al., 2012), monomers and dimers, which have been shown to play an important role in atmospheric new particle formation (Ehn et al., 2014). Less oxygenated dimers (e.g., esters and other accretion products), some of which have similarly low volatility as HOM, and for many of which formation mechanisms are still not known, are major products in aerosol particles from α-pinene ozonolysis, and have been proposed to be key components in organic particle growth in field and laboratory (Kristensen et al., 2014, 2016; Tröstl et al., 2016; Zhang et al., 2015; Mohr et al., 2017).

SOA is highly dynamic and continually evolves in the atmosphere, becoming increasingly oxidized, less volatile, and more hygroscopic (Jimenez et al., 2009). As a consequence, SOA residence time in the atmosphere at different temperature (T) and relative humidity (RH) conditions strongly influences the particles' physicochemical properties such as phase state, and thus their effects on air quality and climate (Tsigaridis et al., 2006; Jimenez et al., 2009; Shiraiwa et al., 2017). Biogenic SOA has been shown to exist in phase states ranging from liquid to amorphous (semi-)solid in the atmosphere (Virtanen et al., 2010; Bateman et al., 2016; Shiraiwa et al., 2017). The phase state can affect gas uptake, gas–particle partitioning, diffusion, the particles' ability to act as cloud condensation nuclei (CCN) and/or ice nuclei (IN), and the particles' lifetime in the atmosphere (Shiraiwa et al., 2011; Price et al., 2015; Lienhard et al., 2015). Water diffusion coefficients in the water-soluble fraction of α-pinene SOA were measured for temperatures between 240 and 280 K. The results showed that water diffusion slowed

down as temperature decreased, indicating increasing viscosity of SOA particles (Price et al., 2015). Diffusivity of organic molecules in SOA particles can show similar behavior, leading to large equilibration times under dry conditions (Shiraiwa et al., 2011) and/or cool conditions (Bastelberger et al., 2017). Observations of particle shape transformations (Järvinen et al., 2016), coalescence times (Pajunoja et al., 2014), and the particle bounce factor (BF; Virtanen et al., 2010; Pajunoja et al., 2015) are other parameters used to indicate the phase state and viscosity of particles. At dry conditions and at temperatures close to room temperature, the viscosity of α-pinene SOA is assumed to range from 10^5 to (higher than) 10^8 Pa s (Song et al., 2016; Renbaum-Wolff et al., 2013; Pajunoja et al., 2014), which corresponds to a semisolid state (Shiraiwa et al., 2011), whereas at an RH of about 90 % and room temperature its consistency is comparable to that of honey ($\sim$ 10 Pa s: Renbaum-Wolff et al., 2013). Generally, SOA is more viscous in cool and dry conditions (shown, e.g., for α-pinene SOA at temperatures ranging from 235 to 295 K and RH ranging from 35 to 90 %; Song et al., 2016; Järvinen et al., 2016; Shiraiwa et al., 2011; Wang et al., 2015; Kidd et al., 2014).

Differences in α-pinene SOA chemical composition were observed for different SOA formation temperatures and RH conditions, such as lower oligomer content at higher RH (up to 87 %, Kidd et al., 2014) or lower temperature (285 K, Zhang et al., 2015). Given that the differences in physicochemical properties of SOA particles observed as a function of temperature and RH only cover part of the range of atmospheric values, it is of great importance for our understanding of SOA climate effects to expand the investigation of SOA evolution to atmospherically relevant conditions, especially at low temperature. More knowledge on SOA at temperature and RH conditions that are representative of the upper troposphere, where SOA particles can be transported to or formed in situ, is required in order to understand their potential importance for phase state, morphology, chemical composition, and thus ultimately SOA cloud formation potential (Zhang et al., 2015; Virtanen et al., 2010; Lienhard et al., 2015; Frege et al., 2018). However, such studies, particularly of SOA at low temperature, are still scarce.

In the present work, we investigate the chemical composition, size distributions, and degree of oligomerization of α-pinene SOA formed at four different conditions corresponding to temperatures of 223 and 296 K and RH between < 1 and 61 % in order to simulate SOA uplifting to and SOA formation in the upper troposphere. Samples for chemical ionization mass spectrometric analysis were taken from the Aerosol Interaction and Dynamics in the Atmosphere (AIDA) chamber at 223 K and collected on Teflon filters at two different times after starting the experiments. We discuss differences in these mass spectra and corresponding molecular desorption profiles when heating the filters from room temperature to 200 °C as well as possible implications for mutual interactions between particle chemical composition and viscosity.

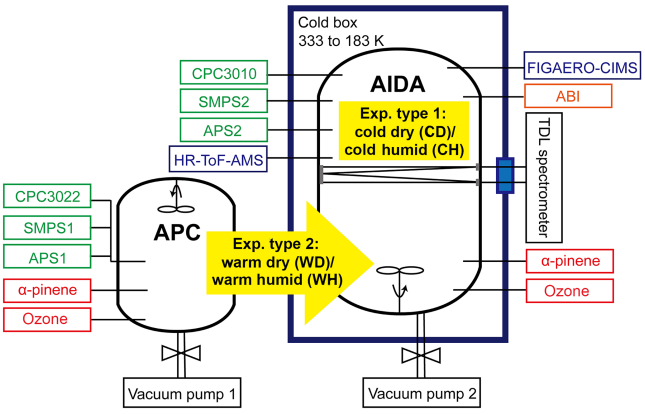

Figure 1. Simple schematic and conditions for the two types of experiments (modified from Wagner et al., 2017). Both chambers at IMK (APC and AIDA) were used in this study. Instruments are annotated in green, blue, and orange, and precursor gases in red. More detailed information on the instruments and precursor gases are explained in the text.

2 Methodology

2.1 Environmental chambers and experimental design

The data for this study were acquired during a 2-month measurement campaign (SOA15) in October and November 2015 at environmental chambers of the Institute of Meteorology and Climate Research (IMK) at the Karlsruhe Institute of Technology (KIT). The measurement campaign investigated yields, physical properties, and chemical composition of SOA from α-pinene ozonolysis as a function of precursor concentration, temperature, RH, and the ice nucleation abilities of the SOA particles (Wagner et al., 2017). The focus on ice cloud formation allowed for the investigation of the particles' physicochemical properties at temperatures as low as 223 K (representative of conditions in the upper troposphere at 8–12 km altitude at the mid-latitudes), a range where detailed characterization is largely missing. Here, we discuss a subset (Table 1) of the large dataset of the SOA15 campaign that is based on experiments investigating the influence and mutual interaction of particle chemical composition and viscosity shortly after SOA formation and after a residence time of $\sim$ 3.5 h. Particles were formed at different temperatures (223–296 K) and RH (< 1–61 %) conditions using both environmental chambers available at IMK (see Fig. 1).

The AIDA (Aerosol Interaction and Dynamics in the Atmosphere) aerosol and cloud chamber is an 84.3 m^3 sized aluminum vessel. It can be operated in the temperature range of 183 to 333 K, pressure range of 1 to 1000 hPa, RH from close to 0 to 200 %, and at different warming and cooling

Table 1. Experimental conditions and precursor concentrations for the four experiments discussed in this study: CH and CD (type 1); WDtoCH and WHtoCH (type 2). Total organic mass (Total org.), CHOI mass concentrations, and elemental oxygen to carbon (O : C) ratios are given for $t0$ and $t1$. RH values (with respect to water) from the APC chamber were measured at room temperature (296 K).

Exp. name	SOA position	T (K)	RH (%)	α-Pinene added (ppm)	O_3 added (ppm)	Total org. ($\mu g\,m^{-3}$)	Total CHOI ($\mu g\,m^{-3}$)	O : C
CH	AIDA	223	61.0	0.714	2.3	67.5/319.5	97.8/247.6	0.26/0.30
CD	AIDA	223	6.0	0.714	2.3	260.1/440.1	110.6/160.4	0.28/0.29
WDtoCH	APC → AIDA	296 → 223	< 1 → 60.6	2.2	1.8	50.9/48.5	40.7/39.3	0.34/0.34
WHtoCH	APC → AIDA	296 → 223	21 → 30.3	2.2	1.8	64.2/58.4	23.4/23.3	0.36/0.37

rates (Schnaiter et al., 2016; Möhler et al., 2003; Saathoff et al., 2009).

The APC (Aerosol Preparation and Characterization) chamber (Möhler et al., 2008) is a 3.7 m^3 sized stainless steel vessel, situated at a distance of 3 m from AIDA and connected to it with a 7 m stainless steel tube of 24 mm inner diameter. The APC chamber can only be operated at room temperature (296 K) and was used to prepare SOA particles in a reproducible manner (Wagner et al., 2017).

We present two types of chamber experiments (Fig. 1): for the first type, SOA from α-pinene ozonolysis was directly formed at 223 K in the AIDA chamber. For the second type, SOA was first produced in the APC chamber kept at room temperature and then transferred to the AIDA chamber kept at 223 K. The second type of experiment thus represents a simplified simulation of particle formation in the boundary layer and subsequent uplifting of particles to higher altitudes with lower temperature conditions. We stress here that for both types of experiments, the particles were sampled from the cold AIDA chamber for chemical analysis. The detailed conditions for these two types of experiments are listed in Table 1. During the first type of chamber experiment, SOA was formed by reaction of an excess of O_3 (initially 2.3 ppm generated by silent discharge in pure oxygen, Semozon 030.2 discharge generator, Sorbios GmbH) with α-pinene (initially 0.714 ppm, 99 %, Aldrich) in the dark AIDA chamber at 223 K at 61 % RH (experiment termed "cold humid", CH) or 6 % RH (experiment termed "cold dry", CD) conditions. For the second type of chamber experiment, SOA was first formed with an excess of O_3 (initially 1.8 ppm) and 2.2 ppm α-pinene in the dark APC chamber at room temperature (296 K), < 1 % RH (experiment termed "warm dry", WD) or 21 % RH (experiment termed "warm humid", WH) conditions. After a residence time of 1–1.5 h in the APC chamber, its pressure was increased by 5 hPa compared to AIDA, and a fraction of the SOA particles was then transferred to the dark AIDA chamber kept at 223 K at 61 % RH (WDtoCH) or 30 % RH (WHtoCH), respectively, resulting in particle number concentrations ranging between 1500 and 2200 cm^{-3} in the AIDA chamber. No OH scavenger was used during SOA formation, and RH was kept constant in AIDA during the course of the experiments. The time series of total particle mass for experiment type 1 (particles formed in situ in AIDA, CH) and experiment type 2 (aerosols formed in APC and transferred to AIDA, WDtoCH) are shown in Fig. 2. The times $t0$ (right after SOA formation in CD and CH, or SOA transfer in WDtoCH and WHtoCH) and $t1$ (∼ 3.5 h later) indicate the points in experiment time which were used for the investigation of the physicochemical evolution of α-pinene SOA.

2.2 Temperature and relative humidity measurements

Temperature (T) in the AIDA chamber was measured by in-house thermocouples (NiCrNi) and in-house PT 100 temperature sensors with an accuracy of ±3 %, which are regularly calibrated with reference sensors traceable to standards of the National Institute of Standards and Technology (NIST). Under static conditions, gas temperature in the AIDA chamber deviated by less than 0.3 K in time and in space. Water vapor concentrations in the AIDA chamber were measured by a in-house tunable diode laser (TDL) spectrometer with an accuracy of ±5 % (Fahey et al., 2014; Skrotzki et al., 2013) and by a dew point mirror hygrometer (MBW373LX, MBW Calibration Ltd.) with an accuracy of ±1 % traceable to different national metrology standards including Federal Institution of Physical Technology (PTB), National Physical Laboratory (NPL), Federal Office of Metrology and Surveying (BEV) and NIST. Both instruments agree within ±2 %. RH in the AIDA chamber was calculated using the measured water vapor concentrations and temperature based on the saturation water vapor pressures given by Murphy and Koop (2005), resulting in an accuracy of ±5 %.

2.3 Particle and gas measurements

Number concentrations of SOA particles formed in APC or AIDA were recorded with two condensation particle counters (CPC3022, CPC3010; TSI Inc.) outside the temperature-controlled housing of the chambers via stainless steel tubes extending 35 cm into the AIDA chamber. The absolute uncertainty of the number concentrations is estimated to be ±20 % by comparison of the different CPCs with each other and with an electrometer (3068, TSI Inc.). Particle size distributions were sampled in the same way from both cham-

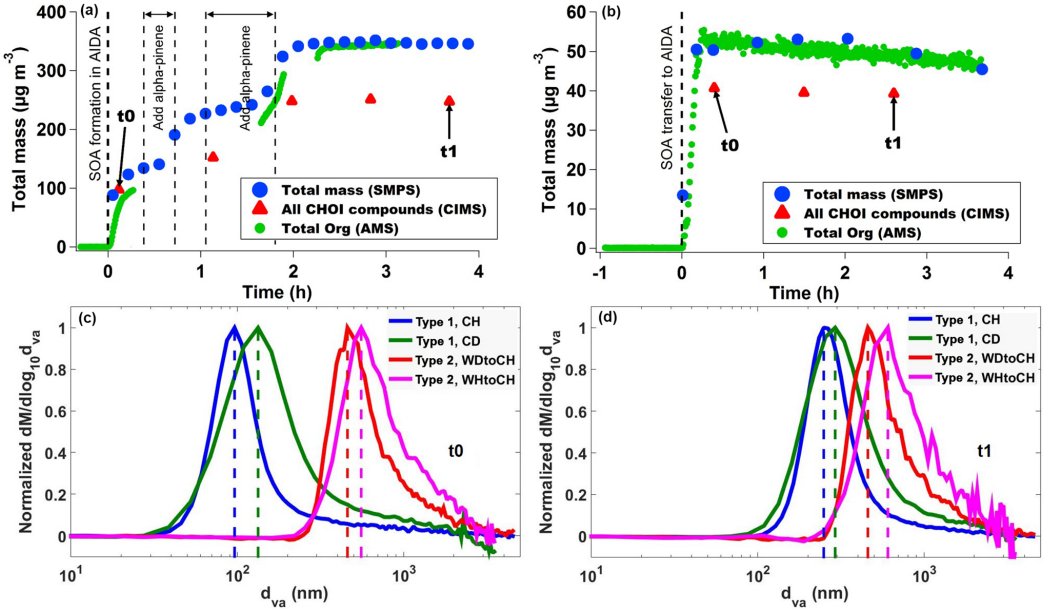

Figure 2. (a) Particle mass concentrations derived from SMPS size distributions (blue circles), CHOI mass concentrations measured by CIMS (red triangles), and organic mass concentrations measured by AMS (green circles) representative of type 1 experiments (here CH), **(b)** representative of type 2 experiments (here WDtoCH). Data were not wall-loss-corrected. $t0$ and $t1$ indicate points in time used for comparisons in this study. Averaged size distributions measured by AMS at $t0$ **(c)** and **(d)** $t1$ for the four experiments.

bers with scanning mobility particle sizers (SMPS; differential mobility analyzer (DMA) 3071 connected to a CPC 3010, TSI Inc.). Mass concentrations were derived from integrated number size distributions and their conversions to mass using their corresponding calculated particle density (1.3–1.5 kg m^{-3}). Particle densities were calculated using the ratio of vacuum aerodynamic diameter (d_{va}) measured by a high-resolution time-of-flight aerosol mass spectrometer (HR-ToF-AMS, hereafter AMS; Aerodyne Research Inc.) and mobility diameter (d_m) measured by the SMPS, assuming particle sphericity (shape factor = 1). O_3 concentrations were measured by an O_3 monitor (O_3 41M, Environment S.A.). The AMS was connected to the AIDA chamber by a stainless steel tube of 1.35 m length (flow rate 0.1 L min^{-1}, residence time 1.6 s). It was equipped with a high-pressure lens (HPL; Williams et al., 2013) and continuously measured total organic particle mass as a function of size (up to 2.5 µm particle d_{va}) at a time resolution of 0.5 min. Elemental oxygen-to-carbon (O : C) and hydrogen-to-carbon (H : C) ratios were derived using the EALight_1_06 procedure in the AMS data analysis software package SQUIRREL (version 1.57H; Canagaratna et al., 2015). An AMS collection efficiency (CE) of 0.4–0.5 was used, except for the CH experiment where CE was 0.7, likely due to higher particle water content (Middlebrook et al., 2012). AMS mass concentrations compare well with the total mass derived from SMPS (slopes are between 0.87 and 1.04 except for the slope of 2.2 in the CD experiment, possibly due to the lower transmission efficiency in the aerodynamic lens of the AMS for sub-100 nm particles; Pearson's correlation coefficients are between 0.87 and 0.98 for the experiments presented here). Individual organic compounds in both the gas and particle phase were measured with a Filter Inlet for Gases and AEROsols coupled to a high-resolution time-of-flight chemical ionization mass spectrometer (FIGAERO-HR-ToF-CIMS, Aerodyne Research Inc., hereafter CIMS) deploying iodide ions (I^-) as reagent ions (Lopez-Hilfiker et al., 2014; Lee et al., 2014). During the gas-phase measurement, gases were sampled via a fluorinated ethylene propylene (FEP) tube of 0.83 m length, while particles were simultaneously collected on a Teflon (Polytetrafluoroethylene, PTFE) filter via a separate sampling port (stainless steel tube of 0.66 m length, flow rate 5 L min^{-1}, residence time 0.9 s). At regular intervals (5–20 min; see Table S1 in the Supplement), the gas-phase measurement was switched off and particles on the filter were desorbed by a flow of ultra-high-purity (99.999 %) nitrogen heated from room temperature to 200 °C over the course of 35 min. The resulting mass spectral signal evolutions as a function of desorption temperature are termed thermograms (Lopez-Hilfiker et al., 2014). Single-mode thermograms of a compound with signal maxima occurring at distinct desorption temperatures (T_{max}), which correlate with the compound's enthalpy of sublimation, can be used to infer its saturation vapor pressure (Lopez-Hilfiker et al., 2015; Mohr et al., 2017). Multi-mode thermograms indicate contributions from isomers having different vapor pressures, or thermal fragmentation of larger molecules during the heating of the filter (Lopez-Hilfiker et al., 2015). Integration of ther-

mograms of individual compounds yielded their total signal in counts per deposition, which were converted to mass concentrations using a sensitivity of 22 counts s^{-1} ppt^{-1} (collisional limit; Lopez-Hilfiker et al., 2016). For each experiment, backgrounds were determined by sampling from the AIDA chamber before adding any precursor gases. For type 2 experiments, backgrounds were negligible with initial particle number concentrations below 1 cm^{-3}. For type 1 experiments, we observed a small increase in both gas mixing ratio and particle mass ($< 0.01\,\mu g\,m^{-3}$) after O_3 addition, which was subtracted from the mass loadings presented here. However, the background and the increase induced by O_3 addition were negligible compared to the increase by the SOA mass (> 1000-fold for particle mass).

All instruments were set up at room temperature, outside the temperature-controlled housing of AIDA. Despite inlet insulation with Armaflex, we calculated a theoretical temperature increase (Fitzer and Fritz, 1989) of ∼ 15 K for the particle inlet of the CIMS (the FIGAERO filter was thus presumably at 238 K during deposition), and cannot entirely rule out partial evaporation of water or semivolatile organic compounds, which is taken into account in our interpretation of results.

3 Results and discussion

3.1 Organic particle mass and size distribution

Figure 2a–b show the time series of total particle mass derived from SMPS size distributions, total organic particle mass measured by AMS, and total mass of particulate oxygenated hydrocarbons ($C_{x>1}H_{y>1}O_{z>1}$ detected as clustered with I^-, termed CHOI compounds) measured by CIMS for both types of experiments. Figure 2a depicts the CH experiment, representative of experiment type 1, where particles were directly formed in AIDA. Figure 2b shows experiment type 2, where aerosol was formed in the APC and transferred to AIDA (here the WDtoCH example; see Table 1). Note that the data were not wall-loss-corrected. Gaps in the AMS time series were due to filter measurements. To investigate the evolution of the SOA particles' physicochemical properties with time, we chose two points in time during the experiments, $t0$ and $t1$. $t0$ is the first FIGAERO filter deposition from AIDA after particle formation (experiment type 1) or particle transfer (experiment type 2), while $t1$ is approximately 3.5 h later. Averaged concentrations of total organics and total CHOI compounds, elemental O : C ratios at $t0$ and $t1$, and an overview of the experimental conditions including temperature (T), RH, and added precursor (α-pinene and O_3) concentrations for all experiments discussed here (WDtoCH, WHtoCH, CH, and CD) are listed in Table 1. Particle size distributions measured by AMS for all four experiments at $t0$ and $t1$ are shown in Fig. 2c–d.

For SOA formed in AIDA (type 1 experiments), at $t0$ and $t1$, mean total organic mass concentrations and mean total concentrations of CHOI compounds were in the range of 67.5–440.1 $\mu g\,m^{-3}$ and 97.8–247.6 $\mu g\,m^{-3}$, respectively. When particles were transferred from the APC chamber (type 2 experiments), organic and CHOI mass concentrations in AIDA reached values of 48.5–64.2 $\mu g\,m^{-3}$ and 23.3–40.7 $\mu g\,m^{-3}$, respectively. We stress here that even though particle mass concentrations in AIDA were higher for the experiments of type 1 (particles formed at 223 K directly in AIDA), the α-pinene concentration for the type 2 experiments was higher by a factor of ∼ 3 (Fig. 2a–b and Table 1). This also led to larger particle sizes for the type 2 experiments. Due to additional α-pinene addition between $t0$ and $t1$ only for the CH experiment, we observed a step increase of total particle mass for this experiment (Fig. 2a).

The discrepancies between AMS and CIMS concentrations are likely due to the CIMS with I^- as reagent ion being more sensitive to more polar oxygenated organic compounds (Lee et al., 2014), and thus only a potential subset of organic compounds are measured by CIMS. Evaporation losses of particulate compounds during filter deposition in the FIGAERO may play a minor role. In addition, by using the collisional limit for the CIMS data, we apply maximum sensitivity and thus present lower limits of CHOI compounds. The differences between the AMS- and SMPS-derived mass concentrations in Fig. 2a are likely due to the lower transmission of sub-100 nm particles in the aerodynamic lens of the AMS used here. The AMS measured lower concentrations than the SMPS at the beginning of the CH experiment (Fig. 2a), when the newly formed particles were much smaller (see Fig. 2c), compared to later in the experiment when they had grown in size (see Fig. 2d). For the WDtoCH experiment (Fig. 2b) with larger particles transferred from the APC to the AIDA chamber, AMS- and SMPS-derived mass concentrations agree very well. The slightly decreasing trend observed during both experiments was due to wall losses (Donahue et al., 2012).

3.2 Chemical characterization of SOA particles

3.2.1 Elemental oxygen-to-carbon ratios

Elemental O : C ratios were calculated using both AMS and CIMS data. The mean AMS O : C ratios for SOA formed in APC and AIDA were 0.34–0.36 and 0.26–0.30, respectively (Table 1). This is representative of O : C ratios for relatively fresh SOA measured in ambient studies (Mohr et al., 2012; Ge et al., 2012; Canagaratna et al., 2015). For CHOI compounds measured by CIMS, the calculated mean O : C ratios for SOA formed in APC and AIDA were 0.59–0.66 and 0.56–0.61, respectively. The AMS O : C ratio is expected to be lower than that of the CHOI compounds measured by iodide CIMS, as the latter is selective towards polar oxygenated compounds. The potential loss of semivolatiles from the filter

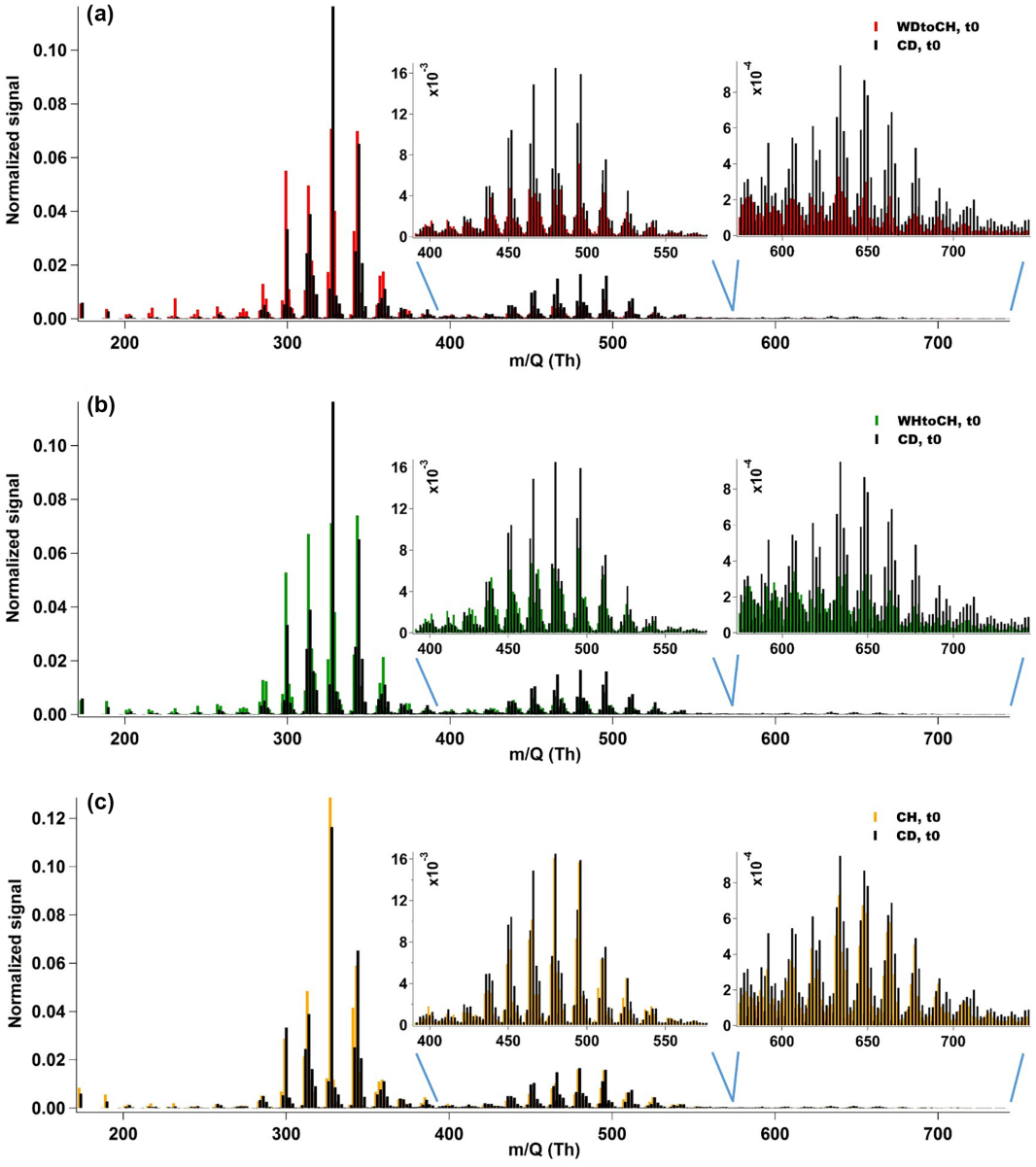

Figure 3. CIMS mass spectra (normalized to the sum of signal of all detected CHOI compounds) of experiments WDtoCH and CD **(a)**, WHtoCH and CD **(b)**, and CH and CD **(c)** at $t0$. Inserts show enlarged regions of dimers (left) and trimers (right).

during FIGAERO deposition may additionally increase the mass-averaged O : C ratio of compounds measured with this instrument. The O : C ratios of SOA formed in the APC were slightly higher than those formed in AIDA, likely a result of the difference in precursor concentrations and temperature and thus partitioning behavior of semivolatile SOA compounds during formation between the particles and chamber walls. We rule out a dilution effect when transferring particles from APC to AIDA since the dilution factor was orders of magnitude smaller than the decrease in saturation vapor pressure due to the temperature reduction from APC (296 K) to AIDA (223 K), and this was confirmed by the absence of a change in particle size after transfer. For all experiments, O : C ratios remained largely constant from $t0$ to $t1$.

3.2.2 CIMS mass spectra

Mass spectra of integrated desorptions from the CIMS are compared for the four experiments and two points in time, $t0$ and $t1$. Mass spectra shown were normalized to the sum of signal of all detected CHOI compounds. The corresponding mass loadings and sampling times (particle collection on filter) for the four experiments are listed in Table S1. Figure 3a, b, and c show a comparison of mass spectral patterns for the experiments WDtoCH and CD, for WHtoCH and CD, and

for CH and CD, respectively, all at $t0$ (the same comparisons for $t1$ are to be found in Fig. S1). Overall, the mass spectral patterns across all experimental conditions and points in time were relatively similar. Monomers ($C_mH_yO_z$ compounds, $m \leq 10$), dimers ($C_nH_yO_z$ compounds, $11 \leq n \leq 20$), and even trimers ($C_pH_yO_z$ compounds, $21 \leq p \leq 30$) clustered with I^- were observed in the mass spectra at $t0$ and $t1$ for all occasions.

Monomers dominated the overall signal of detected compounds, with the largest signal at m/z 327 (mainly $C_{10}H_{16}O_4I_1^-$, likely hydroxy-pinonic acid clustered with I^-). As we can see from Fig. 3, relatively higher contributions of monomers were measured at $t0$ for experiments WDtoCH and WHtoCH compared to CD. The difference in relative monomer contributions for experiments CH and CD was less distinct. At the same time, relatively larger contributions from dimers and trimers (inserts in Fig. 3) were observed for the experiment CD (and to a lesser extent for the CH). This was also the case for $t1$ (Fig. S1).

Figure 4 shows the relative mass contributions of monomers and adducts (this definition includes dimers, trimers, and oligomers in general) for the four experiments at both time points. As already observed in the mass spectral patterns, larger relative mass contributions from monomers were measured for the type 2 experiments (WDtoCH, WHtoCH), and larger relative mass contributions from adducts for the type 1 experiments (CH, CD). There was no significant change for the relative contributions and absolute concentrations of adducts (Fig. S2) between $t0$ and $t1$ for type 2 experiments (WDtoCH, WHtoCH). For type 1 experiments (CH and CD), absolute concentrations of monomers and adducts (Fig. S2) increased from $t0$ to $t1$ due to the addition of α-pinene after $t0$ and hence the continuing production of oxidation products and particle mass (compare to Fig. 2). However, the relative contributions of monomers for type 1 experiments increased from $t0$ to $t1$, which may be partially influenced by smaller FIGAERO sampling time and thus less evaporation losses of semivolatiles at $t1$ (see Table S1 and Supplement), but mostly by increased condensation of semivolatiles or lower-molecular-weight products with increasing particle size (compare Fig. 2c–d).

Figure 5 shows the average mass-weighted number of carbon atoms (numC) and oxygen atoms (numO) for CHOI compounds for the four experiments at $t0$ and $t1$. The corresponding average mass-weighted compounds' formulae for SOA generated in APC and AIDA were $C_{10-12}H_yO_{6-7}$ and $C_{11-13}H_yO_{6-7}$, respectively. Slightly bigger numC were observed for type 1 experiments (CH, CD) than type 2 experiments, with the largest value for experiment CD, followed by CH and WHtoCH. numC was smallest for WDtoCH. There was no obvious trend for numO.

In summary, smaller particles with slightly lower O : C ratios, bigger carbon numbers, and relatively more mass from adducts were observed for type 1 experiments (CH, CD), which had lower α-pinene concentrations and colder formation temperature (223 K) compared to the type 2 experiments. For type 2 experiments (WDtoCH, WHtoCH), higher α-pinene concentrations (by a factor of ∼ 3) and warmer formation temperature (296 K) produced larger particles with slightly higher O : C ratios, smaller carbon numbers, and relatively more mass from monomers. The slightly higher O : C ratio in type 2 experiments is thus not due to bigger oxygen numbers, but due to smaller carbon numbers (Fig. 5), indicating that relatively more small oxygenated molecules were formed for type 2 experiments. This is likely due to higher α-pinene concentrations and faster oxidation at 296 K leading to rapid condensation of monomers, providing enough gaseous oxidation products for the equilibrium of semivolatiles to be shifted into the particle phase. Type 1 experiments, on the other hand, were performed with lower α-pinene concentrations, and particles were formed in situ, favoring higher contributions of larger ELVOC/LVOC compounds, especially at the early stages of particle growth (Tröstl et al., 2016). At the same time, the low-temperature conditions may also have shifted equilibrium to the particle phase and led to condensation of compounds with a relatively lower degree of oxygenation (compared to warm temperature conditions). Overall, the differences observed in mass spectral patterns between the two types of experiments are a consequence of both temperature and precursor concentration differences. They underline the importance of experiment conditions when interpreting laboratory data or using them for modeling.

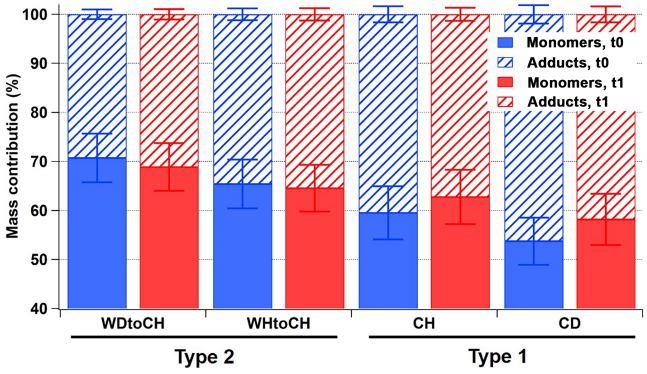

Figure 4. Relative mass contributions of monomers and adducts with error bars at $t0$ (blue) and $t1$ (red).

3.3 Thermograms: variation in T_{max} of SOA compounds for different experiments

In addition to information on mass spectral patterns and mass loadings when peaks are integrated, the FIGAERO also provides signal curves as a function of desorption temperature (referred to as thermograms). Although T_{max} can be used to infer the compound's saturation vapor pressure (Lopez-Hilfiker et al., 2015; Mohr et al., 2017), evaporative behavior and inferred volatility of a particle-bound compound are also

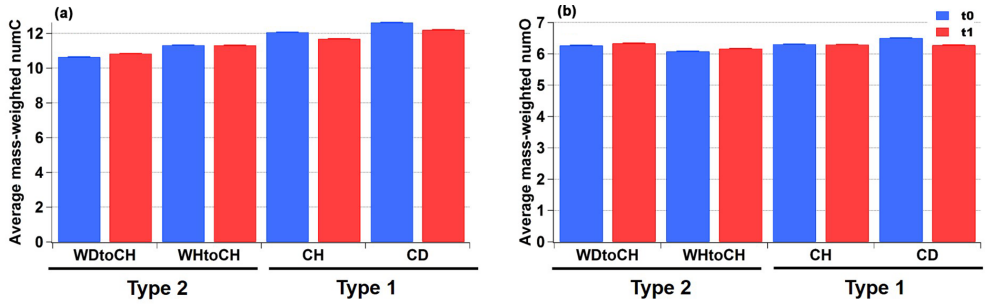

Figure 5. **(a)** Average mass-weighted number of carbon atoms (numC) and **(b)** oxygen atoms (numO) with error bars at $t0$ (blue) and $t1$ (red).

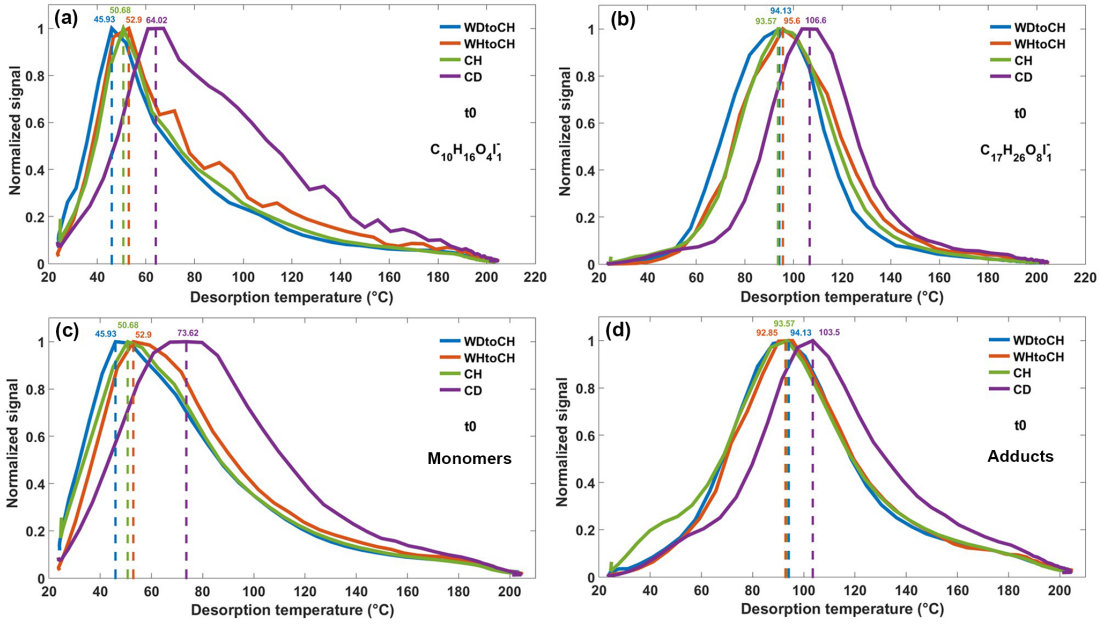

Figure 6. Thermograms of monomer $C_{10}H_{16}O_4$ **(a)** and adduct $C_{17}H_{26}O_8$ **(b),** both clustered with I^- at $t0$, and sum thermograms of monomers **(c)** and adducts **(d)** at $t0$. Dashed lines refer to the corresponding T_{max}.

influenced by the particles' physical phase state, particle-phase diffusivity, and viscosity (Yli-Juuti et al., 2017). Here we show that thermograms may also be used for qualitative information on particle viscosity.

Thermograms resulting from the thermal desorption of deposited SOA particles from the four experiments CH, CD, WDtoCH, and WHtoCH at both time points $t0$ and $t1$ were analyzed. Examples of the thermograms of a monomer ($C_{10}H_{16}O_4$, molecular formula corresponding to hydroxypinonic acid identified by Zhang et al., 2017) and an adduct ($C_{17}H_{26}O_8$, molecular structure identified in SOA from α-pinene ozonolysis as a *cis*-pinyl-diaterpenyl ester by Yasmeen et al., 2010; molecular formula identified in SOA from α-pinene ozonolysis by, e.g., Zhang et al., 2015; Mohr et al., 2017), both clustered with I^- at $t0$ are shown in Fig. 6a–b. Figure 6c shows the sum of thermograms of all monomers, Fig. 6d shows the sum of all adduct thermograms at $t0$. The same plots for $t1$ can be found in Fig. S3. Thermograms and sums of thermograms were normalized to their maximum values. The corresponding mass loadings and sampling times (particle collection on filter) for the four experiments are listed in Table S1. For experiment CD, the $C_{10}H_{16}O_4I_1^-$ thermograms exhibited a multi-modal shape, indicative of contributions from isomers having different vapor pressures, or thermal decomposition of larger molecules. Different isomeric hydroxypinonic acids were found in α-pinene SOA (Zhang et al., 2017) and the decomposition of *cis*-pinyl-hydroxypinonyl diester could have a residue of *cis*-pinic acid and 7-hydroxypinonic acid (Müller et al., 2008). Based on previous FIGAERO data analyses (Lopez-Hilfiker et al., 2015; D'Ambro et al., 2017; Wang et al., 2016), we can safely presume that the first mode corresponds to the monomer.

Figure 6a–b show that T_{max} of an individual compound varied by up to 20 °C, depending on experimental conditions. It has been shown earlier that thermograms and cor-

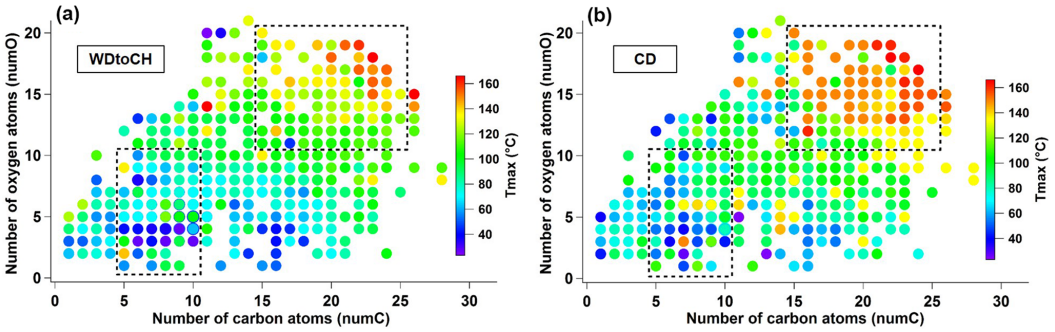

Figure 7. T_{max} distribution for individual CHOI compounds of WDtoCH **(a)** and CD **(b)** experiments at $t0$ according to number of oxygen atoms (numO) vs. number of carbon atoms (numC). Dashed boxes specify the compounds with nominal molecular formulae $C_{5-10}H_yO_{1-10}I^-$ and $C_{15-25}H_yO_{11-20}I^-$ that had bigger T_{max} differences.

responding T_{max} are highly reproducible for stable conditions (Lopez-Hilfiker et al., 2014). In our instrument, T_{max} varied by 2 °C at most for the monomer, $C_{10}H_{16}O_4$, and for another adduct, $C_{16}H_{24}O_6$ (molecular formula identified in SOA from α-pinene ozonolysis by, e.g., Zhang et al., 2015) both clustered with I^-, for six subsequent thermograms under stable conditions (Fig. S4). The variation in T_{max} as a function of experiment types observed here thus indicates that the shape of a thermogram for a given compound and given FIGAERO configuration is not only defined by the compound's enthalpy of evaporation. For both $C_{10}H_{16}O_4I_1^-$ and $C_{17}H_{26}O_8I_1^-$ thermograms, T_{max} was highest for experiment CD, followed by WHtoCH, CH, and WDtoCH. Similar trends were observed for all compounds measured by the CIMS, as shown by the sums of thermograms of all monomer compounds (Fig. 6c), and by the sums of thermograms of all adduct compounds (Fig. 6d). Sum T_{max} of monomers and adducts varied from 46 °C (experiment WDtoCH) to 74 °C (experiment CH) to 93 °C (experiment WHtoCH) to 104 °C (experiment CD).

Variation in T_{max} of the sum of CHOI compounds was larger for monomers (Fig. 6c) than for adducts (Fig. 6d). Monomers are thus the more important contributors to the shifts in T_{max}, likely because at the higher temperatures where adducts desorb, particle matrix effects may become less important. Since the sum of thermograms and its T_{max} is highly influenced by compounds with large signal, we also show a box and whisker diagram of T_{max} for monomers and adducts (Fig. S5). The median T_{max} values showed similar variation as the T_{max} values based on thermogram sums. Examples of the T_{max} distribution of individual CHOI compounds in numO vs. numC space at $t0$ are shown in Fig. 7 for the WDtoCH and CD experiments. Points were color-coded by T_{max}. Compounds with nominal molecular formula $C_{8-10}H_yO_{4-6}I^-$ were the main contributors to mass concentrations (data not shown), and thus also aggregated T_{max} values. Generally, T_{max} for CHOI compounds ranged from 25 to 165 °C, and increased with carbon numbers and oxygen numbers of compounds, as is to be expected given the relationship between enthalpy of evaporation and volatility of a compound (Lopez-Hilfiker et al., 2015; Mohr et al., 2017). The comparison between WDtoCH (Fig. 7a) and CD (Fig. 7b) experiments, however, showed differences in T_{max} values for most compounds. T_{max} values, especially of many compounds with nominal molecular formulae $C_{5-10}H_yO_{1-10}I^-$ and $C_{15-25}H_yO_{11-20}I^-$, were higher for the CD experiment. The similar behavior in the variation of T_{max} of most compounds measured by CIMS indicates that T_{max} is not purely a function of a compound's vapor pressure or volatility, but is influenced by diffusion limitations within particles (particle viscosity; Vaden et al., 2011; Yli-Juuti et al., 2017), interactions between particles deposited on the filter (particle matrix), and/or particle mass on the filter. In the following we will discuss these implications in more detail.

Mass transport limitations within SOA particles, often measured or modeled as evaporation rates of specific compounds (Yli-Juuti et al., 2017; Wilson et al., 2015; Roldin et al., 2014), have been related to the particle viscosity (Vaden et al., 2011; Yli-Juuti et al., 2017). Particle viscosity is highly influenced by temperature and RH (Shiraiwa et al., 2017; Kidd et al., 2014), with higher viscosities at cool and/or dry conditions (Shiraiwa et al., 2011). Since the temperature was 223 K in AIDA for all experiments discussed here, the observed differences in T_{max}, and presumed viscosity, cannot be directly explained by differences in temperature. In addition, during desorption of compounds with the FIGAERO, particles are actively heated (with heat transfer assumed to be immediate), and are not evaporating under equilibrium conditions. Presumed variations in particle viscosity based on observed variations in T_{max} must therefore be due to variations in particle chemical composition, and/or RH differences.

The biggest T_{max} difference in Fig. 6 was between WDtoCH and CD experiments, which was in accordance with the largest differences in mass spectra as discussed above (see Figs. 3a and 4). This is indicative of a relationship between

T_{max} in the thermograms and particle chemical composition. It has been shown earlier that the chemical properties of particulate compounds influence particle viscosity (Kidd et al., 2014; Hosny et al., 2016). Viscosity is expected to be higher with higher oligomer content, due to inter-component hydrogen bonding, especially at low RH (Kidd et al., 2014). This is in accordance with our results, which showed highest T_{max} values for the CD experiment, which also had the highest contribution from adducts.

RH is an additional parameter that greatly influences particle viscosity (Kidd et al., 2014; Hosny et al., 2016; Renbaum-Wolff et al., 2013). Despite the fact that the SOA particles might be dried very quickly by the dry heated nitrogen during particle desorption, we suppose that RH might have a "memory effect" and still influence T_{max}. RH conditions during the four experiments presented here ranged from 6 % (CD) to 30 % (WHtoCH) to 61 % (WDtoCH and CH). Note that these were the conditions of the measurement time in the AIDA chamber; for WDtoCH and WHtoCH, the RH conditions during SOA formation in the APC chamber were 1 and 21 %, respectively. We thus need to differentiate between $RH_{formation}$ and $RH_{measurement}$. As shown in Fig. 8, there was no trend between $RH_{formation}$ and T_{max}, indicating that the RH during particle formation did not play an important role in the observed viscosity variation. However, we observed a negative correlation of $RH_{measurement}$ and T_{max} of all monomer compounds at $t0$, indicating that even under low-temperature conditions of 223 K there is particle water uptake, and an influence of RH on viscosity. Particle water uptake thus seems to influence particle viscosity even at such low temperature and on such short timescales (few hours). To what extent RH and particle water uptake, or chemical properties and adduct content, and their respective influence on water uptake via increased hygroscopicity, contribute to the observed differences in T_{max} and presumed viscosity, we can only speculate. In the CH and WDtoCH experiments, $RH_{measurement}$ was ∼ 60 % for both. The adduct mass fraction was only slightly higher for SOA in the CH experiment, and so was T_{max} and thus potentially particle viscosity. More controlled studies at low temperature are needed to separate these effects.

We also noticed that different mass loadings on the filter due to different sampling times and/or sample concentrations influenced the shape of thermograms and thus T_{max}. T_{max} increased as a function of mass loading on the filter, likely due to the increase in heat capacity of the increasing mass of the particle matrix, and potential interactions between the particles. The dependency of T_{max} on filter mass loading was not linear, and for our FIGAERO, it reached a plateau at mass loadings of 2–4 µg. Our results are therefore not affected by the mass loading effect, but we recommend taking it into account in analyses that involve T_{max}. A detailed discussion can be found in the Supplement.

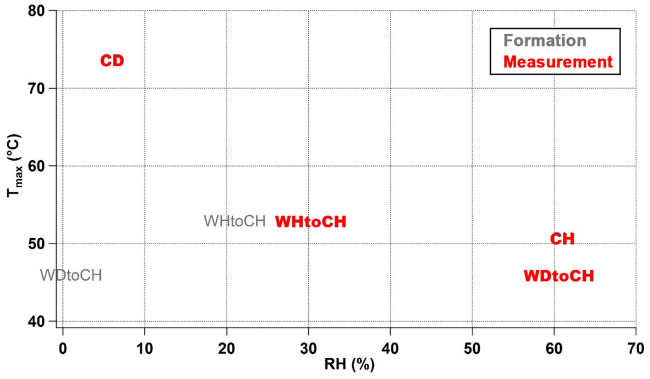

Figure 8. Relationship of $RH_{formation}$ (gray), $RH_{measurement}$ (red), and T_{max} of all CHOI monomer compounds for four experiments at $t0$.

4 Conclusions and atmospheric implications

In this study, α-pinene SOA physicochemical properties such as chemical composition, size distributions, and degree of oligomerization were investigated at low temperature (223 K) and different relative humidity (RH) using two simulation chambers (APC and AIDA). Two types of experiments were performed: for type 1 experiments, SOA was directly generated in the AIDA chamber kept at 223 K at 61 % RH (experiment termed "cold humid", CH) or 6 % RH (experiment termed "cold dry", CD) conditions. For type 2 experiments, SOA was formed in the APC chamber at room temperature (296 K), < 1 % RH (experiment termed "warm dry", WD) or 21 % RH (experiment termed "warm humid", WH) conditions, and then partially transferred to the AIDA chamber kept at 223 K at 61 % RH (WDtoCH) or 30 % RH (WHtoCH) conditions, respectively, to simulate SOA uplifting.

For type 1 experiments (CH, CD) with lower α-pinene concentrations and cold SOA formation temperature (223 K), smaller particles with relatively more mass from adducts were observed. For type 2 experiments (WDtoCH, WHtoCH) with higher α-pinene concentrations (by a factor of ∼ 3) and warm SOA formation temperature (296 K), larger particles with relatively more mass from monomers were produced. The differences observed in mass spectral patterns between the two types of experiments are likely a consequence of both temperature and precursor concentration differences. Higher α-pinene concentrations and faster oxidation at 296 K during SOA formation in the APC chamber shifted the gas–particle equilibrium to the particles, resulting in larger mass fractions of semivolatile and/or monomer compounds. Low-temperature conditions in the AIDA chamber during SOA formation on the other hand may result in condensation of compounds with a relatively lower degree of oxygenation. Our results show that depending on where SOA formation takes place in the atmosphere (e.g., boundary layer or upper troposphere), chemical properties can vary, and with it, reactivity and lifetime.

In addition to the differences in mass spectral patterns for the different experiments, we also observed differences in the shape of thermograms resulting from the desorption of SOA particles collected on the FIGAERO filter: T_{max} of an individual compound in the thermograms varied by up to 20 °C depending on experimental conditions, indicating that T_{max} is not only influenced by a compound's vapor pressure or volatility, but also by diffusion limitations within the particles (particle viscosity). For both $C_{10}H_{16}O_4I_1^-$ and $C_{17}H_{26}O_8I_1^-$ thermograms, T_{max} was highest for experiment CD, followed by WHtoCH, CH, and WDtoCH. We observed higher T_{max} for α-pinene SOA particles with higher oligomer mass fractions, indicating the potential role of intra- and inter-molecular hydrogen bonds between these large and highly functionalized molecules for the increase in particle viscosity (Kidd et al., 2014). Furthermore, T_{max} was negatively correlated with RH in the particle reservoir and particle water content, suggesting that hygroscopic properties and water uptake are important factors even at such low temperature. We also demonstrated an effect of mass deposited on the FIGAERO filter on T_{max}, which needs to be taken into account for further studies relying on T_{max}.

The results suggest that particle physicochemical properties such as viscosity and oligomer content mutually influence each other. More controlled experiments at low temperature are needed to separate the direct effects of RH and particle water uptake as well as chemical properties such as adduct content (i.e., oligomer content), and the indirect effects of chemical properties on water uptake via changes in hygroscopicity on the observed differences in T_{max} and presumed viscosity. The differences in SOA physicochemical properties observed in our set of experiments as a function of temperature, RH, and precursor conditions demonstrate the importance of ambient and laboratory measurements at a wide range of atmospherically relevant conditions, and of taking experimental conditions into careful consideration when interpreting laboratory studies or using them as input in climate models.

Data availability. Data are available upon request to the corresponding author.

The Supplement related to this article is available online at https://doi.org/10.5194/acp-18-2883-2018-supplement.

Author contributions. WH, HS, AP, XS, KHN, AV, TL, and CM designed research; WH, HS, AP, XS, RW, and CM performed research; WH, HS, AP, XS, and CM analyzed data; and WH and CM wrote the paper.

Competing interests. The authors declare that they have no conflict of interest.

Acknowledgements. Technical support by the AIDA staff at IMK-AAF, and financial support by the European Research Council (ERC-StG QAPPA 335478), Academy of Finland (259005 and 272041), and China Scholarship Council (CSC) for Wei Huang and Xiaoli Shen, is gratefully acknowledged.

The article processing charges for this open-access publication were covered by a Research Centre of the Helmholtz Association.

Edited by: David Topping
Reviewed by: two anonymous referees

References

Bastelberger, S., Krieger, U. K., Luo, B., and Peter, T.: Diffusivity measurements of volatile organics in levitated viscous aerosol particles, Atmos. Chem. Phys., 17, 8453–8471, https://doi.org/10.5194/acp-17-8453-2017, 2017.

Bateman, A. P., Gong, Z. H., Liu, P. F., Sato, B., Cirino, G., Zhang, Y., Artaxo, P., Bertram, A. K., Manzi, A. O., Rizzo, L. V., Souza, R. A. F., Zaveri, R. A., and Martin, S. T.: Sub-micrometre particulate matter is primarily in liquid form over Amazon rainforest, Nat. Geosci., 9, 34–37, 2016.

Canagaratna, M. R., Jimenez, J. L., Kroll, J. H., Chen, Q., Kessler, S. H., Massoli, P., Hildebrandt Ruiz, L., Fortner, E., Williams, L. R., Wilson, K. R., Surratt, J. D., Donahue, N. M., Jayne, J. T., and Worsnop, D. R.: Elemental ratio measurements of organic compounds using aerosol mass spectrometry: characterization, improved calibration, and implications, Atmos. Chem. Phys., 15, 253–272, https://doi.org/10.5194/acp-15-253-2015, 2015.

D'Ambro, E. L., Lee, B. H., Liu, J., Shilling, J. E., Gaston, C. J., Lopez-Hilfiker, F. D., Schobesberger, S., Zaveri, R. A., Mohr, C., Lutz, A., Zhang, Z., Gold, A., Surratt, J. D., Rivera-Rios, J. C., Keutsch, F. N., and Thornton, J. A.: Molecular composition and volatility of isoprene photochemical oxidation secondary organic aerosol under low- and high-NO_x conditions, Atmos. Chem. Phys., 17, 159–174, https://doi.org/10.5194/acp-17-159-2017, 2017.

Denjean, C., Formenti, P., Picquet-Varrault, B., Camredon, M., Pangui, E., Zapf, P., Katrib, Y., Giorio, C., Tapparo, A., Temime-Roussel, B., Monod, A., Aumont, B., and Doussin, J. F.: Aging of secondary organic aerosol generated from the ozonolysis of α-pinene: effects of ozone, light and temperature, Atmos. Chem. Phys., 15, 883–897, https://doi.org/10.5194/acp-15-883-2015, 2015.

Donahue, N. M., Henry, K. M., Mentel, T. F., Kiendler-Scharr, A., Spindler, C., Bohn, B., Brauers, T., Dorn, H. P., Fuchs, H., Tillmann, R., Wahner, A., Saathoff, H., Naumann, K. H., Möhler, O., Leisner, T., Müller, L., Reinnig, M. C., Hoffmann, T., Salo, K., Hallquist, M., Frosch, M., Bilde, M., Tritscher, T., Barmet, P., Praplan, A. P., DeCarlo, P. F., Dommen, J., Prévôt, A. S. H., and Baltensperger, U.: Aging of biogenic secondary organic aerosol

via gas-phase OH radical reactions, P. Natl. Acad. Sci. USA, 109, 13503–13508, 2012.

Ehn, M., Kleist, E., Junninen, H., Petäjä, T., Lönn, G., Schobesberger, S., Dal Maso, M., Trimborn, A., Kulmala, M., Worsnop, D. R., Wahner, A., Wildt, J., and Mentel, Th. F.: Gas phase formation of extremely oxidized pinene reaction products in chamber and ambient air, Atmos. Chem. Phys., 12, 5113–5127, https://doi.org/10.5194/acp-12-5113-2012, 2012.

Ehn, M., Thornton, J. A., Kleist, E., Sipilä, M., Junninen, H., Pullinen, I., Springer, M., Rubach, F., Tillmann, R., Lee, B., Lopez-Hilfiker, F., Andres, S., Acir, I. H., Rissanen, M., Jokinen, T., Schobesberger, S., Kangasluoma, J., Kontkanen, J., Nieminen, T., Kurtén, T., Nielsen, L. B., Jørgensen, S., Kjaergaard, H. G., Canagaratna, M., Dal Maso, M., Berndt, T., Petäjä, T., Wahner, A., Kerminen, V. M., Kulmala, M., Worsnop, D. R., Wildt, J., and Mentel, T. F.: A large source of low-volatility secondary organic aerosol, Nature, 506, 476–479, 2014.

Fahey, D. W., Gao, R.-S., Möhler, O., Saathoff, H., Schiller, C., Ebert, V., Krämer, M., Peter, T., Amarouche, N., Avallone, L. M., Bauer, R., Bozóki, Z., Christensen, L. E., Davis, S. M., Durry, G., Dyroff, C., Herman, R. L., Hunsmann, S., Khaykin, S. M., Mackrodt, P., Meyer, J., Smith, J. B., Spelten, N., Troy, R. F., Vömel, H., Wagner, S., and Wienhold, F. G.: The AquaVIT-1 intercomparison of atmospheric water vapor measurement techniques, Atmos. Meas. Tech., 7, 3177–3213, https://doi.org/10.5194/amt-7-3177-2014, 2014.

Fitzer, E. and Fritz, W.: Technische Chemie, 3rd ed., Springer, Berlin, 140 pp., 1989.

Frege, C., Ortega, I. K., Rissanen, M. P., Praplan, A. P., Steiner, G., Heinritzi, M., Ahonen, L., Amorim, A., Bernhammer, A.-K., Bianchi, F., Brilke, S., Breitenlechner, M., Dada, L., Dias, A., Duplissy, J., Ehrhart, S., El-Haddad, I., Fischer, L., Fuchs, C., Garmash, O., Gonin, M., Hansel, A., Hoyle, C. R., Jokinen, T., Junninen, H., Kirkby, J., Kürten, A., Lehtipalo, K., Leiminger, M., Mauldin, R. L., Molteni, U., Nichman, L., Petäjä, T., Sarnela, N., Schobesberger, S., Simon, M., Sipilä, M., Stolzenburg, D., Tomé, A., Vogel, A. L., Wagner, A. C., Wagner, R., Xiao, M., Yan, C., Ye, P., Curtius, J., Donahue, N. M., Flagan, R. C., Kulmala, M., Worsnop, D. R., Winkler, P. M., Dommen, J., and Baltensperger, U.: Influence of temperature on the molecular composition of ions and charged clusters during pure biogenic nucleation, Atmos. Chem. Phys., 18, 65–79, https://doi.org/10.5194/acp-18-65-2018, 2018.

Ge, X. L., Setyan, A., Sun, Y. L., and Zhang, Q.: Primary and secondary organic aerosols in Fresno, California during wintertime: Results from high resolution aerosol mass spectrometry, J. Geophys. Res.-Atmos., 117, D19301, https://doi.org/10.1029/2012jd018026, 2012.

Hallquist, M., Wenger, J. C., Baltensperger, U., Rudich, Y., Simpson, D., Claeys, M., Dommen, J., Donahue, N. M., George, C., Goldstein, A. H., Hamilton, J. F., Herrmann, H., Hoffmann, T., Iinuma, Y., Jang, M., Jenkin, M. E., Jimenez, J. L., Kiendler-Scharr, A., Maenhaut, W., McFiggans, G., Mentel, Th. F., Monod, A., Prévôt, A. S. H., Seinfeld, J. H., Surratt, J. D., Szmigielski, R., and Wildt, J.: The formation, properties and impact of secondary organic aerosol: current and emerging issues, Atmos. Chem. Phys., 9, 5155–5236, https://doi.org/10.5194/acp-9-5155-2009, 2009.

Heald, C. L., Henze, D. K., Horowitz, L. W., Feddema, J., Lamarque, J.-F., Guenther, A., Hess, P. G., Vitt, F., Seinfeld, J. H., Goldstein, A. H., and Fung, I.: Predicted change in global secondary organic aerosol concentrations in response to future climate, emissions, and land use change, J. Geophys. Res.-Atmos., 113, D05211, https://doi.org/10.1029/2007jd009092, 2008.

Hosny, N. A., Fitzgerald, C., Vyšniauskas, A., Athanasiadis, A., Berkemeier, T., Uygur, N., Pöschl, U., Shiraiwa, M., Kalberer, M., Pope, F. D., and Kuimova, M. K.: Direct imaging of changes in aerosol particle viscosity upon hydration and chemical aging, Chem. Sci., 7, 1357–1367, 2016.

IPCC: Climate change 2013: The physical scientific basis, Cambridge University Press, Cambridge, England, 622–623, 2013.

Järvinen, E., Ignatius, K., Nichman, L., Kristensen, T. B., Fuchs, C., Hoyle, C. R., Höppel, N., Corbin, J. C., Craven, J., Duplissy, J., Ehrhart, S., El Haddad, I., Frege, C., Gordon, H., Jokinen, T., Kallinger, P., Kirkby, J., Kiselev, A., Naumann, K.-H., Petäjä, T., Pinterich, T., Prevot, A. S. H., Saathoff, H., Schiebel, T., Sengupta, K., Simon, M., Slowik, J. G., Tröstl, J., Virtanen, A., Vochezer, P., Vogt, S., Wagner, A. C., Wagner, R., Williamson, C., Winkler, P. M., Yan, C., Baltensperger, U., Donahue, N. M., Flagan, R. C., Gallagher, M., Hansel, A., Kulmala, M., Stratmann, F., Worsnop, D. R., Möhler, O., Leisner, T., and Schnaiter, M.: Observation of viscosity transition in α-pinene secondary organic aerosol, Atmos. Chem. Phys., 16, 4423–4438, https://doi.org/10.5194/acp-16-4423-2016, 2016.

Jimenez, J. L., Canagaratna, M. R., Donahue, N. M., Prevot, A. S. H., Zhang, Q., Kroll, J. H., DeCarlo, P. F., Allan, J. D., Coe, H., Ng, N. L., Aiken, A. C., Docherty, K. S., Ulbrich, I. M., Grieshop, A. P., Robinson, A. L., Duplissy, J., Smith, J. D., Wilson, K. R., Lanz, V. A., Hueglin, C., Sun, Y. L., Tian, J., Laaksonen, A., Raatikainen, T., Rautiainen, J., Vaattovaara, P., Ehn, M., Kulmala, M., Tomlinson, J. M., Collins, D. R., Cubison, M. J., Dunlea, E. J., Huffman, J. A., Onasch, T. B., Alfarra, M. R., Williams, P. I., Bower, K., Kondo, Y., Schneider, J., Drewnick, F., Borrmann, S., Weimer, S., Demerjian, K., Salcedo, D., Cottrell, L., Griffin, R., Takami, A., Miyoshi, T., Hatakeyama, S., Shimono, A., Sun, J. Y., Zhang, Y. M., Dzepina, K., Kimmel, J. R., Sueper, D., Jayne, J. T., Herndon, S. C., Trimborn, A. M., Williams, L. R., Wood, E. C., Middlebrook, A. M., Kolb, C. E., Baltensperger, U., and Worsnop, D. R.: Evolution of organic aerosols in the atmosphere, Science, 326, 1525–1529, 2009.

Jokinen, T., Berndt, T., Makkonen, R., Kerminen, V.-M., Junninen, H., Paasonen, P., Stratmann, F., Herrmann, H., Guenther, A. B., Worsnop, D. R., Kulmala, M., Ehn, M., and Sipilä, M.: Production of extremely low volatile organic compounds from biogenic emissions: Measured yields and atmospheric implications, P. Natl. Acad. Sci. USA, 112, 7123–7128, 2015.

Kanakidou, M., Seinfeld, J. H., Pandis, S. N., Barnes, I., Dentener, F. J., Facchini, M. C., Van Dingenen, R., Ervens, B., Nenes, A., Nielsen, C. J., Swietlicki, E., Putaud, J. P., Balkanski, Y., Fuzzi, S., Horth, J., Moortgat, G. K., Winterhalter, R., Myhre, C. E. L., Tsigaridis, K., Vignati, E., Stephanou, E. G., and Wilson, J.: Organic aerosol and global climate modelling: a review, Atmos. Chem. Phys., 5, 1053–1123, https://doi.org/10.5194/acp-5-1053-2005, 2005.

Kidd, C., Perraud, V., Wingen, L. M., and Finlayson-Pitts, B. J.: Integrating phase and composition of secondary organic aerosol

from the ozonolysis of α-pinene, P. Natl. Acad. Sci. USA, 111, 7552–7557, 2014.

Kristensen, K., Cui, T., Zhang, H., Gold, A., Glasius, M., and Surratt, J. D.: Dimers in α-pinene secondary organic aerosol: effect of hydroxyl radical, ozone, relative humidity and aerosol acidity, Atmos. Chem. Phys., 14, 4201–4218, https://doi.org/10.5194/acp-14-4201-2014, 2014.

Kristensen, K., Watne, Å. K., Hammes, J., Lutz, A., Petäjä, T., Hallquist, M., Bilde, M., and Glasius, M.: High-molecular weight dimer esters are major products in aerosols from α-pinene ozonolysis and the boreal forest, Environ. Sci. Tech. Let., 3, 280–285, 2016.

Lee, B. H., Lopez-Hilfiker, F. D., Mohr, C., Kurtén, T., Worsnop, D. R., and Thornton, J. A.: An iodide-adduct high-resolution time-of-flight chemical-ionization mass spectrometer: Application to atmospheric inorganic and organic compounds, Environ. Sci. Technol., 48, 6309–6317, 2014.

Lienhard, D. M., Huisman, A. J., Krieger, U. K., Rudich, Y., Marcolli, C., Luo, B. P., Bones, D. L., Reid, J. P., Lambe, A. T., Canagaratna, M. R., Davidovits, P., Onasch, T. B., Worsnop, D. R., Steimer, S. S., Koop, T., and Peter, T.: Viscous organic aerosol particles in the upper troposphere: diffusivity-controlled water uptake and ice nucleation?, Atmos. Chem. Phys., 15, 13599–13613, https://doi.org/10.5194/acp-15-13599-2015, 2015.

Lopez-Hilfiker, F. D., Mohr, C., Ehn, M., Rubach, F., Kleist, E., Wildt, J., Mentel, Th. F., Lutz, A., Hallquist, M., Worsnop, D., and Thornton, J. A.: A novel method for online analysis of gas and particle composition: description and evaluation of a Filter Inlet for Gases and AEROsols (FIGAERO), Atmos. Meas. Tech., 7, 983–1001, https://doi.org/10.5194/amt-7-983-2014, 2014.

Lopez-Hilfiker, F. D., Mohr, C., Ehn, M., Rubach, F., Kleist, E., Wildt, J., Mentel, Th. F., Carrasquillo, A. J., Daumit, K. E., Hunter, J. F., Kroll, J. H., Worsnop, D. R., and Thornton, J. A.: Phase partitioning and volatility of secondary organic aerosol components formed from a-pinene ozonolysis and OH oxidation: the importance of accretion products and other low volatility compounds, Atmos. Chem. Phys., 15, 7765–7776, https://doi.org/10.5194/acp-15-7765-2015, 2015.

Lopez-Hilfiker, F. D., Iyer, S., Mohr, C., Lee, B. H., D'Ambro, E. L., Kurtén, T., and Thornton, J. A.: Constraining the sensitivity of iodide adduct chemical ionization mass spectrometry to multifunctional organic molecules using the collision limit and thermodynamic stability of iodide ion adducts, Atmos. Meas. Tech., 9, 1505–1512, https://doi.org/10.5194/amt-9-1505-2016, 2016.

McVay, R. C., Zhang, X., Aumont, B., Valorso, R., Camredon, M., La, Y. S., Wennberg, P. O., and Seinfeld, J. H.: SOA formation from the photooxidation of a-pinene: systematic exploration of the simulation of chamber data, Atmos. Chem. Phys., 16, 2785–2802, https://doi.org/10.5194/acp-16-2785-2016, 2016.

Middlebrook, A. M., Bahreini, R., Jimenez, J. L., and Canagaratna, M. R.: Evaluation of composition-dependent collection efficiencies for the Aerodyne Aerosol Mass Spectrometer using field data, Aerosol. Sci. Tech., 46, 258–271, 2012.

Möhler, O., Stetzer, O., Schaefers, S., Linke, C., Schnaiter, M., Tiede, R., Saathoff, H., Krämer, M., Mangold, A., Budz, P., Zink, P., Schreiner, J., Mauersberger, K., Haag, W., Kärcher, B., and Schurath, U.: Experimental investigation of homogeneous freezing of sulphuric acid particles in the aerosol chamber AIDA, Atmos. Chem. Phys., 3, 211–223, https://doi.org/10.5194/acp-3-211-2003, 2003.

Möhler, O., Benz, S., Saathoff, H., Schnaiter, M., Wagner, R., Schneider, J., Walter, S., Ebert, V., and Wagner, S.: The effect of organic coating on the heterogeneous ice nucleation efficiency of mineral dust aerosols, Environ. Res. Lett., 3, 025007, https://doi.org/10.1088/1748-9326/3/2/025007, 2008.

Mohr, C., DeCarlo, P. F., Heringa, M. F., Chirico, R., Slowik, J. G., Richter, R., Reche, C., Alastuey, A., Querol, X., Seco, R., Peñuelas, J., Jiménez, J. L., Crippa, M., Zimmermann, R., Baltensperger, U., and Prévôt, A. S. H.: Identification and quantification of organic aerosol from cooking and other sources in Barcelona using aerosol mass spectrometer data, Atmos. Chem. Phys., 12, 1649–1665, https://doi.org/10.5194/acp-12-1649-2012, 2012.

Mohr, C., Lopez-Hilfiker, F. D., Yli-Juuti, T., Heitto, A., Lutz, A., Hallquist, M., D'Ambro, E. L., Rissanen, M. P., Hao, L. Q., Schobesberger, S., Kulmala, M., Mauldin, R. L., Makkonen, U., Sipilä, M., Petäjä, T., and Thornton, J. A.: Ambient observations of dimers from terpene oxidation in the gas phase: Implications for new particle formation and growth, Geophys. Res. Lett., 44, 2958–2966, 2017.

Müller, L., Reinnig, M.-C., Warnke, J., and Hoffmann, Th.: Unambiguous identification of esters as oligomers in secondary organic aerosol formed from cyclohexene and cyclohexene/a-pinene ozonolysis, Atmos. Chem. Phys., 8, 1423–1433, https://doi.org/10.5194/acp-8-1423-2008, 2008.

Murphy, D. M. and Koop, T.: Review of the vapour pressures of ice and supercooled water for atmospheric applications, Q. J. Roy. Meteor. Soc., 131, 1539–1565, 2005.

Murphy, D. M., Cziczo, D. J., Froyd, K. D., Hudson, P. K., Matthew, B. M., Middlebrook, A. M., Peltier, R. E., Sullivan, A., Thomson, D. S., and Weber, R. J.: Single-particle mass spectrometry of tropospheric aerosol particles, J. Geophys. Res.-Atmos., 111, D23S32, https://doi.org/10.1029/2006jd007340, 2006.

Nel, A.: Air pollution-related illness: Effects of particles, Science, 308, 804–806, 2005.

Nozière, B., Kaberer, M., Claeys, M., Allan, J., D'Anna, B., Decesari, S., Finessi, E., Glasius, M., Grgić, I., Hamilton, J. F., Hoffmann, T., Iinuma, Y., Jaoui, M., Kahno, A., Kampf, C. J., Kourtchev, I., Maenhaut, W., Marsden, N., Saarikoski, S., Schnelle-Kreis, J., Surratt, J. D., Szidat, S., Szmigielski, R., and Wisthaler, A.: The molecular identification of organic compounds in the atmosphere: State of the art and challenges, Chem. Rev., 115, 3919–3983, 2015.

Pajunoja, A., Malila, J., Hao, L. Q., Joutsensaari, J., Lehtinen, K. E. J., and Virtanen, A.: Estimating the viscosity range of SOA particles based on their coalescence Time, Aerosol. Sci. Tech., 48, i–iv, https://doi.org/10.1080/02786826.2013.870325, 2014.

Pajunoja, A., Lambe, A. T., Hakala, J., Rastak, N., Cummings, M. J., Brogan, J. F., Hao, L. Q., Paramonov, M., Hong, J., Prisle, N. L., Malila, J., Romakkaniemi, S., Lehtinen, K. E. J., Laaksonen, A., Kulmala, M., Massoli, P., Onasch, T. B., Donahue, N. M., Riipinen, I., Davidovits, P., Worsnop, D. R., Petäjä, T., and Virtanen, A.: Adsorptive uptake of water by semisolid secondary organic aerosols, Geophys. Res. Lett., 42, 3063–3068, 2015.

Price, H. C., Mattsson, J., Zhang, Y., Bertram, A. K., Davies, J. F., Grayson, J. W., Martin, S. T., O'Sullivan, D., Reid, J. P., Rickards, A. M. J., and Murray, B. J.: Water diffusion in atmo-

spherically relevant α-pinene secondary organic material, Chem. Sci., 6, 4876–4883, 2015.

Renbaum-Wolff, L., Grayson, J. W., Bateman, A. P., Kuwata, M., Sellier, M., Murray, B. J., Shilling, J. E., Martin, S. T., and Bertram, A. K.: Viscosity of α-pinene secondary organic material and implications for particle growth and reactivity, P. Natl. Acad. Sci. USA, 110, 8014–8019, 2013.

Roldin, P., Eriksson, A. C., Nordin, E. Z., Hermansson, E., Mogensen, D., Rusanen, A., Boy, M., Swietlicki, E., Svenningsson, B., Zelenyuk, A., and Pagels, J.: Modelling non-equilibrium secondary organic aerosol formation and evaporation with the aerosol dynamics, gas- and particle-phase chemistry kinetic multilayer model ADCHAM, Atmos. Chem. Phys., 14, 7953–7993, https://doi.org/10.5194/acp-14-7953-2014, 2014.

Rückerl, R., Schneider, A., Breitner, S., Cyrys, J., and Peters, A.: Health effects of particulate air pollution: A review of epidemiological evidence, Inhal. Toxicol., 23, 555–592, 2011.

Saathoff, H., Naumann, K.-H., Möhler, O., Jonsson, Å. M., Hallquist, M., Kiendler-Scharr, A., Mentel, Th. F., Tillmann, R., and Schurath, U.: Temperature dependence of yields of secondary organic aerosols from the ozonolysis of a-pinene and limonene, Atmos. Chem. Phys., 9, 1551–1577, https://doi.org/10.5194/acp-9-1551-2009, 2009.

Schnaiter, M., Järvinen, E., Vochezer, P., Abdelmonem, A., Wagner, R., Jourdan, O., Mioche, G., Shcherbakov, V. N., Schmitt, C. G., Tricoli, U., Ulanowski, Z., and Heymsfield, A. J.: Cloud chamber experiments on the origin of ice crystal complexity in cirrus clouds, Atmos. Chem. Phys., 16, 5091–5110, https://doi.org/10.5194/acp-16-5091-2016, 2016.

Shiraiwa, M., Ammann, M., Koop, T., and Pöschl, U.: Gas uptake and chemical aging of semisolid organic aerosol particles, P. Natl. Acad. Sci. USA, 108, 11003–11008, 2011.

Shiraiwa, M., Li, Y., Tsimpidi, A. P., Karydis, V. A., Berkemeier, T., Pandis, S. N., Lelieveld, J., Koop, T., and Pöschl, U.: Global distribution of particle phase state in atmospheric secondary organic aerosols, Nat. Commun., 8, 15002, https://doi.org/10.1038/ncomms15002, 2017.

Shrivastava, M., Easter, R. C., Liu, X. H., Zelenyuk, A., Singh, B., Zhang, K., Ma, P.-L., Chand, D., Ghan, S., Jimenez, J. L., Zhang, Q., Fast, J., Rasch, P. J., and Tiitta, P.: Global transformation and fate of SOA: Implications of low-volatility SOA and gas-phase fragmentation reactions, J. Geophys. Res.-Atmos., 120, 4169–4195, 2015.

Skrotzki, J., Connolly, P., Schnaiter, M., Saathoff, H., Möhler, O., Wagner, R., Niemand, M., Ebert, V., and Leisner, T.: The accommodation coefficient of water molecules on ice – cirrus cloud studies at the AIDA simulation chamber, Atmos. Chem. Phys., 13, 4451–4466, https://doi.org/10.5194/acp-13-4451-2013, 2013.

Song, Y. C., Haddrell, A. E., Bzdek, B. R., Reid, J. P., Barman, T., Topping, D. O., Percival, C., and Cai, C.: Measurements and predictions of binary component aerosol particle viscosity, J. Phys. Chem. A, 120, 8123–8137, 2016.

Tröstl, J., Chuang, W. K., Gordon, H., Heinritzi, M., Yan, C., Molteni, U., Ahlm, L., Frege, C., Bianchi, F., Wagner, R., Simon, M., Lehtipalo, K., Williamson, C., Craven, J. S., Duplissy, J., Adamov, A., Almeida, J., Bernhammer, A.-K., Breitenlechner, M., Brilke, S., Dias, A., Ehrhart, S., Flagan, R. C., Franchin, A., Fuchs, C., Guida, R., Gysel, M., Hansel, A., Hoyle, C. R., Jokinen, T., Junninen, H., Kangasluoma, J., Keskinen, H., Kim, J., Krapf, M., Kürten, A., Laaksonen, A., Lawler, M., Leiminger, M., Mathot, S., Möhler, O., Nieminen, T., Onnela, A., Petäjä, T., Piel, F. M., Miettinen, P., Rissanen, M. P., Rondo, L., Sarnela, N., Schobesberger, S., Sengupta, K., Sipilä, M., Smith, J. N., Steiner, G., Tomè, A., Virtanen, A., Wagner, A. C., Weingartner, E., Wimmer, D., Winkler, P. M., Ye, P. L., Carslaw, K. S., Curtius, J., Dommen, J., Kirkby, J., Kulmala, M., Riipinen, I., Worsnop, D. R., Donahue, N. M., and Baltensperger, U.: The role of low-volatility organic compounds in initial particle growth in the atmosphere, Nature, 533, 527–531, 2016.

Tsigaridis, K., Krol, M., Dentener, F. J., Balkanski, Y., Lathière, J., Metzger, S., Hauglustaine, D. A., and Kanakidou, M.: Change in global aerosol composition since preindustrial times, Atmos. Chem. Phys., 6, 5143–5162, https://doi.org/10.5194/acp-6-5143-2006, 2006.

Vaden, T. D., Imre, D., Beránek, J., Shrivastava, M., and Zelenyuk, A.: Evaporation kinetics and phase of laboratory and ambient secondary organic aerosol, P. Natl. Acad. Sci. USA, 108, 2190–2195, 2011.

Virtanen, A., Joutsensaari, J., Koop, T., Kannosto, J., Yli-Pirilä, P., Leskinen, J., Mäkelä, J. M., Holopainen, J. K., Pöschl, U., Kulmala, M., Worsnop, D. R., and Laaksonen, A.: An amorphous solid state of biogenic secondary organic aerosol particles, Nature, 467, 824–827, 2010.

Wagner, R., Höhler, K., Huang, W., Kiselev, A., Möhler, O., Mohr, C., Pajunoja, A., Saathoff, H., Schiebel, T., Shen, X. L., and Virtanen, A.: Heterogeneous ice nucleation of α-pinene SOA particles before and after ice cloud processing, J. Geophys. Res.-Atmos., 122, 4924–4943, 2017.

Wang, B. B., O'Brien, R. E., Kelly, S. T., Shilling, J. E., Moffet, R. C., Gilles, M. K., and Laskin, A.: Reactivity of liquid and semisolid secondary organic carbon with chloride and nitrate in atmospheric aerosols, J. Phys. Chem. A, 119, 4498–4508, 2015.

Wang, M. Y., Yao, L., Zheng, J., Wang, X. K., Chen, J. M., Yang, X., Worsnop, D. R., Donahue, N. M., and Wang, L.: Reactions of atmospheric particulate stabilized Criegee intermediates lead to high-molecular-weight aerosol components, Environ. Sci. Technol., 50, 5702–5710, 2016.

Williams, L. R., Gonzalez, L. A., Peck, J., Trimborn, D., McInnis, J., Farrar, M. R., Moore, K. D., Jayne, J. T., Robinson, W. A., Lewis, D. K., Onasch, T. B., Canagaratna, M. R., Trimborn, A., Timko, M. T., Magoon, G., Deng, R., Tang, D., de la Rosa Blanco, E., Prévôt, A. S. H., Smith, K. A., and Worsnop, D. R.: Characterization of an aerodynamic lens for transmitting particles greater than 1 micrometer in diameter into the Aerodyne aerosol mass spectrometer, Atmos. Meas. Tech., 6, 3271–3280, https://doi.org/10.5194/amt-6-3271-2013, 2013.

Wilson, J., Imre, D., Beránek, J., Shrivastava, M., and Zelenyuk, A.: Evaporation kinetics of laboratory-generated secondary organic aerosols at elevated relative humidity, Environ. Sci. Technol., 49, 243–249, 2015.

Winterhalter, R., Van Dingenen, R., Larsen, B. R., Jensen, N. R., and Hjorth, J.: LC-MS analysis of aerosol particles from the oxidation of α-pinene by ozone and OH-radicals, Atmos. Chem. Phys. Discuss., https://doi.org/10.5194/acpd-3-1-2003, in review, 2003.

Yasmeen, F., Vermeylen, R., Szmigielski, R., Iinuma, Y., Böge, O., Herrmann, H., Maenhaut, W., and Claeys, M.: Terpenylic

acid and related compounds: precursors for dimers in secondary organic aerosol from the ozonolysis of α- and β-pinene, Atmos. Chem. Phys., 10, 9383–9392, https://doi.org/10.5194/acp-10-9383-2010, 2010.

Yli-Juuti, T., Pajunoja, A., Tikkanen, O. P., Buchholz, A., Faiola, C., Väisänen, O., Hao, L. Q., Kari, E., Peräkylä, O., Garmash, O., Shiraiwa, M., Ehn, M., Lehtinen, K., and Virtanen, A.: Factors controlling the evaporation of secondary organic aerosol from α-pinene ozonolysis, Geophys. Res. Lett., 44, 2562–2570, 2017.

Zhang, Q., Jimenez, J. L., Canagaratna, M. R., Allan, J. D., Coe, H., Ulbrich, I., Alfarra, M. R., Takami, A., Middlebrook, A. M., Sun, Y. L., Dzepina, K., Dunlea, E., Docherty, K., DeCarlo, P. F., Salcedo, D., Onasch, T., Jayne, J. T., Miyoshi, T., Shimono, A., Hatakeyama, S., Takegawa, N., Kondo, Y., Schneider, J., Drewnick, F., Borrmann, S., Weimer, S., Demerjian, K., Williams, P., Bower, K., Bahreini, R., Cottrell, L., Griffin, R. J., Rautiainen, J., Sun, J. Y., Zhang, Y. M., and Worsnop, D. R.: Ubiquity and dominance of oxygenated species in organic aerosols in anthropogenically-influenced Northern Hemisphere midlatitudes, Geophys. Res. Lett., 34, L13801, https://doi.org/10.1029/2007gl029979, 2007.

Zhang, X., McVay, R. C., Huang, D. D., Dalleska, N. F., Aumont, B., Flagan, R. C., and Seinfeld, J. H.: Formation and evolution of molecular products in α-pinene secondary organic aerosol, P. Natl. Acad. Sci. USA, 112, 14168–14173, 2015.

Zhang, X., Lambe, A. T., Upshur, M. A., Brooks, W. A., Beì, A. G., Thomson, R. J., Geiger, F. M., Surratt, J. D., Zhang, Z. F., Gold, A., Graf, S., Cubison, M. J., Groessl, M., Jayne, J. T., Worsnop, D. R., and Canagaratna, M. R.: Highly oxygenated multifunctional compounds in α-pinene secondary organic aerosol, Environ. Sci. Technol., 51, 5932–5940, 2017.

3 Contribution of highly functionalized organonitrates to organic aerosol and particle growth

Publication title: Chemical characterization of highly functionalized organonitrates contributing to night-time organic aerosol mass loadings and particle growth

Authors: Wei Huang, Harald Saathoff, Xiaoli Shen, Ramakrishna Ramisetty, Thomas Leisner, and Claudia Mohr

In: Environmental Science & Technology, 1165–1174, 2019. DOI: 10.1021/acs.est.8b05826.

Authorship statement

This peer-reviewed scientific journal article was written by me and is based on the field data from a six-week campaign (TRAM01) during July–August 2016 in a rural area near Eggenstein-Leopoldshafen (southwest Germany), located ~12 km north of the city of Karlsruhe, with a focus on the molecular composition of highly functionalized organonitrates, their contribution to night-time OA mass and their role in particle growth. I was responsible for the setup, operation and calibrations of FIGAERO-CIMS and AMS, data analysis, interpretation, and writing of this article.

Environmental Science & Technology

Article

Cite This: Environ. Sci. Technol. 2019, 53, 1165−1174

pubs.acs.org/est

Chemical Characterization of Highly Functionalized Organonitrates Contributing to Night-Time Organic Aerosol Mass Loadings and Particle Growth

Wei Huang,[†,‡] Harald Saathoff,[†] Xiaoli Shen,[†,‡] Ramakrishna Ramisetty,[†,○] Thomas Leisner,[†,§] and Claudia Mohr*[,∥]

[†]Institute of Meteorology and Climate Research, Karlsruhe Institute of Technology, Eggenstein-Leopoldshafen, 76344, Germany

[‡]Institute of Geography and Geoecology, Working Group for Environmental Mineralogy and Environmental System Analysis, Karlsruhe Institute of Technology, Karlsruhe, 76131, Germany

[§]Institute of Environmental Physics, Heidelberg University, Heidelberg, 69120, Germany

[∥]Department of Environmental Science and Analytical Chemistry, Stockholm University, Stockholm, 11418, Sweden

Supporting Information

ABSTRACT: Reactions of volatile organic compounds (VOC) with NO_3 radicals and of reactive intermediates of oxidized VOC with NO_x can lead to the formation of highly functionalized organonitrates (ON). We present quantitative and chemical information on ON contributing to high night-time organic aerosol (OA) mass concentrations measured during July−August 2016 in a rural area in southwest Germany. A filter inlet for gases and aerosols coupled to a high-resolution time-of-flight chemical ionization mass spectrometer (FIGAERO-HR-ToF-CIMS) was used to analyze the molecular composition of ON in both the gas and particle phase. We find larger contributions of ON to OA mass during the night. Identified ON are highly functionalized, with 4 to 12 oxygen atoms. The diel patterns of ON compounds with 5, 7, 10, or 15 carbon atoms per molecule vary, indicating a corresponding behavior of their potential precursor VOC. The temporal behavior of ON after sunset correlates with that of the number concentration of ultrafine particles, indicating a potential role of ON in night-time new particle formation (NPF) regularly observed at this location. We estimate an ON contribution of 18−25% to the mass increase of newly formed particles after sunset. Our study provides insights into the chemical composition of highly functionalized ON in the rural atmosphere and the role of anthropogenic emissions for night-time SOA formation in an area where biogenic VOC emissions dominate.

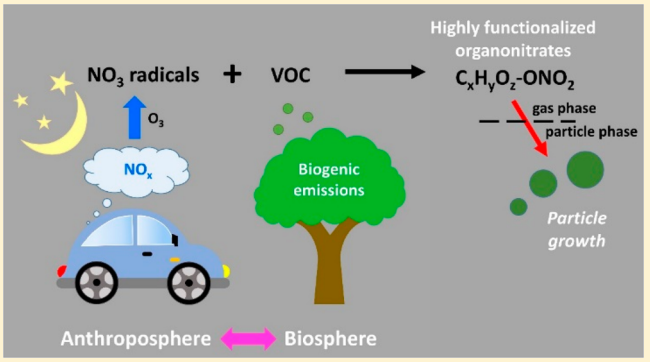

1. INTRODUCTION

Organic aerosols (OA) are ubiquitous in the Earth's atmosphere and have significant impacts on climate,[1] visibility,[2] and health.[3,4] They can be of anthropogenic and/or biogenic origin. OA are either directly emitted into the atmosphere (primary organic aerosol, POA) or formed by gas-phase oxidation of volatile organic compounds (VOC) with hydroxyl radicals (OH), ozone (O_3), or nitrate radicals (NO_3), the products of which can partition into the particle phase either by contributing to forming new particles or by adding mass to pre-existing particles (secondary organic aerosol, SOA).[5−11] OH radicals are the dominant oxidant during the day in the troposphere, while NO_3 radicals are one of the main oxidants during the night in addition to O_3.[12] Ground-level observations have indicated that new particle formation (NPF, the process of atmospheric nucleation and ultrafine particle growth from subnanometers to larger sizes (tens of nanometers)) during the night may be related to organics formed via biogenic VOC (BVOC, e.g., monoterpenes) oxidation by O_3 or NO_3 radicals in the absence of UV and OH or by OH radicals resulting from ozonolysis of BVOC.[13,14]

NO_3 radicals are formed by reaction of nitrogen oxides (NO_x, including NO and NO_2), predominantly emitted by high temperature combustion processes, with O_3.[12,15] The oxidation of BVOC (e.g., monoterpenes, isoprene) by NO_3 radicals during the night can lead to significant formation of SOA mass[16−18] and therefore "converts" biogenic emissions into an anthropogenic source of SOA. Reported SOA yields from the reaction of different BVOC with NO_3 radicals range from close to 0 (α-pinene) to up to 86% (β-caryophyllene).[19−21] The type of BVOC being oxidized by NO_3 radicals

Received: October 16, 2018
Revised: December 7, 2018
Accepted: January 7, 2019
Published: January 7, 2019

also influences the resulting SOA compounds' behavior during photochemical aging, with α-pinene SOA exhibiting more photolabile properties than β-pinene SOA.[22]

In addition to forming NO_3 radicals, NO_x can significantly alter SOA chemistry and influence SOA particle formation, composition, and properties during VOC oxidation.[15,23−25] SOA yields for α-pinene decrease as NO_x levels increase, while SOA yields for isoprene increase at low NO_x conditions and decrease at high NO_x conditions.[26,27] SOA yields for sesquiterpenes (longifolene and aromadendrene) are substantially higher under high NO_x conditions.[24] SOA particles also have lower vapor pressures when formed at high NO_x compared to those formed at low NO_x conditions.[23]

Reactions of VOC with NO_3 radicals during the night can lead to the formation of alkyl nitrates and multifunctional nitrates ($RONO_2$), while during the day organic peroxy radicals (RO_2) can react with NO or NO_2 to form $RONO_2$ or peroxy nitrates (RO_2NO_2).[28,29] Organonitrates (ON, including $RONO_2$ and RO_2NO_2) are therefore an important reservoir or sink (temporary or permanent) of NO_x, depending on the precursor VOC.[22] RO_2NO_2 are mostly thermally unstable or photolabile and can decompose back to NO_x.[28,30,31] It has been shown across different sites in Europe that ON are an important fraction of the total organic aerosol particle mass measured by aerosol mass spectrometers (AMS).[12] Specified ON measurements showed higher contributions during the night (4−8%) and lower contributions during the day (2−4%).[15,32] A large fraction of the particulate ON is highly functionalized, with dominant contributions from ON possessing 6 to 8 oxygen atoms.[22,32,33] The highly functionalized ON are of low volatility, since the addition of different functional groups including the nitrate group (ONO_2) to a hydrocarbon is estimated to lower its saturation vapor pressure by orders of magnitude.[34] ON are thus likely to partition into the particle phase and contribute to SOA particle formation.[24,32] Non-negative matrix factorization (NNMF) and positive matrix factorization (PMF) have been used to separate ON with different diel behaviors (higher contributions during the night, or during the day or early morning hours), indicative of NO_3 radical initiated or NO_x-driven chemistry.[33,35] Despite this, a coherent understanding of interactions between anthropogenic and biogenic emissions and the role of highly functionalized ON in the atmosphere is still needed.

In this paper, we present organic aerosol concentrations and chemical composition measured during July and August 2016 at a rural site in the upper Rhine Valley in southwest Germany. We investigate the molecular composition of ambient ON contributing to high organic aerosol mass loadings during the night and discuss the relationship between these ON and different precursor VOC as well as their potential role in nighttime SOA formation and particle growth.

2. METHODS

2.1. Measurement Site. We performed particle and trace gas measurements from July 8 to September 1, 2016 at a rural area in southwest Germany (49°6′10.54″N, 8°24′26.07″E), located ∼12 km north of the city of Karlsruhe with more than 300000 inhabitants. The area lies in the upper Rhine Valley, a region with inhomogeneous land use for industry, agriculture, settlements, and some forests. The measurement site was set up in a field next to a rural road and tramway tracks. At a 200 m distance in the south, there was a sunflower (*Helianthus annuus* L. cv. Giganteus) field (∼15 km^2), which can contribute to sesquiterpene emissions.[36] The Hardtwald forest is ∼1 km to the east and the Bienwald forest is ∼15 km southwest of the measurement site. Both forests are composed of mainly pine trees. About 40 km away is the Black Forest, a large forested area with mostly pine and oak trees of ∼6000 km^2. These forests can contribute to significant amounts of BVOC emissions from monoterpenes,[37] sesquiterpenes,[36] and also isoprene.[38] There are several industrial emission sources southwest of the measurement site, including refineries with 15.5 Mt/year capacity and a 550 MW hard coal fired power plant.[39] High particle number concentrations were found in this rural location during previous measurements on a tram.[39]

2.2. Meteorological Parameters, Particle, and Trace Gas Measurements. All instruments were set up in a temperature-controlled measurement container kept at ∼298 K. All sampling inlets were located 3.7 m above ground level and 1.5 m above the container roof. An overview on instruments and parameters measured is given in Table S1 in the Supporting Information.

Temperature, relative humidity (RH), wind direction, wind speed, global radiation, pressure, and precipitation data of this site were measured by a meteorological sensor (WS700, Lufft Inc.; see Table S1). As the winds were channeled by the Rhine Valley,[40] the main wind directions during the campaign were southwest and northeast.

Trace gases (O_3, CO_2, NO, NO_2, SO_2) were measured with the corresponding sensors (Table S1). Particle number concentrations were recorded with two condensation particle counters (CPC3022, measuring particles with mobility diameters larger than 7 nm; CPC3776, measuring particles with mobility diameters larger than 2.5 nm, TSI Inc.). Particle size distributions were measured with a scanning mobility particle sizer (SMPS, differential mobility analyzer 3071 connected to a CPC 3776 measuring particles with mobility diameters between 10 and 670 nm, TSI Inc.) and an optical particle counter (OPC FIDAS200, measuring particles with optical diameters between 180 nm and 18 μm, Palas Inc.).

A high-resolution time-of-flight aerosol mass spectrometer (HR-ToF-AMS, Aerodyne Research Inc., hereafter AMS) equipped with a high-pressure lens[41] was deployed to continuously measure total nonrefractory particle mass as a function of size (up to 2.5 μm particle aerodynamic diameter d_{va}) at a time resolution of 0.5 min. The AMS inlet was connected to a $PM_{2.5}$ head (flow rate 1 $m^3\ h^{-1}$) and a stainless steel tube of 3.45 m length (flow rate 0.1 L min^{-1}, residence time 0.9 s). AMS data were analyzed by the AMS data analysis software package SQUIRREL (version 1.60C) and PIKA (version 1.20C). An AMS composition-dependent collection efficiency (CDCE) was used for this data.[42] Individual organic compounds in both the gas and particle phase were measured with a filter inlet for gases and aerosols coupled to a high-resolution time-of-flight chemical ionization mass spectrometer (FIGAERO-HR-ToF-CIMS, Aerodyne Research Inc., hereafter CIMS) deploying iodide (I^-) as the reagent ion.[43,44] During the gas-phase measurement, gases were sampled via a fluorinated ethylene propylene (FEP) tube of 3.46 m length (flow rate 8 L min^{-1}, residence time 0.7 s). At the same time, particles were collected on a Teflon (Polytetrafluoroethylene, PTFE) filter via a separate sampling port connected to a PM_{10} head (flow rate 1 $m^3\ h^{-1}$) and a stainless steel tube of 2.65 m length (flow rate 8.6 L min^{-1}, residence time 1.2 s). At regular intervals (30−60 min), the gas-phase measurement was switched off and particles on the filter were desorbed by a

DOI: 10.1021/acs.est.8b05826
Environ. Sci. Technol. 2019, 53, 1165−1174

flow of ultrahigh-purity (UHP, 99.999%) nitrogen heated from room temperature to 200 °C over the course of 35 min. Integration of the signal evolution of an individual compound during desorption yields its total signal in counts per deposition, which was then converted to mass concentration using a sensitivity of 22 counts s^{-1} ppt^{-1} (reported collisional limit).[33,45,46] The sensitivity at collisional limit in our instrument may slightly vary from the reported value due to small differences in voltage settings of the respective mass spectrometers. Comparison of formic acid calibrations between the two instruments show a lower sensitivity in our instrument, indicating also a potentially lower sensitivity at the collisional limit. We therefore emphasize that our mass concentrations based on CIMS data represent a lower limit. The influence of RH on sensitivity is expected to be negligible for both particle phase (particles are desorbed in UHP N_2 and thus always at dry conditions) and gas phase. In gas phase, calculated water vapor pressures in the ion−molecule reaction (IMR) region fall into a range where sensitivity dependencies are weak.[44] Sensitivity uncertainties were taken into account in the calculation of the overall uncertainties of CIMS concentrations (±60%) following the approach by Thompson et al.[47] Gas phase backgrounds were determined by sampling zero air (high purity synthetic air). Particle phase backgrounds were assessed by putting an additional Teflon filter upstream of the particle phase sampling port during the deposition.[33]

3. RESULTS AND DISCUSSION

3.1. Diel Patterns of Organic Particle Mass and Trace Gases. The average organic mass loading measured by AMS is 5.0 ± 3.3 $\mu g\ m^{-3}$ (average ±1 standard deviation) at this site during the measurement period (Figure S1), comparable to other rural/urban sites in Europe (0.9−8.2 $\mu g\ m^{-3}$).[48] Organic aerosol (OA) is the dominant component and makes up 58.3% of total nonrefractory $PM_{2.5}$ mass measured by AMS (Figure S1a).

The average diel pattern of OA for this period reveals higher OA mass loadings during the night (00:00−06:00, 5.8 ± 1.6 $\mu g\ m^{-3}$) compared to day (12:00−17:00, 4.6 ± 1.3 $\mu g\ m^{-3}$; Figure 1a, S1b). Data in Figure 1a were normalized to total $PM_{2.5}$ measured by AMS to remove the effect of changes in boundary layer height. The shape of the OA diel evolution thus indicates night-time chemistry contributing to OA formation. High night-time OA mass loadings have also been observed at other European locations and US sites.[15,25,49,50] It is suggested that most night-time SOA formation is due to the oxidation of precursor VOC by NO_3 radicals, which are formed by reactions of O_3 with anthropogenic NO_x emissions.[15]

As generally observed,[15,35] NO_2 concentrations during this campaign also exhibit higher concentrations during the night compared to day (Figure 1b), with a peak after sunset (21:00−22:00) and another peak in the early morning after sunrise (06:00−08:00). The late evening peak could be related to the accumulation of anthropogenic NO_2 from nearby emission sources, decreasing ozone concentrations (Figure 1b) and decreasing boundary layer height, so that more NO_3 radicals can be formed.[15,39,51] Besides increasing emissions, the morning peak of NO_2 may be due to rapid NO_2 formation after sunrise from the photolysis of NO_3 and decomposition of N_2O_5[51] and/or photochemical aging of photolabile ON.[22] The OA mass measured by AMS thus can have contributions from both NO_x-driven and NO_3 radical induced chemistry.

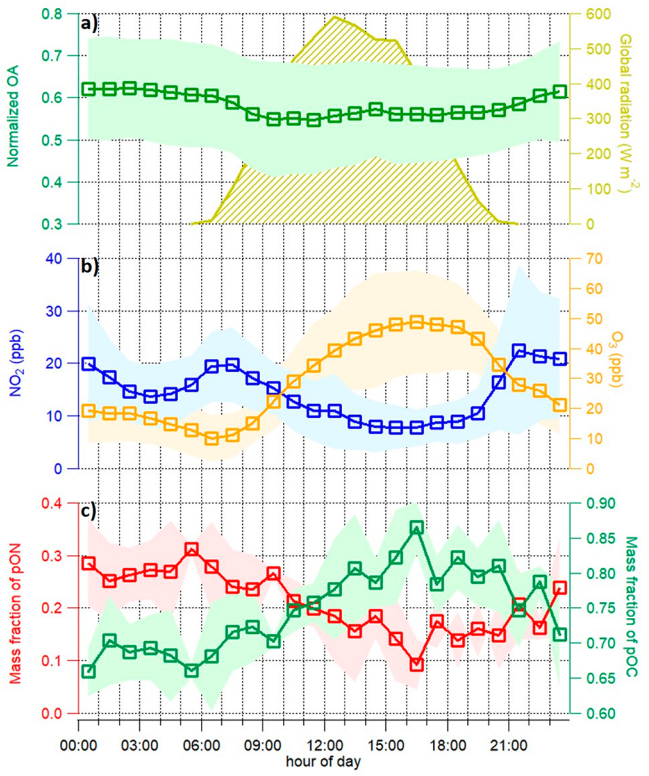

Figure 1. Mean diel patterns of (a) organic aerosol (OA) normalized to the total $PM_{2.5}$ measured by AMS and global radiation, (b) NO_2 and ozone, and (c) of the mass fraction of pON and pOC of total oxygenated hydrocarbons measured by CIMS. The shaded areas represent ±1 standard deviation.

The reaction of NO_2 with O_3 during the night leads to the formation of NO_3 radicals[15,51] which can oxidize VOC and form ON.[28,29] In order to characterize the OA compounds that contribute to the high night-time OA mass loadings measured by AMS, CIMS measurements were used to analyze the molecular composition of OA. The average organic particle size is below 1 μm (Figure S1c), which suggests a minor influence of particle size on total organics measured by AMS and CIMS. The total mass of oxygenated hydrocarbons measured by CIMS (OC-X, 2056 out of a total of 2567 identified compounds, with at least one C atom, one H atom, and one O atom ($C_{x\geq1}H_{y\geq1}O_{z\geq1}X_n$, detected as clustered with I^-)) account for about 31% of OA measured by AMS. Compounds not clustered with I^- (437 compounds) were excluded in this analysis, as their ionization mechanisms and thus sensitivity are highly uncertain. Using the same sensitivity as for the compounds detected as I^--clusters, they only account for 2−4% of particulate OC-X (pOC-X). The differences between CIMS and AMS measurements are likely due to the CIMS measuring only a subset of organics measured by AMS.[44,45,52] Besides, with the maximum sensitivity applied the CIMS concentrations represent a lower limit. Two classes of compounds make up >90% of the mass of OC-X both in gas and particle phase: pure oxygenated hydrocarbons (OC, 61.2−90.8%, 1352 compounds, $C_{x\geq1}H_{y\geq1}O_{z\geq1}$) and nitrogen-containing oxygenated hydrocarbons (ON, 3.6−35.7%, 509 compounds, $C_{x\geq1}H_{y\geq1}O_{z\geq4}N_1$). Oxygenated hydrocarbons with more than one nitrogen atom (e.g., organic dinitrates) were excluded in this analysis. This is in agreement with the study by Lee et al.[33] where dinitrates only represented

DOI: 10.1021/acs.est.8b05826
Environ. Sci. Technol. 2019, 53, 1165−1174

negligible mass fraction of the total mass measured by CIMS. In addition, their molecular identification is rather uncertain due to overlaps with more abundant non-nitrogen containing compounds.[33] We also determined the mass concentration of the organic bound nitrate fraction ($OrgNO_3$, i.e., organonitrates) from AMS data, assuming an NO_2^+/NO^+ ratio of $OrgNO_3$ of 0.1.[12,53] About 47% of the $OrgNO_3$ calculated in this way can be explained by the highly functionalized particulate ON (pON) measured by CIMS (see Figure S1d), similar to what Lee et al.[32] reported for the southeast US (58%).

Particulate OC (pOC) and pON measured by CIMS exhibit distinct diel patterns, with pOC dominating the particle composition during the day and night and pON accounting for significantly more mass during the night (Figure 1c). On average, pON accounts for 4.6% and 9.7% of total organic particle mass measured by AMS during the day (12:00−17:00) and during the night (00:00−06:00), respectively, consistent with previous studies.[15,32,49] In order to find out if the pON formed during the night originate from NO_3 radical chemistry[15] with different precursor VOC, we investigate the molecular composition of these ON in the next section.

3.2. Chemical Composition of Organonitrates. The average mass-weighted chemical compositions for pON and gaseous ON (gON) observed at our measurement site are $C_{11.4}H_{16.2}O_{8.1}N_1$ and $C_{8.3}H_{12.8}O_{6.5}N_1$, respectively (for comparison: pOC: $C_{9.1}H_{14.5}O_{6.7}$ and gaseous OC (gOC): $C_{7.4}H_{12.0}O_{5.5}$). ON are highly functionalized, containing up to 25 carbon atoms and 4 to 12 oxygen atoms. Figure S2a shows the relative contribution of individual ON to the total ON mass as a function of the number of carbon atoms in the gas and particle phase, respectively. For ON with up to 7 carbon atoms, the relative contributions in the gas phase are higher than those in the particle phase; for larger compounds, the relative contributions in the particle phase become higher. For both phases, C_9N and $C_{10}N$ compounds exhibit the highest contributions to total pON and gON (for comparison: C_xHO compounds are more widely distributed across carbon numbers and exhibit highest contributions of $C_{7-9}HO$ to total OC; see Figure S2b). In order to further investigate the potential relationships between these ON and anthropogenic and biogenic precursor VOC such as isoprene (C_5H_8), toluene (C_7H_8), monoterpenes ($C_{10}H_{16}$), and sesquiterpenes ($C_{15}H_{24}$), we selected the C_5N, C_7N, $C_{10}N$, and $C_{15}N$ compounds for further analysis. Together they contribute 41.0% to total pON and 42.4% to total gON. We stress here that assuming a relationship between the different precursor VOC and resulting ON based on carbon number is simplified, as fragmentation and/or accretion reactions[32] can lead to both negative and positive artifacts in assigned concentrations. Thermal decomposition in the FIGAERO[54] of the four particulate C_xN (pC_xN, x = 5, 7, 10, 15) groups can be neglected based on thermogram shapes (Figure S4).

The mass spectra of the four pC_xN groups are shown in Figure 2a in a similar plot as presented by Lee et al.[32] The mass spectral patterns of pON detected at this central European location are similar to those observed in southeastern US and in northern Europe,[32,33] implying similar chemistry and/or instrument sensitivity. The compounds of the $pC_{10}N$ group exhibit a bell-shaped distribution of the mass contribution of individual compounds to the total pON as a function of the number of oxygen atoms. The mass contributions of the pC_5N and pC_7N compounds drop faster after the maximum, and the

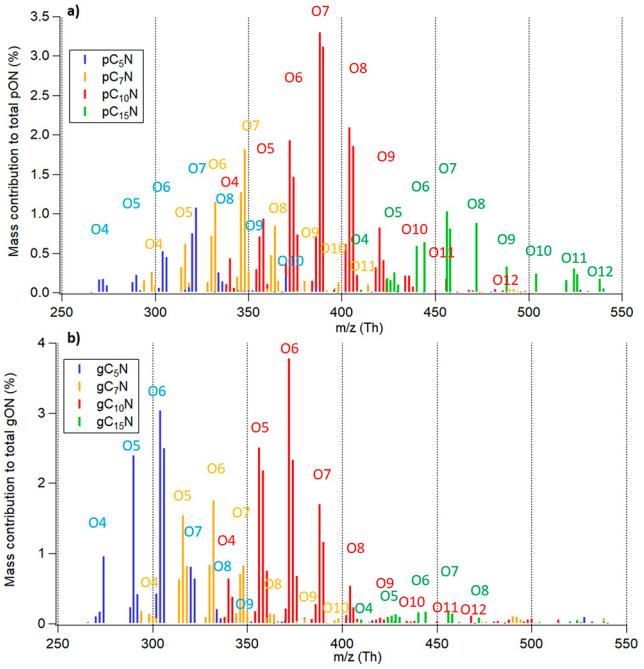

Figure 2. Mass contribution of the compounds of the C_xN (x = 5, 7, 10, 15) groups (a) in the particle phase to total pON and (b) in the gas phase to total gON as a function of m/z (includes mass of I^- ion; m/z 126.9050 Th). The shaded areas represent ±1 standard deviation.

$pC_{15}N$ compounds have a longer tail toward higher elemental oxygen-to-carbon (O:C) ratios, likely related to the length of the carbon backbone influencing the potential number of oxygen atoms that can be added to a molecule. The compounds of the $pC_{10}N$ group in general exhibit the largest contributions with up to 3% of the total pON mass, and significant mass contributions from compounds of the $pC_{15}N$ group are also observed. For all four pON groups, compounds with 6 to 8 oxygen atoms dominate the signal contributions; these pON groups, particularly the $pC_{10}N$ and $pC_{15}N$ groups, have non-negligible contributions from compounds with the number of oxygen atoms up to 10 or even 12, indicating multistep oxidation processes of precursor VOC emissions (e.g., autoxidation).[7] Similar patterns can be found in the mass spectra of the gaseous C_xN (gC_xN, x = 5, 7, 10, 15) compounds (Figure 2b), but here all gC_xN groups have a smaller number of oxygen atoms, with 5 to 7 oxygen atoms dominating the signal contributions. Generally, as expected,[55] the heavier compounds show a stronger tendency to partition into the particle phase (e.g., $C_{15}N$), while the lighter compounds (e.g., C_5N) favor the gas phase. We attribute the compounds in $C_{10}N$ and $C_{15}N$ groups mainly to be nitration products of mono- and sesquiterpenes, as there are important natural (e.g., pine trees in the Hardtwald forest, Bienwald forest, and Black Forest)[36,37] and agricultural (e.g., sunflower plantations)[36] sources of these compounds in the vicinity of the measurement site. Compounds in the C_5N group are assumed to be mainly formed from isoprene, which may originate from oak trees or legume farms present around the site.[38,56] The attribution of the C_7N compounds is more ambiguous, because they may be formed by oxidation of, e.g., toluene,[57] a major compound of anthropogenic emissions related to traffic or industrial activity,[58] but may also stem from the oxidation of monoterpenes, the products of which have

DOI: 10.1021/acs.est.8b05826
Environ. Sci. Technol. 2019, 53, 1165−1174

undergone fragmentation of the carbon backbone.[22,32,59] Due to the multitude of oxidation pathways and the resulting molecular compositions of compounds, it is difficult to distinguish the biogenic and anthropogenic contributions to the different C_xN groups, especially to C_7N.

The average diel patterns of the mass contributions of these pC_xN groups to total pON are shown in Figure 3a. The $pC_{10}N$ and $pC_{15}N$ groups, which include compounds with larger molecular weight, account for more pON mass during the night than during the day. On average, the $pC_{10}N$ group accounts for 21.5 ± 2.4% of total pON during the day (12:00−17:00) and 25.3 ± 1.0% of total pON during the night (00:00−06:00). Due to the fact that the compounds of the $pC_{10}N$ group exhibit the largest signal, they also largely influence the diel pattern of the relative contributions of total pON to all compounds measured by CIMS (see Figure 1c). A total of 45 compounds of the $pC_{10}N$ group contribute 0.9% to OA measured by AMS (3.0 ± 1.4% to pOC-X by CIMS) during the day (12:00−17:00) and 2.5% to OA measured by AMS (7.1 ± 0.9% to pOC-X by CIMS) during the night (00:00−06:00), demonstrating the important role of $pC_{10}N$ compounds in night-time OA mass loadings (see Figure 1a). The pC_5N and pC_7N groups, which include compounds with smaller molecular weight, exhibit a distinct diel trend, with higher contributions during the day compared to the night. This may be due to the different diel behaviors of their precursor VOC emissions[32] and/or different oxidation processes favored during the day, e.g., OH radical induced oxidation of aromatic compounds in the presence of NO_x.

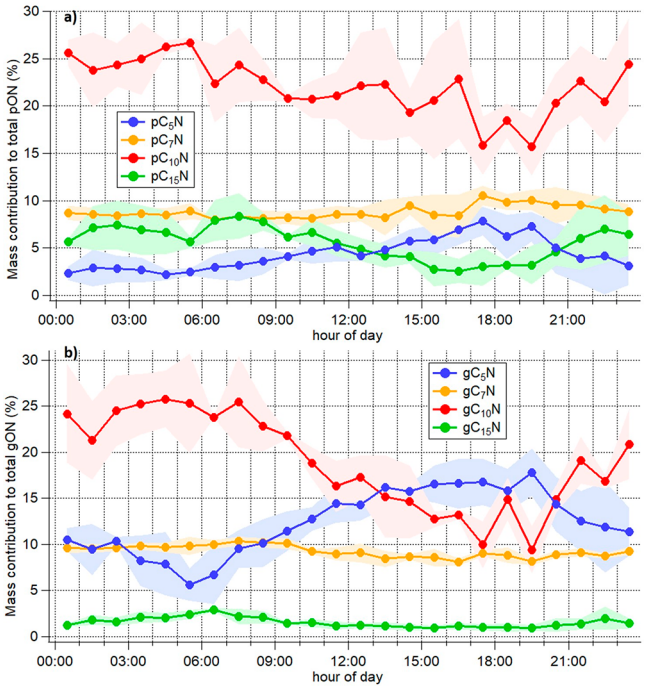

Figure 3. Mean diel patterns of the mass contribution of the C_xN (x = 5, 7, 10, 15) groups (a) in the particle phase to total pON and (b) in the gas phase to total gON. The shaded areas represent ±1 standard deviation.

In the gas phase, similar to the average diel patterns in the particle phase, the $gC_{10}N$ and $gC_{15}N$ groups account for more mass of the total gON during the night and the gC_5N accounts for more mass during the day (Figure 3b). However, the gC_7N group exhibits slightly higher contributions to total gON during the night, which is different from its diel behavior in the particle phase. The differences for the C_7N group in particle phase and gas phase may result from the different partitioning behaviors of oxidation products from monoterpenes[32,59] and from toluene with higher anthropogenic contributions during the day.[57,58] In general, the diel evolutions of the gC_xN groups exhibit a more distinct pattern compared to the pC_xN groups, potentially due to the relatively longer lifetimes of particulate compounds smearing out immediate (local) formation effects in time in the particle phase. The more distinct and structured diel patterns of the gC_xN groups may thus better reflect the corresponding precursor VOC emissions. The diel patterns of the mass contributions of the C_xHO (x = 5, 7, 10) groups to total OC all exhibit a peak during the day (Figure S3), indicative of different oxidation processes (e.g., O_3 and/or OH radical induced oxidation).

These results imply different partitioning behaviors of these C_xN groups as well as different oxidation processes of different precursor VOC (e.g., different terpenes, toluene, etc.) which can be induced by NO_3 during the night or by O_3 or OH in the presence of NO_x during the day.[28,32,35]

3.3. Role of Organonitrates in Particle Growth. During the measurement period, night-time NPF was observed for almost all nights, starting after sunset with particle growth lasting well into the morning of the following day (Figure S5a). A two week long measurement series using the same SMPS was also carried out in the same month (August) of 2018 at KIT campus north (49°5′43.0″N 8°25′46.0″E), located ∼2 km east of the measurement site in 2016 (Figure S5b). Night-time NPF was also observed for this measurement period in a different year and a slightly different location, confirming the robustness of the data set as well as the regional nature of this phenomenon. We stress here that since we did not have the instruments to investigate the molecules or ions involved in the very early stages of NPF, i.e., clustering and early growth of particles from subnanometers to a few nanometer sizes, our discussions are focused on the process of particle growth from a few nanometer size ranges to larger sizes (tens of nanometers). NPF during the night has been reported previously,[13,14,60,61] albeit much less often than day-time NPF. It has been suggested that night-time NPF may be induced by organics formed via BVOC (e.g., monoterpenes) oxidation by O_3 or NO_3 radicals in the absence of UV and OH radicals or by OH radicals resulting from BVOC ozonolysis.[13,14] The average O:C ratios are 0.85 for pON and 0.93 for gON, indicating that they could comprise highly oxygenated molecules (HOMs) formed, e.g., by autoxidation processes,[7] which have been shown to play an important role in atmospheric NPF.[8] The mean diel pattern of the number fraction of ultrafine particles (with mobility diameters between 2.5−7 nm) measured with two CPCs (Table S1) also shows a peak after sunset (20:30−00:00, Figure S6), suggesting emission or formation of small particles for this time period. We observe good correlations (Figure S7) between the number concentrations of these ultrafine particles and the above-mentioned four C_xN groups in both gas phase (Pearson's R: 0.53−0.73) and particle phase (Pearson's R: 0.64−0.83) after sunset (20:30−00:00), particularly for the C_7N and $C_{10}N$ groups, indicative of the potentially important role of these ON in the growth of newly formed particles. With night-time anthropogenic activities assumed to be lower and the very low reaction rate of NO_3 radicals with toluene

DOI: 10.1021/acs.est.8b05826
Environ. Sci. Technol. 2019, 53, 1165−1174

compared to that with α-pinene and isoprene,[62] the C_7N groups may have larger contributions from the fragmentation of oxidation products from monoterpenes[22,32,59] instead of oxidation products from toluene.

In order to investigate the role of NO_x emissions and ON in night-time particle growth and high night-time OA mass loadings, we calculated the production rate of NO_3 radicals ($PNO_3 = k_1[NO_2][O_3]$, $k_1 = 3.5 \times 10^{-17}$ cm^3 molecule^{-1} s^{-1} at 298 K)[63] using the NO_2 and O_3 concentrations measured during the campaign (Figure S8a). N_2O_5 concentrations measured by CIMS are orders of magnitude lower than the NO_2 concentrations. The loss of N_2O_5 (calculated as in Xu et al.,[25] due to homogeneous reaction with water and heterogeneous uptake to aqueous particles)[64−66] is rather slow (lifetime $\geq$ 1700 s), indicating that the main sink of NO_3 is likely its reaction with BVOC. Besides, good correlations are observed between PNO_3 and the C_xN groups in the particle phase (Pearson's R: 0.60−0.91) and gas phase (Pearson's R: 0.72−0.90) after sunset (20:30−00:00, Figure S9). The number concentrations of the ultrafine particles are also well correlated (Pearson's R = 0.64) with PNO_3 (Figure S8a) after sunset (20:30−00:00, Figure S8b). The results together with the good correlation of C_xN and ultrafine particles indicate the potentially important role of NO_3 radicals in night-time VOC oxidation to ON and the resulting growth of newly formed particles. We calculated the particle growth rate (increase rate of count mean diameter) for each night-time NPF (5 events, see Figure S5a) by averaging the diameter difference after sunset until midnight ($\Delta = (\text{diameter}_{\text{midnight}} - \text{diameter}_{\text{sunset}})/(\text{time}_{\text{midnight}} - \text{time}_{\text{sunset}})$). The average particle growth rate is 5.3 ± 3.1 nm hr^{-1} (min to max: 2.2−10.3 nm hr^{-1}), which is close to the growth rates for the night-time NPF observed over the Landes forest (9.0−17.5 nm hr^{-1}).[14] We also calculated the mass increase rate of OA measured by AMS, as well as pON, gON and the C_xN groups measured by CIMS for each night-time NPF observed during the CIMS measurement period (2 events, see Figure S1 and S5a) in a similar way ($\Delta = (\text{mass}_{\text{midnight}} - \text{mass}_{\text{sunset}})/(\text{time}_{\text{midnight}} - \text{time}_{\text{sunset}})$). The average mass increase rate for these two events is 0.48 ± 0.06 μg m^{-3} hr^{-1} for OA, 0.10 ± 0.04 μg m^{-3} hr^{-1} for pON, and 0.043 ± 0.035 μg m^{-3} hr^{-1} (4.0 ± 3.6 ppt hr^{-1}) for gON (see Figure 4). This means that 18−25% of the OA mass increase after sunset can be explained by pON resulting from condensation of gON and/or particle-phase reactions, such as accretion reactions.[67] Within the four C_xN groups in pON and gON, the $C_{10}N$ group shows the largest mass increase (particle phase: 0.029 ± 0.001 μg m^{-3} hr^{-1}, gas phase: 0.024 ± 0.014 μg m^{-3} hr^{-1}), followed by C_7N and $C_{15}N$. The C_5N group has the lowest pON mass increase and decreases a bit in gON, indicating lower emissions of C_5 BVOC (e.g., isoprene) during the night. We rule out a significant influence of the temperature changes between day and night on our observations, as one would expect especially the smaller molecules, of which a larger fraction typically remains in the gas phase, to partition more significantly into the condensed phase. However, we observe the contrary, indicating a smaller influence of temperature-driven partitioning under these conditions. In total, the mass increase rate of these four pC_xN groups accounts for 46.6% of the pON mass increase and 9.7% of the OA mass increase.

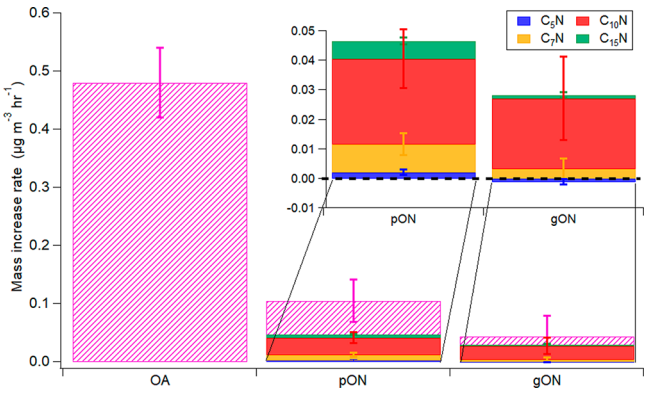

Figure 4. Mass increase rate comparisons of OA, pON and gON (hatched bars). The specified contributions of the different C_xN groups (x = 5, 7, 10, 15) are laid over the hatched areas. The inset shows the enlarged regions of the mass increase rates of the C_xN groups (x = 5, 7, 10, 15) in particle and gas phases; error bars represent ±1 standard deviation.

Our results indicate that these highly functionalized ON observed after sunset result from NO_3 radical initiated oxidation reactions and that they have potential contributions to SOA formation and particle growth via condensation and/or multiphase chemistry.

Given the location of the measurement station (outside the city and in close proximity to large forested areas) and the season during which the measurements were taken (summer), the majority of the precursor VOC for ON presented here are most likely of biogenic origin (also reflected in the emission inventories of the upper Rhine valley[68]). The abundance of $C_{10}N$ compounds, which are very likely to be the reaction products of the oxidation of monoterpenes by NO_3 radicals,[22,32,35] supports this conclusion. Furthermore, the proximity to the city and the nearby industrial emission sources results in high enough NO_x emissions for NO_3 radical oxidation to be a major pathway for OA particle number and mass formation during the night, especially during the summer months. However, a clear distinction between biogenic and anthropogenic contributions to the different C_xN groups is limited within this data set. This is especially evident for the C_7N group, the compounds of which, based on their number of carbon atoms, are hypothesized to partially result from toluene oxidation[57] but may also result from fragmentation products of monoterpene oxidation.[22,32,59]

Night-time NPF events are also frequently observed at our measurement site, similar to recently reported observations over the Landes forest in southwestern France.[14] Monoterpenes have been shown to play an important role for NPF in boreal regions[69] and were shown to reach maximum concentrations during the night-time NPF events over the Landes forest.[14] Isoprene, emissions of which are controlled by temperature and light,[70] however, was shown to significantly inhibit NPF.[71,72] The good correlation of ultrafine particle number concentrations with $C_{10}N$ compounds, together with calculated particle growth rate and mass increase rate of this group, in our study thus corroborates the important role of night-time VOC oxidation, particularly of monoterpenes, for ON in night-time SOA formation and particle growth. More in-depth and comprehensive studies on ON formation from different anthropogenic and biogenic VOC, and their role in NPF and SOA formation, are needed.

Our study provides insights into the chemical composition of ON, their relationship with different precursor VOC, and

DOI: 10.1021/acs.est.8b05826
Environ. Sci. Technol. 2019, 53, 1165−1174

their role in night-time particle growth in an area where BVOC emissions dominate.

■ ASSOCIATED CONTENT

Supporting Information

The Supporting Information is available free of charge on the ACS Publications website at DOI: 10.1021/acs.est.8b05826.

Detailed campaign instrumentation overview; results for time series of aerosol composition measured by AMS and CIMS, and average aerosol contribution to total $PM_{2.5}$ measured by AMS, mean diel trend of OA measured by AMS, average size distribution of organics measured by AMS, time series of total OA, NO_3, $OrgNO_3$, and pON, and correlation of $OrgNO_3$ and pON; mass contribution of C_xN groups to total ON and C_xHO groups to total OC as a function of the number of carbon atoms; mean diel patterns of mass contributions of C_xHO (x = 5, 7, 10, 15) groups in the particle phase to total pOC and in the gas phase to total gOC; average thermograms of pC_xN and pC_xHO groups (x = 5, 7, 10, 15); night-time NPF events during the measurement period and during another year (2018) in KIT campus north; mean diel trend of number fraction of ultrafine particles (with mobility diameters between 2.5−7 nm); correlations of C_xN (x = 5, 7, 10, 15) group concentrations in particle and gas phases with ultrafine particle number concentrations; mean calculated production rate of nitrate radicals (PNO_3) during the night, and correlation of ultrafine particle number concentrations with PNO_3; correlations of C_xN (x = 5, 7, 10, 15) group concentrations with PNO_3 (PDF)

■ AUTHOR INFORMATION

Corresponding Author

*E-mail: claudia.mohr@aces.su.se.

ORCID

Wei Huang: 0000-0002-5049-2117

Present Address

○TSI Instruments India Private Limited, Bangalore, 560102, India.

Notes

The authors declare no competing financial interest.

■ ACKNOWLEDGMENTS

Technical support by the staff at IMK-AAF and financial support by China Scholarship Council (CSC) for W.H. and X.S. is gratefully acknowledged.

■ REFERENCES

(1) IPCC. *Climate change 2013: The physical scientific basis*;Cambridge University Press: Cambridge, England, 2013; p 622−623.

(2) Boers, R.; van Weele, M.; van Meijgaard, E.; Savenije, M.; Siebesma, A. P.; Bosveld, F.; Stammes, P. Observations and projections of visibility and aerosol optical thickness (1956−2100) in the Netherlands: impacts of time-varying aerosol composition and hygroscopicity. *Environ. Res. Lett.* **2015**, *10* (1), 015003.

(3) Nel, A. Air pollution-related illness: Effects of particles. *Science* **2005**, *308* (5723), 804−806.

(4) Rückerl, R.; Schneider, A.; Breitner, S.; Cyrys, J.; Peters, A. Health effects of particulate air pollution: A review of epidemiological evidence. *Inhalation Toxicol.* **2011**, *23* (10), 555−592.

(5) Jimenez, J. L.; Canagaratna, M. R.; Donahue, N. M.; Prevot, A. S. H.; Zhang, Q.; Kroll, J. H.; DeCarlo, P. F.; Allan, J. D.; Coe, H.; Ng, N. L.; Aiken, A. C.; Docherty, K. S.; Ulbrich, I. M.; Grieshop, A. P.; Robinson, A. L.; Duplissy, J.; Smith, J. D.; Wilson, K. R.; Lanz, V. A.; Hueglin, C.; Sun, Y. L.; Tian, J.; Laaksonen, A.; Raatikainen, T.; Rautiainen, J.; Vaattovaara, P.; Ehn, M.; Kulmala, M.; Tomlinson, J. M.; Collins, D. R.; Cubison, M. J.; Dunlea, E. J.; Huffman, J. A.; Onasch, T. B.; Alfarra, M. R.; Williams, P. I.; Bower, K.; Kondo, Y.; Schneider, J.; Drewnick, F.; Borrmann, S.; Weimer, S.; Demerjian, K.; Salcedo, D.; Cottrell, L.; Griffin, R.; Takami, A.; Miyoshi, T.; Hatakeyama, S.; Shimono, A.; Sun, J. Y.; Zhang, Y. M.; Dzepina, K.; Kimmel, J. R.; Sueper, D.; Jayne, J. T.; Herndon, S. C.; Trimborn, A. M.; Williams, L. R.; Wood, E. C.; Middlebrook, A. M.; Kolb, C. E.; Baltensperger, U.; Worsnop, D. R. Evolution of organic aerosols in the atmosphere. *Science* **2009**, *326* (5959), 1525−1529.

(6) Hallquist, M.; Wenger, J. C.; Baltensperger, U.; Rudich, Y.; Simpson, D.; Claeys, M.; Dommen, J.; Donahue, N. M.; George, C.; Goldstein, A. H.; Hamilton, J. F.; Herrmann, H.; Hoffmann, T.; Iinuma, Y.; Jang, M.; Jenkin, M. E.; Jimenez, J. L.; Kiendler-Scharr, A.; Maenhaut, W.; McFiggans, G.; Mentel, T. F.; Monod, A.; Prévôt, A. S. H.; Seinfeld, J. H.; Surratt, J. D.; Szmigielski, R.; Wildt, J. The formation, properties and impact of secondary organic aerosol: current and emerging issues. *Atmos. Chem. Phys.* **2009**, *9* (14), 5155−5236.

(7) Ehn, M.; Thornton, J. A.; Kleist, E.; Sipilä, M.; Junninen, H.; Pullinen, I.; Springer, M.; Rubach, F.; Tillmann, R.; Lee, B.; Lopez-Hilfiker, F.; Andres, S.; Acir, I. H.; Rissanen, M.; Jokinen, T.; Schobesberger, S.; Kangasluoma, J.; Kontkanen, J.; Nieminen, T.; Kurtén, T.; Nielsen, L. B.; Jørgensen, S.; Kjaergaard, H. G.; Canagaratna, M.; Dal Maso, M.; Berndt, T.; Petäjä, T.; Wahner, A.; Kerminen, V. M.; Kulmala, M.; Worsnop, D. R.; Wildt, J.; Mentel, T. F. A large source of low-volatility secondary organic aerosol. *Nature* **2014**, *506* (7489), 476−479.

(8) Bianchi, F.; Tröstl, J.; Junninen, H.; Frege, C.; Henne, S.; Hoyle, C. R.; Molteni, U.; Herrmann, E.; Adamov, A.; Bukowiecki, N.; Chen, X.; Duplissy, J.; Gysel, M.; Hutterli, M.; Kangasluoma, J.; Kontkanen, J.; Kürten, A.; Manninen, H. E.; Münch, S.; Peräkylä, O.; Petäjä, T.; Rondo, L.; Williamson, C.; Weingartner, E.; Curtius, J.; Worsnop, D. R.; Kulmala, M.; Dommen, J.; Baltensperger, U. New particle formation in the free troposphere: A question of chemistry and timing. *Science* **2016**, *352* (6289), 1109−1112.

(9) Tröstl, J.; Chuang, W. K.; Gordon, H.; Heinritzi, M.; Yan, C.; Molteni, U.; Ahlm, L.; Frege, C.; Bianchi, F.; Wagner, R.; Simon, M.; Lehtipalo, K.; Williamson, C.; Craven, J. S.; Duplissy, J.; Adamov, A.; Almeida, J.; Bernhammer, A.-K.; Breitenlechner, M.; Brilke, S.; Dias, A.; Ehrhart, S.; Flagan, R. C.; Franchin, A.; Fuchs, C.; Guida, R.; Gysel, M.; Hansel, A.; Hoyle, C. R.; Jokinen, T.; Junninen, H.; Kangasluoma, J.; Keskinen, H.; Kim, J.; Krapf, M.; Kürten, A.; Laaksonen, A.; Lawler, M.; Leiminger, M.; Mathot, S.; Möhler, O.; Nieminen, T.; Onnela, A.; Petäjä, T.; Piel, F. M.; Miettinen, P.; Rissanen, M. P.; Rondo, L.; Sarnela, N.; Schobesberger, S.; Sengupta, K.; Sipilä, M.; Smith, J. N.; Steiner, G.; Tomè, A.; Virtanen, A.; Wagner, A. C.; Weingartner, E.; Wimmer, D.; Winkler, P. M.; Ye, P. L.; Carslaw, K. S.; Curtius, J.; Dommen, J.; Kirkby, J.; Kulmala, M.; Riipinen, I.; Worsnop, D. R.; Donahue, N. M.; Baltensperger, U. The role of low-volatility organic compounds in initial particle growth in the atmosphere. *Nature* **2016**, *533* (7604), 527−531.

(10) Kirkby, J.; Duplissy, J.; Sengupta, K.; Frege, C.; Gordon, H.; Williamson, C.; Heinritzi, M.; Simon, M.; Yan, C.; Almeida, J.; Tröstl, J.; Nieminen, T.; Ortega, I. K.; Wagner, R.; Adamov, A.; Amorim, A.; Bernhammer, A.-K.; Bianchi, F.; Breitenlechner, M.; Brilke, S.; Chen, X. M.; Craven, J.; Dias, A.; Ehrhart, S.; Flagan, R. C.; Franchin, A.; Fuchs, C.; Guida, R.; Hakala, J.; Hoyle, C. R.; Jokinen, T.; Junninen, H.; Kangasluoma, J.; Kim, J.; Krapf, M.; Kürten, A.; Laaksonen, A.; Lehtipalo, K.; Makhmutov, V.; Mathot, S.; Molteni, U.; Onnela, A.; Peräkylä, O.; Piel, F.; Petäjä, T.; Praplan, A. P.; Pringle, K.; Rap, A.; Richards, N. A. D.; Riipinen, I.; Rissanen, M. P.; Rondo, L.; Sarnela, N.; Schobesberger, S.; Scott, C. E.; Seinfeld, J. H.; Sipilä, M.; Steiner, G.; Stozhkov, Y.; Stratmann, F.; Tomé, A.; Virtanen, A.; Vogel, A. L.;

Wagner, A. C.; Wagner, P. E.; Weingartner, E.; Wimmer, D.; Winkler, P. M.; Ye, P. L.; Zhang, X.; Hansel, A.; Dommen, J.; Donahue, N. M.; Worsnop, D. R.; Baltensperger, U.; Kulmala, M.; Carslaw, K. S.; Curtius, J. Ion-induced nucleation of pure biogenic particles. *Nature* **2016**, *533* (7604), 521−526.

(11) Kulmala, M.; Kontkanen, J.; Junninen, H.; Lehtipalo, K.; Manninen, H. E.; Nieminen, T.; Petäjä, T.; Sipilä, M.; Schobesberger, S.; Rantala, P.; Franchin, A.; Jokinen, T.; Järvinen, E.; Äijälä, M.; Kangasluoma, J.; Hakala, J.; Aalto, P. P.; Paasonen, P.; Mikkilä, J.; Vanhanen, J.; Aalto, J.; Hakola, H.; Makkonen, U.; Ruuskanen, T.; Mauldin, R. L., III; Duplissy, J.; Vehkamäki, H.; Bäck, J.; Kortelainen, A.; Riipinen, I.; Kurtén, T.; Johnston, M. V.; Smith, J. N.; Ehn, M.; Mentel, T. F.; Lehtinen, K. E. J.; Laaksonen, A.; Kerminen, V.-M.; Worsnop, D. R. Direct observations of atmospheric aerosol nucleation. *Science* **2013**, *339* (6122), 943−946.

(12) Kiendler-Scharr, A.; Mensah, A. A.; Friese, E.; Topping, D.; Nemitz, E.; Prevot, A. S. H.; Äijälä, M.; Allan, J.; Canonaco, F.; Canagaratna, M.; Carbone, S.; Crippa, M.; Dall Osto, M.; Day, D. A.; De Carlo, P.; Di Marco, C. F.; Elbern, H.; Eriksson, A.; Freney, E.; Hao, L.; Herrmann, H.; Hildebrandt, L.; Hillamo, R.; Jimenez, J. L.; Laaksonen, A.; McFiggans, G.; Mohr, C.; O'Dowd, C.; Otjes, R.; Ovadnevaite, J.; Pandis, S. N.; Poulain, L.; Schlag, P.; Sellegri, K.; Swietlicki, E.; Tiitta, P.; Vermeulen, A.; Wahner, A.; Worsnop, D.; Wu, H.-C. Ubiquity of organic nitrates from nighttime chemistry in the European submicron aerosol. *Geophys. Res. Lett.* **2016**, *43* (14), 7735−7744.

(13) Lee, S.-H.; Young, L.-H.; Benson, D. R.; Suni, T.; Kulmala, M.; Junninen, H.; Campos, T. L.; Rogers, D. C.; Jensen, J. Observations of nighttime new particle formation in the troposphere. *J. Geophys. Res.* **2008**, *113* (D10), D10210.

(14) Kammer, J.; Perraudin, E.; Flaud, P. M.; Lamaud, E.; Bonnefond, J. M.; Villenave, E. Observation of nighttime new particle formation over the French Landes forest. *Sci. Total Environ.* **2018**, *621*, 1084−1092.

(15) Rollins, A. W.; Browne, E. C.; Min, K.-E.; Pusede, S. E.; Wooldridge, P. J.; Gentner, D. R.; Goldstein, A. H.; Liu, S.; Day, D. A.; Russell, L. M.; Cohen, R. C. Evidence for NOx control over nighttime SOA formation. *Science* **2012**, *337* (6099), 1210−1212.

(16) Pye, H. O. T.; Chan, A. W. H.; Barkley, M. P.; Seinfeld, J. H. Global modeling of organic aerosol: the importance of reactive nitrogen (NOx and NO3). *Atmos. Chem. Phys.* **2010**, *10* (22), 11261−11276.

(17) Brown, S. S.; deGouw, J. A.; Warneke, C.; Ryerson, T. B.; Dubé, W. P.; Atlas, E.; Weber, R. J.; Peltier, R. E.; Neuman, J. A.; Roberts, J. M.; Swanson, A.; Flocke, F.; McKeen, S. A.; Brioude, J.; Sommariva, R.; Trainer, M.; Fehsenfeld, F. C.; Ravishankara, A. R. Nocturnal isoprene oxidation over the Northeast United States in summer and its impact on reactive nitrogen partitioning and secondary organic aerosol. *Atmos. Chem. Phys.* **2009**, *9* (9), 3027−3042.

(18) Ayres, B. R.; Allen, H. M.; Draper, D. C.; Brown, S. S.; Wild, R. J.; Jimenez, J. L.; Day, D. A.; Campuzano-Jost, P.; Hu, W.; de Gouw, J.; Koss, A.; Cohen, R. C.; Duffey, K. C.; Romer, P.; Baumann, K.; Edgerton, E.; Takahama, S.; Thornton, J. A.; Lee, B. H.; Lopez-Hilfiker, F. D.; Mohr, C.; Wennberg, P. O.; Nguyen, T. B.; Teng, A.; Goldstein, A. H.; Olson, K.; Fry, J. L. Organic nitrate aerosol formation via NO3 + biogenic volatile organic compounds in the southeastern United States. *Atmos. Chem. Phys.* **2015**, *15* (23), 13377−13392.

(19) Spittler, M.; Barnes, I.; Bejan, I.; Brockmann, K. J.; Benter, T.; Wirtz, K. Reactions of NO3 radicals with limonene and alpha-pinene: Product and SOA formation. *Atmos. Environ.* **2006**, *40*, S116−S127.

(20) Fry, J. L.; Draper, D. C.; Barsanti, K. C.; Smith, J. N.; Ortega, J.; Winkle, P. M.; Lawler, M. J.; Brown, S. S.; Edwards, P. M.; Cohen, R. C.; Lee, L. Secondary organic aerosol formation and organic nitrate yield from NO3 oxidation of biogenic hydrocarbons. *Environ. Sci. Technol.* **2014**, *48* (20), 11944−11953.

(21) Ng, N. L.; Kwan, A. J.; Surratt, J. D.; Chan, A. W. H.; Chhabra, P. S.; Sorooshian, A.; Pye, H. O. T.; Crounse, J. D.; Wennberg, P. O.; Flagan, R. C.; Seinfeld, J. H. Secondary organic aerosol (SOA) formation from reaction of isoprene with nitrate radicals (NO3). *Atmos. Chem. Phys.* **2008**, *8* (14), 4117−4140.

(22) Nah, T.; Sanchez, J.; Boyd, C. M.; Ng, N. L. Photochemical aging of alpha-pinene and beta-pinene secondary organic aerosol formed from nitrate radical oxidation. *Environ. Sci. Technol.* **2016**, *50* (1), 222−231.

(23) D'Ambro, E. L.; Lee, B. H.; Liu, J. M.; Shilling, J. E.; Gaston, C. J.; Lopez-Hilfiker, F. D.; Schobesberger, S.; Zaveri, R. A.; Mohr, C.; Lutz, A.; Zhang, Z. F.; Gold, A.; Surratt, J. D.; Rivera-Rios, J. C.; Keutsch, F. N.; Thornton, J. A. Molecular composition and volatility of isoprene photochemical oxidation secondary organic aerosol under low- and high-NOx conditions. *Atmos. Chem. Phys.* **2017**, *17* (1), 159−174.

(24) Ng, N. L.; Chhabra, P. S.; Chan, A. W. H.; Surratt, J. D.; Kroll, J. H.; Kwan, A. J.; McCabe, D. C.; Wennberg, P. O.; Sorooshian, A.; Murphy, S. M.; Dalleska, N. F.; Flagan, R. C.; Seinfeld, J. H. Effect of NOx level on secondary organic aerosol (SOA) formation from the photooxidation of terpenes. *Atmos. Chem. Phys.* **2007**, *7* (19), 5159−5174.

(25) Xu, L.; Guo, H. Y.; Boyd, C. M.; Klein, M.; Bougiatioti, A.; Cerully, K. M.; Hite, J. R.; Isaacman-VanWertz, G.; Kreisberg, N. M.; Knote, C.; Olson, K.; Koss, A.; Goldstein, A. H.; Hering, S. V.; de Gouw, J.; Baumann, K.; Lee, S.-H.; Nenes, A.; Weber, R. J.; Ng, N. L. Effects of anthropogenic emissions on aerosol formation from isoprene and monoterpenes in the southeastern United States. *Proc. Natl. Acad. Sci. U. S. A.* **2015**, *112* (1), 37−42.

(26) Xu, L.; Kollman, M. S.; Song, C.; Shilling, J. E.; Ng, N. L. Effects of NOx on the volatility of secondary organic aerosol from isoprene photooxidation. *Environ. Sci. Technol.* **2014**, *48* (4), 2253−2262.

(27) Kroll, J. H.; Ng, N. L.; Murphy, S. M.; Flagan, R. C.; Seinfeld, J. H. Secondary organic aerosol formation from isoprene photooxidation. *Environ. Sci. Technol.* **2006**, *40* (6), 1869−1877.

(28) Sobanski, N.; Thieser, J.; Schuladen, J.; Sauvage, C.; Song, W.; Williams, J.; Lelieveld, J.; Crowley, J. N. Day and night-time formation of organic nitrates at a forested mountain site in south-west Germany. *Atmos. Chem. Phys.* **2017**, *17* (6), 4115−4130.

(29) Faxon, C.; Hammes, J.; Le Breton, M.; Pathak, R. K.; Hallquist, M. Characterization of organic nitrate constituents of secondary organic aerosol (SOA) from nitrate-radical-initiated oxidation of limonene using high-resolution chemical ionization mass spectrometry. *Atmos. Chem. Phys.* **2018**, *18* (8), 5467−5481.

(30) Fisher, J. A.; Jacob, D. J.; Travis, K. R.; Kim, P. S.; Marais, E. A.; Miller, C. C.; Yu, K. R.; Zhu, L.; Yantosca, R. M.; Sulprizio, M. P.; Mao, J. Q.; Wennberg, P. O.; Crounse, J. D.; Teng, A. P.; Nguyen, T. B.; St Clair, J. M.; Cohen, R. C.; Romer, P.; Nault, B. A.; Wooldridge, P. J.; Jimenez, J. L.; Campuzano-Jost, P.; Day, D. A.; Hu, W. W.; Shepson, P. B.; Xiong, F. L. Z.; Blake, D. R.; Goldstein, A. H.; Misztal, P. K.; Hanisco, T. F.; Wolfe, G. M.; Ryerson, T. B.; Wisthaler, A.; Mikoviny, T. Organic nitrate chemistry and its implications for nitrogen budgets in an isoprene- and monoterpene-rich atmosphere: constraints from aircraft (SEAC4RS) and ground-based (SOAS) observations in the Southeast US. *Atmos. Chem. Phys.* **2016**, *16* (9), 5969−5991.

(31) Singh, H. B.; Hanst, P. L. Peroxyacetyl nitrate (PAN) in the unpolluted atmosphere: An important reservoir for nitrogen oxides. *Geophys. Res. Lett.* **1981**, *8* (8), 941−944.

(32) Lee, B. H.; Mohr, C.; Lopez-Hilfiker, F. D.; Lutz, A.; Hallquist, M.; Lee, L.; Romer, P.; Cohen, R. C.; Iyer, S.; Kurtén, T.; Hu, W. W.; Day, D. A.; Campuzano-Jost, P.; Jimenez, J. L.; Xu, L.; Ng, N. L.; Guo, H. Y.; Weber, R. J.; Wild, R. J.; Brown, S. S.; Koss, A.; de Gouw, J.; Olson, K.; Goldstein, A. H.; Seco, R.; Kim, S.; McAvey, K.; Shepson, P. B.; Starn, T.; Baumann, K.; Edgerton, E. S.; Liu, J. M.; Shilling, J. E.; Miller, D. O.; Brune, W.; Schobesberger, S.; D'Ambro, E. L.; Thornton, J. A. Highly functionalized organic nitrates in the southeast United States: Contribution to secondary organic aerosol and reactive nitrogen budgets. *Proc. Natl. Acad. Sci. U. S. A.* **2016**, *113* (6), 1516−1521.

DOI: 10.1021/acs.est.8b05826
Environ. Sci. Technol. 2019, 53, 1165−1174

(33) Lee, B. H.; Lopez-Hilfiker, F. D.; D'Ambro, E. L.; Zhou, P. T.; Boy, M.; Petäjä, T.; Hao, L. Q.; Virtanen, A.; Thornton, J. A. Semi-volatile and highly oxygenated gaseous and particulate organic compounds observed above a boreal forest canopy. *Atmos. Chem. Phys.* **2018**, *18* (15), 11547−11562.
(34) Capouet, M.; Müller, J.-F. A group contribution method for estimating the vapour pressures of alpha-pinene oxidation products. *Atmos. Chem. Phys.* **2006**, *6*, 1455−1467.
(35) Massoli, P.; Stark, H.; Canagaratna, M. R.; Krechmer, J. E.; Xu, L.; Ng, N. L.; Mauldin, R. L.; Yan, C.; Kimmel, J.; Misztal, P. K.; Jimenez, J. L.; Jayne, J. T.; Worsnop, D. R. Ambient measurements of highly oxidized gas-phase molecules during the Southern Oxidant and Aerosol Study (SOAS) 2013. *ACS Earth Space Chem.* **2018**, *2*, 653−672.
(36) Duhl, T. R.; Helmig, D.; Guenther, A. Sesquiterpene emissions from vegetation: a review. *Biogeosciences* **2008**, *5* (3), 761−777.
(37) Komenda, M.; Koppmann, R. Monoterpene emissions from Scots pine (Pinus sylvestris): Field studies of emission rate variabilities. *J. Geophys. Res.* **2002**, *107* (D13), ACH1-1−ACH 1-13.
(38) Langford, B.; Cash, J.; Acton, W. J. F.; Valach, A. C.; Hewitt, C. N.; Fares, S.; Goded, I.; Gruening, C.; House, E.; Kalogridis, A.-C.; Gros, V.; Schafers, R.; Thomas, R.; Broadmeadow, M.; Nemitz, E. Isoprene emission potentials from European oak forests derived from canopy flux measurements: an assessment of uncertainties and inter-algorithm variability. *Biogeosciences* **2017**, *14* (23), 5571−5594.
(39) Hagemann, R.; Corsmeier, U.; Kottmeier, C.; Rinke, R.; Wieser, A.; Vogel, B. Spatial variability of particle number concentrations and NOx in the Karlsruhe (Germany) area obtained with the mobile laboratory 'AERO-TRAM'. *Atmos. Environ.* **2014**, *94*, 341−352.
(40) Duine, G.-J.; Hedde, T.; Roubin, P.; Durand, P.; Lothon, M.; Lohou, F.; Augustin, P.; Fourmentin, M. Characterization of valley flows within two confluent valleys under stable conditions: observations from the KASCADE field experiment. *Q. J. R. Meteorol. Soc.* **2017**, *143* (705), 1886−1902.
(41) Williams, L. R.; Gonzalez, L. A.; Peck, J.; Trimborn, D.; McInnis, J.; Farrar, M. R.; Moore, K. D.; Jayne, J. T.; Robinson, W. A.; Lewis, D. K.; Onasch, T. B.; Canagaratna, M. R.; Trimborn, A.; Timko, M. T.; Magoon, G.; Deng, R.; Tang, D.; Blanco, E. D. L. R.; Prévôt, A. S. H.; Smith, K. A.; Worsnop, D. R. Characterization of an aerodynamic lens for transmitting particles greater than 1 micrometer in diameter into the Aerodyne aerosol mass spectrometer. *Atmos. Meas. Tech.* **2013**, *6* (11), 3271−3280.
(42) Middlebrook, A. M.; Bahreini, R.; Jimenez, J. L.; Canagaratna, M. R. Evaluation of composition-dependent collection efficiencies for the Aerodyne Aerosol Mass Spectrometer using field data. *Aerosol Sci. Technol.* **2012**, *46* (3), 258−271.
(43) Lopez-Hilfiker, F. D.; Mohr, C.; Ehn, M.; Rubach, F.; Kleist, E.; Wildt, J.; Mentel, T. F.; Lutz, A.; Hallquist, M.; Worsnop, D.; Thornton, J. A. A novel method for online analysis of gas and particle composition: description and evaluation of a Filter Inlet for Gases and AEROsols (FIGAERO). *Atmos. Meas. Tech.* **2014**, *7* (4), 983−1001.
(44) Lee, B. H.; Lopez-Hilfiker, F. D.; Mohr, C.; Kurtén, T.; Worsnop, D. R.; Thornton, J. A. An iodide-adduct high-resolution time-of-flight chemical-ionization mass spectrometer: Application to atmospheric inorganic and organic compounds. *Environ. Sci. Technol.* **2014**, *48* (11), 6309−6317.
(45) Lopez-Hilfiker, F. D.; Iyer, S.; Mohr, C.; Lee, B. H.; D'Ambro, E. L.; Kurtén, T.; Thornton, J. A. Constraining the sensitivity of iodide adduct chemical ionization mass spectrometry to multifunctional organic molecules using the collision limit and thermodynamic stability of iodide ion adducts. *Atmos. Meas. Tech.* **2016**, *9* (4), 1505−1512.
(46) Huang, W.; Saathoff, H.; Pajunoja, A.; Shen, X. L.; Naumann, K.-H.; Wagner, R.; Virtanen, A.; Leisner, T.; Mohr, C. α-Pinene secondary organic aerosol at low temperature: chemical composition and implications for particle viscosity. *Atmos. Chem. Phys.* **2018**, *18* (4), 2883−2898.
(47) Thompson, S. L.; Yatavelli, R. L. N.; Stark, H.; Kimmel, J. R.; Krechmer, J. E.; Day, D. A.; Hu, W. W.; Isaacman-VanWertz, G.; Yee, L.; Goldstein, A. H.; Khan, M. A. H.; Holzinger, R.; Kreisberg, N.; Lopez-Hilfiker, F. D.; Mohr, C.; Thornton, J. A.; Jayne, J. T.; Canagaratna, M.; Worsnop, D. R.; Jimenez, J. L. Field intercomparison of the gas/particle partitioning of oxygenated organics during the Southern Oxidant and Aerosol Study (SOAS) in 2013. *Aerosol Sci. Technol.* **2017**, *51* (1), 30−56.
(48) Crippa, M.; Canonaco, F.; Lanz, V. A.; Äijälä, M.; Allan, J. D.; Carbone, S.; Capes, G.; Ceburnis, D.; Dall'Osto, M.; Day, D. A.; DeCarlo, P. F.; Ehn, M.; Eriksson, A.; Freney, E.; Hildebrandt Ruiz, L.; Hillamo, R.; Jimenez, J. L.; Junninen, H.; Kiendler-Scharr, A.; Kortelainen, A.-M.; Kulmala, M.; Laaksonen, A.; Mensah, A.; Mohr, C.; Nemitz, E.; O'Dowd, C.; Ovadnevaite, J.; Pandis, S. N.; Petäjä, T.; Poulain, L.; Saarikoski, S.; Sellegri, K.; Swietlicki, E.; Tiitta, P.; Worsnop, D. R.; Baltensperger, U.; Prévôt, A. S. H. Organic aerosol components derived from 25 AMS data sets across Europe using a consistent ME-2 based source apportionment approach. *Atmos. Chem. Phys.* **2014**, *14* (12), 6159−6176.
(49) Xu, L.; Suresh, S.; Guo, H.; Weber, R. J.; Ng, N. L. Aerosol characterization over the southeastern United States using high-resolution aerosol mass spectrometry: spatial and seasonal variation of aerosol composition and sources with a focus on organic nitrates. *Atmos. Chem. Phys.* **2015**, *15* (13), 7307−7336.
(50) Fountoukis, C.; Megaritis, A. G.; Skyllakou, K.; Charalampidis, P. E.; Pilinis, C.; van der Gon, H. A. C. D.; Crippa, M.; Canonaco, F.; Mohr, C.; Prévôt, A. S. H.; Allan, J. D.; Poulain, L.; Petäjä, T.; Tiitta, P.; Carbone, S.; Kiendler-Scharr, A.; Nemitz, E.; O'Dowd, C.; Swietlicki, E.; Pandis, S. N. Organic aerosol concentration and composition over Europe: insights from comparison of regional model predictions with aerosol mass spectrometer factor analysis. *Atmos. Chem. Phys.* **2014**, *14* (17), 9061−9076.
(51) Sobanski, N.; Tang, M. J.; Thieser, J.; Schuster, G.; Pöhler, D.; Fischer, H.; Song, W.; Sauvage, C.; Williams, J.; Fachinger, J.; Berkes, F.; Hoor, P.; Platt, U.; Lelieveld, J.; Crowley, J. N. Chemical and meteorological influences on the lifetime of NO3 at a semi-rural mountain site during PARADE. *Atmos. Chem. Phys.* **2016**, *16* (8), 4867−4883.
(52) Mohr, C.; Lopez-Hilfiker, F. D.; Yli-Juuti, T.; Heitto, A.; Lutz, A.; Hallquist, M.; D'Ambro, E. L.; Rissanen, M. P.; Hao, L. Q.; Schobesberger, S.; Kulmala, M.; Mauldin, R. L.; Makkonen, U.; Sipilä, M.; Petäjä, T.; Thornton, J. A. Ambient observations of dimers from terpene oxidation in the gas phase: Implications for new particle formation and growth. *Geophys. Res. Lett.* **2017**, *44* (6), 2958−2966.
(53) Farmer, D. K.; Matsunaga, A.; Docherty, K. S.; Surratt, J. D.; Seinfeld, J. H.; Ziemann, P. J.; Jimenez, J. L. Response of an aerosol mass spectrometer to organonitrates and organosulfates and implications for atmospheric chemistry. *Proc. Natl. Acad. Sci. U. S. A.* **2010**, *107* (15), 6670−6675.
(54) Lopez-Hilfiker, F. D.; Mohr, C.; Ehn, M.; Rubach, F.; Kleist, E.; Wildt, J.; Mentel, T. F.; Carrasquillo, A. J.; Daumit, K. E.; Hunter, J. F.; Kroll, J. H.; Worsnop, D. R.; Thornton, J. A. Phase partitioning and volatility of secondary organic aerosol components formed from α-pinene ozonolysis and OH oxidation: the importance of accretion products and other low volatility compounds. *Atmos. Chem. Phys.* **2015**, *15* (14), 7765−7776.
(55) Donahue, N. M.; Epstein, S. A.; Pandis, S. N.; Robinson, A. L. A two-dimensional volatility basis set: 1. organic-aerosol mixing thermodynamics. *Atmos. Chem. Phys.* **2011**, *11* (7), 3303−3318.
(56) Monson, R. K.; Jones, R. T.; Rosenstiel, T. N.; Schnitzler, J. P. Why only some plants emit isoprene. *Plant, Cell Environ.* **2013**, *36* (3), 503−516.
(57) Stroud, C. A.; Makar, P. A.; Michelangeli, D. V.; Mozurkewich, M.; Hastie, D. R.; Barbu, A.; Humble, J. Simulating organic aerosol formation during the photooxidation of toluene/NOx mixtures: Comparing the equilibrium and kinetic assumption. *Environ. Sci. Technol.* **2004**, *38* (5), 1471−1479.

DOI: 10.1021/acs.est.8b05826
Environ. Sci. Technol. 2019, 53, 1165−1174

(58) EPA. Locating and estimating air emissions from sources of toluene, EPA-454/R-93−047; Research Triangle Park: North Carolina, United States, 1994; pp 3−*1*, 3−4.
(59) Zhang, H. F.; Yee, L. D.; Lee, B. H.; Curtis, M. P.; Worton, D. R.; Isaacman-VanWertz, G.; Offenberg, J. H.; Lewandowski, M.; Kleindienst, T. E.; Beaver, M. R.; Holder, A. L.; Lonneman, W. A.; Docherty, K. S.; Jaoui, M.; Pye, H. O. T.; Hu, W. W.; Day, D. A.; Campuzano-Jost, P.; Jimenez, J. L.; Guo, H. Y.; Weber, R. J.; de Gouw, J.; Koss, A. R.; Edgerton, E. S.; Brune, W.; Mohr, C.; Lopez-Hilfiker, F. D.; Lutz, A.; Kreisberg, N. M.; Spielman, S. R.; Hering, S. V.; Wilson, K. R.; Thornton, J. A.; Goldstein, A. H. Monoterpenes are the largest source of summertime organic aerosol in the southeastern United States. *Proc. Natl. Acad. Sci. U. S. A.* **2018**, *115* (9), 2038−2043.
(60) Salimi, F.; Rahman, M. M.; Clifford, S.; Ristovski, Z.; Morawska, L. Nocturnal new particle formation events in urban environments. *Atmos. Chem. Phys.* **2017**, *17* (1), 521−530.
(61) Wiedensohler, A.; Hansson, H.-C.; Orsini, D.; Wendisch, M.; Wagner, F.; Bower, K. N.; Chourlarton, T. W.; Wells, M.; Parkin, M.; Acker, K.; Wieprecht, W.; Facchini, M. C.; Lind, J. A.; Fuzzi, S.; Arends, B. G.; Kulmala, M. Night-time formation and occurrence of new particles associated with orographic clouds. *Atmos. Environ.* **1997**, *31* (16), 2545−2559.
(62) Atkinson, R.; Aschmann, S. M.; Winer, A. M.; Pitts, J. N., Jr Gas phase reaction of NO2 with alkenes and dialkenes. *Int. J. Chem. Kinet.* **1984**, *16* (6), 697−706.
(63) *International Union of Pure and Applied Chemistry*http://iupac.pole-ether.fr/.
(64) Fry, J. L.; Draper, D. C.; Zarzana, K. J.; Campuzano-Jost, P.; Day, D. A.; Jimenez, J. L.; Brown, S. S.; Cohen, R. C.; Kaser, L.; Hansel, A.; Cappellin, L.; Karl, T.; Roux, A. H.; Turnipseed, A.; Cantrell, C.; Lefer, B. L.; Grossberg, N. Observations of gas- and aerosol-phase organic nitrates at BEACHON-RoMBAS 2011. *Atmos. Chem. Phys.* **2013**, *13* (17), 8585−8605.
(65) Gaston, C. J.; Thornton, J. A.; Ng, N. L. Reactive uptake of N2O5 to internally mixed inorganic and organic particles: the role of organic carbon oxidation state and inferred organic phase separations. *Atmos. Chem. Phys.* **2014**, *14* (11), 5693−5707.
(66) Crowley, J. N.; Thieser, J.; Tang, M. J.; Schuster, G.; Bozem, H.; Beygi, Z. H.; Fischer, H.; Diesch, J.-M.; Drewnick, F.; Borrmann, S.; Song, W.; Yassaa, N.; Williams, J.; Pöhler, D.; Platt, U.; Lelieveld, J. Variable lifetimes and loss mechanisms for NO3 and N2O5 during the DOMINO campaign: contrasts between marine, urban and continental air. *Atmos. Chem. Phys.* **2011**, *11* (21), 10853−10870.
(67) Kroll, J. H.; Seinfeld, J. H. Chemistry of secondary organic aerosol: Formation and evolution of low-volatility organics in the atmosphere. *Atmos. Environ.* **2008**, *42* (16), 3593−3624.
(68) Ponche, J.-L.; Schneider, C. Mirabel, P. Methodology and results of the REKLIP atmospheric emission inventory of the upper Rhine valley transborder region. *Water, Air, Soil Pollut.* **2000**, *124* (1−2), 61−93.
(69) Tunved, P.; Hansson, H.-C.; Kerminen, V.-M.; Ström, J.; Dal Maso, M.; Lihavainen, H.; Viisanen, Y.; Aalto, P. P.; Komppula, M.; Kulmala, M. High natural aerosol loading over boreal forests. *Science* **2006**, *312* (5771), 261−263.
(70) Guenther, A.; Hewitt, C. N.; Erickson, D.; Fall, R.; Geron, C.; Graedel, T.; Harley, P.; Klinger, L.; Lerdau, M.; Mckay, W. A.; Pierce, T.; Scholes, B.; Steinbrecher, R.; Tallamraju, R.; Taylor, J.; Zimmerman, P. A global model of natural volatile organic compound emissions. *J. Geophys. Res.* **1995**, *100* (D5), 8873−8892.
(71) Kiendler-Scharr, A.; Wildt, J.; Dal Maso, M.; Hohaus, T.; Kleist, E.; Mentel, T. F.; Tillmann, R.; Uerlings, R.; Schurr, U.; Wahner, A. New particle formation in forests inhibited by isoprene emissions. *Nature* **2009**, *461* (7262), 381−384.
(72) Lee, S.-H.; Uin, J.; Guenther, A. B.; de Gouw, J. A.; Yu, F. Q.; Nadykto, A. B.; Herb, J.; Ng, N. L.; Koss, A.; Brune, W. H.; Baumann, K.; Kanawade, V. P.; Keutsch, F. N.; Nenes, A.; Olsen, K.; Goldstein, A.; Ouyang, Q. Isoprene suppression of new particle formation: Potential mechanisms and implications. *J. Geophys. Res.* **2016**, *121* (24), 14621−14635.

DOI: 10.1021/acs.est.8b05826
Environ. Sci. Technol. 2019, 53, 1165−1174

4 Seasonal variation of organic aerosol chemical composition and volatility

Publication title: Seasonal characteristics of organic aerosol chemical composition and volatility in Stuttgart, Germany

Authors: Wei Huang, Harald Saathoff, Xiaoli Shen, Ramakrishna Ramisetty, Thomas Leisner, and Claudia Mohr

In: Atmospheric Chemistry and Physics Discussions, 1–22, 2019. DOI: 10.5194/acp-2019-364.

Authorship statement

This article was written by me and is based on the field data from two campaigns during July–August 2017 (Stuttgart01) and February–March 2018 (Stuttgart02) in the city of Stuttgart, one of the most polluted cities in Germany (Schwartz et al., 1991; Süddeutsche Zeitung, 2016; Office for Environmental Protection, 2016), with a focus on the seasonal variations of the molecular composition and volatility of OA. I was responsible for the operation and calibrations of AMS, filter sampling and analysis by FIGAERO-CIMS in the laboratory, as well as the data analysis, interpretation, and the writing of this article. Currently this article is under review in *Atmospheric Chemistry and Physics*.

Atmos. Chem. Phys. Discuss., https://doi.org/10.5194/acp-2019-364
Manuscript under review for journal Atmos. Chem. Phys.
Discussion started: 30 April 2019

Atmospheric Chemistry and Physics Discussions

Seasonal characteristics of organic aerosol chemical composition and volatility in Stuttgart, Germany

Wei Huang[1,2], Harald Saathoff[1], Xiaoli Shen[1,2], Ramakrishna Ramisetty[1,3], Thomas Leisner[1,4], Claudia Mohr[5,*]

[1]Institute of Meteorology and Climate Research, Karlsruhe Institute of Technology, Eggenstein-Leopoldshafen, 76344, Germany

[2]Institute of Geography and Geoecology, Working Group for Environmental Mineralogy and Environmental System Analysis, Karlsruhe Institute of Technology, Karlsruhe, 76131, Germany

[3]Now at: TSI Instruments India Private Limited, Bangalore, 560102, India

[4]Institute of Environmental Physics, Heidelberg University, Heidelberg, 69120, Germany

[5]Department of Environmental Science and Analytical Chemistry, Stockholm University, Stockholm, 11418, Sweden

**Correspondence to*: claudia.mohr@aces.su.se

Abstract. Chemical composition and volatility of organic aerosol (OA) particles were investigated during July–August 2017 and February–March 2018 in the city of Stuttgart, one of the most polluted cities in Germany. Total non-refractory particle mass was measured with a high-resolution time-of-flight aerosol mass spectrometer (HR-ToF-AMS; hereafter AMS). Aerosol particles were collected on filters and analyzed in the laboratory with a filter inlet for gases and aerosols coupled to a high-resolution time-of-flight chemical ionization mass spectrometer (FIGAERO-HR-ToF-CIMS; hereafter CIMS), yielding the molecular composition of oxygenated OA (OOA) compounds. While the average organic mass loadings are lower in the summer period (5.1 ± 3.2 µg m^{-3}) than in the winter period (8.4 ± 5.6 µg m^{-3}), we find relatively larger mass contributions of organics measured by AMS in summer (68.8 ± 13.4 %) compared to winter (34.8 ± 9.5 %). CIMS mass spectra show OOA compounds in summer have O:C ratios of 0.82 ± 0.02 and are more influenced by biogenic emissions, while OOA compounds in winter have O:C ratios of 0.89 ± 0.06 and are more influenced by biomass burning emissions. Volatility parametrization analysis shows that OOA in winter is less volatile with higher contributions of low volatile organic compounds (LVOC) and extremely low volatile organic compounds (ELVOC). We partially explain this by the higher contributions of compounds with shorter carbon chain lengths and higher number of oxygen atoms, i.e. higher O:C ratios in winter. Organic compounds desorbing from the particles deposited on the filter samples also exhibit a shift of signal to higher desorption temperatures (i.e. lower apparent volatility) in winter. This is consistent with the relatively higher O:C ratios in winter, but may also be related to higher particle viscosity due to the higher contributions of larger molecular-weight LVOC and ELVOC, interactions between different species and/or particles (particle matrix), and/or thermal decomposition of larger molecules. The results suggest that whereas lower temperature in winter may lead to increased partitioning of semi-volatile organic compounds (SVOC) into the particle phase, this does not result in a higher overall volatility of OOA in winter, and that the difference in

Atmos. Chem. Phys. Discuss., https://doi.org/10.5194/acp-2019-364
Manuscript under review for journal Atmos. Chem. Phys.
Discussion started: 30 April 2019

Atmospheric Chemistry and Physics Discussions

sources and/or chemistry between the seasons plays a more important role. Our study provides insights into the seasonal variation of molecular composition and volatility of ambient OA particles, and into their potential sources.

1 Introduction

Air pollution has significant impacts on human health (D'Amato et al., 2014), visibility (Majewski et al., 2014), and also interacts with climate change (Seinfeld and Pandis, 2016). Due to rapid urbanization, industrialization, and growing human population, air quality in urban environments has become a severe issue in more and more cities all over the world, particularly in densely populated megacities (Guttikunda et al., 2014; Chan and Yao, 2008; Mayer, 1999; Marlier et al., 2016). Air quality in urban environments is influenced by emissions, e.g. from sources such as industrial processes, automobile traffic, and domestic heating, and also by meteorological conditions (e.g. solar radiation, wind, temperature, precipitation), atmospheric dispersion, chemical transformation, location, and topography (D'Amato et al., 2014; Baumbach and Vogt, 2003; Kinney, 2018). Moreover, air pollution is not limited within the boundaries of urban areas, but can be transported over long distances and contribute to background pollution on the regional to global scale (Baklanov et al., 2016).

The most abundant air pollutants are nitrogen dioxide (NO_2), ozone (O_3), sulfur dioxide (SO_2), and particulate matter (PM; D'Amato et al., 2014). Despite its abundance and important impacts on climate and health, PM sources, physicochemical transformation, and fate in the atmosphere still remain to be fully understood in urban areas. This is especially true for the organic fraction (Hallquist et al., 2009; Fuzzi et al., 2015). Organic aerosol (OA) often makes up a significant fraction of submicron particulate mass in urban areas (Hallquist et al., 2009; Jimenez et al., 2009). OA can be directly emitted into the atmosphere from sources such as fossil fuel combustion and biomass burning (primary organic aerosol, POA), or be formed in the atmosphere from the oxidation of gas-phase precursors (secondary organic aerosol, SOA). POA is dominated by vehicular emissions in urban environments (Bhattu, 2018). SOA, which dominates the global budget of OA (Shrivastava et al., 2015), can be of biogenic and/or anthropogenic origin with biogenic sources dominating on a global scale (Heald et al., 2008). SOA also generally makes up the biggest mass fraction of OA in urban areas, as observed e.g. in Mexico City (Volkamer et al., 2006; Kleinman et al., 2008), some heavily urbanized areas in the U.S. (de Gouw et al., 2005; Zhang et al., 2005), and during the severe haze pollution events in the big cities in China (Huang et al., 2014). In European cities, most of the OA mass observed consists of oxygenated compounds (oxygenated organic aerosol, OOA), and most OOA is of secondary origin and thus SOA (Lanz et al., 2007; Jimenez et al., 2009; Zhang et al., 2007; El Haddad et al., 2013). Robinson et al. (2007) suggested that semi-volatile and intermediate VOC may play a dominant role in SOA formation in urban locations. In order to design effective mitigation strategies for urban air pollution, it is therefore of great importance to identify the sources of OA, and especially SOA, in urban areas.

Source apportionment of OA has been advanced by the application of positive matrix factorization (PMF) to aerosol mass spectrometer (AMS) or aerosol chemical speciation monitor (ACSM) data (Canonaco et al., 2015; Crippa et al., 2014; Ulbrich et al., 2009). However, the distinction of OOA sources (biogenic or anthropogenic) by AMS- or ACSM-PMF remains difficult due to excessive fragmentation and thus loss of molecular information in the AMS or ACSM. The recent advent of new methods provides more insights into the molecular composition of OA, such as linear trap quadrupole (LTQ) Orbitrap mass spectrometry (Daellenbach et al., 2019), filter inlet for gases and aerosols coupled to a high-resolution time-of-flight chemical ionization mass spectrometer (FIGAERO-HR-ToF-CIMS; Huang et al., 2019), and the newly developed extractive electrospray ionization time-of-flight

Atmos. Chem. Phys. Discuss., https://doi.org/10.5194/acp-2019-364
Manuscript under review for journal Atmos. Chem. Phys.
Discussion started: 30 April 2019

Atmospheric Chemistry and Physics Discussions

mass spectrometer (EESI-ToF; Qi et al., 2019). Whereas AMS-/ACSM-PMF is not directly able to reveal OOA sources, it separates OOA into factors with different degrees of oxygenation and thus presumed volatility, such as semi-volatile oxygenated organic aerosol (SV-OOA) and low-volatile oxygenated organic aerosol (LV-OOA; Ulbrich et al., 2009; Jimenez et al., 2009; Lanz et al., 2007). Abovementioned state-of-the-art instruments (e.g. Orbitrap, FIGAERO-HR-ToF-CIMS, EESI-ToF) enable the link between the molecular composition of OA and its physicochemical properties by use of molecular information in volatility parameterizations to calculate effective saturation mass concentrations (C_{sat}) of different compounds (Li et al., 2016; Donahue et al., 2011). This can be used to define e.g. volatility basis sets (VBS), a framework that has been proposed and widely used for grouping the organic compounds into volatility classes (or bins) based on their C_{sat} values (Donahue et al., 2006; 2011; 2012; Cappa and Jimenez, 2010).

Volatility determines whether an organic compound partitions into the particle phase and contributes to OA particulate mass. It is thus an important physicochemical property of OA that influences the lifetime of OA and with that air quality. As a consequence of the connection between a compound's molecular composition and structure with its volatility, different types of OA fall into different categories of volatility. For e.g. OA measured in Mexico City, biomass burning OA (BBOA) was found to be the most volatile, followed by hydrocarbon-like OA (HOA), SV-OOA, and LV-OOA (Cappa and Jimenez, 2010). Isoprene epoxydiol (IEPOX) derived SOA was observed to have the highest volatility of the OA measured in the southeastern U.S. (Lopez-Hilfiker et al., 2016). As ambient particles generally consist of a matrix of thousands of different compounds, OA apparent volatility can also be influenced by particle-phase diffusion limitations, e.g. due to amorphous phase state and/or the presence of a high mass fraction of oligomers (Vaden et al., 2011; Roldin et al., 2014; Cappa and Wilson, 2011; Yli-Juuti et al., 2017; Huang et al., 2018). Overall, the relationship between OA molecular composition and its volatility, and how this relationship is influenced by environmental conditions and particle physicochemical properties, are not well characterized, particularly for field data.

Here we present detailed chemical composition measurements of OA from July–August 2017 and February–March 2018 in the city of Stuttgart, Germany. We investigate the molecular composition and volatility of OA particles, and discuss their seasonal variations as well as their potential sources. Stuttgart, a city located in southwest Germany with a population of more than 600000 in a metropolitan area of 2.6 million inhabitants, is an important industrial center in Germany. It is situated in the steep valley of the Neckar river, in a "bowl" surrounded by a variety of hills, small mountains, and valleys. The complex topography can prevent the dispersion of air pollutants, and the location is characterized by low wind speeds and weak air circulation (Schwartz et al., 1991; Hebbert and Webb, 2012). Air quality has been a long-standing concern in Stuttgart, as it is one of the most polluted cities in Germany (Schwartz et al., 1991; Süddeutsche Zeitung, 2016; Office for Environmental Protection, 2016); however only few detailed studies are available. For the year 2017, the state environmental protection agency, LUBW (Landesanstalt für Umwelt Baden-Württemberg), attributes 58 % of the annual mean PM_{10} at their monitoring station "Am Neckartor" in downtown Stuttgart to road traffic (45 % abrasion, 7 % exhaust, 6 % secondary formation), 8 % to small and middle size combustion sources, and 27 % to regional background (LUBW, 2019). Mayer (1999) showed the temporal variability of urban air pollutants (NO, NO_2, O_3, and O_x (sum of NO_2 and O_3)) caused by motor traffic in Stuttgart based on more than 10 years of observations, with higher NO concentrations in winter and higher O_x concentrations in summer. Bari et al. (2011) characterized air pollutants such as polycyclic aromatic hydrocarbons (PAHs) and other wood smoke tracer compounds (levoglucosan, methoxyphenols) from wood-burning in the residential areas of Dettenhausen (about 30 km south of Stuttgart) and

Atmos. Chem. Phys. Discuss., https://doi.org/10.5194/acp-2019-364
Manuscript under review for journal Atmos. Chem. Phys.
Discussion started: 30 April 2019

Atmospheric Chemistry and Physics Discussions

attributed 57% of the ambient PM_{10} pollution to hardwood combustion during wintertime. Our study therefore adds an important piece of information on air quality in Stuttgart by investigating the chemical composition, physicochemical properties, and potential sources of the OA particles in this city.

2 Methodology

2.1 Measurement site

We performed particle and trace gas measurements from July 5th to August 17th, 2017 and from February 5th to March 5th, 2018 in the city of Stuttgart, Germany (48°47'55.1"N, 9°12'13.5"E). The measurement site was located near the park "Unterer Schlossgarten" of Stuttgart and can be classified as an urban background site. The only nearby source is a parcel distribution center with delivery trucks passing by with low frequency during daytime. It was set up on a bridge over a train track about 2.2 km northeast of the Stuttgart main station with frequent train traffic (electric). The air quality monitoring station of LUBW, "Am Neckartor", is 1.5 km southwest and one of the busiest roads in Stuttgart, B14 (LUBW, 2019), is about 360 m southwest of the measurement location.

All instruments were set up in a temperature-controlled measurement container kept at ~298 K. The container has been described elsewhere (Huang et al., 2019; Shen et al., 2018). All sampling inlets were located 3.7 m above ground level and 1.5 m above the container roof. An overview of instruments and parameters measured is given in Table S1 in the Supplement.

2.2 Meteorological, particle and trace gas measurements

Temperature, relative humidity, wind direction, wind speed, global radiation, pressure, and precipitation data were measured by a meteorological sensor (WS700, Lufft GmbH; see Table S1). The main wind directions during the campaign were southwest during the summer and northeast during the winter. Trace gases (O_3, CO_2, NO_2, SO_2) were measured with the corresponding sensors (Table S1). Particle number concentrations were recorded with two condensation particle counters (a CPC3022, measuring particles with mobility diameters larger than 7 nm, and a CPC3776, measuring particles with mobility diameters larger than 2.5 nm, both TSI Inc.). Particle size distributions were measured with a nanoscan scanning mobility particle sizer (NanoScan SMPS3910, measuring particles with mobility diameters between 10 nm and 420 nm, TSI Inc.). Black carbon (BC) concentrations were measured with an Aethalometer (AE51, Aethlabs Inc.).

A high-resolution time-of-flight aerosol mass spectrometer (HR-ToF-AMS, Aerodyne Research Inc., hereafter AMS) equipped with an aerodynamic high-pressure lens (Williams et al., 2013) was deployed to continuously measure total non-refractory particle mass as a function of size (up to 2.5 µm particle aerodynamic diameter d_{va}) at a time resolution of 0.5 min. The AMS inlet was connected to a $PM_{2.5}$ head (flow rate 1 $m^3\ h^{-1}$, Comde-Derenda GmbH) and a stainless steel tube of 3.45 m length (flow rate 0.1 L min^{-1}, residence time 0.9 s). AMS data were analyzed with the AMS data analysis software packages SQUIRREL (version 1.60C) and PIKA (version 1.20C). Polytetrafluoroethylene (PTFE) filters (Zefluor PTFE membrane, 2 µm pore size, 25 mm diameter, Pall Corp.), which were prebaked at 200 °C in an oven overnight and stored in clean filter slides, were deposited during daytime (between 10:00 and 16:00) using a stainless steel filter holder connected to a PM_{10} head (flow rate 1 $m^3\ h^{-1}$, Comde-Derenda GmbH) via a stainless steel tube and conductive tubing of 2.85 m length (flow rate 8.7 L min^{-1} (summer) or 10 L min^{-1} (winter), residence time 0.75 s (summer) or 0.72 s (winter)). Deposition times were varied (20–260

Atmos. Chem. Phys. Discuss., https://doi.org/10.5194/acp-2019-364
Manuscript under review for journal Atmos. Chem. Phys.
Discussion started: 30 April 2019

Atmospheric Chemistry and Physics Discussions

min) based on ambient organic mass concentrations in order to achieve similar mass concentrations deposited on the filter to avoid mass loading effects (Huang et al., 2018; Wang and Ruiz, 2018). A total of 21 filter samples were collected in the summer and 10 in the winter. After deposition, each filter sample was stored in a filter slide, wrapped in aluminium foil, and then stored in a freezer at −20 °C until analysis in the laboratory by a filter inlet for gases and aerosols coupled to a high-resolution time-of-flight chemical ionization mass spectrometer (FIGAERO-HR-ToF-CIMS, Aerodyne Research Inc., hereafter CIMS) deploying iodide (I^-) as reagent ion. Particles collected on the filter were thermally desorbed by a flow of ultra-high purity (99.999 %) nitrogen heated to 200 °C over the course of 35 min. The resulting mass spectral desorption signals are termed thermograms (Lopez-Hilfiker et al., 2014). For individual compounds, signals that peak at distinct desorption temperatures (T_{max}) correlate with their saturation vapor pressure (Lopez-Hilfiker et al., 2015; Mohr et al., 2017); however, interference from isomers with different vapor pressures or thermal fragmentation of larger oligomeric molecules can lead to more complex, multimodal thermograms (Lopez-Hilfiker et al., 2015). Integration of thermograms of individual compounds yields their total particle-phase signal. We assume the sensitivity to be the same for all compounds measured by CIMS (Huang et al., 2019) and convert the signal to mass so that the molecular weight of a compound is taken into account. In this study we do not attempt to derive any atmospheric mass concentrations from these filter measurements, since the actual deposited area of aerosol particles on the filter was larger than the area of the desorption flow, and the deposition was not evenly distributed across the filter. We therefore focus on the molecular composition and volatility distributions of OA particles, their seasonal variations, and the interpretation of these observations for potential sources. In order to correct for filter backgrounds, we collected prebaked clean filters from the measurement site without deposition flow for both winter and summer. Field blank samples for winter and summer were analyzed by CIMS in the laboratory and used for background subtraction.

3 Results and discussion

3.1 Particulate OA mass loadings

We observe higher total non-refractory $PM_{2.5}$ mass concentrations measured by AMS in winter (27.0 ± 11.9 μg m^{-3}, average ± 1 standard deviation) than in summer (7.1 ± 3.3 μg m^{-3}) at this measurement site (Figure S1). Similar observations were also made for other central European locations, e.g. Zurich, Switzerland (Jimenez et al., 2009; Zhang et al., 2007). Reasons for this observation are differences in emission sources between the seasons, boundary layer height dynamics, and/or meteorological conditions (Canonaco et al., 2015; Daellenbach et al., 2019; Baumbach and Vogt, 2003). The surface inversion, which develops by radiative cooling of the ground and is dissolved from the bottom up by solar radiation and heating up of the ground (Baumbach and Vogt, 2003), is expected to be stronger in winter due to lower ambient temperature and global radiation (Figure S2), weaker air circulation (i.e. wind speed, Figure S3), and less precipitation. Air pollutants are therefore more likely to be kept beneath this inversion and have longer local residence time in the atmosphere in winter. While the average organic mass loadings measured by AMS are lower in summer (5.1 ± 3.2 μg m^{-3}) than in winter (8.4 ± 5.6 μg m^{-3}; see Fig. S1), organics contribute relatively more mass to total non-refractory $PM_{2.5}$ measured by AMS in summer (68.8 ± 13.4 %) compared to winter (34.8 ± 9.5 %; see Fig. S1). Contributions of fragments containing only C and H atoms (CH) or also one oxygen atom (CHO_1) or more than one oxygen atoms (CHO_{gt1}) to total OA measured by AMS are similar, with slightly higher contributions of CH and CHO_1 in summer (CH: 29.4 ± 3.9 %; CHO_1: 15.7 ± 1.6

Atmos. Chem. Phys. Discuss., https://doi.org/10.5194/acp-2019-364
Manuscript under review for journal Atmos. Chem. Phys.
Discussion started: 30 April 2019

Atmospheric Chemistry and Physics Discussions

%) compared to winter (CH: 27.9 ± 4.6 %; CHO_1: 15.3 ± 1.9 %) and slightly lower contributions of CHO_{gt1} in summer (14.0 ± 2.6 %) compared to winter (15.8 ± 2.8 %). This is also reflected in the higher elemental oxygen-to-carbon (O:C) ratios measured by AMS in winter (0.61 ± 0.12) than in summer (0.55 ± 0.10). The results imply that OA is more oxygenated in winter. Due to fragmentation of organic molecules during the ionization process in the AMS, molecular information of OA is lost. This information is able to retrieve from the filter samples analyzed by CIMS. Due to the fact that the iodide CIMS is selective towards polarizable and thus oxygenated compounds (Lee et al., 2014), the organic compounds measured by CIMS are oxygenated organic aerosol (OOA). In the next section we will discuss the molecular composition of OOA measured by CIMS.

3.2 Molecular composition of OOA

Figure 1a and 1c show a comparison of CIMS mass spectral patterns of all CHOX compounds ($C_{x\geq1}H_{y\geq1}O_{z\geq1}X_{0-n}$ detected as clustered with I^-, with X being different atoms like N, S, Cl, or a combination thereof; 1808 out of a total of 2138 identified compounds and accounting for >96 % of total signals), and CHON compounds only for summer and winter (panels b, d). Mass spectra shown were normalized to the sum of the deposited mass of all detected CHOX compounds. Although the absolute CHOX mass concentrations are uncertain, the time series of the sum of the deposited mass of all detected CHOX compounds follows the trend of the OA concentrations measured by AMS quite well. CHO compounds (compounds containing only C, H, and O atoms) are the dominating group and make up 79.4 ± 3.3 % of total CHOX in summer and 74.6 ± 2.2 % of total CHOX in winter, followed by CHON compounds with 20.1 ± 3.4 % of total CHOX in summer and 24.6 ± 2.4 % of total CHOX in winter. CHON compounds contribute relatively more mass in winter (also reflected in the organic bound nitrate fraction ($OrgNO_3$, i.e., organonitrates) from AMS data (summer: 0.3 ± 0.2 µg m^{-3}; winter: 1.7 ± 1.1 µg m^{-3}), determined assuming an NO_2^+/NO^+ ratio of $OrgNO_3$ of 0.1; Farmer et al., 2010; Kiendler-Scharr et al., 2016; see Figure S4 and S5), while CHO compounds contribute relatively more mass in summer. This is possibly due to the higher daytime O_3 concentrations in summer and higher daytime NO_2 concentrations in winter (Figure S6) as well as different emission sources. Contributions of some biogenic marker compounds are higher in summer (Fig. 1a–b), particularly $C_8H_{12}O_5$ (molecular formula corresponding to 2-hydroxyterpenylic acid identified in α-pinene SOA by Claeys et al., 2009; Kahnt et al., 2014) and $C_8H_{11}O_7N$ (identified in the laboratory as α-pinene oxidation product by Lee et al., 2016). We also observe good correlations (Pearson's R: 0.85; Figure S7a) between our summer mass spectra and the summer daytime mass spectra acquired in 2016 near Karlsruhe (a city in southwest Germany, about 70 km northwest of Stuttgart; Huang et al., 2019), indicative of the regional nature of sources and/or chemistry in summer. We therefore conclude that the majority of the precursor VOC for OOA presented here in summer are most likely of biogenic origin, despite the urban location of the measurement site.

Significantly higher contributions of $C_6H_{10}O_5$ (molecular formula corresponding to levoglucosan, a tracer for biomass burning; Saarnio et al., 2010) are observed in winter compared to summer (Fig. 1c). Besides, higher contributions of $C_6H_5O_3N$, $C_7H_7O_3N$, $C_6H_5O_4N$, and $C_7H_7O_4N$ (molecular formulae corresponding to nitrated phenols, tracers for biomass burning identified by Mohr et al., 2013) are also observed in winter (Fig. 1d). Some of these compounds were also observed in the central European city of Zurich, Switzerland in winter (Daellenbach et al., 2019). We cannot completely exclude that these compounds may have contributions from vehicular emissions (Tong et al., 2016). However, significantly higher contributions of levoglucosan and nitrated phenols indicate that biomass burning emissions are a dominant contributor to OOA in Stuttgart in winter. In addition to compounds from biomass burning, we also observe similar patterns of contributions of CHON compounds with

Atmos. Chem. Phys. Discuss., https://doi.org/10.5194/acp-2019-364
Manuscript under review for journal Atmos. Chem. Phys.
Discussion started: 30 April 2019

Atmospheric Chemistry and Physics Discussions

m/z between 300–400 Th (also dominated by $C_8H_{11}O_7N$), and high contributions of $C_8H_{12}O_4$ (molecular formula corresponding to terpenylic acid identified in α-pinene SOA by Claeys et al., 2009) and $C_8H_{12}O_6$ (molecular formula corresponding to 3-methyl-1,2,3-butanetricarboxylic acid (MBTCA) in α-pinene SOA identified by Szmigielski et al., 2007; Müller et al., 2012) in winter. After removing the five biomass burning tracer compounds ($C_6H_{10}O_5$, $C_6H_5O_3N$, $C_7H_7O_3N$, $C_6H_5O_4N$, and $C_7H_7O_4N$), good correlations (Pearson's R: 0.70; Figure S7b) are observed between summer mass spectra and winter mass spectra, indicating that biogenic emissions may also contribute significantly to the OOA particulate mass in winter. In addition, in both summer and winter, contributions of $C_7H_8O_5$ (identified in the laboratory as toluene oxidation product by Hinks et al., 2018; Molteni et al., 2018) are also observed, with relatively higher contributions in winter than in summer, indicating anthropogenic influences related to traffic or industrial activities (EPA, 1994).

In the following we will have a closer look at the bulk molecular composition for winter and summer daytime OOA measured by CIMS. Consistent with the O:C ratios measured by AMS (winter: 0.61 ± 0.12; summer: 0.55 ± 0.10), higher O:C ratios are also observed by CIMS in winter (0.89 ± 0.06) compared to summer (0.82 ± 0.02), despite lower ambient temperature and weaker global radiation in winter (see Fig. S2). The AMS O:C ratios are expected to be lower than those of the organic compounds measured by iodide CIMS, as the latter is selective towards oxygenated compounds (Lee et al., 2014). Mass contributions of CHO and CHON with different number of oxygen atoms per molecule to total CHOX compounds as a function of the number of carbon atoms are shown in Figure 2. C_8HO compounds exhibit the highest mass contributions in summer, while C_6HO compounds surpass C_8HO compounds in winter due to the large contributions of levoglucosan ($C_6H_{10}O_5$; see Fig. 2a and 2c). The mass distribution of CHO compounds in winter also exhibits higher contributions from compounds with 1–6 carbon atoms and 4, 5 (levoglucosan), 7–9 oxygen atoms, while in summer higher contributions from compounds with 7–10 carbon atoms and 5–7 oxygen atoms are observed. This indicates that the slightly higher oxidation levels (or O:C ratios) in winter are related to both shorter carbon chain lengths and higher number of oxygen atoms of the OOA compounds compared to summer (see also Figure S8). In addition, relatively higher contributions of compounds with larger number of carbon atoms (C16–23) are also observed in winter (Fig. 2). A similar pattern can be found for CHON compounds (Fig. 2b and 2d). $C_{9-10}HON$ compounds exhibit the highest mass contributions in summer, similar to what we observed in 2016 in summer near the city of Karlsruhe, where these compounds were determined to originate from biogenic VOC emissions (Huang et al., 2019). However, the filters in Stuttgart were deposited during daytime, therefore the chemistry involved in the formation of these CHON compounds likely involves the reaction of organic peroxy radicals (RO_2) with NO_x instead of night-time NO_3 radical chemistry. In winter, C_6HON relative contributions exceed those from $C_{9-10}HON$ compounds, similar to the pattern of CHO compounds, indicative of similar sources (biomass burning emissions). Furthermore, in summer CHON compounds are dominated by compounds with 6–9 oxygen atoms, while in winter significantly higher contributions from compounds with 5–7 carbon atoms and 3–4 oxygen atoms are observed, mostly due to nitrated phenols ($C_{6-7}H_{5,7}O_{3-4}N$; see also Fig. 1d).

The results imply the importance of non-fossil OA formation from biogenic and/or biomass burning influences in different seasons even in a city with high traffic emissions mainly based on fossil fuel combustion (LUBW, 2019). This is similar to previous studies in other European cities such as Barcelona, Spain (Mohr et al., 2012) and some megacities in China (Ni et al., 2019). In the next section, we investigate the volatility of OOA compounds measured by CIMS, which can influence their lifetime in the atmosphere and thus air quality.

Atmos. Chem. Phys. Discuss., https://doi.org/10.5194/acp-2019-364
Manuscript under review for journal Atmos. Chem. Phys.
Discussion started: 30 April 2019

Atmospheric Chemistry and Physics Discussions

3.3 Seasonal changes of volatility of OOA

3.3.1 Volatility distribution

Effective saturation mass concentrations (C_{sat}), a measure for volatility of a compound, were parameterized for each CHO and CHON compound using the approach by Li et al. (2016). The CHO and CHON compounds were then grouped into a 25-bin volatility basis set (VBS; Donahue et al., 2006) based on their $\log_{10}C_{sat}$ values (Figure 3). Organic compounds with C_{sat} lower than 10^{-5} µg m^{-3}, between 10^{-4}–10^{-2} µg m^{-3}, and higher than 10^{-1} µg m^{-3} are termed extremely low volatile organic compounds (ELVOC), low volatile organic compounds (LVOC), and semi-volatile organic compounds (SVOC), respectively. As shown in Fig. 3a, organic compounds with C_{sat} between 10^{2}–10^{3} µg m^{-3} make up the biggest mass contributions during daytime in both summer and winter, suggesting that SVOC is the dominating group in both seasons (summer: 74.2 ± 3.4 %; winter: 66.7 ± 4.9 %; see Fig. 3b–c). The dominating compounds in these volatility bins come from the group of $C_{8–12}HO$ compounds in summer and from the group of $C_{1–7}HO$ compounds with relatively higher O:C ratios in winter (Figure S9a and S9c). Dominant compounds are 2-hydroxyterpenylic acid ($C_8H_{12}O_5$) and levoglucosan ($C_6H_{10}O_5$) for summer and winter, respectively (compare also to Fig. 1a and 1c). Non-negligible contributions from $C_{1–7}HON$ compounds are also observed in these volatility bins in winter (Fig. S9b and S9d), mainly from nitrated phenols ($C_{6–7}H_{5,\ 7}O_{3–4}N$; compare also to Fig. 1d). In winter we also observe significant contributions of SVOC with C_{sat} between 10^{5}–10^{6} µg m^{-3} in the particle phase. Since winter is much colder compared to summer (Fig. S2), compounds of higher volatility are expected to be able to condense in winter. However, we may also have contributions from thermal decomposition products of oligomers to some of these low-molecular weight SVOC (also reflected in the multi-mode thermograms for CHOX compounds with 1–5 carbon atoms; see Figure S10). But for the larger compounds, such as dimers and trimers, contributions of thermal decomposition products become negligible (i.e. thermograms are unimodal; Huang et al., 2018; Wang and Ruiz, 2018). LVOC and ELVOC, which include compounds with larger molecular weight, exhibit higher mass contributions in winter (LVOC: 26.4 ± 3.1 %; ELVOC: 6.9 ± 1.9 %) than in summer (LVOC: 21.7 ± 2.5 %; ELVOC: 4.1 ± 1.1 %; see Fig. 3). The average mass-weighted $\log_{10}C_{sat}$ value is 1.05 ± 0.28 µg m^{-3} for summer and 0.63 ± 0.44 µg m^{-3} for winter.

The results indicate that even though the lower ambient temperatures in winter may lead to increased partitioning of SVOC into the particle phase, the bulk winter OOA is less volatile. Similar results were also observed in Zurich, Switzerland by Canonaco et al. (2015) based on AMS data. The lower volatility of OOA in Stuttgart in winter compared to summer can be partially explained by the higher contributions of compounds with shorter carbon chain lengths and higher number of oxygen atoms in winter (i.e. higher O:C ratios; see Fig. S8), and the relatively higher contribution of larger molecules (number of carbons atoms >16; see also Fig. 2). Differences in aging processes (functionalization, fragmentation, and oligomerization; Jimenez et al., 2009) between the seasons may also play a role, since Keller and Burtscher (2017) found that aging processes reduce the volatility of OA from biomass burning.

3.3.2 Variation of the maximum desorption temperatures (T_{max})

Thermograms resulting from the thermal desorption of the filter samples were analyzed. T_{max}, the maximum desorption temperatures at which the signals of a compound peak, were compared for summer and winter. Figure 4a–b shows the campaign-average high resolution two-dimensional (2D) thermogram of CHOX compounds, a

Atmos. Chem. Phys. Discuss., https://doi.org/10.5194/acp-2019-364
Manuscript under review for journal Atmos. Chem. Phys.
Discussion started: 30 April 2019

framework developed recently to investigate the OOA thermal desorption behavior over the entire *m/z* and T_{max} range (Wang and Ruiz, 2018). Each thermogram of each individual compound in the 2D space was normalized to its maximum signal. Due to the CHOX compounds containing at least 1 carbon atom, 1 hydrogen atom, and 1 oxygen atom, and being detected as clustered with I^- (*m/z* 126.9050 Th), the smallest *m/z* in the 2D thermogram is 168 Th. As shown in Fig. 4a–b, the majority of the OOA compounds exhibit higher T_{max} with a wider spread across different CHOX compounds in winter (114.4 ± 17.1 °C, average ± 1 standard deviation) compared to summer (96.8 ± 18.2 °C; see also Figure S11). For the summer period, T_{max} decreases from 160 °C to 60 °C for *m/z* 168–280 Th, stays relatively constant at 60–110 °C for *m/z* 280–550 Th, and increases from 60 °C to 120 °C for *m/z* >550 Th; for the winter period, T_{max} decreases from 160 °C to 80 °C for *m/z* 168–280 Th, stays relatively constant at 2 T_{max} regions (one region at 80–100 °C and the other one at 110–130 °C) for *m/z* 280–550 Th, and increases from 80 °C to 130 °C for *m/z* >550 Th (see also Fig. S11). The high T_{max} values for *m/z* <280 Th (SVOC range) result from multi-mode thermograms with thermal decomposition of larger molecules (Lopez-Hilfiker et al., 2015). A similar picture can be seen in the campaign-average thermograms for the sum of the signals of all CHOX, CHO, and CHON compounds detected (normalized to the maximum; Fig. 4c). The pattern of the summer 2D thermogram in Stuttgart, particularly the "zigzag"-like behavior of e.g. *m/z* 280–380 Th (see Figure S12a), is comparable to that from alkane-Cl SOA at high RH (67 %) and high NO_x conditions observed by Wang and Ruiz (2018), and was explained by increased hydroxyl functionalization over ketone functionalization. The winter 2D thermogram in Stuttgart also has a "zigzag"-like pattern but less pronounced and at higher T_{max} (see Fig. S12b).

The results indicate a generally lower apparent volatility (i.e. higher T_{max}) of bulk OOA in winter, in agreement with the results based on the C_{sat} parametrization (see also Fig. 3). Recent studies show that T_{max} of a compound can be influenced by isomers (Thompson et al., 2017), thermal fragmentation of larger molecules during the heating of the filter (Lopez-Hilfiker et al., 2015), variations in filter mass loading (Huang et al., 2018; Wang and Ruiz, 2018), and/or differences in particles' viscosity (Huang et al., 2018). Since deposited organic mass loadings on the filter samples were similar for summer and winter, we can exclude a mass loading effect on the T_{max} results presented here. However, we also observed by eye that the filter samples in winter were more blackish, possibly due to the higher black carbon (BC) concentrations during daytime (10:00–16:00) in winter (1247 ± 112 ng m^{-3}) compared to summer (1032 ± 311 ng m^{-3}). If (and how) the higher BC concentrations can affect the desorption behaviors of organic compounds (i.e. interactions between organic compounds and BC) is still unknown and requires further laboratory studies. Higher O:C ratios (Buchholz et al., 2019), and/or higher oligomer mass fractions (Huang et al., 2019; compare to LVOC and ELVOC mass contributions in Fig. 3b–c) have been shown to be correlated with higher T_{max}, which is in agreement with our mass spectral observations in winter. Besides, higher inorganic sulfate concentrations in winter (see Fig. S1) might also play a role in the formation of low volatile but thermally unstable organic compounds which can only be detected as their decomposition products with FIGAERO-CIMS (Gaston et al., 2016; Riva et al., 2019). If assuming that the winter thermograms are more influenced by thermal decomposition of oligomers than the summer thermograms, which artificially shifts the molecular formula-based volatility distribution towards higher volatility, the winter OOA are expected to be even less volatile.

4 Conclusions and atmospheric implications

Atmos. Chem. Phys. Discuss., https://doi.org/10.5194/acp-2019-364
Manuscript under review for journal Atmos. Chem. Phys.
Discussion started: 30 April 2019

Atmospheric Chemistry and Physics Discussions

In this paper, chemical composition and volatility of OA particles were investigated during July–August 2017 and February–March 2018 in the city of Stuttgart, one of the most polluted cities in Germany. The average organic mass loadings measured by AMS are lower in summer (5.1 ± 3.2 μg m^{-3}) than in winter (8.4 ± 5.6 μg m^{-3}), but the relative contributions of OA to total non-refractory $PM_{2.5}$ mass measured by AMS are higher in summer (68.8 ± 13.4 %) compared to winter (34.8 ± 9.5 %). This can be explained by the differences in emission sources between the seasons, boundary layer height dynamics, and/or meteorological conditions (Canonaco et al., 2015; Daellenbach et al., 2019; Baumbach and Vogt, 2003). CIMS mass spectra from filter samples collected at the measurement site during daytime (10:00–16:00) show OOA compounds in summer have O:C ratios of 0.82 ± 0.02 and are more influenced by biogenic emissions (as shown by e.g. tracers of α-pinene oxidation products), while OOA compounds in winter have slightly higher O:C ratios (0.89 ± 0.06) and are more influenced by biomass burning emissions (as shown by e.g. signals of levoglucosan and nitrated phenols).

The apparent volatility of the OOA compounds varies between the two seasons. OOA in winter is found to be less volatile, which is reflected in the higher contributions of LVOC and ELVOC in the VBS, as well as in the higher maximum desorption temperatures (T_{max}) of the organic compounds desorbing from the particles deposited on the filter samples. Potential possible reason for the lower apparent volatility of winter OOA is the increased residence time of air masses over Stuttgart due to the stronger surface inversion and thus longer atmospheric aging time of the OOA compounds, leading to a reduction in volatility (Keller and Burtscher, 2017; Jimenez et al., 2009). This is also consistent with the higher O:C ratios and the higher mass contributions of larger molecular-weight LVOC and ELVOC in winter. Since the OOA observed in the winter period also shows influence from biogenic emissions, the sources for the LVOC and ELVOC may partly be biogenic. In addition, interactions between different species and/or particles (particle matrix; Huang et al., 2018) due to higher BC, OA and inorganic concentrations, such as the intermolecular interactions between biomass burning compounds and biogenic/anthropogenic organic compounds and/or the interactions between organic compounds, inorganic compounds, and BC, might also play a role in the reduction of volatility of aerosol particles in winter. Overall, the lower apparent volatility of the winter OOA compounds could be caused by higher O:C ratios, but may also be related to the higher particle viscosity due to the higher mass contributions of larger molecular-weight LVOC and ELVOC, interactions between different species and/or particles deposited on the filter (particle matrix; Huang et al., 2018), and/or thermal decomposition of large molecules.

The results suggest that whereas lower temperatures in winter may lead to increased partitioning of SVOC into the particle phase, this does not result in a higher overall volatility of OOA in winter, and that the difference in sources and/or chemistry between the seasons plays a more important role. Our study provides insights into the seasonal variation of molecular composition and volatility of ambient OA particles during daytime, and into their potential sources, which is important for air pollution mitigation in urban locations. Our study shows the important contributions of non-fossil OA from biogenic and biomass burning even in an urban area with high traffic emissions mainly based on fossil fuel combustion (LUBW, 2019). As a consequence, in addition to mitigating traffic emissions, reducing emissions of anthropogenic OOA precursors from e.g. industry and biomass burning may contribute to reducing the environmental and health effects of air pollution.

Data availability

Data are available upon request to the corresponding author.

Atmos. Chem. Phys. Discuss., https://doi.org/10.5194/acp-2019-364
Manuscript under review for journal Atmos. Chem. Phys.
Discussion started: 30 April 2019

Atmospheric Chemistry and Physics Discussions

Author contributions

WH operated AMS and took the filter samples during the two field campaigns, analyzed the filters by CIMS in the laboratory, did the CIMS and AMS data analysis, produced all figures, and wrote and edited the manuscript; HS organized the campaign, did the trace gas, CPC, and black carbon data analysis, and provided suggestions for the data interpretation and discussion; XS operated AMS and took the filter samples during the field campaigns; RR took the filter samples during the summer campaign; TL gave general advice and comments for this manuscript; CM provided suggestions for the data analysis, interpretation, discussion, and edited the manuscript. All authors contributed to the final text.

Competing interests

The authors declare no conflict of interest.

Acknowledgements

Technical support by the staff at IMK-AAF, and financial support by China Scholarship Council (CSC) for Wei Huang and Xiaoli Shen, is gratefully acknowledged. Support by the Deutsche Bahn AG, the University of Stuttgart, and the partners of the project “Three-Dimensional Observation of Atmospheric Processes in Cities (3DO)” (uc2-3do.org/) is gratefully acknowledged.

References

Baklanov, A., Molina, L. T., and Gauss, M.: Megacities, air quality and climate, Atmos Environ, 126, 235–249, https://doi.org/10.1016/j.atmosenv.2015.11.059, 2016.

Bari, M. A., Baumbach, G., Kuch, B., and Scheffknecht, G.: Air pollution in residential areas from wood-fired heating, Aerosol Air Qual Res, 11, 749–757, https://doi.org/10.4209/aaqr.2010.09.0079, 2011.

Baumbach, G., and Vogt, U.: Influence of inversion layers on the distribution of air pollutants in urban areas, Water, Air, & Soil Pollution: Focus, 3, 67–78, https://doi.org/10.1023/A:1026098305581, 2003.

Bhattu, D.: Primary Organic Aerosols. In: Sharma N., Agarwal A., Eastwood P., Gupta T., Singh A. (eds) Air pollution and Control. Energy, Environment, and Sustainability, Springer, Singapore, 109–117 pp., 2018.

Buchholz, A., Lambe, A. T., Ylisirniö, A., Li, Z., Tikkanen, O.-P., Faiola, C., Kari, E., Hao, L. Q., Luoma, O., Huang, W., Mohr, C., Worsnop, D. R., Nizkorodov, S. A., Yli-Juuti, T., Schobesberger, S., and Virtanen, A.: Insights into the O:C dependent mechanisms controlling the evaporation of α-pinene secondary organic aerosol particles, Atmos Chem Phys, 19, 4061–4073, https://doi.org/10.5194/acp-19-4061-2019, 2019.

Canonaco, F., Slowik, J. G., Baltensperger, U., and Prévôt, A. S. H.: Seasonal differences in oxygenated organic aerosol composition: implications for emissions sources and factor analysis, Atmos Chem Phys, 15, 6993–7002, https://doi.org/10.5194/acp-15-6993-2015, 2015.

Cappa, C. D., and Jimenez, J. L.: Quantitative estimates of the volatility of ambient organic aerosol, Atmos Chem Phys, 10, 5409–5424, https://doi.org/10.5194/acp-10-5409-2010, 2010.

Atmos. Chem. Phys. Discuss., https://doi.org/10.5194/acp-2019-364
Manuscript under review for journal Atmos. Chem. Phys.
Discussion started: 30 April 2019

Cappa, C. D., and Wilson, K. R.: Evolution of organic aerosol mass spectra upon heating: implications for OA phase and partitioning behavior, Atmos Chem Phys, 11, 1895–1911, https://doi.org/10.5194/acp-11-1895-2011, 2011.

Chan, C. K., and Yao, X.: Air pollution in mega cities in China, Atmos Environ, 42, 1–42, https://doi.org/10.1016/j.atmosenv.2007.09.003, 2008.

Claeys, M., Iinuma, Y., Szmigielski, R., Surratt, J. D., Blockhuys, F., Van Alsenoy, C., Böge, O., Sierau, B., Gómez-González, Y., Vermeylen, R., Van der Veken, P., Shahgholi, M., Chan, A. W. H., Herrmann, H., Seinfeld, J. H., and Maenhaut, W.: Terpenylic acid and related compounds from the oxidation of α-pinene: Implications for new particle formation and growth above forests, Environ Sci Technol, 43, 6976–6982, https://doi.org/10.1021/es9007596, 2009.

Crippa, M., Canonaco, F., Lanz, V. A., Äijälä, M., Allan, J. D., Carbone, S., Capes, G., Ceburnis, D., Dall'Osto, M., Day, D. A., DeCarlo, P. F., Ehn, M., Eriksson, A., Freney, E., Hildebrandt Ruiz, L., Hillamo, R., Jimenez, J. L., Junninen, H., Kiendler-Scharr, A., Kortelainen, A.-M., Kulmala, M., Laaksonen, A., Mensah, A., Mohr, C., Nemitz, E., O'Dowd, C., Ovadnevaite, J., Pandis, S. N., Petäjä, T., Poulain, L., Saarikoski, S., Sellegri, K., Swietlicki, E., Tiitta, P., Worsnop, D. R., Baltensperger, U., and Prévôt, A. S. H.: Organic aerosol components derived from 25 AMS data sets across Europe using a consistent ME-2 based source apportionment approach, Atmos Chem Phys, 14, 6159–6176, https://doi.org/10.5194/acp-14-6159-2014, 2014.

D'Amato, G., Bergmann, K. C., Cecchi, L., Annesi-Maesano, I., Sanduzzi, A., Liccardi, G., Vitale, C., Stanziola, A., and D'Amato, M.: Climate change and air pollution: Effects on pollen allergy and other allergic respiratory diseases, Allergo J Int, 23, 17–23, https://doi.org/10.1007/s40629-014-0003-7, 2014.

Daellenbach, K. R., Kourtchev, I., Vogel, A. L., Bruns, E. A., Jiang, J., Petäjä, T., Jaffrezo, J.-L., Aksoyoglu, S., Kalberer, M., Baltensperger, U., El Haddad, I., and Prévôt, A. S. H.: Impact of anthropogenic and biogenic sources on the seasonal variation of the molecular composition of urban organic aerosols: a field and laboratory study using ultra-high resolution mass spectrometry, Atmos Chem Phys Discuss, 1–40, https://doi.org/10.5194/acp-2018-1128, 2019.

de Gouw, J. A., Middlebrook, A. M., Warneke, C., Goldan, P. D., Kuster, W. C., Roberts, J. M., Fehsenfeld, F. C., Worsnop, D. R., Canagaratna, M. R., Pszenny, A. A. P., Keene, W. C., Marchewka, M., Bertman, S. B., and Bates, T. S.: Budget of organic carbon in a polluted atmosphere: Results from the New England Air Quality Study in 2002, J Geophys Res-Atmos, 110, D16305, https://doi.org/10.1029/2004JD005623, 2005.

Donahue, N. M., Robinson, A. L., Stanier, C. O., and Pandis, S. N.: Coupled partitioning, dilution, and chemical aging of semivolatile organics, Environ Sci Technol, 40, 2635-2643, https://doi.org/10.1021/es052297c, 2006.

Donahue, N. M., Epstein, S. A., Pandis, S. N., and Robinson, A. L.: A two-dimensional volatility basis set: 1. organic-aerosol mixing thermodynamics, Atmos Chem Phys, 11, 3303–3318, https://doi.org/10.5194/acp-11-3303-2011, 2011.

Donahue, N. M., Kroll, J. H., Pandis, S. N., and Robinson, A. L.: A two-dimensional volatility basis set – Part 2: Diagnostics of organic-aerosol evolution, Atmos Chem Phys, 12, 615–634, https://doi.org/10.5194/acp-12-615-2012, 2012.

El Haddad, I., D'Anna, B., Temime-Roussel, B., Nicolas, M., Boreave, A., Favez, O., Voisin, D., Sciare, J., George, C., Jaffrezo, J.-L., Wortham, H., and Marchand, N.: Towards a better understanding of the origins, chemical composition and aging of oxygenated organic aerosols: case study of a Mediterranean industrialized environment, Marseille, Atmos Chem Phys, 13, 7875–7894, https://doi.org/10.5194/acp-13-7875-2013, 2013.

Atmos. Chem. Phys. Discuss., https://doi.org/10.5194/acp-2019-364
Manuscript under review for journal Atmos. Chem. Phys.
Discussion started: 30 April 2019

EPA: Locating and estimating air emissions from sources of toluene, EPA-454/R-93-047, in, Research Triangle Park, North Carolina, United States, 3-1, 3-4, 1994.

Farmer, D. K., Matsunaga, A., Docherty, K. S., Surratt, J. D., Seinfeld, J. H., Ziemann, P. J., and Jimenez, J. L.: Response of an aerosol mass spectrometer to organonitrates and organosulfates and implications for atmospheric chemistry, P Natl Acad Sci USA, 107, 6670–6675, https://doi.org/10.1073/pnas.0912340107, 2010.

Fuzzi, S., Baltensperger, U., Carslaw, K., Decesari, S., Denier van der Gon, H., Facchini, M. C., Fowler, D., Koren, I., Langford, B., Lohmann, U., Nemitz, E., Pandis, S., Riipinen, I., Rudich, Y., Schaap, M., Slowik, J. G., Spracklen, D. V., Vignati, E., Wild, M., Williams, M., and Gilardoni, S.: Particulate matter, air quality and climate: lessons learned and future needs, Atmos Chem Phys, 15, 8217–8299, http://doi.org/10.5194/acp-15-8217-2015, 2015.

Gaston, C. J., Lopez-Hilfiker, F. D., Whybrew, L. E., Hadley, O., McNair, F., Gao, H. L., Jaffe, D. A., and Thornton, J. A.: Online molecular characterization of fine particulate matter in Port Angeles, WA: Evidence for a major impact from residential wood smoke, Atmos Environ, 138, 99–107, https://doi.org/10.1016/j.atmosenv.2016.05.013, 2016.

Guttikunda, S. K., Goel, R., and Pant, P.: Nature of air pollution, emission sources, and management in the Indian cities, Atmos Environ, 95, 501–510, https://doi.org/10.1016/j.atmosenv.2014.07.006, 2014.

Hallquist, M., Wenger, J. C., Baltensperger, U., Rudich, Y., Simpson, D., Claeys, M., Dommen, J., Donahue, N. M., George, C., Goldstein, A. H., Hamilton, J. F., Herrmann, H., Hoffmann, T., Iinuma, Y., Jang, M., Jenkin, M. E., Jimenez, J. L., Kiendler-Scharr, A., Maenhaut, W., McFiggans, G., Mentel, T. F., Monod, A., Prévôt, A. S. H., Seinfeld, J. H., Surratt, J. D., Szmigielski, R., and Wildt, J.: The formation, properties and impact of secondary organic aerosol: current and emerging issues, Atmos Chem Phys, 9, 5155−5236, https://doi.org/10.5194/acp-9-5155-2009, 2009.

Heald, C. L., Henze, D. K., Horowitz, L. W., Feddema, J., Lamarque, J.-F., Guenther, A., Hess, P. G., Vitt, F., Seinfeld, J. H., Goldstein, A. H., and Fung, I.: Predicted change in global secondary organic aerosol concentrations in response to future climate, emissions, and land use change, J Geophys Res-Atmos, 113, D05211, https://doi.org/10.1029/2007JD009092, 2008.

Hebbert, M., and Webb, B.: Towards a Liveable Urban Climate: Lessons from Stuttgart, in: C. Gossop and S. Nan (Eds) Liveable Cities: Urbanising World (ISOCARP 07), Routledge, London, 2012.

Hinks, M. L., Montoya-Aguilera, J., Ellison, L., Lin, P., Laskin, A., Laskin, J., Shiraiwa, M., Dabdub, D., and Nizkorodov, S. A.: Effect of relative humidity on the composition of secondary organic aerosol from the oxidation of toluene, Atmos Chem Phys, 18, 1643–1652, https://doi.org/10.5194/acp-18-1643-2018, 2018.

Huang, R.-J., Zhang, Y., Bozzetti, C., Ho, K.-F., Cao, J.-J., Han, Y., Daellenbach, K. R., Slowik, J. G., Platt, S. M., Canonaco, F., Zotter, P., Wolf, R., Pieber, S. M., Bruns, E. A., Crippa, M., Ciarelli, G., Piazzalunga, A., Schwikowski, M., Abbaszade, G., Schnelle-Kreis, J., Zimmermann, R., An, Z., Szidat, S., Baltensperger, U., El Haddad, I., and Prévôt, A. S. H.: High secondary aerosol contribution to particulate pollution during haze events in China, Nature, 514, 218–222, https://doi.org/10.1038/nature13774, 2014.

Huang, W., Saathoff, H., Pajunoja, A., Shen, X. L., Naumann, K.-H., Wagner, R., Virtanen, A., Leisner, T., and Mohr, C.: α-Pinene secondary organic aerosol at low temperature: chemical composition and implications for particle viscosity, Atmos Chem Phys, 18, 2883–2898, https://doi.org/10.5194/acp-18-2883-2018, 2018.

Huang, W., Saathoff, H., Shen, X., Ramisetty, R., Leisner, T., and Mohr, C.: Chemical characterization of highly functionalized organonitrates contributing to night-time organic aerosol mass loadings and particle growth, Environ Sci Technol, 53, 1165–1174, https://doi.org/10.1021/acs.est.8b05826, 2019.

Atmos. Chem. Phys. Discuss., https://doi.org/10.5194/acp-2019-364
Manuscript under review for journal Atmos. Chem. Phys.
Discussion started: 30 April 2019

Jimenez, J. L., Canagaratna, M. R., Donahue, N. M., Prevot, A. S. H., Zhang, Q., Kroll, J. H., DeCarlo, P. F., Allan, J. D., Coe, H., Ng, N. L., Aiken, A. C., Docherty, K. S., Ulbrich, I. M., Grieshop, A. P., Robinson, A. L., Duplissy, J., Smith, J. D., Wilson, K. R., Lanz, V. A., Hueglin, C., Sun, Y. L., Tian, J., Laaksonen, A., Raatikainen, T., Rautiainen, J., Vaattovaara, P., Ehn, M., Kulmala, M., Tomlinson, J. M., Collins, D. R., Cubison, M. J., Dunlea, E. J., Huffman, J. A., Onasch, T. B., Alfarra, M. R., Williams, P. I., Bower, K., Kondo, Y., Schneider, J., Drewnick, F., Borrmann, S., Weimer, S., Demerjian, K., Salcedo, D., Cottrell, L., Griffin, R., Takami, A., Miyoshi, T., Hatakeyama, S., Shimono, A., Sun, J. Y., Zhang, Y. M., Dzepina, K., Kimmel, J. R., Sueper, D., Jayne, J. T., Herndon, S. C., Trimborn, A. M., Williams, L. R., Wood, E. C., Middlebrook, A. M., Kolb, C. E., Baltensperger, U., and Worsnop, D. R.: Evolution of organic aerosols in the atmosphere, Science, 326, 1525−1529, https://doi.org/10.1126/science.1180353 2009.

Kahnt, A., Iinuma, Y., Mutzel, A., Böge, O., Claeys, M., and Herrmann, H.: Campholenic aldehyde ozonolysis: a mechanism leading to specific biogenic secondary organic aerosol constituents, Atmos Chem Phys, 14, 719–736, https://doi.org/10.5194/acp-14-719-2014, 2014.

Keller, A., and Burtscher, H.: Characterizing particulate emissions from wood burning appliances including secondary organic aerosol formation potential, J Aerosol Sci, 114, 21–30, https://doi.org/10.1016/j.jaerosci.2017.08.014, 2017.

Kiendler-Scharr, A., Mensah, A. A., Friese, E., Topping, D., Nemitz, E., Prevot, A. S. H., Äijälä, M., Allan, J., Canonaco, F., Canagaratna, M., Carbone, S., Crippa, M., Dall Osto, M., Day, D. A., De Carlo, P., Di Marco, C. F., Elbern, H., Eriksson, A., Freney, E., Hao, L., Herrmann, H., Hildebrandt, L., Hillamo, R., Jimenez, J. L., Laaksonen, A., McFiggans, G., Mohr, C., O'Dowd, C., Otjes, R., Ovadnevaite, J., Pandis, S. N., Poulain, L., Schlag, P., Sellegri, K., Swietlicki, E., Tiitta, P., Vermeulen, A., Wahner, A., Worsnop, D., and Wu, H.-C.: Ubiquity of organic nitrates from nighttime chemistry in the European submicron aerosol, Geophys Res Lett, 43, 7735–7744, https://doi.org/10.1002/2016GL069239, 2016.

Kinney, P. L.: Interactions of climate change, air pollution, and human health, Curr Environ Health Rep, 5, 179–186, https://doi.org/10.1007/s40572-018-0188-x, 2018.

Kleinman, L. I., Springston, S. R., Daum, P. H., Lee, Y.-N., Nunnermacker, L. J., Senum, G. I., Wang, J., Weinstein-Lloyd, J., Alexander, M. L., Hubbe, J., Ortega, J., Canagaratna, M. R., and Jayne, J.: The time evolution of aerosol composition over the Mexico City plateau, Atmos Chem Phys, 8, 1559–1575, https://doi.org/10.5194/acp-8-1559-2008, 2008.

Lanz, V. A., Alfarra, M. R., Baltensperger, U., Buchmann, B., Hueglin, C., and Prévôt, A. S. H.: Source apportionment of submicron organic aerosols at an urban site by factor analytical modelling of aerosol mass spectra, Atmos Chem Phys, 7, 1503–1522, https://doi.org/10.5194/acp-7-1503-2007, 2007.

Lee, B. H., Lopez-Hilfiker, F. D., Mohr, C., Kurtén, T., Worsnop, D. R., and Thornton, J. A.: An iodide-adduct high-resolution time-of-flight chemical-ionization mass spectrometer: Application to atmospheric inorganic and organic compounds, Environ Sci Technol, 48, 6309−6317, https://doi.org/10.1021/es500362a, 2014.

Lee, B. H., Mohr, C., Lopez-Hilfiker, F. D., Lutz, A., Hallquist, M., Lee, L., Romer, P., Cohen, R. C., Iyer, S., Kurtén, T., Hu, W. W., Day, D. A., Campuzano-Jost, P., Jimenez, J. L., Xu, L., Ng, N. L., Guo, H. Y., Weber, R. J., Wild, R. J., Brown, S. S., Koss, A., de Gouw, J., Olson, K., Goldstein, A. H., Seco, R., Kim, S., McAvey, K., Shepson, P. B., Starn, T., Baumann, K., Edgerton, E. S., Liu, J. M., Shilling, J. E., Miller, D. O., Brune, W., Schobesberger, S., D'Ambro, E. L., and Thornton, J. A.: Highly functionalized organic nitrates in the southeast United States:

Atmos. Chem. Phys. Discuss., https://doi.org/10.5194/acp-2019-364
Manuscript under review for journal Atmos. Chem. Phys.
Discussion started: 30 April 2019

Contribution to secondary organic aerosol and reactive nitrogen budgets, P Natl Acad Sci USA, 113, 1516–1521, https://doi.org/10.1073/pnas.1508108113, 2016.

Li, Y., Pöschl, U., and Shiraiwa, M.: Molecular corridors and parameterizations of volatility in the chemical evolution of organic aerosols, Atmos Chem Phys, 16, 3327–3344, https://doi.org/10.5194/acp-16-3327-2016, 2016.

Lopez-Hilfiker, F. D., Mohr, C., Ehn, M., Rubach, F., Kleist, E., Wildt, J., Mentel, T. F., Lutz, A., Hallquist, M., Worsnop, D., and Thornton, J. A.: A novel method for online analysis of gas and particle composition: description and evaluation of a Filter Inlet for Gases and AEROsols (FIGAERO), Atmos Meas Tech, 7, 983−1001, https://doi.org/10.5194/amt-7-983-2014, 2014.

Lopez-Hilfiker, F. D., Mohr, C., Ehn, M., Rubach, F., Kleist, E., Wildt, J., Mentel, T. F., Carrasquillo, A. J., Daumit, K. E., Hunter, J. F., Kroll, J. H., Worsnop, D. R., and Thornton, J. A.: Phase partitioning and volatility of secondary organic aerosol components formed from α-pinene ozonolysis and OH oxidation: the importance of accretion products and other low volatility compounds, Atmos Chem Phys, 15, 7765−7776, https://doi.org/10.5194/acp-15-7765-2015, 2015.

Lopez-Hilfiker, F. D., Mohr, C., D'Ambro, E. L., Lutz, A., Riedel, T. P., Gaston, C. J., Iyer, S., Zhang, Z., Gold, A., Surratt, J. D., Lee, B. H., Kurten, T., Hu, W. W., Jimenez, J., Hallquist, M., and Thornton, J. A.: Molecular composition and volatility of organic aerosol in the Southeastern U.S.: Implications for IEPOX derived SOA, Environ Sci Technol, 50, 2200–2209, https://doi.org/10.1021/acs.est.5b04769, 2016.

LUBW: Luftreinhaltepläne für Baden-Württemberg (Grundlagenband 2017), in, LUBW State Institute for the Environment Baden-Württemberg, Karlsruhe, Germany, 2019.

Majewski, G., Czechowski, P. O., Badyda, A., and Brandyk, A.: Effect of air pollution on visibility in urban conditions. Warsaw case study, Environ Prot Eng, 40, 47−64, https://doi.org/10.5277/epe140204, 2014.

Marlier, M. E., Jina, A. S., Kinney, P. L., and DeFries, R. S.: Extreme air pollution in global megacities, Curr Clim Change Rep, 2, 15−27, https://doi.org/10.1007/s40641-016-0032-z, 2016.

Mayer, H.: Air pollution in cities, Atmos Environ, 33, 4029−4037, https://doi.org/10.1016/S1352-2310(99)00144-2, 1999.

Mohr, C., DeCarlo, P. F., Heringa, M. F., Chirico, R., Slowik, J. G., Richter, R., Reche, C., Alastuey, A., Querol, X., Seco, R., Peñuelas, J., Jiménez, J. L., Crippa, M., Zimmermann, R., Baltensperger, U., and Prévôt, A. S. H.: Identification and quantification of organic aerosol from cooking and other sources in Barcelona using aerosol mass spectrometer data, Atmos Chem Phys, 12, 1649−1665, https://doi.org/10.5194/acp-12-1649-2012, 2012.

Mohr, C., Lopez-Hilfiker, F. D., Zotter, P., Prévôt, A. S. H., Xu, L., Ng, N. L., Herndon, S. C., Williams, L. R., Franklin, J. P., Zahniser, M. S., Worsnop, D. R., Knighton, W. B., Aiken, A. C., Gorkowski, K. J., Dubey, M. K., Allan, J. D., and Thornton, J. A.: Contribution of nitrated phenols to wood burning brown carbon light absorption in Detling, United Kingdom during winter time, Environ Sci Technol, 47, 6316−6324, https://doi.org/10.1021/es400683v, 2013.

Mohr, C., Lopez-Hilfiker, F. D., Yli-Juuti, T., Heitto, A., Lutz, A., Hallquist, M., D'Ambro, E. L., Rissanen, M. P., Hao, L. Q., Schobesberger, S., Kulmala, M., Mauldin III, R. L., Makkonen, U., Sipilä, M., Petäjä, T., and Thornton, J. A.: Ambient observations of dimers from terpene oxidation in the gas phase: Implications for new particle formation and growth, Geophys Res Lett, 44, 2958−2966, https://doi.org/10.1002/2017gl072718, 2017.

Molteni, U., Bianchi, F., Klein, F., El Haddad, I., Frege, C., Rossi, M. J., Dommen, J., and Baltensperger, U.: Formation of highly oxygenated organic molecules from aromatic compounds, Atmos Chem Phys, 18, 1909−1921, https://doi.org/10.5194/acp-18-1909-2018, 2018.

Atmos. Chem. Phys. Discuss., https://doi.org/10.5194/acp-2019-364
Manuscript under review for journal Atmos. Chem. Phys.
Discussion started: 30 April 2019

Müller, L., Reinnig, M.-C., Naumann, K. H., Saathoff, H., Mentel, T. F., Donahue, N. M., and Hoffmann, T.: Formation of 3-methyl-1,2,3-butanetricarboxylic acid via gas phase oxidation of pinonic acid - a mass spectrometric study of SOA aging, Atmos Chem Phys, 12, 1483–1496, https://doi.org/10.5194/acp-12-1483-2012, 2012.

Ni, H., Huang, R.-J., Cao, J., Dai, W., Zhou, J., Deng, H., Aerts-Bijma, A., Meijer, H. A. J., and Dusek, U.: High contributions of fossil sources to more volatile organic carbon, Atmos Chem Phys Discuss, 1–34, https://doi.org/10.5194/acp-2018-1343, 2019.

Office for Environmental Protection. Luft: Erfolgreiche Maßnahmen zur Luftreinhaltung in Stuttgart: https://www.stuttgart.de/item/show/15638, 2016.

Qi, L., Chen, M., Stefenelli, G., Pospisilova, V., Tong, Y., Bertrand, A., Hueglin, C., Ge, X., Baltensperger, U., Prévôt, A. S. H., and Slowik, J. G.: Organic aerosol source apportionment in Zurich using an extractive electrospray ionization time-of-flight mass spectrometry (EESI-TOF): Part II, biomass burning influences in winter, Atmos Chem Phys Discuss, 1–42, https://doi.org/10.5194/acp-2019-64, 2019.

Riva, M., Heikkinen, L., Bell, D. M., Peräkylä, O., Zha, Q., Schallhart, S., Rissanen, M. P., Imre, D., Petäjä, T., Thornton, J. A., Zelenyuk, A., and Ehn, M.: Chemical transformations in monoterpene-derived organic aerosol enhanced by inorganic composition, npj Clim Atmos Sci, 2, 1–9, https://doi.org/10.1038/s41612-018-0058-0, 2019.

Robinson, A. L., Donahue, N. M., Shrivastava, M. K., Weitkamp, E. A., Sage, A. M., Grieshop, A. P., Lane, T. E., Pierce, J. R., and Pandis, S. N.: Rethinking organic aerosols: Semivolatile emissions and photochemical aging, Science, 315, 1259–1262, https://doi.org/10.1126/science.1133061, 2007.

Roldin, P., Eriksson, A. C., Nordin, E. Z., Hermansson, E., Mogensen, D., Rusanen, A., Boy, M., Swietlicki, E., Svenningsson, B., Zelenyuk, A., and Pagels, J.: Modelling non-equilibrium secondary organic aerosol formation and evaporation with the aerosol dynamics, gas- and particle-phase chemistry kinetic multilayer model ADCHAM, Atmos Chem Phys, 14, 7953–7993, https://doi.org/10.5194/acp-14-7953-2014, 2014.

Saarnio, K., Aurela, M., Timonen, H., Saarikoski, S., Teinilä, K., Mäkelä, T., Sofiev, M., Koskinen, J., Aalto, P. P., Kulmala, M., Kukkonen, J., and Hillamo, R.: Chemical composition of fine particles in fresh smoke plumes from boreal wild-land fires in Europe, Sci Total Environ, 408, 2527–2542, https://doi.org/10.1016/j.scitotenv.2010.03.010, 2010.

Schwartz, J., Spix, C., Wichmann, H. E., and Malin, E.: Air pollution and acute respiratory illness in five German communities, Environ Res, 56, 1–14, https://doi.org/10.1016/S0013-9351(05)80104-5, 1991.

Seinfeld, J. H., and Pandis, S. N.: Atmospheric Chemistry and Physics: From Air Pollution to Climate Change, 3. ed., John Wiley & Sons, Inc., Hoboken, New Jersey, 2016.

Shen, X., Ramisetty, R., Mohr, C., Huang, W., Leisner, T., and Saathoff, H.: Laser ablation aerosol particle time-of-flight mass spectrometer (LAAPTOF): performance, reference spectra and classification of atmospheric samples, Atmos Meas Tech, 11, 2325–2343, https://doi.org/10.5194/amt-11-2325-2018, 2018.

Shrivastava, M., Easter, R. C., Liu, X., Zelenyuk, A., Singh, B., Zhang, K., Ma, P.-L., Chand, D., Ghan, S., Jimenez, J. L., Zhang, Q., Fast, J., Rasch, P. J., and Tiitta, P.: Global transformation and fate of SOA: Implications of low-volatility SOA and gas-phase fragmentation reactions, J Geophys Res-Atmos, 120, 4169–4195, https://doi.org/10.1002/2014JD022563, 2015.

Süddeutsche Zeitung. Stuttgart löst als erste Stadt in Deutschland den Feinstaubalarm aus: http://www.sueddeutsche.de/panorama/luftverschmutzung-stuttgart-loest-als-erste-stadt-in-deutschland-feinstaubalarm-aus-1.2822775, 2016.

Atmos. Chem. Phys. Discuss., https://doi.org/10.5194/acp-2019-364
Manuscript under review for journal Atmos. Chem. Phys.
Discussion started: 30 April 2019

Szmigielski, R., Surratt, J. D., Gómez-González, Y., Van der Veken, P., Kourtchev, I., Vermeylen, R., Blockhuys, F., Jaoui, M., Kleindienst, T. E., Lewandowski, M., Offenberg, J. H., Edney, E. O., Seinfeld, J. H., Maenhaut, W., and Claeys, M.: 3-methyl-1,2,3-butanetricarboxylic acid: An atmospheric tracer for terpene secondary organic aerosol, Geophys Res Lett, 34, L24811, https://doi.org/10.1029/2007GL031338, 2007.

Thompson, S. L., Yatavelli, R. L. N., Stark, H., Kimmel, J. R., Krechmer, J. E., Day, D. A., Hu, W. W., Isaacman-VanWertz, G., Yee, L., Goldstein, A. H., Khan, M. A. H., Holzinger, R., Kreisberg, N., Lopez-Hilfiker, F. D., Mohr, C., Thornton, J. A., Jayne, J. T., Canagaratna, M., Worsnop, D. R., and Jimenez, J. L.: Field intercomparison of the gas/particle partitioning of oxygenated organics during the Southern Oxidant and Aerosol Study (SOAS) in 2013, Aerosol Sci Tech, 51, 30–56, https://doi.org/10.1080/02786826.2016.1254719, 2017.

Tong, H., Kourtchev, I., Pant, P., Keyte, I. J., O'Connor, I. P., Wenger, J. C., Pope, F. D., Harrison, R. M., and Kalberer, M.: Molecular composition of organic aerosols at urban background and road tunnel sites using ultra-high resolution mass spectrometry, Faraday Discuss, 189, 51–68, https://doi.org/10.1039/c5fd00206k, 2016.

Ulbrich, I. M., Canagaratna, M. R., Zhang, Q., Worsnop, D. R., and Jimenez, J. L.: Interpretation of organic components from positive matrix factorization of aerosol mass spectrometric data, Atmos Chem Phys, 9, 2891–2918, https://doi.org/10.5194/acp-9-2891-2009, 2009.

Vaden, T. D., Imre, D., Beránek, J., Shrivastava, M., and Zelenyuk, A.: Evaporation kinetics and phase of laboratory and ambient secondary organic aerosol, P Natl Acad Sci USA, 108, 2190–2195, https://doi.org/10.1073/pnas.1013391108, 2011.

Volkamer, R., Jimenez, J. L., San Martini, F., Dzepina, K., Zhang, Q., Salcedo, D., Molina, L. T., Worsnop, D. R., and Molina, M. J.: Secondary organic aerosol formation from anthropogenic air pollution: Rapid and higher than expected, Geophys Res Lett, 33, L17811, https://doi.org/10.1029/2006GL026899, 2006.

Wang, D. S., and Ruiz, L. H.: Chlorine-initiated oxidation of n-alkanes under high-NOx conditions: insights into secondary organic aerosol composition and volatility using a FIGAERO-CIMS, Atmos Chem Phys, 18, 15535–15553, https://doi.org/10.5194/acp-18-15535-2018, 2018.

Williams, L. R., Gonzalez, L. A., Peck, J., Trimborn, D., McInnis, J., Farrar, M. R., Moore, K. D., Jayne, J. T., Robinson, W. A., Lewis, D. K., Onasch, T. B., Canagaratna, M. R., Trimborn, A., Timko, M. T., Magoon, G., Deng, R., Tang, D., Blanco, E. D. L. R., Prévôt, A. S. H., Smith, K. A., and Worsnop, D. R.: Characterization of an aerodynamic lens for transmitting particles greater than 1 micrometer in diameter into the Aerodyne aerosol mass spectrometer, Atmos Meas Tech, 6, 3271–3280, https://doi.org/10.5194/amt-6-3271-2013, 2013.

Yli-Juuti, T., Pajunoja, A., Tikkanen, O.-P., Buchholz, A., Faiola, C., Väisänen, O., Hao, L., Kari, E., Peräkylä, O., Garmash, O., Shiraiwa, M., Ehn, M., Lehtinen, K., and Virtanen, A.: Factors controlling the evaporation of secondary organic aerosol from α-pinene ozonolysis, Geophys Res Lett, 44, 2562–2570, https://doi.org/10.1002/2016GL072364, 2017.

Zhang, Q., Worsnop, D. R., Canagaratna, M. R., and Jimenez, J. L.: Hydrocarbon-like and oxygenated organic aerosols in Pittsburgh: insights into sources and processes of organic aerosols, Atmos Chem Phys, 5, 3289–3311, https://doi.org/10.5194/acp-5-3289-2005, 2005.

Zhang, Q., Jimenez, J. L., Canagaratna, M. R., Allan, J. D., Coe, H., Ulbrich, I., Alfarra, M. R., Takami, A., Middlebrook, A. M., Sun, Y. L., Dzepina, K., Dunlea, E., Docherty, K., DeCarlo, P. F., Salcedo, D., Onasch, T., Jayne, J. T., Miyoshi, T., Shimono, A., Hatakeyama, S., Takegawa, N., Kondo, Y., Schneider, J., Drewnick, F., Borrmann, S., Weimer, S., Demerjian, K., Williams, P., Bower, K., Bahreini, R., Cottrell, L., Griffin, R. J., Rautiainen, J., Sun, J. Y., Zhang, Y. M., and Worsnop, D. R.: Ubiquity and dominance of oxygenated species in

Atmos. Chem. Phys. Discuss., https://doi.org/10.5194/acp-2019-364
Manuscript under review for journal Atmos. Chem. Phys.
Discussion started: 30 April 2019

organic aerosols in anthropogenically-influenced Northern Hemisphere midlatitudes, Geophys Res Lett, 34, L13801, https://doi.org/10.1029/2007GL029979, 2007.

665

Atmos. Chem. Phys. Discuss., https://doi.org/10.5194/acp-2019-364
Manuscript under review for journal Atmos. Chem. Phys.
Discussion started: 30 April 2019

Atmospheric Chemistry and Physics Discussions
Open Access
EGU

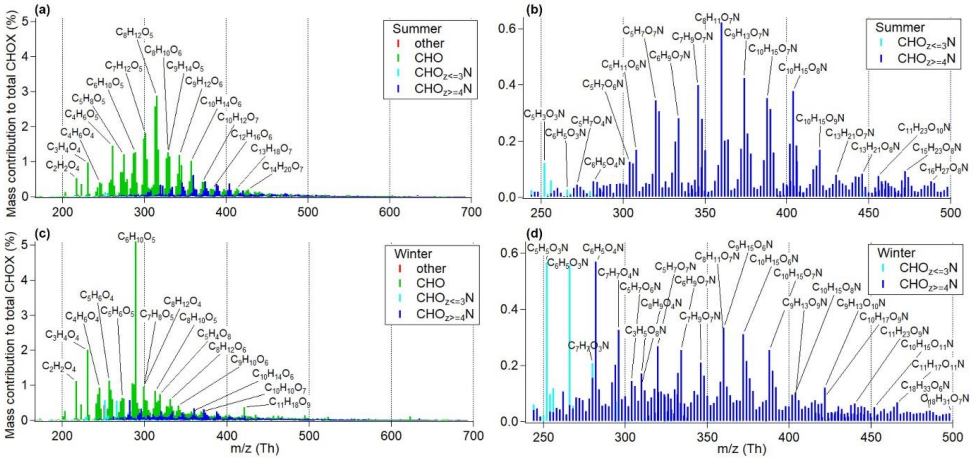

Figure 1. CIMS mass spectra comparison of CHOX compounds (separated into CHO, CHON and other compounds) (a), and CHON compounds (b) in the summer period, CHOX compounds (c) and CHON compounds (b) in the winter period as a function of *m/z* (includes mass of I^- ion; *m/z* 126.9050 Th). Mass contributions of each compound were normalized to the sum of the mass of all detected CHOX compounds.

Atmos. Chem. Phys. Discuss., https://doi.org/10.5194/acp-2019-364
Manuscript under review for journal Atmos. Chem. Phys.
Discussion started: 30 April 2019

Atmospheric Chemistry and Physics Discussions
Open Access
EGU

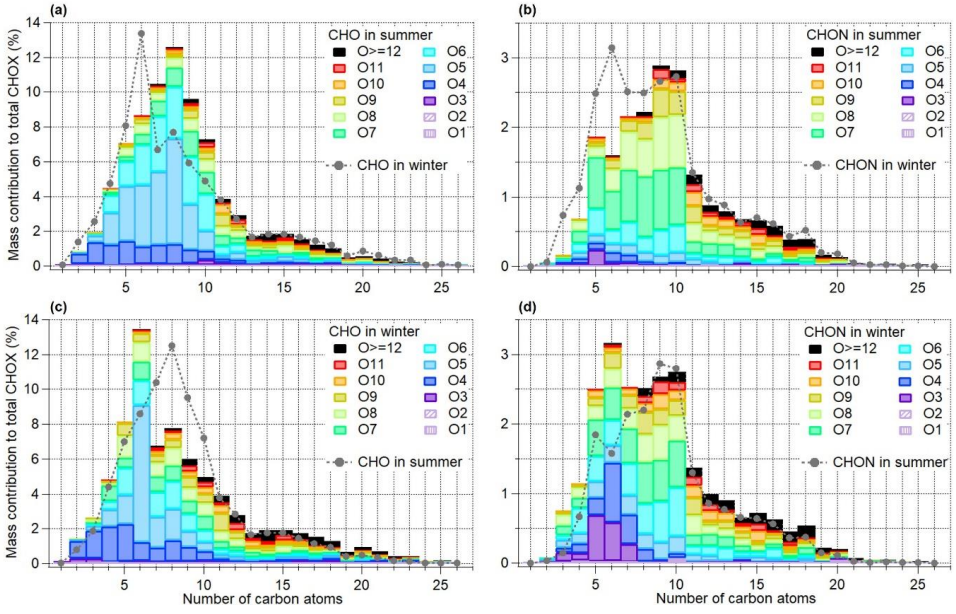

Figure 2. Mass contribution of CHO and CHON compounds with different number of oxygen atoms as a function of the number of carbon atoms to total CHOX compounds for the summer (a, c) and winter (b, d) periods. The corresponding distribution for the other season is plotted as a gray dotted line.

Atmos. Chem. Phys. Discuss., https://doi.org/10.5194/acp-2019-364
Manuscript under review for journal Atmos. Chem. Phys.
Discussion started: 30 April 2019

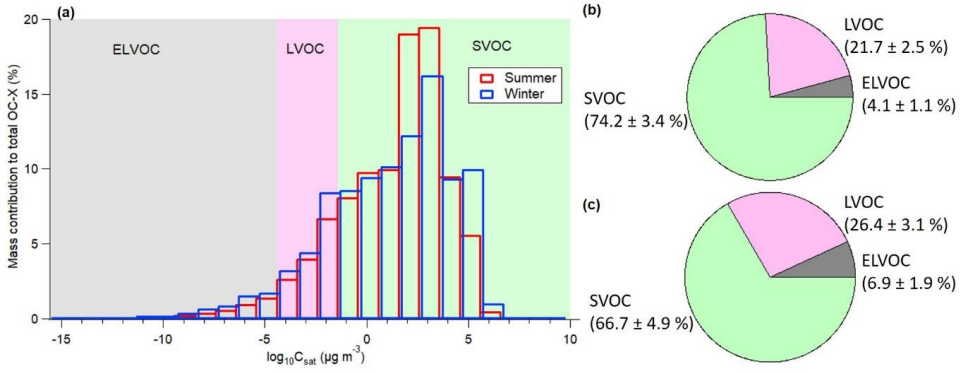

675

Figure 3. (a) Volatility distribution based on the molecular formula parameterization by Li et al. (2016); resulting pie chart for the mass contributions of SVOC, LVOC, and ELVOC in the summer (b) and winter (c) periods.

Atmos. Chem. Phys. Discuss., https://doi.org/10.5194/acp-2019-364
Manuscript under review for journal Atmos. Chem. Phys.
Discussion started: 30 April 2019

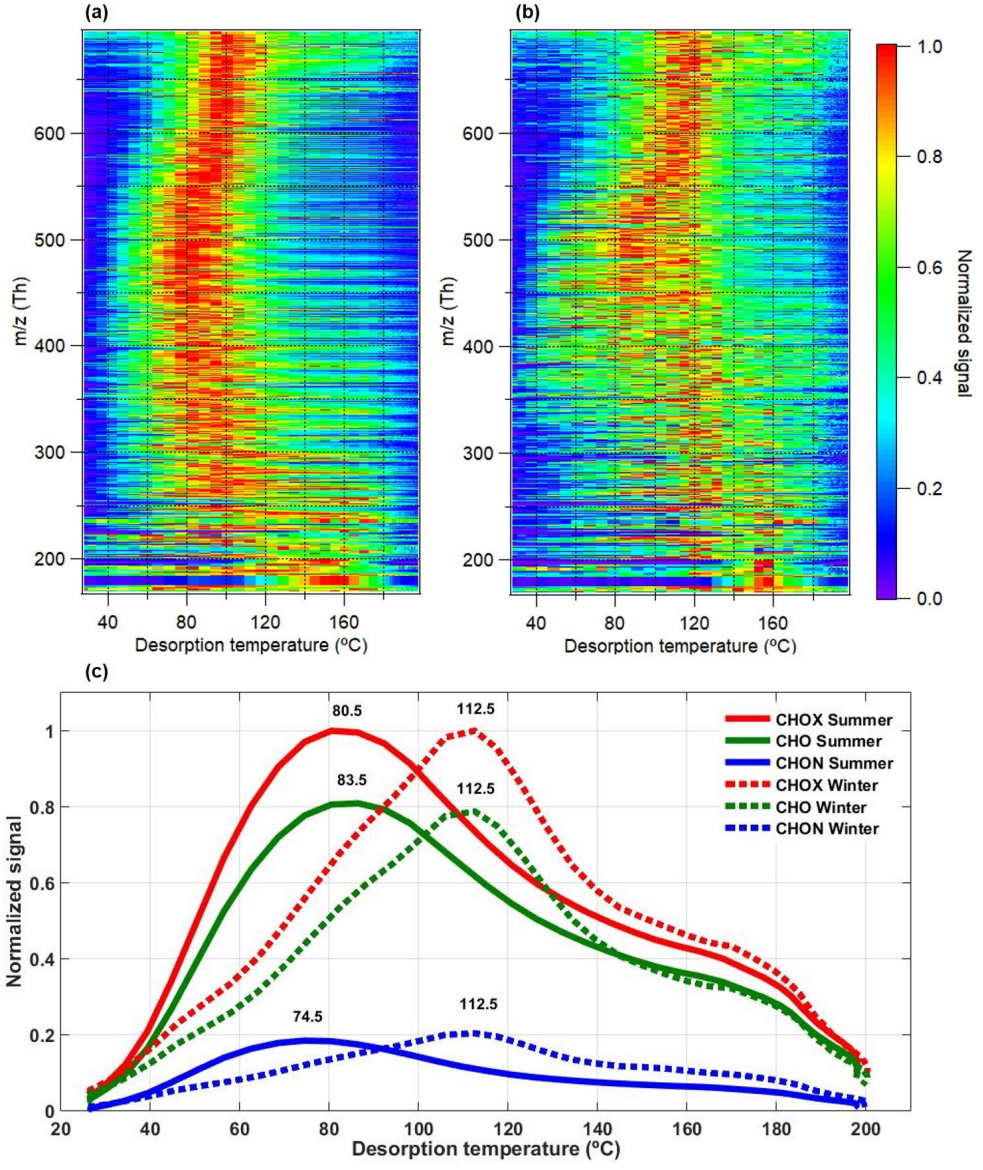

Figure 4. Comparison of campaign-average high resolution two-dimensional (2D) thermograms of CHOX compounds for the summer (a) and winter (b) periods vs *m/z* (includes mass of I^- ion; *m/z* 126.9050 Th), and the sum thermograms of CHOX, CHO, and CHON compounds (c). The 2D thermograms and sum thermograms were normalized to their maximum values.

5 Conclusions and outlook

Due to the complexity of SOA chemical composition and physicochemical properties, as well as its incompletely understood impacts on air quality and climate, I have performed SOA characterization both in the atmospheric simulation chambers and in the field in order to understand whether molecular composition of SOA is correlated with its physicochemical properties and whether different organic compounds formed from different sources play different roles (e.g., NPF, particle growth, ice nucleation). Based on the scientific results collected from chamber studies (section 2, Appendix A.1, B.1–B.3) and field measurements (section 3 and 4, Appendix A.2, A.3, B.4–B.6) of this dissertation, the main conclusions and atmospheric implications will be summarized in section 5.1, and the results leading to new scientific questions will be discussed in section 5.2.

5.1 Conclusions and atmospheric implications

In this dissertation, chemical composition of α-pinene SOA was investigated in the atmospheric simulation chambers at KIT. By the deployment of FIGAERO-CIMS and AMS, I characterized two types of α-pinene SOA at low temperature (223 K) and different RH conditions, with the first type simulating SOA formation at upper troposphere and the second type simulating SOA uplifting from boundary layer to upper troposphere. SOA particles formed directly at 223 K in the AIDA chamber was found to be smaller (100–300 nm d_{va}) and comprise of higher mass fraction of oligomers (>40 %) than those formed at room temperature (296 K) in the APC chamber and then transferred to the AIDA chamber kept at 223 K (particle size: ~500 nm d_{va}; oligomer content: <35 %). Differences in the oligomer contents are due to differences in formation temperatures and precursor VOC concentrations. Higher precursor VOC concentrations and faster oxidation at warm formation temperatures are expected to shift the gas-particle equilibrium of SOA to the particle phase, resulting in higher mass fraction of SVOC and/or monomers in SOA particles; whereas lower α-pinene concentrations and lower formation temperatures favor higher contributions of oligomers, especially at the early stages of particle growth (Tröstl et al., 2016; Mohr et al., 2017). Difference in the evaporation behaviors of SOA particles (based on the T_{max} (maximum desorption temperatures) values in the thermograms of FIGAERO-CIMS; see more details about T_{max} in section 1.4.1.2; Figure 15) was also observed, with slower evaporation for SOA particles comprising of a higher oligomer content. The results demonstrate that SOA particle

evaporation is not only related to a compound's volatility, but also influenced by other factors, such as diffusion limitations within the particles (particle viscosity) caused by higher oligomer contents as well as interactions between particles (particle matrix). Higher particle viscosity is also reflected in its suppression for SOA particles to liquefy and nucleate ice (Wagner et al., 2017; section Appendix B.1). The results show that chemical composition can vary depending on where SOA is formed (e.g., boundary layer or upper troposphere). It can also be deduced that particle physicochemical properties such as viscosity and oligomer content affect each other and that differences in SOA particle evaporation behaviors can provide implications for different particle viscosity and particle matrix effects.

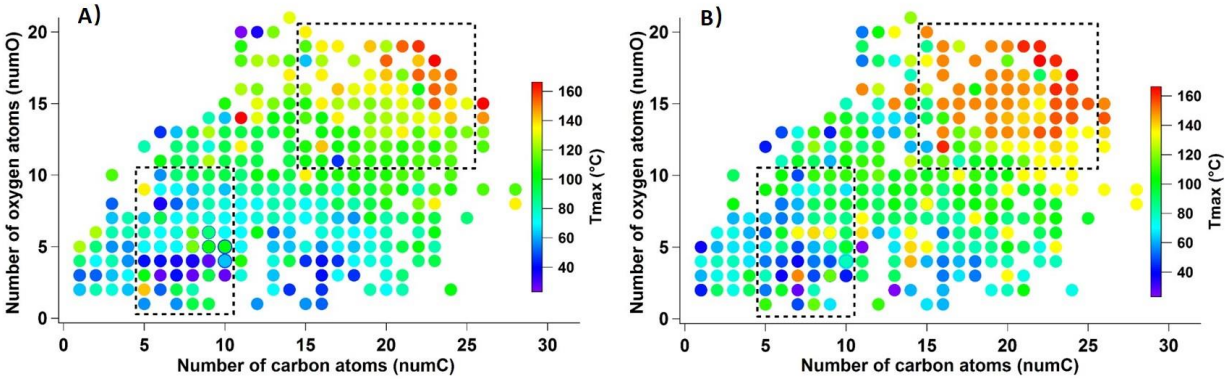

Figure 15. Volatility distribution (color-coded and shown as T_{max} values) for one experiment example simulating SOA uplifting (A) and one experiment example simulating SOA formation at upper troposphere (B), as a function of different number of carbon atoms (numC) and oxygen atoms (numO). Dashed boxes specify the compounds with molecular formulae of $C_{5-10}H_yO_{1-10}$ and $C_{15-25}H_yO_{11-20}$ that had bigger T_{max} differences. Higher T_{max} values were found for SOA comprising a higher oligomer content. Reprint from Huang et al. (2018). Copyright © Huang et al. (2018).

Due to the abundant sources and oxidation mechanisms in the field, ambient SOA are expected to be more complex compared to SOA formed in chambers. I used the knowledge of chemical composition and physicochemical properties obtained from the chamber studies to identify SOA in four field measurements. I characterized atmospheric organic compounds at a rural site near Eggenstein-Leopoldshafen, an urban background site in Stuttgart (both summer and winter), and a remote site near La Paz in Bolivia. Some organic tracer compounds identified in α-pinene SOA, toluene SOA, and biomass burning from my chamber studies were also found in the field, indicating contributions of different sources (e.g., forests, industry, and city) to OA measured in these measurement sites.

For the rural site near Eggenstein-Leopoldshafen influenced by BVOC emissions (also reflected in the emission inventories of the upper Rhine valley; Ponche et al., 2000) but also

anthropogenic emissions (Hagemann et al., 2014), I found some organic tracer compounds identified in the α-pinene SOA from my previous chamber studies, indicating biogenic contributions to the OA mass in this measurement site. The average OA mass loadings measured by AMS were 5.0 ± 3.3 μgm^{-3}, and OA were the dominant component (58 % of total non-refractory $PM_{2.5}$ mass) at this measurement site in the summer period. Larger contributions of highly functionalized organonitrates (ON; Sobanski et al., 2017; Faxon et al., 2018) to night-time OA mass loadings were also observed. They are the products of the interaction between anthropogenic and biogenic emissions. The diel patterns of ON compounds with 5, 7, 10, 15 carbon atoms per molecule varied, indicating a corresponding behavior of their potential precursor VOC isoprene, toluene, monoterpenes, and sesquiterpenes, respectively. The majority of the precursor VOC for these highly functionalized ON are assumed to originate from biogenic source considering the measurement location that is outside the city and close to large forests, as well as the summer time when the measurements were taken. The abundance of ON compounds with 10 carbon atoms, which are most likely to be the oxidation products of monoterpenes with NO_3 radicals (Nah et al., 2016; Lee et al., 2016a; Massoli et al., 2018), supports this conclusion. The high anthropogenic NO_x emissions, resulting from the proximity to the city and the nearby industrial emission sources, are a major chemical pathway for night-time OA formation through the NO_3 radical initiated chemistry formed from the night-time reaction of O_3 with anthropogenic NO_x emissions (Rollins et al., 2012). Good correlations were also observed between the temporal behavior of ON and the number concentration of ultrafine particles after sunset, indicating a potential role of ON in night-time NPF which were regularly observed at this measurement site. ON were found to contribute 18–25 % to the mass increase of newly formed particles after sunset. Considering that monoterpenes have been shown to play an important role in day-time NPF over boreal forests (Tunved et al., 2006), and shown to reach maximum concentrations during night-time NPF over the Landes forest in southwestern France (Kammer et al., 2018); whereas isoprene, emissions of which are dependent on e.g. light and temperature (Guenther et al., 1995), has been shown to significantly inhibit NPF (Kiendler-Scharr et al., 2009; Lee et al., 2016b) and reduce α-pinene SOA yields (McFiggans et al., 2019), ON formed from monoterpenes are therefore more likely to contribute to night-time particle growth compared to those from isoprene. The results reveal that these highly functionalized ON observed after sunset are formed from NO_3 radical initiated oxidations with different precursor VOC, and that they contribute to night-time SOA formation

and particle growth (Figure 16). It is also one of the rare evidences yet, for night-time NPF events (Kammer et al., 2018).

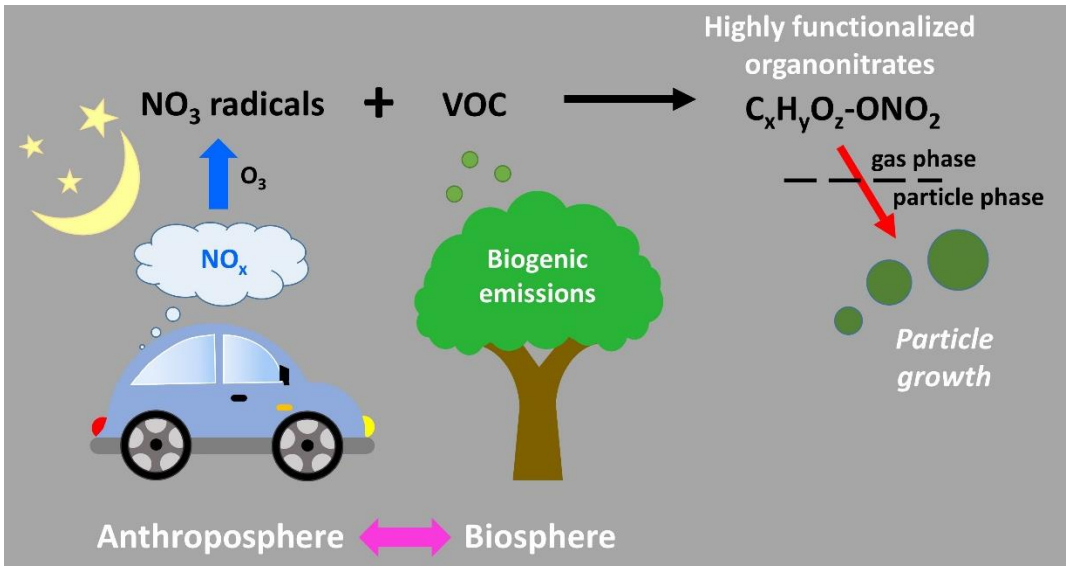

Figure 16. Schematic representation of formation chemistry of highly functionalized ON and their contribution to particle growth. Reprint from Huang et al. (2019). Copyright © 2019, American Chemical Society.

Despite the higher BVOC emissions and thus higher SOA formation in summer, OA can even exhibit higher mass concentrations in winter as a result of the differences in emission sources between the seasons, boundary layer height dynamics, and/or meteorological conditions (Canonaco et al., 2015; Daellenbach et al., 2019; Baumbach and Vogt, 2003). For the urban locations influenced by more anthropogenic emissions such as Stuttgart, one of the most polluted cities in Germany (Schwartz et al., 1991; Süddeutsche Zeitung, 2016; Office for Environmental Protection, 2016), seasonal differences for the OA molecular composition were observed. I also found the abundance of different organic tracer compounds identified in the α-pinene SOA, toluene SOA and biomass burning from my chamber studies, indicating contributions from different sources (biogenic and anthropogenic) to the OA mass in this measurement site. The average OA mass loadings were found to be higher in winter (8.4 ± 5.6 µg m^{-3}) compared to summer (5.1 ± 3.2 µg m^{-3}), but the relative contributions of OA to total non-refractory $PM_{2.5}$ mass measured by AMS were higher in summer (69 %) than winter (35 %). OA particles in summer (as shown by e.g. organic tracer compounds of α-pinene SOA) were more influenced by biogenic emissions (similar to Eggenstein-Leopoldshafen), while biomass burning emissions (both primary and secondary) were an important source in winter (as shown by e.g. signals of levoglucosan and nitrated phenols).

The apparent volatility of the detected organic compounds also varied between the two seasons. Winter OA particles were found to be less volatile (i.e., higher T_{max} values) compared to summer OA particles. It can be partly due to the longer atmospheric aging time of organic compounds (Keller and Burtscher, 2017; Jimenez et al., 2009), resulting from the stronger surface inversion induced longer residence time of OA. This is consistent with the higher O:C ratios in winter and in agreement with the results by Buchholz et al. (2019; section Appendix B.3) that lower apparent volatility is correlated with higher O:C ratios. Other reasons that result in the apparent volatility decrease for OA particles in winter could be higher particle viscosity due to larger mass fraction of large organic compounds (i.e., oligomers) and interactions between different species and/or particle types (particle matrix; Huang et al., 2018), which are also consistent with the results from my chamber studies (section 2 and Appendix A.1). The results demonstrate that differences in sources and/or chemistry between these two seasons are more important than partitioning. The results also show the important contributions of non-fossil OA from biogenic and biomass burning emissions even in an urban area with high traffic emissions mainly using fossil fuels (LUBW, 2019). Therefore, in order to reduce the environmental and health effects of air pollution in urban locations, particularly in densely populated megacities, apart from mitigating traffic emissions, emissions from anthropogenic precursor VOC, e.g., industry and biomass burning, should also be reduced.

For the remote site near La Paz in Bolivia, I identified organic tracer compounds from biogenic emissions (e.g., isoprene and monoterpenes) via e.g. regional transport of Amazon basin, as well as strong anthropogenic pollution (e.g., toluene, black carbon) from the La Paz city. The results demonstrate the influences from regional transport and vertical mixing of SOA even at such a remote location. The results from my chamber studies on simulating SOA formation at upper troposphere and SOA uplifting from boundary layer to upper troposphere, as well as the different organic compounds specific for anthropogenic and biogenic sources identified in chambers can help to better interpret the contributions of anthropogenic and biogenic influences at this remote mountain site in Bolivia.

In this dissertation, the knowledge of SOA chemical composition and physicochemical properties I obtained from chamber studies are proved to be useful for the identification and interpretation of SOA in the field. Vice versa, organic compounds observed in the field (such as organonitrates) and incompletely understood observations also initiated more of my chamber

studies on their oxidation mechanisms and characterization e.g. from anthropogenic and biogenic interactions. This dissertation demonstrates the advantages of combining laboratory and field studies for the chemical characterization of atmospheric OA. All of the chamber studies and field work support the hypothesis that SOA molecular composition is responsible for its physicochemical properties like particle viscosity and volatility, and different organic compounds specific for anthropogenic and biogenic sources can interact with each other and lead to changes in particle properties and to particle growth. This dissertation provides new insights on a molecular basis for the understanding of the organic compounds in the atmosphere, and can be used to further help to assess their lifetime, fate, role/influences in the atmosphere and with that the air quality and climate effects.

5.2 Innovation and outlook

This dissertation discussed the molecular composition of atmospheric organic compounds at different experimental/environmental conditions (i.e., sources, formation conditions (temperature and RH), chemistry, seasons, environments (rural, urban, and remote)), their temporal and spatial variations, and their physicochemical properties (e.g., volatility and viscosity). Major points and/or knowledge gaps this dissertation stresses or contributes to fill in are summarized below and shown in a simplified way in Figure 17:

a) SOA composition and volatility at low temperature conditions representative of the upper troposphere where SOA can be transported to or formed in-situ, and for which only limited literature data exists (section 2 and Appendix A.1);
b) The apparent volatility of organic compounds is influenced by higher particle viscosity due to a higher oligomer content, by higher O:C ratios, and/or particle matrix effects (shown/reflected in section 2 and 4 as well as Appendix A.1, A.3, B.1, B.3), which is a significant contribution to the actual discussion on volatility distributions of SOA components and their modellings;
c) Substantial contributions of ON (i.e., interactions of anthropogenic and biogenic emissions) to OA mass, which are in line with some recent publications also showing high fractions of ON in OA (e.g., Lee et al., 2016; Lee et al., 2018). They are formed from different sources and contribute to particle growth (section 3 and Appendix A.2);

d) NO_x chemistry contributing to night-time SOA formation in a rural area is one of the rare examples demonstrating the potential role of night-time chemistry especially for NPF and particle growth (section 3 and Appendix A.2);

e) Non-fossil OA from biogenic and biomass burning emissions dominates even in an urban area with high traffic emissions like Stuttgart (section 4 and Appendix A.3);

f) The molecular composition of OA on the top of the Bolivian Andes show influence from biogenic emissions from the Amazon basin but also strong influence from pollution of the La Paz city.

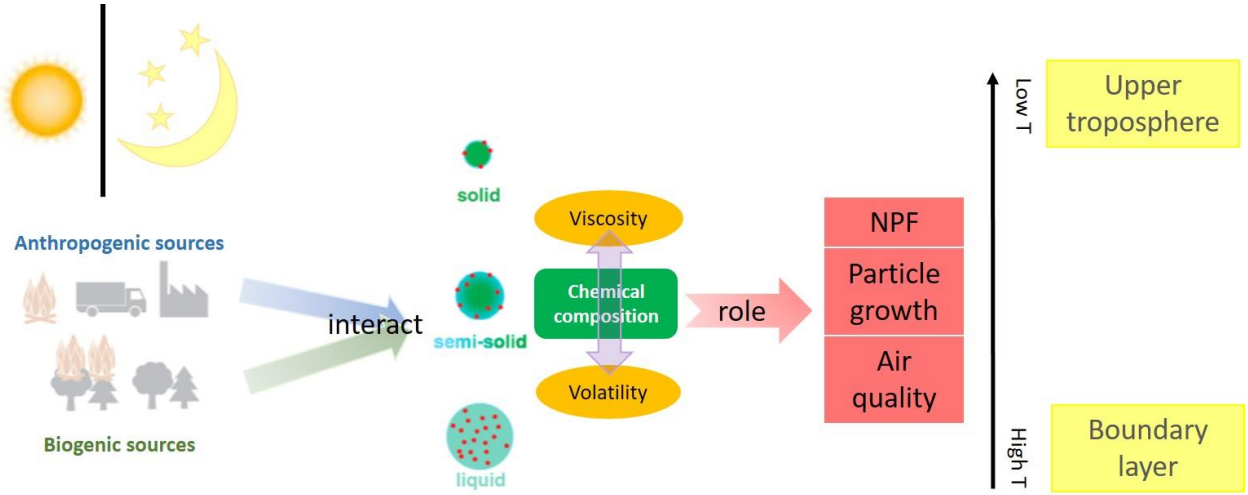

Figure 17. Concept figure of the results about atmospheric processes of OA. Biogenic and anthropogenic emissions can interact to form SOA at boundary layer or upper troposphere with different oligomer contents and physicochemical properties (e.g., volatility, viscosity). SOA chemical composition can interact with its volatility and viscosity, and also play a role in NPF, particle growth and air quality.

Despite this, the dissertation also initiates new scientific questions, some of which could be the research focus for future studies:

a) Differences in the oligomer contents of SOA formed from α-pinene ozonolysis at low temperatures were observed to result from the differences in formation temperatures and precursor VOC concentrations. Within these two factors, which factor is more influencing? How variable and sensitive is the oligomer contents in response to different temperatures and precursor VOC concentrations? How different is the oligomer contents if we change the oxidants from O_3 to e.g. OH radicals or NO_3 radicals, or if we mix different oxidants together/ sequentially (more atmospherically relevant)? What about other relevant precursor VOC such as isoprene, toluene, and sesquiterpenes?

b) Differences in the apparent volatility of OA particles were observed both in the chamber studies and in the field due to either the higher O:C ratios and/or higher particle viscosity caused by larger mass fraction of large organic compounds (i.e., oligomers) and particle matrix effects (interactions between different species and/or particles). How variable is the apparent volatility of individual organic compounds in response to different environments (rural, urban, and remote)? Can we utilize the differences in apparent volatility to infer other physicochemical properties, lifetime, and/or climate effects? Considering the higher e.g. black carbon content in Stuttgart in winter, if (and how) the refractory component such as black carbon can affect the evaporation behaviors of organic compounds (i.e., interactions between non-refractory and refractory components)? How will our understanding of the effects of OA on air quality and climate change if we reconsider the apparent volatility of SOA?

c) Highly functionalized ON observed in the field after sunset were formed from NO_3 radical initiated oxidation with different precursor VOC. However, these ON compounds can the monomer products of their corresponding precursor VOC but may also originate from the fragmentation/oligomerization products of bigger/smaller precursor VOC. How can we distinguish the different VOC contributions to individual ON compounds? In addition to their role in particle growth, what about the other roles they may play in the atmosphere (e.g., their optical properties, CCN activity)? How about the other products of the interactions of anthropogenic and biogenic emissions, such as organosulfates? What is their major oxidation chemistry and their role in the atmosphere?

d) Differences in sources and/or chemistry resulted in different chemical composition and physicochemical properties of atmospheric OA measured in Stuttgart. Can we fully separate the biogenic and anthropogenic contributions to individual organic compounds which may serve as robust tracers? How do the OA compare to other polluted cities? How do the OA measured near Eggenstein-Leopoldshafen and in Stuttgart in Germany (Northern Hemisphere) compare to the OA at the remote mountain site in Bolivia (Southern Hemisphere)?

These questions underscore the need for continued data analysis as well as more in-depth and comprehensive studies, such as controlled experiments at low temperatures, detailed characterization of OA at different formation conditions including the products of the interactions

of different anthropogenic and biogenic emissions, as well as model comparison. In order to fully understand the sources, chemical mechanisms, and molecular composition during the OA formation, as well as to fully understand the interactions between anthroposphere and biosphere, the relationship between OA molecular composition and its physicochemical properties, as well as the effects of OA on air quality and climate, continued efforts are required in simulation chamber studies, field observations as well as model development. The data obtained in this dissertation also provides a good basis to test and improve e.g. parameterizations in volatility basis sets for predicting OA evolutions in transport models.

References

Ammann, C., Spirig, C., Neftel, A., Steinbacher, M., Komenda, M., and Schaub, A.: Application of PTR-MS fro measurements of biogenic VOC in a deciduous forest, Int J Mass Spectrom, 239, 87–101, https://doi.org/10.1016/j.ijms.2004.08.012, 2004.

Atkinson, R., and Arey, J.: Atmospheric degradation of volatile organic compounds, Chem Rev, 103, 4605–4638, https://doi.org/10.1021/cr0206420, 2003.

Atkinson, R.: Rate constants for the atmospheric reactions of alkoxy radicals: An updated estimation method, Atmos Environ, 41, 8468–8485, https://doi.org/10.1016/j.atmosenv.2007.07.002, 2007.

Bai, J., Sun, X. M., Zhang, C. X., Xu, Y. S., and Qi, C. S.: The OH-initiated atmospheric reaction mechanism and kinetics for levoglucosan emitted in biomass burning, Chemosphere, 93, 2004–2010, https://doi.org/10.1016/j.chemosphere.2013.07.021, 2013.

Bateman, A. P., Gong, Z. H., Liu, P. F., Sato, B., Cirino, G., Zhang, Y., Artaxo, P., Bertram, A. K., Manzi, A. O., Rizzo, L. V., Souza, R. A. F., Zaveri, R. A., and Martin, S. T.: Sub-micrometre particulate matter is primarily in liquid form over Amazon rainforest, Nature Geoscience, 9, 34−37, https://doi.org/10.1038/ngeo2599, 2016.

Baumbach, G., and Vogt, U.: Influence of inversion layers on the distribution of air pollutants in urban areas, Water, Air, & Soil Pollution: Focus, 3, 67–78, https://doi.org/10.1023/A:1026098305581, 2003.

Berresheim, H., Elste, T., Plass-Dulmer, C., Eisele, F. L., and Tanner, D. J.: Chemical ionization mass spectrometer for long-term measurements of atmospheric OH and H2SO4, Int J Mass Spectrom, 202, 91–109, https://doi.org/10.1016/S1387-3806(00)00233-5, 2000.

Bianchi, F., Tröstl, J., Junninen, H., Frege, C., Henne, S., Hoyle, C. R., Molteni, U., Herrmann, E., Adamov, A., Bukowiecki, N., Chen, X., Duplissy, J., Gysel, M., Hutterli, M., Kangasluoma, J., Kontkanen, J., Kürten, A., Manninen, H. E., Münch, S., Peräkylä, O., Petäjä, T., Rondo, L., Williamson, C., Weingartner, E., Curtius, J., Worsnop, D. R., Kulmala, M., Dommen, J., and Baltensperger, U.: New particle formation in the free troposphere: A question of chemistry and timing, Science, 352, 1109–1112, https://doi.org/10.1126/science.aad5456 2016.

Bianchi, F., Kurtén, T., Riva, M., Mohr, C., Rissanen, M. P., Roldin, P., Berndt, T., Crounse, J. D., Wennberg, P. O., Mentel, T. F., Wildt, J., Junninen, H., Jokinen, T., Kulmala, M., Worsnop, D. R., Thornton, J. A., Donahue, N., Kjaergaard, H. G., and Ehn, M.: Highly oxygenated

organic molecules (HOM) from gas-phase autoxidation involving peroxy radicals: A key contributor to atmospheric aerosol, Chem Rev, 119, 3472–3509, https://doi.org/10.1021/acs.chemrev.8b00395, 2019.

Boers, R., van Weele, M., van Meijgaard, E., Savenije, M., Siebesma, A. P., Bosveld, F., and Stammes, P.: Observations and projections of visibility and aerosol optical thickness (1956-2100) in the Netherlands: impacts of time-varying aerosol composition and hygroscopicity, Environmental Research Letters, 10, 015003, https://doi.org/10.1088/1748-9326/10/1/015003, 2015.

Breitmaier, E.: Hemi- and Monoterpenes, in: Terpenes: Flavors, Fragrances, Pharmaca, Pheromones, Wiley-VCH, Weinheim, 2006.

Buchholz, A., Lambe, A. T., Ylisirniö, A., Li, Z., Tikkanen, O.-P., Faiola, C., Kari, E., Hao, L. Q., Luoma, O., Huang, W., Mohr, C., Worsnop, D. R., Nizkorodov, S. A., Yli-Juuti, T., Schobesberger, S., and Virtanen, A.: Insights into the O:C-dependent mechanisms controlling the evaporation of α-pinene secondary organic aerosol particles, Atmos Chem Phys, 19, 4061–4073, https://doi.org/10.5194/acp-19-4061-2019, 2019.

Caldwell, G. W., Masucci, J. A., and Ikonomou, M. G.: Negative-ion chemical ionization mass-spectrometry binding of molecules to bromide and iodide Anions, Org Mass Spectrom, 24, 8–14, https://doi.org/10.1002/oms.1210240103, 1989.

Canagaratna, M. R., Jayne, J. T., Jimenez, J. L., Allan, J. D., Alfarra, M. R., Zhang, Q., Onasch, T. B., Drewnick, F., Coe, H., Middlebrook, A., Delia, A., Williams, L. R., Trimborn, A. M., Northway, M. J., DeCarlo, P. F., Kolb, C. E., Davidovits, P., and Worsnop, D. R.: Chemical and microphysical characterization of ambient aerosols with the aerodyne aerosol mass spectrometer, Mass Spectrometry Reviews, 26, 185–222, https://doi.org/10.1002/mas.20115, 2007.

Canagaratna, M. R., Jimenez, J. L., Kroll, J. H., Chen, Q., Kessler, S. H., Massoli, P., Hildebrandt Ruiz, L., Fortner, E., Williams, L. R., Wilson, K. R., Surratt, J. D., Donahue, N. M., Jayne, J. T., and Worsnop, D. R.: Elemental ratio measurements of organic compounds using aerosol mass spectrometry: characterization, improved calibration, and implications, Atmos Chem Phys, 15, 253−272, https://doi.org/10.5194/acp-15-253-2015, 2015.

Canonaco, F., Slowik, J. G., Baltensperger, U., and Prévôt, A. S. H.: Seasonal differences in oxygenated organic aerosol composition: implications for emissions sources and factor analysis, Atmos Chem Phys, 15, 6993–7002, https://doi.org/10.5194/acp-15-6993-2015, 2015.

Cappa, C. D., and Jimenez, J. L.: Quantitative estimates of the volatility of ambient organic aerosol, Atmos Chem Phys, 10, 5409–5424, https://doi.org/10.5194/acp-10-5409-2010, 2010.

Cappa, C. D., and Wilson, K. R.: Evolution of organic aerosol mass spectra upon heating: implications for OA phase and partitioning behavior, Atmos Chem Phys, 11, 1895–1911, https://doi.org/10.5194/acp-11-1895-2011, 2011.

Carlton, A. G., Wiedinmyer, C., and Kroll, J. H.: A review of Secondary Organic Aerosol (SOA) formation from isoprene, Atmos Chem Phys, 9, 4987–5005, https://doi.org/10.5194/acp-9-4987-2009, 2009.

Claeys, M., Graham, B., Vas, G., Wang, W., Vermeylen, R., Pashynska, V., Cafmeyer, J., Guyon, P., Andreae, M. O., Artaxo, P., and Maenhaut, W.: Formation of secondary organic aerosols through photooxidation of isoprene, Science, 303, 1173–1176, https://doi.org/10.1126/science.1092805, 2004.

Constable, J. V. H., Litvak, M. E., Greenberg, J. P., and Monson, R. K.: Monoterpene emission from coniferous trees in response to elevated CO2 concentration and climate warming, Glob Change Biol, 5, 255–267, https://doi.org/10.1046/j.1365-2486.1999.00212.x, 1999.

Crutzen, P. J., and Andreae, M. O.: Biomass burning in the tropics: Impact on atmospheric chemistry and biogeochemical cycles, Science, 250, 1669–1678, https://doi.org/10.1126/science.250.4988.1669, 1990.

D'Amato, G., Bergmann, K. C., Cecchi, L., Annesi-Maesano, I., Sanduzzi, A., Liccardi, G., Vitale, C., Stanziola, A., and D'Amato, M.: Climate change and air pollution: Effects on pollen allergy and other allergic respiratory diseases, Allergo J Int, 23, 17–23, https://doi.org/10.1007/s40629-014-0003-7, 2014.

D'Ambro, E. L., Lee, B. H., Liu, J. M., Shilling, J. E., Gaston, C. J., Lopez-Hilfiker, F. D., Schobesberger, S., Zaveri, R. A., Mohr, C., Lutz, A., Zhang, Z. F., Gold, A., Surratt, J. D., Rivera-Rios, J. C., Keutsch, F. N., and Thornton, J. A.: Molecular composition and volatility of isoprene photochemical oxidation secondary organic aerosol under low- and high-NOx conditions, Atmos Chem Phys, 17, 159–174, https://doi.org/10.5194/acp-17-159-2017, 2017.

Daellenbach, K. R., Kourtchev, I., Vogel, A. L., Bruns, E. A., Jiang, J., Petäjä, T., Jaffrezo, J.-L., Aksoyoglu, S., Kalberer, M., Baltensperger, U., El Haddad, I., and Prévôt, A. S. H.: Impact of anthropogenic and biogenic sources on the seasonal variation of the molecular composition of urban organic aerosols: a field and laboratory study using ultra-high resolution mass spectrometry, Atmos Chem Phys Discuss, 1–40, https://doi.org/10.5194/acp-2018-1128, 2019.

DeCarlo, P. F., Kimmel, J. R., Trimborn, A., Northway, M. J., Jayne, J. T., Aiken, A. C., Gonin, M., Fuhrer, K., Horvath, T., Docherty, K. S., Worsnop, D. R., and Jimenez, J. L.: Field-deployable, high-resolution, time-of-flight aerosol mass spectrometer, Analytical Chemistry, 78, 8281–8289, https://doi.org/10.1021/ac061249n, 2006.

Denjean, C., Formenti, P., Picquet-Varrault, B., Camredon, M., Pangui, E., Zapf, P., Katrib, Y., Giorio, C., Tapparo, A., Temime-Roussel, B., Monod, A., Aumont, B., and Doussin, J. F.: Aging of secondary organic aerosol generated from the ozonolysis of α-pinene: effects of ozone, light and temperature, Atmos Chem Phys, 15, 883−897, https://doi.org/10.5194/acp-15-883-2015, 2015.

Docherty, K. S., Wu, W., Lim, Y. B., and Ziemann, P. J.: Contributions of organic peroxides to secondary aerosol formed from reactions of monoterpenes with O3, Environ Sci Technol, 39, 4049−4059, https://doi.org/10.1021/es050228s, 2005.

Donahue, N. M., Robinson, A. L., Stanier, C. O., and Pandis, S. N.: Coupled partitioning, dilution, and chemical aging of semivolatile organics, Environ Sci Technol, 40, 2635–2643, https://doi.org/10.1021/es052297c, 2006.

Donahue, N. M., Epstein, S. A., Pandis, S. N., and Robinson, A. L.: A two-dimensional volatility basis set: 1. organic-aerosol mixing thermodynamics, Atmos Chem Phys, 11, 3303–3318, https://doi.org/10.5194/acp-11-3303-2011, 2011.

Donahue, N. M., Kroll, J. H., Pandis, S. N., and Robinson, A. L.: A two-dimensional volatility basis set – Part 2: Diagnostics of organic-aerosol evolution, Atmos Chem Phys, 12, 615–634, https://doi.org/10.5194/acp-12-615-2012, 2012.

Donahue, N. M., Chuang, W., Epstein, S. A., Kroll, J. H., Worsnop, D. R., Robinson, A. L., Adams, P. J., and Pandis, S. N.: Why do organic aerosols exist? Understanding aerosol lifetimes using the two-dimensional volatility basis set, Environ Chem, 10, 151−157, https://doi.org/10.1071/En13022, 2013.

Edney, E. O., Kleindienst, T. E., Jaoui, M., Lewandowski, M., Offenberg, J. H., Wang, W., and Claeys, M.: Formation of 2-methyl tetrols and 2-methylglyceric acid in secondary organic aerosol from laboratory irradiated isoprene/NO(X)/SO(2)/air mixtures and their detection in ambient PM(2.5) samples collected in the eastern United States, Atmos Environ, 39, 5281–5289, https://doi.org/10.1016/j.atmosenv.2005.05.031, 2005.

Ehn, M., Kleist, E., Junninen, H., Petäjä, T., Lönn, G., Schobesberger, S., Dal Maso, M., Trimborn, A., Kulmala, M., Worsnop, D. R., Wahner, A., Wildt, J., and Mentel, T. F.: Gas phase formation of extremely oxidized pinene reaction products in chamber and ambient air, Atmos Chem Phys, 12, 5113−5127, https://doi.org/10.5194/acp-12-5113-2012, 2012.

Ehn, M., Thornton, J. A., Kleist, E., Sipilä, M., Junninen, H., Pullinen, I., Springer, M., Rubach, F., Tillmann, R., Lee, B., Lopez-Hilfiker, F., Andres, S., Acir, I. H., Rissanen, M., Jokinen, T., Schobesberger, S., Kangasluoma, J., Kontkanen, J., Nieminen, T., Kurtén, T., Nielsen, L. B., Jørgensen, S., Kjaergaard, H. G., Canagaratna, M., Dal Maso, M., Berndt, T., Petäjä, T., Wahner, A., Kerminen, V. M., Kulmala, M., Worsnop, D. R., Wildt, J., and Mentel, T. F.: A large source of low-volatility secondary organic aerosol, Nature, 506, 476−479, https://doi.org/10.1038/nature13032, 2014.

Enami, S., Hoffmann, M. R., and Colussi, A. J.: Criegee Intermediates React with Levoglucosan on Water, J Phys Chem Lett, 8, 3888–3894, https://doi.org/10.1021/acs.jpclett.7b01665, 2017.

EPA: Locating and estimating air emissions from sources of toluene, EPA-454/R-93-047, in, Research Triangle Park, North Carolina, United States, 3-1, 3-4, 1994.

Fares, S., Gentner, D. R., Park, J. H., Ormeno, E., Karlik, J., and Goldstein, A. H.: Biogenic emissions from Citrus species in California, Atmos Environ, 45, 4557–4568, https://doi.org/10.1016/j.atmosenv.2011.05.066, 2011.

Faxon, C., Hammes, J., Le Breton, M., Pathak, R. K., and Hallquist, M.: Characterization of organic nitrate constituents of secondary organic aerosol (SOA) from nitrate-radical-initiated oxidation of limonene using high-resolution chemical ionization mass spectrometry, Atmos Chem Phys, 18, 5467–5481, https://doi.org/10.5194/acp-18-5467-2018, 2018.

Forstner, H. J. L., Flagan, R. C., and Seinfeld, J. H.: Secondary organic aerosol from the photooxidation of aromatic hydrocarbons: Molecular composition, Environ Sci Technol, 31, 1345–1358, https://doi.org/10.1021/es9605376, 1997.

Fraser, M. P., and Lakshmanan, K.: Using levoglucosan as a molecular marker for the long-range transport of biomass combustion aerosols, Environ Sci Technol, 34, 4560–4564, https://doi.org/10.1021/es991229l, 2000.

Gilardoni, S., Massoli, P., Paglione, M., Giulianelli, L., Carbone, C., Rinaldi, M., Decesari, S., Sandrini, S., Costabile, F., Gobbi, G. P., Pietrogrande, M. C., Visentin, M., Scotto, F., Fuzzi, S., and Facchini, M. C.: Direct observation of aqueous secondary organic aerosol from biomass-burning emissions, P Natl Acad Sci USA, 113, 10013–10018, https://doi.org/10.1073/pnas.1602212113, 2016.

Gramlich, Y. N.: Characterization of anthropogenic fractions in secondary organic aerosol, Master, Karlsruhe Institute of Technology, Karlsruhe, 2018.

Greve, H.-H.: Rubber, 2. Natural, in: Ullmann's Encyclopedia of Industrial Chemistry, Wiley-VCH, Weinheim, 2000.

Gross, J. H.: Mass Spectrometry, 3 ed., Springer International Publishing, Cham, 2017.

Guenther, A., Hewitt, C. N., Erickson, D., Fall, R., Geron, C., Graedel, T., Harley, P., Klinger, L., Lerdau, M., Mckay, W. A., Pierce, T., Scholes, B., Steinbrecher, R., Tallamraju, R., Taylor, J., and Zimmerman, P.: A global model of natural volatile organic compound emissions, J Geophys Res-Atmos, 100, 8873–8892, https://doi.org/10.1029/94jd02950, 1995.

Hagemann, R., Corsmeier, U., Kottmeier, C., Rinke, R., Wieser, A., and Vogel, B.: Spatial variability of particle number concentrations and NOx in the Karlsruhe (Germany) area obtained with the mobile laboratory 'AERO-TRAM', Atmos Environ, 94, 341–352, https://doi.org/10.1016/j.atmosenv.2014.05.051, 2014.

Hallquist, M., Wenger, J. C., Baltensperger, U., Rudich, Y., Simpson, D., Claeys, M., Dommen, J., Donahue, N. M., George, C., Goldstein, A. H., Hamilton, J. F., Herrmann, H., Hoffmann, T., Iinuma, Y., Jang, M., Jenkin, M. E., Jimenez, J. L., Kiendler-Scharr, A., Maenhaut, W., McFiggans, G., Mentel, T. F., Monod, A., Prévôt, A. S. H., Seinfeld, J. H., Surratt, J. D., Szmigielski, R., and Wildt, J.: The formation, properties and impact of secondary organic aerosol: current and emerging issues, Atmos Chem Phys, 9, 5155–5236, https://doi.org/10.5194/acp-9-5155-2009, 2009.

Heald, C. L., Henze, D. K., Horowitz, L. W., Feddema, J., Lamarque, J.-F., Guenther, A., Hess, P. G., Vitt, F., Seinfeld, J. H., Goldstein, A. H., and Fung, I.: Predicted change in global secondary

organic aerosol concentrations in response to future climate, emissions, and land use change, J Geophys Res-Atmos, 113, D05211, https://doi.org/10.1029/2007JD009092, 2008.

Henze, D. K., Seinfeld, J. H., Ng, N. L., Kroll, J. H., Fu, T. M., Jacob, D. J., and Heald, C. L.: Global modeling of secondary organic aerosol formation from aromatic hydrocarbons: high- vs. low-yield pathways, Atmos Chem Phys, 8, 2405–2420, https://doi.org/10.5194/acp-8-2405-2008, 2008.

Hildebrandt, L., Donahue, N. M., and Pandis, S. N.: High formation of secondary organic aerosol from the photo-oxidation of toluene, Atmos Chem Phys, 9, 2973–2986, https://doi.org/10.5194/acp-9-2973-2009, 2009.

Hinks, M. L., Montoya-Aguilera, J., Ellison, L., Lin, P., Laskin, A., Laskin, J., Shiraiwa, M., Dabdub, D., and Nizkorodov, S. A.: Effect of relative humidity on the composition of secondary organic aerosol from the oxidation of toluene, Atmos Chem Phys, 18, 1643–1652, https://doi.org/10.5194/acp-18-1643-2018, 2018.

Holmes, B. J., and Petrucci, G. A.: Water-soluble oligomer formation from acid-catalyzed reactions of levoglucosan in proxies of atmospheric aqueous aerosols, Environ Sci Technol, 40, 4983–4989, https://doi.org/10.1021/es060646c, 2006.

Holmes, B. J., and Petrucci, G. A.: Oligomerization of levoglucosan by Fenton chemistry in proxies of biomass burning aerosols, J Atmos Chem, 58, 151–166, https://doi.org/10.1007/s10874-007-9084-8, 2007.

Hu, W., Hu, M., Hu, W. W., Zheng, J., Chen, C., Wu, Y. S., and Guo, S.: Seasonal variations in high time-resolved chemical compositions, sources, and evolution of atmospheric submicron aerosols in the megacity Beijing, Atmos Chem Phys, 17, 9979–10000, https://doi.org/10.5194/acp-17-9979-2017, 2017.

Huang, W., Saathoff, H., Pajunoja, A., Shen, X. L., Naumann, K.-H., Wagner, R., Virtanen, A., Leisner, T., and Mohr, C.: α-Pinene secondary organic aerosol at low temperature: chemical composition and implications for particle viscosity, Atmos Chem Phys, 18, 2883–2898, https://doi.org/10.5194/acp-18-2883-2018, 2018.

Huang, W., Saathoff, H., Shen, X., Ramisetty, R., Leisner, T., and Mohr, C.: Chemical characterization of highly functionalized organonitrates contributing to night-time organic aerosol mass loadings and particle growth, Environ Sci Technol, 53, 1165–1174, https://doi.org/10.1021/acs.est.8b05826, 2019.

IPCC: Climate change 2013: The physical scientific basis, in, Cambridge University Press, Cambridge, England, 622−623, 2013.

Jang, M. S., and Kamens, R. M.: Characterization of secondary aerosol from the photooxidation of toluene in the presence of NOx and 1-propene, Environ Sci Technol, 35, 3626–3639, https://doi.org/10.1021/es010676+, 2001.

Järvinen, E., Ignatius, K., Nichman, L., Kristensen, T. B., Fuchs, C., Hoyle, C. R., Höppel, N., Corbin, J. C., Craven, J., Duplissy, J., Ehrhart, S., El Haddad, I., Frege, C., Gordon, H., Jokinen, T., Kallinger, P., Kirkby, J., Kiselev, A., Naumann, K.-H., Petäjä, T., Pinterich, T., Prevot, A. S. H., Saathoff, H., Schiebel, T., Sengupta, K., Simon, M., Slowik, J. G., Tröstl, J., Virtanen, A., Vochezer, P., Vogt, S., Wagner, A. C., Wagner, R., Williamson, C., Winkler, P. M., Yan, C., Baltensperger, U., Donahue, N. M., Flagan, R. C., Gallagher, M., Hansel, A., Kulmala, M., Stratmann, F., Worsnop, D. R., Möhler, O., Leisner, T., and Schnaiter, M.: Observation of viscosity transition in α-pinene secondary organic aerosol, Atmos Chem Phys, 16, 4423−4438, https://doi.org/10.5194/acp-16-4423-2016, 2016.

Jayne, J. T., Leard, D. C., Zhang, X. F., Davidovits, P., Smith, K. A., Kolb, C. E., and Worsnop, D. R.: Development of an aerosol mass spectrometer for size and composition analysis of submicron particles, Aerosol Sci Tech, 33, 49–70, https://doi.org/10.1080/027868200410840, 2000.

Ji, Y. M., Zhao, J., Terazono, H., Misawa, K., Levitt, N. P., Li, Y. X., Lin, Y., Peng, J. F., Wang, Y., Duan, L., Pan, B. W., Zhang, F., Feng, X. D., An, T. C., Marrero-Ortiz, W., Secrest, J., Zhang, A. L., Shibuya, K., Molina, M. J., and Zhang, R. Y.: Reassessing the atmospheric oxidation mechanism of toluene, P Natl Acad Sci USA, 114, 8169–8174, https://doi.org/10.1073/pnas.1705463114, 2017.

Jimenez, J. L., Canagaratna, M. R., Donahue, N. M., Prevot, A. S. H., Zhang, Q., Kroll, J. H., DeCarlo, P. F., Allan, J. D., Coe, H., Ng, N. L., Aiken, A. C., Docherty, K. S., Ulbrich, I. M., Grieshop, A. P., Robinson, A. L., Duplissy, J., Smith, J. D., Wilson, K. R., Lanz, V. A., Hueglin, C., Sun, Y. L., Tian, J., Laaksonen, A., Raatikainen, T., Rautiainen, J., Vaattovaara, P., Ehn, M., Kulmala, M., Tomlinson, J. M., Collins, D. R., Cubison, M. J., Dunlea, E. J., Huffman, J. A., Onasch, T. B., Alfarra, M. R., Williams, P. I., Bower, K., Kondo, Y., Schneider, J., Drewnick, F., Borrmann, S., Weimer, S., Demerjian, K., Salcedo, D., Cottrell, L., Griffin, R., Takami, A., Miyoshi, T., Hatakeyama, S., Shimono, A., Sun, J. Y., Zhang, Y. M., Dzepina, K.,

Kimmel, J. R., Sueper, D., Jayne, J. T., Herndon, S. C., Trimborn, A. M., Williams, L. R., Wood, E. C., Middlebrook, A. M., Kolb, C. E., Baltensperger, U., and Worsnop, D. R.: Evolution of organic aerosols in the atmosphere, Science, 326, 1525–1529, https://doi.org/10.1126/science.1180353 2009.

Junninen, H., Ehn, M., Petäjä, T., Luosujärvi, L., Kotiaho, T., Kostiainen, R., Rohner, U., Gonin, M., Fuhrer, K., Kulmala, M., and Worsnop, D. R.: A high-resolution mass spectrometer to measure atmospheric ion composition, Atmos Meas Tech, 3, 1039–1053, https://doi.org/10.5194/amt-3-1039-2010, 2010.

Juuti, S., Arey, J., and Atkinson, R.: Monoterpene Emission Rate Measurements from a Monterey Pine, J Geophys Res-Atmos, 95, 7515–7519, https://doi.org/10.1029/JD095iD06p07515, 1990.

Kammer, J., Perraudin, E., Flaud, P. M., Lamaud, E., Bonnefond, J. M., and Villenave, E.: Observation of nighttime new particle formation over the French Landes forest, Science of the Total Environment, 621, 1084–1092, https://doi.org/10.1016/j.scitotenv.2017.10.118, 2018.

Kanakidou, M., Seinfeld, J. H., Pandis, S. N., Barnes, I., Dentener, F. J., Facchini, M. C., Van Dingenen, R., Ervens, B., Nenes, A., Nielsen, C. J., Swietlicki, E., Putaud, J. P., Balkanski, Y., Fuzzi, S., Horth, J., Moortgat, G. K., Winterhalter, R., Myhre, C. E. L., Tsigaridis, K., Vignati, E., Stephanou, E. G., and Wilson, J.: Organic aerosol and global climate modelling: a review, Atmos Chem Phys, 5, 1053−1123, https://doi.org/10.5194/acp-5-1053-2005, 2005.

Karban, R., Shiojiri, K., Huntzinger, M., and McCall, A. C.: Damage-induced resistance in sagebrush: Volatiles are key to intra- and interplant communication, Ecology, 87, 922–930, https://doi.org/10.1890/0012-9658(2006)87[922:Drisva]2.0.Co;2, 2006.

Keller, A., and Burtscher, H.: Characterizing particulate emissions from wood burning appliances including secondary organic aerosol formation potential, J Aerosol Sci, 114, 21–30, https://doi.org/10.1016/j.jaerosci.2017.08.014, 2017.

Kessler, A., and Baldwin, I. T.: Defensive function of herbivore-induced plant volatile emissions in nature, Science, 291, 2141–2144, https://doi.org/10.1126/science.291.5511.2141, 2001.

Kidd, C., Perraud, V., Wingen, L. M., and Finlayson-Pitts, B. J.: Integrating phase and composition of secondary organic aerosol from the ozonolysis of α-pinene, P Natl Acad Sci USA, 111, 7552−7557, https://doi.org/10.1073/pnas.1322558111, 2014.

Kiendler-Scharr, A., Wildt, J., Dal Maso, M., Hohaus, T., Kleist, E., Mentel, T. F., Tillmann, R., Uerlings, R., Schurr, U., and Wahner, A.: New particle formation in forests inhibited by isoprene emissions, Nature, 461, 381–384, https://doi.org/10.1038/nature08292, 2009.

Kinney, P. L.: Interactions of climate change, air pollution, and human health, Curr Environ Health Rep, 5, 179–186, https://doi.org/10.1007/s40572-018-0188-x, 2018.

Komenda, M., and Koppmann, R.: Monoterpene emissions from Scots pine (Pinus sylvestris): Field studies of emission rate variabilities, J Geophys Res-Atmos, 107, ACH 1-1–ACH 1-13, https://doi.org/10.1029/2001JD000691, 2002.

Kristensen, K., Cui, T., Zhang, H., Gold, A., Glasius, M., and Surratt, J. D.: Dimers in α-pinene secondary organic aerosol: Effect of hydroxyl radical, ozone, relative humidity and aerosol acidity, Atmos Chem Phys, 14, 4201−4218, https://doi.org/10.5194/acp-14-4201-2014, 2014.

Kristensen, K., Watne, Å. K., Hammes, J., Lutz, A., Petäjä, T., Hallquist, M., Bilde, M., and Glasius, M.: High-molecular weight dimer esters are major products in aerosols from α-pinene ozonolysis and the boreal forest, Environmental Science & Technology Letters, 3, 280−285, https://doi.org/10.1021/acs.estlett.6b00152, 2016.

Kroll, J. H., Ng, N. L., Murphy, S. M., Flagan, R. C., and Seinfeld, J. H.: Secondary organic aerosol formation from isoprene photooxidation under high-NOx conditions, Geophys Res Lett, 32, L18808, https://doi.org/10.1029/2005gl023637, 2005.

Kroll, J. H., and Seinfeld, J. H.: Chemistry of secondary organic aerosol: Formation and evolution of low-volatility organics in the atmosphere, Atmos Environ, 42, 3593–3624, https://doi.org/10.1016/j.atmosenv.2008.01.003, 2008.

Kulmala, M., Kontkanen, J., Junninen, H., Lehtipalo, K., Manninen, H. E., Nieminen, T., Petäjä, T., Sipilä, M., Schobesberger, S., Rantala, P., Franchin, A., Jokinen, T., Järvinen, E., Äijälä, M., Kangasluoma, J., Hakala, J., Aalto, P. P., Paasonen, P., Mikkilä, J., Vanhanen, J., Aalto, J., Hakola, H., Makkonen, U., Ruuskanen, T., Mauldin III, R. L., Duplissy, J., Vehkamäki, H., Bäck, J., Kortelainen, A., Riipinen, I., Kurtén, T., Johnston, M. V., Smith, J. N., Ehn, M., Mentel, T. F., Lehtinen, K. E. J., Laaksonen, A., Kerminen, V.-M., and Worsnop, D. R.: Direct observations of atmospheric aerosol nucleation, Science, 339, 943–946, https://doi.org/10.1126/science.1227385, 2013.

Langford, B., Cash, J., Acton, W. J. F., Valach, A. C., Hewitt, C. N., Fares, S., Goded, I., Gruening, C., House, E., Kalogridis, A.-C., Gros, V., Schafers, R., Thomas, R., Broadmeadow, M., and

Nemitz, E.: Isoprene emission potentials from European oak forests derived from canopy flux measurements: an assessment of uncertainties and inter-algorithm variability, Biogeosciences, 14, 5571–5594, https://doi.org/10.5194/bg-14-5571-2017, 2017.

Lee, B. H., Lopez-Hilfiker, F. D., Mohr, C., Kurtén, T., Worsnop, D. R., and Thornton, J. A.: An iodide-adduct high-resolution time-of-flight chemical-ionization mass spectrometer: Application to atmospheric inorganic and organic compounds, Environ Sci Technol, 48, 6309−6317, https://doi.org/10.1021/es500362a, 2014.

Lee, B. H., Lopez-Hilfiker, F. D., D'Ambro, E. L., Zhou, P. T., Boy, M., Petäjä, T., Hao, L. Q., Virtanen, A., Thornton, J. A.: Semi-volatile and highly oxygenated gaseous and particulate organiccompounds observed above a boreal forest canopy. Atmos Chem Phys, 18, 11547−11562, https://doi.org/10.5194/acp-18-11547-2018, 2018.

Lee, B. H., Mohr, C., Lopez-Hilfiker, F. D., Lutz, A., Hallquist, M., Lee, L., Romer, P., Cohen, R. C., Iyer, S., Kurtén, T., Hu, W. W., Day, D. A., Campuzano-Jost, P., Jimenez, J. L., Xu, L., Ng, N. L., Guo, H. Y., Weber, R. J., Wild, R. J., Brown, S. S., Koss, A., de Gouw, J., Olson, K., Goldstein, A. H., Seco, R., Kim, S., McAvey, K., Shepson, P. B., Starn, T., Baumann, K., Edgerton, E. S., Liu, J. M., Shilling, J. E., Miller, D. O., Brune, W., Schobesberger, S., D'Ambro, E. L., and Thornton, J. A.: Highly functionalized organic nitrates in the southeast United States: Contribution to secondary organic aerosol and reactive nitrogen budgets, P Natl Acad Sci USA, 113, 1516–1521, https://doi.org/10.1073/pnas.1508108113, 2016a.

Lee, S.-H., Uin, J., Guenther, A. B., de Gouw, J. A., Yu, F. Q., Nadykto, A. B., Herb, J., Ng, N. L., Koss, A., Brune, W. H., Baumann, K., Kanawade, V. P., Keutsch, F. N., Nenes, A., Olsen, K., Goldstein, A., and Ouyang, Q.: Isoprene suppression of new particle formation: Potential mechanisms and implications, J Geophys Res-Atmos, 121, 14621–14635, https://doi.org/10.1002/2016jd024844, 2016b.

Li, Y., Pöschl, U., and Shiraiwa, M.: Molecular corridors and parameterizations of volatility in the chemical evolution of organic aerosols, Atmos Chem Phys, 16, 3327–3344, https://doi.org/10.5194/acp-16-3327-2016, 2016.

Lienhard, D. M., Huisman, A. J., Krieger, U. K., Rudich, Y., Marcolli, C., Luo, B. P., Bones, D. L., Reid, J. P., Lambe, A. T., Canagaratna, M. R., Davidovits, P., Onasch, T. B., Worsnop, D. R., Steimer, S. S., Koop, T., and Peter, T.: Viscous organic aerosol particles in the upper

troposphere: diffusivity-controlled water uptake and ice nucleation?, Atmos Chem Phys, 15, 13599−13613, https://doi.org/10.5194/acp-15-13599-2015, 2015.

Lopez-Hilfiker, F. D., Mohr, C., Ehn, M., Rubach, F., Kleist, E., Wildt, J., Mentel, T. F., Lutz, A., Hallquist, M., Worsnop, D., and Thornton, J. A.: A novel method for online analysis of gas and particle composition: description and evaluation of a Filter Inlet for Gases and AEROsols (FIGAERO), Atmos Meas Tech, 7, 983−1001, https://doi.org/10.5194/amt-7-983-2014, 2014.

Lopez-Hilfiker, F. D., Mohr, C., Ehn, M., Rubach, F., Kleist, E., Wildt, J., Mentel, T. F., Carrasquillo, A. J., Daumit, K. E., Hunter, J. F., Kroll, J. H., Worsnop, D. R., and Thornton, J. A.: Phase partitioning and volatility of secondary organic aerosol components formed from α-pinene ozonolysis and OH oxidation: the importance of accretion products and other low volatility compounds, Atmos Chem Phys, 15, 7765−7776, https://doi.org/10.5194/acp-15-7765-2015, 2015.

Lopez-Hilfiker, F. D., Iyer, S., Mohr, C., Lee, B. H., D'Ambro, E. L., Kurtén, T., and Thornton, J. A.: Constraining the sensitivity of iodide adduct chemical ionization mass spectrometry to multifunctional organic molecules using the collision limit and thermodynamic stability of iodide ion adducts, Atmos Meas Tech, 9, 1505−1512, https://doi.org/10.5194/amt-9-1505-2016, 2016a.

Lopez-Hilfiker, F. D., Mohr, C., D'Ambro, E. L., Lutz, A., Riedel, T. P., Gaston, C. J., Iyer, S., Zhang, Z., Gold, A., Surratt, J. D., Lee, B. H., Kurten, T., Hu, W. W., Jimenez, J., Hallquist, M., and Thornton, J. A.: Molecular composition and volatility of organic aerosol in the Southeastern U.S.: Implications for IEPOX derived SOA, Environ Sci Technol, 50, 2200–2209, https://doi.org/10.1021/acs.est.5b04769, 2016b.

Lopez-Hilfiker, F. D., Pospisilova, V., Huang, W., Kalberer, M., Mohr, C., Stefenelli, G., Thornton, J. A., Baltensperger, U., Prevot, A. S. H., and Slowik, J. G.: An Extractive Electrospray Ionization Time-of-Flight Mass Spectrometer (EESI-TOF) for online measurement of atmospheric aerosol particles, Atmospheric Chemistry and Physics Discussions, 1–40, https://doi.org/10.5194/amt-2019-45, 2019.

LUBW: Luftreinhaltepläne für Baden-Württemberg (Grundlagenband 2017), in, LUBW State Institute for the Environment Baden-Württemberg, Karlsruhe, Germany, 2019.

Massoli, P., Stark, H., Canagaratna, M. R., Krechmer, J. E., Xu, L., Ng, N. L., Mauldin, R. L., Yan, C., Kimmel, J., Misztal, P. K., Jimenez, J. L., Jayne, J. T., and Worsnop, D. R.: Ambient

measurements of highly oxidized gas-phase molecules during the Southern Oxidant and Aerosol Study (SOAS) 2013, Acs Earth Space Chem, 2, 653–672, https://doi.org/10.1021/acsearthspacechem.8b00028, 2018.

McFiggans, G., Mentel, T. F., Wildt, J., Pullinen, I., Kang, S., Kleist, E., Schmitt, S., Springer, M., Tillmann, R., Wu, C., Zhao, D. F., Hallquist, M., Faxon, C., Le Breton, M., Hallquist, A. M., Simpson, D., Bergström, R., Jenkin, M. E., Ehn, M., Thornton, J. A., Alfarra, M. R., Bannan, T. J., Percival, C. J., Priestley, M., Topping, D., and Kiendler-Scharr, A.: Secondary organic aerosol reduced by mixture of atmospheric vapours, Nature, 565, 587–593, https://doi.org/10.1038/s41586-018-0871-y, 2019.

McVay, R. C., Zhang, X., Aumont, B., Valorso, R., Camredon, M., La, Y. S., Wennberg, P. O., and Seinfeld, J. H.: SOA formation from the photooxidation of α-pinene: systematic exploration of the simulation of chamber data, Atmos Chem Phys, 16, 2785−2802, https://doi.org/10.5194/acp-16-2785-2016, 2016.

Mofikoya, A. O., Kim, T. H., El-Raheem, A. M. A., Blande, J. D., Kivimaedenpaa, M., and Holopainen, J. K.: Passive adsorption of volatile monoterpene in pest control: Aided by proximity and disrupted by ozone, J Agr Food Chem, 65, 9579–9586, https://doi.org/10.1021/acs.jafc.7b03251, 2017.

Möhler, O., Stetzer, O., Schaefers, S., Linke, C., Schnaiter, M., Tiede, R., Saathoff, H., Krämer, M., Mangold, A., Budz, P., Zink, P., Schreiner, J., Mauersberger, K., Haag, W., Kärcher, B., and Schurath, U.: Experimental investigation of homogeneous freezing of sulphuric acid particles in the aerosol chamber AIDA, Atmos Chem Phys, 3, 211−223, https://doi.org/10.5194/acp-3-211-2003, 2003.

Mohr, C., DeCarlo, P. F., Heringa, M. F., Chirico, R., Slowik, J. G., Richter, R., Reche, C., Alastuey, A., Querol, X., Seco, R., Peñuelas, J., Jiménez, J. L., Crippa, M., Zimmermann, R., Baltensperger, U., and Prévôt, A. S. H.: Identification and quantification of organic aerosol from cooking and other sources in Barcelona using aerosol mass spectrometer data, Atmos Chem Phys, 12, 1649−1665, https://doi.org/10.5194/acp-12-1649-2012, 2012.

Mohr, C., Lopez-Hilfiker, F. D., Yli-Juuti, T., Heitto, A., Lutz, A., Hallquist, M., D'Ambro, E. L., Rissanen, M. P., Hao, L. Q., Schobesberger, S., Kulmala, M., Mauldin, R. L., Makkonen, U., Sipilä, M., Petäjä, T., and Thornton, J. A.: Ambient observations of dimers from terpene

oxidation in the gas phase: Implications for new particle formation and growth, Geophys Res Lett, 44, 2958−2966, https://doi.org/10.1002/2017GL072718, 2017.

Molteni, U., Bianchi, F., Klein, F., El Haddad, I., Frege, C., Rossi, M. J., Dommen, J., and Baltensperger, U.: Formation of highly oxygenated organic molecules from aromatic compounds, Atmos Chem Phys, 18, 1909−1921, https://doi.org/10.5194/acp-18-1909-2018, 2018.

Monson, R. K., Jones, R. T., Rosenstiel, T. N., and Schnitzler, J. P.: Why only some plants emit isoprene, Plant Cell and Environment, 36, 503–516, https://doi.org/10.1111/pce.12015, 2013.

Müller, L., Reinnig, M.-C., Warnke, J., and Hoffmann, T.: Unambiguous identification of esters as oligomers in secondary organic aerosol formed from cyclohexene and cyclohexene/α-pinene ozonolysis, Atmos Chem Phys, 8, 1423−1433, https://doi.org/10.5194/acp-8-1423-2008, 2008.

Munson, B.: Development of chemical ionization mass spectrometry, Int J Mass Spectrom, 200, 243–251, https://doi.org/10.1016/S1387-3806(00)00301-8, 2000.

Murphy, D. M., Cziczo, D. J., Froyd, K. D., Hudson, P. K., Matthew, B. M., Middlebrook, A. M., Peltier, R. E., Sullivan, A., Thomson, D. S., and Weber, R. J.: Single-particle mass spectrometry of tropospheric aerosol particles, J Geophys Res-Atmos, 111, D23S32, https://doi.org/10.1029/2006JD007340, 2006.

Nah, T., Sanchez, J., Boyd, C. M., and Ng, N. L.: Photochemical aging of α-pinene and β-pinene secondary organic aerosol formed from nitrate radical oxidation, Environ Sci Technol, 50, 222–231, https://doi.org/10.1021/acs.est.5b04594, 2016.

Nash, D. G., Baer, T., and Johnston, M. V.: Aerosol mass spectrometry: An introductory review, Int J Mass Spectrom, 258, 2–12, https://doi.org/10.1016/j.ijms.2006.09.017, 2006.

Nel, A.: Air pollution-related illness: Effects of particles, Science, 308, 804−806, https://doi.org/10.1126/science.1108752 2005.

Nestorowicz, K., Jaoui, M., Rudzinski, K. J., Lewandowski, M., Kleindienst, T. E., Spólnik, G., Danikiewicz, W., and Szmigielski, R.: Chemical composition of isoprene SOA under acidic and non-acidic conditions: effect of relative humidity, Atmos Chem Phys, 18, 18101–18121, https://doi.org/10.5194/acp-18-18101-2018, 2018.

Ng, N. L., Kroll, J. H., Chan, A. W. H., Chhabra, P. S., Flagan, R. C., and Seinfeld, J. H.: Secondary organic aerosol formation from m-xylene, toluene, and benzene, Atmos Chem Phys, 7, 3909–3922, https://doi.org/10.5194/acp-7-3909-2007, 2007.

Nozière, B., Kaberer, M., Claeys, M., Allan, J., D'Anna, B., Decesari, S., Finessi, E., Glasius, M., Grgić, I., Hamilton, J. F., Hoffmann, T., Iinuma, Y., Jaoui, M., Kahno, A., Kampf, C. J., Kourtchev, I., Maenhaut, W., Marsden, N., Saarikoski, S., Schnelle-Kreis, J., Surratt, J. D., Szidat, S., Szmigielski, R., and Wisthaler, A.: The molecular identification of organic compounds in the atmosphere: State of the art and challenges, Chem Rev, 115, 3919−3983, https://doi.org/10.1021/cr5003485, 2015.

Office for Environmental Protection. Luft: Erfolgreiche Maßnahmen zur Luftreinhaltung in Stuttgart: https://www.stuttgart.de/item/show/15638, 2016.

Pajunoja, A., Malila, J., Hao, L. Q., Joutsensaari, J., Lehtinen, K. E. J., and Virtanen, A.: Estimating the viscosity range of SOA particles based on their coalescence Time, Aerosol Sci Tech, 48, i−iv, https://doi.org/10.1080/02786826.2013.870325, 2014.

Pandis, S. N., Paulson, S. E., Seinfeld, J. H., and Flagan, R. C.: Aerosol formation in the photooxidation of isoprene and β-pinene, Atmos Environ, 25, 997–1008, https://doi.org/10.1016/0960-1686(91)90141-S, 1991.

Paulsen, D., Dommen, J., Kalberer, M., Prévôt, A. S. H., Richter, R., Sax, M., Steinbacher, M., Weingartner, E., and Baltensperger, U.: Secondary organic aerosol formation by irradiation of 1,3,5-trimethylbenzene-NOx-H2O in a new reaction chamber for atmospheric chemistry and physics, Environ Sci Technol, 39, 2668–2678, https://doi.org/10.1021/es0489137, 2005.

Perry, R. A., Atkinson, R., and Pitts, J. N.: Kinetics and mechanism of gas phase reaction of OH radicals with aromatic hydrocarbons over temperature range 296-473 K, J Phys Chem-Us, 81, 296–304, https://doi.org/10.1021/j100519a004, 1977.

Ponche, J.-L., Schneider, C., and Mirabel, P.: Methodology and results of the REKLIP atmospheric emission inventory of the upper Rhine Valley transborder region, Water Air Soil Poll, 124, 61–93, https://doi.org/10.1023/A:1005252525013, 2000.

Pospisilova, V., Lopez-Hilfiker, F. D., Bell, D., El Haddad, I., Mohr, C., Huang, W., Heikkinen, L., Xiao, M., Dommen, J., Prévôt, A. S. H., Baltensperger, U., and Slowik, J. G.: On the fate of oxygenated organic molecules in atmospheric aerosol particles, Science Advances, in review, 2019.

Price, H. C., Mattsson, J., Zhang, Y., Bertram, A. K., Davies, J. F., Grayson, J. W., Martin, S. T., O'Sullivan, D., Reid, J. P., Rickards, A. M. J., and Murray, B. J.: Water diffusion in

atmospherically relevant α-pinene secondary organic material, Chemical Science, 6, 4876−4883, https://doi.org/10.1039/c5sc00685f, 2015.

Qi, L., Chen, M., Stefenelli, G., Pospisilova, V., Tong, Y., Bertrand, A., Hueglin, C., Ge, X., Baltensperger, U., Prévôt, A. S. H., and Slowik, J. G.: Organic aerosol source apportionment in Zurich using an extractive electrospray ionization time-of-flight mass spectrometry (EESI-TOF): Part II, biomass burning influences in winter, Atmos Chem Phys Discuss, 1−42, https://doi.org/10.5194/acp-2019-64, 2019.

Renbaum-Wolff, L., Grayson, J. W., Bateman, A. P., Kuwata, M., Sellier, M., Murray, B. J., Shilling, J. E., Martin, S. T., and Bertram, A. K.: Viscosity of α-pinene secondary organic material and implications for particle growth and reactivity, P Natl Acad Sci USA, 110, 8014−8019, https://doi.org/10.1073/pnas.1219548110, 2013.

Reyes-Villegas, E., Bannan, T., Le Breton, M., Mehra, A., Priestley, M., Percival, C., Coe, H., and Allan, J. D.: Online chemical characterization of food-cooking organic aerosols: Implications for source apportionment, Environ Sci Technol, 52, 5308−5318, https://doi.org/10.1021/acs.est.7b06278, 2018.

Riva, M., Budisulistiorini, S. H., Zhang, Z. F., Gold, A., and Surratt, J. D.: Chemical characterization of secondary organic aerosol constituents from isoprene ozonolysis in the presence of acidic aerosol, Atmos Environ, 130, 5–13, https://doi.org/10.1016/j.atmosenv.2015.06.027, 2016.

Roldin, P., Eriksson, A. C., Nordin, E. Z., Hermansson, E., Mogensen, D., Rusanen, A., Boy, M., Swietlicki, E., Svenningsson, B., Zelenyuk, A., and Pagels, J.: Modelling non-equilibrium secondary organic aerosol formation and evaporation with the aerosol dynamics, gas- and particle-phase chemistry kinetic multilayer model ADCHAM, Atmos Chem Phys, 14, 7953−7993, https://doi.org/10.5194/acp-14-7953-2014, 2014.

Rollins, A. W., Browne, E. C., Min, K.-E., Pusede, S. E., Wooldridge, P. J., Gentner, D. R., Goldstein, A. H., Liu, S., Day, D. A., Russell, L. M., and Cohen, R. C.: Evidence for NOx control over nighttime SOA formation, Science, 337, 1210–1212, https://doi.org/10.1126/science.1221520, 2012.

Rückerl, R., Schneider, A., Breitner, S., Cyrys, J., and Peters, A.: Health effects of particulate air pollution: A review of epidemiological evidence, Inhal Toxicol, 23, 555−592, https://doi.org/10.3109/08958378.2011.593587, 2011.

Rudich, Y., Donahue, N. M., and Mentel, T. F.: Aging of organic aerosol: Bridging the gap between laboratory and field studies, Annu Rev Phys Chem, 58, 321–352, https://doi.org/10.1146/annurev.physchem.58.032806.104432, 2007.

Saarnio, K., Aurela, M., Timonen, H., Saarikoski, S., Teinilä, K., Mäkelä, T., Sofiev, M., Koskinen, J., Aalto, P. P., Kulmala, M., Kukkonen, J., and Hillamo, R.: Chemical composition of fine particles in fresh smoke plumes from boreal wild-land fires in Europe, Sci Total Environ, 408, 2527−2542, https://doi.org/10.1016/j.scitotenv.2010.03.010, 2010.

Saathoff, H., Naumann, K.-H., Möhler, O., Jonsson, Å. M., Hallquist, M., Kiendler-Scharr, A., Mentel, T. F., Tillmann, R., and Schurath, U.: Temperature dependence of yields of secondary organic aerosols from the ozonolysis of α-pinene and limonene, Atmos Chem Phys, 9, 1551−1577, https://doi.org/10.5194/acp-9-1551-2009, 2009.

Sanchez, J., Tanner, D. J., Chen, D. X., Huey, L. G., and Ng, N. L.: A new technique for the direct detection of HO2 radicals using bromide chemical ionization mass spectrometry (Br-CIMS): initial characterization, Atmos Meas Tech, 9, 3851–3861, https://doi.org/10.5194/amt-9-3851-2016, 2016.

Sato, K., Hatakeyama, S., and Imamura, T.: Secondary organic aerosol formation during the photooxidation of toluene: NOx dependence of chemical composition, J Phys Chem A, 111, 9796–9808, https://doi.org/10.1021/jp071419f, 2007.

Schauer, J. J., Rogge, W. F., Hildemann, L. M., Mazurek, M. A., Cass, G. R., and Simoneit, B. R. T.: Source apportionment of airborne particulate matter using organic compounds as tracers, Atmos Environ, 30, 3837–3855, https://doi.org/10.1016/1352-2310(96)00085-4, 1996.

Schauer, J. J., Kleeman, M. J., Cass, G. R., and Simoneit, B. R. T.: Measurement of emissions from air pollution sources. 3. C1-C29 organic compounds from fireplace combustion of wood, Environ Sci Technol, 35, 1716–1728, https://doi.org/10.1021/es001331e, 2001.

Schnaiter, M., Järvinen, E., Vochezer, P., Abdelmonem, A., Wagner, R., Jourdan, O., Mioche, G., Shcherbakov, V. N., Schmitt, C. G., Tricoli, U., Ulanowski, Z., and Heymsfield, A. J.: Cloud chamber experiments on the origin of ice crystal complexity in cirrus clouds, Atmos Chem Phys, 16, 5091−5110, https://doi.org/10.5194/acp-16-5091-2016, 2016.

Schwartz, J., Spix, C., Wichmann, H. E., and Malin, E.: Air pollution and acute respiratory illness in five German communities, Environ Res, 56, 1−14, https://doi.org/10.1016/S0013-9351(05)80104-5, 1991.

Sharkey, T. D., and Yeh, S. S.: Isoprene emission from plants, Annu Rev Plant Phys, 52, 407–436, https://doi.org/10.1146/annurev.arplant.52.1.407, 2001.

Sharkey, T. D., Wiberley, A. E., and Donohue, A. R.: Isoprene emission from plants: Why and how, Ann Bot-London, 101, 5–18, https://doi.org/10.1093/aob/mcm240, 2008.

Shen, X., Ramisetty, R., Mohr, C., Huang, W., Leisner, T., and Saathoff, H.: Laser ablation aerosol particle time-of-flight mass spectrometer (LAAPTOF): performance, reference spectra and classification of atmospheric samples, Atmos Meas Tech, 11, 2325−2343, https://doi.org/10.5194/amt-11-2325-2018, 2018.

Shen, X., Vogel, H., Vogel, B., Huang, W., Mohr, C., Ramisetty, R., Leisner, T., Prévôt, A. S. H., and Saathoff, H.: Composition and origin of PM2.5 aerosol particles in the upper Rhine valley in summer, Atmos Chem Phys, in review, 2019a.

Shen, X., Saathoff, H., Huang, W., Mohr, C., Ramisetty, R., and Leisner, T.: Understanding atmospheric aerosol particles with improved particle identification and quantification by single-particle mass spectrometry, Atmos Meas Tech, 12, 2219–2240, https://doi.org/10.5194/amt-12-2219-2019, 2019b.

Shiraiwa, M., Ammann, M., Koop, T., and Pöschl, U.: Gas uptake and chemical aging of semisolid organic aerosol particles, P Natl Acad Sci USA, 108, 11003−11008, https://doi.org/10.1073/pnas.1103045108, 2011.

Shiraiwa, M., Li, Y., Tsimpidi, A. P., Karydis, V. A., Berkemeier, T., Pandis, S. N., Lelieveld, J., Koop, T., and Pöschl, U.: Global distribution of particle phase state in atmospheric secondary organic aerosols, Nature Communications, 8, 15002, https://doi.org/10.1021/acsearthspacechem.7b00120, 2017.

Shrivastava, M., Easter, R. C., Liu, X., Zelenyuk, A., Singh, B., Zhang, K., Ma, P.-L., Chand, D., Ghan, S., Jimenez, J. L., Zhang, Q., Fast, J., Rasch, P. J., and Tiitta, P.: Global transformation and fate of SOA: Implications of low-volatility SOA and gas-phase fragmentation reactions, J Geophys Res-Atmos, 120, 4169−4195, https://doi.org/10.1002/2014JD022563, 2015.

Simoneit, B. R. T., Schauer, J. J., Nolte, C. G., Oros, D. R., Elias, V. O., Fraser, M. P., Rogge, W. F., and Cass, G. R.: Levoglucosan, a tracer for cellulose in biomass burning and atmospheric particles, Atmos Environ, 33, 173–182, https://doi.org/10.1016/S1352-2310(98)00145-9, 1999.

Simoneit, B. R. T., Elias, V. O., Kobayashi, M., Kawamura, K., Rushdi, A. I., Medeiros, P. M., Rogge, W. F., and Didyk, B. M.: Sugars - Dominant water-soluble organic compounds in soils

and characterization as tracers in atmospheric particulate matter, Environ Sci Technol, 38, 5939–5949, https://doi.org/10.1021/es0403099, 2004.

Singh, H. B., and Hanst, P. L.: Peroxyacetyl nitrate (PAN) in the unpolluted atmosphere: An important reservoir for nitrogen oxides, Geophys Res Lett, 8, 941–944, https://doi.org/10.1029/Gl008i008p00941, 1981.

Sobanski, N., Thieser, J., Schuladen, J., Sauvage, C., Song, W., Williams, J., Lelieveld, J., and Crowley, J. N.: Day and night-time formation of organic nitrates at a forested mountain site in south-west Germany, Atmos Chem Phys, 17, 4115–4130, https://doi.org/10.5194/acp-17-4115-2017, 2017.

Song, Y. C., Haddrell, A. E., Bzdek, B. R., Reid, J. P., Barman, T., Topping, D. O., Percival, C., and Cai, C.: Measurements and predictions of binary component aerosol particle viscosity, J Phys Chem A, 120, 8123−8137, https://doi.org/10.1021/acs.jpca.6b07835, 2016.

Spolnik, G., Wach, P., Rudzinski, K. J., Skotak, K., Danikiewicz, W., and Szmigielski, R.: Improved UHPLC-MS/MS methods for analysis of isoprene-derived organosulfates, Analytical Chemistry, 90, 3416–3423, https://doi.org/10.1021/acs.analchem.7b05060, 2018.

Süddeutsche Zeitung. Stuttgart löst als erste Stadt in Deutschland den Feinstaubalarm aus: http://www.sueddeutsche.de/panorama/luftverschmutzung-stuttgart-loest-als-erste-stadt-in-deutschland-feinstaubalarm-aus-1.2822775, 2016.

Suess, D. T., and Prather, K. A.: Mass spectrometry of aerosols, Chem Rev, 99, 3007–3035, https://doi.org/10.1021/cr980138o, 1999.

Sullivan, R. C., and Prather, K. A.: Recent advances in our understanding of atmospheric chemistry and climate made possible by on-line aerosol analysis instrumentation, Analytical Chemistry, 77, 3861–3885, https://doi.org/10.1021/ac050716i, 2005.

Surratt, J. D., Murphy, S. M., Kroll, J. H., Ng, N. L., Hildebrandt, L., Sorooshian, A., Szmigielski, R., Vermeylen, R., Maenhaut, W., Claeys, M., Flagan, R. C., and Seinfeld, J. H.: Chemical composition of secondary organic aerosol formed from the photooxidation of isoprene, J Phys Chem A, 110, 9665–9690, https://doi.org/10.1021/jp061734m, 2006.

Surratt, J. D., Kroll, J. H., Kleindienst, T. E., Edney, E. O., Claeys, M., Sorooshian, A., Ng, N. L., Offenberg, J. H., Lewandowski, M., Jaoui, M., Flagan, R. C., and Seinfeld, J. H.: Evidence for organosulfates in secondary organic aerosol, Environ Sci Technol, 41, 517–527, https://doi.org/10.1021/es062081q, 2007.

Takekawa, H., Minoura, H., and Yamazaki, S.: Temperature dependence of secondary organic aerosol formation by photo-oxidation of hydrocarbons, Atmos Environ, 37, 3413–3424, https://doi.org/10.1016/S1352-2310(03)00359-5, 2003.

Tröstl, J., Chuang, W. K., Gordon, H., Heinritzi, M., Yan, C., Molteni, U., Ahlm, L., Frege, C., Bianchi, F., Wagner, R., Simon, M., Lehtipalo, K., Williamson, C., Craven, J. S., Duplissy, J., Adamov, A., Almeida, J., Bernhammer, A.-K., Breitenlechner, M., Brilke, S., Dias, A., Ehrhart, S., Flagan, R. C., Franchin, A., Fuchs, C., Guida, R., Gysel, M., Hansel, A., Hoyle, C. R., Jokinen, T., Junninen, H., Kangasluoma, J., Keskinen, H., Kim, J., Krapf, M., Kürten, A., Laaksonen, A., Lawler, M., Leiminger, M., Mathot, S., Möhler, O., Nieminen, T., Onnela, A., Petäjä, T., Piel, F. M., Miettinen, P., Rissanen, M. P., Rondo, L., Sarnela, N., Schobesberger, S., Sengupta, K., Sipilä, M., Smith, J. N., Steiner, G., Tomè, A., Virtanen, A., Wagner, A. C., Weingartner, E., Wimmer, D., Winkler, P. M., Ye, P. L., Carslaw, K. S., Curtius, J., Dommen, J., Kirkby, J., Kulmala, M., Riipinen, I., Worsnop, D. R., Donahue, N. M., and Baltensperger, U.: The role of low-volatility organic compounds in initial particle growth in the atmosphere, Nature, 533, 527−531, https://doi.org/10.1038/nature18271, 2016.

Tsigaridis, K., Krol, M., Dentener, F. J., Balkanski, Y., Lathière, J., Metzger, S., Hauglustaine, D. A., and Kanakidou, M.: Change in global aerosol composition since preindustrial times, Atmos Chem Phys, 6, 5143−5162, https://doi.org/10.5194/acp-6-5143-2006, 2006.

Tunved, P., Hansson, H.-C., Kerminen, V.-M., Ström, J., Dal Maso, M., Lihavainen, H., Viisanen, Y., Aalto, P. P., Komppula, M., and Kulmala, M.: High natural aerosol loading over boreal forests, Science, 312, 261–263, https://doi.org/10.1126/science.1123052, 2006.

Ulbrich, I. M., Canagaratna, M. R., Zhang, Q., Worsnop, D. R., and Jimenez, J. L.: Interpretation of organic components from positive matrix factorization of aerosol mass spectrometric data, Atmos Chem Phys, 9, 2891–2918, https://doi.org/10.5194/acp-9-2891-2009, 2009.

Vaden, T. D., Imre, D., Beránek, J., Shrivastava, M., and Zelenyuk, A.: Evaporation kinetics and phase of laboratory and ambient secondary organic aerosol, P Natl Acad Sci USA, 108, 2190−2195, https://doi.org/10.1073/pnas.1013391108, 2011.

van der Werf, G. R., Randerson, J. T., Giglio, L., Collatz, G. J., Kasibhatla, P. S., and Arellano Jr., A. F.: Interannual variability in global biomass burning emissions from 1997 to 2004, Atmos Chem Phys, 6, 3423–3441, https://doi.org/10.5194/acp-6-3423-2006, 2006.

Virtanen, A., Joutsensaari, J., Koop, T., Kannosto, J., Yli-Pirilä, P., Leskinen, J., Mäkelä, J. M., Holopainen, J. K., Pöschl, U., Kulmala, M., Worsnop, D. R., and Laaksonen, A.: An amorphous solid state of biogenic secondary organic aerosol particles, Nature, 467, 824−827, https://doi.org/10.1038/nature09455, 2010.

Wagner, R., Höhler, K., Huang, W., Kiselev, A., Möhler, O., Mohr, C., Pajunoja, A., Saathoff, H., Schiebel, T., Shen, X. L., and Virtanen, A.: Heterogeneous ice nucleation of α-pinene SOA particles before and after ice cloud processing, J Geophys Res-Atmos, 122, 4924−4943, https://doi.org/10.1002/2016JD026401, 2017.

Wang, B. B., O'Brien, R. E., Kelly, S. T., Shilling, J. E., Moffet, R. C., Gilles, M. K., and Laskin, A.: Reactivity of liquid and semisolid secondary organic carbon with chloride and nitrate in atmospheric aerosols, J Phys Chem A, 119, 4498−4508, https://doi.org/10.1021/jp510336q, 2015.

Williams, L. R., Gonzalez, L. A., Peck, J., Trimborn, D., McInnis, J., Farrar, M. R., Moore, K. D., Jayne, J. T., Robinson, W. A., Lewis, D. K., Onasch, T. B., Canagaratna, M. R., Trimborn, A., Timko, M. T., Magoon, G., Deng, R., Tang, D., Blanco, E. D. L. R., Prévôt, A. S. H., Smith, K. A., and Worsnop, D. R.: Characterization of an aerodynamic lens for transmitting particles greater than 1 micrometer in diameter into the Aerodyne aerosol mass spectrometer, Atmos Meas Tech, 6, 3271−3280, https://doi.org/10.5194/amt-6-3271-2013, 2013.

Winterhalter, R., Van Dingenen, R., Larsen, B. R., Jensen, N. R., and Hjorth, J.: LC-MS analysis of aerosol particles from the oxidation of α-pinene by ozone and OH radicals, Atmospheric Chemistry and Physics Discussions, 3, 1−39, https://doi.org/10.5194/acpd-3-1-2003, 2003.

Xu, L., Williams, L. R., Young, D. E., Allan, J. D., Coe, H., Massoli, P., Fortner, E., Chhabra, P., Herndon, S., Brooks, W. A., Jayne, J. T., Worsnop, D. R., Aiken, A. C., Liu, S., Gorkowski, K., Dubey, M. K., Fleming, Z. L., Visser, S., Prévôt, A. S. H., and Ng, N. L.: Wintertime aerosol chemical composition, volatility, and spatial variability in the greater London area, Atmos Chem Phys, 16, 1139–1160, https://doi.org/10.5194/acp-16-1139-2016, 2016.

Yang, L. M., Nguyen, D. M., and Yu, L. E.: Photooxidation of levoglucosan in atmospheric aqueous aerosols, Geochim Cosmochim Ac, 73, A1477–A1477, 2009.

Yasmeen, F., Vermeylen, R., Szmigielski, R., Iinuma, Y., Böge, O., Herrmann, H., Maenhaut, W., and Claeys, M.: Terpenylic acid and related compounds: precursors for dimers in secondary

organic aerosol from the ozonolysis of α- and β-pinene, Atmos Chem Phys, 10, 9383−9392, https://doi.org/10.5194/acp-10-9383-2010, 2010.

Yli-Juuti, T., Pajunoja, A., Tikkanen, O.-P., Buchholz, A., Faiola, C., Väisänen, O., Hao, L., Kari, E., Peräkylä, O., Garmash, O., Shiraiwa, M., Ehn, M., Lehtinen, K., and Virtanen, A.: Factors controlling the evaporation of secondary organic aerosol from α-pinene ozonolysis, Geophys Res Lett, 44, 2562−2570, https://doi.org/10.1002/2016GL072364, 2017.

Zare, A., Romer, P. S., Nguyen, T., Keutsch, F. N., Skog, K., and Cohen, R. C.: A comprehensive organic nitrate chemistry: insights into the lifetime of atmospheric organic nitrates, Atmos Chem Phys, 18, 15419−15436, https://doi.org/10.5194/acp-18-15419-2018, 2018.

Zhang, Q., Jimenez, J. L., Canagaratna, M. R., Allan, J. D., Coe, H., Ulbrich, I., Alfarra, M. R., Takami, A., Middlebrook, A. M., Sun, Y. L., Dzepina, K., Dunlea, E., Docherty, K., DeCarlo, P. F., Salcedo, D., Onasch, T., Jayne, J. T., Miyoshi, T., Shimono, A., Hatakeyama, S., Takegawa, N., Kondo, Y., Schneider, J., Drewnick, F., Borrmann, S., Weimer, S., Demerjian, K., Williams, P., Bower, K., Bahreini, R., Cottrell, L., Griffin, R. J., Rautiainen, J., Sun, J. Y., Zhang, Y. M., and Worsnop, D. R.: Ubiquity and dominance of oxygenated species in organic aerosols in anthropogenically-influenced Northern Hemisphere midlatitudes, Geophys Res Lett, 34, L13801, https://doi.org/10.1029/2007GL029979, 2007.

Zhang, X., McVay, R. C., Huang, D. D., Dalleska, N. F., Aumont, B., Flagan, R. C., and Seinfeld, J. H.: Formation and evolution of molecular products in α-pinene secondary organic aerosol, P Natl Acad Sci USA, 112, 14168−14173, https://doi.org/10.1073/pnas.1517742112, 2015.

Zhao, R., Mungall, E. L., Lee, A. K. Y., Aljawhary, D., and Abbatt, J. P. D.: Aqueous-phase photooxidation of levoglucosan - a mechanistic study using aerosol time-of-flight chemical ionization mass spectrometry (Aerosol ToF-CIMS), Atmos Chem Phys, 14, 9695–9706, https://doi.org/10.5194/acp-14-9695-2014, 2014.

Zheng, M., Cass, G. R., Schauer, J. J., and Edgerton, E. S.: Source apportionment of PM2.5 in the southeastern United States using solvent-extractable organic compounds as tracers, Environ Sci Technol, 36, 2361–2371, https://doi.org/10.1021/es011275x, 2002.

Publications during the PhD study

[1] **Huang, W.**, Saathoff, H., Shen, X., Ramisetty, R., Leisner, T., and Mohr, C.: Chemical characterization of highly functionalized organonitrates contributing to night-time organic aerosol mass loadings and particle growth, ***Environ Sci Technol***, 53 (3), 1165–1174, https://doi.org/10.1021/acs.est.8b05826, 2019.

[2] **Huang, W.**, Saathoff, H., Pajunoja, A., Shen, X., Naumann, K.-H., Wagner, R., Virtanen, A., Leisner, T., and Mohr, C.: α-Pinene secondary organic aerosol at low temperature: chemical composition and implications for particle viscosity, ***Atmos Chem Phys***, 18, 2883–2898, https://doi.org/10.5194/acp-18-2883-2018, 2018.

[3] **Huang, W.**, Saathoff, H., Shen, X., Ramisetty, R., Leisner, T., and Mohr, C.: Seasonal characteristics of organic aerosol chemical composition and volatility in Stuttgart, Germany. ***Atmos Chem Phys Discuss***, https://doi.org/10.5194/acp-2019-364, in review, 2019.

[4] Shen, X., Saathoff, H., **Huang, W.**, Mohr, C., Ramisetty, R., Leisner, T.: Understanding atmospheric aerosol particles with improved particle identification and quantification by single-particle mass spectrometry, ***Atmos Meas Tech***, 12, 2219–2240, https://doi.org/10.5194/amt-12-2219-2019, 2019.

[5] Buchholz, A., Lambe, A., Ylisirniö, A., Li, Z., Tikkanen, O.-P., Faiola, C., Kari, E., Hao, L., Luoma, O., **Huang, W.**, Mohr, C., Worsnop. D.R., Nizkorodov, S., Yli-Juuti, T., Schobesberger, S., Virtanen, A.: Insights into the O:C-dependent mechanisms controlling the evaporation of α-pinene secondary organic aerosol particles, ***Atmos Chem Phys***, 19, 4061–4073, https://doi.org/10.5194/acp-19-4061-2019, 2019.

[6] Shen, X., Ramisetty, R., Mohr, C., **Huang, W.**, Leisner, T., and Saathoff, H.: Laser ablation aerosol particle time-of-flight mass spectrometer (LAAPTOF): performance, reference spectra and classification of atmospheric samples, ***Atmos Meas Tech***, 11, 2325–2343, https://doi.org/10.5194/amt-11-2325-2018, 2018.

[7] Wagner, R., Höhler, K., **Huang, W.**, Kiselev, A., Möhler, O., Mohr, C., Pajunoja, A., Saathoff, H., Schiebel, T., Shen, X. L., and Virtanen, A.: Heterogeneous ice nucleation of α-pinene SOA particles before and after ice cloud processing, ***J Geophys Res Atmos***, 122, 4924–4943, https://doi.org/10.1002/2016JD026401, 2017.

[8] Lopez-Hilfiker, F. D., Pospisilova, V., **Huang, W.**, Kalberer, M., Mohr, C., Stefenelli, G., Thornton, J. A., Baltensperger, U., Prevot, A. S. H., and Slowik, J. G. An Extractive Electrospray Ionization Time-of-Flight Mass Spectrometer (EESI-TOF) for online measurement of atmospheric aerosol particles, ***Atmos Meas Tech Discuss***, https://doi.org/10.5194/amt-2019-45, in review, 2019.

[9] Shen, X., Vogel, H., Vogel, B., Huang, W., Mohr, C., Ramisetty, R., Leisner, T., Prévôt, A. S. H., and Saathoff, H.: Composition and origin of $PM_{2.5}$ aerosol particles in the upper Rhine valley in summer, ***Atmos Chem Phys***, in review, 2019.

[10] Pospisilova, V., Lopez-Hilfiker, F. D., Bell, D., El Haddad, I., Mohr, C., **Huang, W.**, Heikkinen, L., Xiao, M., Dommen, J., Prevot, A. S. H., Baltensperger, U., Slowik, J. G.: On the fate of oxygenated organic molecules in atmospheric aerosol particles, ***Science Advances***, in review, 2019.

Acknowledgements

The whole PhD project cannot be finished without the support of many people and many organizations! I sincerely want to say thank you!

Firstly, I would like to thank Prof. Dr. Stefan Norra and Prof. Dr. Thomas Leisner for being my first and second supervisors at BGU and providing me the opportunity and platform to study here at IMK-AAF at KIT. I also want to thank them for always being positive about my PhD progress, and giving me advices how to proceed.

Secondly, I would like to sincerely thank Prof. Dr. Claudia Mohr for being my direct supervisor and giving me so much selfless care, encouragement, and help during my PhD study. Due to my analytical chemistry and environmental toxicology research background during my master study, I had really hard time at the beginning of my PhD to get into this completely new research topic, atmospheric science. But Claudia is always so patient and nice to help me to get familiar with all the new things I have to learn in my pace, and help me to find solutions how to deal with all the problems I had during my scientific research, such as how to solve the instrumental problems, how to analyze and interpret the data, and how to think and write publications in a scientific way, etc. In addition to as my direct supervisor in my PhD work, Claudia is also my friend, my sister, and my mentor of life. She is always willing to listen to my uneasiness, confusion, anxiety, and all the other bad feelings both from work and life, encourages me what I could try or even help me to solve these problems by e.g. reducing the overwhelming workload for me and making me feel comfortable and cheered up when I'm not. She is such a thoughtful and considerate person for always understanding my feelings! She shows me herself as a best example and thus influences me to treat science seriously, be simple towards life, stick to the things I like to do, and bravely choose and pursue the life I feel happy about. We had a lot of nice memories together in Karlsruhe (e.g., having hotpot party for New Year's Eve, making Chinese dumplings, playing Bowling together, eating Chinese food at Yangda Restaurant, taking care of our MS babies during TRAM01, swimming in the lake near Leopoldshafen) before she went to Stockholm in April 2017. After she left KIT, she didn't "give up" on me but continued to supervise me till the end of my PhD even with the big spatial distance. She even provided me the chance to go to Stockholm for one-month research stay there to get to know a slightly different scientific atmosphere, which was really nice and comfortable. Ever since after my research stay and the discussion with her and other scientists there, I was more and more certain that I want to do the things I like to do, i.e.,

continue doing science after my PhD. Also without her careful and meticulous attitude towards science, great supervision for my PhD work, and considerate personality, I cannot make any progress at all, not even to mention publishing any papers during my PhD! I feel so grateful for everything she has done for me from the bottom of my heart!

Thirdly, I want to thank all the colleagues at IMK-AAF for all the scientific and technical support. I especially want to thank Dr. Harald Saathoff for organizing the AIDA and field campaigns I participated in Germany and providing useful suggestions for the data interpretation and discussions. Harald is a chemist with solid and rich knowledge on chemistry, and I can always consult him whenever I have any questions about chemistry! Besides, he is a really nice and easygoing person. From him and many other colleagues, I learnt that we should always have a young mind no matter how old we are and that it is extremely important to balance work and life, since the latter provides so much motivation when the work is tough. All the best for him and his family! I also want to especially thank Xiaoli for providing me the textbook of atmospheric science and helping me a lot to learn the basic knowledge of atmospheric science at the beginning of my PhD, sharing the workload for the AMS operation and data analysis (we were always extremely efficient when we worked together!), having a lot of beneficial scientific discussions, as well as all the unforgettable time for the lunch, chat, and walk we had during the work and for the conferences we participated in together, sightseeings we did together (e.g., Wuppertal, Sicily island, Venice, Zurich, Lucerne, Washington DC, New York, etc.), different kind of tasty food we had together, and all the crazy things we did together during our spare time. She is the most special friend of mine in Germany considering how much time we have spent together! Sincere wishes for her postdoc as well as her life! I also want to thank Yvette for supporting me to operate the FIGAERO-CIMS during the SALTENA campaign in Bolivia, FIGAERO-CIMS data analysis, interpretation and discussions. Yvette is a very studious and observant girl, and I always believe in her to finish the work excellently and accomplish her goals. Hope her PhD study in Stockholm University is a great success! And of course, I thank all of them as well as Tobi, Lena, Barbara, Linyu, and Junwei for all the nice coffee breaks together and mutual cheering up.

Moreover, I also want to thank the support by the colleagues at PSI during PSI campaign 2016 (particularly Felipe and Veronika for performing the lab experiments, and the help in the instrument setup, operation and data discussion), all the members of the SALTENA campaign in Bolivia (particularly Wiebke and Eva from Innsbruck University for helping us setup the ion

source with corona; Cheng from Stockholm University for the CIMS operation, data analysis, interpretation, and discussion; George and Federico from Helsinki University for the CIMS data analysis and discussion), as well as the financial support by China Scholarship Council (CSC) for providing me the funding for my four-year PhD study at KIT, and also by KIT Graduate School for Climate and Environment (GRACE) for providing me the funding for me to participate in four international conferences (EAC2016, CIMS users meeting 2017, EAC2017, and EGU2019) and two research stays abroad (two-month for SALTENA campaign in Bolivia and one-month in Stockholm University in Sweden).

Last but not least I want to thank my parents, family members for supporting me to do all the things I want to do! Despite the huge spatial distance and time difference between China and Germany, they are always supportive for I am doing and affirmative for my work. I also want to thank my friends for cheering me up and sharing my happiness and sorrow. Special thanks go to my boyfriend, Junning, for all the love, support, and motivation. We met each other in Stutensee (~12 km away from Karlsruhe) and fell in love there. He was always there during the several worst moments of my time in Germany. Without his gentle comfort and encouragement, those moments would be much more horrible, tough, and suffering! Also without all the tasty food (e.g., handmade noodles, dumplings, Zongzi, Mooncake) he cooked and the accompany and beautiful memories we shared together in Karlsruhe and other countries (e.g., Netherlands, Belgium, Luxembourg, Italy, France, Spain, Sweden, Norway, Greece, Morocco) for the last four years, I would not have lived such an enriched and happy life in Karlsruhe! Best wishes for our future.

In the end, I want to thank you all again for the precious gather and the rare memories we had together during these four years! No matter how unwilling and sad, we always have to face countless parting all over our life! However, may we all be blessed though far apart, and I genuinely hope to see you again soon!

黄 薇 Huang, Wei

Karlsruhe, in July 2019.

A Appendix-Supplement for first-authored scientific publications

A.1 α-Pinene secondary organic aerosol at low temperature: chemical composition and implications for particle viscosity

Supplement of Atmos. Chem. Phys., 18, 2883–2898, 2018
https://doi.org/10.5194/acp-18-2883-2018-supplement

Atmospheric Chemistry and Physics Open Access EGU

Supplement of

α-Pinene secondary organic aerosol at low temperature: chemical composition and implications for particle viscosity

Wei Huang et al.

Correspondence to: Claudia Mohr (claudia.mohr@aces.su.se)

A Appendix

Table S1. Particle mass loadings (μg) on the filter and corresponding sampling times (min) at t0 and t1.

Exp. name	t0		t1	
	Mass loadings (μg)	Sampling time (min)	Mass loadings (μg)	Sampling time (min)
WDtoCH	4.07	20	3.93	20
WHtoCH	2.34	20	2.33	20
CH	6.60	13.5	6.19	5
CD	11.06	20	4.01	5

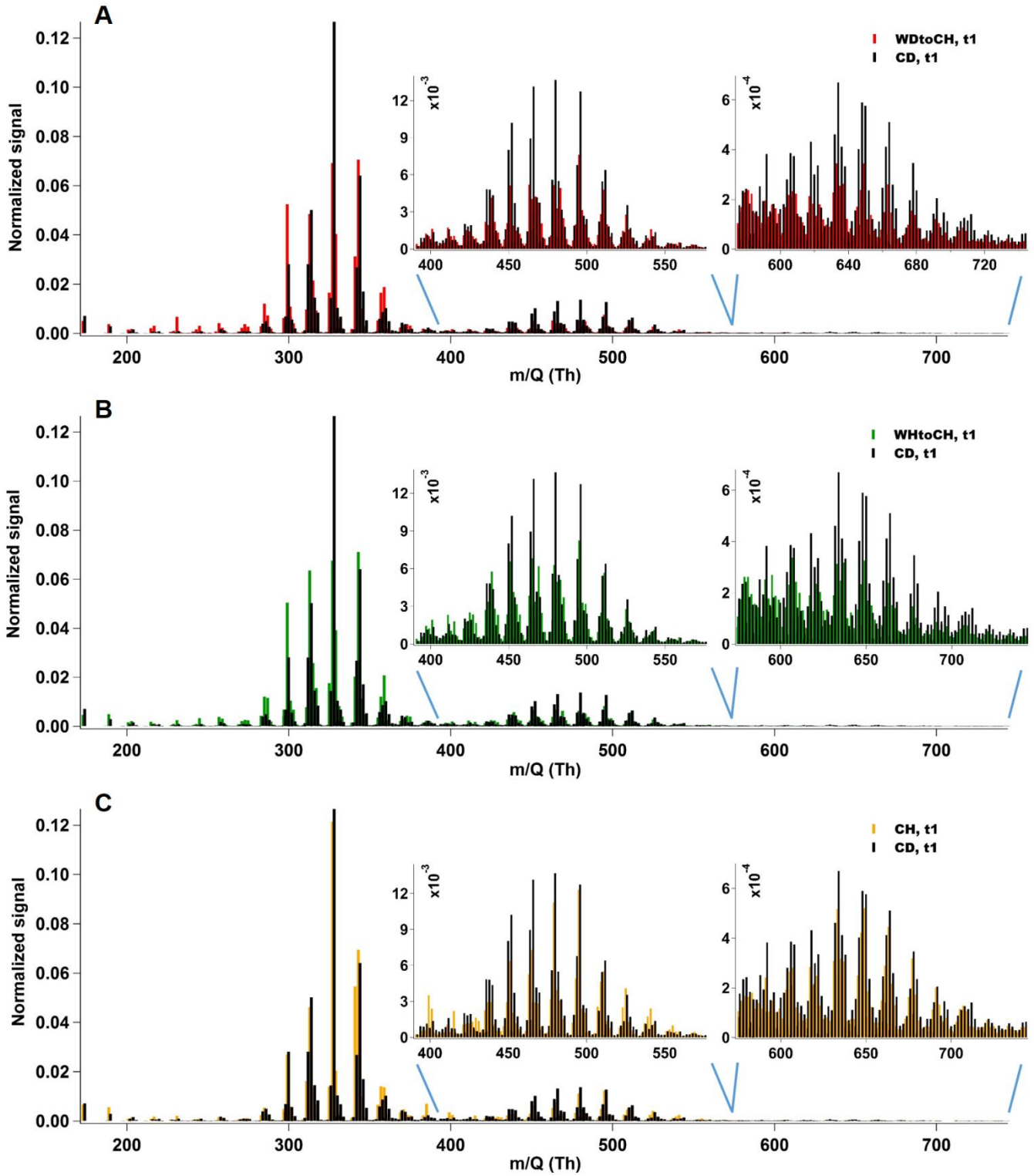

Figure S1. FIGAERO-CIMS mass spectra (normalized to the sum of signal of all detected CHOI compounds) of experiments WDtoCH and CD (A), WHtoCH and CD (B), CH and CD (C) at t1. Inserts show enlarged regions of dimers (left) and trimers (right).

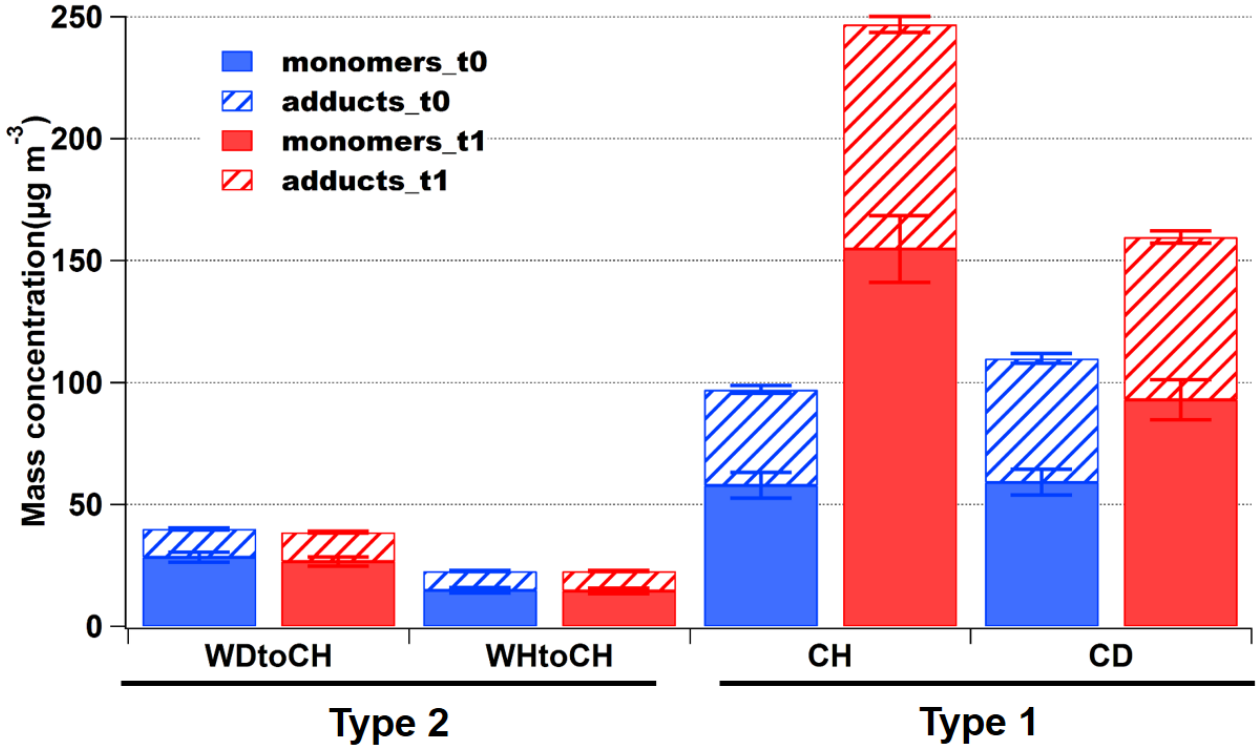

Figure S2. Absolute mass concentrations of monomers and adducts with error bars at t0 (blue) and t1 (red).

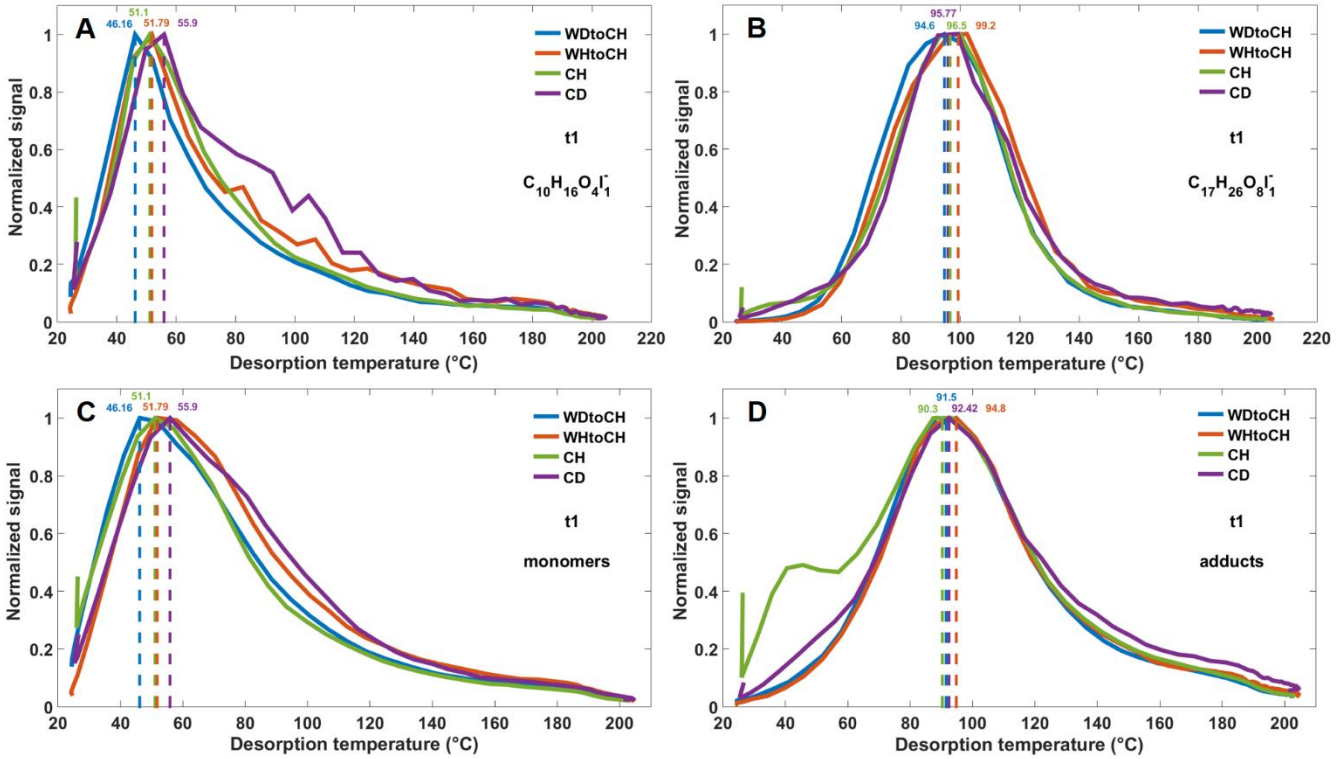

Figure S3. Thermograms of a monomer, $C_{10}H_{16}O_4$ (A) and an adduct, $C_{17}H_{26}O_8$ (B) both clustered with I^- at t1; sum thermograms of monomers (C) and adducts (D) at t1. Dashed lines refer to the corresponding T_{max}.

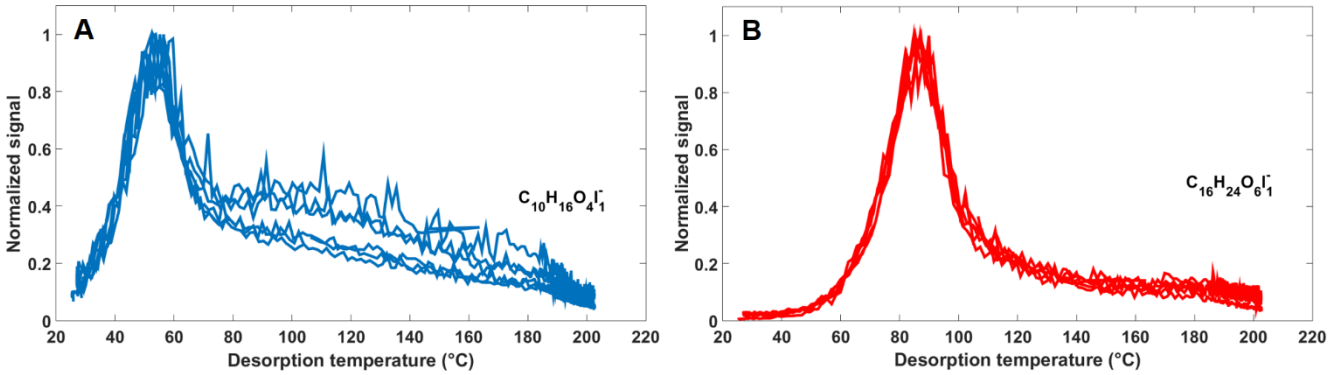

Figure S4. Thermograms of a monomer, $C_{10}H_{16}O_4$ (A) and an adduct, $C_{16}H_{24}O_6$ (B) both clustered with I^- under stable conditions.

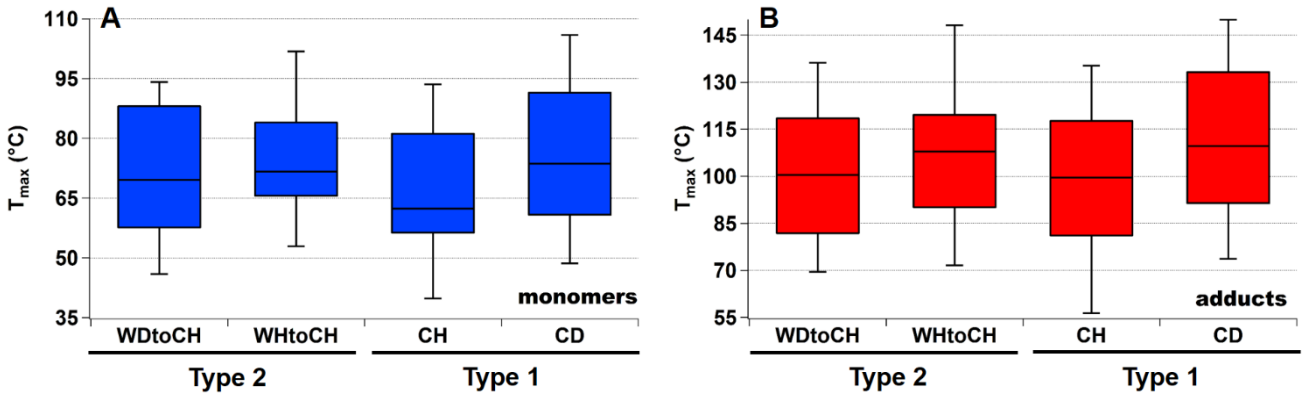

Figure S5. T_{max} box plot for monomers (A) and adducts (B) for four experiments at t0.

Mass loading effects

Different mass loadings on the filter due to different sampling times and/or sample concentrations influence thermogram shapes and thus T_{max}. Thermograms of the sums of all CHOI compounds, monomers and adducts for different filter mass loadings for WHtoCH and CD experiments were compared (Figure S6). The corresponding filter mass loadings are listed in Table S2. The box plot of T_{max} of all CHOI compounds, monomers and adducts increased with increasing mass loading on the filter (Figure S7). Beyond filter mass loadings of 2−4 µg the curves levelled off (saturation effect). Potential reasons for the observed effect of filter mass loading on T_{max} values are increased heat capacity of the increasing mass of the particle matrix, particle-particle interactions, and diffusion limitations due to several particle layers.

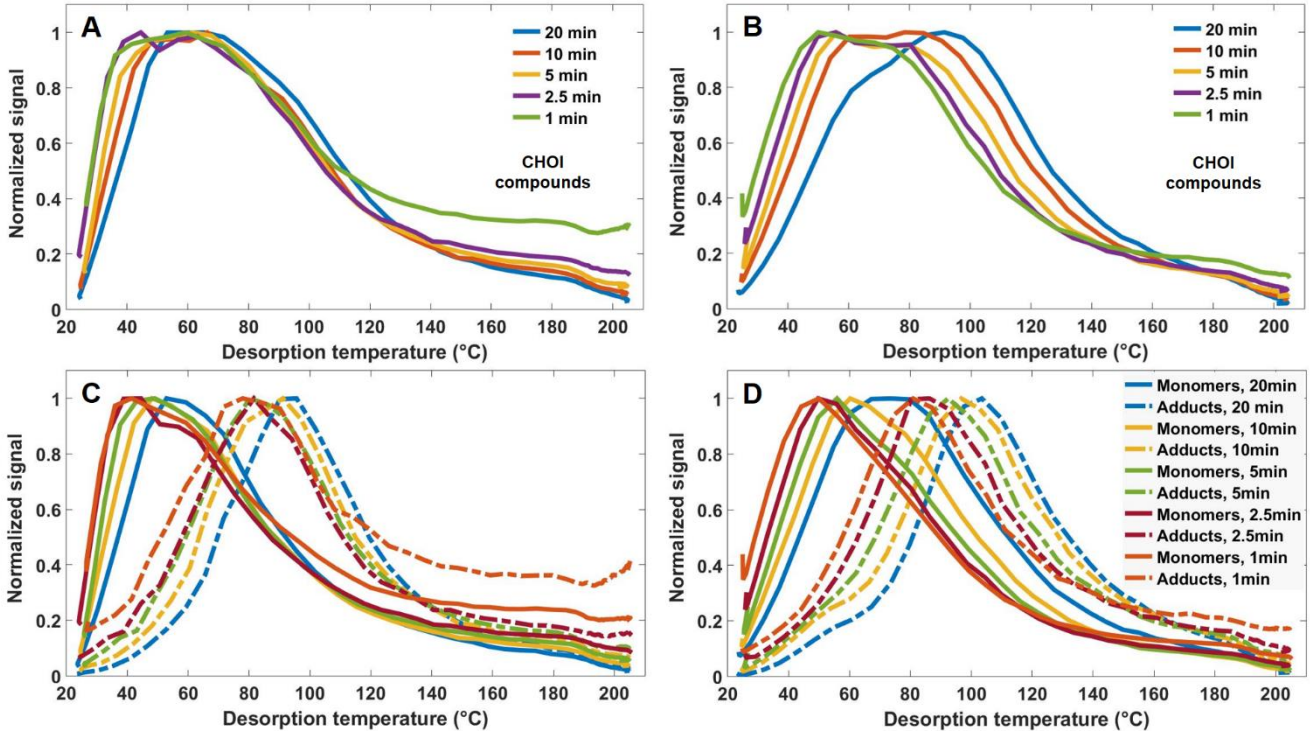

Figure S6. Sum thermograms of CHOI compounds with different sampling time for WHtoCH (A) and CD (B) experiments, and sum thermograms of monomers (solid lines) and adducts (dashed lines) for WHtoCH (C) and CD (D) experiments.

Table S2. Mass loadings (μg) on the filter with different sampling time for WHtoCH and CD experiments.

Exp. name	Mass loadings (μg)				
	20 min	10 min	5 min	2.5 min	1 min
WHtoCH	2.36	1.24	0.60	0.38	0.20
CD	11.06	7.25	4.01	2.08	0.94

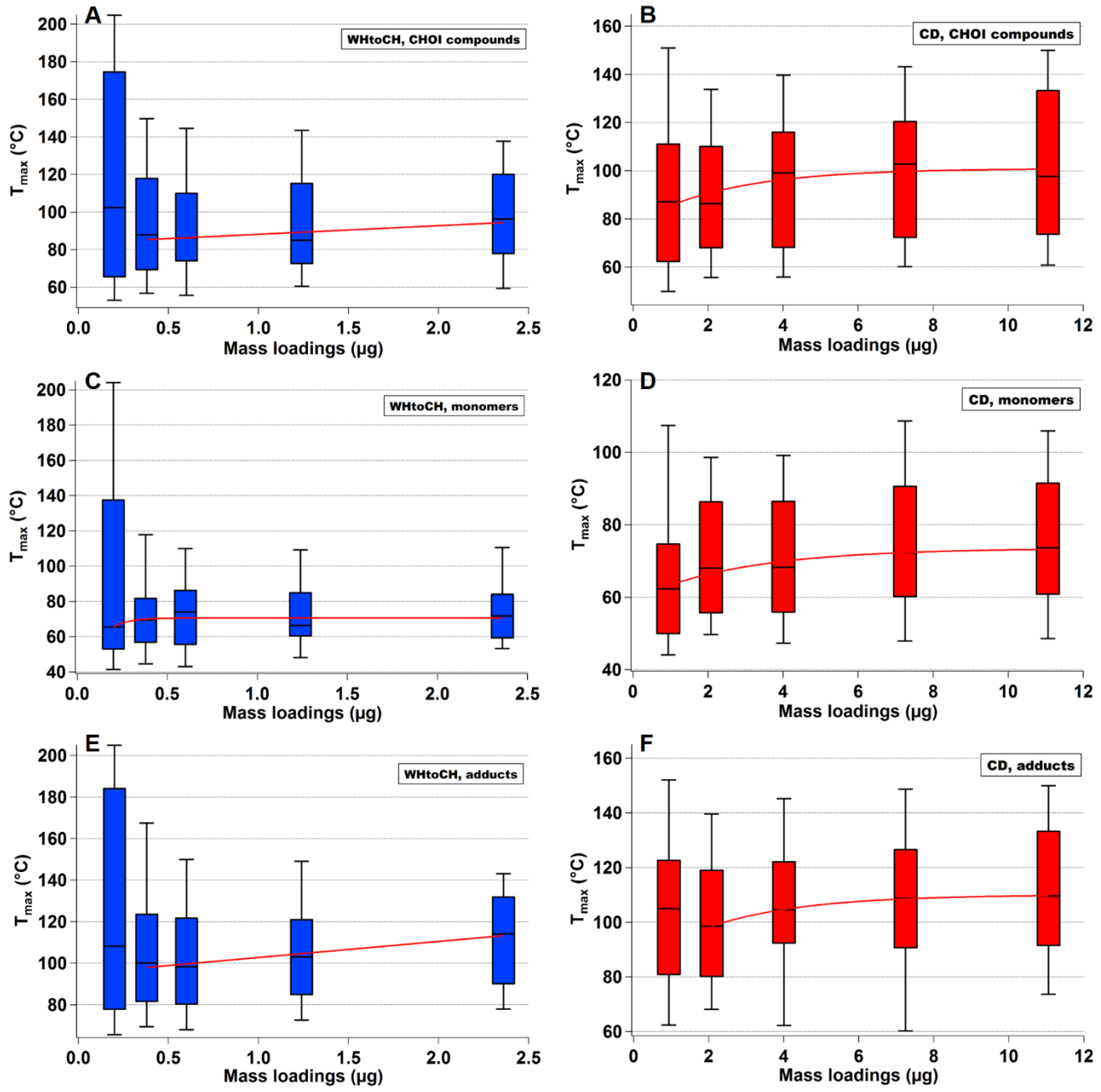

Figure S7. Box plot of T_{max} at different mass loadings for CHOI compounds (A−B), monomers (C−D) and adducts (E−F) for WHtoCH (left) and CD (right) experiments. Red lines refer to the exponential curves fitted for the median T_{max} in (A−D) and (F) except for linear fit in (E).

A.2 Chemical characterization of highly functionalized organonitrates contributing to night-time organic aerosol mass loadings and particle growth

Supporting Information

Chemical Characterization of Highly Functionalized Organonitrates Contributing to Night-Time Organic Aerosol Mass Loadings and Particle Growth

Wei Huang,[†,‡] Harald Saathoff,[†] Xiaoli Shen,[†,‡] Ramakrishna Ramisetty,[†,○] Thomas Leisner,[†,§] Claudia Mohr[*,‖]

[†]Institute of Meteorology and Climate Research, Karlsruhe Institute of Technology, Eggenstein-Leopoldshafen, 76344, Germany

[‡]Institute of Geography and Geoecology, Working Group for Environmental Mineralogy and Environmental System Analysis, Karlsruhe Institute of Technology, Karlsruhe, 76131, Germany

[○]Now at: TSI Instruments India Private Limited, Bangalore, 560102, India

[§]Institute of Environmental Physics, Heidelberg University, Heidelberg, 69120, Germany

[‖]Department of Environmental Science and Analytical Chemistry, Stockholm University, Stockholm, 11418, Sweden

15 pages: Page S1–S15

17 1 table: Table S1

18 9 figures: Figure S1–S9

19

20 **Corresponding Authors**

21 *E-mail: claudia.mohr@aces.su.se.

22 Table S1. Instruments installed in the measurement container during the field campaign 2016.

Measured parameter	**Instrument**	**Data period**
Ambient temperature	WS700 (Lufft GmbH)	July 8–Sept 1
Container temperature	WS700 (Lufft GmbH)	July 8–Sept 1
Dew point temperature	WS700 (Lufft GmbH)	July 8–Sept 1
RH	WS700 (Lufft GmbH)	July 8–Sept 1
Pressure	WS700 (Lufft GmbH)	July 8–Sept 1
Wind speed	WS700 (Lufft GmbH)	July 8–Sept 1
Wind vertical	WS700 (Lufft GmbH)	July 8–Sept 1
Wind direction	WS700 (Lufft GmbH)	July 8–Sept 1
Rain	WS700 (Lufft GmbH)	July 8–Sept 1
Rain type	WS700 (Lufft GmbH)	July 8–Sept 1
Rain rate	WS700 (Lufft GmbH)	July 8–Sept 1
Radiation	WS700 (Lufft GmbH)	July 8–Sept 1
Particle number concentration (>7 nm)	CPC3022 (TSI Inc.)	July 15–Sept 1
Particle number concentration (>2.5 nm)	CPC3776 (TSI Inc.)	July 15–Sept 1
O_3	O341M (Environment SA)	July 15–Sept 1
CO_2	NGA2000 (Rosemount Inc.)	July 15–Sept 1
SO_2	AF22M (Environment SA)	July 15–Sept 1
NO_2	AS32M (Environment SA)	July 15–Sept 1

NO	CLD 77 (Eco Physics AG)	July 15–Sept 1
Particle optical diameter (0.18–18 µm)	FIDAS 200 (Palas GmbH)	July 27–Sept 1
Particle size (10–670 nm, d_m)	SMPS (TSI Inc.)	August 19–31
Black carbon (BC)	AE33-7 Aethalometer (Magee Scientific Co.)	August 5–Sept 1
Single particle composition and size (0.2–2.5 µm, d_{va})	LAAPTOF (AeroMegt GmbH)	July 26–August 31
Particle mass and size (0.07–2.5 µm, d_{va})	AMS (Aerodyne Research Inc.)	July 26–August 31
Particle-phase and gas-phase oxygenated organic molecules	FIGAERO CIMS (Aerodyne Research Inc.)	August 18–Sept 1

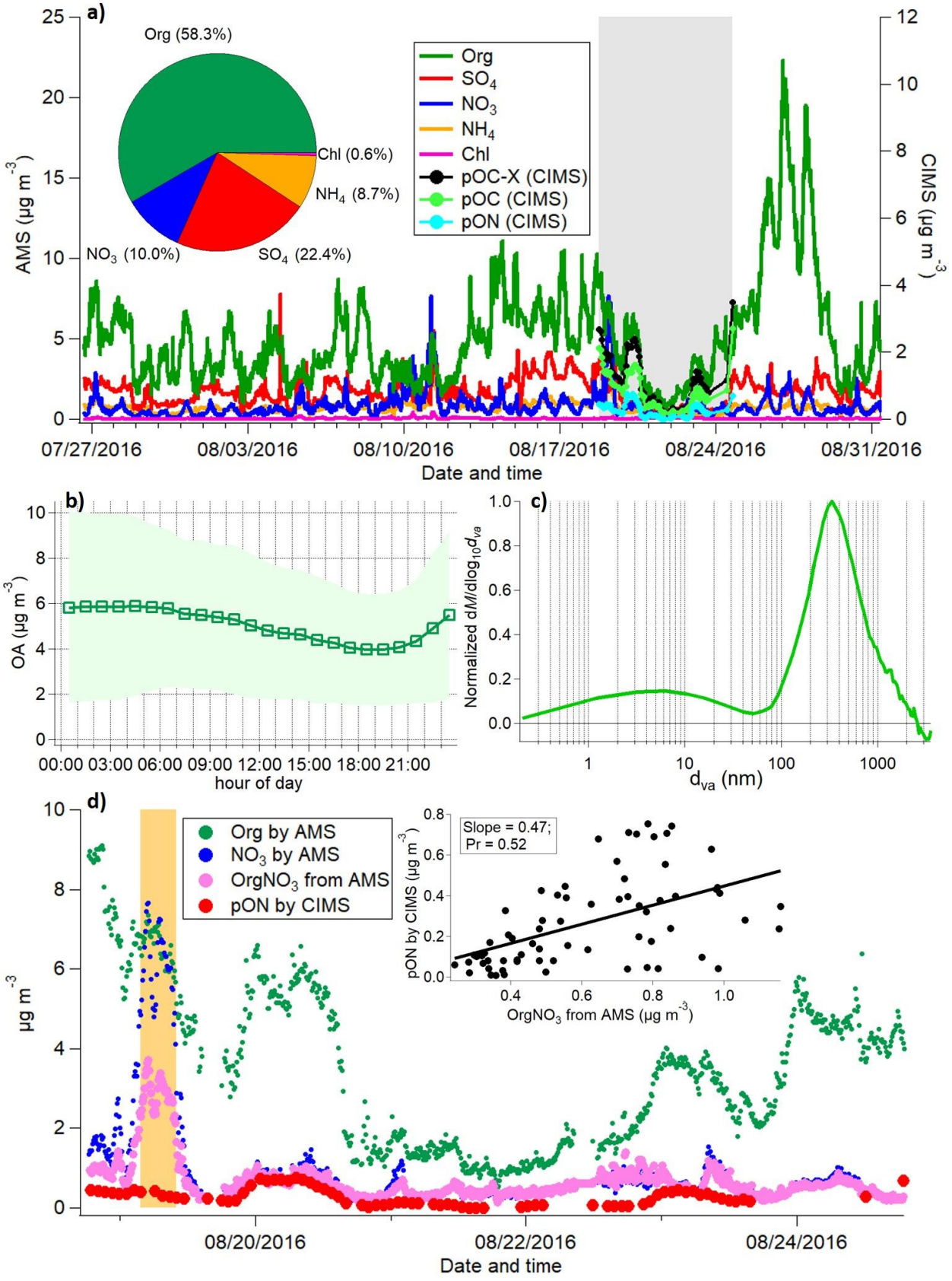
a)
Org (58.3%)
Chl (0.6%)
NH4 (8.7%)
NO3 (10.0%)
SO4 (22.4%)
Org
SO4
NO3
NH4
Chl
pOC-X (CIMS)
pOC (CIMS)
pON (CIMS)
AMS (μg m-3)
CIMS (μg m-3)
07/27/2016
08/03/2016
08/10/2016
08/17/2016
08/24/2016
08/31/2016
Date and time
b)
OA (μg m-3)
00:00 03:00 06:00 09:00 12:00 15:00 18:00 21:00
hour of day
c)
Normalized dM/dlog10dva
dva (nm)
d)
Org by AMS
NO3 by AMS
OrgNO3 from AMS
pON by CIMS
μg m-3
Slope = 0.47;
Pr = 0.52
pON by CIMS (μg m-3)
OrgNO3 from AMS (μg m-3)
08/20/2016
08/22/2016
08/24/2016
Date and time

23

Figure S1. (a) Time series of aerosol composition measured by AMS and CIMS, with the insert showing the campaign average aerosol contribution to total $PM_{2.5}$ measured by AMS. The CIMS measurement period is shaded in gray; (b) mean diel trend of OA measured by AMS during the whole campaign with the shaded area representing ±1 standard deviation; (c) average size distribution of organics measured by AMS during the CIMS measurement period; (d) time series of total OA and NO_3 measured by AMS, $OrgNO_3$ derived from AMS, and pON measured by CIMS. The insert shows the correlation of pON measured by CIMS and $OrgNO_3$, with the period shaded in orange excluded (likely moslty inorganic nitrates that contribute overproportionally to NO_x^+ fragments in the AMS)[1].

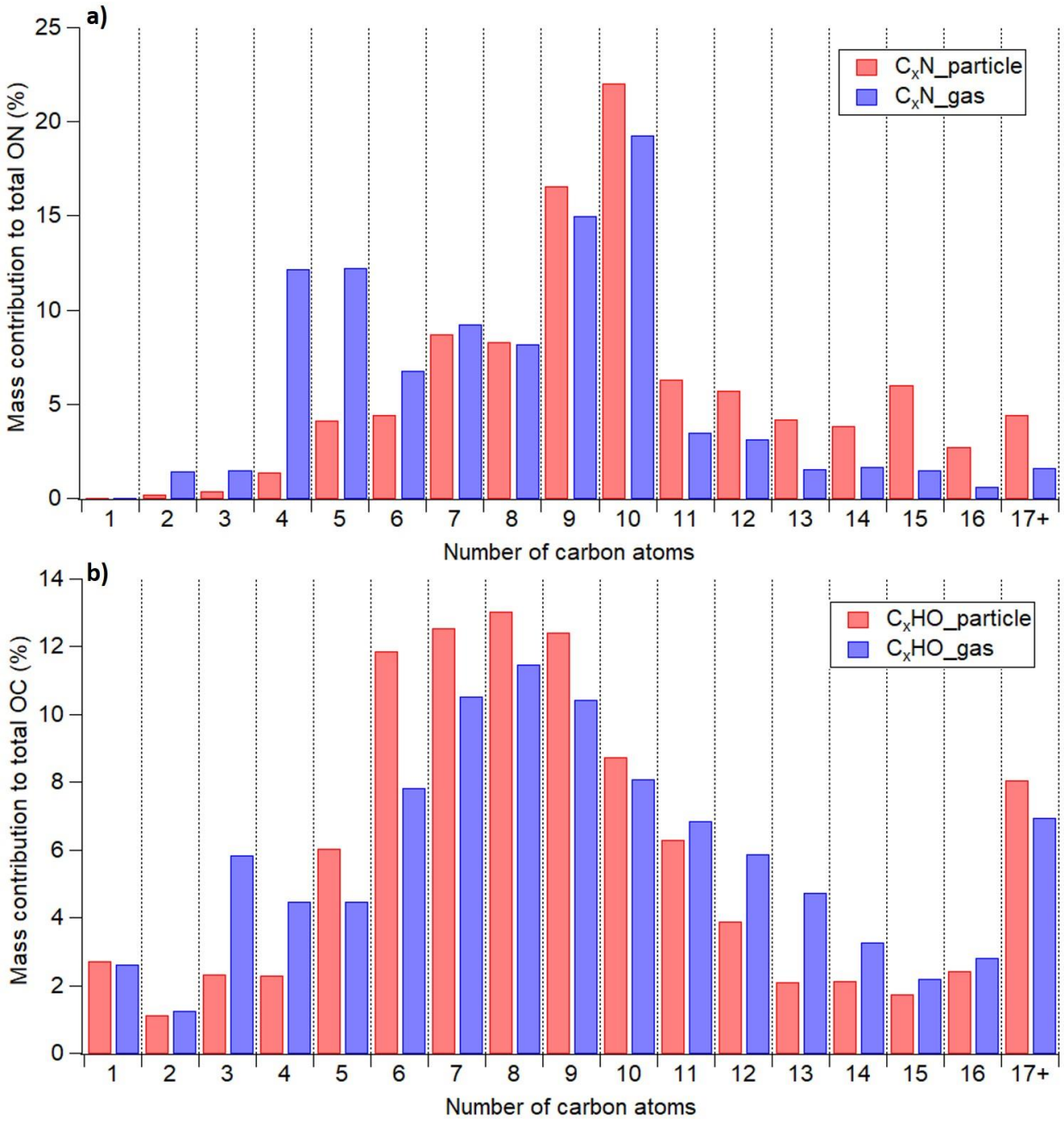

33

34 Figure S2. Mass contribution of (a) C_xN groups to total ON, and (b) of C_xHO groups to total OC

35 as a function of the number of carbon atoms.

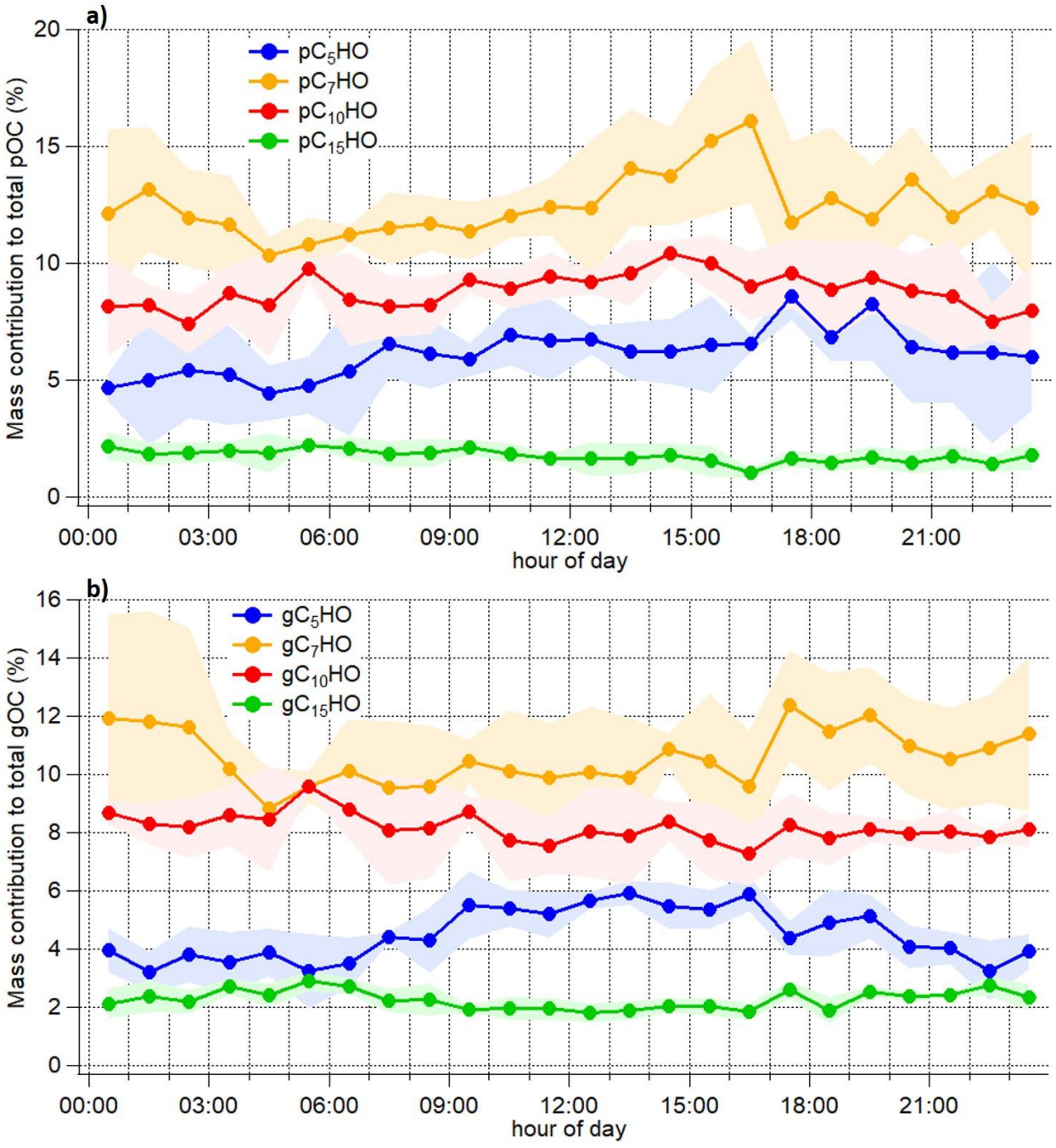

Figure S3. Mean diel patterns of the mass contribution of C_xHO (x=5, 7, 10, 15) groups (a) in the particle phase to total pOC, and (b) in the gas phase to total gOC. The shaded areas represent ±1 standard deviation.

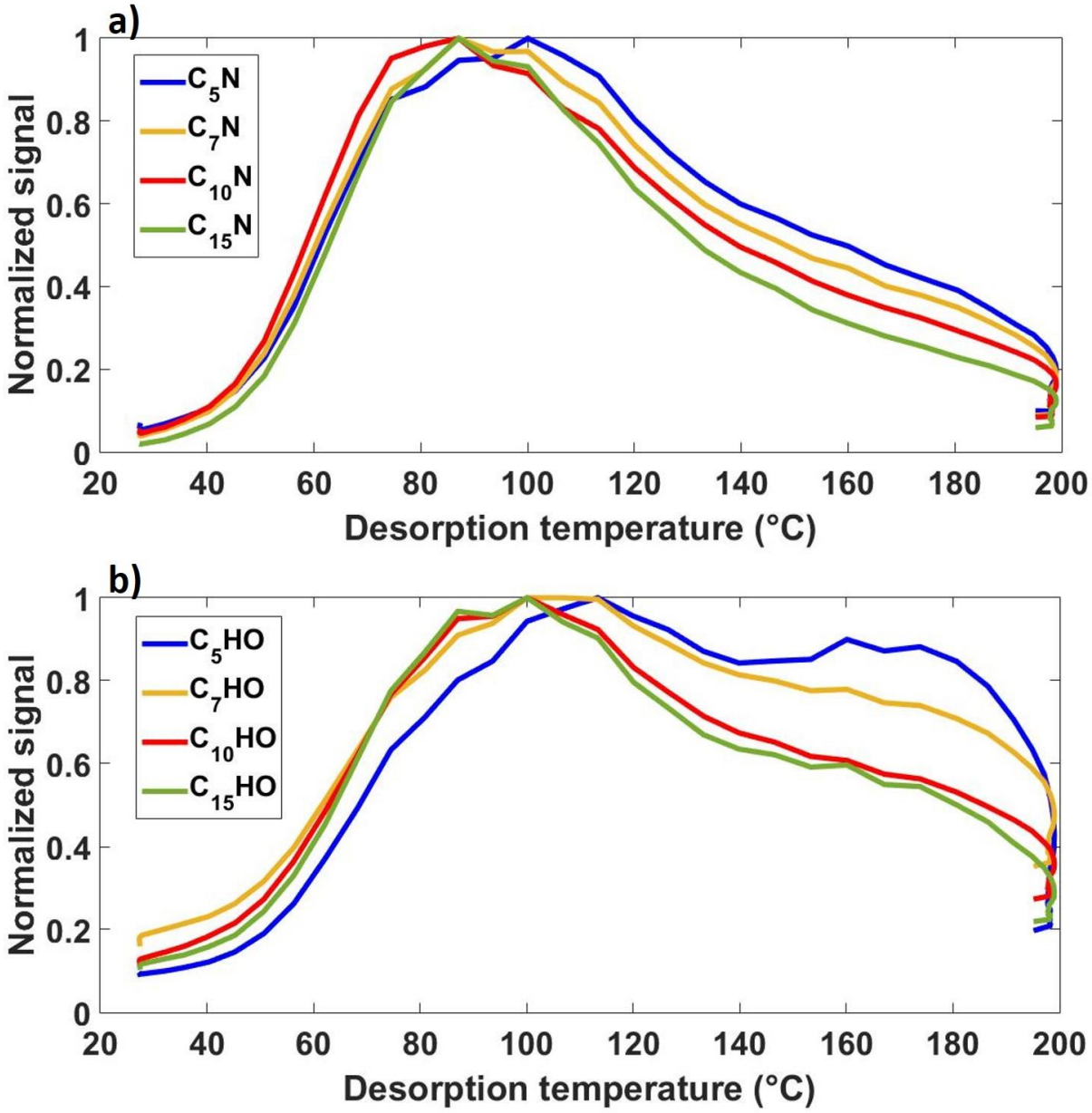

Figure S4. Average thermograms (mass spectral signal evolution as a function of desorption temperature) of pC_xN and pC_xHO groups (x=5, 7, 10, 15). Compared to the single-mode thermograms of the pC_xN groups and most pC_xHO groups, the thermogram of the pC_5HO group exhibits a multi-modal shape, indicative of contributions from isomers having different vapor pressures, or thermal decomposition of larger molecules.[2]

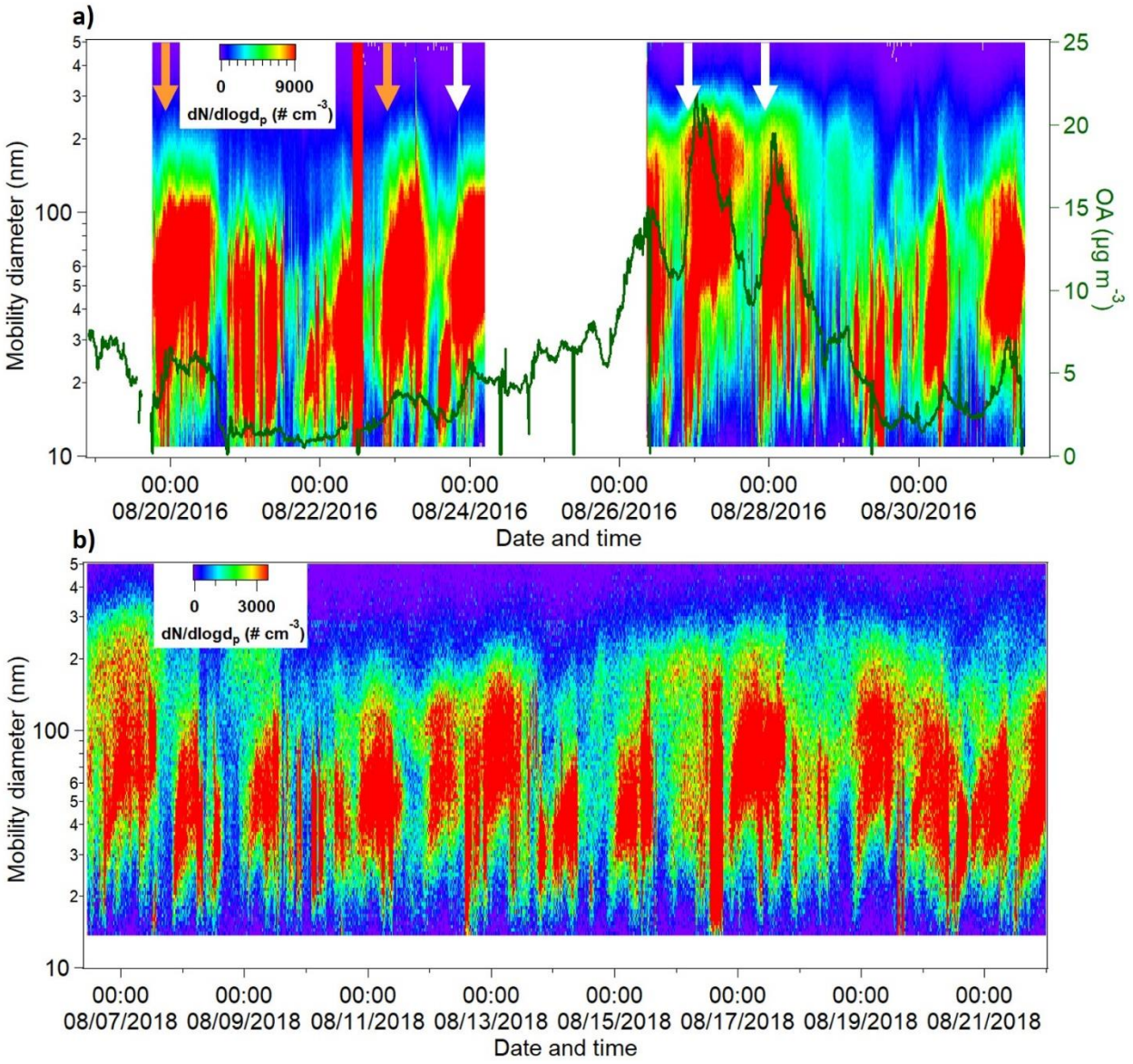

Figure S5. Night-time NPF events during the measurement period. (a) Particle size evolution measured by SMPS and OA particle mass measured by AMS, with the five arrows indicating the five NPF events used for particle growth rate calculations, and the two orange arrows indicating the two events used for mass increase rate calculations; (b) similar measurement during August 2018 at KIT campus north about 2 km east of the measurement site.

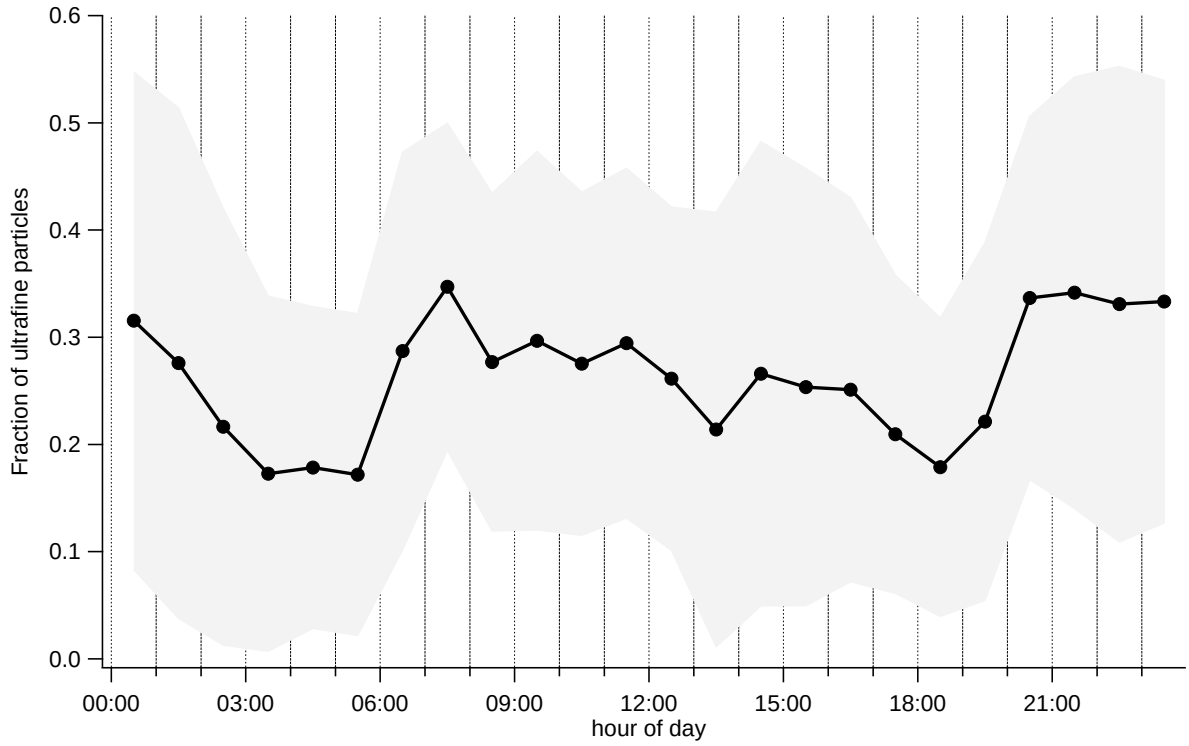

Figure S6. Mean diel trend of the number fraction of ultrafine particles (with mobility diameters between 2.5–7 nm), with the shaded area representing ±1 standard deviation.

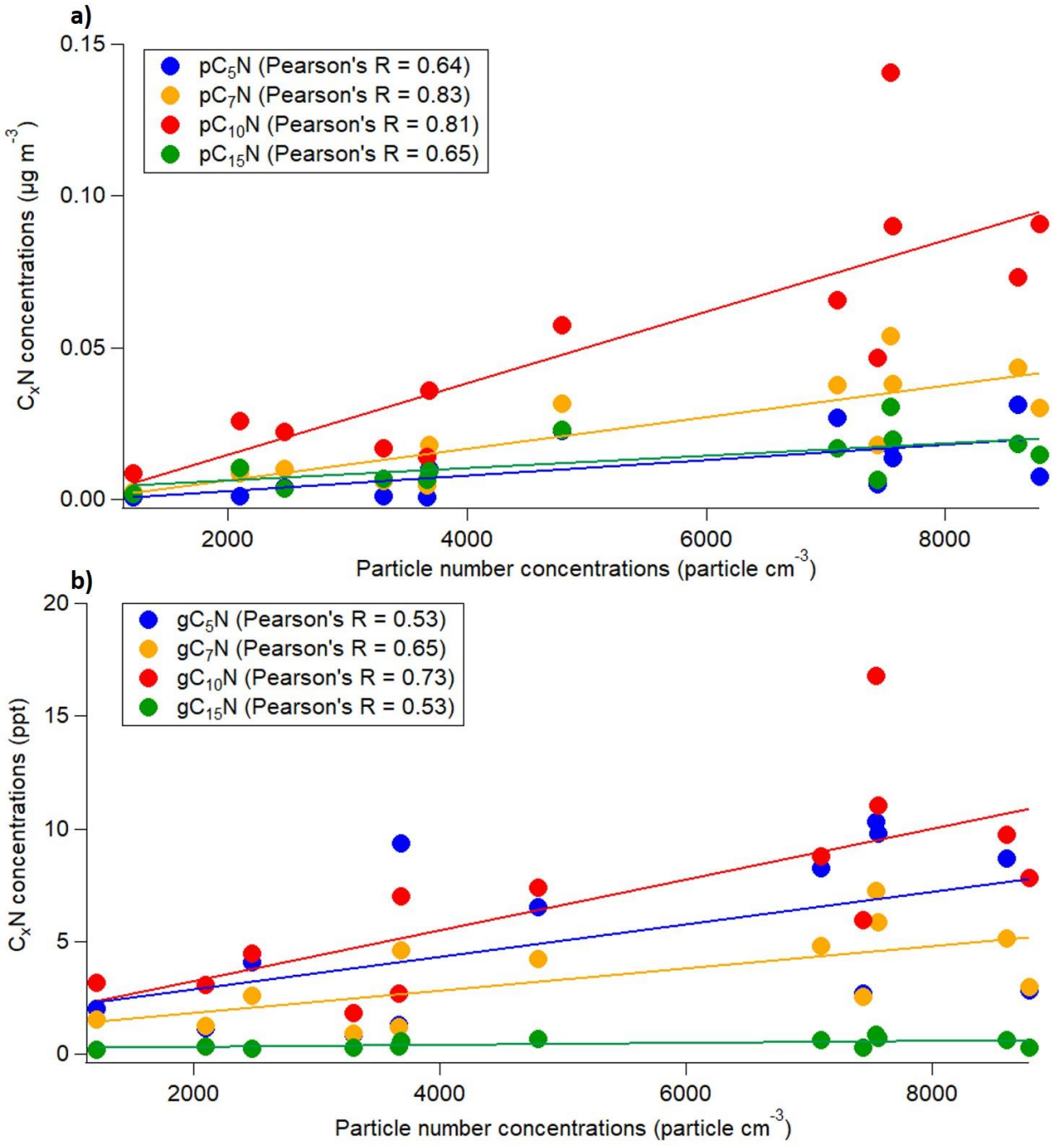

Figure S7. Correlations of C_xN (x=5, 7, 10, 15) group concentrations in particle (a) and gas (b) phases with number concentrations of ultrafine particles (with mobility diameters between 2.5–7 nm).

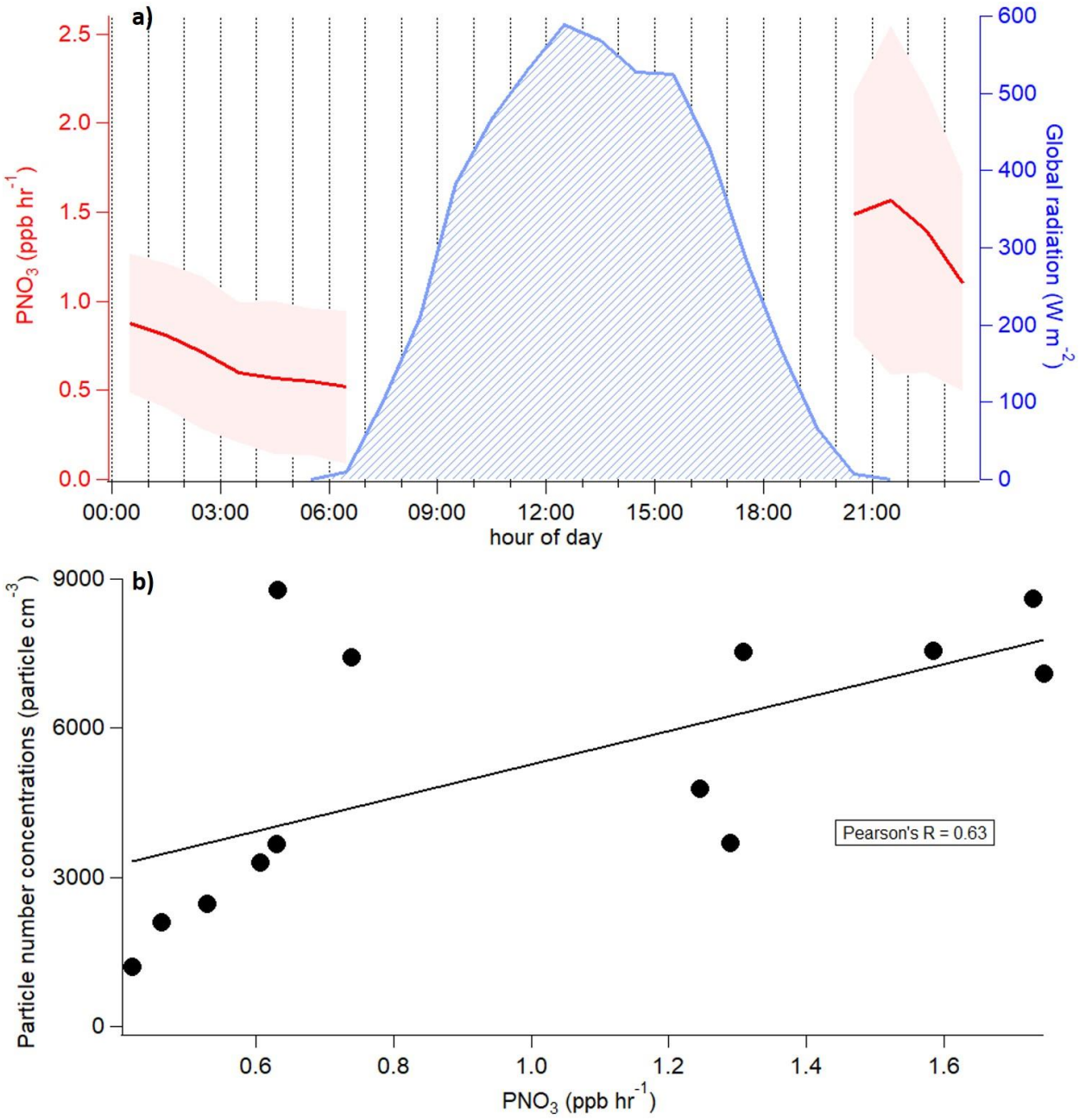

Figure S8. (a) Mean calculated production rate of nitrate radicals (PNO_3) during the night with the shaded area representing ±1 standard deviation, and mean global radiation during the day; (b) correlation of the number concentrations of ultrafine particles (with mobility diameters between 2.5–7 nm) with PNO_3.

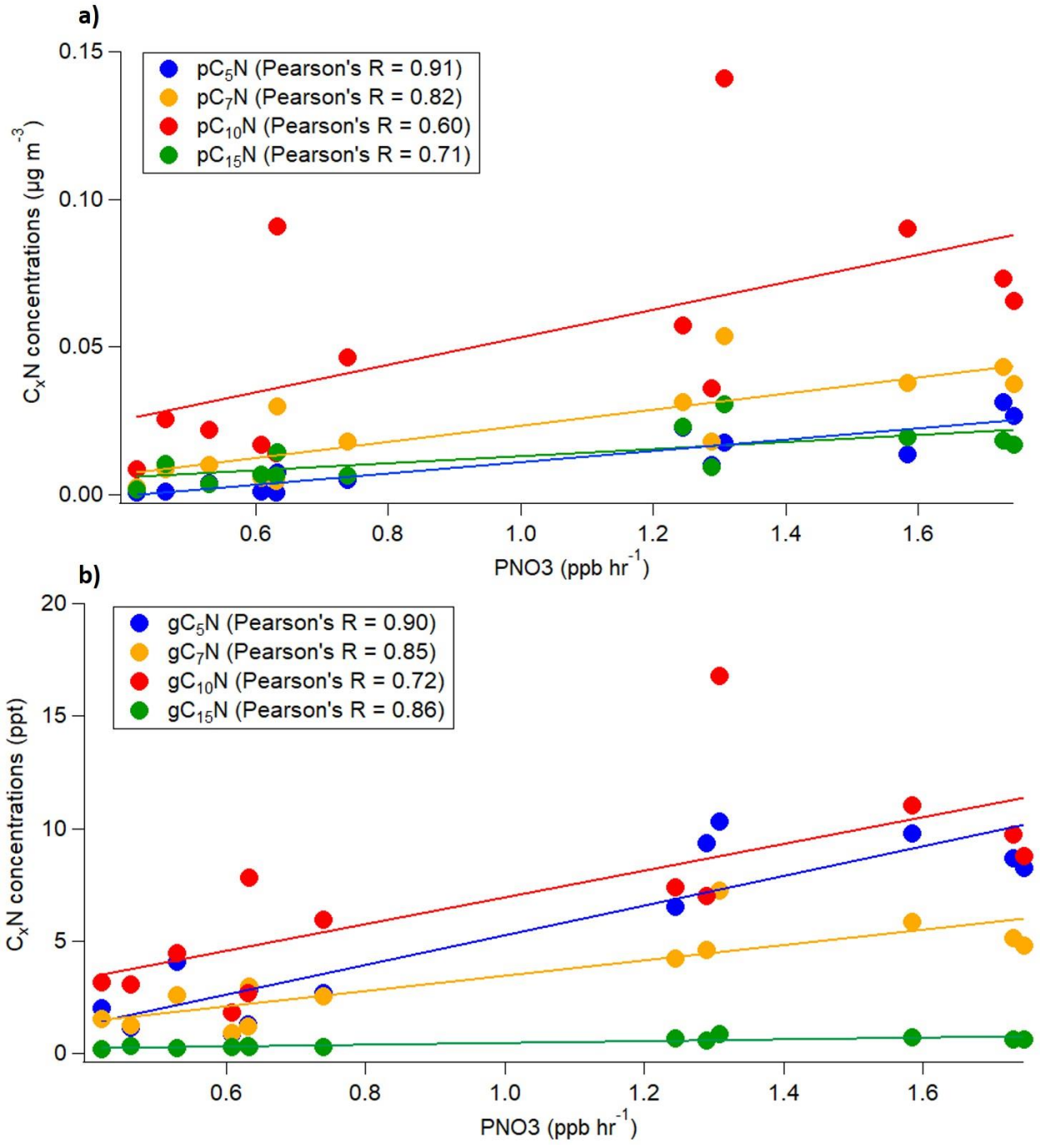

Figure S9. Correlations of C_xN (x=5, 7, 10, 15) group concentrations in particle (a) and gas (b) phases with PNO_3.

REFERENCES

1. Farmer, D. K.; Matsunaga, A.; Docherty, K. S.; Surratt, J. D.; Seinfeld, J. H.; Ziemann, P. J.; Jimenez, J. L. Response of an aerosol mass spectrometer to organonitrates and organosulfates and implications for atmospheric chemistry. *Proc. Natl. Acad. Sci. U. S. A.* **2010**, *107* (15), 6670-6675.
2. Lopez-Hilfiker, F. D.; Mohr, C.; Ehn, M.; Rubach, F.; Kleist, E.; Wildt, J.; Mentel, T. F.; Carrasquillo, A. J.; Daumit, K. E.; Hunter, J. F.; Kroll, J. H.; Worsnop, D. R.; Thornton, J. A. Phase partitioning and volatility of secondary organic aerosol components formed from α-pinene ozonolysis and OH oxidation: the importance of accretion products and other low volatility compounds. *Atmos. Chem. Phys.* **2015**, *15* (14), 7765−7776.

A.3 Seasonal characteristics of organic aerosol chemical composition and volatility in Stuttgart, Germany

Table S1. Instruments installed in the measurement container.

Measured parameter	Instrument	Data period	
		Summer 2017	**Winter 2018**
Ambient temperature	WS700 (Lufft GmbH)	July 7–August 17	February 5–March 5
Container temperature	WS700 (Lufft GmbH)	July 7–August 17	February 5–March 5
Dew point temperature	WS700 (Lufft GmbH)	July 7–August 17	February 5–March 5
RH	WS700 (Lufft GmbH)	July 7–August 17	February 5–March 5
Pressure	WS700 (Lufft GmbH)	July 7–August 17	February 5–March 5
Wind speed	WS700 (Lufft GmbH)	July 7–August 17	February 5–March 5
Wind vertical	WS700 (Lufft GmbH)	July 7–August 17	February 5–March 5
Wind direction	WS700 (Lufft GmbH)	July 7–August 17	February 5–March 5
Rain	WS700 (Lufft GmbH)	July 7–August 17	February 5–March 5
Rain type	WS700 (Lufft GmbH)	July 7–August 17	February 5–March 5
Rain rate	WS700 (Lufft GmbH)	July 7–August 17	February 5–March 5
Radiation	WS700 (Lufft GmbH)	July 7–August 17	February 5–March 5
Particle number concentration (>7 nm)	CPC3022 (TSI Inc.)	July 5–August 17	February 5–March 5
Particle number concentration (>2.5 nm)	CPC3776 (TSI Inc.)	July 5–August 17	February 5–March 5
O_3	O341M (Environment SA)	July 5–August 17	February 5–March 5
CO_2	NGA2000 (Rosemount Inc.)	July 5–August 17	February 5–March 5
SO_2	AF22M (Environment SA)	July 5–August 17	February 5–March 5
NO_2	AS32M (Environment SA)	July 5–August 17	February 5–March 5
Particle optical diameter (0.18–18 µm)	OPC FIDAS200 (Palas GmbH)	July 5–August 17	February 5–March 5
Particle size (10–410 nm, d_m)	NanoScan-SMPS (TSI Inc.)	July 5–July 26	/
Black carbon (BC)	AE51 Aethalometer (Aethlabs Inc.)	July 5–August 17	February 5–March 5
Single particle composition and size (0.2–2.5 µm, d_{va})	LAAPTOF (AeroMegt GmbH)	July 5–August 17	February 5–March 5
Particle mass and size (0.07–2.5 µm, d_{va})	AMS (Aerodyne Research Inc.)	July 5–August 17	February 5–March 5
Particle-phase oxygenated organic molecules (offline filters)	FIGAERO-CIMS (Aerodyne Research Inc.)	July 5–August 14	February 8–March 5

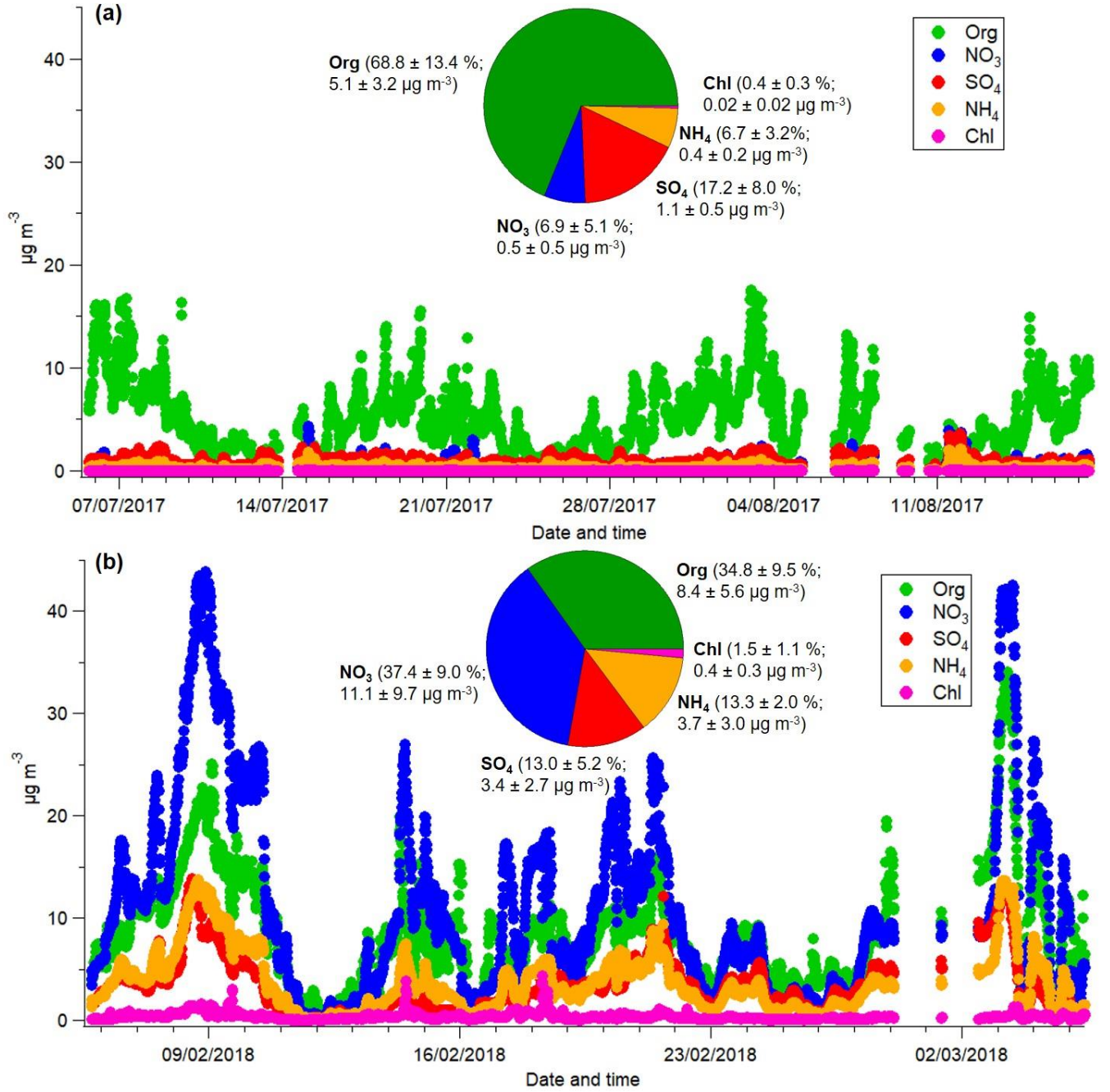

Figure S1. Time series of aerosol composition measured by AMS (Organics (Org), Nitrate (NO_3), Sulfate (SO_4), Ammonium (NH_4), and Chloride (Chl)) in the summer (a) and winter (b) periods.

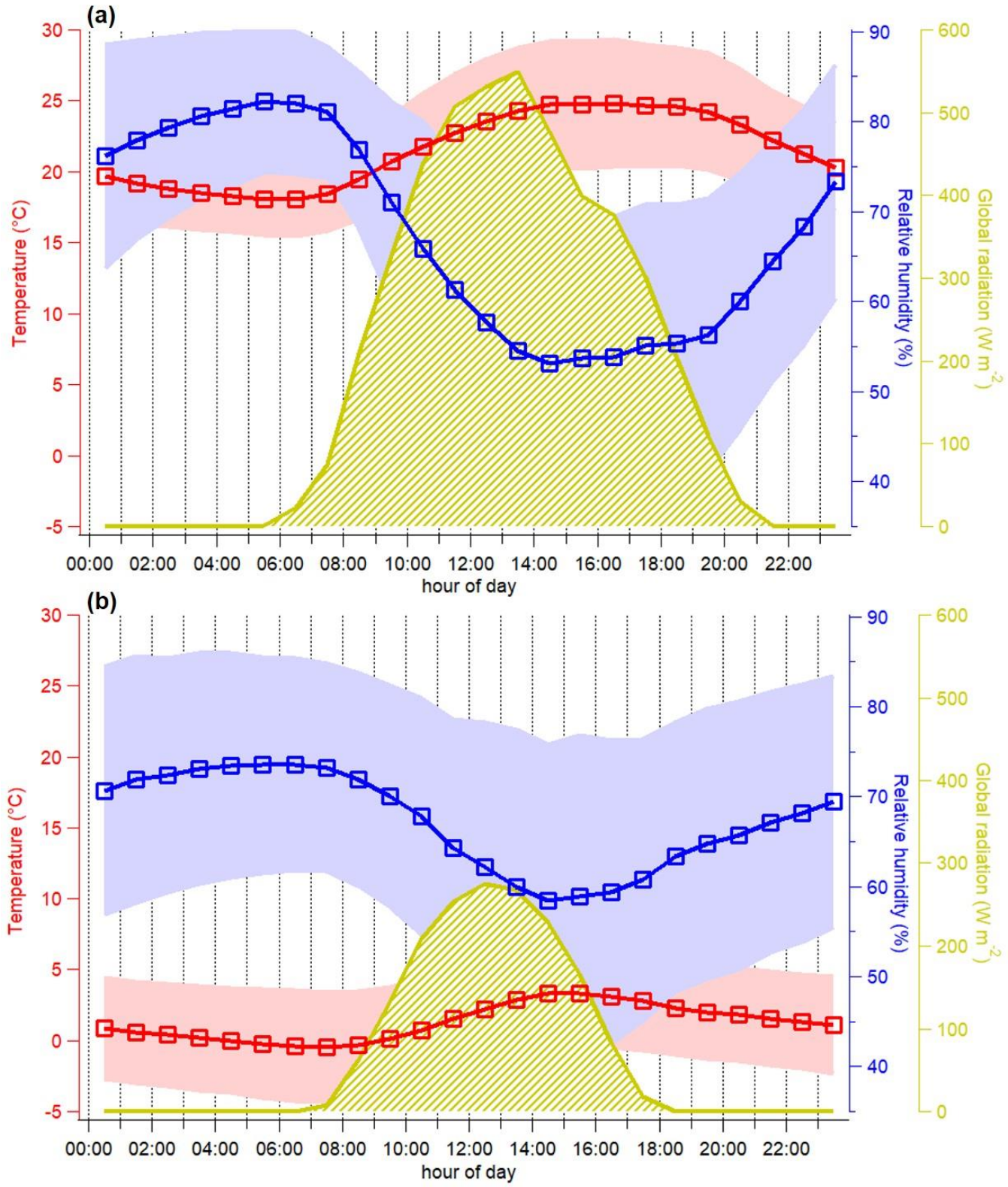

Figure S2. Mean diel patterns of ambient temperature, relative humidity, and global radiation in the summer (a) and winter (b) periods. The shaded areas represent ±1 standard deviation.

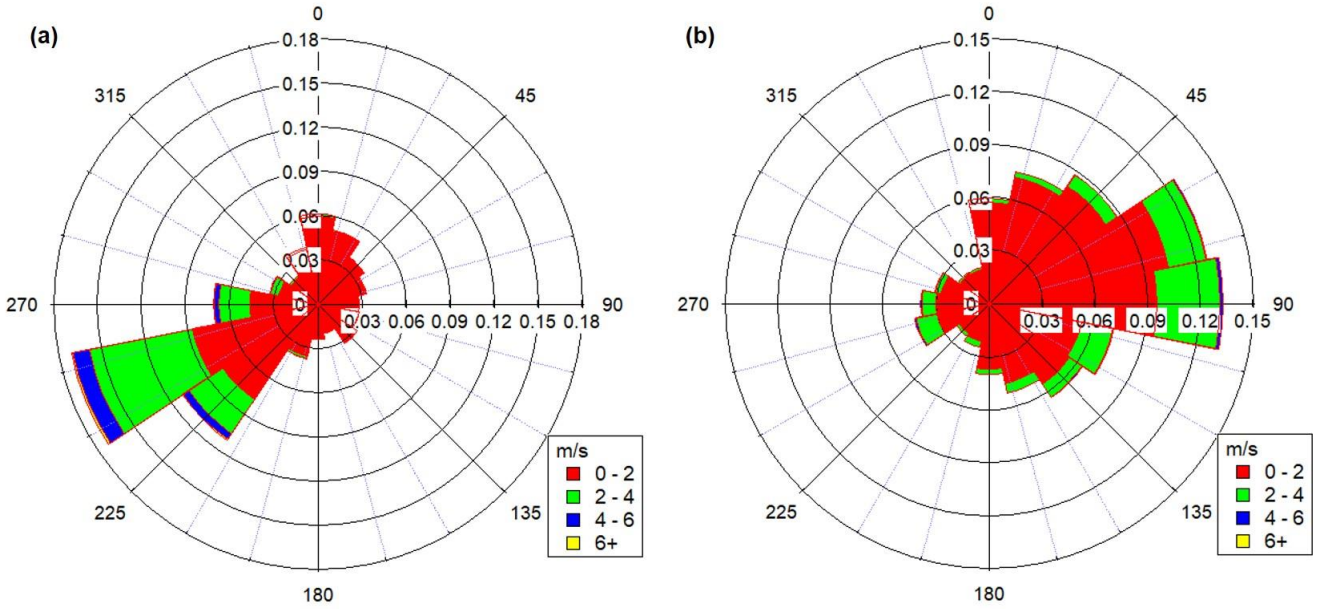

Figure S3. Wind speeds and directions for the summer (a) and winter (b) periods.

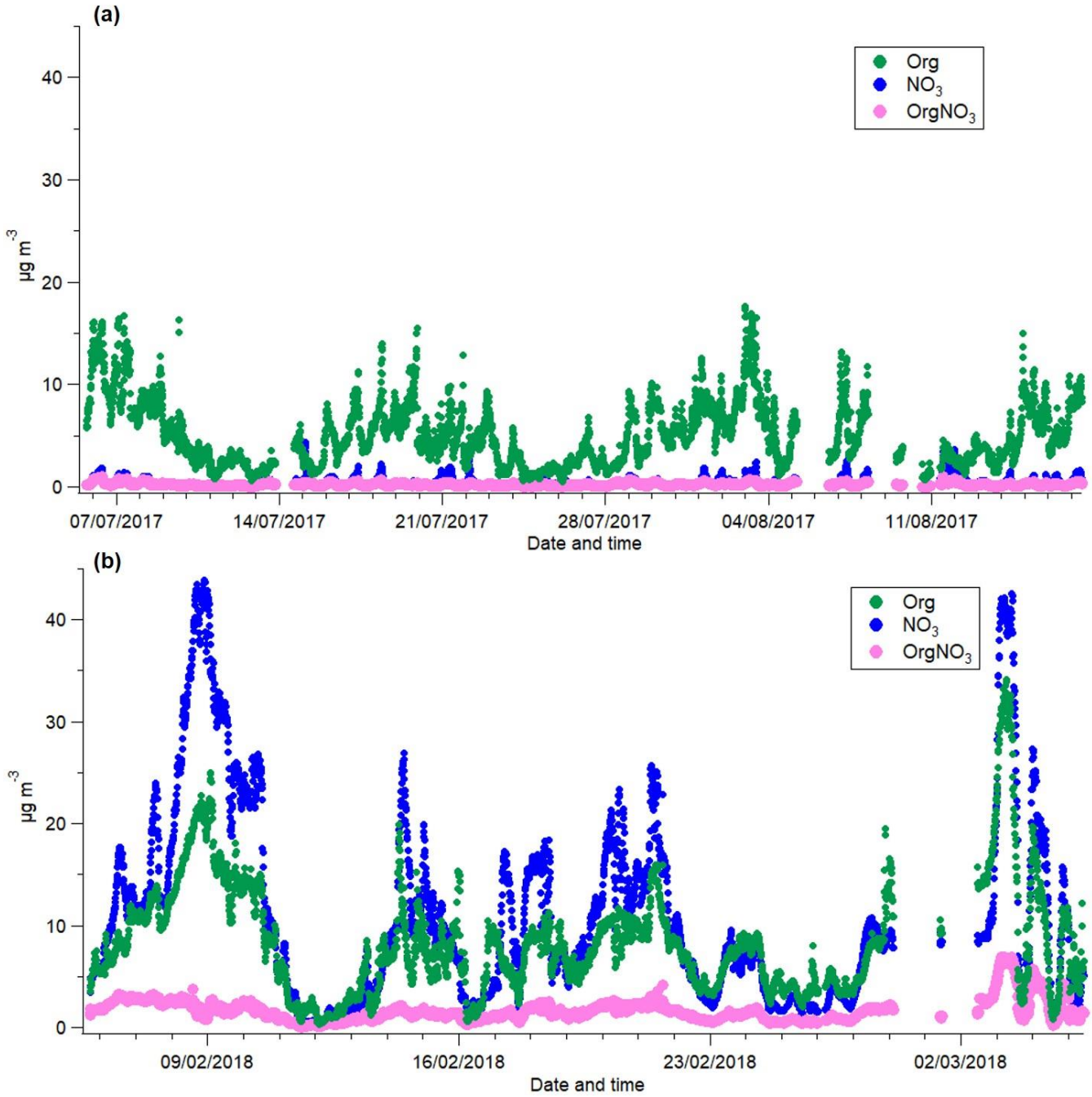

Figure S4. Comparison of time series of Organonitrates ($OrgNO_3$) with Organics (Org) and Nitrate (NO_3) by AMS for the summer (a) and winter (b) periods. $OrgNO_3$ concentrations were estimated based on the NO_2^+/NO^+ ion ratio measured by AMS and assuming a ratio of 0.1 for $OrgNO_3$ (Farmer et al., 2010; Kiendler-Scharr et al., 2016).

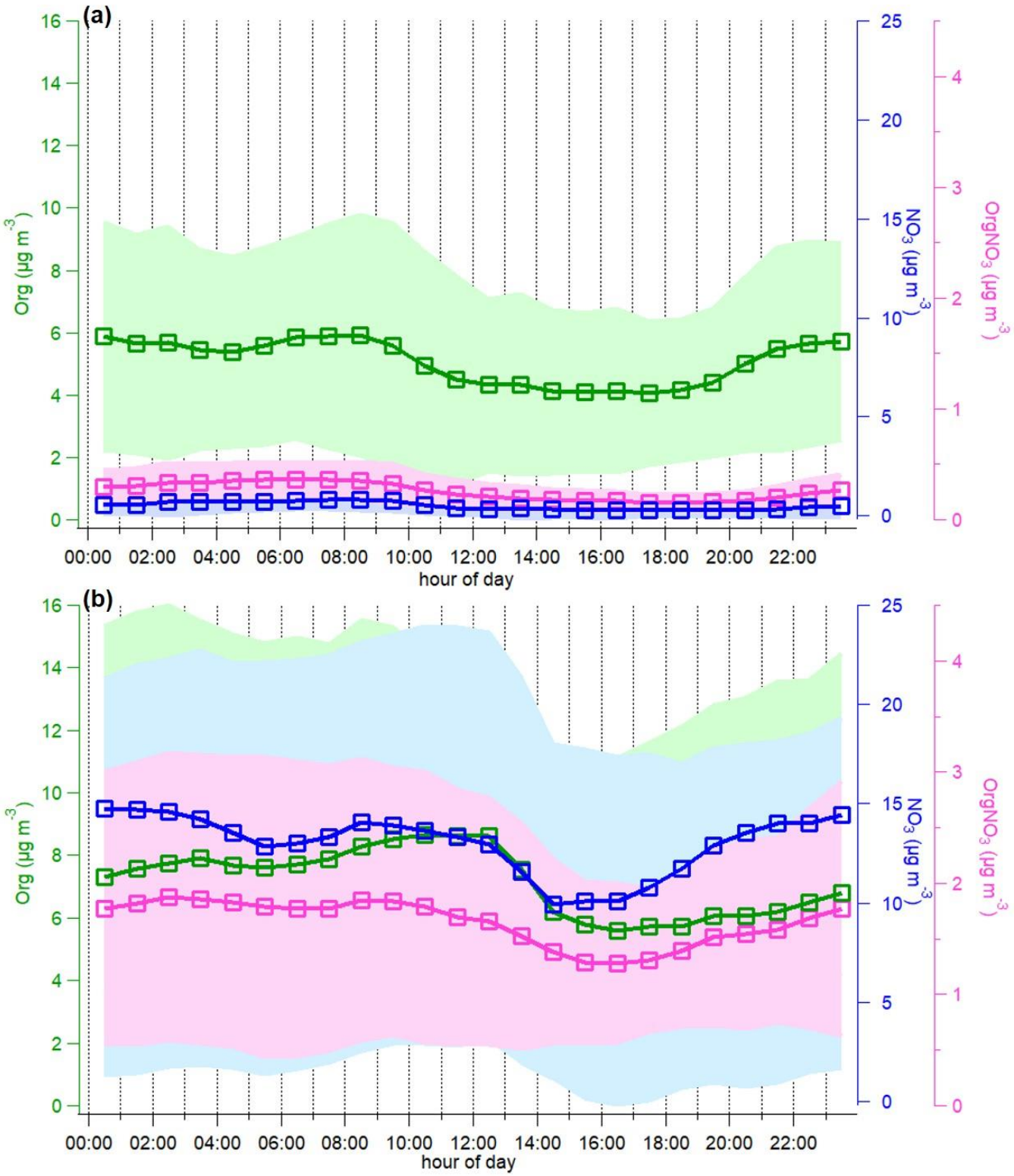

Figure S5. Mean diel patterns of Organics (Org), Nitrate (NO_3), and Organonitrates ($OrgNO_3$) by AMS for the summer (a) and winter (b) periods. The shaded areas represent ±1 standard deviation.

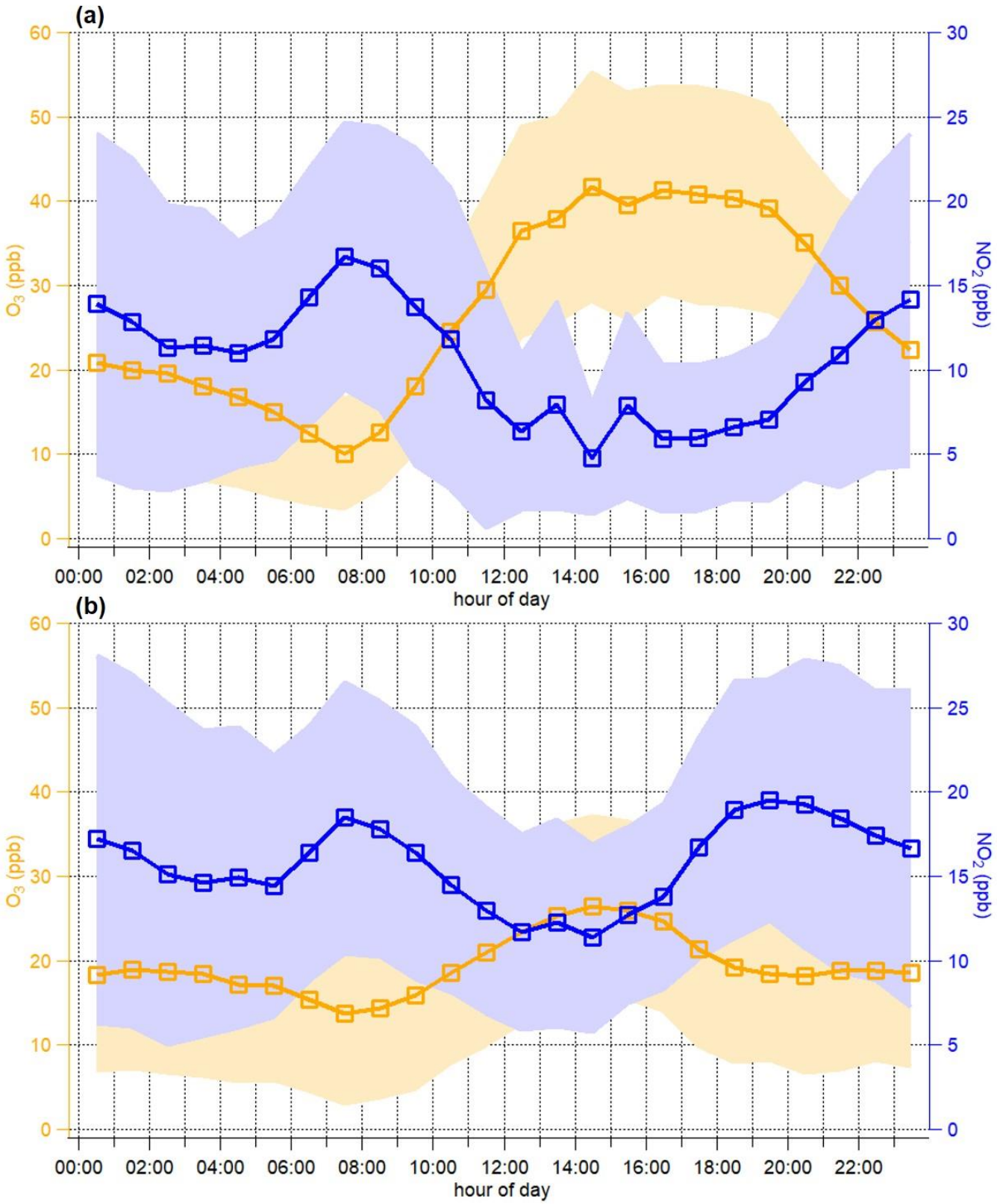

Figure S6. Mean diel patterns of O_3 and NO_2 mixing ratios for the summer (a) and winter (b) periods. The shaded areas represent ±1 standard deviation.

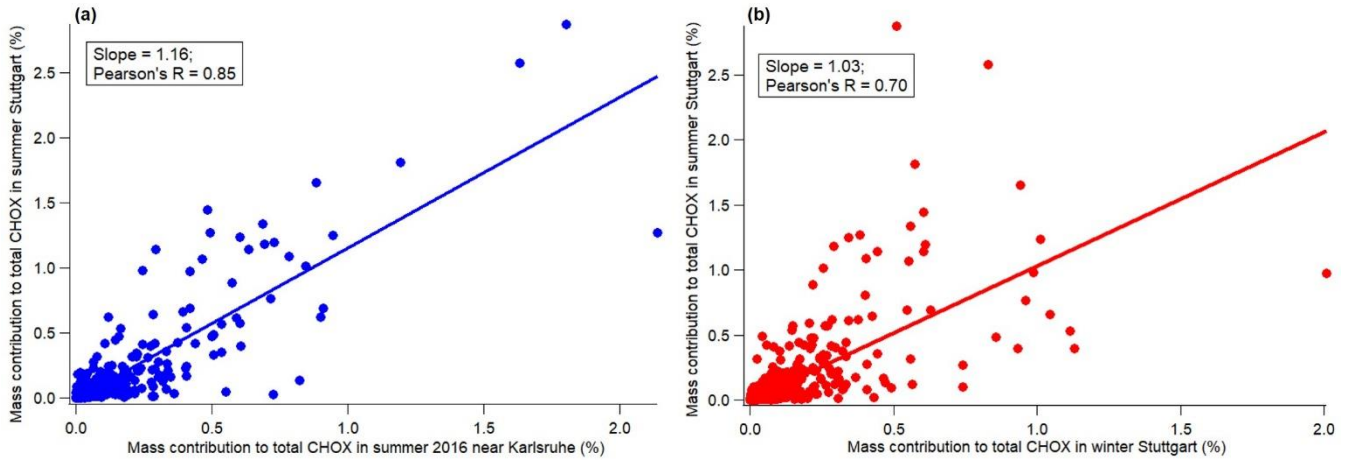

Figure S7. Correlations of CHOX compounds in summer 2017 in Stuttgart (a) with CHOX compounds in summer 2016 near Karlsruhe (Huang et al., 2019) and (b) with CHOX compounds in winter 2018 in Stuttgart after removing five prominent biomass burning tracer compounds ($C_6H_{10}O_5$, $C_6H_5O_3N$, $C_7H_7O_3N$, $C_6H_5O_4N$, and $C_7H_7O_4N$).

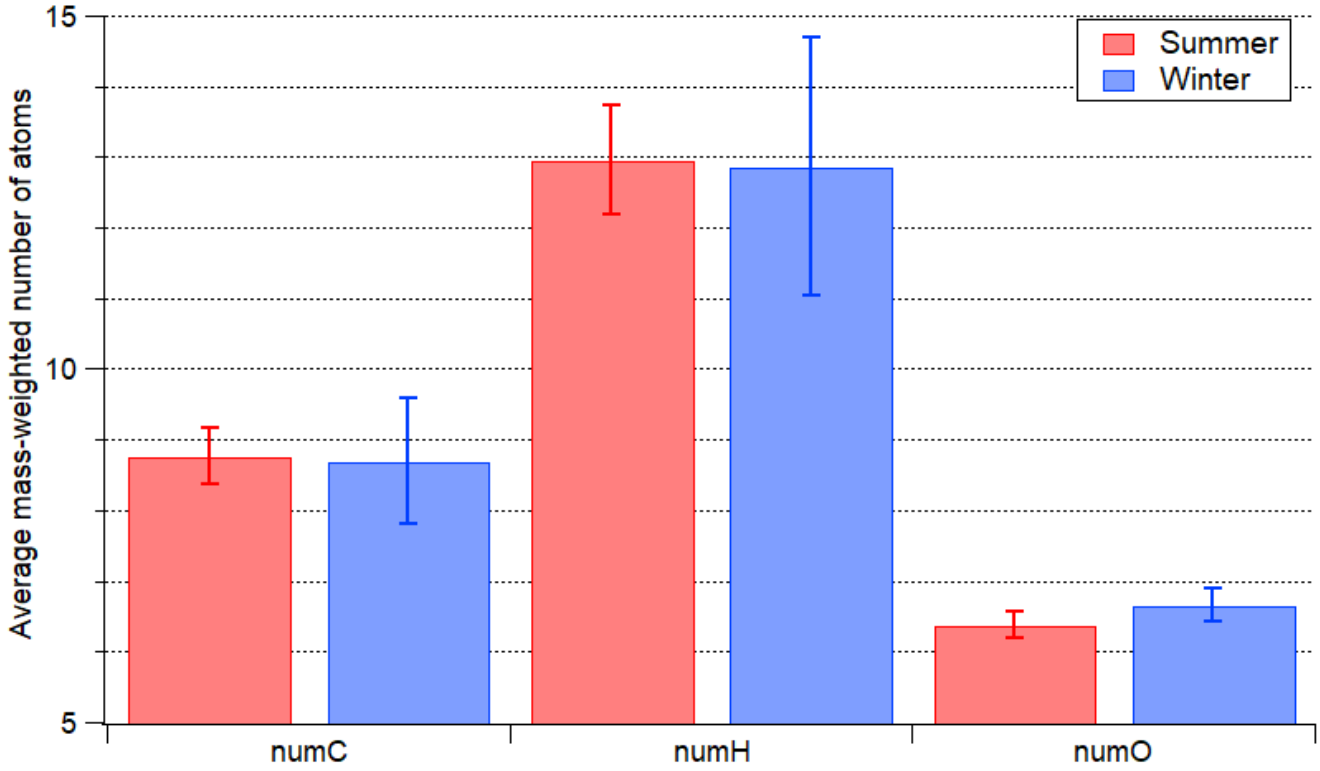

Figure S8. Average mass-weighted number of carbon atoms (numC), hydrogen atoms (numH), and oxygen atoms (numO) of the CHOX compounds for the summer and winter periods.

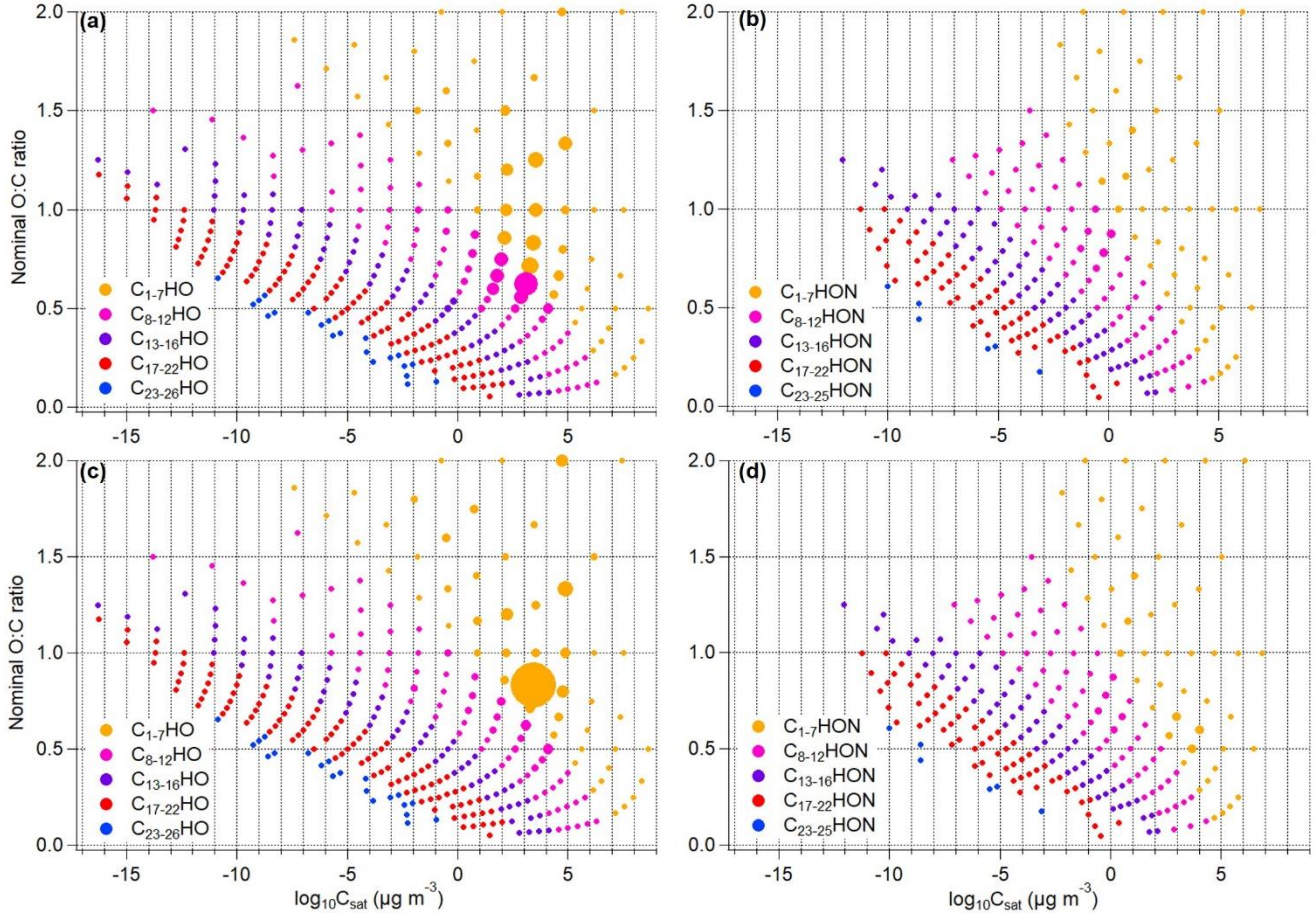

Figure S9. Volatility distribution of CHO compounds (a) and CHON compounds (b) in the summer period, CHO compounds (a) and CHON compounds (b) in the winter period vs their corresponding nominal O:C ratio. Markers were colored by different number of carbon atoms and sized by their corresponding mass contributions to total CHOX compounds.

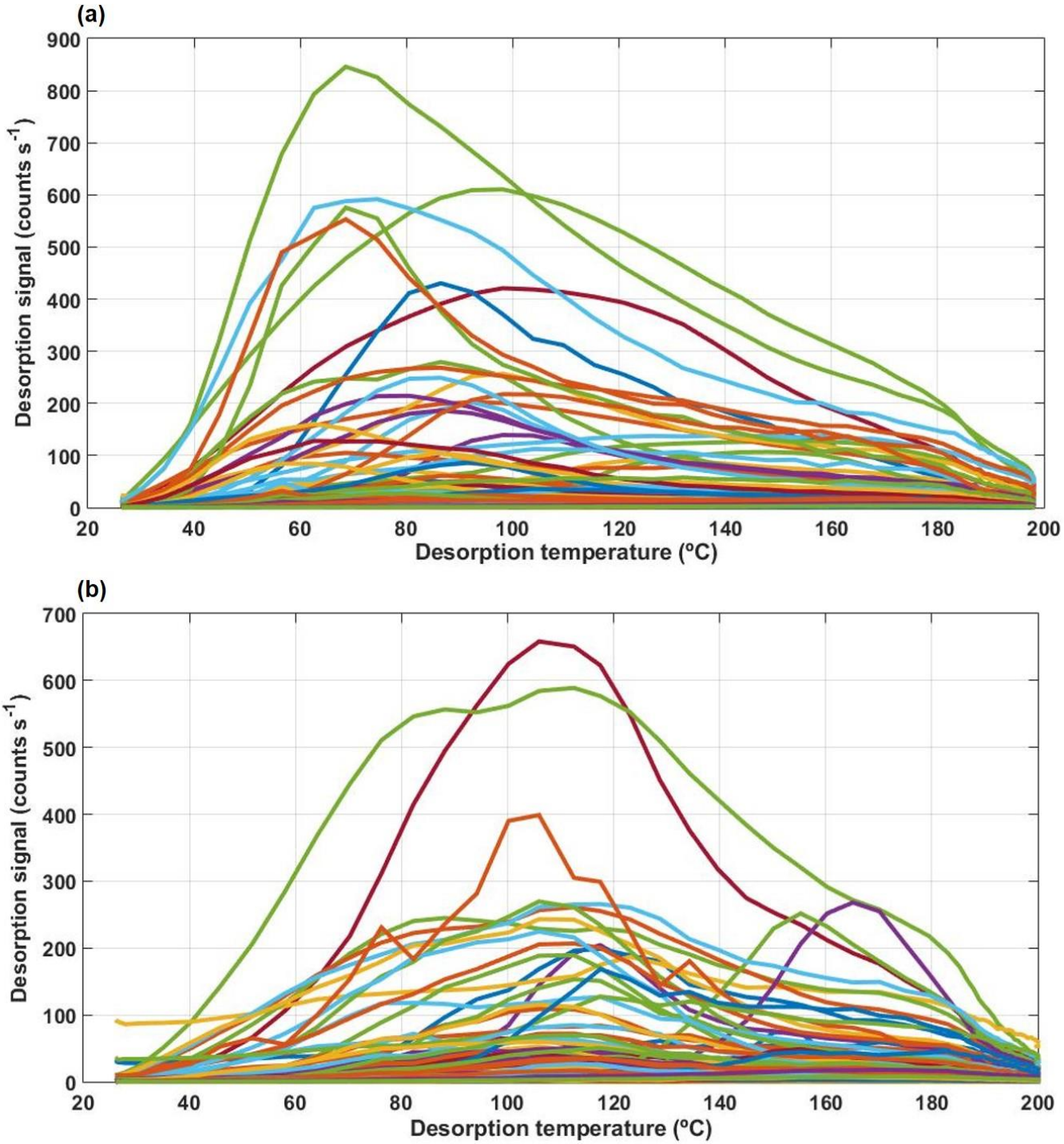

Figure S10. Thermograms of CHOX compounds with 1–5 carbon atoms for the summer (a) and winter (b) periods.

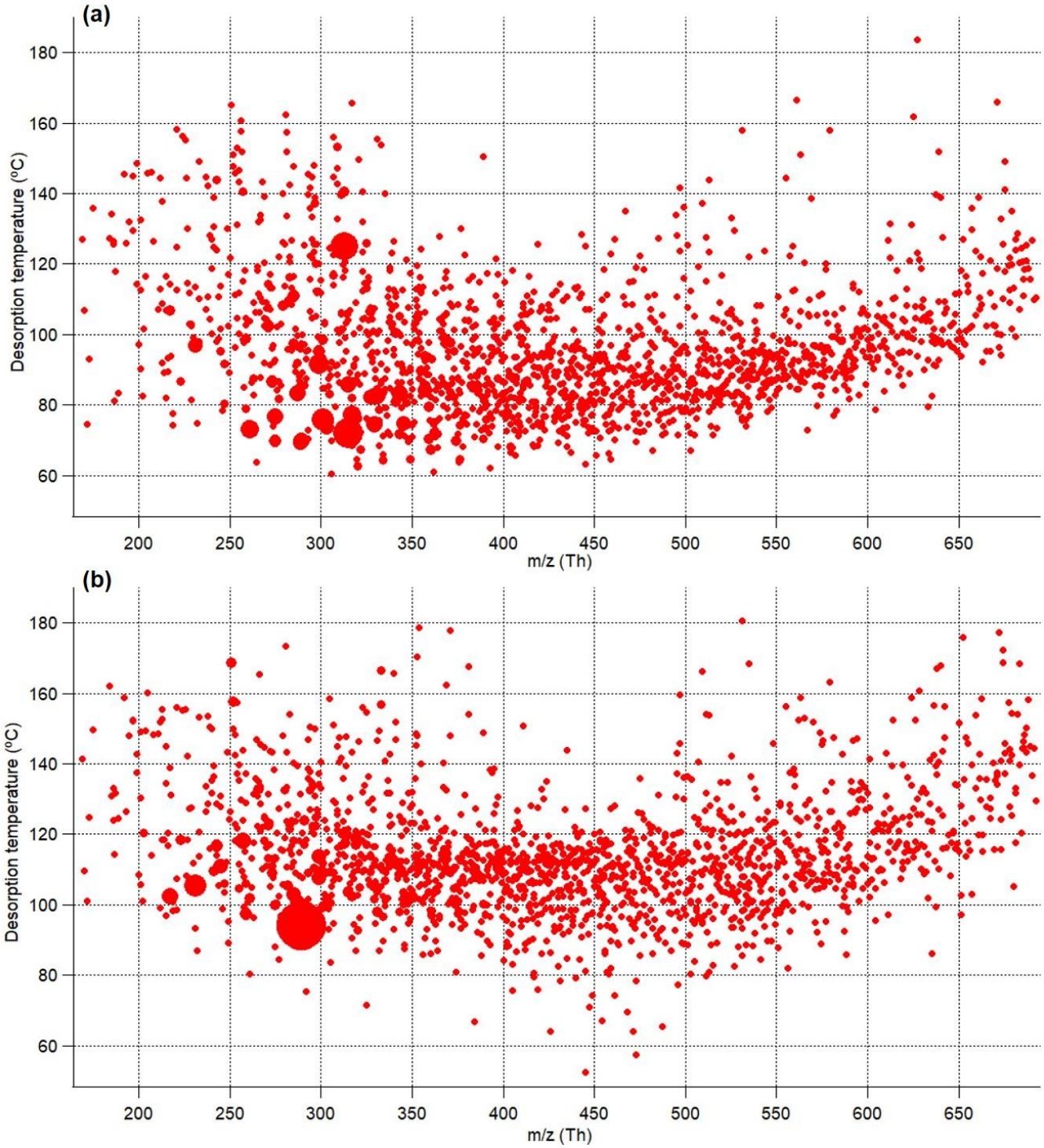

Figure S11. Mean T_{max} distribution of CHOX compounds as a function of *m/z* (includes mass of I^- ion; *m/z* 126.9050 Th) for the summer (a) and winter (b) periods. Markers were sized by their corresponding mass contributions to total CHOX compounds. Mean T_{max} were calculated as the campaign-average of the T_{max} for each CHOX compound.

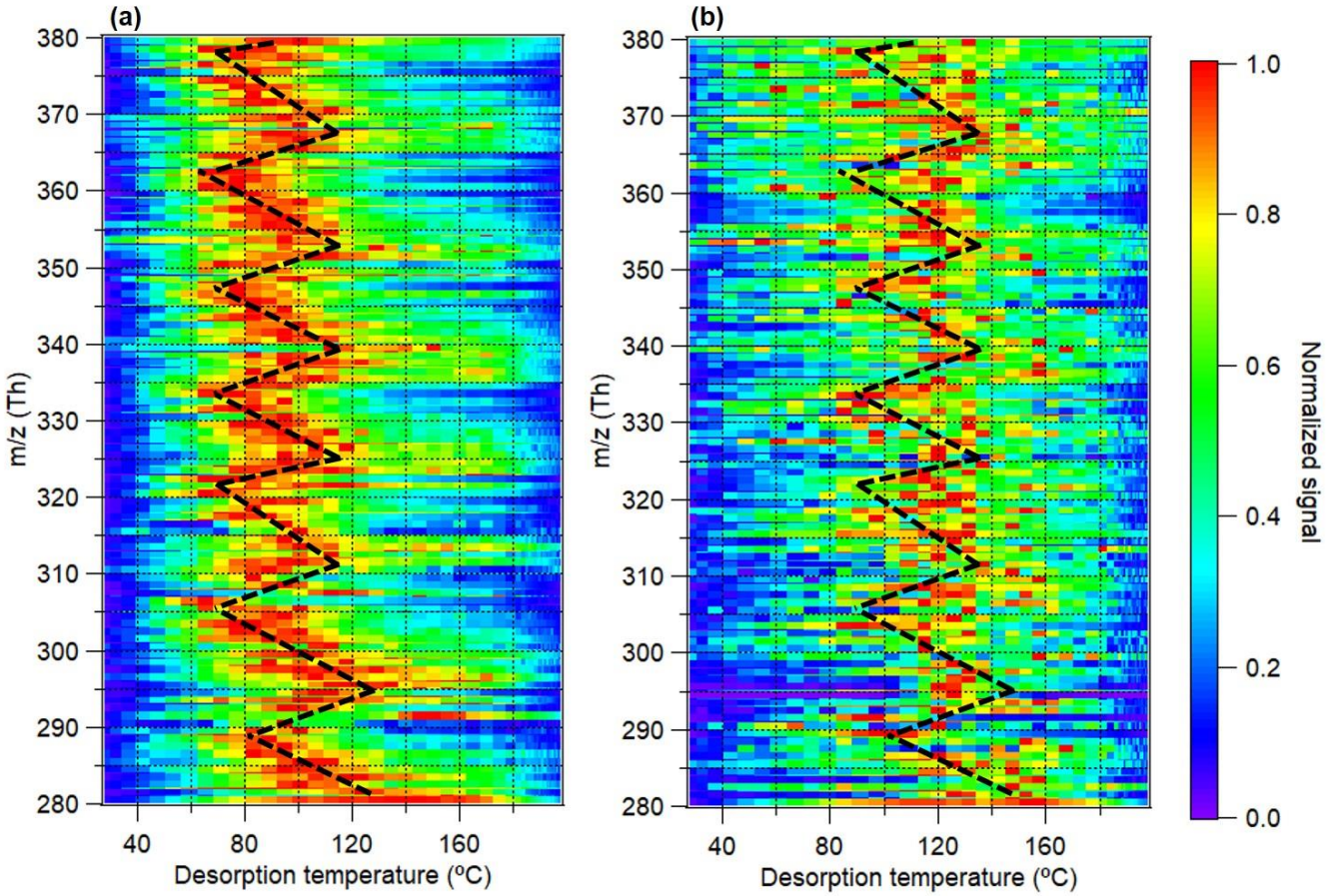

Figure S12. Comparison of high resolution 2D thermograms of CHOX compounds for mass range 280–380 Th of Figure 4 for the summer (a) and winter (b) periods. The 2D thermograms were normalized to their maximum values. A black dotted line was plotted by hand to guide the eye.

References

Farmer, D. K., Matsunaga, A., Docherty, K. S., Surratt, J. D., Seinfeld, J. H., Ziemann, P. J., and Jimenez, J. L.: Response of an aerosol mass spectrometer to organonitrates and organosulfates and implications for atmospheric chemistry, P Natl Acad Sci USA, 107, 6670–6675, https://doi.org/10.1073/pnas.0912340107, 2010.

Huang, W., Saathoff, H., Shen, X., Ramisetty, R., Leisner, T., and Mohr, C.: Chemical characterization of highly functionalized organonitrates contributing to night-time organic aerosol mass loadings and particle growth, Environ Sci Technol, 53, 1165–1174, https://doi.org/10.1021/acs.est.8b05826, 2019.

Kiendler-Scharr, A., Mensah, A. A., Friese, E., Topping, D., Nemitz, E., Prevot, A. S. H., Äijälä, M., Allan, J., Canonaco, F., Canagaratna, M., Carbone, S., Crippa, M., Dall Osto, M., Day, D. A., De Carlo, P., Di Marco, C. F., Elbern, H., Eriksson, A., Freney, E., Hao, L., Herrmann, H., Hildebrandt, L., Hillamo, R., Jimenez, J. L., Laaksonen, A., McFiggans, G., Mohr, C., O'Dowd, C., Otjes, R., Ovadnevaite, J., Pandis, S. N., Poulain, L., Schlag, P., Sellegri, K., Swietlicki, E., Tiitta, P., Vermeulen, A., Wahner, A., Worsnop, D., and Wu, H.-C.: Ubiquity of organic nitrates from nighttime chemistry in the European submicron aerosol, Geophys Res Lett, 43, 7735–7744, https://doi.org/10.1002/2016GL069239, 2016.

B Appendix-Full papers for co-authored scientific publications

B.1 Heterogeneous ice nucleation of α-pinene SOA particles before and after ice cloud processing

Authors: Robert Wagner, Kristina Höhler, **Wei Huang**, Alexei Kiselev, Ottmar Möhler, Claudia Mohr, Aki Pajunoja, Harald Saathoff, Thea Schiebel, Xiaoli Shen, and Annele Virtanen.

In: Journal of Geophysical Research: Atmospheres, 122, 4924–4943, 2017. DOI: 10.1002/2016JD026401.

Authorship statement

This peer-reviewed scientific journal article is based on the chamber data from a two-month measurement campaign (SOA15) in October and November 2015 at simulation chambers at KIT, with a focus on the ice nucleation abilities of the SOA particles. In particular, I was responsible for the operation and calibrations of AMS, AMS data analysis, and participated in the data interpretation and discussion of this article.

AGU PUBLICATIONS

JGR

Journal of Geophysical Research: Atmospheres

RESEARCH ARTICLE

10.1002/2016JD026401

Key Points:
- Pristine α-pinene SOA particles reveal poor heterogeneous ice nucleation ability in the cirrus cloud regime of the upper troposphere
- Ice cloud processing of α-pinene SOA particles in a convective cloud system leads to formation of highly porous particles
- Freeze-dried SOA particles show heterogeneous ice formation in the mixed-phase cloud regime via the CCN-induced ice growth mode

Correspondence to:
R. Wagner,
robert.wagner2@kit.edu

Citation:
Wagner, R., et al. (2017), Heterogeneous ice nucleation of α-pinene SOA particles before and after ice cloud processing, *J. Geophys. Res. Atmos.*, *122*, 4924–4943, doi:10.1002/2016JD026401.

Received 19 DEC 2016
Accepted 11 APR 2017
Accepted article online 18 APR 2017
Published online 3 MAY 2017

Heterogeneous ice nucleation of α-pinene SOA particles before and after ice cloud processing

Robert Wagner[1], Kristina Höhler[1], Wei Huang[1], Alexei Kiselev[1], Ottmar Möhler[1], Claudia Mohr[1], Aki Pajunoja[2], Harald Saathoff[1], Thea Schiebel[1], Xiaoli Shen[1], and Annele Virtanen[2]

[1]Institute of Meteorology and Climate Research, Karlsruhe Institute of Technology, Karlsruhe, Germany, [2]Department of Applied Physics, University of Eastern Finland, Kuopio, Finland

Abstract The ice nucleation ability of α-pinene secondary organic aerosol (SOA) particles was investigated at temperatures between 253 and 205 K in the Aerosol Interaction and Dynamics in the Atmosphere cloud simulation chamber. Pristine SOA particles were nucleated and grown from pure gas precursors and then subjected to repeated expansion cooling cycles to compare their intrinsic ice nucleation ability during the first nucleation event with that observed after ice cloud processing. The unprocessed α-pinene SOA particles were found to be inefficient ice-nucleating particles at cirrus temperatures, with nucleation onsets (for an activated fraction of 0.1%) as high as for the homogeneous freezing of aqueous solution droplets. Ice cloud processing at temperatures below 235 K only marginally improved the particles' ice nucleation ability and did not significantly alter their morphology. In contrast, the particles' morphology and ice nucleation ability was substantially modified upon ice cloud processing in a simulated convective cloud system, where the α-pinene SOA particles were first activated to supercooled cloud droplets and then froze homogeneously at about 235 K. As evidenced by electron microscopy, the α-pinene SOA particles adopted a highly porous morphology during such a freeze-drying cycle. When probing the freeze-dried particles in succeeding expansion cooling runs in the mixed-phase cloud regime up to 253 K, the increase in relative humidity led to a collapse of the porous structure. Heterogeneous ice formation was observed after the droplet activation of the collapsed, freeze-dried SOA particles, presumably caused by ice remnants in the highly viscous material or the larger surface area of the particles.

1. Introduction

The ice nucleation ability of organic aerosol particles is a rapidly developing field of research. This is exemplified by the large number of experimental and theoretical investigations on that issue, which have been published since the release of the latest comprehensive review on laboratory measurements of ice nucleation on atmospheric aerosols [*Hoose and Möhler*, 2012]. A key question of the recent studies was the identification of organic compounds that are able to contribute to the abundance of ice-nucleating particles (INPs) in the atmosphere, i.e., particles that are responsible for heterogeneous ice nucleation [*Vali et al.*, 2015].

Some organic compounds, like various monocarboxylic and dicarboxylic acids, exist in the crystalline solid state and were shown to promote heterogeneous ice nucleation via deposition nucleation when prevalent as bare substances [*Baustian et al.*, 2010; *Schill and Tolbert*, 2012; *Shilling et al.*, 2006; *Wagner et al.*, 2010] or via immersion freezing when embedded as crystalline inclusions in water or aqueous solution droplets [*Wagner et al.*, 2011, 2015; *Zobrist et al.*, 2006]. Organic compounds also frequently form amorphous semisolid or amorphous solid (glassy) states at low temperature and/or relative humidity [*Koop et al.*, 2011; *Virtanen et al.*, 2010; *Zobrist et al.*, 2008]. In such cases, the glass transition relative humidity (RH_g) and the timescale for water diffusion in the particles will control the mode of ice nucleation during an atmospheric updraft [*Berkemeier et al.*, 2014]. Depositional ice nucleation on the surface of the particles may occur before passing the RH_g line during humidification of the air upon an adiabatic expansion, as first experimentally evidenced with glassy citric acid aerosol particles [*Murray et al.*, 2010]. The RH_g threshold denotes the onset of the humidity-induced phase transition from the glassy into the liquid region, also termed as amorphous deliquescence [*Mikhailov et al.*, 2009]. In an updraft with fast relative humidity increase, the water diffusion in the glassy organic particles may be too slow for immediately transforming them into entirely liquid solution droplets above RH_g, resulting in core-shell morphologies with glassy cores and liquid outer layers [*Berkemeier et al.*, 2014]. Such partially deliquesced particles can trigger ice nucleation via immersion

Journal of Geophysical Research: Atmospheres 10.1002/2016JD026401

freezing. Further humidification leads to a continuous shrinkage of the glassy core, until entirely liquid particles are finally formed at the full deliquescence relative humidity [*Berkemeier et al*., 2014]. Above that limit, homogeneous freezing remains the only feasible ice nucleation mechanism [*Koop et al*., 2000].

After the first measurements of heterogeneous ice nucleation on glassy materials using citric acid [*Murray et al*., 2010], further experimental work was performed with other proxies for atmospherically abundant organic aerosol particles, e.g., with single compounds like raffinose, levoglucosan, HMMA (4-hydroxy-3-methoxy-DL-mandelic acid), sucrose, and glucose [*Baustian et al*., 2013; *Wilson et al*., 2012] and with multicomponent mixtures like raffinose/M5/AS (M5: mixture of five dicarboxylic acids, AS: ammonium sulfate), citric acid/AS, glucose/AS, sucrose/AS, and 1,2,6-hexanetriol/2,2,6,6-tetrakis(hydroxymethyl)cyclohexanol [*Baustian et al*., 2013; *Schill and Tolbert*, 2013; *Wilson et al*., 2012]. In an attempt to categorize the ice nucleation abilities of amorphous organic (semi)solids, the latter compounds were grouped into the class "simple sugars/acids" to differentiate them from organic aerosol components that are formed by chemical reactions in the atmosphere (secondary organic aerosol, SOA) [*Schill et al*., 2014]. Ice nucleation studies with SOA compounds include the reaction products from the gas phase oxidation of naphthalene with OH radicals [*Wang et al*., 2012], the aqueous phase reaction of methylglyoxal with methylamine [*Schill et al*., 2014], and the ozonolysis of alkenes and α-pinene [*Ignatius et al*., 2016; *Ladino et al*., 2014; *Möhler et al*., 2008; *Prenni et al*., 2009], the latter being one of the most abundant monoterpene SOA precursor compounds [*Hallquist et al*., 2009].

The organic compounds belonging to the class of simple sugars/acids reveal a higher ability to act as INPs at cirrus temperatures compared to the SOA species. This is illustrated by comparatively low onset ice saturation ratios, S_{ice}, for heterogeneous ice nucleation, which are typically in the range from 1.1 to 1.4 for temperatures between 235 and 200 K and thereby clearly fall below the homogeneous freezing threshold that ranges from about 1.45 to 1.6 in the same temperature regime [*Schill et al*., 2014]. With freezing onsets in terms of S_{ice} between about 1.4 at 235 K and 1.5 at 200 K, the ice nucleation data for the naphthalene + OH and methylglyoxal + methylamine SOA particles can still be unambiguously assigned to the heterogeneous nucleation regime. This assignment is less definite for the α-pinene SOA particles where the experimental findings are partly inconsistent. The currently most extensive data set for the ice nucleation ability of freshly generated α-pinene SOA particles from *Ladino et al*. [2014] shows freezing onsets at or even slightly above the homogeneous freezing line at temperatures between 233 and 213 K. This poor ice nucleation ability for α-pinene SOA is substantiated by the measurement from *Möhler et al*. [2008] conducted at a temperature of 205 K, where the onset of ice nucleation only occurred at an ice saturation ratio as high as 1.7. In contrast, one of the most recent ice nucleation studies with α-pinene SOA particles revealed freezing onsets below the homogeneous freezing limit at temperatures around 235 K [*Ignatius et al*., 2016]. Specifically, ice saturation ratios between 1.3 and 1.4 for the nucleation onset as well as ice-active fractions of up to 20% were found [*Ignatius et al*., 2016].

These experimental findings can be compared to recent measurements of the low-temperature water diffusion coefficients in SOA material generated from the oxidation of α-pinene with OH radicals and ozone [*Lienhard et al*., 2015; *Price et al*., 2015]. As outlined above, kinetic limitations in water diffusion would favor the particles' ability to act as heterogeneous ice nuclei during humidification because the process of amorphous deliquescence would be slowed down. Data and model calculations from *Lienhard et al*. [2015] suggest that for temperatures above 220 K the SOA particles equilibrate with the ambient relative humidity for an updraft velocity as high as 3 m s^{-1}, meaning that heterogeneous ice nucleation is unlikely under such conditions. Below 220 K, a glassy or highly viscous core might persist when the particles' trajectory reaches the regime of ice supersaturation, thereby enabling heterogeneous ice nucleation in the immersion freezing mode. At very cold temperatures below 195 K, water diffusion could be limited to such a degree that homogeneous ice nucleation of the particles would be delayed, even for small updrafts of 0.1 m s^{-1} [*Lienhard et al*., 2015]. *Price et al*. [2015] conclude that at a starting temperature of 220 K and an updraft speed in the range of 0.02–2 m s^{-1} or at a starting temperature of 230 K and an updraft speed of 2 m s^{-1}, the core of the α-pinene SOA particles might still prevail in an amorphous solid state when the relative humidity of the environment exceeds ice saturation.

Obviously, there is a need to reconcile the water diffusion measurements in α-pinene SOA with at least part of the ice nucleation experiments, as, e.g., *Ignatius et al*. [2016] observed heterogeneous ice nucleation at a temperature where the particles are supposed to be fully equilibrated with the gas phase humidity

Journal of Geophysical Research: Atmospheres 10.1002/2016JD026401

[*Lienhard et al*., 2015]. However, the comparison between various studies is not straightforward because the chemical composition of the generated SOA materials (as, e.g., expressed by their elemental oxygen-to-carbon and hydrogen-to-carbon ratios) may vary due to different oxidants (OH radicals and ozone), precursor concentrations, residence times, and oxidation temperatures employed [*Grayson et al*., 2016]. Also, particle processing like precooling was shown to have an influence on the ice nucleation ability [*Ladino et al*., 2014].

A drawback of most laboratory studies is that the determination of the onset conditions for ice nucleation in the case of SOA particles does not automatically disclose the underlying ice nucleation mechanism because it is difficult to probe the particle morphology in situ during the trajectory of humidification. Let us, e.g., consider the results from *Ladino et al*. [2014] who found freezing onsets close to the homogeneous freezing line for α-pinene SOA. This could mean (i) that the particles had completely been liquefied and frozen homogeneously; (ii) that the particles had a core-shell morphology at the freezing onset, with the glassy core just being inefficient in triggering ice nucleation by immersion freezing before the homogeneous freezing limit was reached and the surrounding liquid layer nucleated ice; and (iii) that the particles had remained entirely in the glassy state during humidification, and the onset of ice nucleation via deposition nucleation on the glassy surface just accidentally coincided with the homogeneous freezing threshold. Recently, the use of in situ, near-backscattering depolarization measurements was explored to detect temperature- and humidity-induced viscosity transitions in α-pinene SOA particles [*Järvinen et al*., 2016]. The applicability of this technique, however, is limited to laboratory experiments with very high number concentrations and particle sizes above 0.6 μm, where nonspherical SOA particle aggregates can be formed, whose transition to less viscous and thereby spherical particle morphologies can be detected by a decrease in the depolarization ratio.

An indirect measure to infer the ice nucleation mechanism for glassy SOA particles could be the degree of morphology change during ice cloud processing (atmospheric freeze drying) [*Adler et al*., 2013; *Wagner et al*., 2012]. Provided that the glassy particles liquefy during the updraft and homogeneous freezing occurs, the ice growth within the liquefied droplets will lead to a revitrification of the freeze-concentrated organic solution, and the subsequent sublimation of ice will leave behind highly porous aerosol particles. Evidence for such porous aerosol formation comes from freeze-drying experiments with particles generated from a reference sample for natural organic matter (Suwannee River Natural Organic Matter, International Humic Substances Society), where the particle morphology before and after the freeze-drying step was inferred from electron microscopy [*Adler et al*., 2013]. The formation of a porous structure with potential surface defects and a larger surface area compared to a smooth sphere could also explain experimental findings from previous Aerosol Interaction and Dynamics in the Atmosphere (AIDA) measurements with amorphous organic aerosol particles of the simple sugars/acids category [*Wagner et al*., 2012], where an increase in the ice nucleation efficiency of the aerosol particles was detected after a preceding homogeneous ice freezing experiment. Such structural change will not occur if the organic particles remain glassy in the course of an ice nucleation event and act as INPs in the deposition mode. Repeated ice nucleation experiments with the same load of organic aerosol particles, together with the analysis of associated changes in the morphology and the ice nucleation ability of the particles, could therefore be a valuable tool to gain further information about the ice nucleation mechanism.

In the present study, we first provide a new temperature-dependent data set for the ice nucleation ability of pristine SOA particles generated from the ozonolysis of α-pinene. The ice nucleation experiments were performed in the AIDA (Aerosol Interaction and Dynamics in the Atmosphere) cloud chamber, which has already successfully been employed in previous studies with glassy materials [*Möhler et al*., 2008; *Murray et al*., 2010; *Saathoff et al*., 2009; *Wagner et al*., 2012; *Wilson et al*., 2012]. Specifically, our new study extends the former ice nucleation measurement for α-pinene SOA at 205 K [*Möhler et al*., 2008] to a temperature range from 243 to 205 K, which immediately allows the comparison of the new data with those from *Ladino et al*. [2014] and *Ignatius et al*. [2016] for the same SOA precursor compound.

In addition to the ice nucleation measurements with pristine α-pinene SOA particles, the second main goal of this work is to explore to what extent freeze drying and porous aerosol particle formation occur at different temperatures and what the associated effect on the particles' ice nucleation efficiency would be. Our paper is structured as follows: After describing the instrumentation and technical operation of the AIDA chamber in section 2, we analyze in section 3 the ice nucleation experiments with pristine, unprocessed SOA particles from the ozonolysis of α-pinene, compare our results to previous literature studies, and discuss the

Journal of Geophysical Research: Atmospheres 10.1002/2016JD026401

potential freezing mechanisms. Section 4 investigates the ice cloud processing of the α-pinene SOA particles and the modification of their ice nucleation ability in repeated ice nucleation experiments. We then conclude our article with a summary and an outlook on future experiments in section 5.

2. Experimental

2.1. General Setup

The AIDA facility consists of two aerosol vessels, (i) an 84.3 m^3-sized aluminum chamber, referred to as the AIDA chamber and (ii) a 3.7 m^3-sized stainless steel chamber, referred to as the aerosol preparation and characterization (APC) vessel (Figure 1) [*Möhler et al*., 2008]. The APC vessel can only be operated at ambient temperature (295 K) and was used to generate the α-pinene SOA particles in a reproducible manner (section 2.2). A fraction of the SOA particles was then transferred through a stainless steel tube into the AIDA vessel for the ice nucleation experiments. The AIDA chamber is located in an isolating containment and can be cooled to any temperature between ambient and 183 K. Supersaturations with respect to ice are achieved by expansion cooling, as conducted by a controlled reduction of the chamber pressure with a mechanical pump that is typically operated at volume flow rates between 1.5 and 3 m^3/min (section 2.3). During the freeze-drying experiments, the evacuated APC vessel served as additional expansion volume to induce a rapid increase in the ice supersaturation (section 2.4).

2.2. Aerosol Generation and Characterization

Before aerosol preparation, the APC vessel was evacuated to a pressure below 1 hPa and then filled with particle-free synthetic air to ambient pressure. SOA particles were generated by reacting (1S)-(−)-α-pinene (99%, Aldrich) and ozone (Semozon 030.2 discharge generator, Sorbios) in the dark at low relative humidity with respect to water ($RH_w < 10\%$). First, 2 ppmv of ozone was added to the APC vessel, followed by the addition of 2 ppmv of α-pinene. A few experiments were also conducted with (S)-(−)-limonene (>97%, Merck) instead of α-pinene as the SOA precursor compound. The number concentration of the nucleated SOA particles was measured with condensation particle counters (CPC3010 and CPC3022, TSI) and their size distribution recorded with a scanning mobility particle sizer (SMPS, TSI) and an aerodynamic particle spectrometer (APS, TSI). After a reaction and growth period of 1 h, the SOA particles had a number concentration of $\sim 3 \cdot 10^5$ cm^{-3} and formed a unimodal size distribution that could accurately be fitted with a lognormal function, yielding a median mobility-equivalent diameter, d_{me}, of ~300 nm and a mode width, σ_g, of ~1.3. A fraction of the SOA particles from the APC vessel was then transferred through a stainless steel tube into the cooled AIDA chamber. The connection between APC and AIDA was closed when the number concentration of particles in the AIDA chamber reached a value of 1500 cm^{-3}. The size distribution of the SOA particles in AIDA was recorded with a second set of SMPS and APS instruments. An exemplary size distribution as measured in the AIDA chamber is shown in the top left part of Figure 1. The AIDA chamber was held at temperatures between 243 and 205 K, representing the starting conditions for the ice nucleation experiments described in section 2.3. RH_w in AIDA was controlled by an ice layer on the chamber walls and varied between ~70% at 243 K and ~55% at 205 K. For each individual ice nucleation experiment at a different AIDA temperature, a fresh load of α-pinene SOA particles was generated in the APC vessel using the same experimental procedure and transferred to AIDA, guaranteeing reproducible and uniform particle properties in terms of number concentration, size, and chemical composition. The composition of the SOA particles in AIDA was characterized with a high-resolution time-of-flight aerosol mass spectrometer (HR-ToF-AMS, Aerodyne). For all experiments, the mean oxygen-to-carbon (O/C) and hydrogen-to-carbon (H/C) ratios of the SOA particles as inferred from the AMS measurements were 0.35 and 1.55, respectively.

The ice nucleation experiments discussed in this article were part of an extended measurement campaign on the chemical and physical properties of α-pinene SOA particles in the temperature range from 298 to 205 K. Further information about the individual organic compounds in the SOA particles, as inferred from high-resolution time-of-flight chemical ionization mass spectrometer measurements (FIGAERO-HR-ToF-CIMS, Aerodyne) [*Lopez-Hilfiker et al*., 2014], will be discussed in a forthcoming article. In addition to the CIMS analyses, the bounce characteristics of the SOA particles were measured by the Aerosol Bounce Instrument (ABI) [*Pajunoja et al*., 2015]. The ABI, however, could only be operated down to a temperature of 258 K inside the isolating containment of the AIDA chamber (Figure 1), thereby probing the particles at conditions as prevalent in the AIDA chamber itself. Below 258 K, the ABI had to be removed from the cold housing, meaning that

Journal of Geophysical Research: Atmospheres 10.1002/2016JD026401

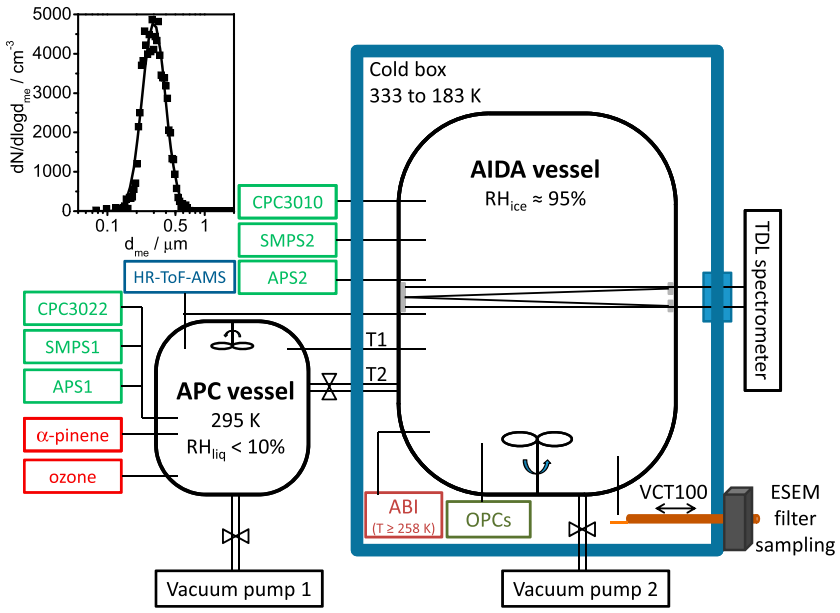

Figure 1. Simplified scheme of the AIDA aerosol and cloud chamber facility with the relevant scientific instrumentation used in this study. Both the volumes of the AIDA and the APC chamber are stirred by mixing fans mounted at the bottom and at the top of the vessels, respectively. T1 is a 25 mm stainless steel connection tube to transfer the α-pinene SOA particles from the APC to the AIDA aerosol vessel. T2 is a 100 mm stainless steel connection tube between the two aerosol vessels, whose valve is opened during the freeze-drying experiments to provoke an additional expansion of the AIDA volume into the evacuated APC vessel (section 2.4). All instruments and abbreviations are discussed in sections 2.1 to 2.4. The insert in the top left shows a typical number size distribution of the SOA particles after having them transferred from the APC into the AIDA chamber at 243 K. The SMPS data points (squares) could be accurately fitted with a unimodal lognormal distribution function, yielding $\sigma_g = 1.32$ and $d_{me} = 0.30$ µm.

it was not possible to measure the bounced fraction of the particles in the temperature regime covered by the ice nucleation experiments. Also, the specific demands with respect to particle number concentration and size for depolarization measurements to be sensitive to probe the phase state of the SOA particles, as estimated to be 10,000 cm^{-3} particles with a diameter of at least 600 nm [*Järvinen et al.*, 2016], were not met in our study.

We have therefore no direct information about the phase state of the α-pinene SOA particles after injecting them into the AIDA at $T \leq 243$ K and $RH_w \leq 70\%$. From a particular freeze-drying experiment conducted at an initial temperature of 243 K, however, we obtained unambiguous evidence that the SOA particles resided in a highly viscous state even at 243 K and 70% RH_w, i.e., at the highest temperature and relative humidity conditions before starting the expansion cooling experiments. This could be concluded because the freeze-dried SOA particles adopted and conserved a highly porous structure under these conditions and did not immediately collapse into spherical, less viscous particles. For the sake of clarity, we will discuss this experiment only later in this article (section 4.1) and presume for the discussion in section 3 that at the starting conditions of the ice nucleation experiments, highly viscous or glassy α-pinene SOA particles were present. This assumption is also in agreement with the temperature-and humidity-dependent parameterization of the viscosities of α-pinene SOA [*Wang et al.*, 2015].

2.3. Standard Ice Nucleation Experiments

Figure 2 (left) shows time series of the most important AIDA data during a typical ice nucleation experiment with α-pinene SOA particles at an initial temperature of 233 K, where the start of expansion cooling is denoted by time zero. Panel A depicts the evolution of the AIDA pressure (black line) and mean gas temperature (red line, computed from the average of a series of vertically arranged thermocouple sensors, uncertainty ±0.3 K). The controlled reduction of the chamber pressure leads to a decrease in the gas temperature and an increase in the ice saturation ratio, S_{ice}, and the saturation ratio with respect to supercooled water, S_{liq} (panel

Journal of Geophysical Research: Atmospheres 10.1002/2016JD026401

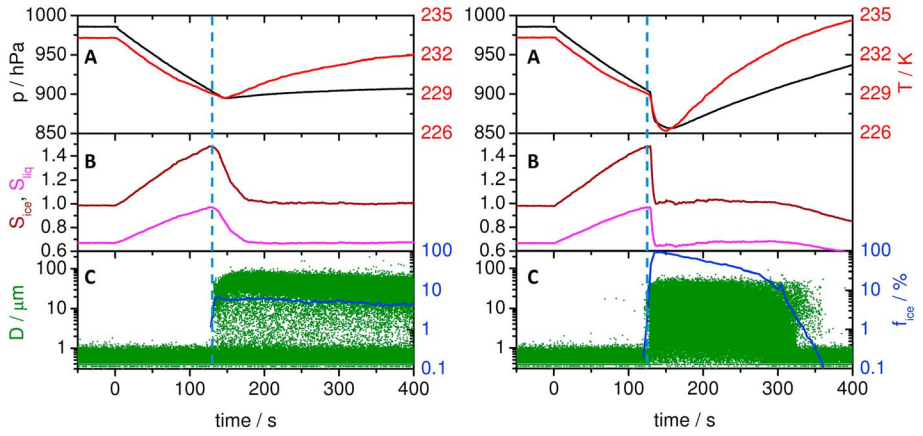

Figure 2. Ice nucleation characteristics of α-pinene SOA particles during (left) a standard ice nucleation and (right) a freeze-drying experiment. Panel A: AIDA pressure (black line) and mean gas temperature (red line). Panel B: Saturation ratio with respect to ice (S_{ice}, brown line) and liquid supercooled water (S_{liq}, magenta line). Panel C: Aerosol and cloud particle size distribution (green dots) and ice-active fraction of the aerosol population (f_{ice}, blue line).

B, brown and magenta lines, respectively). The latter two quantities were computed from the equations by *Murphy and Koop* [2005], based on water vapor concentrations that were measured in situ in the AIDA chamber by a tunable diode laser (TDL) spectrometer with an uncertainty of ±5% [*Fahey et al.*, 2014]. The onset of ice nucleation was measured with two optical particle counters (OPC, type welas 2000, Palas, overall size range 0.3–240 µm) that were mounted inside the isolating containment of the AIDA chamber (Figure 1). The OPC data are illustrated as a scatterplot (green dots in panel C), where each dot represents the signal of an individual particle that was categorized into a specific size channel of the OPC according to its scattering intensity. Initially, only the smaller-sized seed aerosol particles with optical diameters up to 1 µm are visible in the OPC records. The onset of ice formation at about t = 130 s (vertical line) is then clearly defined by the appearance of the nucleation mode of larger particles with optical diameters above 10 µm. By introducing an optical threshold size, the nucleated ice crystals can be separately counted, and by dividing the ice particle number concentration through the number concentration of the α-pinene SOA seed aerosol particles, the ice-active fraction of the aerosol population can be inferred (f_{ice}, blue line in panel C, estimated uncertainty ±20%). From each expansion cooling run, a data pair consisting of temperature and ice saturation ratio at the nucleation onset can be inferred, such as T = 229.1 K and S_{ice} = 1.47 for the experiment shown in Figure 2.

2.4. Freeze-Drying Experiments

In order to detect changes in the ice nucleation ability of the α-pinene SOA particles in repeated expansion cooling cycles, it is a prerequisite to activate and process as many seed aerosol particles as possible in the first ice nucleation run. As can be seen from the AIDA records of the standard ice nucleation experiment (Figure 2, left), only a small fraction of 6% of the particle ensemble was activated. This is because the ice supersaturation was rapidly depleted after the onset of ice nucleation so that no further ice crystals could nucleate. We therefore employed a special procedure to activate a larger fraction of the seed aerosol population (Figure 2, right). The freeze-drying experiment was started with a similar pumping speed as in the preceding standard ice nucleation run, but then, just when reaching the afore determined nucleation threshold (S_{ice} = 1.47, vertical line), a valve to the evacuated APC vessel was opened. The additional expansion provoked a further, almost instant decrease of the gas temperature by 2.5 K and led to the formation of a strong nucleation mode with an ice-active fraction close to 100%. After a short observation period of about 30 s, the AIDA vessel was refilled with dry synthetic air to ambient pressure, leading to the rapid sublimation of the nucleated ice crystals and leaving behind the population of ice cloud processed α-pinene SOA particles. In a subsequent ice nucleation experiment, we could then probe whether freeze drying had modified the ice nucleation ability of the seed aerosols compared to the behavior of the unprocessed particles shown in Figure 2 (left).

Two methods were used to probe a potential morphology change of the freeze-dried α-pinene SOA particles. Necessarily, these methods have to keep the SOA particles at cold temperatures as prevalent in the AIDA

Journal of Geophysical Research: Atmospheres 10.1002/2016JD026401

chamber in order to not modify their phase state upon warming. On the one hand, the records from the optical particle counters, mounted in the thermostated housing of the AIDA chamber, proved to be useful to discriminate between compact and highly porous particle morphologies, in accordance with previous findings that the optical properties of these two particle types are substantially different [*Adler et al*., 2014]. On the other, we developed a method to obtain electron microscope images of the aerosol particles before and after freeze drying. For that purpose, we used a vacuum cryotransfer system (EM VCT100, Leica) to ensure an unbroken cold chain from particle sampling to electron microscopic analysis. The cryotransfer unit includes a liquid-nitrogen cooled transfer shuttle with a silicon substrate mounted on a copper sample holder. For particle sampling, the Si substrate was introduced through a pneumatic lock into a sampling chamber located inside the isolating containment of the AIDA chamber. To achieve efficient sampling of SOA particles, the aerosol flow from AIDA was directed through a neutralizer (model 3077A, TSI) onto the sampling substrate connected to a high-voltage power supply set to 2 kV. After sampling, the substrate was retracted into the precooled shuttle. Thereafter, under continuous supply of liquid nitrogen, the shuttle was detached from the AIDA lock, transferred to a nearby laboratory, and attached to the lock of an environmental scanning electron microscope (ESEM, Quanta 650 FEG, FEI). This newly developed technique was successfully deployed during a freeze-drying experiment performed at 243 K. We plan to refine its operation in order to establish it as a standard diagnostic tool for future AIDA measurement campaigns. In the context of this work, we are limited to the results from this single experiment.

3. Ice Nucleation Experiments With Pristine, Unprocessed α-Pinene SOA Particles

3.1. Ice Nucleation Onsets and Potential Nucleation Mechanisms

Figure 3a shows the ice saturation ratios required to activate 0.1% of the unprocessed α-pinene SOA particles (dark green squares), as inferred from the standard ice nucleation experiments described in section 2.3. The error bars represent the 5% uncertainty of the water vapor measurements with the TDL spectrometer. A single expansion cooling run was conducted with limonene SOA particles at a starting temperature of 223 K. Its corresponding ice nucleation onset is shown as the dark green circle in Figure 3a. The data are compared to several nucleation onsets for various aerosol types reported previously, two of which we first want to take into consideration in our discussion: (i) the previous AIDA measurement with α-pinene SOA particles at 205 K (dark green diamond) [*Möhler et al*., 2008] and (ii) the homogeneous freezing of aqueous sulfuric acid solution droplets (cyan stars), as also inferred from previous AIDA expansion cooling experiments [*Möhler et al*., 2003]. *Möhler et al*. [2008] had also used the APC vessel to generate the SOA particles from α-pinene and ozone at room temperature in the dark. Hence, the α-pinene SOA particles should have been of similar, albeit unspecified, composition as those generated in the present study. The good agreement of the formerly derived nucleation onset for α-pinene SOA at 205 K with that from the present study supports this assumption and illustrates the excellent repeatability of the AIDA ice nucleation experiments.

The most striking observation from the data in Figure 3a is the similarity of the freezing onsets for α-pinene SOA particles and aqueous H_2SO_4/H_2O solution droplets. The latter are in reasonable agreement with the parameterization of the homogeneous freezing threshold from *Koop et al*. [2000], although the AIDA measurements tend to follow a slightly steeper slope, as already discussed in *Möhler et al*. [2003]. As mentioned in section 2.4, we postulate that the α-pinene SOA particles are initially in a highly viscous or glassy state before the expansion cooling runs are started. A possible explanation for the observed freezing behavior is thus the fast equilibration of the SOA particles with the increasing relative humidity during expansion cooling, meaning that the thickness of the diluted outer particle layer was at least equal to or larger than the diameter of the critical ice nucleus before the homogeneous freezing threshold was reached [*Lienhard et al*., 2015]. In case the particles were only partially liquefied and still contained a glassy core, the absence of ice formation before the homogeneous freezing threshold would indicate the immersion freezing mode to be rather inefficient. Further conclusions on the prevailing ice nucleation mechanism cannot be drawn from the measurements of the ice nucleation onsets only, a drawback that has already been mentioned in section 1.

As an additional step in the analysis, we therefore investigated the ice-active fractions of the seed aerosol population during the expansion cooling cycles, as shown in Figure 3b (see also *Murray et al*. [2010, Figure 2] for a similar graphical representation). The black curves are the measured T-S_{ice} trajectories of the ice

Journal of Geophysical Research: Atmospheres 10.1002/2016JD026401

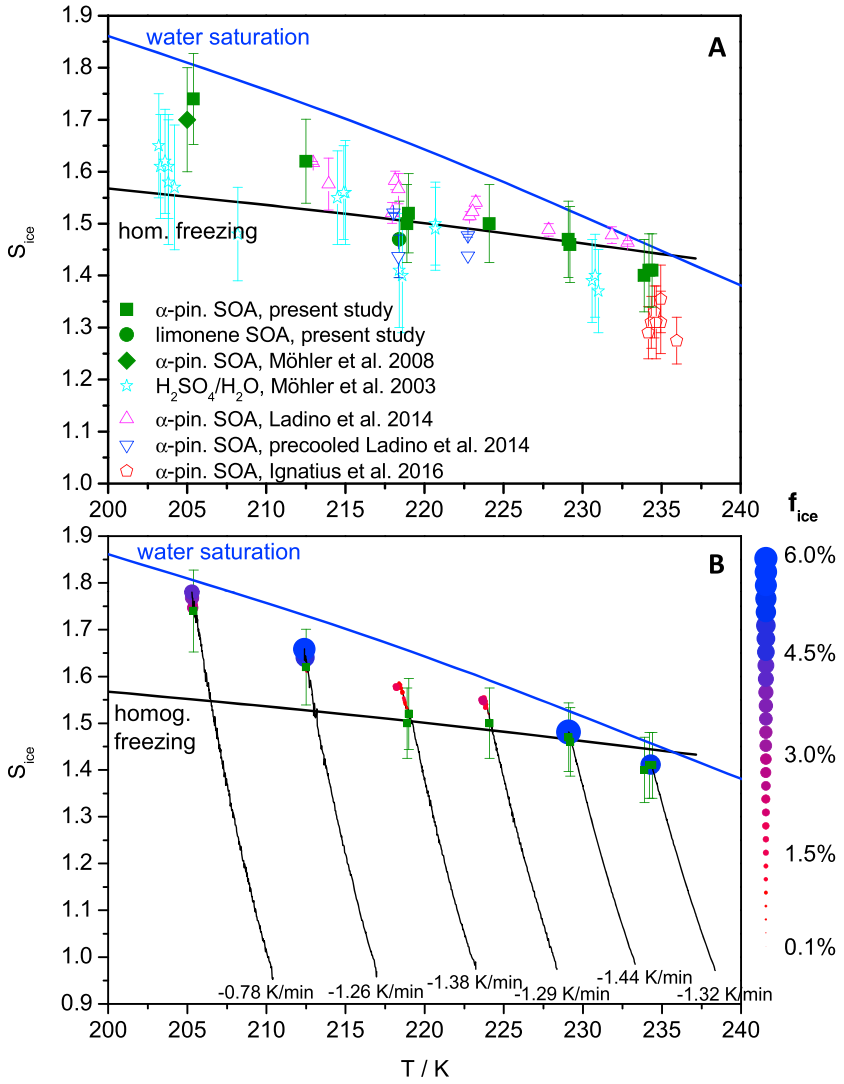

Figure 3. (a) Ice nucleation onsets of α-pinene and limonene SOA particles from this study in comparison with previously reported nucleation onsets for α-pinene SOA particles and aqueous sulfuric acid solution droplets, which are discussed in detail in section 3. The blue line is the saturation curve with respect to liquid supercooled water, and the black line represents the homogeneous freezing threshold [*Koop et al.*, 2000]. (b) T-S_{ice} trajectories of the expansion cooling experiments with the α-pinene SOA particles from this study (black curves), superimposed with the detected freezing onsets (dark green squares, same data as in Figure 3a) and the fractions of aerosol particles that activated to ice (size of the colored circles). The number at the bottom of each trajectory denotes the cooling rate at the ice nucleation onset. See section 3 for further discussion of this panel.

nucleation experiments with α-pinene SOA particles, covering the period from the start of expansion cooling at slightly ice-subsaturated conditions until the time when the maximum ice saturation ratio was reached. The numbers at the bottom of each trajectory denote the respective cooling rates at the ice nucleation onsets, the latter again marked by the dark green squares (same data as in Figure 3a). The size of the colored dots superimposed on the trajectories represents the ice-active fraction of the seed aerosol particles. For starting temperatures of 238, 233, and 223 K, two separate ice nucleation experiments were conducted, and for each of those, a fresh load of α-pinene SOA particles, afore generated in the APC vessel, was used. As can be seen from Figure 3a, the ice nucleation onsets for these pairs of expansion cooling experiments closely agree. The same is true for the time evolution of the ice-active fractions, and hence, for the sake of clarity, only a single trajectory is shown in Figure 3b for these temperatures. The selected experimental trajectory for the starting temperature of 233 K corresponds to the data shown in Figure 2 (left).

Journal of Geophysical Research: Atmospheres 10.1002/2016JD026401

At initial temperatures of 238 and 233 K, the temporal development of the f_{ice} data displays the expected behavior for liquid or liquefied aerosol particles in which ice nucleates homogeneously. As soon as the homogeneous freezing threshold is reached, f_{ice} rapidly increases and the growth of the nucleated ice crystals almost immediately quenches the supersaturation and prevents further nucleation. As a result, the peak ice saturation ratio almost coincides with the nucleation onset. Such behavior is commonly observed for AIDA expansion cooling experiments with aqueous sulfuric acid solution droplets when similar cooling rates as in the α-pinene SOA experiments are employed. More importantly, the sharply defined homogeneous nucleation threshold with the immediate, strong increase in f_{ice} is also observed at temperatures down to about 200 K. Only when the expansion cooling runs are conducted at temperatures below 200 K, a nonequilibrium effect may delay the burst of homogeneously nucleated ice crystals, because the supercooled liquid particles do not reach their equilibrium water activity due to the small absolute amount of water vapor prevalent in the gas phase [*Haag et al*., 2003]. This implicates that there is not such a sharp, sudden increase in f_{ice} at the homogeneous freezing threshold at $T < 200$ K. In addition, the nucleated ice crystals only slowly grow into the detection range of the OPCs at these low temperatures [*Möhler et al*., 2003], thereby leading to an artificial delay in the measured evolution of f_{ice}. These two factors, however, do not count in the temperature regime of the SOA experiments considered in Figure 3. As an example, a sudden burst of homogeneously nucleated ice crystals was also detected for aqueous citric acid aerosol particles at a starting temperature of 215 K and contrasted with the behavior observed at lower temperatures in the glassy regime [*Murray et al*., 2010]. Here the much more gradual increase in f_{ice} after the nucleation onset was attributed to a heterogeneous nucleation mode. For the α-pinene SOA particles, there is also a clear change in the evolution of f_{ice} with temperature (Figure 3b). At intermediate starting temperatures of 228 and 223 K, the number concentration of ice crystals that nucleate after exceeding the homogeneous freezing threshold is much smaller compared to the experiments at higher temperatures, even though similar cooling rates were encountered at the nucleation onsets. As a result, the ice supersaturation is not instantly depleted but rises clearly above the value of the nucleation onset, in which course f_{ice} gradually increases. Overall, the maximum ice-active fractions are by a factor of 3 to 4 smaller than at 238 and 233 K. Interestingly, the nucleation characteristics change again at even lower temperatures. At starting temperatures of 217 and 211 K, f_{ice} again more rapidly increases after the nucleation onset, limiting the peak ice supersaturation to a value only slightly above the nucleation onset. Also, the maximum ice-active fractions are again as high as during the experiments that started at 238 and 233 K; although particularly at the lowest starting temperature of 211 K the cooling rate at the nucleation onset is clearly reduced.

These variations in the evolution of f_{ice} are an indirect but robust indication for a change in the underlying ice nucleation mechanisms over the considered temperature range. Most likely, the nucleation modes observed at starting temperatures of 238 and 233 K can be attributed to homogeneous freezing, without being able to clarify whether the entire particle or just a sufficiently thick outer layer of the α-pinene SOA particles liquefies during expansion cooling. The retarded evolution of f_{ice} during the 228 and 223 K experiments can be interpreted as delayed homogeneous freezing, meaning that the glassy SOA particles just start to soften in the vicinity of the homogenous freezing limit. A slow formation of liquid layers would explain the observed gradual increase of the number concentration of nucleated ice crystals at elevated humidities above the homogeneous freezing limit [*Lienhard et al*., 2015]. The again different behavior at lower temperatures could be due to the transition to yet another nucleation regime. According to our line of reasoning that condensed-phase diffusion is already slowed down during the expansion cooling experiments that started at 228 and 223 K, it seems unlikely that the α-pinene SOA particles would liquefy at all at even lower temperatures. This suggests deposition nucleation to be the prevailing ice formation mechanism for SOA particles at these temperatures, with just the accidental situation that the heterogeneous nucleation onsets for the SOA particles coincide with the homogeneous freezing thresholds for aqueous solution droplets.

3.2. Comparison With Literature Data

We now turn toward the comparison of our freezing onsets with those measured in preceding ice nucleation studies, thereby addressing the additional data displayed in Figure 3a. Our interpretation of a homogeneous freezing mode during the expansion cooling experiments at 238 and 233 K is in contradiction to the results of *Ignatius et al*. [2016], who observed heterogeneous ice nucleation when probing the ice nucleation ability of α-pinene SOA particles in a continuous flow diffusion chamber (CFDC) at 238 K (red pentagons in Figure 3a,

Journal of Geophysical Research: Atmospheres 10.1002/2016JD026401

representing the onset values for f_{ice} = 10%). The SOA particles were also generated from the reaction of α-pinene with ozone, which, however, was carried out at lower temperatures (263–235 K) and under irradiation with UV light. The average specified O/C ratio of the α-pinene SOA particles was lower than in our study (0.25 compared to 0.35), which could affect the particles' viscosity and response to a change in relative humidity [*Berkemeier et al*., 2014; *Pajunoja et al*., 2015]. An important issue could also be the abrupt humidification and short residence time (about 10 s) of the aerosol particles in the nucleation region of the CFDC chamber. Compared to these conditions, the α-pinene SOA particles probed in a typical AIDA expansion cooling experiment have more time to adjust to the increasing relative humidity, thus making liquefaction and homogeneous freezing more likely.

Nonetheless, our reported freezing onsets for α-pinene SOA are in good agreement with a different ice nucleation study that was carried out with a CFDC chamber [*Ladino et al*., 2014]. *Ladino et al*. [2014] have used a flow tube and a smog chamber set up to generate SOA particles from the ozonolysis of α-pinene at room temperature. The O/C ratio of the particles was not specified. The pink, upward pointing triangles in Figure 3a denote the reported ice saturation ratios to activate 0.1% of the particles, comprising experiments with freshly formed α-pinene SOA, as well as studies where samples of the water-soluble fraction of filter-collected particles were atomized and probed in the CFDC chamber. Similar to the AIDA results, the S_{ice} onsets are located at or slightly above the homogeneous freezing threshold. In a different type of experiment, the particles generated from the samples of the water-soluble organic fraction were precooled for 30 s at 233 K in a cooling flow tube prior to the injection into the CFDC chamber. The concomitant onset S_{ice} values, shown as the blue, downward pointing triangles in Figure 3a, are slightly lower than those determined for the particles that were not precooled. Precooling could lead to hardening of the organic material, thereby favoring the particles' ability to promote heterogeneous ice nucleation. However, the authors could not exclude that the improved ice nucleation ability of the precooled particles was due to preactivation in the cooling flow tube [*Ladino et al*., 2014].

The discussion makes clear that measured onset values for ice nucleation by highly viscous or glassy materials will crucially depend on the humidification conditions of the specific experiment. The cooling rates shown along the T-S_{ice} trajectories in Figure 3b correspond to dry adiabatic cooling rates at 1.3 to 2.5 m/s updraft velocities in the troposphere, representing values at the high end of atmospheric updrafts taken into account in the recent model simulations of the water uptake by α-pinene SOA particles [*Lienhard et al*., 2015; *Price et al*., 2015]. With our interpretation of a delayed homogeneous freezing mode during the expansion cooling experiments that started at 228 and 223 K, we are in agreement with the simulations by *Price et al*. [2015] who predicted kinetically limited water diffusion already at these temperatures. According to *Lienhard et al*. [2015], homogeneous ice nucleation should only be delayed at very cold conditions (195 K) near the tropical tropopause. Concerning the reliability of the model simulations, one should state that the underlying measurements of the water diffusion coefficients were only performed at relative humidities below ice saturation and, in the case of the *Price et al*. [2015] study, only down to a temperature of 240 K. Therefore, the model simulations rely on an extrapolation of the water diffusion coefficient parameterization to higher relative humidities and, in part, to lower temperatures.

4. Atmospheric Freeze-Drying Experiments

4.1. Freeze-Drying Experiments Simulating a Convective Cloud System

4.1.1. Formation of Highly Porous Aerosol Particles

We have introduced the freeze-drying experiments as a tool to gain further insights into the ice nucleation mechanism of the α-pinene SOA particles at cirrus temperatures. Before addressing this subject in section 4.2, we want to explore whether the observations from the atmospheric freeze-drying cycle of the Suwannee River NOM particles [*Adler et al*., 2013], namely, the formation of highly porous aerosol particles, can be reproduced for the α-pinene SOA particles. The laboratory freeze-drying cycles performed by *Adler et al*. [2013] were not started in the cirrus regime but mimicked a deep convective cloud system, entailing droplet activation of the aerosol particles at warm temperatures, homogeneous freezing of the cloud droplets below 237 K, and release of the freeze-dried particles after the sublimation of ice in an ice-subsaturated environment. To simulate such a process in AIDA, we have started an expansion cooling run with the α-pinene SOA particles at 243 K, following the usual procedure of particle

Journal of Geophysical Research: Atmospheres 10.1002/2016JD026401

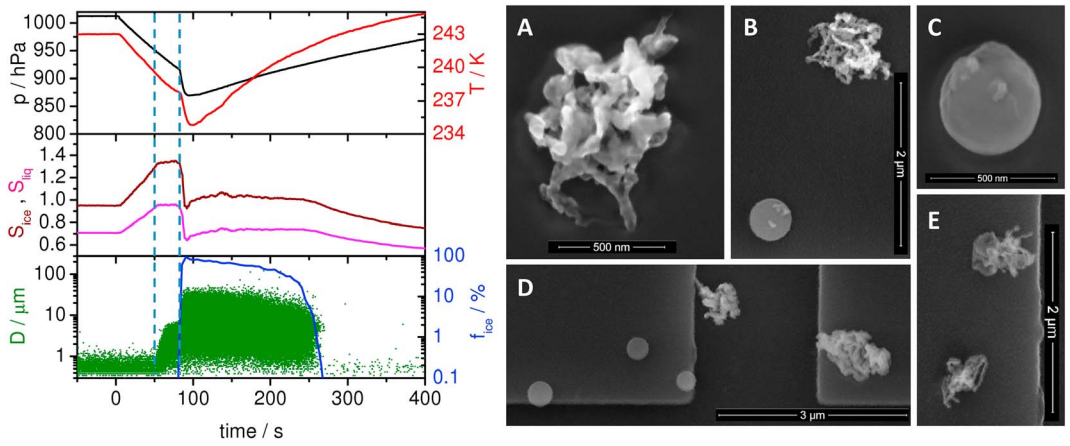

Figure 4. (left) Ice nucleation characteristics of α-pinene SOA particles during a freeze-drying experiment that started at 243 K. The data types are the same as shown in Figure 2. (right) Selection of ESEM images of α-pinene SOA particles collected on a Si substrate before and after the freeze-drying step, following the experimental procedure described in section 2.4. Note that both the unprocessed and the freeze-dried α-pinene SOA particles were deposited on the same substrate.

generation in the APC chamber at room temperature and transfer to the AIDA vessel. The AIDA records of the freeze-drying experiment are shown in Figure 4 (left). During expansion cooling, the α-pinene SOA particles were first activated to a cloud of supercooled water droplets (first vertical line) when the relative humidity exceeded water saturation. At the time of droplet activation, the gas temperature had dropped to about 239 K. After two further degrees of cooling during continued pumping, the gas temperature approached the homogeneous freezing temperature of micron-sized supercooled water droplets (second vertical line). No heterogeneously formed ice crystals were detected until reaching the homogeneous freezing limit. At that moment, we induced an extra expansion by opening the valve to the evacuated APC chamber. The intention of this action was the same as in the freeze-drying experiment that started at 233 K (Figure 2, right), namely, to ensure that the complete population of seed aerosol particles, respectively, cloud droplets, was involved in the freeze-drying step. The additional expansion led to an almost instant decrease of the gas temperature by additional 2.5 K, causing the whole cloud of supercooled water droplets to freeze with f_{ice} close to 100%. Thereafter, the nucleated ice crystals were rapidly sublimed by refilling the AIDA chamber with dry synthetic air, thereby minimizing sedimentation losses of large ice crystals and releasing the freeze-dried α-pinene SOA particles in an ice-subsaturated environment.

As an immediate consequence of the freeze-drying experiment, the ice cloud processed α-pinene SOA particles almost completely disappeared from the records of the optical particle counters. Before the start of the expansion cooling cycle at $t < 0$, the OPC measurements have captured about 5% of the overall aerosol particle number concentration. This fraction corresponds to the largest α-pinene SOA particles of the size distribution shown in Figure 1, which are detected at optical diameters below 1 µm by the OPCs. After the freeze-drying step, the dilution-corrected fraction of seed aerosol particles that are still captured by the OPCs is less than 0.25%. This points to a severe change of the optical properties of the freeze-dried compared to the unprocessed α-pinene SOA particles, given that the size classification of the OPCs is based on the particles' light scattering intensities at scattering angles of 90 ± 12 ° [*Benz et al.*, 2005]. Such large modification of the optical properties upon freeze drying, apparent as a reduction of the extinction efficiencies of the freeze-dried NOM aerosols compared to those of the nonporous particles, was also observed by *Adler et al.* [2013, 2014]. The fact that the freeze-dried α-pinene SOA particles appear "less visible" than the unprocessed particles in the OPC records is therefore a first indication for the formation of highly porous aerosol particles. The porosity of the freeze-dried α-pinene SOA particles is confirmed by the ESEM images of SOA particles collected on the Si substrate as shown in Figure 4 (right). Collection of SOA particles with the liquid-nitrogen cooled transfer shuttle was performed in a way that both the unprocessed and the freeze-dried α-pinene SOA particles were deposited on the same substrate, with sampling periods of 30 min at $t < 0$ before the start of expansion cooling and another 30 min at $t > 300$ s after the sublimation of the ice crystals. The ESEM images B and D show proof of

Journal of Geophysical Research: Atmospheres 10.1002/2016JD026401

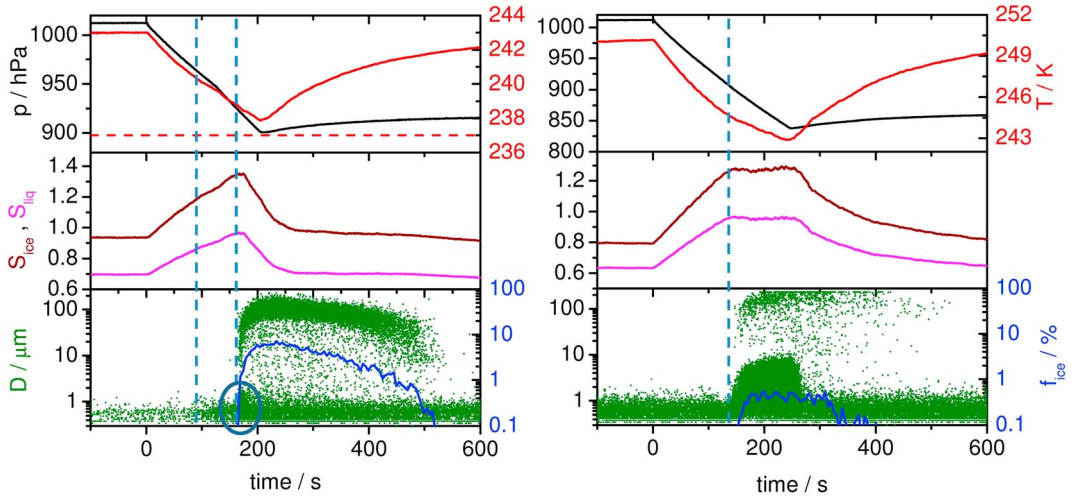

Figure 5. Ice nucleation characteristics of α-pinene SOA particles after the freeze-drying experiment shown in Figure 4. (left) expansion cooling run started at the same temperature as the freeze-drying experiment (243 K). The horizontal dashed line in the first panel represents the onset of homogeneous freezing observed in the ice nucleation experiment with the unprocessed α-pinene SOA particles (Figure 4, left). (right) Expansion cooling run started after warming the freeze-dried SOA particles to 250 K. The data types are the same as shown in Figure 2.

two different particle morphologies: compact, near-spherical particles (see also image C), representing the unprocessed particle ensemble, and highly irregular, porous particles (see also images A and E), representing the freeze-dried population of α-pinene SOA particles.

4.1.2. Ice Nucleation Ability of the Highly Porous Aerosol Particles

Adler et al. [2014] have performed a detailed analysis of the optical properties of the highly porous aerosol particles. The AIDA facility represents an ideal extension for the characterization of such aerosols, insofar as we can immediately probe whether the freeze-dried particles reveal a modified ice nucleation ability compared to the nonporous SOA particles. For that purpose, we performed a subsequent ice nucleation experiment with the porous α-pinene SOA particles at 243 K, which was started 1 h after the initial freeze-drying experiment. Its records are shown in Figure 5 (left). In the course of expansion cooling, there is clear indication for a humidity-induced collapse of the porous structure of the freeze-dried SOA particles. Starting at about 240 K and RH_w = 85% (first vertical line at t = 90 s), there is a rapid increase in the count rate of the OPCs at optical diameters below 1 µm, as visually evident from a much denser scatterplot in the OPC records than before the beginning of pumping. Taking into account particle dilution due to pumping, the fraction of seed aerosol particles that is detected by the OPCs again approaches the initial value from before the freeze-drying experiment. Such increase in the OPC count rate upon humidification was not observed in the expansion cooling experiments with the unprocessed α-pinene SOA particles at 243 K, i.e., it cannot simply be related to the hygroscopic growth of the aerosol particles. Similar to the depolarization method explored by *Järvinen et al.* [2016], also, the OPC measurements thereby prove to be a tool for detecting a morphology change of the α-pinene SOA particles which is related to a change of the particles' viscosity. For the particles probed by *Järvinen et al.* [2016], whose ice nucleation characteristics were investigated by *Ignatius et al.* [2016], the detected viscosity transition RH_w (55–62% at 243 K and 69–79% at 235 K) was somewhat lower than in our study, pointing to a different chemical composition of the generated SOA materials. We only detected a small structural change of the freeze-dried α-pinene SOA particles while they were suspended in the AIDA chamber for 1 h at T = 243 K and S_{ice} = 0.95 (RH_w = 70%) between the two expansion cooling cycles shown in Figures 4 and 5 (left). During that time, the fraction of aerosol particles detected by the OPCs slightly increased from about 0.25% to 0.5% but remained 1 order of magnitude lower than before the freeze-drying experiment, where a 5% fraction of the SOA particles was captured in the OPC records.

With the further increase of the relative humidity in the course of expansion cooling, the collapsed, freeze-dried α-pinene particles finally acted as cloud condensation nuclei (CCN) (second vertical line in Figure 5, left). The evolving cloud droplet mode, however, is barely visible in the OPC records and only persists for a short

Journal of Geophysical Research: Atmospheres 10.1002/2016JD026401

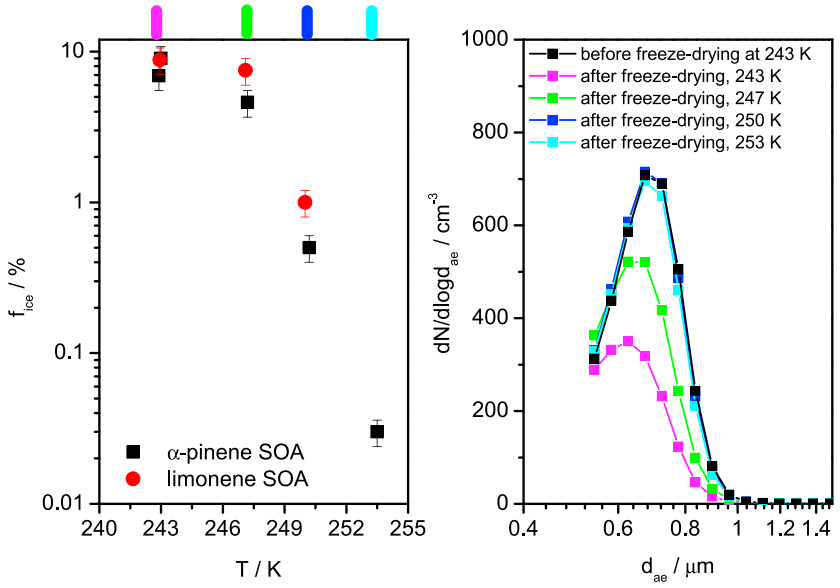

Figure 6. (left) Temperature-dependent ice-active fractions of freeze-dried α-pinene and limonene SOA particles in the CCN-induced ice growth mode. The colored bars on the top axis denote the times of individual size distribution measurements with the APS, which are shown with the same color coding in the right panel. In addition to the size distributions that were recorded after freeze drying, the initial APS distribution from before the freeze-drying experiment is also shown (black squares). As explained in the text, the maximum in the APS size distributions is only artificial and arises due to the decreasing detection efficiency at d_{ae} smaller than 0.7 µm (see also exemplary SMPS size distribution of the α-pinene SOA particles shown in the top left of Figure 1).

time period of about 20 s (as highlighted by the blue circle in Figure 5), because instantaneously with the CCN activation of the seed aerosol particles a large number concentration of ice crystals was formed with f_{ice} close to 10%. At the time of CCN activation, the gas temperature was still 2 K above the homogeneous freezing temperature of supercooled water droplets at about 237 K where the homogeneous ice nucleation of the CCN-activated, unprocessed α-pinene SOA particles was observed (Figure 4, left, second vertical line). This homogeneous freezing threshold for the unprocessed SOA particles is shown as the horizontal dashed line in the first panel of Figure 5 (left). It can be seen that during the expansion run with the freeze-dried SOA particles the temperature has never dropped below the homogeneous freezing line, meaning that the observed ice nucleation mode must be due to a heterogeneous freezing mechanism. Heterogeneous ice formation upon CCN activation was also detected when the freeze-dried particles were probed at warmer temperatures. Figure 5 (right) shows an experiment where a fresh load of α-pinene SOA particles was generated in the APC chamber, transferred to the AIDA vessel, subjected to a freeze-drying cycle at 243 K as shown in Figure 4, and then directly warmed to 250 K to probe the ice nucleation ability of the freeze-dried particles at that temperature. The expansion cooling run at 250 K was started about 3 h after the freeze-drying cycle at 243 K. Upon warming, there was a full recovery of the OPC count rate for the seed aerosol particles, which, similar to the data shown in Figure 4, had decreased by a factor of 20 immediately after the freeze-drying step. This observation points to a complete collapse of the porous structure of the freeze-dried α-pinene SOA particles during warming to 250 K. After CCN activation of the seed aerosol particles (vertical line, Figure 5, right), the droplet cloud evolves more clearly in the OPC records and persists for a much longer time period in comparison with the expansion cooling cycle started at 243 K (Figure 5, left). Nonetheless, there is still a distinct number concentration of ice crystals heterogeneously formed after CCN activation with an ice-active fraction of about 1%. Figure 6 (left) summarizes the f_{ice} values of the freeze-dried SOA particles as a function of temperature. Each data point corresponds to an individual experiment with freshly generated SOA particles, freeze dried at 243 K, and then probed for their heterogeneous ice nucleation ability in an expansion cooling experiment that started at the indicated temperature. In addition to the freeze-drying cycles with α-pinene SOA, we conducted three such experiments with limonene SOA, whose results, as evidenced by the data from Figure 6, closely agree with those for α-pinene SOA. Note again that all ice nucleation data displayed in Figure 6 represent

Journal of Geophysical Research: Atmospheres 10.1002/2016JD026401

heterogeneous freezing modes that were exclusively observed for the freeze-dried SOA particles after CCN activation at temperatures above 237 K. CCN-activated, unprocessed SOA particles only promoted homogeneous ice nucleation at $T < 237$ K.

In the following, we refer to the improved ice nucleation ability of the freeze dried compared to the unprocessed SOA particles as preactivation. The term "preactivation" has been introduced in the context of repeated ice nucleation experiments with insoluble INPs like mineral dust where the particles do not significantly change their morphology during ice-cloud processing [*Pruppacher and Klett*, 1997; *Vali et al*., 2015]. One might therefore be tempted to discuss the ice nucleation ability of the freeze-dried particles as a separate class of particles, i.e., unrelated to the properties of the compact SOA particles. On the other hand, the occurrence of the ice nucleation modes of the freeze-dried SOA particles displayed in Figure 5 inevitably requires a preceding ice nucleation event with the compact SOA particles, which suggests applying the concept of preactivation in the interpretation of our results. The preactivation efficiency of the freeze-dried SOA particles gradually decreases with increasing temperature (Figure 6, left), but preactivation is still detectable even for a temperature at or slightly above 250 K, where the OPC records point to a collapse of the porous network of the freeze-dried particles due to their reduced viscosity at higher temperatures. But obviously, the particles' viscosity is still sufficiently high that a memory effect from the preceding ice nucleation event is conserved in the viscous medium, which allows for the immediate growth of ice crystals after the droplet activation of the SOA particles at ice-supersaturated conditions. Whether the heterogeneous freezing mode of the freeze-dried SOA particles is induced by genuine, microscopic ice germs that are trapped in the viscous material during revitrification in the freeze-drying step, by a residual imprint of the ice lattice, or just by the particles' enhanced surface area even in the collapsed state remains a matter of speculation. Due to the observation of the ice nucleation mode only appearing after the droplet activation of the SOA particles, we propose to term the preactivation mode as "CCN-induced ice growth mode."

During the experiments depicted in Figure 6 (left), we were able to assess a different technique to at least qualitatively probe the morphology change of the α-pinene SOA particles after freeze drying and subsequent warming. *Adler et al*. [2013] have detected a clear increase of the mode diameter of the NOM particles in the SMPS size distribution measurement after freeze drying. Our SMPS instrument is located outside of the cold housing of the AIDA chamber, and the overall residence time of the particles in the sampling line, electrostatic classifier, and subsequent CPC is about 16 s. This gives the freeze-dried particles sufficient time for potential restructuring at warm temperatures and might be the reason why we could not detect a systematic change in the SMPS size distributions in the course of the freeze-drying experiments. This was different for the APS instrument, which is also situated outside the isolating containment but keeps the residence time of the particles in the warm environment at less than 1 s. Figure 6 (right) shows exemplary number size distributions as a function of the aerodynamic diameter, which were recorded before and after freeze drying of α-pinene SOA at 243 K (black and magenta squares, respectively), as well as after subsequent warming to 247, 250, and 253 K (green, blue, and cyan squares, respectively). All size distributions were corrected for the overall dilution of the particle number concentration during the experiment. Similar to the OPC records, the APS only detects the largest particles of the size distribution, and the apparent maximum at $d_{ae} = 0.7$ μm is due to the decreasing detection efficiency at smaller diameters. After freeze drying, there is clear decrease of the number concentration of SOA particles that are captured in the detection range of the APS instrument, pointing to the reduced settling velocities and aerodynamic diameters of the porous particles. Upon warming to 250 K and above, the initially detected size distribution is fully recovered as a result of the collapse of the particles' porous network.

4.1.3. Estimating the Viscosity of the α-Pinene SOA Particles

The porous particle morphology of the freeze-dried α-pinene SOA particles shown in Figure 4 results from the vitrification of the freeze-concentrated organic solution on the nucleated ice crystals and the subsequent sublimation of the ice pockets. Freezing must occur at a temperature in the region of the so-called T_g', denoting the temperature where the glass transition curve and the ice melting point curve in the SOA/water phase diagram intersect [*Zobrist et al*., 2008]. Even at a temperature slightly above T_g', a porous particle morphology could be formed provided that the viscosity is high enough to prevent a structural rearrangement on the experimental time frame. For a generic SOA material, T_g' was estimated to be about 233 K [*Koop et al*., 2011]. The freezing of the CCN-activated α-pinene SOA particles during the freeze-drying cycle performed in the AIDA chamber occurred at a similar temperature (Figure 4). We also observed that the investigated

Journal of Geophysical Research: Atmospheres 10.1002/2016JD026401

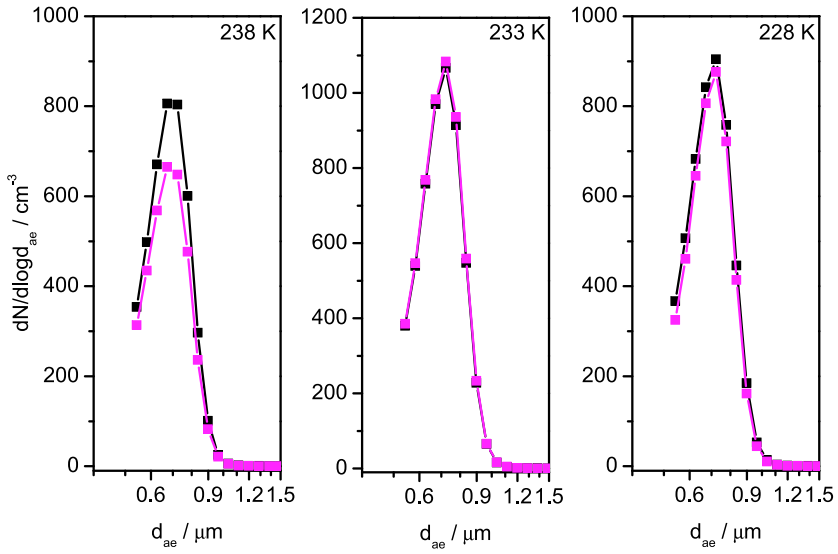

Figure 7. APS size distribution measurements of the unprocessed (black squares) and the freeze-dried (magenta squares) populations of α-pinene SOA particles during the freeze-drying experiments conducted at 238, 233, and 228 K.

particles were still highly viscous at 243 K in an almost ice-saturated environment (corresponding to about 70% RH_w), because the OPC records only indicated a minor structural rearrangement of the freeze-dried particles over a timescale of 1 h. We can use the OPC data for a rough estimate of the viscosity of the α-pinene SOA particles under these conditions, following an approach that relates the relaxation time of coalescing amorphous particles to their viscosity [*Pajunoja et al.*, 2014]. Quantitatively, the decrease in the OPC count rate of the SOA particles immediately after freeze drying was only recovered by about 5% within of an observation period of 1 h at 243 K and 70% RH_w. Assuming that this translates into a total relaxation time of 20 h for the full recovery of the OPC count rate, and approximating the porous SOA particles as aggregates with a primary particle size of 100 nm and a surface tension of 35 mN m^{-1} [*Pajunoja et al.*, 2014], the estimated viscosity would be in the range of 10^{10} Pa s. Accordingly, the particles' phase state would fall into the highly viscous, semisolid regime [*Koop et al.*, 2011]. A recent temperature-dependent parameterization of the viscosities of α-pinene SOA even predicted the transition into the solid state with a viscosity of 10^{12} Pa s at 243 K and 70% RH_w [*Wang et al.*, 2015]. Based on these data, we conclude that the unprocessed α-pinene SOA particles, which were probed on their ice nucleation ability at even lower temperatures in the cirrus regime (Figure 3), were initially also in the highly viscous, semisolid or even glassy solid state before the expansion cooling cycles were started.

4.2. Freeze-Drying Experiments at Cirrus Temperatures

An immediate question is whether the dominant morphological change of the α-pinene SOA particles after freeze drying at 243 K is also evident when the freeze-drying experiments are performed at cirrus temperatures. This would be a hint at the underlying ice nucleation mechanism, as it would indicate whether liquefaction of the aerosol particles has occurred during humidification or not. The AIDA data from one freeze-drying experiment that started at 233 K are already displayed in Figure 2 (right). In obvious contrast to the respective experiment at 243 K (Figure 4), there is no reduction of the number concentration of aerosol particles counted by the OPCs after the freeze-drying step. The same behavior was observed at starting temperatures below 233 K. Only for freeze-drying experiments that started at 238 K, the dilution-corrected count rate of the OPCs was lowered by a small factor of 1.2 compared to the unprocessed α-pinene SOA particles. This factor, however, is much smaller than the factor of 20 observed during the corresponding experiment that started at 243 K. Obviously, there is much less structural change during the trajectories in the cirrus regime compared to a simulated convective-cloud system where the SOA particles are processed at warmer temperatures. Also, the APS measurements substantiate this conclusion. Similar to Figure 6 (right), Figure 7 shows the dilution-corrected number size distributions of the SOA particles as a function of the aerodynamic diameter from before (black squares) and after the freeze-drying experiments (magenta squares)

Journal of Geophysical Research: Atmospheres 10.1002/2016JD026401

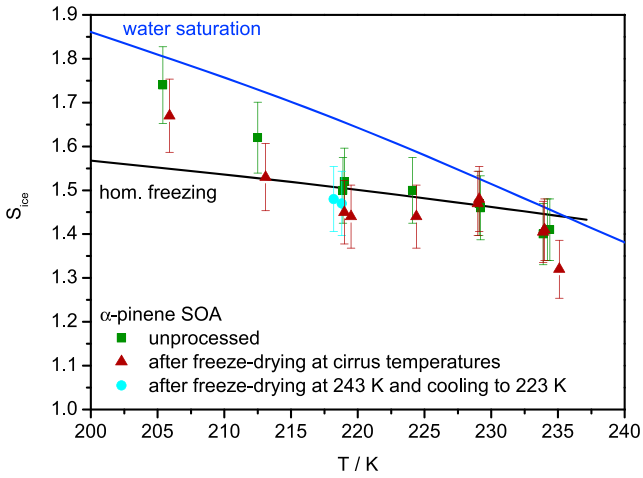

Figure 8. Comparison of the ice nucleation onsets for unprocessed and freeze-dried α-pinene SOA particles at cirrus temperatures. See text for details.

that started at 238, 233, and 228 K. Only for the experiment that started at 238 K, there is a slight reduction of the number concentration measured with the APS after freeze drying, which is due to a decrease of the aerodynamic diameter of the ice cloud processed SOA particles.

These observations can now be linked to the tentative assignment of the temperature-dependent ice nucleation mechanism of the α-pinene SOA particles detailed in section 3. For the experiment that started at 238 K, we assumed that ice has nucleated homogeneously. At least a small degree of structural change of the SOA particles could be indirectly evidenced from the observation of the freeze-dried particles having a slightly reduced count rate in the OPC and APS records at this temperature in comparison with the unprocessed particles. Most likely, the particles adopted a core-shell morphology at the freezing onset, with the solid core being inefficient in triggering ice formation by immersion freezing before the homogeneous freezing threshold of the liquefied outer layer was reached. The formation of porous material by vitrification and ice sublimation was then restricted to the particles' outer layer and could not lead to the formation of such highly porous particles as displayed in Figure 4, which explains the less pronounced changes in the OPC and APS measurements after freeze drying at 238 K. The sharp nucleation onset observed for the experiment that started at 233 K (Figure 3) was also interpreted as a homogeneous nucleation mode. If true, homogeneous freezing would be limited to a very thin liquefied layer because there was no indication for a morphological change of the particles upon freeze drying at this temperature. Following this interpretation, the onset of the homogeneous freezing mode should likely be delayed when the starting temperature of the expansion cooling cycle is further decreased. This reasoning is in good agreement with the more gradually evolving ice nucleation modes observed at starting temperatures of 228 and 223 K (Figure 3), which were already tentatively assigned as delayed homogeneous freezing modes.

The remaining question is how the ice nucleation ability of the SOA particles that were freeze dried at cirrus temperatures changes with respect to that of the unprocessed particles. Figure 8 again shows the onset conditions for ice nucleation of 0.1% of the unprocessed α-pinene SOA particles as the dark green squares and compares them to the respective S_{ice} thresholds after the particle ensembles were subjected to freeze-drying cycles at cirrus temperatures as described in section 2.4 (brown triangles). For starting temperatures of 228 K and below, there is a systematic, albeit small decrease in the onset S_{ice} value of the freeze dried compared to the unprocessed α-pinene SOA particles. As we do not expect a substantial change of the overall particle morphology during freeze drying at these temperatures, the small preactivation ability can be attributed to a memory effect of ice from the preceding nucleation event on the glassy material. The slightly reduced ice nucleation onsets observed for precooled α-pinene SOA particles by *Ladino et al.* [2014] could therefore also be due to preactivation in their cooling flow tube setup. For most experiments at starting temperatures above 228 K, we did not observe any change in the particles' ice nucleation ability after freeze drying. This indicates that the memory effect on the glassy material is small, meaning that at warmer temperatures preactivation cannot compete with the liquefaction of the outer particle layers during humidification and homogeneous freezing is also the dominant ice nucleation mechanism after freeze drying. There was only one exception to this general behavior, where we observed a small heterogeneous ice nucleation mode after freeze drying at 238 K. Ice formation initiated at S_{ice} = 1.32 but involved less than 1% of the overall particle population. In two other freeze-drying experiments conducted at 238 K, we did not observe this early preactivation mode and also the freeze-dried α-pinene SOA particles nucleated ice homogeneously. The temperature of 238 K is just the threshold where the APS and OPC measurements still indicate

Journal of Geophysical Research: Atmospheres 10.1002/2016JD026401

a small morphological change of the SOA particles during freeze drying. This could explain why the ice nucleation behavior of the freeze-dried SOA particles is more complex and variable at 238 K than at colder temperatures.

Figure 8 also includes the ice nucleation onsets for two experiments where the freeze-drying cycle was conducted at 243 K, and the highly porous α-pinene SOA particles were then cooled to 223 K to probe their ice nucleation ability in the cirrus regime (cyan circles). The freezing onsets remain almost unchanged compared to the compact, unprocessed SOA particles, indicating that the larger surface area of the porous particles alone does not make them better INPs. This substantiates the interpretation that the CCN-induced ice growth mode of the porous particles at warmer temperatures is induced by ice pockets that are enclosed in the glassy matrix. Such ice pockets can be released and trigger ice formation upon liquefaction at warm temperatures but will remain completely shielded and do not enhance the particles' ice nucleation ability during expansion cooling experiments at colder temperatures. We want to emphasize that this interpretation is only valid provided that the SOA particles probed at 223 K have conserved their highly porous morphology from the freeze-drying cycle performed at 243 K. Due to the cooling of the AIDA chamber from 243 to 223 K, there was a time delay of about 6 h between the freeze-drying cycle at 243 K and the succeeding expansion cooling run at 223 K, during which the OPC measurements detected a small structural change of the freeze-dried α-pinene SOA particles. The fraction of aerosol particles detected by the OPCs, which had dropped from 5 to 0.25% immediately after the freeze-drying step at 243 K, increased to 0.6% during cooling to 223 K. In an ideal experiment, as, e.g., feasible by the joint operation of the AIDA chamber with a continuous flow diffusion chamber (see section 5), highly porous aerosol particles could be generated in AIDA at 243 K and immediately probed for their ice nucleation ability at cirrus temperatures by the CFDC chamber.

5. Conclusions and Outlook

Our results suggest that monoterpene SOA particles are of minor importance for heterogeneous ice nucleation in the cirrus cloud regime of the upper troposphere. Although we assigned the ice nucleation mode that is dominant at temperatures below 218 K to deposition nucleation, its efficiency is very low in view of the high values for the ice saturation ratio which are needed to initiate ice formation ($S_{ice} > 1.6$). Other abundant INPs like mineral dust require much lower values for S_{ice} to trigger heterogeneous ice formation at these temperatures [*Hoose and Möhler*, 2012]. For example, two types of mineral dust particles from the Takla Makan desert in Asia and the Sahara with median diameters between 0.35 and 0.40 μm showed ice-active fractions in the deposition nucleation mode of at least 25% at $T < 223$ K and $S_{ice} < 1.35$ in previous AIDA measurements [*Möhler et al.*, 2006]. For the present SOA ice nucleation experiments, we estimate to be sensitive to an ice-active fraction of 0.01%, when assuming a detection limit of 0.1 cm^{-3} for the ice particle number concentration in combination with a seed aerosol number concentration of around 1000 cm^{-3}. This means that a very small fraction of the SOA particles could have nucleated ice at lower ice saturation ratios, but we would have been unable to detect this nucleation mode. The ratio of the ice-active fraction observed for mineral dust (25%) and the detection limit for the SOA particles (0.01%) yields a value of 2500, meaning that the number concentration of SOA particles must be higher by at least 3 orders of magnitude than that of the mineral dust particles to obtain a similar number concentration of nucleated ice crystals at lower ice saturation ratios. Aircraft-based single-particle mass spectrometer measurements of the aerosol composition for several altitude ranges indicated that the TTL region was enriched in organic material and depleted in mineral dust [*Froyd et al.*, 2009]. However, the number fraction of dust particles was only reduced by a factor of about 5 in the TTL region above 12 km compared to the convective region with altitudes from 4 to 12 km [*Froyd et al.*, 2009]. So we expect that the higher abundance of organic aerosol particles in the TTL region only compensates to a small extent for their much lower ice nucleation activity compared to mineral dust particles.

At temperatures above 218 K, we ascribed ice formation to homogeneous or delayed homogeneous freezing of the partly liquefied SOA particles and did not find any indication for an immersion freezing ability of a potentially still existing glassy particle core. Our experiments substantiate the conclusion that SOA compounds reveal a lower ability to act as INPs at cirrus temperatures compared to organic species belonging to the class of simple sugars/acids, part of which were also investigated using the AIDA cloud chamber and showed clearly lower S_{ice} thresholds to initiate ice formation compared to the α-pinene and limonene

Journal of Geophysical Research: Atmospheres 10.1002/2016JD026401

SOA particles [*Wilson et al*., 2012]. The current study also supports the observation from previous AIDA experiments that the heterogeneous ice nucleation efficiency of mineral dust particles is greatly reduced by a coating with SOA material [*Möhler et al*., 2008].

A particular pathway by which the SOA particles could be preactivated was atmospheric freeze drying and in particular freeze drying in a convective cloud system as first proposed by *Adler et al*. [2013]. This process could lead to the encapsulation of ice pockets in the revitrified glassy matrix. These ice pockets, however, seem to be completely shielded because we did not observe instant ice particle growth when the freeze-dried particles were again exposed to an ice-supersaturated environment. Heterogeneous ice formation only occurred after droplet activation via the so-called CCN-induced ice growth mode, which was observed up to a temperature of about 253 K in the mixed-phase cloud regime. These findings are again in contrast with repeated ice nucleation experiments conducted with organic species of the simple sugars/acids category, where ice cloud processing improved the particles' ice nucleation ability more significantly [*Wagner et al*., 2012].

The most important objective for future experiments is the systematic investigation of the dependence of the ice nucleation ability of the SOA particles on their chemical composition. One could select a fixed starting temperature for a series of AIDA expansion cooling experiments, as, e.g., 228 or 223 K which are just in the transition regime where ice nucleation was ascribed to delayed homogeneous freezing. With varying SOA formation conditions like temperature, relative humidity, or reactants (e.g., different types of monoterpenes and oxidants), SOA particles with different O/C ratios could be generated and probed for their ability to nucleate ice heterogeneously. Less viscous particles than those probed in the current study could provoke a more distinct, sharply defined homogeneous freezing mode at 228 or 223 K, whereas hardening of the glassy matrix could favor the particles' ability to nucleate ice via deposition nucleation. The implementation of low-temperature filter sampling for ESEM analyses as a new standard measurement technique could help to ascertain the proposed ice nucleation mechanisms, as it would yield direct proof of a potential morphological change of the particles during freeze drying.

Similarly important, one could conduct a series of ice nucleation experiments at a fixed starting temperature where SOA particles with the same O/C ratio are probed at varying humidification rates, which can be controlled by adjusting the pumping speed in the adiabatic expansion experiments. Different humidification rates or updraft velocities would alter the time that the SOA particles have to adjust to the increasing relative humidity, which in turn could influence the ice nucleation characteristics (sharply defined versus delayed homogeneous freezing). A series of such experiments would also deliver a robust data set which could be fitted by model calculations with a kinetic multilayer model, using the water diffusion coefficient of the SOA material as a tunable parameter [*Lienhard et al*., 2015].

Concerning the freeze-drying experiments, a major experimental step forward would be the joint operation of AIDA with a continuous flow diffusion chamber via a low-temperature connection line, in which the particles do not experience transient warm conditions and thereby preserve their morphology and preactivation ability. Freeze-dried SOA particles could so be routinely produced and maintained in the AIDA chamber and then systemically probed for their ice nucleation ability by the CFDC chamber over a wide range of temperatures.

Acknowledgments

We gratefully acknowledge the continuous support by all members of the Engineering and Infrastructure group of IMK-AAF, in particular by Olga Dombrowski, Rainer Buschbacher, Tomasz Chudy, Steffen Vogt, and Georg Scheurig. We also thank Volker Zibat at KIT LEM for his enthusiastic help with Cryo-ESEM. We thank Luis Ladino for providing the data shown in Figure 3. The work has been funded by the Helmholtz-Gemeinschaft Deutscher Forschungszentren as part of the program "Atmosphere and Climate," by the Deutsche Forschungsgemeinschaft (DFG) as part of the Ice Nuclei Research Unit INUIT (FOR 1525, project MO 668/4-2), by the European Research Council (ERC-StG-QAPPA, grant 335478), and by the Academy of Finland (grants 259005 and 272041). All data sets used in this manuscript are stored in the IMK-AAF data base and will be made available upon request to the authors.

References

Adler, G., T. Koop, C. Haspel, I. Taraniuk, T. Moise, I. Koren, R. H. Heiblum, and Y. Rudich (2013), Formation of highly porous aerosol particles by atmospheric freeze-drying in ice clouds, *Proc. Natl. Acad. Sci. U.S.A.*, *110*(51), 20414–20419.

Adler, G., C. Haspel, T. Moise, and Y. Rudich (2014), Optical extinction of highly porous aerosol following atmospheric freeze drying, *J. Geophys. Res. Atmos.*, *119*, 6768–6787, doi:10.1002/2013JD021314.

Baustian, K. J., M. E. Wise, and M. A. Tolbert (2010), Depositional ice nucleation on solid ammonium sulfate and glutaric acid particles, *Atmos. Chem. Phys.*, *10*(5), 2307–2317.

Baustian, K. J., M. E. Wise, E. J. Jensen, G. P. Schill, M. A. Freedman, and M. A. Tolbert (2013), State transformations and ice nucleation in amorphous (semi-)solid organic aerosol, *Atmos. Chem. Phys.*, *13*(11), 5615–5628.

Benz, S., K. Megahed, O. Möhler, H. Saathoff, R. Wagner, and U. Schurath (2005), T-dependent rate measurements of homogeneous ice nucleation in cloud droplets using a large atmospheric simulation chamber, *J. Photochem. Photobiol. A*, *176*(1–3), 208–217.

Berkemeier, T., M. Shiraiwa, U. Pöschl, and T. Koop (2014), Competition between water uptake and ice nucleation by glassy organic aerosol particles, *Atmos. Chem. Phys.*, *14*(22), 12513–12531.

Fahey, D. W., et al. (2014), The AquaVIT-1 intercomparison of atmospheric water vapor measurement techniques, *Atmos. Meas. Tech.*, *7*(9), 3177–3213.

Journal of Geophysical Research: Atmospheres 10.1002/2016JD026401

Froyd, K. D., D. M. Murphy, T. J. Sanford, D. S. Thomson, J. C. Wilson, L. Pfister, and L. Lait (2009), Aerosol composition of the tropical upper troposphere, *Atmos. Chem. Phys.*, *9*(13), 4363–4385.

Grayson, J. W., Y. Zhang, A. Mutzel, L. Renbaum-Wolff, O. Boge, S. Kamal, H. Herrmann, S. T. Martin, and A. K. Bertram (2016), Effect of varying experimental conditions on the viscosity of alpha-pinene derived secondary organic material, *Atmos. Chem. Phys.*, *16*(10), 6027–6040.

Haag, W., B. Kärcher, S. Schaefers, O. Stetzer, O. Möhler, U. Schurath, M. Krämer, and C. Schiller (2003), Numerical simulations of homogeneous freezing processes in the aerosol chamber AIDA, *Atmos. Chem. Phys.*, *3*(1), 195–210.

Hallquist, M., et al. (2009), The formation, properties and impact of secondary organic aerosol: Current and emerging issues, *Atmos. Chem. Phys.*, *9*(14), 5155–5236.

Hoose, C., and O. Möhler (2012), Heterogeneous ice nucleation on atmospheric aerosols: A review of results from laboratory experiments, *Atmos. Chem. Phys.*, *12*(20), 9817–9854.

Ignatius, K., et al. (2016), Heterogeneous ice nucleation of viscous secondary organic aerosol produced from ozonolysis of alpha-pinene, *Atmos. Chem. Phys.*, *16*(10), 6495–6509.

Järvinen, E., et al. (2016), Observation of viscosity transition in alpha-pinene secondary organic aerosol, *Atmos. Chem. Phys.*, *16*(7), 4423–4438.

Koop, T., B. P. Luo, A. Tsias, and T. Peter (2000), Water activity as the determinant for homogeneous ice nucleation in aqueous solutions, *Nature*, *406*, 611–614.

Koop, T., J. Bookhold, M. Shiraiwa, and U. Pöschl (2011), Glass transition and phase state of organic compounds: Dependency on molecular properties and implications for secondary organic aerosols in the atmosphere, *Phys. Chem. Chem. Phys.*, *13*(43), 19238–19255.

Ladino, L. A., S. Zhou, J. D. Yakobi-Hancock, D. Aljawhary, and J. P. D. Abbatt (2014), Factors controlling the ice nucleating abilities of alpha-pinene SOA particles, *J. Geophys. Res. Atmos.*, *119*, 9041–9051, doi:10.1002/2014JD021578.

Lienhard, D. M., et al. (2015), Viscous organic aerosol particles in the upper troposphere: Diffusivity-controlled water uptake and ice nucleation?, *Atmos. Chem. Phys.*, *15*(23), 13599–13613.

Lopez-Hilfiker, F. D., et al. (2014), A novel method for online analysis of gas and particle composition: Description and evaluation of a Filter Inlet for Gases and AEROsols (FIGAERO), *Atmos. Meas. Tech.*, *7*(4), 983–1001.

Mikhailov, E., S. Vlasenko, S. T. Martin, T. Koop, and U. Pöschl (2009), Amorphous and crystalline aerosol particles interacting with water vapor: Conceptual framework and experimental evidence for restructuring, phase transitions and kinetic limitations, *Atmos. Chem. Phys.*, *9*(24), 9491–9522.

Möhler, O., et al. (2003), Experimental investigation of homogeneous freezing of sulphuric acid particles in the aerosol chamber AIDA, *Atmos. Chem. Phys.*, *3*(1), 211–223.

Möhler, O., et al. (2006), Efficiency of the deposition mode ice nucleation on mineral dust particles, *Atmos. Chem. Phys.*, *6*(10), 3007–3021.

Möhler, O., S. Benz, H. Saathoff, M. Schnaiter, R. Wagner, J. Schneider, S. Walter, V. Ebert, and S. Wagner (2008), The effect of organic coating on the heterogeneous ice nucleation efficiency of mineral dust aerosols, *Environ. Res. Lett.*, *3*(2), 025007), doi:10.1088/1748-9326/3/2/025007.

Murphy, D. M., and T. Koop (2005), Review of the vapour pressures of ice and supercooled water for atmospheric applications, *Q. J. R. Meteorol. Soc.*, *131*(608), 1539–1565.

Murray, B. J., et al. (2010), Heterogeneous nucleation of ice particles on glassy aerosols under cirrus conditions, *Nat. Geosci.*, *3*(4), 233–237.

Pajunoja, A., J. Malila, L. Q. Hao, J. Joutsensaari, K. E. J. Lehtinen, and A. Virtanen (2014), Estimating the viscosity range of SOA particles based on their coalescence time, *Aerosol Sci. Technol.*, *48*(2), i–iv.

Pajunoja, A., et al. (2015), Adsorptive uptake of water by semisolid secondary organic aerosols, *Geophys. Res. Lett.*, *42*, 3063–3068, doi:10.1002/2015GL063142.

Prenni, A. J., M. D. Petters, A. Faulhaber, C. M. Carrico, P. J. Ziemann, S. M. Kreidenweis, and P. J. DeMott (2009), Heterogeneous ice nucleation measurements of secondary organic aerosol generated from ozonolysis of alkenes, *Geophys. Res. Lett.*, *36*, L06808, doi:10.1029/2008GL036957.

Price, H. C., et al. (2015), Water diffusion in atmospherically relevant alpha-pinene secondary organic material, *Chem. Sci.*, *6*(8), 4876–4883.

Pruppacher, H. R., and J. D. Klett (1997), *Microphysics of Clouds and Precipitation*, pp. 330–341, Kluwer Acad., Dordrecht, Sect. 9.2.3.5.

Saathoff, H., K. H. Naumann, O. Möhler, A. M. Jonsson, M. Hallquist, A. Kiendler-Scharr, T. F. Mentel, R. Tillmann, and U. Schurath (2009), Temperature dependence of yields of secondary organic aerosols from the ozonolysis of alpha-pinene and limonene, *Atmos. Chem. Phys.*, *9*(5), 1551–1577.

Schill, G. P., and M. A. Tolbert (2012), Depositional ice nucleation on monocarboxylic acids: Effect of the O:C ratio, *J. Phys. Chem. A*, *116*(25), 6817–6822.

Schill, G. P., and M. A. Tolbert (2013), Heterogeneous ice nucleation on phase-separated organic-sulfate particles: Effect of liquid vs. glassy coatings, *Atmos. Chem. Phys.*, *13*(9), 4681–4695.

Schill, G. P., D. O. De Haan, and M. A. Tolbert (2014), Heterogeneous ice nucleation on simulated secondary organic aerosol, *Environ. Sci. Technol.*, *48*(3), 1675–1682.

Shilling, J. E., T. J. Fortin, and M. A. Tolbert (2006), Depositional ice nucleation on crystalline organic and inorganic solids, *J. Geophys. Res.*, *111*, D12204, doi:10.1029/2005JD006664.

Vali, G., P. J. DeMott, O. Möhler, and T. F. Whale (2015), Technical note: A proposal for ice nucleation terminology, *Atmos. Chem. Phys.*, *15*(18), 10263–10270.

Virtanen, A., et al. (2010), An amorphous solid state of biogenic secondary organic aerosol particles, *Nature*, *467*(7317), 824–827.

Wagner, R., O. Möhler, H. Saathoff, M. Schnaiter, and T. Leisner (2010), High variability of the heterogeneous ice nucleation potential of oxalic acid dihydrate and sodium oxalate, *Atmos. Chem. Phys.*, *10*(16), 7617–7641.

Wagner, R., O. Möhler, H. Saathoff, M. Schnaiter, and T. Leisner (2011), New cloud chamber experiments on the heterogeneous ice nucleation ability of oxalic acid in the immersion mode, *Atmos. Chem. Phys.*, *11*(5), 2083–2110.

Wagner, R., O. Möhler, H. Saathoff, M. Schnaiter, J. Skrotzki, T. Leisner, T. W. Wilson, T. L. Malkin, and B. J. Murray (2012), Ice cloud processing of ultra-viscous/glassy aerosol particles leads to enhanced ice nucleation ability, *Atmos. Chem. Phys.*, *12*(18), 8589–8610.

Wagner, R., K. Höhler, O. Möhler, H. Saathoff, and M. Schnaiter (2015), Crystallization and immersion freezing ability of oxalic and succinic acid in multicomponent aqueous organic aerosol particles, *Geophys. Res. Lett.*, *42*, 2464–2472, doi:10.1002/2015GL063075.

Wang, B. B., A. T. Lambe, P. Massoli, T. B. Onasch, P. Davidovits, D. R. Worsnop, and D. A. Knopf (2012), The deposition ice nucleation and immersion freezing potential of amorphous secondary organic aerosol: Pathways for ice and mixed-phase cloud formation, *J. Geophys. Res.*, *117*, D16209, doi:10.1029/2012JD018063.

Wang, B. B., R. E. O'Brien, S. T. Kelly, J. E. Shilling, R. C. Moffet, M. K. Gilles, and A. Laskin (2015), Reactivity of liquid and semisolid secondary organic carbon with chloride and nitrate in atmospheric aerosols, *J. Phys. Chem. A*, *119*(19), 4498–4508.

Journal of Geophysical Research: Atmospheres 10.1002/2016JD026401

Wilson, T. W., et al. (2012), Glassy aerosols with a range of compositions nucleate ice heterogeneously at cirrus temperature, *Atmos. Chem. Phys.*, *12*(18), 8611–8632.

Zobrist, B., C. Marcolli, D. A. Pedernera, and T. Koop (2008), Do atmospheric aerosols form glasses?, *Atmos. Chem. Phys.*, *8*(17), 5221–5244.

Zobrist, B., et al. (2006), Oxalic acid as a heterogeneous ice nucleus in the upper troposphere and its indirect aerosol effect, *Atmos. Chem. Phys.*, *6*(10), 3115–3129.

B.2 An Extractive Electrospray Ionization Time-of-Flight Mass Spectrometer (EESI-TOF) for online measurement of atmospheric aerosol particles

Authors: Felipe D. Lopez-Hilfiker, Veronika Pospisilova, **Wei Huang**, Markus Kalberer, Claudia Mohr, Giulia Stefenelli, Joel A. Thornton, Urs Baltensperger, Andre S. H. Prevot, and Jay G. Slowik

In: Atmospheric Measurement Techniques Discussions, 1–40, 2019. DOI: 10.5194/amt-2019-45.

Authorship statement

This article is based on the chamber data from a five-week measurement campaign (PSI2016) performed in April and early May 2016 at Paul Scherrer Institute (PSI) in Switzerland, with a focus on the performance of a newly developed instrument, EESI-TOF, and the data comparison with FIGAERO-CIMS. I was responsible for the operation and calibrations of FIGAERO-CIMS, and participated in the FIGAERO-CIMS data analysis, data interpretation and discussion of this article. Currently this article is under review in *Atmospheric Measurement Techniques*.

Atmos. Meas. Tech. Discuss., https://doi.org/10.5194/amt-2019-45
Manuscript under review for journal Atmos. Meas. Tech.
Discussion started: 5 March 2019

Atmospheric Measurement Techniques Discussions

An Extractive Electrospray Ionization Time-of-Flight Mass Spectrometer (EESI-TOF) for online measurement of atmospheric aerosol particles.

Felipe D. Lopez-Hilfiker[1,a], Veronika Pospisilova[1], Wei Huang[2], Markus Kalberer[3,4], Claudia Mohr[5], Giulia Stefenelli[1], Joel A. Thornton[6], Urs Baltensperger[1], Andre S. H. Prevot[1], Jay G. Slowik[1]

[1]Laboratory of Atmospheric Chemistry, Paul Scherrer Institute (PSI), 5232 Villigen PSI, Switzerland

[2]Institute of Meteorology and Climate Research, Karlsruhe Institute of Technology, 76131 Karlsruhe, Germany

[3]Department of Chemistry, University of Cambridge, Cambridge CB2 1EW, United Kingdom

[4]Department of Environmental Sciences, University of Basel, 4056 Basel, Switzerland

[5]Department of Environmental Science and Analytical Chemistry, Stockholm University, 106 91 Stockholm, Sweden

[6]Department of Atmospheric Sciences, University of Washington, Seattle, WA 98195, Washington, USA

[a]*Now at*: Tofwerk AG, 3600 Thun, Switzerland

Correspondence to: Jay G. Slowik (jay.slowik@psi.ch)

Atmos. Meas. Tech. Discuss., https://doi.org/10.5194/amt-2019-45
Manuscript under review for journal Atmos. Meas. Tech.
Discussion started: 5 March 2019

Atmospheric Measurement Techniques Discussions

Abstract

Real-time, online measurements of atmospheric organic aerosol (OA) composition are an essential tool for determining the emissions sources and physicochemical processes governing aerosol effects on climate and health. However, the reliance of current techniques on thermal desorption, hard ionization, and/or separated collection/analysis stages introduces significant uncertainties into OA composition measurements, hindering progress towards these goals. To address this gap, we present a novel, field-deployable extractive electrospray ionization time-of-flight mass spectrometer (EESI-TOF), which provides online, near-molecular OA measurements at atmospherically relevant concentrations without analyte fragmentation or decomposition. Aerosol particles are continuously sampled into the EESI-TOF, where they intersect a spray of charged droplets generated by a conventional electrospray probe. Soluble components are extracted, and then ionized as the droplets are evaporated. The EESI-TOF achieves a linear response to mass, with detection limits on the order of 1 to 10 ng m^{-3} for typical atmospherically-relevant compounds. In contrast to conventional electrospray systems, the EESI-TOF response is not significantly affected by a changing OA matrix, while a slight decrease in sensitivity in response to increasing absolute humidity is observed for some ions. Although the relative sensitivities to a variety of commercially available organic standards vary by approximately a factor of 30, the bulk sensitivity to most SOA compounds varies by only a factor of 6. Further, the ratio of compound-by-compound sensitivities between the EESI-TOF and an iodide adduct FIGAERO-CIMS vary by only ±50%, suggesting that EESI-TOF mass spectra indeed reflect the actual distribution of detectable compounds in the particle phase. Successful deployments of the EESI-TOF for laboratory environmental chamber measurements, ground-based ambient sampling, and proof-of-concept measurements aboard a research aircraft highlight the versatility and potential of the EESI-TOF system.

Atmos. Meas. Tech. Discuss., https://doi.org/10.5194/amt-2019-45
Manuscript under review for journal Atmos. Meas. Tech.
Discussion started: 5 March 2019

Atmospheric Measurement Techniques Discussions

1. Introduction

Aerosol particles adversely affect respiratory and cardiovascular systems, scatter and absorb radiation, influence cloud formation processes and properties, provide surfaces for heterogeneous reactions, and affect trace gas concentrations by providing an adsorptive medium for semi-volatile gases. As a result, aerosols have a significant effect on public health, climate, and overall atmospheric reactivity. Of particular importance are aerosol particles smaller than 1 μm in diameter, a significant and ubiquitous fraction of which is secondary organic aerosol (SOA) formed from atmospheric reactions of organic gases (Hallquist et al., 2009; Jimenez et al., 2009). The sources, aging, and chemical properties of SOA remain highly uncertain, and these uncertainties can lead to large errors between modeled and measured aerosol loadings (Volkamer et al., 2006). These errors limit our ability to predict future changes in aerosol particle composition and concentration under a warming climate and to link SOA to its atmospheric emission sources. To develop adequate model parameterizations of organic aerosol (OA) and its formation, growth, and loss, there remains a need to improve source apportionment capabilities and to identify chemical mechanisms governing the conversion and partitioning of organic compounds between gas and particle phase. Measurements of specific chemical tracers on timescales similar to the typical variability in emissions, photochemical activity, and meteorology, approximately minutes to hours, would improve source apportionment, mechanistic studies, and characterization of bulk molecular properties such as the distribution of average oxidation state across carbon number (Kroll et al., 2011) against mechanistic photochemical models.

The chemical complexity of OA makes highly time-resolved, chemically-specific measurements extremely challenging. OA consists of thousands of individual components, many of which are present at only trace amounts (Goldstein and Galbally, 2007). Most organic aerosol chemical speciation to date has come from offline analysis of filter samples. Offline samplers typically concentrate particles on a filter or impactor for 2-24 hours, after which particles are extracted or thermally desorbed for offline chemical analysis. The main disadvantages of offline techniques are their low time resolution, which is much slower than many atmospheric processes, and the potential for chemical changes due to evaporation, adsorption, and/or reaction during sample collection, transfer, and/or storage. The extraction process is also time consuming and can introduce additional artifacts into the measurements (e.g. decomposition during derivatization or hydrolysis in aqueous solutions). A recent study addresses the issue of low time resolution and

Atmos. Meas. Tech. Discuss., https://doi.org/10.5194/amt-2019-45
Manuscript under review for journal Atmos. Meas. Tech.
Discussion started: 5 March 2019

Atmospheric Measurement Techniques Discussions

reaction on the collection substrate by collecting samples at 5 min time resolution using a particle-into-liquid sampler (PILS) coupled to collection vials on a rotating carousel, followed by offline ultra-performance liquid chromatography/electrospray ionization quadrupole time-of-flight mass spectrometry (UPLC/ESI-Q-TOFMS) analysis (Zhang et al., 2015; Zhang et al., 2016). This approach yielded time-resolved molecular speciation for water-soluble components, but remains subject to sample transfer and storage artifacts.

Traditional techniques for rapid online measurements of OA without sample handling rely on the combination of mass spectrometry with thermal desorption. Most single particle instruments, e.g. ATOFMS (Gard et al., 1997), SPLAT (Zelenyuk and Imre, 2005), and PALMS (Murphy et al., 2006), utilize simultaneous laser desorption/ionization, which is not quantitative due to matrix effects and can also result in fragmentation of organic molecules. In contrast, the Aerodyne aerosol mass spectrometer (AMS) utilizes a high vaporization temperature (600 C) and electron ionization (EI, 70 eV) to remain quantitative, but at the cost of extensive thermal decomposition and ionization-induced fragmentation (Canagaratna et al., 2007). More recently, the CHARON-PTR couples an aerodynamic particle lens with a heated inlet and a softer ionization scheme (via proton transfer reaction) for measurements of particles between 100 and 750 nm (Eichler et al., 2015). This provides improved chemical speciation for some atmospherically-relevant compounds; e.g. oleic acid and 5α-cholestane (Müller et al., 2017). However, proton transfer is too energetic for studies of the oxygenated compounds characteristic of SOA; for example, only ~10% of *cis*-pinonic acid is detected as the parent ion $[M]H^+$, with the rest distributed across several fragments. Extensive fragmentation in the CHARON-PTR also occurs for oxygenated primary compounds such as levoglucosan limiting its usefulness in mechanistic studies. Another recent development, the AeroFAPA-MS (aerosol flowing atmospheric-pressure afterglow mass spectrometer) (Brüggemann et al., 2015; Brüggemann et al., 2017) couples thermal vaporization with ionization by the outflow of a low-temperature plasma. The AeroFAPA-MS has detection limits suitable for ambient aerosol measurements and when detecting ions in negative mode is subject to significantly less fragmentation than is PTR, but due to the variety of ions produced in the plasma is subject to various competing ionization pathways, complicating spectral interpretation and quantitative analysis.

The need for molecular-level information (without ionization-induced fragmentation) led to the development of a number of semi-continuous online measurements that follow a general two-step

Atmos. Meas. Tech. Discuss., https://doi.org/10.5194/amt-2019-45
Manuscript under review for journal Atmos. Meas. Tech.
Discussion started: 5 March 2019

Atmospheric Measurement Techniques Discussions

collection and analysis procedure. Aerosol is typically collected for 10-60 minutes either by impaction or on a filter, then thermally desorbed for gas chromatography with prior online derivatization (Isaacman et al., 2014), proton transfer reaction mass spectrometry (PTR-MS) (Holzinger et al., 2010), or chemical ionization mass spectrometry (CIMS) (Lopez-Hilfiker et al., 2014). These techniques offer significantly improved chemical resolution relative to online systems, but remain subject to thermal decomposition during desorption (though to a lesser degree than the AMS), as well as reaction or partitioning effects on the collection substrate. In some systems which feature a temperature ramp, thermal decomposition products can be identified as such, although links to the parent molecules are unclear (Lopez-Hilfiker et al., 2015). Further, there remain fundamental limits to the detection of highly oxidized compounds, as well accretion products for which there is currently no satisfactory online detection technique. Finally, the time delay between aerosol collection and detection can compromise detection of fast intra-particle reactions (Pospisilova et al., submitted). Therefore, there remains a need for fast, online aerosol analysis without decomposition or fragmentation.

Electrospray ionization (ESI) is a well-known method for transferring low volatility, high molecular weight molecules (e.g. proteins and peptides) into gas phase ions without the need for direct heating. ESI has been successfully coupled to mass spectrometry for offline analysis of atmospheric aerosol both by direct infusion of aerosol extracts (Reemstsma et al., 2006; Zhang et al., 2011) and surface sampling techniques (Laskin et al., 2010; Roach et al., 2010). Extractive electrospray ionization (EESI) is a technique that couples the advantages of ESI with online continuous measurement (Chen et al., 2006). In extractive electrospray ionization, a solvent is delivered through a conventional electrospray probe generating a plume of charged electrospray droplets. The primary spray is directed into a sample flow of gases and/or aerosol whereby the collision between aerosol and electrospray droplets results in the extraction of the soluble components into the bulk electrospray droplet. During the rapid evaporation of the solvent from the electrospray droplets, surface charge is concentrated and ions are ejected into the gas phase, presumably by the Coulomb explosion mechanism (Kebarle and Peschke, 2000). These ions are then sampled directly into a mass spectrometer for analysis.

There have been several previous attempts to apply extractive electrospray ionization to atmospheric gas and particle studies. However, the detection limits achieved by these techniques are one or more orders of magnitude too high to be useful in the atmosphere or for laboratory

Atmos. Meas. Tech. Discuss., https://doi.org/10.5194/amt-2019-45
Manuscript under review for journal Atmos. Meas. Tech.
Discussion started: 5 March 2019

Atmospheric Measurement Techniques Discussions

experiments at atmospherically-relevant concentrations (i.e. ~1-10 μg/m^3). Doezema et al. (2012) identified a limited number of compounds in α-pinene SOA at aerosol mass loadings of 1500-2500 μg m^{-3}. Ambient ESI, a conceptually similar technique to EESI, detected particle-phase organic compounds, including some oligomers, at 26 μg m^{-3} of SOA from α-pinene ozonolysis, although instabilities in the mass analyzer precluded quantitative analysis (Horan et al., 2012). A more recent EESI system (Gallimore and Kalberer, 2013; Gallimore et al., 2017) attained individual compound detection limits of ~1 μg m^{-3}, which were further reduced to as low as 0.25 μg m^{-3} using tandem mass spectrometry (MS^2) and collisionally-induced dissociation (CID). While a significant improvement compared to previous work, these detection limits remain insufficient for most atmospheric systems, where even the most abundant compounds in OA are typically present in concentrations of 10-100 ng m^{-3}. However, EESI was shown to be linear over several orders of magnitude, independent of particle size or morphology up to 200 nm, and reproducible, highlighting its potential benefits for atmospheric OA analysis with soft ionization and without thermal desorption.

Here we present the development and characterization of a novel EESI interface coupled to a portable high-resolution time-of-flight mass spectrometer (EESI-TOF). Our design, while conceptually similar to previous EESI work, provides detection limits as low as 1 ng m^{-3} at 1 Hz through a combination of source optimization and efficient ion transfer into and through the mass spectrometer. We present comprehensive characterization of the source, including sensitivity, linearity, time response, as well as water vapor and matrix sampling effects. We also present proof of concept measurements from the reaction of α-pinene and ozone in a laboratory flow tube, ambient measurements in Zurich, Switzerland, and airborne wildfire measurements in the central United States.

2. Instrument Description

In brief, the EESI-TOF system consists of a custom built EESI inlet and ionization source coupled to a commercially available mass spectrometer (APi-TOF, Tofwerk, Thun, Switzerland). In addition to the physical inlet design, selection of working fluid and ionization scheme are critical for optimal EESI-TOF operation.

2.1.EESI design

Atmos. Meas. Tech. Discuss., https://doi.org/10.5194/amt-2019-45
Manuscript under review for journal Atmos. Meas. Tech.
Discussion started: 5 March 2019

Atmospheric Measurement Techniques Discussions

The EESI source was developed with the specific goal to measure OA at a near-molecular level, however it can more generally be applied to gas or combined gas/particle measurements. Figure 1 shows a schematic of the main components of the EESI. For particle measurements, the instrument automatically alternates between direct sampling and sampling through a Teflon filter with a 1 µm pore size (Fig. 1, orange). The difference between the direct and filter blank measurements is the background-corrected particle-phase signal. Particles and gases enter the EESI source through a 6 mm inner diameter (ID) 5 cm long multi-channel extruded carbon denuder (Fig. 1, black). At this flow rate, the denuder removes most gas phase species with high efficiency (e.g. pinonic acid > 99.6%). The denuder is housed in a stainless steel tube that can be biased relative to the entrance of the mass spectrometer, but is typically set to ground. The denuder improves instrument detection limits by reducing the gas-phase background. In addition, it removes from the particle flow any sticky gases that may be lost to the filter and otherwise misclassified as particulate material.

After the sample passes through the denuder, particles collide with the primary electrospray droplets in a laminar sample flow and the soluble components are extracted. The electrospray is generated by a commercially available 360 µm OD untreated fused silica capillary with an inner diameter of 50 µm (BGB Analytik AG, Boeckten, Germany), with no further treatment. The ESI probe is positioned approximately 1 cm away from the mass spectrometer inlet. A high voltage liquid junction and electrospray fluid reservoir (80 mL) is used to deliver the solvent to the ESI capillary. We find that fluid flow rates between 0.1-10.0 µL/min leads to the formation of a stable primary spray without requiring a sheath gas. Initially, the ESI working fluid was delivered using a commercially available syringe pump (KD Scientific, Holliston, MA, USA) via a 250 µL syringe. However, a combination of unstable fluid delivery rates (pulsed flow) and limited run time (i.e. several hours) led to the replacement of the syringe pump with a high precision pressure regulator for fluid flow (MFCS-EZ 1000 mbar, Fluigent, Inc., Lowell, MA, USA) coupled to a large liquid reservoir. This system allows continuous solvent delivery for months at a time and ensures ultra-stable fluid flow rates.

The droplet-laden flow enters the mass spectrometer through a heated stainless steel capillary to evaporate excess electrospray solvent and facilitate efficient ion formation (Figure 1, blue). The inlet flow rate is between 0.7 and 1.0 L min^{-1} and determined by the capillary temperature. We use a commercially available stainless steel capillary (0.5 mm inner diameter (ID), 1/16” OD 70 mm long; VICI AG International, Schenkon, Switzerland), which is housed in a conical capillary heater

Atmos. Meas. Tech. Discuss., https://doi.org/10.5194/amt-2019-45
Manuscript under review for journal Atmos. Meas. Tech.
Discussion started: 5 March 2019

Atmospheric Measurement Techniques Discussions

manifold fabricated from aluminum. A tight fit between the heating manifold and capillary helps to ensure uniform heating and efficient heat-transfer to the capillary from the heater block controlled by two cartridge heaters. The capillary manifold is operated at ~250 °C to ensure that electrospray droplets evaporate during the ~1 ms transit through the capillary tube. Note that the combined effects of gas expansion, solvent evaporation, capillary temperature, finite heat transfer, and short residence time results in a sample gas of significantly lower absolute temperature than the 250 °C heater would suggest. The spray probe and assembly is coupled to the mass spectrometer via a PTFE manifold (Fig. 1, green), which thermally isolates the sample flow from the heated capillary manifold (Fig. 1, blue). An aluminum heat sink plate compresses the EESI mounting manifold to the sample cone of the capillary inlet and draws heat away from the sample flow using a small fan. In this way, the sample flow remains unheated until after extraction into the ESI droplets, minimizing volatilization of labile particle phase components and thermal decomposition.

Evaporation of the charged droplets yields ions via the Coulomb explosion mechanism. These ions are analyzed by a portable high-resolution time of flight mass spectrometer with an atmospheric pressure interface (APi-TOF, Tofwerk, Thun, Switzerland), which has been described in detail previously (Junninen et al., 2010) but modified with a heated capillary inlet. We find that maximum ion transmission is achieved by maximizing the flow rate into the mass spectrometer, which for our pumping configuration is nominally 1 L min^{-1}.

2.2. Extraction and ionization

Conceptually, the EESI solution consists of two components: (1) a working fluid for aerosol extraction and spray formation and (2) a dopant for control of ionization pathways. Note that changing one or both of these components alters the set of detectable compounds, increasing the versatility of the EESI-TOF system. In this initial study, we focus on efficient, stable detection of a broad range of organic compounds, with an emphasis on oxygenated SOA. The working fluid and ionization dopant were optimized for the detection of a-pinene ozonolysis products.

Regardless of working fluid, the electrospray solution is doped with 100 ppm NaI to promote ionization by sodium ion attachment (Na^+), and suppress alternative pathways such as proton transfer ($[M]H^+$), formation of adducts with other ions (e.g. Li^+ or K^+), charge transfer, and proton

Atmos. Meas. Tech. Discuss., https://doi.org/10.5194/amt-2019-45
Manuscript under review for journal Atmos. Meas. Tech.
Discussion started: 5 March 2019

Atmospheric Measurement Techniques Discussions

abstraction ($[M-H]^-$). Positive ion detection is therefore employed. In principle, any compound may be added to the ESI working fluid to control the ionization process, provided that the ion-adduct binding energies are sufficiently strong to survive droplet evaporation. (For example, detection of I^- adducts in negative mode has so far been unsuccessful, as the $[M]I^-$ adducts dissociate into [M] and I^-, presumably during transit through the heated capillary). However, we find that Na^+ ions generate strong enough molecular adducts with a wide range of organic molecules present in atmospheric aerosol, including sugars, acids, alcohols, organic nitrates, and highly oxidized multifunctional molecules. In principle, Li^+ likely provides stronger adducts and may thus facilitate quantification and improve detection of weakly bound species (Zhao et al., 2017). However, Na^+ also has the advantage of only a single peak (no isotopes), which simplifies peak identification and reduces spectral clutter. The detected molecular classes include nearly all compounds present in secondary organic aerosol, with the important exception of organosulfates, which are typically detected as negative ions in electrospray-based studies (Surratt et al., 2008). This ionization scheme is also not sensitive to non-oxygenated compounds such as alkanes, alkenes, and aromatic hydrocarbons. The detectable species are observed exclusively as adducts with Na^+. Indeed, the only molecule in ambient or laboratory aerosol that we have identified as ionizing without Na^+ attachment is nicotine, where the ionization instead proceeds via net proton transfer, yielding $[M]H^+$ (Stefenelli et al., in preparation; Qi et al., submitted). It may be that other reduced nitrogen species follow a similar pathway.

Additional benefits of the Na^+ dopant include provision of (1) an internal measure of spray stability and (2) reference ions for *m/z* calibration. For the former, we typically monitor the $[NaI]Na^+$ ion (*m/z* 172.883), as for some experiments it is desirable to set the quadrupole guides to block transmission from low *m/z* ions (including Na^+ and working fluid-related signals) to increase detector lifetime. For *m/z* calibration, we utilize a series of $[(NaI)_n]Na^+$ clusters, which are well-spaced across the entire *m/z* of interest for ambient aerosol and also have a strong negative mass defect, reducing interferences with organic analytes.

For the ESI working fluid, mixtures of acetonitrile (ACN) (HPLC grade, ≥99.9% purity, Sigma-Aldrich, St. Louis, USA) and methanol (MeOH) (UHPLC-MS LiChrosolv, ≥99.9% purity, Sigma-Aldrich, St. Louis, USA) in a variable ratio with ultrapure water (19.2 MΩ cm, total-organic carbon < 5 ppb) were selected for testing; all solutions included the 100 ppm NaI dopant. The solvent blend was optimized with the goals of (1) maximizing the overall OA detection (extraction

Atmos. Meas. Tech. Discuss., https://doi.org/10.5194/amt-2019-45
Manuscript under review for journal Atmos. Meas. Tech.
Discussion started: 5 March 2019

Atmospheric Measurement Techniques Discussions

+ ionization) efficiency and (2) generating a spray that is stable over long timescales. We tested a 1:1 MeOH:H_2O mixture and compared this to ACN:H_2O mixtures, as these are the two most common electrospray solvents used in traditional analysis (HPLC and direct infusion ESI) and should have a high overall extraction efficiency of OA. Both solvent blends formed stable electrospray as determined by the stability of detected ion currents over long timescales (days to weeks) and gave similar sensitivities for products from a-pinene SOA.

We found that the MeOH:H_2O spray produces significant background peaks throughout the spectrum, presumably due to impurities, which are efficiently ionized by the primary electrospray probe. These background signals increase detection limits and complicate interpretation of blank subtraction during the EESI process. Significant effort to ensure the cleanliness of the primary solution is therefore of critical importance for maintaining low detection limits. We found that using a mixture of ACN:H_2O for the primary spray generation reduced these backgrounds by approximately an order of magnitude, leading to a net decrease in detection limits. This reduction could simply be due to a more pure acetonitrile solvent compared to methanol. We observe that the effective binding energy of the acetonitrile adduct with sodium [$(ACN)_n$]Na^+) is significantly stronger than that of methanol. Irrespective of solvent purity, we expect this stronger binding energy to yield a somewhat cleaner spectrum by suppressing subsequent ionization processes. In our test system (α-pinene SOA), we observe the ACN:H_2O working fluid can yield clusters of analyte molecules with acetonitrile (i.e., [M(ACN)]Na^+), with abundances on the order of 10% of the parent ion ([M]Na^+). This effect remains to be characterized in other chemical systems. Note that the cluster abundance depends on the electric fields in the interface and capillary temperature, both of which can be adjusted. Increasing either will decrease the cluster abundance, however at some point the additional energy required to decluster solvent from the organic adducts will reach the binding energy of the organic sodium adducts, thereby reducing overall sensitivity. Note that the sensitivity vs. declustering tradeoff does not affect all species equally and is of greatest importance for the most weakly bound adducts. Herein we present results using mostly the MeOH:H_2O spray, unless otherwise explicitly noted.

Preliminary investigations using an H_2O-only working fluid (with NaI dopant). This working fluid is of interest because it yields backgrounds even lower than those of the ACN:H_2O mixture. However, in our preliminary tests the primary ion count for H_2O is also lower by a factor of ~20 relative to ACN:H_2O. Further, unlike the MeOH:H_2O and ACN:H_2O sprays, sampling of ~30 to

Atmos. Meas. Tech. Discuss., https://doi.org/10.5194/amt-2019-45
Manuscript under review for journal Atmos. Meas. Tech.
Discussion started: 5 March 2019

Atmospheric Measurement Techniques Discussions

35 µg m^{-3} of aerosol from re-nebulized ambient filter extracts resulted in a 10 to 15% decrease in the primary ion signal from the H_2O spray, increasing the possibility of ion suppression artifacts or other non-linear behavior. Therefore, while the H_2O spray may be of interest for background-limited applications, it cannot be assumed to perform similarly to the MeOH:H_2O and ACN:H_2O sprays, and detailed characterization is needed.

3. Performance and characterization

The EESI-TOF performance was assessed using a variety of single components and atmospherically relevant multi-component aerosol. We focus on assessing sensitivity and detection limits, linearity of response to aerosol mass, and the effects of changes in the OA matrix or water vapor concentrations on EESI-TOF performance.

3.1. Test aerosol generation and basic operation

To characterize and optimize EESI-TOF performance we used both single-component aerosol generated by a conventional nebulizer system as well as multi-component aerosol produced from the reaction of α-pinene and O_3 in a flowtube, the configuration of which is described in detail elsewhere (Molteni et al., 2018). The α-pinene is delivered by a diffusion vial from a pure liquid at room temperature into a carrier gas flow of 1-10 L min^{-1} of zero air at the entrance of the flow tube. O_3 (0.25-5 ppmv) is produced from a commercially available ozone generator and is mixed into the main flow at the flowtube entrance. This leads to the prompt formation of SOA during the (~1-5 min) residence time in the flow tube. While SOA generated under such conditions is likely not entirely representative of real atmospheric conditions, it contains a suite of highly oxygenated organic monomers, dimers, and higher-order oligomers and therefore provides a useful test aerosol matrix beyond what can be interrogated using a single compound. In this way, we are able to provide a more comprehensive characterization of instrument performance.

Figure 2 shows a sample time series of $[C_{10}H_{16}O_8]Na^+$ measured in SOA generated from α-pinene ozonolysis, with an expanded view shown in the lower panel. Over this measurement period, maximum SOA concentrations reach approximately 30 µg m^{-3}. Here the EESI-TOF alternates between 3 min of direct sampling and a 30 s filter blank, denoted by red circles. The background concentration measured during the filter blank is a small fraction of the total signal and is stable over time, typical of our experience for laboratory and atmospheric concentrations of up to at least

Atmos. Meas. Tech. Discuss., https://doi.org/10.5194/amt-2019-45
Manuscript under review for journal Atmos. Meas. Tech.
Discussion started: 5 March 2019

Atmospheric Measurement Techniques Discussions

100 μg m^{-3}. The system rapidly responds to filter actuation, with the signal equilibrating on the order of 5 s. Interposing the filter into the sampled flow causes a small pressure drop, which may slightly perturb the spray; deviations in the $[NaI]Na^+$ signal of up to 2% are typical.

Fundamentally, the EESI-TOF measurement is in terms of the ion flux reaching the detector (Hz), as shown on the left axis of Fig. 2. However, the particle phase is typically described in terms of mass for both absolute and relative concentrations. In principle, the EESI-TOF ion signal for a molecule *x* can be converted to a mass concentration according to Eq. (1):

$$Mass_x = I_x \left(\frac{MW_x}{EE_x * CE_x * IE_x * TE_{m/z}} \right) * \frac{1}{F} \quad (1)$$

Here $Mass_x$ denotes the ambient mass concentration of molecule *x*, I_x is the measured ion flux, *F* is the inlet flowrate (0.7 to 1.0 L min^{-1}, depending on inlet capillary temperature), and MW_x is the molecular weight of *x*. Note that MW_x does not generally correspond to the *m/z* at which *x* is measured, which is typically an Na^+ adduct of *x*. The remaining terms address the probability that a molecule exposed to the electrospray is detected as an ion. The probability that a molecule dissolves in the spray is defined as the extraction efficiency (EE_x). The probability that the analyte-laden droplet enters the inlet capillary is defined as the collection efficiency (CE_x). Ions are generated as the droplets evaporate; the probability that an ion forms and survives declustering forces induced by evaporation and electric fields is defined as ionization efficiency (IE_x). Finally, the probability that a generated ion is transmitted to the detector is defined as transmission efficiency ($TE_{m/z}$) and is independent of chemical identity, depending only on *m/z*. We cannot at present distinguish between effects of the four efficiency terms, and so define their product as an empirically-determined compound-dependent response factor (RF_x), such that:

$$Mass_x = I_x * \frac{MW_x}{RF_x} * \frac{1}{F} \quad (2)$$

The RF_x parameter denotes the total number of ions detected per molecule incident to the spray (i.e. probability that a sampled molecule is detected). In the absence of fragmentation or decomposition, which has not been observed for any system presented herein, RF_x may be equivalently treated in terms of mass. At present, RF_x has been measured only for a few compounds, and we do not have a reliable parameterization for the many unknowns sampled in laboratory and atmospheric aerosol. Nevertheless, we can arrive at a closer approximation of sampled mass by applying MW_x to calculate the mass flux of *x* to the detector (MF_x):

Atmos. Meas. Tech. Discuss., https://doi.org/10.5194/amt-2019-45
Manuscript under review for journal Atmos. Meas. Tech.
Discussion started: 5 March 2019

Atmospheric Measurement Techniques Discussions

$$MF_x = I_x * MW_x \quad (3)$$

The quantity MF_x is used herein for assessment of bulk properties (e.g. comparison of total EESI-TOF signal to external mass measurements and investigation of relative composition). For reference, we show on the right axis of Fig. 3 the MF_x (in attograms (10^{-18} g) per second, ag s^{-1}) corresponding to the measured I_x; however for the remainder of the basic characterization experiments presented herein we show instead the directly measured I_x.

3.2. Linearity and sensitivity

To assess EESI-TOF linearity, single-component aerosols were nebulized and sampled simultaneously by the EESI-TOF and a scanning mobility particle sizer (model 3080 differential mobility analyzer and model 3022 condensation particle counter, TSI, Inc., Shoreview, MN, USA). Figure 3 shows the background-subtracted EESI-TOF signal as a function of calibrant mass for two model compounds: raffinose ($C_{18}H_{32}O_{16}$, a surrogate for α-pinene dimers) and dipentaeryrithritol ($C_{10}H_{22}O_7$, a surrogate for isoprene accretion products). Concentrations vary from approximately 1 to 1000 ng m^{-3}, thereby covering an atmospherically relevant range of concentrations for single components. In both cases, the molecular species is detected exclusively as adducts of the original molecule with Na^+, and both compounds exhibit a linear response to mass in agreement with previous work (Gallimore and Kalberer, 2013). Critically, individual component concentrations of only 10 ng m^{-3} are readily detectable by the EESI-TOF. Detection limits based on 3-σ variation of adjacent filter blank measurements (i.e. the instrument and spray background) are on the order of a few ng m^{-3}. These detection limits improve on the most sensitive previously reported EESI-based aerosol systems by approximately 2 orders of magnitude (or 2-3 orders of magnitude for non-MS^2 systems) (Doezema et al., 2012; Horan et al., 2012; Gallimore and Kalberer, 2013) and are sufficient to allow for the first time the detection of OA components in real atmospheric aerosol.

The different slopes observed between raffinose and dipentaerythritol (4.49 vs. 108 Hz / μg m^{-3}) correspond to response factors of RF_{raff} = 1.88 x 10^{-8} ions $molec^{-1}$ and RF_{dpe} = 2.93 x 10^{-7} ions $molec^{-1}$, assuming spherical particles with the material density of the pure component. This implies significant differences in the relative sensitivity of the EESI-TOF to different compounds, although as shown later in Fig. 4 dipentaerythritol is an extreme case. Differences are in RF_x expected,

Atmos. Meas. Tech. Discuss., https://doi.org/10.5194/amt-2019-45
Manuscript under review for journal Atmos. Meas. Tech.
Discussion started: 5 March 2019

Atmospheric Measurement Techniques Discussions

however, and may arise from thermodynamic and/or kinetic limitations on extraction efficiency, as well as ion-adduct binding energies. (In principle, ion suppression, matrix effects, and multiple ionization pathways can also affect sensitivity, though as discussed above and in the next section we do not believe that these issues significantly affect the EESI-TOF). In Fig. 4, we compare the RF_x of a suite of saccharides, polyols, and carboxylic acids, as well as bulk SOA generated by reaction of precursor VOCs with OH radicals in a potential aerosol mass (PAM) flow reactor (Lambe et al., 2011). Because the absolute sensitivity of the EESI-TOF depends on instrument setup (spray optimization, mass spectrometer tuning, etc.), we define a relative response factor (RRF_x), using sucrose as a reference:

$$RRF_x = \frac{RF_x}{RF_{sucrose}} \quad (4)$$

Sucrose is chosen as a reference due to its ease of use (i.e. low volatility and high water solubility) and because it is the standard which we have measured most frequently. The pure component RF_x are calculated from SMPS distributions assuming spherical particles with the material density of the pure component, while the SOA RF_x are calculated from the total organic mass of a co-located AMS. Figure 4 primarily shows RF_x determined with the MeOH:H_2O system, although a few ACN:H_2O measurements are included as well.

Several features are evident from Fig. 4. There is a strong decrease in saccharide sensitivity with increasing molecular weight, with the sensitivity of glucose (6 carbons) being nearly 10 times greater than that of glycogen (24 carbons). The relative sensitivities of carboxylic acids and polyols each also span approximately an order of magnitude, although for these classes a clear molecular weight dependence is not observed. The measured polyols also appear to have somewhat higher sensitivities than the other molecular classes, although this feature should be interpreted with caution due to the small number of compounds tested.

The measured SOA mostly follows a trend of decreasing sensitivity with decreasing molecular weight of the precursors, although the high sensitivity of 1,3,5-trimethylbenzene makes it a slight outlier. Calculation of these sensitivities requires the assumption of SOA molecular weights, which were estimated from the EESI-TOF mass spectrum to be 181 g mol^{-1} (benzene), 173 g mol^{-1} (phenol), 195 g mol^{-1} (toluene), 209 g mol^{-1} (naphthalene), 199 g mol^{-1} (α-pinene), and 220 g mol^{-1} (1,3,5-trimethylbenzene). Neglecting benzene (which is an outlier), the RRF_x observed for the SOAs span a much smaller range than do the pure components (i.e. factor 6 between phenol and

Atmos. Meas. Tech. Discuss., https://doi.org/10.5194/amt-2019-45
Manuscript under review for journal Atmos. Meas. Tech.
Discussion started: 5 March 2019

Atmospheric Measurement Techniques Discussions

1,3,5-trimethylbenzene compared to a factor of ~30 between citric acid and dipentaerythritol). The smaller RRF_x range exhibited by the SOA experiments is more consistent with ambient observations, where we do not observe major composition-dependent variations in overall EESI-TOF sensitivity to bulk ambient OA (Stefenelli et al., in preparation; Qi et al., submitted). However, direct calibration is clearly advisable for compounds for which absolute quantification is desired.

The SOA species shown in Fig. 4 are comprised of many individual compounds, and it is highly desirable to constrain their relative concentrations and thus RRF_x. However, direct calibration of every compound is not feasible due to the large number of species present; in addition, many SOA compounds are not commercially available and cannot be readily synthesized. Therefore, to better understand the relative sensitivities of the individual ions, we utilize as a reference the well-characterized FIGAERO-I-CIMS (filter inlet for gases and aerosols, coupled to iodide chemical ionization mass spectrometry) (Lopez-Hilfiker et al., 2014). The FIGAERO collects particles for 30 min, after which a 45 min thermal desorption program is applied and the resulting organic vapor is detected by I-CIMS. Reaction rates in the FIGAERO-I-CIMS are collision-limited, which in conjunction with ion-adduct binding energies and operational characterization of the declustering potential within the ion transfer optics allows estimation of the sensitivity of the instrument to compounds for which standards do not exist. A direct compound-to-compound comparison between the EESI-TOF and FIGAERO-I-CIMS thus allows us to assess how RRF_x obtained by the EESI-TOF compare to an ionization/detection scheme that can be well-described theoretically in terms of fundamental principles (Iyer et al., 2016; Lopez-Hilfiker et al., 2016).

As a test aerosol, we again select SOA from α-pinene ozonolysis, for which many of the product compounds are detected at or near the collision limit by the FIGAERO-I-CIMS. Figure 5a shows EESI-TOF signals as a function of the FIGAERO-I-CIMS for selected ions, specifically the $[C_9H_{14}O_x]Na^+$ (red) and $[C_{10}H_{16}O_x]Na^+$ (blue) series. Although this comparison is shown on a logarithmic scale due to the range of signal intensities recorded, strong linear correlations are observed for every ion. Moreover, a single line can reasonably describe the EESI-TOF vs. FIGAERO-I-CIMS correlation, regardless of ion identity. This is further highlighted in Fig. 5b, where the slopes of every ion from the comparison in Fig. 5a are shown; the spread of slopes describes the range of relative sensitivities in the EESI-TOF relative to the FIGAERO-I-CIMS. The mean slope is 0.51, with a standard deviation of 0.11, indicating that the instrument-to-

Atmos. Meas. Tech. Discuss., https://doi.org/10.5194/amt-2019-45
Manuscript under review for journal Atmos. Meas. Tech.
Discussion started: 5 March 2019

Atmospheric Measurement Techniques Discussions

instrument sensitivity typically varies by only ±20%, and all ions are within ±40% of the mean. Also of note is a slight reduction in the relative sensitivity of the EESI-TOF to the FIGAERO-I-CIMS for the smaller $[C_9H_{14}O_x]Na^+$ series (0.45 ± 0.09) compared to $[C_{10}H_{16}O_x]Na^+$ (0.57 ± 0.08); however, additional measurements are needed to validate this trend. In all, the strong correlation of the EESI-TOF with the collision-limited FIGAERO-I-CIMS suggests that the FIGAERO-I-CIMS strategy of drawing on a fundamental limit to parameterize sensitivity to unknown compounds may likewise be applicable to the EESI-TOF. Further, the correlation indicates that the spectral patterns observed in the EESI-TOF likely reflect to a large degree the actual distribution of compounds in the particle phase.

3.3. Matrix effects

Matrix effects and ion suppression processes are common in direct infusion electrospray sources, introducing non-linear responses to analyte concentration and impeding quantification efforts. We therefore characterized EESI-TOF sensitivity to a test compound (dipentaerythritol) in the presence of a complex and variable particle-phase organic matrix produced from α-pinene ozonolysis, used again here as a surrogate for the multi-component aerosol particles present in the atmosphere. Dipentaerythritol was chosen as a reference because it does not evaporate during transit through the flow tube, is relatively unreactive, and has a chemical formula ($C_{10}H_{22}O_7$) not found in α-pinene ozonolysis products (maximum of 18 hydrogens for a C_{10} molecule). A constant concentration of pure dipentaerythritol particles was introduced into the flow tube, and coated with SOA formed from α-pinene ozonolysis, generated as described above. Coating thickness was controlled by varying the O_3 concentration. The initial dipentaerythritol particles are approximately 20 nm in diameter and increase to ~70 nm by coating with α-pinene SOA, corresponding to approximately 75 μg m^{-3} of SOA. At these high SOA concentrations, the α-pinene ozonolysis reaction produces sufficient concentrations of low-volatility organics to induce nucleation, which competes with the dipentaerythritol test particles as a surface for condensing SOA. At the maximum SOA concentration, approximately 40% of the mass corresponds to coated dipentaerythritol, and 60% to nucleated α-pinene SOA.

A change in the measured concentration of dipentaerythritol in response to the SOA coating would indicate a matrix-dependent instrument response. Figure 6 shows the measured dipentaerythritol

Atmos. Meas. Tech. Discuss., https://doi.org/10.5194/amt-2019-45
Manuscript under review for journal Atmos. Meas. Tech.
Discussion started: 5 March 2019

Atmospheric Measurement Techniques Discussions

signal ($[C_{10}H_{22}O_7]Na^+$) as a function of $[C_{10}H_{16}O_7]Na^+$, a major ion in α-pinene SOA that is approximately proportional to the total SOA mass. Measurements are colored by time. Even at the thickest coatings, the dependentaerythritol signal is unaffected, indicating that particle-phase matrix effects do not significantly affect the measurement.

3.4. Water vapor dependence

Atmospheric water vapor concentrations are high in absolute terms and highly variable, and as a result affect the response of instruments based on chemical ionization (Vlasenko et al., 2010; Lee et al., 2014; Iyer et al., 2016; Zhao et al., 2017). We therefore investigated the water vapor-dependent response of the α-pinene ozonolysis SOA mass spectrum. For these tests, SOA was generated at constant concentration in a flow tube and programmatically diluted by a dry and a wet flow. The wet flow was humidified by passing through a water bubbler held at room temperature (~25 C). The total dilution was kept constant, but the ratio of the wet and dry flows was systematically varied to obtain relative humidities ranging from 0 to 80% Water vapor has a significant memory effect in the denuder used in the EESI-TOF for removing semi-volatile gases from the sample flow, therefore despite step changes in the dilution relative humidity the water vapor seen by the instrument changes much more smoothly. As a surrogate for water vapor concentration, we monitor a sodium iodide adduct generated in the spray and determine the ratio of its water-clustered and water-free forms, i.e. $[NaI(H_2O)]Na^+$ / $[NaI]Na^+$. Note that the particulate water content is insignificant compared to the ESI droplets and thus does not perturb either the $[NaI(H_2O)]Na^+$ / $[NaI]Na^+$ ratio or the EESI-TOF sensitivity.

The left axis of Fig. 7a (black dots) shows an example of the $[C_{10}H_{16}O_7]Na^+$ ion as a function of the $NaI(H_2O)Na^+$ / $NaINa^+$ ratio. For this ion, the instrument response is constant independent of water vapor concentration, i.e. the ratio of the ion signal (I) at a given RH to the ion signal at 0% RH ($I/I_{RH=0}$) is ~1. On the right axis (red line and shading), we show the median, 10th, and 90th percentiles for $I/I_{RH=0}$ across all detected ions as a function of $[NaI(H_2O)]Na^+$ / $[NaI]Na^+$; $I/I_{RH=0}$ = 1 is shown as a dashed green line for reference. Probability distributions of $I/I_{RH=0}$ at $[NaI(H_2O)]Na^+$ / $[NaI]Na^+$ = 0.1, 0.5, and 0.9 (with the latter condition corresponding to ~80% RH) are shown in Fig. 7b. As water vapor increases, the $I/I_{RH=0}$ distribution broadens, and the median signal decreases slightly (~15% lower at 80% RH). Note that the broadening takes place

Atmos. Meas. Tech. Discuss., https://doi.org/10.5194/amt-2019-45
Manuscript under review for journal Atmos. Meas. Tech.
Discussion started: 5 March 2019

Atmospheric Measurement Techniques Discussions

on the low-sensitivity side of the $I/I_{RH=0}$ distribution; Fig. 7b shows that many ions have a humidity-independent response, similar to $[C_{10}H_{16}O_7]Na^+$. Even for ions with the most extreme humidity dependence, at the highest water vapor concentrations measured for 90% of ions $I/I_{RH=0} > 0.60$ and for 99% $I/I_{RH=0} > 0.45$. This weak perturbation by ambient water vapor simplifies spectral interpretation, and suggests that ion chemistry occurs predominantly in the droplet phase.

3.5. Effect of particle size

Particle size can in theory affect detection in the EESI-TOF system via two mechanisms. First, particle losses may occur within the denuder by diffusion or impaction, affecting small and large particles, respectively. Second, larger particles may be incompletely extracted in the spray. These two possibilities are investigated separately. Figure 8a shows the denuder transmission efficiency as a function of particle size, as measured by a scanning mobility particle sizer (SMPS). For this test, the denuder is removed from the EESI inlet and placed within a segment of straight tubing. SMPS measurements before and after the denuder are compared to determine transmission efficiency. The figure shows that particles are transmitted with better than 80% efficiency over the measured size range of 20 to 750 nm.

The size dependent response of the EESI extraction/ionization processes was characterized using pure dipentaerythritol particles nebulized from an aqueous solution. The polydisperse particles were dried and quantified using an SMPS system that sampled in parallel with the EESI-TOF. The size of the nebulized particles was controlled by changing the nebulizer flowrate and solution concentration. Figure 8b shows the measured sensitivity of the EESI-TOF to dipentaerythritol ($C_{10}H_{22}O_7$) as a function of the (polydisperse) particle volume distribution geometric mean diameter, which ranges between approximately 50 and 250 nm. The same sensitivity is measured independent of particle diameter, indicating complete extraction into the droplet phase and a lack of any size-dependent ionization due to solvation kinetics or incomplete extraction. Previous investigations of this effect in EESI-based aerosol systems have yielded conflicting results; our results are consistent with those of Gallimore and Kalberer (Gallimore and Kalberer, 2013), who observed no size dependence for single component OA particles with diameters ≤200 nm. For ambient aerosol, we observe a linear relationship with mass for particles of up to ~500 nm diameter (with larger sizes not yet investigated) for both methanol:water and acetonitrile:water working

Atmos. Meas. Tech. Discuss., https://doi.org/10.5194/amt-2019-45
Manuscript under review for journal Atmos. Meas. Tech.
Discussion started: 5 March 2019

Atmospheric Measurement Techniques Discussions

fluids (Stefenelli et al., in preparation; Qi et al., submitted). In contrast, Kumbhani et al. (Kumbhani et al., 2018) observed incomplete extraction of $NaNO_3$ particles coated with glutaric acid, also using 1:1 methanol:water as the working fluid. One possibility is that the characteristics of the generated electrospray are significantly different in the EESI-TOF, e.g. larger droplet diameter (the inner diameter of the EESI-TOF electrospray capillary is 5 times larger), increased droplet number density, and/or longer droplet/analyte contact time.

We expect that the electrospray droplets are significantly larger than the sampled aerosol (Wortmann et al., 2007). In principle, as particles grow to larger diameters the aerosol particle diameter could begin to approach the diameter of the electrospray droplets. In such a limit, the extraction process would become less efficient, as particles may bounce or incompletely dissolve in the electrospray droplet plume (Wang et al., 2012). The electrospray liquid flow rate controls the electrospray droplet size distribution; therefore it is important to ensure that the flow rate is sufficiently high to keep the electrospray droplet diameter much larger than the particles to be analyzed. Low electrospray flow rates increase instrument sensitivity by up to a factor of two (a similar trend is frequently observed for conventional ESI), but decrease response time and can introduce a size-dependent extraction efficiency at larger particle sizes. We hypothesize that these effects are due to slower flushing of the electrospray tip and surrounding areas, as well as a shift of the primary electrospray droplets towards a smaller size distribution, affecting charge density. In addition, we performed some preliminary experiments during the development of the EESI-TOF using drawn electrospray tips to generate the primary EESI droplets. Although drawn tips are known to be very efficient at generating ions in conventional electrospray sources, we found that with 15-30 μm drawn capillary tips (New Objective, Inc., Woburn, MA, USA) aerosol extraction was not efficient despite higher total primary spray ion currents, presumably due to the electrospray droplet size distribution being much smaller than our standard electrospray capillary.

4. Proof of concept measurements and applications

To assess the versatility and robustness of the EESI-TOF, proof-of-concept measurements were conducted across several laboratory and field-based platforms. Here we present sample results from the measurement of SOA generated from α-pinene ozonolysis in an environmental chamber, ground-based ambient measurements, and a proof-of-concept deployment aboard a research

Atmos. Meas. Tech. Discuss., https://doi.org/10.5194/amt-2019-45
Manuscript under review for journal Atmos. Meas. Tech.
Discussion started: 5 March 2019

Atmospheric Measurement Techniques Discussions

aircraft. The EESI-TOF performed successfully in each of these environments, demonstrating its potential for a wide range of measurement applications.

4.1. Laboratory chambers

Dark ozonolysis of α-pinene was investigated using the 27 m^3 PSI environmental chamber (Paulsen et al., 2005). Briefly, the chamber was filled with 40 to 50 ppb of ozone at 40 % RH, after which 30 ppb of α-pinene was injected and the ensuing reaction proceeded undisturbed under dark conditions for approximately 16 hours. The EESI-TOF monitored the composition of SOA particles with 1 s time resolution. A detailed analysis of the chemical composition and evolution of SOA from the α-pinene ozonolysis system as determined by the EESI-TOF is provided elsewhere, and only proof-of-concept sample data is shown here (Pospisilova et al., submitted). The time series of the summed signal of all $[C_xH_yO_z]Na^+$ ions recorded by the EESI-TOF and the measured SMPS mass are shown in Fig. 9a, with these two values compared as a scatterplot in Fig. 9b. A strong linear correlation between the EESI-TOF and SMPS signal is observed throughout the experiment.

Figures 9c and 9d show an averaged EESI-TOF mass spectrum collected from the period of maximum suspended aerosol mass. The raw (background-subtracted) spectrum is shown in Fig. 9c. To aid the eye, $[(NaI)_n]Na^+$ clusters are removed; the background-subtracted of $[(NaI)_n]Na^+$ is close to zero, but as the difference of two high-intensity signals remains large relative to most ions in the mass spectrum. Distinct regions are clearly visible for monomers, dimers, and higher-order oligomeric species. The dimer region is shown (on a linear axis) in the inset. Figure 9d summarizes the chemical composition in terms of a mass defect plot (difference between ion exact mass and the nearest integer, as a function of integer mass) for ions having between 7 and 10 carbons. The ions are colored by carbon number and the points are sized by the signal intensity. This highlights the detailed chemical information provided by the EESI-TOF, as well providing an example of the compositional trends running throughout the spectrum.

4.2. Ambient ground-based measurements

The EESI-TOF was deployed at an urban site in Zurich, Switzerland for approximately 3 weeks during summer 2016. Stable operation was achieved for >85% of the sampling period. The EESI-TOF mass spectral time series were used to identify sources and processes governing OA in Zurich,

Atmos. Meas. Tech. Discuss., https://doi.org/10.5194/amt-2019-45
Manuscript under review for journal Atmos. Meas. Tech.
Discussion started: 5 March 2019

Atmospheric Measurement Techniques Discussions

both by direct inspection of chemical signatures and using the positive matrix factorization source apportionment technique (Stefenelli et al., in preparation). Figure 10 shows the EESI-TOF mass spectrum averaged over the entire campaign, colored to highlight specific ions and families. In dark blue, we show again the set of the $[C_{7\text{-}10}H_xO_y]Na^+$ ions observed in α-pinene SOA in the PSI environmental chamber (see Fig. 9d). These ions are among the strongest contributors to the ambient OA signal during this campaign. These ions are not necessarily unique to α-pinene ozonolysis, as many can also be generated as reaction products of other terpenes and/or different oxidants (e.g. OH, NO_3 radicals). A subset of these ions may also derive from ring-opening oxidation products of aromatics. However, in a general sense, they highlight the strong contribution of biogenic emissions to summer OA in Zurich, consistent with previous studies (Daellenbach et al., 2017).

Several other species of note are highlighted in Fig. 10. The single most intense peak in the spectrum ($[C_6H_{10}O_5]Na^+$, *m/z* 185.042) is attributed to levoglucosan and its isomers. The high intensity occurs because of the significant contribution of levoglucosan to OA from biomass combustion, as well as the high sensitivity of the EESI-TOF to small saccharides (see Fig. 4). Another high intensity ion is attributed to nicotine ($[C_{10}H_{14}N_2]H^+$, *m/z* 163.123), which as a reduced nitrogen species ionizes by hydrogen abstraction rather than Na^+ adduct formation. This introduces considerable uncertainty into both the sensitivity and linearity of the EESI-TOF response to nicotine. However, the AMS nicotine tracer $C_5H_{10}N^+$ (Struckmeier et al., 2016) exhibits a strong linear correlation with the EESI-TOF nicotine measurement, suggesting that no significant non-linearities are present under the conditions encountered in Zurich (Qi et al., submitted). Finally, the spectrum shows a significant contribution from $[C_xH_yO_zN_{1\text{-}2}]Na^+$ ions, which are mostly assigned to organonitrates as discussed in detail elsewhere (Stefenelli et al., in preparation).

4.3. Aircraft deployment

Mobile sampling platforms, such as aircraft and ground vehicles, require highly time-resolved measurements. As discussed above, current OA measurements used in mobile measurements require a tradeoff between extensive thermal decomposition (AMS), ionization-induced fragmentation (AMS, CHARON-PTRMS), or time resolution (FIGAERO-CIMS). The EESI-TOF

Atmos. Meas. Tech. Discuss., https://doi.org/10.5194/amt-2019-45
Manuscript under review for journal Atmos. Meas. Tech.
Discussion started: 5 March 2019

Atmospheric Measurement Techniques Discussions

thus addresses an important gap in mobile aerosol instrumentation. As a proof of concept, the EESI-TOF was deployed aboard the NOAA C-130 aircraft during the Airborne Research Instrumentation Testing Opportunity (ARISTO) 2016 test flight campaign from August 1 to 19, 2016. For these flights, the EESI inlet was installed on an API-TOF previously configured for research flights by the University of Washington (Lee et al., 2018) and operated on a pressure-controlled sampling line. In general, good performance and stability were achieved. The main difficulty encountered was icing on the sampling inlet outside the aircraft, which reduced the line pressure and flow and thereby altered the ESI spray.

Figure 11a shows a time series of $[C_6H_{10}O_5]Na^+$, which corresponds to levoglucosan and its isomers. Also shown are $[C_{10}H_{16}O_4]Na^+$ and $[C_{10}H_{16}O_5]Na^+$, which are major products of SOA formed from monoterpene oxidation. EESI-TOF data were collected at 1 Hz; each point in the figure corresponds to a 20 s re-average. At approximately 17:35, the aircraft intersects a wildfire plume. A dramatic increase in $[C_6H_{10}O_5]Na^+$ is observed, compared to only minor changes in the $[C_{10}H_{16}O_x]Na^+$ ions. The high time resolution of the EESI-TOF is critical for accurate characterization of this plume, as the entire period of intersection lasts only ~3 min. Figure 11b shows a 20 s average mass spectrum, corresponding to the period of maximum $[C_6H_{10}O_5]Na^+$ concentration. The spectrum is normalized to levoglucosan, which is the most intense peak. However, even for such a short averaging interval, many other ions are evident throughout the mass spectrum, indicating the wealth of chemical information accessible even for highly time-resolved and/or mobile measurements.

5. Conclusions

We present an extractive electrospray ionization (EESI) source coupled to TOF-MS for laboratory and field measurement of OA on a near-molecular level. The EESI-TOF achieves detection limits compatible with operation at ambient aerosol concentrations, making it the first instrument capable of real-world OA measurements without thermal decomposition, ionization-induced fragmentation, competitive ionization pathways, or separated collection/analysis stages. We observe an instrument response that is linear with mass and without a detectable dependence on the composition of the OA matrix. Changing water vapor concentrations only slightly affect the instrument response to most ions, with a ~50% decrease in sensitivity observed for the most

Atmos. Meas. Tech. Discuss., https://doi.org/10.5194/amt-2019-45
Manuscript under review for journal Atmos. Meas. Tech.
Discussion started: 5 March 2019

Atmospheric Measurement Techniques Discussions

extreme cases. Particle transmission to the EESI source is greater than 80% between 20 and 750 nm, with particles of at least 250 nm (and likely 500 nm) completely extracted in the spray (larger particles remain to be tested). The EESI-TOF was successfully deployed for environmental chamber experiments, ground-based ambient sampling, and tests flights aboard a research aircraft, highlighting its versatility and range of potential applications.

The EESI-TOF sensitivity to SOA generated from a range of individual precursor gases varies within a factor of 6 for most precursors. Larger variations in sensitivity were found between pure organic standards. However, compound-by-compound sensitivities in laboratory-generated SOA are proportional to those determined by the collisionally-limited FIGAERO-I-CIMS within ±50%. This shows promise for an eventual parameterization of the EESI-TOF sensitivity to unknown species, and further suggests that the EESI-TOF responds in a similar way to collision-limited CIMS approaches and that the mass spectra thus approximately reflect the actual distribution of detectable compounds.

The working fluid and ionization scheme plays an important role in both instrument stability/performance and the set of detectable compounds. Here we have focused on positive ion detection using a 1:1 methanol:water system (with a subset of data using 1:1 acetonitrile:water), with 100 ppm NaI added to suppress all ionization pathways except for Na^+-adduct formation. This controlled ionization is highly desirable, and contributes to the system linearity, lack of matrix effects, and spectral interpretation. These Na^+-based systems allow detection of most compounds comprising atmospheric OA, with the notable exceptions of non-oxygenated species and organosulfates. However, different extraction/ionization schemes could be envisaged for different chemical targets, increasing the overall utility of the EESI-TOF.

Acknowledgements

This work was supported by the Swiss National Science Foundation (starting grant BSSGI0_155846). The ARISTO test flight program is funded by the U.S. National Science Foundation Deployment Pool. We thank Tofwerk AG and the PSI machine shop for supporting the construction and integration of the EESI source. We also thank David Bell, Deepika Bhattu, and Yandong Tong (PSI) for useful discussions on acetonitrile clustering, H_2O working fluid, and

Atmos. Meas. Tech. Discuss., https://doi.org/10.5194/amt-2019-45
Manuscript under review for journal Atmos. Meas. Tech.
Discussion started: 5 March 2019

Atmospheric Measurement Techniques Discussions

large particle detection. Rene Richter and Christoph Hueglin are gratefully acknowledged for logistical support of the Zurich deployment.

Atmos. Meas. Tech. Discuss., https://doi.org/10.5194/amt-2019-45
Manuscript under review for journal Atmos. Meas. Tech.
Discussion started: 5 March 2019

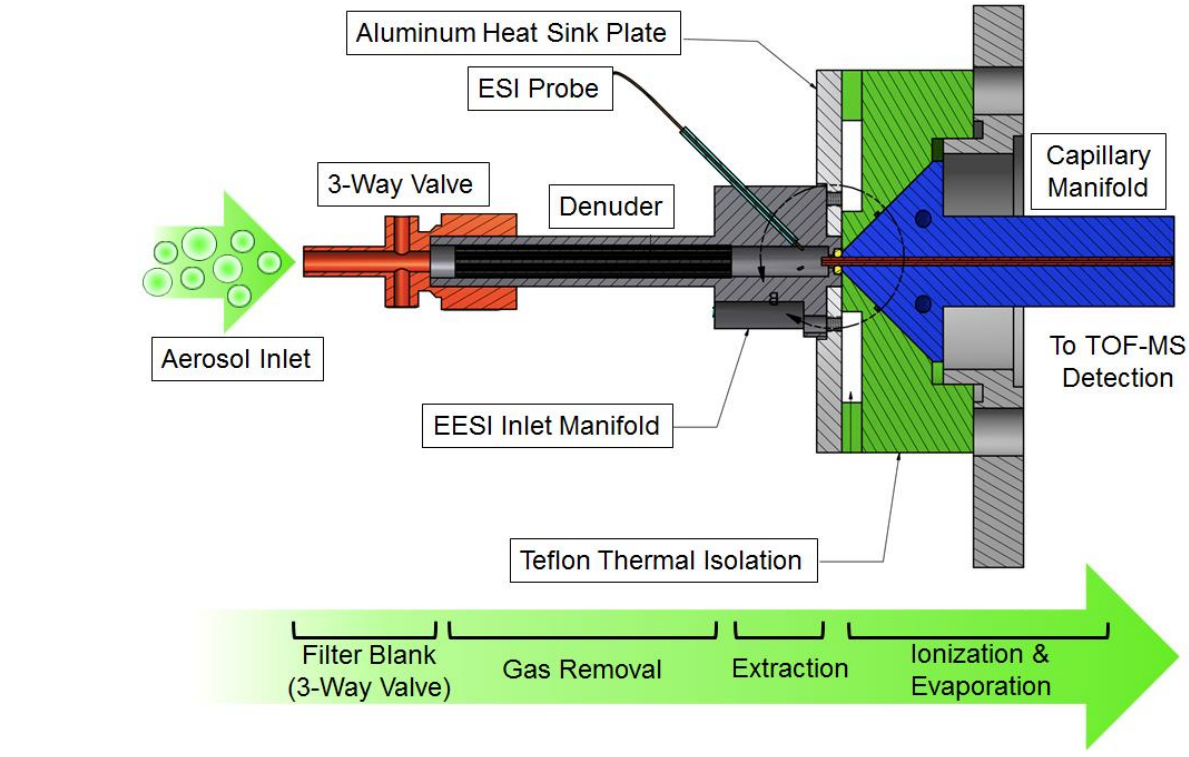

Figure 1. Schematic of the EESI-TOF inlet and ion source, including connection to TOF-MS.

Atmos. Meas. Tech. Discuss., https://doi.org/10.5194/amt-2019-45
Manuscript under review for journal Atmos. Meas. Tech.
Discussion started: 5 March 2019

Atmospheric Measurement Techniques Discussions

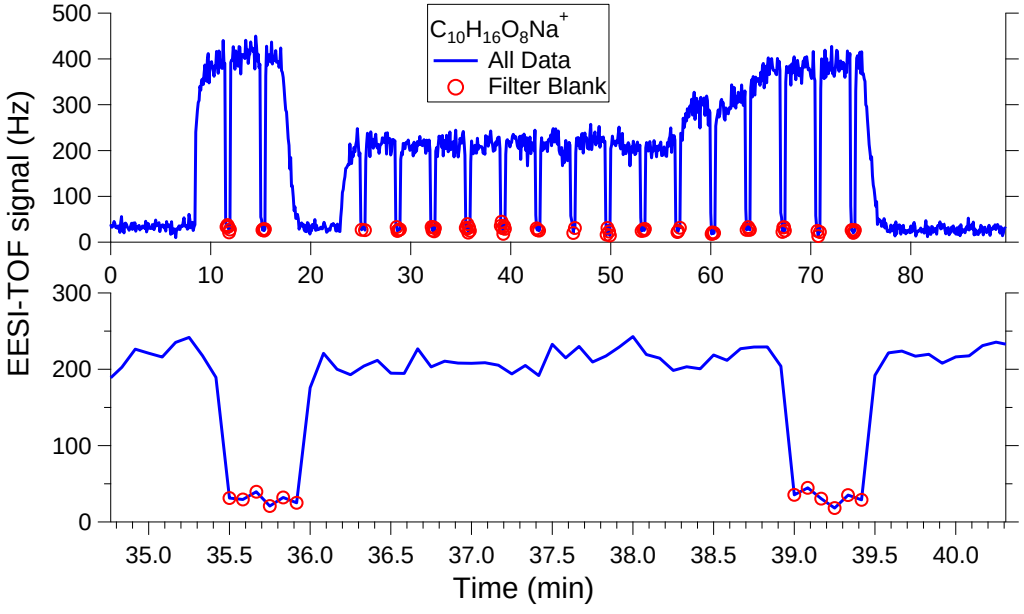

Figure 2. (a) Sample time series of $[C_{10}H_{16}O_8]Na^+$ measured in SOA generated from α-pinene ozonolysis, showing aerosol measurement periods (3 min) interspersed with filter blanks (30 s). The difference between these two conditions yields the signal due to sampled particles. (b) Expanded view of two measurement/filter cycles showing; instrument response to filter switching is ~5 s.

Atmos. Meas. Tech. Discuss., https://doi.org/10.5194/amt-2019-45
Manuscript under review for journal Atmos. Meas. Tech.
Discussion started: 5 March 2019

Atmospheric Measurement Techniques Discussions

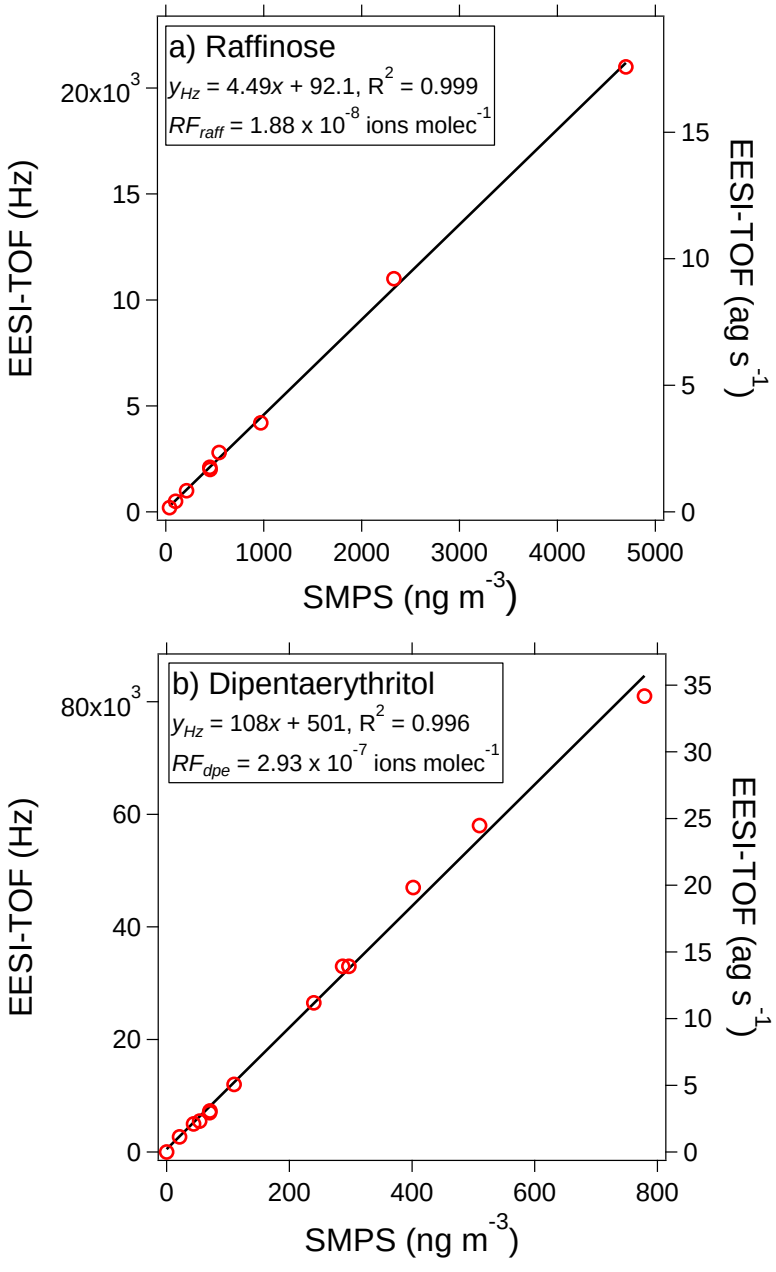

Figure 3. EESI-TOF signal as a function of mass concentration measured by an SMPS, assuming spherical particles with the material density of the pure compound, for raffinose (a) and dipentaerythritol (b). The EESI-TOF signal is represented both in terms of the flux of ions (left axis) and mass (right axis) reaching the detector.

Atmos. Meas. Tech. Discuss., https://doi.org/10.5194/amt-2019-45
Manuscript under review for journal Atmos. Meas. Tech.
Discussion started: 5 March 2019

Atmospheric Measurement Techniques Discussions

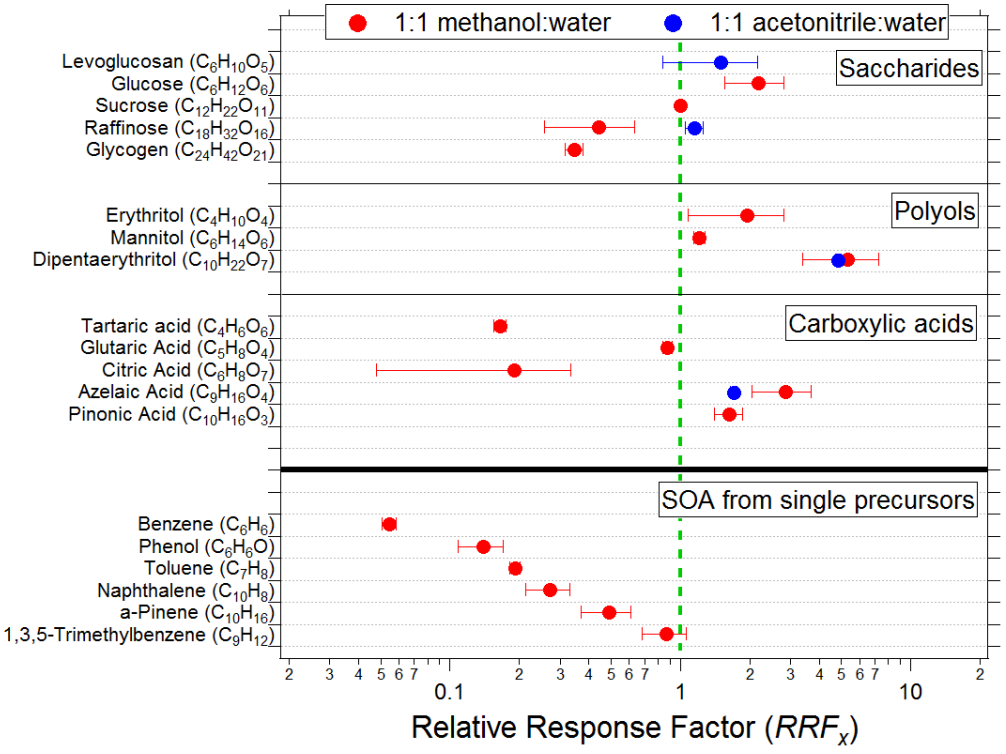

Figure 4. EESI-TOF sensitivity (ions molecule^{-1}, see Eq. 1) relative to that of sucrose for pure components and SOA formed by OH-initiated oxidation of single precursors in a PAM flow reactor. Red points denote a 1:1 methanol:water working fluid; blue denotes 1:1 acetonitrile:water. All configurations use 100 ppm NaI as a dopant, and all ions are detected as $[M]Na^+$.

Atmos. Meas. Tech. Discuss., https://doi.org/10.5194/amt-2019-45
Manuscript under review for journal Atmos. Meas. Tech.
Discussion started: 5 March 2019

Atmospheric Measurement Techniques Discussions

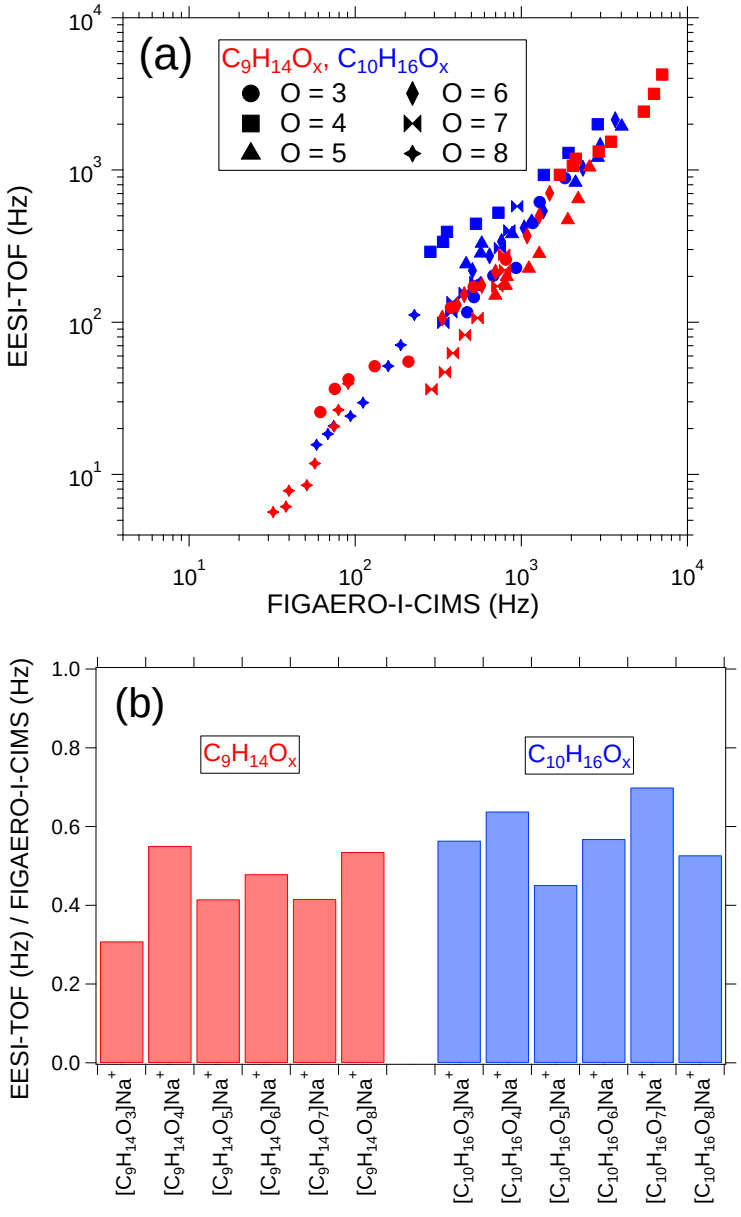

Figure 5. (a) EESI-TOF signal (Hz) as a function of FIGAERO-I-CIMS (Hz) for the $[C_9H_{14}O_x]Na^+$ (red) and $[C_{10}H_{16}O_x]Na^+$ (blue) ion series. Marker shape denotes number of oxygen atoms. (b) Slopes of linear fits to individual ions for the $[C_9H_{14}O_x]Na^+$ (red) and $[C_{10}H_{16}O_x]Na^+$ (blue) ion series.

Atmos. Meas. Tech. Discuss., https://doi.org/10.5194/amt-2019-45
Manuscript under review for journal Atmos. Meas. Tech.
Discussion started: 5 March 2019

Atmospheric Measurement Techniques Discussions

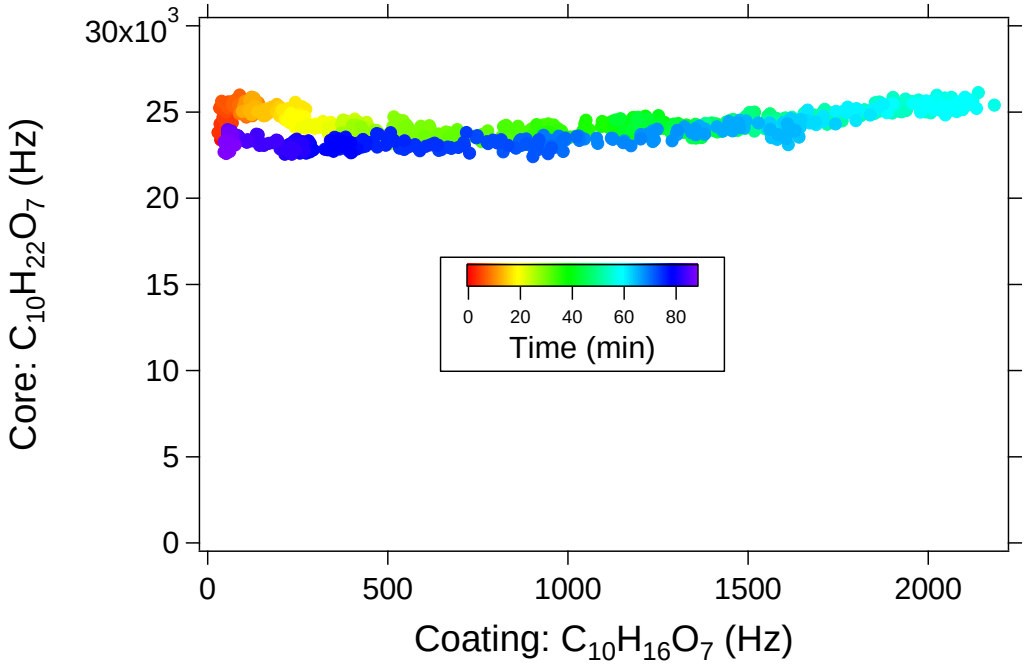

Figure 6. Dipentaerythritol $[C_{10}H_{22}O_7]Na^+$ signal measured in a flow tube as a function of $[C_{10}H_{H16}O_7]Na^+$ signal, which is proportional to condensed SOA mass. The maximum $[C_{10}H_{H16}O_7]Na^+$ signal corresponds to approximately 75 µg m^{-3} of SOA, of which approximately 40% occurs as a coating on the dipentaerythritol seed, increasing the particle diameter from 20 to 70 nm. Points are colored by time, showing an increase and then decrease of coating material.

Atmos. Meas. Tech. Discuss., https://doi.org/10.5194/amt-2019-45
Manuscript under review for journal Atmos. Meas. Tech.
Discussion started: 5 March 2019

Atmospheric Measurement Techniques Discussions

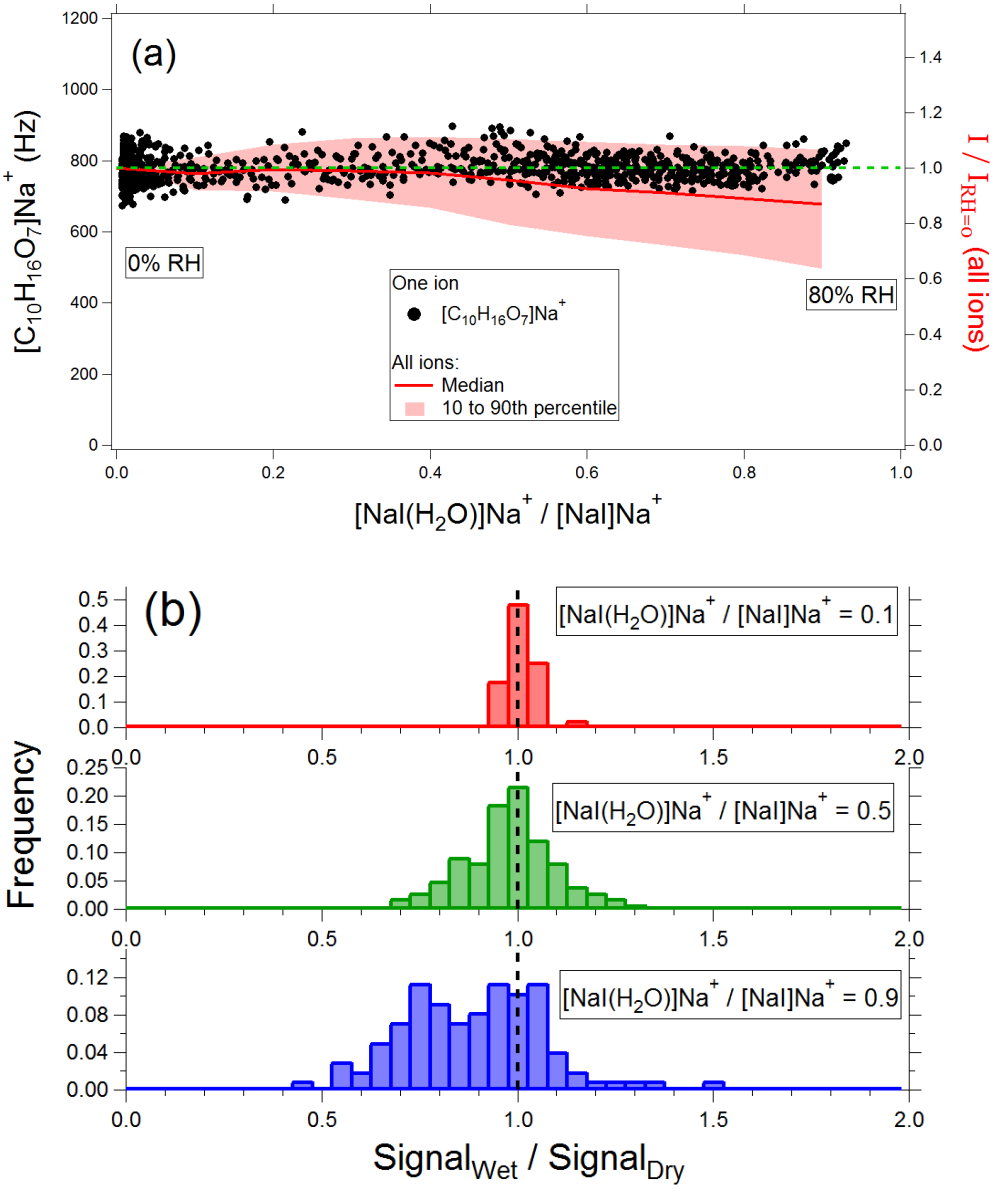

Figure 7. Effect of water vapor on EESI-TOF response. (a) Left axis, black points: $[C_{10}H_{16}O_7]Na^+$ signal as a function of $[NaI](H_2O)]Na^+$ / $[NaI]Na^+$. Right axis, red shading: median, 10th, and 90th percentiles of $I/I_{RH=0}$ for all measured ions. (b) Probability distributions of $I/I_{RH=0}$ at $[NaI](H_2O)]Na^+$ / $[NaI]Na^+$ = 0.1, 0.5, and 0.9, where $[NaI](H_2O)]Na^+$ / $[NaI]Na^+$ = 0.9 corresponds to 80% RH.

Atmos. Meas. Tech. Discuss., https://doi.org/10.5194/amt-2019-45
Manuscript under review for journal Atmos. Meas. Tech.
Discussion started: 5 March 2019

Atmospheric Measurement Techniques Discussions

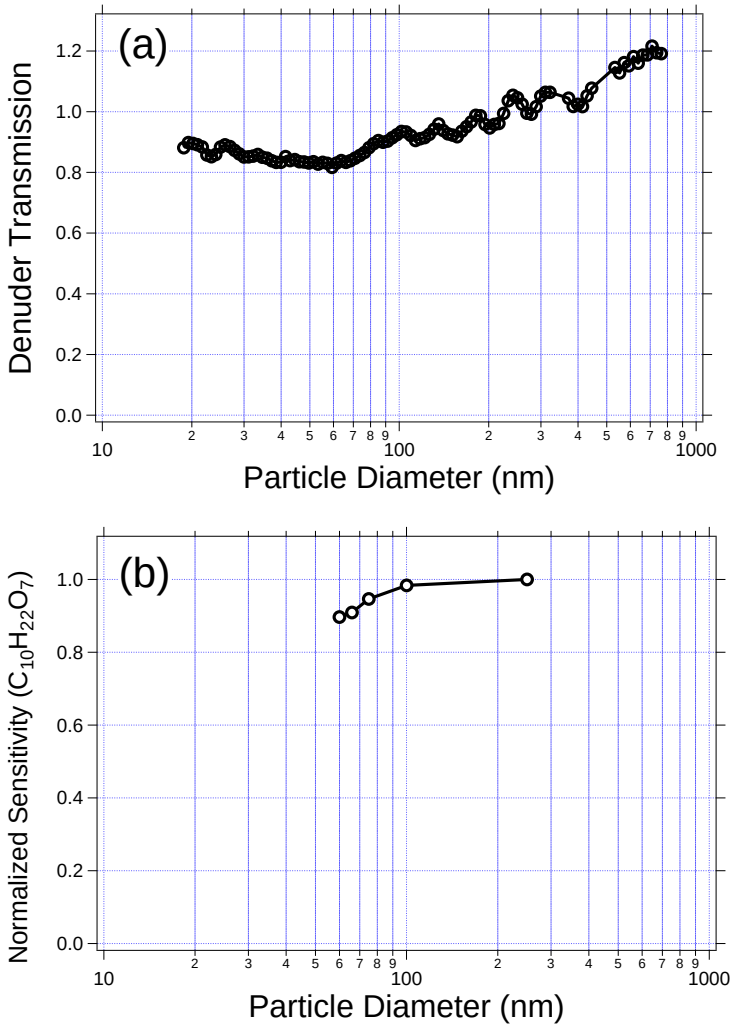

Figure 8. (a) Particle transmission through the denuder as a function of diameter. (b) Measured sensitivity of dipentaerythritol as a function of particle diameter.

Atmos. Meas. Tech. Discuss., https://doi.org/10.5194/amt-2019-45
Manuscript under review for journal Atmos. Meas. Tech.
Discussion started: 5 March 2019

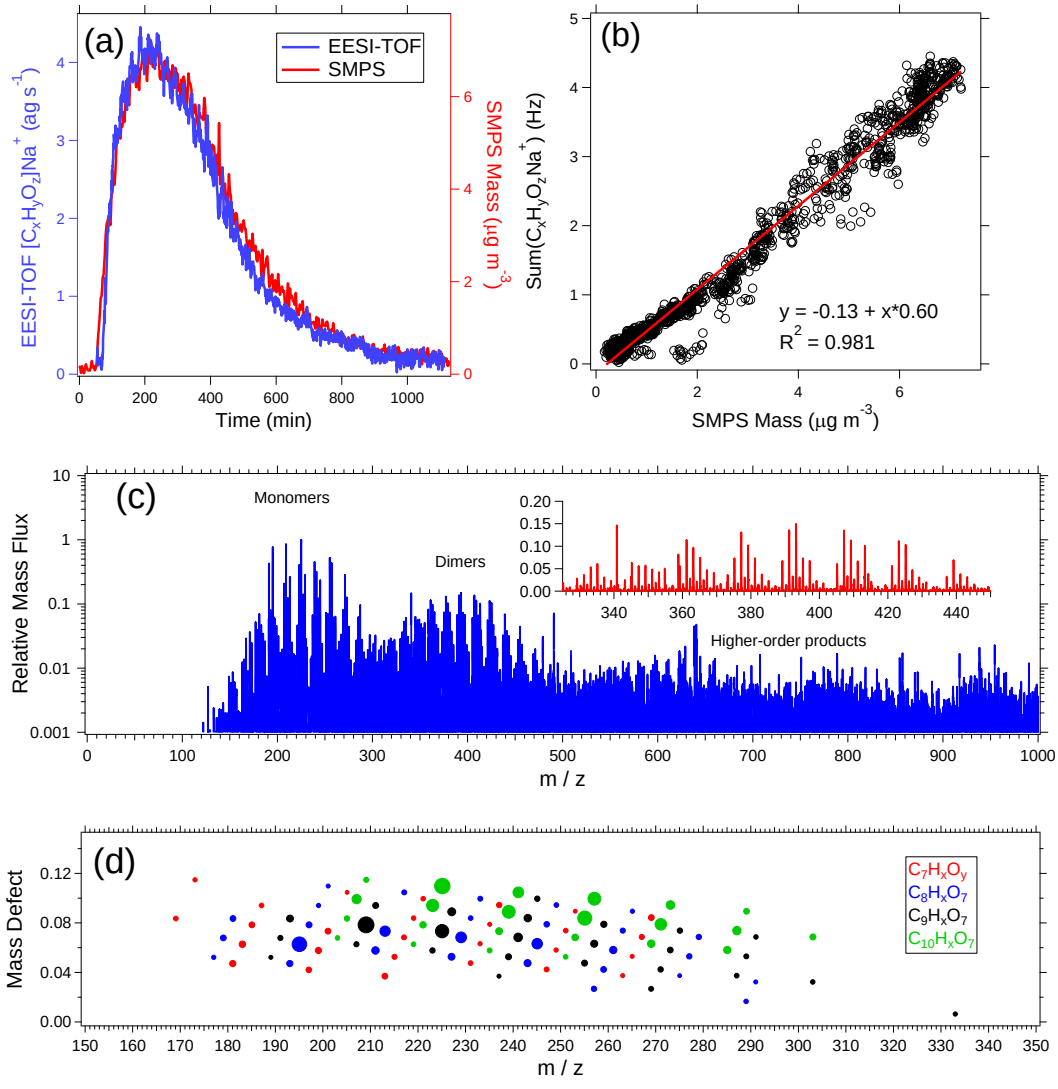

Figure 9. Sample EESI-TOF data from α-pinene ozonolysis in an environmental chamber. (a) Summed signal from all $[C_xH_yO_z]Na^+$ ions measured by the EESI-TOF and particle mass measured by the SMPS as a function of time after beginning of reaction. (b) EESI-TOF $[C_xH_yO_z]Na^+$ signal as a function of SMPS mass. (c) Averaged EESI-TOF mass spectrum, with dimer region expanded on linear scale in inset. (d) Mass defect plot of monomer region, with markers sized by signal intensity and colored by number of carbon atoms.

Atmos. Meas. Tech. Discuss., https://doi.org/10.5194/amt-2019-45
Manuscript under review for journal Atmos. Meas. Tech.
Discussion started: 5 March 2019

Atmospheric Measurement Techniques Discussions

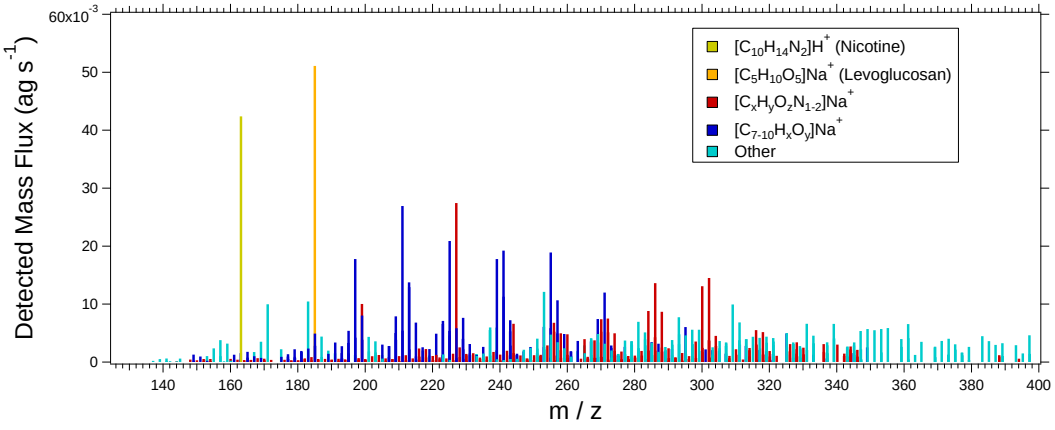

Figure 10. Campaign average EESI-TOF mass spectrum from summer measurements in Zurich, Switzerland. Selected ions and families are colored as shown in the legend. Note the x-axis begins at *m/z* 125 due to blanking of smaller ions by the quadrupole ion guides.

Atmos. Meas. Tech. Discuss., https://doi.org/10.5194/amt-2019-45
Manuscript under review for journal Atmos. Meas. Tech.
Discussion started: 5 March 2019

Atmospheric Measurement Techniques Discussions

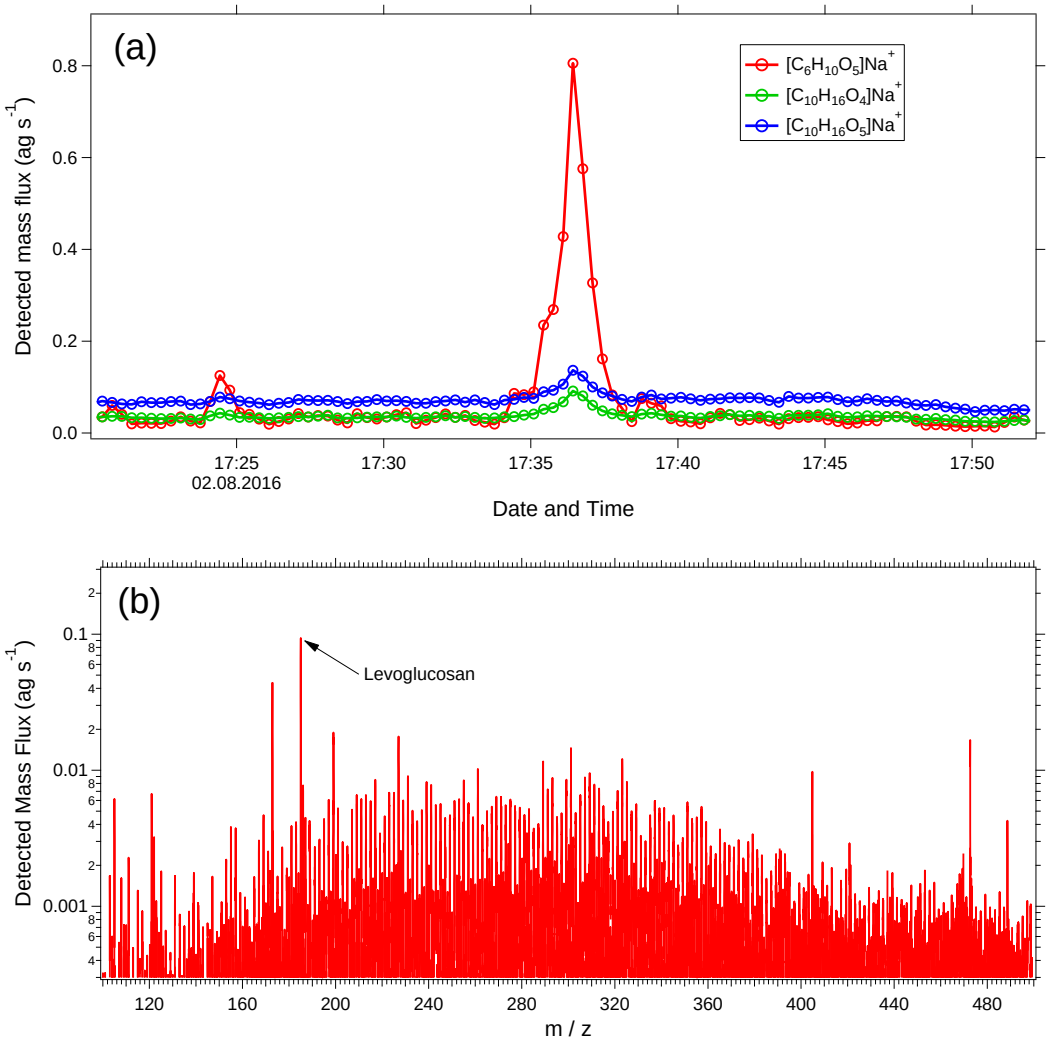

Figure 11. (a) Time series of selected ions showing transect of a wildfire plume. Shown are $[C_6H_{10}O_5]Na^+$ (levoglucosan and its isomers) and the monoterpene SOA-influenced ions $[C_{10}H_{16}O_4]Na^+$ and $[C_{10}H_{16}O_5]Na^+$. (b) Mass spectrum (20 s average) during the peak of the wildfire plume with levoglucosan labelled.

Atmos. Meas. Tech. Discuss., https://doi.org/10.5194/amt-2019-45
Manuscript under review for journal Atmos. Meas. Tech.
Discussion started: 5 March 2019

Atmospheric Measurement Techniques Discussions

References

Brüggemann, M., Karu, E., Stelzer, T., and Hoffmann, T.: Real-time analysis of ambient organic aerosols using aerosol flowing atmospheric-pressure afterglow mass spectrometry (AeroFAPA-MS), Environ. Sci. Technol., 49, 5571-5578, 10.1021/es506186c, 2015.

Brüggemann, M., Poulain, L., Held, A., Stelzer, T., Zuth, C., Richters, S., Mutzel, A., van Pinxteren, D., Iinuma, Y., Katkevica, S., Rabe, R., Herrmann, H., and Hoffmann, T.: Real-time detection of highly oxidized organosulfates and BSOA marker compounds during the F-BEACh 2014 field study, Atmos. Chem. Phys., 17, 1453-1469, 10.5194/acp-17-1453-2017, 2017.

Canagaratna, M. R., Jayne, J. T., Jimenez, J. L., Allan, J. D., Alfarra, M. R., Zhang, Q., Onasch, T. B., Drewnick, F., Coe, H., Middlebrook, A., Delia, A., Williams, L. R., Trimborn, A. M., Northway, M. J., DeCarlo, P. F., Kolb, C. E., Davidovits, P., and Worsnop, D. R.: Chemical and microphysical characterization of ambient aerosols with the Aerodyne aerosol mass spectrometer, Mass Spec. Rev., 26, 185-222, 10.1002/mas.20115, 2007.

Chen, H., Venter, A., and Cooks, R. G.: Extractive electrospray ionization for direct analysis of undiluted urine, milk and other complex mixtures without sample preparation, Chem. Commun., 19, 2042-2044, 10.1039/b602614a, 2006.

Daellenbach, K. R., Stefenelli, G., Bozzetti, C., Vlachou, A., Fermo, P., Gonzalez, R., Piazzalunga, A., Colombi, C., Canonaco, F., Hueglin, C., Kaspar-Giebl, A., Jaffrezo, J.-L., Bianchi, F., Slowik, J. G., Baltensperger, U., El Haddad, I., and Prévôt, A. S. H.: Long-term chemical analysis and organic aerosol source apportionment at nine sites in Central Europe: source identification and uncertainty assessment, Atmos. Chem. Phys., 17, 13265-13282, 10.5194/acp-17-13265-2017, 2017.

Doezema, L. A., Longin, T., Cody, W., Perraud, V., Dawson, M. L., Ezell, M. J., Greaves, J., Johnson, K. R., and Finlayson-Pitts, B. J.: Analysis of secondary organic aerosols in air using extractive electrospray ionization mass spectrometry (EESI-MS), RSC Advances, 2, 2930-2938, 10.1039/C2RA00961G, 2012.

Eichler, P., Müller, M., D'Anna, B., and Wisthaler, A.: A novel inlet system for online chemical analysis of semi-volatile submicron particulate matter, Atmos. Meas. Tech., 8, 1353-1360, 10.5194/amt-8-1353-2015, 2015.

Gallimore, P. J., and Kalberer, M.: Characterizing an extractive electrospray ionization (EESI) source for the online mass spectrometry analysis of organic aerosols, Environ. Sci. Technol., 47, 7324-7331, 10.1021/es305199h, 2013.

Gallimore, P. J., Giorio, C., Mahon, B. M., and Kalberer, M.: Online molecular characterisation of organic aerosols in an atmospheric chamber using extractive electrospray ionisation mass spectrometry, Atmos. Chem. Phys., 17, 14485-14500, 10.5194/acp-17-14485-2017, 2017.

Gard, E., Mayer, J. E., Morrical, B. D., Dienes, T., Fergenson, D. P., and Prather, K. A.: Real-time analysis of individual atmospheric aerosol particles: design and performance of a portable ATOFMS, Anal. Chem., 69, 4083-4091, 10.1021/ac970540n, 1997.

Atmos. Meas. Tech. Discuss., https://doi.org/10.5194/amt-2019-45
Manuscript under review for journal Atmos. Meas. Tech.
Discussion started: 5 March 2019

Atmospheric Measurement Techniques Discussions

Goldstein, A. H., and Galbally, I. E.: Known and unexplored organic constituents in the earth's atmosphere, Environ. Sci. Technol., 41, 1514-1521, Doi 10.1021/Es072476p, 2007.

Hallquist, M., Wenger, J. C., Baltensperger, U., Rudich, Y., Simpson, D., Claeys, M., Dommen, J., Donahue, N. M., George, C., Goldstein, A. H., Hamilton, J. F., Herrmann, H., Hoffmann, T., Iinuma, Y., Jang, M., Jenkin, M. E., Jimenez, J. L., Kiendler-Scharr, A., Maenhaut, W., McFiggans, G., Mentel, T. F., Monod, A., Prevot, A. S. H., Seinfeld, J. H., Surratt, J. D., Szmigielski, R., and Wildt, J.: The formation, properties and impact of secondary organic aerosol: current and emerging issues, Atmos. Chem. Phys., 9, 5155-5236, 2009.

Holzinger, R., Williams, J., Herrmann, F., Lelieveld, J., Donahue, N. M., and Röckmann, T.: Aerosol analysis using a Thermal-Desorption Proton-Transfer-Reaction Mass Spectrometer (TD-PTR-MS): a new approach to study processing of organic aerosols, Atmos. Chem. Phys., 10, 2257-2267, 10.5194/acp-10-2257-2010, 2010.

Horan, A. J., Gao, Y., Hall, W. A., and Johnston, M. V.: Online characterization of particles and gases with an ambient electrospray ionization source, Anal. Chem., 84, 9253-9258, 10.1021/ac302024y, 2012.

Isaacman, G., Kreisberg, N. M., Yee, L. D., Worton, D. R., Chan, A. W. H., Moss, J. A., Hering, S. V., and Goldstein, A. H.: Online derivatization for hourly measurements of gas- and particle-phase semi-volatile oxygenated organic compounds by thermal desorption aerosol gas chromatography (SV-TAG), Atmos. Meas. Tech., 7, 4417-4429, 10.5194/amt-7-4417-2014, 2014.

Iyer, S., Lopez-Hilfiker, F. D., Lee, B. H., Thornton, J. A., and Kurtén, T.: Modeling the detection of organic and inorganic compounds using iodide-based chemical ionization, J. Phys. Chem. A, 120, 576-587, 2016.

Jimenez, J. L., Canagaratna, M. R., Donahue, N. M., Prevot, A. S., Zhang, Q., Kroll, J. H., DeCarlo, P. F., Allan, J. D., Coe, H., Ng, N. L., Aiken, A. C., Docherty, K. S., Ulbrich, I. M., Grieshop, A. P., Robinson, A. L., Duplissy, J., Smith, J. D., Wilson, K. R., Lanz, V. A., Hueglin, C., Sun, Y. L., Tian, J., Laaksonen, A., Raatikainen, T., Rautiainen, J., Vaattovaara, P., Ehn, M., Kulmala, M., Tomlinson, J. M., Collins, D. R., Cubison, M. J., Dunlea, E. J., Huffman, J. A., Onasch, T. B., Alfarra, M. R., Williams, P. I., Bower, K., Kondo, Y., Schneider, J., Drewnick, F., Borrmann, S., Weimer, S., Demerjian, K., Salcedo, D., Cottrell, L., Griffin, R., Takami, A., Miyoshi, T., Hatakeyama, S., Shimono, A., Sun, J. Y., Zhang, Y. M., Dzepina, K., Kimmel, J. R., Sueper, D., Jayne, J. T., Herndon, S. C., Trimborn, A. M., Williams, L. R., Wood, E. C., Middlebrook, A. M., Kolb, C. E., Baltensperger, U., and Worsnop, D. R.: Evolution of organic aerosols in the atmosphere, Science, 326, 1525-1529, 10.1126/science.1180353, 2009.

Junninen, H., Ehn, M., Petäjä, T., Luosujärvi, L., Kotiaho, T., Kostiainen, R., Rohner, U., Gonin, M., Fuhrer, K., Kulmala, M., and Worsnop, D. R.: A high-resolution mass spectrometer to measure atmospheric ion composition, Atmos. Meas. Tech., 3, 1039-1053, 10.5194/amt-3-1039-2010, 2010.

Atmos. Meas. Tech. Discuss., https://doi.org/10.5194/amt-2019-45
Manuscript under review for journal Atmos. Meas. Tech.
Discussion started: 5 March 2019

Atmospheric Measurement Techniques Discussions

Kebarle, P., and Peschke, M.: On the mechanisms by which the charged droplets produced by electrospray lead to gas phase ions, Anal. Chim. Act., 406, 11-35, 10.1016/s0003-2670(99)00598-x, 2000.

Kroll, J. H., Donahue, N. M., Jimenez, J. L., Kessler, S. H., Canagaratna, M. R., Wilson, K. R., Altieri, K. E., Mazzoleni, L. R., Wozniak, A. S., Bluhm, H., Mysak, E. R., Smith, J. D., Kolb, C. E., and Worsnop, D. R.: Carbon oxidation state as a metric for describing the chemistry of atmospheric organic aerosol, Nature Chemistry, 3, 133-139, 10.1038/NCHEM.948, 2011.

Kumbhani, S., Longin, T., Wingen, L. M., Kidd, C., Perraud, V., and Finlayson-Pitts, B. J.: New mechanism of extractive electrospray ionization mass spectrometry for heterogeneous solid particles, Anal. Chem., 90, 2055-2062, 10.1021/acs.analchem.7b04164, 2018.

Lambe, A. T., Ahern, A. T., Williams, L. R., Slowik, J. G., Wong, J. P. S., Abbatt, J. P. D., Brune, W. H., Ng, N. L., Wright, J. P., Croasdale, D. R., Worsnop, D. R., Davidovits, P., and Onasch, T. B.: Characterization of aerosol photooxidation flow reactors: heterogeneous oxidation, secondary organic aerosol formation and cloud condensation nuclei activity measurements, Atmos. Meas. Tech., 4, 445-461, 10.5194/amt-4-445-2011, 2011.

Laskin, J., Laskin, A., Roach, P. J., Slysz, G. W., Anderson, G. A., Nizkorodov, S. A., Bones, D. L., and Nguyen, L. Q.: High-resolution desorption electrospray ionization mass spectrometry for chemical characterization of organic aerosols, Anal. Chem., 82, 2048-2058, 10.1021/ac902801f, 2010.

Lee, B. H., Lopez-Hilfiker, F. D., Mohr, C., Kurtén, T., Worsnop, D. R., and Thornton, J. A.: An iodide-adduct high-resolution time-of-flight chemical-ionization mass spectrometer: application to atmospheric inorganic and organic compounds, Environ. Sci. Technol., 48, 6309-6317, 2014.

Lee, B. H., Lopez-Hilfiker, F. D., Veres, P. R., McDuffie, E. E., Fibiger, D. L., Sparks, T. L., Ebben, C. J., Green, J. R., Schroder, J. C., Campuzano-Jost, P., Iyer, S., D'Ambro, E. L., Schobesberger, S., Brown, S. S., Wooldridge, P. J., Cohen, R. C., Fiddler, M. N., Bililign, S., Jimenez, J. L., Kurtén, T., Weinheimer, A. J., Jaegle, L., and Thornton, J. A.: Flight deployment of a high-resolution time-of-flight chemical ionization mass spectrometer: observations of reactive halogen and nitrogen oxide species, J. Geophys. Res. - Atmos., 123, 7670-7686, 10.1029/2017JD028082, 2018.

Lopez-Hilfiker, F. D., Mohr, C., Ehn, M., Rubach, F., Kleist, E., Wildt, J., Mentel, T. F., Lutz, A., Hallquist, M., Worsnop, D., and Thornton, J. A.: A novel method for online analysis of gas and particle composition: description and evaluation of a Filter Inlet for Gases and AEROsols (FIGAERO), Atmos. Meas. Tech., 7, 983-1001, 10.5194/amt-7-983-2014, 2014.

Lopez-Hilfiker, F. D., Mohr, C., Ehn, M., Rubach, F., Kleist, E., Wildt, J., Mentel, T. F., Carrasquillo, A. J., Daumit, K. E., Hunter, J. F., Kroll, J. H., Worsnop, D. R., and Thornton, J. A.: Phase partitioning and volatility of secondary organic aerosol components formed from α-pinene ozonolysis and OH oxidation: the importance of accretion products and other low volatility compounds, Atmos. Chem. Phys., 15, 7765-7776, 10.5194/acp-15-7765-2015, 2015.

Atmos. Meas. Tech. Discuss., https://doi.org/10.5194/amt-2019-45
Manuscript under review for journal Atmos. Meas. Tech.
Discussion started: 5 March 2019

Atmospheric Measurement Techniques Discussions

Lopez-Hilfiker, F. D., Iyer, S., Mohr, C., Lee, B. H., D'Ambro, E. L., Kurtén, T., and Thornton, J. A.: Constraining the sensitivity of iodide adduct chemical ionization mass spectrometry to multifunctional organic molecules using the collision limit and thermodynamic stability of iodide ion adducts, Atmos. Meas. Tech., 9, 1505-1512, 10.5194/amt-9-1505-2016, 2016.

Molteni, U., Bianchi, F., Klein, F., El Haddad, I., Frege, C., Rossi, M. J., Dommen, J., and Baltensperger, U.: Formation of highly oxygenated organic molecules from aromatic compounds, Atmos. Chem. Phys., 18, 1909-1921, 10.5194/acp-18-1909-2018, 2018.

Müller, M., Eichler, P., D'Anna, B., Tan, W., and Wisthaler, A.: Direct sampling and analysis of atmospheric particulate organic matter by proton-transfer-reaction mass spectrometry, Anal. Chem., 89, 10889-10897, 10.1021/acs.analchem.7b02582, 2017.

Murphy, D. M., Cziczo, D. J., Froyd, K. D., Hudson, P. K., Matthew, B. M., Middlebrook, A. M., Peltier, R. E., Sullivan, A., Thomson, D. S., and Weber, R. J.: Single-particle mass spectrometry of tropospheric aerosol particles, J. Geophys. Res. - Atmos., 111, 10.1029/2006jd007340, 2006.

Paulsen, D., Dommen, J., Kalberer, M., Prévôt, A. S. H., Richter, R., Sax, M., Steinbacher, M., Weingartner, E., and Baltensperger, U.: Secondary organic aerosol formation by irradiation of 1,3,5-trimethylbenzene-NO_x-H_2O in a new reaction chamber for environmental chemistry and physics, Environ. Sci. Technol., 39, 2668-2678, 2005.

Pospisilova, V., Lopez-Hilfiker, F. D., Bell, D., El Haddad, I., Mohr, C., Huang, W., Heikkinen, L., Xiao, M., Dommen, J., Prévôt, A. S. H., Baltensperger, U., and Slowik, J. G.: On the fate of oxygenated organic molecules in atmospheric aerosol particles, Proc. Nat. Acad. Sci., submitted.

Qi, L., Chen, M.-D., Stefenelli, G., Pospisilova, V., Tong, Y.-D., Bertrand, A., Hueglin, C., Rigler, M., Ge, X.-L., Baltensperger, U., Prévôt, A. S. H., and Slowik, J. G.: Real-time source quantification of wintertime secondary organic aerosol in Zurich using an extractive electrospray ionization time-of-flight mass spectrometer (EESI-TOF), Atmos. Chem. Phys., submitted.

Reemstsma, T., These, A., Venkatachari, P., Xia, X. Y., Hopke, P. K., Springer, A., and Linscheid, M.: Identification of fulvic acids and sulfated and nitrated analogues in atmospheric aerosol by electrospray ionization Fourier transform ion cyclotron resonance mass spectrometry, Anal. Chem., 78, 8299-8304, 2006.

Roach, P. J., Laskin, J., and Laskin, A.: Nanospray desorption electrospray ionization: an ambient method for liquid-extraction surface sampling in mass spectrometry, Analyst, 135, 2233-2236, 10.1039/c0an00312c, 2010.

Stefenelli, G., Lopez-Hilfiker, F. D., Pospisilova, V., Vogel, A., Hüglin, C., Baltensperger, U., Prévôt, A. S. H., and Slowik, J. G.: Source apportionment of ambient organic aerosol by online extractive electrospray ionization time-of-flight mass spectrometry (EESI-TOF), in preparation.

Struckmeier, C., Drewnick, F., Fachinger, F., Gobbi, G. P., and Borrmann, S.: Atmospheric aerosols in Rome, Italy: sources, dynamics and spatial variations during two seasons, Atmos. Chem. Phys., 16, 15277-15299, 10.5194/acp-16-15277-2016, 2016.

Atmos. Meas. Tech. Discuss., https://doi.org/10.5194/amt-2019-45
Manuscript under review for journal Atmos. Meas. Tech.
Discussion started: 5 March 2019

Atmospheric Measurement Techniques Discussions

Surratt, J. D., Gomez-Gonzalez, Y., Chan, A. W., Vermeylen, R., Shahgholi, M., Kleindienst, T. E., Edney, E. O., Offenberg, J. H., Lewandowski, M., Jaoui, M., Maenhaut, W., Claeys, M., Flagan, R. C., and Seinfeld, J. H.: Organosulfate formation in biogenic secondary organic aerosol, J. Phys. Chem. A, 112, 8345-8378, 10.1021/jp802310p, 2008.

Vlasenko, A., Macdonald, A. M., Sjostedt, S. J., and Abbatt, J. P. D.: Formaldehyde measurements by proton transfer reaction - mass spectrometry (PTR-MS): correction for humidity effects, Atmos. Meas. Tech., 3, 1055-1062, 10.5194/amt-3-1055-2010, 2010.

Volkamer, R., Jimenez, J. L., San Martini, F., Dzepina, K., Zhang, Q., Salcedo, D., Molina, L. T., Worsnop, D. R., and Molina, M. J.: Secondary organic aerosol formation from anthropogenic air pollution: rapid and higher than expected, Geophys. Res. Lett., 33, L17811, 2006.

Wang, R., Groehn, A. J., Zhu, L., Dietiker, R., Wegner, K., Guenther, D., and Zenobi, R.: On the mechanism of extractive electrospray ionization (EESI) in the dual-spray configuration, Anal. Bioanal. Chem., 402, 2633-2643, 10.1007/s00216-011-5471-8, 2012.

Wortmann, A., Kistler-Momotova, A., Zenobi, R., Heine, M. C., and Wilhelm, O. P., S. E.: Shrinking droplets in electrospray ionization and their influence on chemical equilibria, J. Am. Soc. Mass Spec., 18, 385-393, 10.1016/j.jasms.2006.10.010, 2007.

Zelenyuk, A., and Imre, D.: Single particle laser ablation time-of-flight mass spectrometer: an introduction to SPLAT, Aerosol Sci. Technol., 39, 554-568, 10.1080/027868291009242, 2005.

Zhang, H., Surratt, J. D., Lin, Y.-H., Bapat, J., and Kamens, R. M.: Effect of relative humidity on SOA formation from isoprene/NO photooxidation: enhancement of 2-methylglyceric acid and its corresponding oligoesters under dry conditions, Atmos. Chem. Phys., 11, 6411-6424, 10.5194/acp-11-6411-2011, 2011.

Zhang, X., McVay, R. C., Huang, D. D., Dalleska, N. F., Aumont, B., Flagan, R. c., and Seinfeld, J. H.: Formation and evolution of molecular products in a-pinene secondary organic aerosol, Proc. Nat. Acad. Sci., 112, 14168-14173, 10.1073/pnas.1517742112, 2015.

Zhang, X., Dalleska, N. F., Huang, D. D., Bates, K. H., Sorooshian, A., Flagan, R. C., and Seinfeld, J. H.: Time-resolved molecular characterization of organic aerosols by PILS + UPLC/ESI-Q-TOFMS, Atmos. Environ., 130, 180-189, 10.1016/j.atmosenv.2015.08.049, 2016.

Zhao, Y., Chan, J. K., Lopez-Hilfiker, F. D., McKeown, M. A., D'Ambro, E. L., Slowik, J. G., Riffell, J. A., and Thornton, J. A.: An electrospray chemical ionization source for real-time measurement of atmospheric organic and inorganic vapors, Atmos. Meas. Tech., 10, 3609-3625, 10.5194/amt-10-3609-2017, 2017.

B.3 Insights into the O:C-dependent mechanisms controlling the evaporation of α-pinene secondary organic aerosol particles

Authors: Angela Buchholz, Andrew T. Lambe, Arttu Ylisirniö, Zijun Li, Olli-Pekka Tikkanen, Celia Faiola, Eetu Kari, Liqing Hao, Olli Luoma, **Wei Huang**, Claudia Mohr, Douglas R. Worsnop, Sergey A. Nizkorodov, Taina Yli-Juuti, Siegfried Schobesberger, and Annele Virtanen

In: Atmospheric Chemistry and Physics, 19, 4061–4073, 2019. DOI: 10.5194/acp-19-4061-2019.

Authorship statement

This peer-reviewed scientific journal article is based on the chamber data from a four-week laboratory campaign (Kuopio2016) in University of Eastern Finland in September 2016, with a focus on the volatility of SOA particles from α-pinene oxidation with different concentrations of oxidants. I participated in the FIGAERO-CIMS data analysis, interpretation, and discussion of this article.

Atmos. Chem. Phys., 19, 4061–4073, 2019
https://doi.org/10.5194/acp-19-4061-2019

Atmospheric Chemistry and Physics
Open Access
EGU

Insights into the O : C-dependent mechanisms controlling the evaporation of α-pinene secondary organic aerosol particles

Angela Buchholz[1], Andrew T. Lambe[2], Arttu Ylisirniö[1], Zijun Li[1], Olli-Pekka Tikkanen[1], Celia Faiola[3], Eetu Kari[1], Liqing Hao[1], Olli Luoma[1], Wei Huang[4], Claudia Mohr[4,5], Douglas R. Worsnop[1,2], Sergey A. Nizkorodov[6], Taina Yli-Juuti[1], Siegfried Schobesberger[1], and Annele Virtanen[1]

[1]Department of Applied Physics, University of Eastern Finland, Kuopio, Finland
[2]Aerodyne Research Inc., Billerica, MA, USA
[3]Department of Ecology and Evolutionary Biology, University of California, Irvine, CA, USA
[4]Institute of Meteorology and Climate Research, Karlsruhe Institute of Technology, Karlsruhe, Germany
[5]Department of Environmental Science and Analytical Chemistry, Stockholm University, Stockholm, Sweden
[6]Department of Chemistry, University of California, Irvine, CA, USA

Correspondence: Angela Buchholz (angela.buchholz@uef.fi)

Received: 18 December 2018 – Discussion started: 2 January 2019
Revised: 21 March 2019 – Accepted: 22 March 2019 – Published: 2 April 2019

Abstract. The volatility of oxidation products of volatile organic compounds (VOCs) in the atmosphere is a key factor to determine if they partition into the particle phase contributing to secondary organic aerosol (SOA) mass. Thus, linking volatility and measured particle composition will provide insights into SOA formation and its fate in the atmosphere. We produced α-pinene SOA with three different oxidation levels (characterized by average oxygen-to-carbon ratio; $\overline{\mathrm{O:C}} = 0.53$, 0.69, and 0.96) in an oxidation flow reactor. We investigated the particle volatility by isothermal evaporation in clean air as a function of relative humidity (RH < 2 %, 40 %, and 80 %) and used a filter-based thermal desorption method to gain volatility and chemical composition information.

We observed reduced particle evaporation for particles with increasing $\overline{\mathrm{O:C}}$ ratio, indicating that particles become more resilient to evaporation with oxidative aging. Particle evaporation was increased in the presence of water vapour and presumably particulate water; at the same time the resistance of the residual particles to thermal desorption was increased as well. For SOA with $\overline{\mathrm{O:C}} = 0.96$, the unexpectedly large increase in mean thermal desorption temperature and changes in the thermogram shapes under wet conditions (80 % RH) were an indication of aqueous phase chemistry. For the lower $\overline{\mathrm{O:C}}$ cases, some water-induced composition changes were observed. However, the enhanced evaporation under wet conditions could be explained by the reduction in particle viscosity from the semi-solid to liquid-like range, and the observed higher desorption temperature of the residual particles is a direct consequence of the increased removal of high-volatility and the continued presence of low-volatility compounds.

1 Introduction

Secondary organic aerosol (SOA) accounts for a major fraction of the global atmospheric aerosol burden (Hallquist et al., 2009; Jimenez et al., 2009). Understanding the mechanism of formation and properties of SOA is therefore of utmost importance to estimate its effects on climate, air quality and human health. SOA – by definition – is formed when low-volatility oxidation products of volatile organic compounds (VOCs) deposit onto existing particles or form new particles. While the scientific community has made significant improvements in characterizing the precursors and gas phase oxidation products at the molecular level with new measurement techniques (e.g. Ehn et al., 2014; Lopez-Hilfiker et al., 2014; Mohr et al., 2017), the particle phase is still proving to be complicated. There are technical challenges as chemical composition analysis techniques typically operate with liquid or gaseous samples, and thus aerosol par-

ticle samples need to be extracted or desorbed which can introduce artefacts. In addition, there are a multitude of compounds in aerosol particles (Goldstein and Galbally, 2007), and the particle phase is far from static once it is formed. Many different chemical processes can occur in the particle phase, especially if water is present; e.g. larger molecules may be formed by polymerization reactions or there may be oxidation with oxidants taken up from the gas phase (Herrmann et al., 2015; Kroll and Seinfeld, 2008). In addition, aerosol particles interact with the gas phase constantly. Compounds will partition between the gas and particle phase depending, e.g., on their vapour pressures and concentrations in the different phases (Donahue et al., 2006).

Gas–particle partitioning has been described in detail and applied to model SOA formation (Pankow, 1994a, b; Pankow et al., 2001). Donahue et al. (2006) bypassed the issue of having to define the phase diagram for each compound in the SOA system by introducing the volatility basis set (VBS) framework which utilizes the effective saturation concentration (C^*) to group the compounds into volatility classes (or bins). This framework can then be used to follow changes in partitioning, and thus bulk volatility, with time and to predict SOA formation, e.g. in global modelling (e.g. Bergström et al., 2012; Jimenez et al., 2009). More comprehensive schemes have since been developed linking volatility with other properties, e.g. oxidation level represented by the elemental oxygen-to-carbon $\overline{\mathrm{O:C}}$ ratio (Donahue et al., 2011, 2012) or a certain functionality (Krapf et al., 2016).

In principle, VBS distributions can be derived from any type of volatility measurements. Besides the SOA yield studies, the most common approaches are to measure the evaporation of SOA particles at elevated temperatures (typically 30–300 °C) or by removing the gas phase around the particles through isothermal dilution. Thermal methods include measurements of particle mass loss after passing through a thermodenuder (An et al., 2007; Cappa and Wilson, 2011; Huffman et al., 2008; Kolesar et al., 2015) and methods where particles are collected and then desorbed with a heated carrier gas flow (e.g. the filter inlet for gas and aerosol sampling unit, FIGAERO; Lopez-Hilfiker et al., 2014). Typically, the remaining SOA mass or volume fraction is determined or the changes in chemical composition with temperature are monitored. With any thermal method, there is the potential of thermal decomposition at elevated temperatures prior to detection, and some studies report strong indication of decomposition and particle phase reactions (Hall and Johnston, 2012; Kolesar et al., 2015; Lopez-Hilfiker et al., 2015; Stark et al., 2017). This may lead to an overestimation of the (semi-)volatile fraction of the SOA (Lopez-Hilfiker et al., 2015; Schobesberger et al., 2018). This issue may be constrained by combining isothermal dilution and thermodenuder measurements (Grieshop et al., 2009; Louvaris et al., 2017).

Vaden et al. (2011) proposed an isothermal dilution method utilizing a differential mobility analyser (DMA) for particle size selection coupled to an evaporation–residence time chamber at room temperature with active carbon as an absorber for the evaporating vapours. This method avoids issues associated with thermal decomposition in thermodenuders and wall loss artefacts in smog chamber experiments. It enables studying evaporation times of up to 2 days. With this method, it was shown that dry particles evaporate much slower than expected from SOA yield experiments (Vaden et al., 2011). Combining this type of data with detailed process modelling suggested that mass transport limitations in the most likely semi-solid, and thus highly viscous, dry particles were responsible for the observed slow evaporation (Yli-Juuti et al., 2017). In this context, particulate water can play a crucial role as it can act as a plasticizer, reducing particle viscosity and thus enhancing evaporation (Wilson et al., 2015; Yli-Juuti et al., 2017). Aqueous phase chemical reactions may also have an impact on SOA volatility, enhancing the formation of larger molecules or, conversely, hydrolysing especially peroxy compounds. To distinguish between the physical (viscosity decrease) and chemical (aqueous phase reactions) role of particulate water in particle evaporation, it is necessary to investigate the chemical composition of SOA particles during isothermal evaporation at ambient temperatures under a range of RH conditions. Although the thermal desorption in FIGAERO–CIMS (chemical ionization mass spectrometer) may cause decomposition as described above, it can still be useful for this purpose by combining measurements of fresh SOA particles and of particles that have been left to evaporate for long times. Whereas D'Ambro et al. (2018) left the collected SOA particles on the FIGAERO filter in a clean nitrogen flow for up to 24 h, we utilized our residence time chamber (RTC) to probe the particle phase composition after different evaporation times.

In this study we investigated the volatility of SOA particles formed from α-pinene at different oxidation levels with a combination of isothermal evaporation and thermal desorption. In addition, we monitored the evolution of the chemical composition of the residual particle after evaporation using FIGAERO–CIMS. Special focus was on the role of particulate water in the evaporation behaviour to determine whether water simply affected the rate transfer through the particles or also induced chemical reactions in the particles. Understanding particle phase processes is crucial to improving our ability to model SOA formation and to predict its behaviour in the atmosphere.

2 Methods

2.1 Measurements

The experiments were conducted in the same fashion as described in Yli-Juuti et al. (2017) with the main difference that here SOA was formed in a potential aerosol mass reactor (PAM; Aerodyne Research Inc., Kang et al., 2007; Lambe

et al., 2011) through ozonolysis and photooxidation of α-pinene instead of pure ozonolysis. A schematic of the experimental set-up is shown in Fig. S1 in the Supplement. α-Pinene vapour was introduced to the PAM reactor by flowing nitrogen over a vial of α-pinene ($\geq 98\,\%$ purity, Sigma Aldrich) placed in a diffusion source resulting in a mixing ratio of 190 parts per billion by volume (ppb). The α-pinene mixing ratio input to the PAM reactor was 190 ppb as monitored with a high-resolution time-of-flight proton transfer reaction mass spectrometer (PTR-MS, Ionicon model 8000). Concentrations of α-pinene were checked periodically at the outlet of the PAM reactor and were < 1 ppb for all settings (i.e. the precursor reacted completely). The PAM reactor was operated at a constant temperature of 27 °C and RH of 40 %. Hydroxyl radicals (OH) were formed from ozone (O_3) photolysis and reaction of the generated $O(^1D)$ with water vapour inside the PAM reactor. The O_3 concentration and the irradiation level in the PAM reactor were varied to create SOA with a range of effective oxidation ages (see Tables 1 and S1). The polydisperse SOA was characterized with a scanning mobility particle sizer (SMPS; TSI Inc., model 3082+3775) and a high-resolution time-of-flight aerosol mass spectrometer (AMS; Aerodyne Research Inc., DeCarlo et al., 2006).

To conduct the isothermal evaporation measurements, two nano differential mobility analysers (NanoDMAs, TSI Inc., model 3085) were used in parallel to select a narrow distribution of monodisperse particles (mobility diameter 80 nm). Two NanoDMAs were utilized to double the available sample flow without compromising on the sheath-to-sample-flow ratio. Each NanoDMA was operated with an open loop sheath flow, and the residence time inside the NanoDMA was ≤ 0.3 s, which limits the diffusional mixing of gas phase compounds into the selected sample flow. This led to a high dilution of the gas phase compounds (by more than 1 order of magnitude) and resulted in a sudden shift from the gas–particle equilibrium at the NanoDMA outlet, which initiated the particle evaporation. Due to some length of tubing always required for sampling, the shortest particle evaporation time, i.e. the minimum time between exiting the NanoDMA and reaching subsequent measurement devices, was 2 s. Evaporation times of up to 160 s were achieved by simply adding tubing to the sample line and/or reducing the sample flow. Size and composition of the size-selected particles were monitored using an SMPS, an AMS, and a FIGAERO (Aerodyne Research Inc.; Lopez-Hilfiker et al., 2014) in combination with a CIMS (Aerodyne Research Inc.; Lee et al., 2014) using iodide as reagent ion. The overall RH during the evaporation experiment was controlled with the sheath flow of the NanoDMAs at three different levels: dry (RH $< 2\,\%$), RH40 %, and RH80 %. For RH40 % and RH80 %, the sheath flow was humidified with a Nafion humidifier (Permapure, model PD-200T).

Longer evaporation times, ranging from 0.5 to 11 h, were achieved by passing the sample flow into a 100 L cylindrically shaped stainless-steel chamber (RTC), which had an inlet at the top and an outlet at the bottom. Our earlier study showed that the stainless-steel walls of the evaporation chamber act as nearly perfect sinks for the compounds evaporating from the particles (Yli-Juuti et al., 2017). Before each evaporation experiment, the NanoDMAs, connected tubing, and RTC were flushed for at least 12 h with clean air at the RH of the next experiment. This ensured that all parts of the system had adjusted to the new conditions. RTC experiments were initiated by adding monodisperse SOA through the top inlet for 20 min while displacing clean air, which exited via the bottom outlet. At the end of filling the RTC, the average particle number concentration was 200–1500 cm^{-3} and the average particle mass concentration was 0.1–0.6 $\mu\mathrm{g\,m}^{-3}$. Then the chamber was closed off and periodically opened again to sample for 9 to 15 min intervals with the SMPS and AMS. Clean air with the same RH was admitted into the chamber during sampling intervals to maintain constant pressure and humidity, with corresponding dilution factors of typically 1.2 or less. As we base our analysis on changes in measured particle size, and not on the change in total particle mass, the particle losses and further dilution only limit the number of times it is possible to sample from the RTC. The size selection unit, the RTC, and all particle phase measurement instruments were located in a temperature-controlled room (21 °C) to minimize the effect of ambient temperature fluctuations on particle evaporation and on RH. For the RH80 % experiments, the closed-loop sheath flow of the SMPS was also humidified to ensure that the RH stayed within $\pm 2\,\%$ between size selection, evaporation, and size measurements.

For FIGAERO–CIMS measurements, the above-described procedure had to be adjusted to accommodate the need for higher particle mass loadings: (1) "fresh" samples were collected directly after size selection for 20 or 30 min; (2) RTC fill times were increased from 20 to 75 min; and (3) the FIGAERO–CIMS sampled the remaining SOA particles in the RTC once after 3 to 4 hours of evaporation (data labelled "RTC" in the following). The upper limit of collected mass was estimated from the particle mass concentration and sampling time. Collected particulate material was 140–260 ng for fresh and 20–70 ng for RTC samples (Table S3). Due to the collection time needed, the fresh filter sample contained particles which had been on the filter for 0 to 20 or 30 min. As the particle evaporation starts when the gas phase is diluted in the NanoDMAs and no new particle–gas-phase equilibrium can be reached, the evaporation continues while particles are being deposited on the FIGAERO filter. Thus, some volatile compounds may have already evaporated before the thermal desorption begins and cannot be captured with this method.

2.2 Data analysis

The SMPS data were inverted with the Aerosol Instrument Manager software (TSI). To check the selected sizes of the NanoDMAs, ammonium sulfate particles, which are non-

Table 1. Average oxidation state and average molecular formula derived from FIGAERO–CIMS and AMS measurements.

OH exposure	Instrument			$\overline{\mathrm{O:C}}$	$\overline{\mathrm{H:C}}$	$\overline{\mathrm{Osc}}$	Average composition
Low	AMS			0.53	1.53	−0.46	
	FIGAERO	dry	fresh	0.66	1.62	−0.30	$C_{9.7}H_{16.0}O_{5.8}$
			RTC	0.68	1.63	−0.28	$C_{10.8}H_{17.9}O_{6.8}$
		RH80 %	fresh	0.68	1.62	−0.25	$C_{10.2}H_{16.8}O_{6.5}$
			RTC	0.71	1.61	−0.20	$C_{10.6}H_{17.4}O_{6.8}$
Medium	AMS			0.69	1.42	−0.05	
	FIGAERO	dry	fresh	0.75	1.52	−0.03	$C_{9.0}H_{14.0}O_{6.3}$
			RTC	0.74	1.53	−0.04	$C_{9.3}H_{14.4}O_{6.4}$
		RH80 %	fresh	0.76	1.52	0.00	$C_{9.0}H_{14.0}O_{6.4}$
			RTC	0.77	1.55	−0.02	$C_{9.8}H_{15.5}O_{6.9}$
High	AMS			0.96	1.26	0.63	
	FIGAERO	dry	fresh	0.84	1.46	0.23	$C_{8.2}H_{12.3}O_{6.3}$
			RTC	0.83	1.47	0.19	$C_{8.4}H_{12.7}O_{6.3}$
		RH80 %	fresh	0.85	1.43	0.27	$C_{8.0}H_{11.7}O_{6.1}$
			RTC	0.84	1.46	0.22	$C_{8.5}H_{12.8}O_{6.2}$

volatile at room temperature, were sampled for each sheath flow setting. This actual measured size was then used as "set" size. The evaporation factor (EF) was calculated as the ratio of the measured sizes (D_{meas}) and the set sizes (D_{set}):

$$\mathrm{EF} = \frac{D_{\mathrm{meas}}}{D_{\mathrm{set}}}. \quad (1)$$

Assuming spherical particles, the volume fraction remaining (VFR) can be calculated as

$$\mathrm{VFR} = \mathrm{EF}^3. \quad (2)$$

In the following, the evolution of VFR as a function of the residence time in the RTC will be called "evapogram".

The high-resolution AMS data were analysed with the SQUIRREL (version 1.59D) and PIKA toolkits (version 1.19, DeCarlo et al., 2006). The improved parameterization from Canagaratna et al. (2015) was used to perform the elemental analysis which yields average oxygen-to-carbon and hydrogen-to-carbon ratios for the sampled SOA ($\overline{\mathrm{O:C}}$ and $\overline{\mathrm{H:C}}$ ratios). The average carbon oxidation state, $\overline{\mathrm{OSc}}$, was calculated following the approximation in Kroll et al. (2011):

$$\overline{\mathrm{OSc}} = 2 \cdot \overline{\mathrm{O:C}} - \overline{\mathrm{H:C}}. \quad (3)$$

Raw data from FIGAERO desorption temperature scans were processed using tofTools, a MATLAB-based software package developed for analysing ToF-CIMS data (Junninen et al., 2010). The raw data were averaged to provide average mass spectra spaced by 20 s, and baseline correction was applied before fitting the high-resolution mass spectral data. Details about the magnitude and impact of the instrument background (filter blank measurements) on our analysis are discussed in the Supplement (Sect S1.2). The average $\overline{\mathrm{O:C}}$ and $\overline{\mathrm{H:C}}$ ratios and composition were calculated as signal weighted sums from the elemental composition defined by the sum formulas. Details are given in the Supplement (Sect. S1.3).

Thermal desorption of a FIGAERO filter sample via a nitrogen gas flow heated from 25 to 210 °C yields thermograms, i.e. the total or selected ion count rate vs. desorption temperature. The sum over all ions (except the reagent ions) will be referred to as "total thermogram". Where noted, we normalized the thermograms with the time integral of the respective total thermogram to help compare thermogram shapes. We characterize the thermograms mainly by the temperature of peak desorption (thermogram maximum, T_{max}), as is common practice (Huang et al., 2018; Lopez-Hilfiker et al., 2014). We also use the median desorption temperature (T_{median}), i.e. the temperature dividing the thermogram into two equal areas. This value may reflect the overall desorption characteristics better than T_{max} because thermograms (individual or total) may feature poorly defined peaks and contain large fractions of signal at temperatures very different from (typically higher than) T_{max}. Integrated normalized FIGAERO mass spectra were obtained by calculating the time integral of each ion's count rate over the full desorption cycle and then normalizing to the sum over all non-reagent ions. The above-described normalization procedures were designed to account for differences between experiments in the amount of particle mass collected on the filter, and it allows us to directly compare the thermogram shapes and the relative contributions of certain ions between different experiments while not affecting T_{max} and T_{median}.

In the CIMS instrument, the major class of ions were clusters of iodide (I^-) and organic compounds (M) in the sample flow, detected as $[M+I]^-$. In this study, the voltage settings in the CIMS's ion guidance elements led to a relatively

high level of ion declustering, which included the formation of ions not containing iodide and with an odd number of hydrogen atoms likely dominated by $[M+I]^-$ ions that lost HI resulting in $[M-H]^-$ and by other fragmentation processes described in the Supplement. These "declustered ions" accounted for 15 %–25 % of the total ion signal (see Supplement Sect. S1.1 for further information). We analysed the data treating the declustered and adduct ions separately. However, for plotting the integrated spectra of all observed species, all ions were included, and it was assumed that deprotonation to form $[M-H]^-$ was the only declustering reaction. The observed ion formulas were converted into neutral compound formulas by adding the mass of H^+ for $[M-H]^-$ or subtracting the mass of I^- for $[M+I]^-$.

3 Results and discussion

3.1 SOA chemical composition

For the low, medium, and high OH exposure in the PAM reactor, the $\overline{O:C}$ ratios derived from AMS data of size-selected α-pinene SOA were 0.53, 0.69, and 0.96, respectively. These $\overline{O:C}$ values are representative of fresh and aged ambient SOA in monoterpene-rich environments (Aiken et al., 2008; Ng et al., 2010; Ortega et al., 2016). From here on we refer to these three cases as low-, medium-, or high-$\overline{O:C}$ experiments. Overall, FIGAERO and AMS measurements show the same trends in the $\overline{O:C}$ ratios; however, the AMS derived values show a larger difference in $\overline{O:C}$ ratios between the low and high OH exposures (see Table 1). With increasing overall $\overline{O:C}$, the FIGAERO–CIMS mass spectra show an increasing fraction of monomers (defined as compounds with 10 or fewer C atoms, i.e. compounds derivable from a single monoterpene precursor, roughly corresponding to masses < 300 Da) as shown in Fig. S2. In the high-$\overline{O:C}$ case, there is a strong increase in the contribution of smaller molecules with high O : C (see Figs. S2 and S5c), due to the dominance of fragmentation reactions at high OH exposure (Lambe et al., 2012; Palm et al., 2016). It was not expected to find such a large contribution of low molecular weight (MW) compounds such as $C_3H_4O_4$ at 104 Da (detected mostly as $[C_3H_4O_4+I]^-$) or $C_4H_6O_4$ at 118 Da (detected mostly as $C_4H_5O_4^-$) in the particle phase. Given that the majority of compounds of this size should be too volatile to stay in the particle phase, a likely cause for the appearance of these low-MW compounds is thermal decomposition of higher-MW compounds during the desorption from the FIGAERO filter. Then the increase in low-MW compounds at higher $\overline{O:C}$ indicates that particulate organics become overall more susceptible to thermal decomposition when SOA is formed under higher OH exposure in the PAM reactor. However, at this point we cannot determine if the increased detection of these low-MW compounds is driven by a higher degree of fragmentation reactions at high OH exposure in PAM or the thermal decomposition of higher-MW compounds in the FIGAERO.

3.2 Linking isothermal evaporation and thermal desorption in FIGAERO

Plots showing the VFR of α-pinene SOA as a function of residence time (i.e. evapograms) are presented in Fig. 1a–c for the three $\overline{O:C}$ cases. The dependence of the evaporation rate on RH follows the trends reported in earlier studies: at dry conditions, the evaporation is substantially slower than at RH40 % and RH80 % conditions, for all oxidation levels (Vaden et al., 2011; Wilson et al., 2015; Yli-Juuti et al., 2017). In the studies of Wilson et al. (2015) and Yli-Juuti et al. (2017), the slower evaporation under dry conditions was related to increased diffusional limitations, due to higher viscosity than under humid conditions. We note that the evaporation rate at RH40 % is higher than at RH80 % (Fig. 1a–c). This observation is explained by the solution or Raoult effect, i.e. the decrease in the equilibrium vapour pressure over more dilute humidified particles, as demonstrated by the evaporation modelling presented in the Supplement (Sect. S1.4 and Fig. S4c) and in the study of Yli-Juuti et al. (2017). This indicates that diffusion limitations do not play a major role in aerosol evaporation at room temperature when the RH is at atmospherically relevant levels.

The dependence of the isothermal evaporation rate on the oxidation level is reported for the first time in this study. As the $\overline{O:C}$ ratio of the produced SOA increases, the overall rate of evaporation decreases. After 6 h of evaporation, SOA particle volume decreased by only 10 % under dry and ~ 40 % under RH40 % conditions in the high-$\overline{O:C}$ case. For the low-$\overline{O:C}$ case, the corresponding numbers are 40 % (dry) and 60 % (RH40 %). These trends suggest that the more highly oxygenated SOA is less volatile, as expected from thermodenuder measurements (e.g. Donahue et al., 2012).

In Fig. 1d–f, we show FIGAERO total thermograms (signal-weighted sum of the thermograms for all individual compositions) measured at different time periods during isothermal evaporation at dry and RH80 % conditions. The FIGAERO filter sampling periods of each thermogram are marked by coloured boxes in the evapograms in Fig. 1a–c. Fresh SOA thermograms were shifted to higher temperatures with increasing $\overline{O:C}$, both at dry and RH80 % conditions. For the low-, medium-, and high-$\overline{O:C}$ cases, the peak evaporation temperatures, T_{max}, were 50, 60, and 71 °C under dry conditions and 61, 70, and 92 °C at RH80 %. These shifts are in line with our isothermal evaporation measurements suggesting a decreasing vapour pressure of SOA compounds with increasing $\overline{O:C}$ and are also consistent with a larger role of thermal decomposition during desorption, as indicated by the increased contribution of small highly oxidized molecules discussed above.

When examining the T_{max} of fresh SOA in more detail, it can be seen that at a fixed $\overline{O:C}$ ratio,

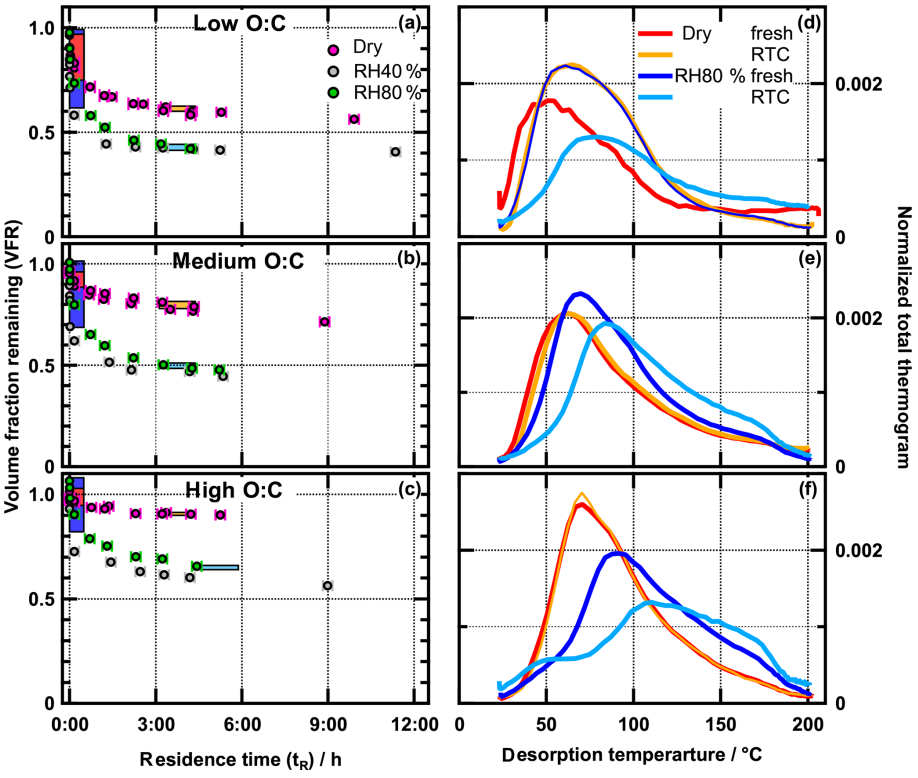

Figure 1. Evapograms **(a–c)** and total thermograms **(d–f)** for low $\overline{\mathrm{O:C}}$ **(a, d)**, medium $\overline{\mathrm{O:C}}$ **(b, e)**, and high $\overline{\mathrm{O:C}}$ **(c, f)**. Coloured boxes in evapograms indicate FIGAERO sampling time. Thermograms are normalized with total signal area.

$T_{\mathrm{max}}(\mathrm{RH80\,\%}) > T_{\mathrm{max}}(\mathrm{dry})$. This trend can be explained with the evapogram measurements: the particles evaporate more quickly at higher humidity as seen in the evapograms; hence a larger fraction of higher-volatility compounds is already lost during the 20 or 30 min period of FIGAERO filter collection before the thermal desorption. Thus, the collected residual particles are less volatile, characterized by a higher T_{max}. When sampling from the RTC after longer evaporation time, the VFR is even lower (i.e. a larger volume fraction has been lost due to evaporation). Correspondingly, the thermogram peak is shifted further toward higher temperatures in all studied $\overline{\mathrm{O:C}}$ cases, again indicating an increasing fraction of lower volatility compounds in the residual particles.

Only for the high-$\overline{\mathrm{O:C}}$ case is an absolute increase in the amount of material desorbing at $> 150\,^{\circ}\mathrm{C}$ also observed when comparing the fresh SOA at RH80 % and dry conditions (see non-normalized thermograms in Fig. S3). Because the estimated organic mass loadings on the filter were comparable, this indicates that when the high-$\overline{\mathrm{O:C}}$ particles, generated in the PAM at RH40 %, are exposed to elevated RH (RH80 %), compounds with high desorption (and/or decomposition) temperatures are formed in the particle phase. We will corroborate this suggestion below.

In Fig. 2, VFR is plotted as a function of T_{median}. The figure visualizes two phenomena: generally, T_{median} and VFR are positively correlated with the $\overline{\mathrm{O:C}}$ ratio. As laid out above, this observation is explained by the negative relationship of $\overline{\mathrm{O:C}}$ and volatility. At the same time, however, for a certain $\overline{\mathrm{O:C}}$ ratio, VFR and T_{median} are negatively correlated. As mentioned above, this can be explained by the properties of the residual particles after a certain period of evaporation. We will explore this further now, together with the possibility of water-induced particle phase reactions.

In low- and medium-$\overline{\mathrm{O:C}}$ cases, the trends of the VFR vs. T_{median} behaviour are comparable, and the increase in T_{median} is clearly associated with the decreasing VFR, regardless of the RH and hence water content of the particles. The behaviour in the high-$\overline{\mathrm{O:C}}$ case is different and cannot be explained by the evaporation of higher-volatility material alone. For the high-$\overline{\mathrm{O:C}}$ cases, T_{median} of fresh SOA increases from 86 to 104 °C between the dry and RH80 % case despite a change of only 9 % in VFR. Combining this observation with the fact that there is an absolute increase in material desorbed $> 150\,^{\circ}\mathrm{C}$ suggests that in the high-$\overline{\mathrm{O:C}}$ cases the particle phase water alters the SOA particle composition, resulting in an increased resistance to thermal desorption or decomposition (i.e. large change in T_{median}) even if the particles lost only a small volume fraction due to isothermal evaporation (i.e. small change in VFR). We note that these composition changes are not clearly visible in the average $\overline{\mathrm{O:C}}$ or $\overline{\mathrm{OSc}}$ values (see Table 1), and we will elaborate on possible reactions in Sect. 3.4.

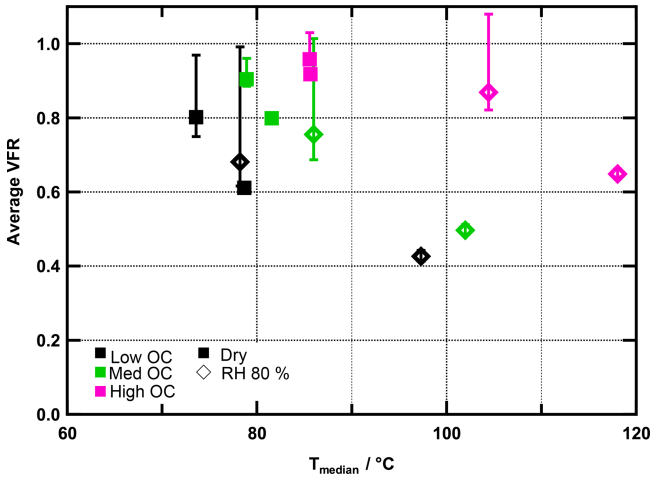

Figure 2. Average VFR during FIGAERO sampling vs. median desorption temperature (T_{median}) for all experiments. Colours indicate $\overline{O:C}$ ratios. Measurements under dry conditions are marked with squares, those under RH80 % with diamonds. Error bars indicate minimum and maximum VFR observed during sampling time.

3.3 Residual particle composition during evaporation under dry and humid conditions

During the evaporation the initial $\overline{O:C}$ changed very little (Table 1). This is consistent with earlier observations reported by Yli-Juuti et al. (2017), who interpreted this as evidence for the presence of low-volatility oligomers in the particles. These should have very similar O : C ratios to the corresponding monomers. To examine detailed changes in particle composition along the isothermal evaporation at dry conditions, we show the difference between the normalized integrated FIGAERO–CIMS mass spectra measured at the beginning (fresh) and after 3 to 4 h of isothermal evaporation (RTC) in Fig. 3 (panels a and c for the low- and high-$\overline{O:C}$ case, respectively). To investigate the changes in composition due to the humidification, panels (b) and (d) in Fig. 3 show the differences between FIGAERO–CIMS mass spectra measured at dry and RH80 % conditions in the beginning (fresh SOA) of the isothermal evaporation. As the low-$\overline{O:C}$ SOA particles evaporate (Fig. 3a), a clear decrease in the fractional contribution of low-MW compounds (< 300 Da, $\sim$ monomers) is observed, whereas the contribution of compounds with MW > 300 Da (predominantly dimers) increases. Correspondingly, the contribution of compounds with $C > 10$ increases with evaporation, while that of $C < 7$ decreases. The relative contributions of intermediate masses are more likely to increase during evaporation if they contain more oxygen atoms (Fig. S5a). It is not possible to tell if these C_7–C_9 compounds really remain in the particles or if they are simply thermal decomposition products of the more abundant dimers. However, this suggests that lighter and/or less oxidized molecules are indeed lost more readily during isothermal evaporation in the RTC than the heavier dimers and more oxidized compounds, which are expected to have very low vapour pressure (Mohr et al., 2017). The more detailed investigation of changes in the mass spectra (Fig. S5a and b, c and d) shows some indications of particle phase water-driven chemical transformation both for low and medium $\overline{O:C}$, but the differences are not as clear as in the high-$\overline{O:C}$ case (Fig. S5e and f). It should be noted that in the low-$\overline{O:C}$ case the molecules affected by particle phase water account for approximately 10 % of the total signal. Therefore overall, the enhanced evaporation during FIGAERO filter collection under wet conditions is very similar to the evaporation happening under dry conditions in the RTC, and the water-driven chemistry plays only a minor role in low-$\overline{O:C}$ cases. This points to particulate water mainly reducing the viscosity and thus accelerating the mass transport in the particles as described in Yli-Juuti et al. (2017). In the high-$\overline{O:C}$ case (Fig. 3c), there is also a relative decrease in masses $<$ 300 Da with isothermal evaporation under dry conditions, but the overall picture is less clear, consistent with very few changes in VFR and in the sum thermogram shape in this case (high-$\overline{O:C}$ dry; Fig. 1c and d). Conversely, humidifying fresh high-$\overline{O:C}$ SOA particles leads to an increase in masses $<$ 200 Da (Fig. 3d), which is a very different behaviour compared to the low-$\overline{O:C}$ cases (Fig. 3a and b) or to the isothermal evaporation of high-$\overline{O:C}$ SOA particles at dry conditions (Fig. 3c). Again, this suggests changes in particle composition upon humidification in the high-$\overline{O:C}$ case. The mass fraction of compounds showing water-driven chemical transformation makes up approximately 30 % of the signal in high-$\overline{O:C}$ cases. This should be taken into account when process level modelling of systems comparable to the high-$\overline{O:C}$ case is considered.

To gain a better understanding of these compositional changes related to humidification, we examined the individual desorption thermograms of a few major ions (Fig. 4): $C_4H_3O_6^-$ (a), $C_5H_5O_6^-$ (b), and $[C_{10}H_{14}O_6+I]^-$ (c), which show an increase when the particles are humidified, and $[C_{10}H_{16}O_7+I]^-$ (d), which exhibits a net decrease in the high-$\overline{O:C}$ RH80 % case. In the low-$\overline{O:C}$ case, only small shifts (0–6 °C) in T_{max} are observed for all four ions when RH is increased. This and the changes in the thermogram shape are consistent with the behaviour observed for the total thermograms, described and explained above. In the high-$\overline{O:C}$ case, only a small shift in T_{max} is visible for $[C_{10}H_{16}O_7+I]^-$ as well (Fig. 4d), but for the other ions (Fig. 4a–c), we see a clear shift in the thermograms, with T_{max} increasing for the humidified case from 63 to 84, 67 to 84, and 70.5 to 95.5 °C for $C_4H_3O_5^-$, $C_5H_5O_6^-$, and $[C_{10}H_{14}O_6+I]^-$, respectively. This behaviour is unique for the high-$\overline{O:C}$ case. The collected organic mass loading on the FIGAERO filter was comparable (within 20 %) for dry and RH80 % conditions. Thus, the apparent shift in T_{max} for $[C_{10}H_{16}O_7+I]^-$ (Fig. 4d) could be explained by volatile material (with lower T_{max}) leaving the particles during evaporation in the same way as in the low-$\overline{O:C}$ case. But for the

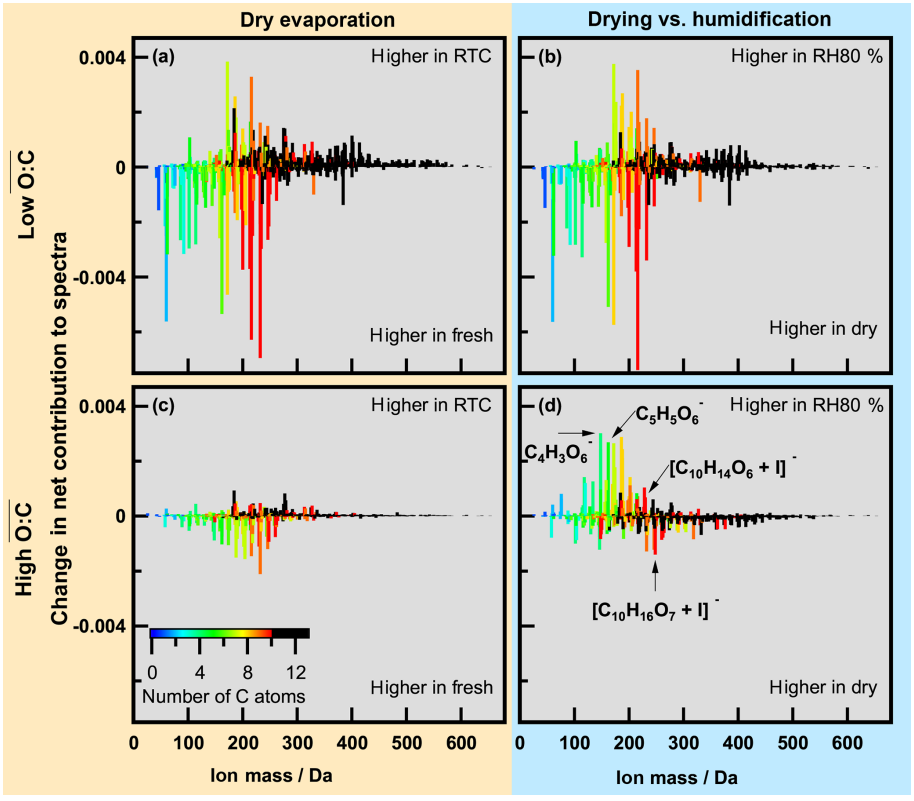

Figure 3. Changes in normalized spectra for low $\overline{O:C}$ **(a, b)** and high $\overline{O:C}$ **(c, d)**. **(a, c)** Changes due to evaporation under dry conditions; **(b, d)** changes between dry and wet conditions. Colour indicates number of C atoms in the identified ions (black corresponds to C number larger than 10). Mass spectra were normalized by total signal, and then the difference was calculated.

ions in Fig. 4a–c, new material with higher T_{max} has clearly been formed. This must be triggered by the presence of larger amounts of water under RH80 % conditions, via either of two scenarios: (a) there are two different isomers dominating the thermogram for the respective composition at dry vs. RH80 % conditions and the desorption temperatures of these isomers differ considerably; (b) the individual thermograms are dominated by the evaporation of monomers at dry conditions (or the decomposition of relatively unstable larger compounds into the observed compositions) but by thermal decomposition of (more stable) larger compounds at RH80 % conditions. Isomers with higher T_{max} may be formed and at the same time the isomers with lower T_{max} are lost, either through reactions or through more rapid evaporation or decomposition than in the dry case. Alternatively, other low-volatility material is formed that thermally decomposes into the observed compounds. With this data set, we cannot exclude either of these two explanations, but the very broad shape of the RH80 % thermogram for $[C_{10}H_{14}O_6 + I]^-$ at high temperatures (see Fig. 4c) is an indication that at least for this ion the mechanism including thermal decomposition is more likely.

3.4 Possible aqueous phase processes

The FIGAERO–CIMS combined composition and thermogram measurements provided insights into the chemical composition of the residual SOA particles after humidification and/or evaporation. The observed changes in the high-$\overline{O:C}$ RH80 % case can only be explained by the formation of low-volatility compounds in the particle phase and removal of the corresponding higher-volatility compound at the same elemental composition. Thus, we briefly consider possible processes that can explain the formation of these less volatile and/or thermally more stable compounds in highly oxidized SOA at 80 %RH in the sections below.

Liquid water can have several effects on particle chemical composition. First, water may initiate hydration and hydrolysis reactions. Second, water may catalyse reactions between organics (e.g. Dong et al., 2018; Kaur and Vikas, 2017). Third, water reduces SOA viscosity (Hosny et al., 2016; Renbaum-Wolff et al., 2013), thereby reducing diffusional limitations to particle phase reactions. Whereas hydrolysis generally reduces the average molecular weight of the reactants, other processes in principle enable the formation of higher-MW but thermally labile products. Water may also enhance the uptake of O_3 from the gas phase (Berke-

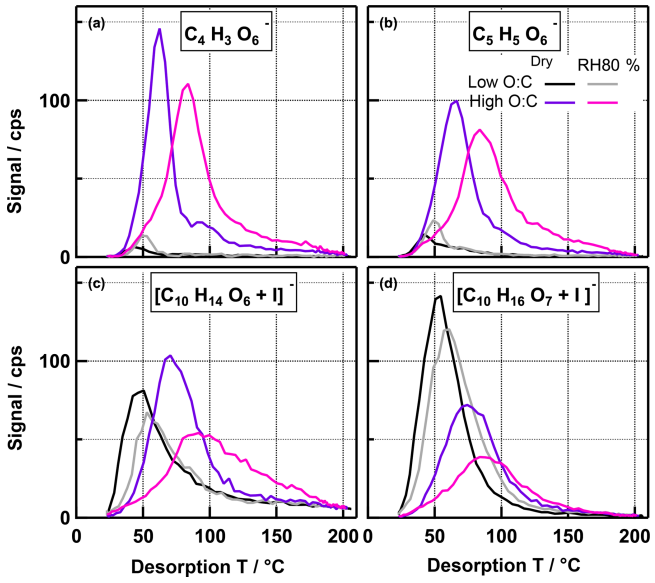

Figure 4. Non-normalized thermograms for four single ions for low- and high-$\overline{\mathrm{O:C}}$ cases. Ions in panels **(a)**, **(b)**, and **(c)** showed a net increase in the RH80 % case, while the ion in panel **(d)** had a net decrease in the high-$\overline{\mathrm{O:C}}$ ratio case. Note that the amount of SOA mass collected on the FIGAERO filter was 5 %–20 % higher in the RH80 % cases and is also different between the $\overline{\mathrm{O:C}}$ cases.

meier et al., 2016; Gallimore et al., 2011), but as the average $\overline{\mathrm{O:C}}$ ratio did not change with increased RH, any oxidizing reaction can be excluded.

3.4.1 Homolysis of peroxy bonds (O-O) in organic peroxides (ROOH)

Organic hydro peroxides (ROOH) species are known to occur in SOA (Sanchez and Myers, 2000) and have been observed to decompose in the particle phase on timescales < 1 h under dark and wet (~ 40 % RH) conditions (Krapf et al., 2016). Liquid-water-induced homolysis of the O-O bond in ROOH yields alkoxy (RO•) radicals that may initiate oligomerization reactions (Tong et al., 2016). Under dry conditions organic (hydro-)peroxides (ROOH) may be more stable and persist in the particle phase but decompose upon desorption and be detected as RO or R fragments in FIGAERO–CIMS. The oligomers (RO-OR) formed in the RH80 % case will most likely have a lower volatility than the educts, but they may still be prone to decompose upon desorption due to their relatively weak O-O bond. Thus, they would also be detected as RO or R fragments but at a higher apparent desorption T than the monomers.

3.4.2 Addition and accretion reactions

As generally no significant change in the $\overline{\mathrm{O:C}}$ ratio was observed, only non-oxidative oligomerization ("accretion") reactions such as aldol addition (aldehyde + aldehyde/ketone, (hemi)acetal formation (aldehyde/ketone + alcohol), peroxy(hemi)acetal formation (aldehyde/ketone + peroxide), and esterification (alcohol + (per)acid) are likely (Herrmann et al., 2015; Kroll and Seinfeld, 2008). All these reactions have reaction pathways which are enhanced by the presence of an acid catalyst in the aqueous phase. Thus, the complete lack of water in dry particles may sufficiently prevent these reactions preserving the monomer educts. To explain our results, there would have to be an additional factor in the high-$\overline{\mathrm{O:C}}$ case, e.g. a much higher fraction of organic peroxides and peroxy acids that form peroxy hemiacetals instead of the more stable hemiacetals. These peroxy hemiacetals would then most likely decompose at a higher temperature than the desorption temperature of the educts but be detected as low-MW compounds, while hemiacetals may be stable enough to be detected without decomposition.

4 Summary and conclusions

We present the first study linking the oxidative age of α-pinene SOA, quantified by the $\overline{\mathrm{O:C}}$ ratio, and isothermal evaporation, for a wide range of RH (< 2 % to 80 % RH). By utilizing an RTC at room temperature and FIGAERO–CIMS as a thermal desorption technique, we were able to determine SOA volatility independent of artefacts due to thermal decomposition. At the same time, the thermal desorption data gave insights into the possible particle phase chemistry during evaporation especially under wet conditions. It has to be kept in mind though that the particles measured with FIGAERO–CIMS are always the residual particles after minutes to hours of isothermal evaporation either during filter collection or in the RTC.

We found a strong correlation between increased oxidation level of the initial particles and lower particle volatility expressed by less isothermal evaporation and higher T_{max} values in FIGAERO–CIMS thermograms. This suggests that atmospheric particles become more resistant to evaporation as they age over time, possibly increasing their lifetime in the atmosphere. This also means that the oxidation level needs to be kept in mind when investigating aerosol volatility in chamber or flow tube experiments. For example, for deriving VBS distributions from smog chamber yield experiments, care has to be taken that the oxidation level stays in the same range for all SOA mass loadings.

Increasing RH enhances particle evaporation as described in previous studies (Wilson et al., 2015; Yli-Juuti et al., 2017) while the T_{max} values of the residual particles was also increased. The observed changes under wet conditions in the low- and medium-$\overline{\mathrm{O:C}}$ cases could be explained with the lowering of the particle phase viscosity alone, but there were some indications for water-induced changes in the chemical composition. However, the compounds exhibiting these changes accounted for approximately 10 % of the detected mass, and thus these changes are minor compared to the shift

in composition due to evaporation. In the high-$\overline{\mathrm{O:C}}$ case, strong evidence for aqueous phase reactions were found with approx. 30 % of the mass being affected. Further evidence for different processes happening in the high-$\overline{\mathrm{O:C}}$ case was found in the relationship between the isothermal evaporation (as VFR) and thermal desorption (as T_{median}). It was similar for the low- and medium-$\overline{\mathrm{O:C}}$ cases and independent of the RH. For the high-$\overline{\mathrm{O:C}}$ case, VFR changed very little during the isothermal evaporation at RH80 %, while a large increase in T_{median} was observed. We attribute this different behaviour to the overall different chemical composition and most likely much higher concentration of organic peroxides (ROOH) in the high-$\overline{\mathrm{O:C}}$ case. We hypothesize that water-induced (1) homo- and heterolytic breaking of weaker O-O bonds present in ROOH and/or (2) the formation of peroxy hemiacetals may form thermally labile oligomers with enhanced yields in high-$\overline{\mathrm{O:C}}$ SOA at RH80 %. To further verify this explanation, direct measurements of the organic peroxide concentration for the different $\overline{\mathrm{O:C}}$ cases would be needed but were not part of this study.

Our data suggest that the degree of thermal decomposition in FIGAERO–CIMS and its impact on derived volatility most likely depends on the initial composition of the SOA and may be changed by the presence of particulate water. Another recent study has shown that chemical composition changes induced by the presence of acidic inorganic seeds may also produce low-volatility, but thermally instable compounds, which can only be detected as their decomposition products with FIGAERO–CIMS (Riva et al., 2019). This highlights the benefit of isothermal methods for studying SOA particle volatility.

The SOA particles studied here had $\overline{\mathrm{O:C}}$ ratios comparable with atmospheric SOA (typically in the 0.3–1.0 range, e.g. Aiken et al., 2008; Ng et al., 2010; Ortega et al., 2016), but the high-$\overline{\mathrm{O:C}}$ case in particular was probably not fully representative of atmospheric SOA as extremely high O_3 and OH radical exposure levels were applied in the PAM reactor. This may have led to a larger degree of fragmentation of the precursor molecules than expected in the atmosphere, i.e. the particle phase is dominated by $C_{4–6}$ compounds instead of the expected $C_{8–10}$ compounds and their oligomers (Lambe et al., 2012). Some of the suggested aqueous phase reactions may be more likely for short carbon chain compounds (e.g. glyoxal like chemistry). Also, we can only speculate that there was a larger fraction of peroxy compounds in the particles in the high-$\overline{\mathrm{O:C}}$ case as we had no direct measurement. However, recent studies with ambient SOA have shown that these particles can contain large amounts of environmental persistent radicals and are prone to form C- and O-centred organic radicals when wetted, which can start oligomerization reactions in the particle phase (Arangio et al., 2016). So, although we formed the high-$\overline{\mathrm{O:C}}$ SOA in a PAM reactor under extreme conditions, the particles produced and their behaviour allowed us to study processes which are most likely atmospherically relevant. Hence, our study substantially increases the understanding of complicated and inadequately studied particle phase processes and the results highlights the importance of water-driven chemistry in SOA.

Data availability. The data set is available upon request from Angela Buchholz (angela.buchholz@uef.fi) or Annele Virtanen (annele.virtanen@uef.fi).

Supplement. The supplement related to this article is available online at: https://doi.org/10.5194/acp-19-4061-2019-supplement.

Author contributions. AV, TYJ, and AB designed the study; AB, ATL, AY, ZL, CF, EK, LH, CM, and SAN performed the measurements; AB, AY, ZL, EK, LH, WH, CM, DRW, SAN, TYJ, SS, and AV participated in data analysis and/or interpretation; OPT, OL, and TYJ performed the model calculations; AB, AV, and SS wrote the paper.

Competing interests. The authors declare that they have no conflict of interest.

Acknowledgements. We thank the European Research Council (ERC StG QAPPA 335478), the Academy of Finland Centre of Excellence program (decision 307331), the Academy of Finland (grants 299544, 317373 and 310682), and the University of Eastern Finland Doctoral Program in Environmental Physics, Health and Biology for financial support. Sergey A. Nizkorodov acknowledges the Fulbright Finland Foundation and the Saastamoinen Foundation that funded his visit to the University of Eastern Finland. Andrew T. Lambe acknowledges support from the Atmospheric Chemistry Program of the US National Science Foundation under grant no. AGS-1537446.

Review statement. This paper was edited by Barbara Ervens and reviewed by two anonymous referees.

References

Aiken, A. C., DeCarlo, P. F., Kroll, J. H., Worsnop, D. R., Huffman, J. A., Docherty, K. S., Ulbrich, I. M., Mohr, C., Kimmel, J. R., Sueper, D., Sun, Y., Zhang, Q., Trimborn, A., Northway, M., Ziemann, P. J., Canagaratna, M. R., Onasch, T. B., Alfarra, M. R., Prevot, A. S. H., Dommen, J., Duplissy, J., Metzger, A., Baltensperger, U., and Jimenez, J. L.: O / C and OM / OC Ratios of Primary, Secondary, and Ambient Organic Aerosols with High-Resolution Time-of-Flight Aerosol Mass Spectrometry, Environ. Sci. Technol., 42, 4478–4485, https://doi.org/10.1021/es703009q, 2008.

An, W. J., Pathak, R. K., Lee, B.-H., and Pandis, S. N.: Aerosol volatility measurement using an improved thermodenuder: Ap-

plication to secondary organic aerosol, J. Aerosol Sci., 38, 305–314, https://doi.org/10.1016/j.jaerosci.2006.12.002, 2007.

Arangio, A. M., Tong, H., Socorro, J., Pöschl, U., and Shiraiwa, M.: Quantification of environmentally persistent free radicals and reactive oxygen species in atmospheric aerosol particles, Atmos. Chem. Phys., 16, 13105–13119, https://doi.org/10.5194/acp-16-13105-2016, 2016.

Bergström, R., Denier van der Gon, H. A. C., Prévôt, A. S. H., Yttri, K. E., and Simpson, D.: Modelling of organic aerosols over Europe (2002–2007) using a volatility basis set (VBS) framework: application of different assumptions regarding the formation of secondary organic aerosol, Atmos. Chem. Phys., 12, 8499–8527, https://doi.org/10.5194/acp-12-8499-2012, 2012.

Berkemeier, T., Steimer, S. S., Krieger, U. K., Peter, T., Pöschl, U., Ammann, M., and Shiraiwa, M.: Ozone uptake on glassy, semi-solid and liquid organic matter and the role of reactive oxygen intermediates in atmospheric aerosol chemistry, Phys. Chem. Chem. Phys., 18, 12662–12674, https://doi.org/10.1039/C6CP00634E, 2016.

Canagaratna, M. R., Jimenez, J. L., Kroll, J. H., Chen, Q., Kessler, S. H., Massoli, P., Hildebrandt Ruiz, L., Fortner, E., Williams, L. R., Wilson, K. R., Surratt, J. D., Donahue, N. M., Jayne, J. T., and Worsnop, D. R.: Elemental ratio measurements of organic compounds using aerosol mass spectrometry: characterization, improved calibration, and implications, Atmos. Chem. Phys., 15, 253–272, https://doi.org/10.5194/acp-15-253-2015, 2015.

Cappa, C. D. and Wilson, K. R.: Evolution of organic aerosol mass spectra upon heating: implications for OA phase and partitioning behavior, Atmos. Chem. Phys., 11, 1895–1911, https://doi.org/10.5194/acp-11-1895-2011, 2011.

D'Ambro, E. L., Schobesberger, S., Zaveri, R. A., Shilling, J. E., Lee, B. H., Lopez-Hilfiker, F. D., Mohr, C., and Thornton, J. A.: Isothermal evaporation of α-pinene ozonolysis SOA: volatility, phase state, and oligomeric composition, ACS Earth Sp. Chem., 2, 1058–1067, https://doi.org/10.1021/acsearthspacechem.8b00084, 2018.

DeCarlo, P. F., Kimmel, J. R., Trimborn, A., Northway, M. J., Jayne, J. T., Aiken, A. C., Gonin, M., Fuhrer, K., Horvath, T., Docherty, K. S., Worsnop, D. R., and Jimenez, J. L.: Field-Deployable, High-Resolution, Time-of-Flight Aerosol Mass Spectrometer, Anal. Chem., 78, 8281–8289, https://doi.org/10.1021/ac061249n, 2006.

Donahue, N. M., Robinson, A. L., Stanier, C. O., and Pandis, S. N.: Coupled partitioning, dilution, and chemical aging of semivolatile organics, Environ. Sci. Technol., 40, 2635–2643, https://doi.org/10.1021/es052297c, 2006.

Donahue, N. M., Epstein, S. A., Pandis, S. N., and Robinson, A. L.: A two-dimensional volatility basis set: 1. organic-aerosol mixing thermodynamics, Atmos. Chem. Phys., 11, 3303–3318, https://doi.org/10.5194/acp-11-3303-2011, 2011.

Donahue, N. M., Kroll, J. H., Pandis, S. N., and Robinson, A. L.: A two-dimensional volatility basis set – Part 2: Diagnostics of organic-aerosol evolution, Atmos. Chem. Phys., 12, 615–634, https://doi.org/10.5194/acp-12-615-2012, 2012.

Dong, Z.-G., Xu, F., and Long, B.: The energetics and kinetics of the $CH_3CHO + (CH_3)_2NH/CH_3NH_2$ reactions catalyzed by a single water molecule in the atmosphere, Comput. Theor. Chem., 1140, 7–13, https://doi.org/10.1016/J.COMPTC.2018.07.013, 2018.

Ehn, M., Thornton, J. A., Kleist, E., Sipilä, M., Junninen, H., Pullinen, I., Springer, M., Rubach, F., Tillmann, R., Lee, B., Lopez-Hilfiker, F., Andres, S., Acir, I. H., Rissanen, M., Jokinen, T., Schobesberger, S., Kangasluoma, J., Kontkanen, J., Nieminen, T., Kurtén, T., Nielsen, L. B., Jørgensen, S., Kjaergaard, H. G., Canagaratna, M., Maso, M. D., Berndt, T., Petäjä, T., Wahner, A., Kerminen, V. M., Kulmala, M., Worsnop, D. R., Wildt, J., and Mentel, T. F.: A large source of low-volatility secondary organic aerosol, Nature, 506, 476–479, https://doi.org/10.1038/nature13032, 2014.

Gallimore, P. J., Achakulwisut, P., Pope, F. D., Davies, J. F., Spring, D. R., and Kalberer, M.: Importance of relative humidity in the oxidative ageing of organic aerosols: case study of the ozonolysis of maleic acid aerosol, Atmos. Chem. Phys., 11, 12181–12195, https://doi.org/10.5194/acp-11-12181-2011, 2011.

Goldstein, A. H. and Galbally, I. E.: Known and Unexplored Organic Constituents in the Earth's Atmosphere, Environ. Sci. Technol., 41, 1514–1521, https://doi.org/10.1021/es072476p, 2007.

Grieshop, A. P., Miracolo, M. A., Donahue, N. M., and Robinson, A. L.: Constraining the volatility distribution and gas-particle partitioning of combustion aerosols using isothermal dilution and thermodenuder measurements, Environ. Sci. Technol., 43, 4750–4756, https://doi.org/10.1021/es8032378, 2009.

Hall IV, W. A. and Johnston, M. V.: The thermal-stability of oligomers in alpha-pinene secondary organic aerosol, Aerosol Sci. Tech., 46, 983–989, https://doi.org/10.1080/02786826.2012.685114, 2012.

Hallquist, M., Wenger, J. C., Baltensperger, U., Rudich, Y., Simpson, D., Claeys, M., Dommen, J., Donahue, N. M., George, C., Goldstein, A. H., Hamilton, J. F., Herrmann, H., Hoffmann, T., Iinuma, Y., Jang, M., Jenkin, M. E., Jimenez, J. L., Kiendler-Scharr, A., Maenhaut, W., McFiggans, G., Mentel, Th. F., Monod, A., Prévôt, A. S. H., Seinfeld, J. H., Surratt, J. D., Szmigielski, R., and Wildt, J.: The formation, properties and impact of secondary organic aerosol: current and emerging issues, Atmos. Chem. Phys., 9, 5155–5236, https://doi.org/10.5194/acp-9-5155-2009, 2009.

Herrmann, H., Schaefer, T., Tilgner, A., Styler, S. A., Weller, C., Teich, M., and Otto, T.: Tropospheric Aqueous-Phase Chemistry: Kinetics, Mechanisms, and Its Coupling to a Changing Gas Phase, Chem. Rev., 115, 4259–4334, https://doi.org/10.1021/cr500447k, 2015.

Hosny, N. A., Fitzgerald, C., Vyšniauskas, A., Athanasiadis, A., Berkemeier, T., Uygur, N., Pöschl, U., Shiraiwa, M., Kalberer, M., Pope, F. D., and Kuimova, M. K.: Direct imaging of changes in aerosol particle viscosity upon hydration and chemical aging, Chem. Sci., 7, 1357–1367, https://doi.org/10.1039/C5SC02959G, 2016.

Huang, W., Saathoff, H., Pajunoja, A., Shen, X., Naumann, K.-H., Wagner, R., Virtanen, A., Leisner, T., and Mohr, C.: α-Pinene secondary organic aerosol at low temperature: chemical composition and implications for particle viscosity, Atmos. Chem. Phys., 18, 2883–2898, https://doi.org/10.5194/acp-18-2883-2018, 2018.

Huffman, J. A., Ziemann, P. J., Jayne, J. T., Worsnop, D. R., and Jimenez, J. L.: Development and Characterization of a Fast-Stepping/Scanning Thermodenuder for Chemically-Resolved

Aerosol Volatility Measurements, Aerosol Sci. Tech., 42, 395–407, https://doi.org/10.1080/02786820802104981, 2008.

Jimenez, J. L., Canagaratna, M. R., Donahue, N. M., Prévôt, A. S. H., Zhang, Q., Kroll, J. H., DeCarlo, P. F., Allan, J. D., Coe, H., Ng, N. L., Aiken, A. C., Docherty, K. D., Ulbrich, I. M., Grieshop, A. P., Robinson, A. L., Duplissy, J., Smith, J. D., Wilson, K. R., Lanz, V. A., Hueglin, C., Sun, Y. L., Laaksonen, A., Raatikainen, T., Rautiainen, J., Vaattovaara, P., Ehn, M., Kulmala, M., Tomlinson, J. M., Collins, D. R., Cubison, M. J., Dunlea, E. J., Huffman, J. A., Onasch, T. B., Alfarra, M. R., Williams, P. I., Bower, K., Kondo, Y., Schneider, J., Drewnick, F., Borrmann, S., Weimer, S., Demerjian, K., Salcedo, D., Cottrell, L., Griffin, R., Takami, A., Miyoshi, T., Hatakeyama, S., Shimono, A., Sun, J. Y., Zhang, Y. M., Dzepina, K., Kimmel, J. R., Sueper, D., Jayne, J. T., Herndon, S. C., Trimborn, A. M., Williams, L. R., Wood, E. C., Kolb, C. E., Baltensperger, U., and Worsnop, D. R.: Evolution of Organic Aerosols in the Atmosphere: A New Framework Connecting Measurements to Models, Science, 326, 1525–1529, https://doi.org/10.1126/science.1180353, 2009.

Junninen, H., Ehn, M., Petäjä, T., Luosujärvi, L., Kotiaho, T., Kostiainen, R., Rohner, U., Gonin, M., Fuhrer, K., Kulmala, M., and Worsnop, D. R.: A high-resolution mass spectrometer to measure atmospheric ion composition, Atmos. Meas. Tech., 3, 1039–1053, https://doi.org/10.5194/amt-3-1039-2010, 2010.

Kang, E., Root, M. J., Toohey, D. W., and Brune, W. H.: Introducing the concept of Potential Aerosol Mass (PAM), Atmos. Chem. Phys., 7, 5727–5744, https://doi.org/10.5194/acp-7-5727-2007, 2007.

Kaur, R. and Vikas: A case of a single water molecule accelerating the atmospheric reactions of hydroxyl radical at temperatures near 200 K, Chem. Phys. Lett., 685, 270–274, https://doi.org/10.1016/j.cplett.2017.07.080, 2017.

Kolesar, K. R., Li, Z., Wilson, K. R., and Cappa, C. D.: Heating-Induced Evaporation of Nine Different Secondary Organic Aerosol Types, Environ. Sci. Technol., 49, 12242–12252, https://doi.org/10.1021/acs.est.5b03038, 2015.

Krapf, M., El Haddad, I., Bruns, E. A., Molteni, U., Daellenbach, K. R., Prévôt, A. S. H., Baltensperger, U., and Dommen, J.: Labile Peroxides in Secondary Organic Aerosol, Chem, 1, 603–616, https://doi.org/10.1016/j.chempr.2016.09.007, 2016.

Kroll, J. H. and Seinfeld, J. H.: Chemistry of secondary organic aerosol: Formation and evolution of low-volatility organics in the atmosphere, Atmos. Environ., 42, 3593–3624, https://doi.org/10.1016/j.atmosenv.2008.01.003, 2008.

Kroll, J. H., Donahue, N. M., Jimenez, J. L., Kessler, S. H., Canagaratna, M. R., Wilson, K. R., Altieri, K. E., Mazzoleni, L. R., Wozniak, A. S., Bluhm, H., Mysak, E. R., Smith, J. D., Kolb, C. E., and Worsnop, D. R.: Carbon oxidation state as a metric for describing the chemistry of atmospheric organic aerosol, Nat. Chem., 3, 133–139, https://doi.org/10.1038/nchem.948, 2011.

Lambe, A. T., Ahern, A. T., Williams, L. R., Slowik, J. G., Wong, J. P. S., Abbatt, J. P. D., Brune, W. H., Ng, N. L., Wright, J. P., Croasdale, D. R., Worsnop, D. R., Davidovits, P., and Onasch, T. B.: Characterization of aerosol photooxidation flow reactors: heterogeneous oxidation, secondary organic aerosol formation and cloud condensation nuclei activity measurements, Atmos. Meas. Tech., 4, 445–461, https://doi.org/10.5194/amt-4-445-2011, 2011.

Lambe, A. T., Onasch, T. B., Croasdale, D. R., Wright, J. P., Martin, A. T., Franklin, J. P., Massoli, P., Kroll, J. H., Canagaratna, M. R., Brune, W. H., Worsnop, D. R., and Davidovits, P.: Transitions from Functionalization to Fragmentation Reactions of Laboratory Secondary Organic Aerosol (SOA) Generated from the OH Oxidation of Alkane Precursors, Environ. Sci. Technol., 46, 5430–5437, https://doi.org/10.1021/es300274t, 2012.

Lee, B. H., Lopez-Hilfiker, F. D., Mohr, C., Kurtén, T., Worsnop, D. R., and Thornton, J. A.: An iodide-adduct high-resolution time-of-flight chemical-ionization mass spectrometer: Application to atmospheric inorganic and organic compounds, Environ. Sci. Technol., 48, 6309–6317, https://doi.org/10.1021/es500362a, 2014.

Lopez-Hilfiker, F. D., Mohr, C., Ehn, M., Rubach, F., Kleist, E., Wildt, J., Mentel, Th. F., Lutz, A., Hallquist, M., Worsnop, D., and Thornton, J. A.: A novel method for online analysis of gas and particle composition: description and evaluation of a Filter Inlet for Gases and AEROsols (FIGAERO), Atmos. Meas. Tech., 7, 983–1001, https://doi.org/10.5194/amt-7-983-2014, 2014.

Lopez-Hilfiker, F. D., Mohr, C., Ehn, M., Rubach, F., Kleist, E., Wildt, J., Mentel, Th. F., Carrasquillo, A. J., Daumit, K. E., Hunter, J. F., Kroll, J. H., Worsnop, D. R., and Thornton, J. A.: Phase partitioning and volatility of secondary organic aerosol components formed from a-pinene ozonolysis and OH oxidation: the importance of accretion products and other low volatility compounds, Atmos. Chem. Phys., 15, 7765–7776, https://doi.org/10.5194/acp-15-7765-2015, 2015.

Louvaris, E. E., Karnezi, E., Kostenidou, E., Kaltsonoudis, C., and Pandis, S. N.: Estimation of the volatility distribution of organic aerosol combining thermodenuder and isothermal dilution measurements, Atmos. Meas. Tech., 10, 3909–3918, https://doi.org/10.5194/amt-10-3909-2017, 2017.

Mohr, C., Lopez-Hilfiker, F. D., Yli-Juuti, T., Heitto, A., Lutz, A., Hallquist, M., D'Ambro, E. L., Rissanen, M. P., Hao, L., Schobesberger, S., Kulmala, M., Mauldin, R. L., Makkonen, U., Sipilä, M., Petäjä, T.- and Thornton, J. A.: Ambient observations of dimers from terpene oxidation in the gas phase: Implications for new particle formation and growth, Geophys. Res. Lett., 44, 2958–2966, https://doi.org/10.1002/2017GL072718, 2017.

Ng, N. L., Canagaratna, M. R., Zhang, Q., Jimenez, J. L., Tian, J., Ulbrich, I. M., Kroll, J. H., Docherty, K. S., Chhabra, P. S., Bahreini, R., Murphy, S. M., Seinfeld, J. H., Hildebrandt, L., Donahue, N. M., DeCarlo, P. F., Lanz, V. A., Prévôt, A. S. H., Dinar, E., Rudich, Y., and Worsnop, D. R.: Organic aerosol components observed in Northern Hemispheric datasets from Aerosol Mass Spectrometry, Atmos. Chem. Phys., 10, 4625–4641, https://doi.org/10.5194/acp-10-4625-2010, 2010.

Ortega, A. M., Hayes, P. L., Peng, Z., Palm, B. B., Hu, W., Day, D. A., Li, R., Cubison, M. J., Brune, W. H., Graus, M., Warneke, C., Gilman, J. B., Kuster, W. C., de Gouw, J., Gutiérrez-Montes, C., and Jimenez, J. L.: Real-time measurements of secondary organic aerosol formation and aging from ambient air in an oxidation flow reactor in the Los Angeles area, Atmos. Chem. Phys., 16, 7411–7433, https://doi.org/10.5194/acp-16-7411-2016, 2016.

Palm, B. B., Campuzano-Jost, P., Ortega, A. M., Day, D. A., Kaser, L., Jud, W., Karl, T., Hansel, A., Hunter, J. F., Cross, E. S., Kroll, J. H., Peng, Z., Brune, W. H., and Jimenez, J. L.: In situ secondary organic aerosol formation from ambient pine forest air

using an oxidation flow reactor, Atmos. Chem. Phys., 16, 2943–2970, https://doi.org/10.5194/acp-16-2943-2016, 2016.

Pankow, J. F.: An absorption model of gas/particle partitioning of organic compounds in the atmosphere, Atmos. Environ., 28, 185–188, https://doi.org/10.1016/1352-2310(94)90093-0, 1994a.

Pankow, J. F.: An absorption model of the gas/aerosol partitioning involved in the formation of secondary organic aerosol, Atmos. Environ., 28, 189–193, https://doi.org/10.1016/1352-2310(94)90094-9, 1994b.

Pankow, J. F., Seinfeld, J. H., Asher, W. E., and Erdakos, G. B.: Modeling the formation of secondary organic aerosol. 1. Application of theoretical principles to measurements obtained in the α-pinene/, β-pinene/, sabinene/, Δ3-carene/, and cyclohexene/ozone systems, Environ. Sci. Technol., 35, 1164–1172, https://doi.org/10.1021/es001321d, 2001.

Renbaum-Wolff, L., Grayson, J. W., Bateman, A. P., Kuwata, M., Sellier, M., Murray, B. J., Shilling, J. E., Martin, S. T., and Bertram, A. K.: Viscosity of α-pinene secondary organic material and implications for particle growth and reactivity, P. Natl. Acad. Sci. USA, 110, 8014–8019, https://doi.org/10.1073/pnas.1219548110, 2013.

Riva, M., Heikkinen, L., Bell, D. M., Peräkylä, O., Zha, Q., Schallhart, S., Rissanen, M. P., Imre, D., Petäjä, T., Thornton, J. A., Zelenyuk, A., and Ehn, M.: Chemical transformations in monoterpene-derived organic aerosol enhanced by inorganic composition, Clim. Atmos. Sci., 2, 1–9, https://doi.org/10.1038/s41612-018-0058-0, 2019.

Sanchez, J. and Myers, T. N.: Peroxides and Peroxide Compounds, Organic Peroxides, in: Kirk-Othmer Encyclopedia of Chemical Technology, John Wiley & Sons, Inc., Hoboken, NJ, USA, 2000.

Schobesberger, S., D'Ambro, E. L., Lopez-Hilfiker, F. D., Mohr, C., and Thornton, J. A.: A model framework to retrieve thermodynamic and kinetic properties of organic aerosol from composition-resolved thermal desorption measurements, Atmos. Chem. Phys., 18, 14757–14785, https://doi.org/10.5194/acp-18-14757-2018, 2018.

Stark, H., Yatavelli, R. L. N., Thompson, S. L., Kang, H., Krechmer, J. E., Kimmel, J. R., Palm, B. B., Hu, W., Hayes, P. L., Day, D. A., Campuzano-Jost, P., Canagaratna, M. R., Jayne, J. T., Worsnop, D. R., and Jimenez, J. L.: Impact of Thermal Decomposition on Thermal Desorption Instruments: Advantage of Thermogram Analysis for Quantifying Volatility Distributions of Organic Species, Environ. Sci. Technol., 51, 8491–8500, https://doi.org/10.1021/acs.est.7b00160, 2017.

Tong, H., Arangio, A. M., Lakey, P. S. J., Berkemeier, T., Liu, F., Kampf, C. J., Brune, W. H., Pöschl, U., and Shiraiwa, M.: Hydroxyl radicals from secondary organic aerosol decomposition in water, Atmos. Chem. Phys., 16, 1761–1771, https://doi.org/10.5194/acp-16-1761-2016, 2016.

Vaden, T. D., Imre, D., Beranek, J., Shrivastava, M., Zelenyuk, A., Beránek, J., Shrivastava, M., and Zelenyuk, A.: Evaporation kinetics and phase of laboratory and ambient secondary organic aerosol., P. Natl. Acad. Sci. USA, 108, 2190–2195, https://doi.org/10.1073/pnas.1013391108, 2011.

Wilson, J., Imre, D., Beránek, J., Shrivastava, M., and Zelenyuk, A.: Evaporation kinetics of laboratory-generated secondary organic aerosols at elevated relative humidity, Environ. Sci. Technol., 49, 243–249, https://doi.org/10.1021/es505331d, 2015.

Yli-Juuti, T., Pajunoja, A., Tikkanen, O. P., Buchholz, A., Faiola, C., Väisänen, O., Hao, L., Kari, E., Peräkylä, O., Garmash, O., Shiraiwa, M., Ehn, M., Lehtinen, K., and Virtanen, A.: Factors controlling the evaporation of secondary organic aerosol from a-pinene ozonolysis, Geophys. Res. Lett., 44, 2562–2570, https://doi.org/10.1002/2016GL072364, 2017.

B.4 Laser ablation aerosol particle time-of-flight mass spectrometer (LAAPTOF): performance, reference spectra and classification of atmospheric samples

Authors: Xiaoli Shen, Ramakrishna Ramisetty, Claudia Mohr, **Wei Huang**, Thomas Leisner, and Harald Saathoff

In: Atmospheric Measurement Techniques, 11, 2325–2343, 2018. DOI: 10.5194/amt-11-2325-2018.

Authorship statement

This peer-reviewed scientific journal article is based on the laboratory data and some field data from a six-week campaign (TRAM01) during July–August 2016 in a rural area near Eggenstein-Leopoldshafen (southwest Germany), located ~12 km north of the city of Karlsruhe, with a focus on reference mass spectra determination for different particle types measured by LAAPTOF and its application in the field data. In particular, I was responsible for the operation and calibrations of AMS, and provided scientific support in the data interpretation and discussion of this article.

Atmos. Meas. Tech., 11, 2325–2343, 2018
https://doi.org/10.5194/amt-11-2325-2018

Atmospheric Measurement Techniques
Open Access
EGU

Laser ablation aerosol particle time-of-flight mass spectrometer (LAAPTOF): performance, reference spectra and classification of atmospheric samples

Xiaoli Shen[1,2], Ramakrishna Ramisetty[1], Claudia Mohr[1,a], Wei Huang[1,2], Thomas Leisner[1], and Harald Saathoff[1]

[1]Institute of Meteorology and Climate Research (IMK-AAF), Karlsruhe Institute of Technology (KIT), Hermann-von-Helmholtz-Platz 1, 76344 Eggenstein-Leopoldshafen, Germany
[2]Institute of Geography and Geoecology (IfGG), Karlsruhe Institute of Technology (KIT), Kaiserstr. 12, 76131 Karlsruhe, Germany
[a]now at: Department of Environmental Science and Analytical Chemistry, Stockholm University, Stockholm, 11418, Sweden

Correspondence: Harald Saathoff (harald.saathoff@kit.edu)

Received: 18 September 2017 – Discussion started: 8 November 2017
Revised: 2 February 2018 – Accepted: 28 March 2018 – Published: 24 April 2018

Abstract. The laser ablation aerosol particle time-of-flight mass spectrometer (LAAPTOF, AeroMegt GmbH) is able to identify the chemical composition and mixing state of individual aerosol particles, and thus is a tool for elucidating their impacts on human health, visibility, ecosystem, and climate. The overall detection efficiency (ODE) of the instrument we use was determined to range from $\sim(0.01 \pm 0.01)$ to $\sim(4.23 \pm 2.36)\,\%$ for polystyrene latex (PSL) in the size range of 200 to 2000 nm, $\sim(0.44 \pm 0.19)$ to $\sim(6.57 \pm 2.38)\,\%$ for ammonium nitrate (NH_4NO_3), and $\sim(0.14 \pm 0.02)$ to $\sim(1.46 \pm 0.08)\,\%$ for sodium chloride (NaCl) particles in the size range of 300 to 1000 nm. Reference mass spectra of 32 different particle types relevant for atmospheric aerosol (e.g. pure compounds NH_4NO_3, K_2SO_4, NaCl, oxalic acid, pinic acid, and pinonic acid; internal mixtures of e.g. salts, secondary organic aerosol, and metallic core–organic shell particles; more complex particles such as soot and dust particles) were determined. Our results show that internally mixed aerosol particles can result in spectra with new clusters of ions, rather than simply a combination of the spectra from the single components. An exemplary 1-day ambient data set was analysed by both classical fuzzy clustering and a reference-spectra-based classification method. Resulting identified particle types were generally well correlated. We show how a combination of both methods can greatly improve the interpretation of single-particle data in field measurements.

1 Introduction

Atmospheric aerosol particles impact visibility, interact with trace gases, can act as cloud condensation and ice nuclei, and influence the Earth's radiation budget (Seinfeld and Pandis, 2006). Especially the continuously evolving chemical composition of aerosol particles is of scientific interest, as it influences all aerosol effects (Burkholder et al., 2017; Pöschl, 2005). However, large knowledge gaps still exist related to the chemical composition of the organic and inorganic components and their mutual interaction (Jimenez et al., 2009; Murphy et al., 2006; Schill and Tolbert, 2013; Zhang et al., 2007).

Aerosol particles can contain various components, ranging from volatile to refractory species (Pratt and Prather, 2012). The global aerosol mass burden was estimated to consist of 73.6 % dust, 16.7 % sea salt, 2.8 % biogenic secondary organic aerosols (SOA), 2.3 % primary organic aerosols (POA), 1.3 % sulfate, 1.3 % ammonium, 1.2 % nitrate, 0.4 % black carbon (soot), 0.2 % anthropogenic SOA, and 0.2 % methane sulfonic acid (Tsigaridis et al., 2006). During the ambient aerosols' lifetime, ranging from hours to a few weeks (Pöschl, 2005), the complexity of their chemical composition usually increases by coagulation, cloud processing, and chemical reactions (Seinfeld and Pandis, 2006; Usher et al., 2003). This modifies the particles' mixing state, with both internal (individual particles consisting of mixed

compounds, e.g. coating structures) and external mixtures, e.g. mixture of particles consisting of different compounds (Li et al., 2016). The aforementioned findings underscore the importance of measuring aerosol chemical composition and its changes on short timescales and on a single-particle basis, which can be realized by online mass spectrometry.

Online mass spectrometry includes bulk and single-particle measurements (Pratt and Prather, 2012). Single-particle mass spectrometry, which can be dated back to the 1970s, aims at in situ and real-time identification of the chemical composition of individual aerosol particles, hereby elucidating a particle's external and internal mixing properties (Noble and Prather, 2000). Online single-particle mass spectrometers (SPMSs) commonly use pulsed lasers for particle desorption and ionization (LDI), with the advantage of ionizing nearly all atmospheric particle components, including both non-refractory and refractory materials (Kulkarni et al., 2011). To the best of our knowledge, so far there is no quantitative analysis of particle composition by SPMS, since the ablation/ionization laser cannot interact with the entire particle and the generated ion fragments/clusters are susceptible to matrix effects (Ramisetty et al., 2017). In addition, ionization mechanisms are not fully understood (Murphy, 2007). SPMSs have identified many different ambient particle types in different regions of the atmosphere, such as elemental carbon and organic carbon (ECOC), organic sulfate, aged sea salt, biological, soil dust, and different metal dominated types (Dall'Osto et al., 2016; Moffet et al., 2008; Murphy et al., 2006; Schmidt et al., 2017). These measurements all confirmed the complexity of individual particles' mixing state and demonstrated the usefulness of single-particle mass spectra for apportionment of individual particle sources, including e.g. fossil fuel and biomass burning combustion, cooking, marine, and shipping sources (Arndt et al., 2017; Schmidt et al., 2017).

Currently, there are only two commercially available SPMSs, i.e. the single-particle aerosol mass spectrometer (SPAMS, Hexin Analytical Instrument Co., Ltd., China; Li et al., 2011; Lin et al., 2017) and the laser ablation aerosol particle time-of-flight mass spectrometer (LAAPTOF, AeroMegt GmbH, Germany). LAAPTOF uses two laser diodes (405 nm wavelength, ~ 40 mW, ~ 50 µm beam spot diameter; Marsden et al., 2016; Zawadowicz et al., 2017) for optical counting and size recording by light scattering, and one excimer laser (ArF, 193 nm, ~ 4 mJ) for one-step ablation/ionization. The overall detection efficiency (ODE) of this instrument, defined as the number of single-particle mass spectra obtained from the total number of aerosol particles in the sampled air, was determined to range from ~ 0.15 to ~ 2.2 % for polystyrene latex (PSL) particles with geometric diameters (d_p) between 350 nm and 800 nm (Gemayel et al., 2016; Marsden et al., 2016). The instrument used by Gemayel et al. (2016) exhibited a maximum ODE of ~ 2.2 % for PSL particle diameters of 450 nm, while ~ 1 % at 600 nm was the peak ODE reported by Marsden et al. (2016) before the instrument modification. Neither the response of the LAAPTOF to spherical PSL particles smaller than 350 nm and bigger than 800 nm nor the response to other particle types with different shapes has been investigated systematically. The scattering efficiency (SE), defined as the number fraction of particles detected by light scattering compared to the number of particles in the sampled air in front of the aerodynamic inlet lens (ADL) of the instrument (refer to Fig. 1), is determined by the laser diodes, the detection optics, and the photomultiplier tubes (PMT), and it has a strong influence on the ODE of the instrument. Therefore, several groups have tried to improve this part of the instrument. Marsden et al. (2016) modified the detection stage geometry by replacing the detection laser with a fibre-coupled 532 nm, 1 W Nd:YAG solid-state laser system with a collimated laser beam, accomplishing an order-of-magnitude improvement in light detection sensitivity to PSL particles with 500–800 nm diameter. Zawadowicz et al. (2017) modified the optical path of the laser diodes with a better laser beam of < 1 mrad full-angle divergence and 100 µm detection beam spot size, and applied light guides to enhance the scattered-light collection. This resulted in improvement of 2–3 orders of magnitude in optical counting efficiency of incident PSL particles with 500–2000 nm vacuum aerodynamic diameter (d_{va}). There are only very few studies so far that discuss mass spectral patterns of different particle types measured by LAAPTOF. Gemayel et al. (2016) presented spectra from ambient particles collected in the city centre of Marseille, France; spectra (positive only) from pure soot and SOA-coated soot particles were shown by Ahern et al. (2016); spectra from potassium rich feldspar, soot, Argentinian soil dust, and Snomax (commercial ice nuclei) were shown by Zawadowicz et al. (2017); PSL and potassium rich feldspar spectra were measured by Marsden et al. (2018); and radiolytically formed particles spectra were measured by Wonaschuetz et al. (2017). Reitz et al. (2016) presented peak assignments for pure ammonium nitrate and sulfate particles, as well as for ambient particles measured at a suburban site of Düsseldorf, Germany, but did not show any spectra. Marker ions generated from SPMS are likely instrument specific, as pointed out by Schmidt et al. (2017). Therefore, there is a need for publicly available spectral information of this relatively new instrument.

There exists several techniques to group the large number of individual particle types and spectra resulting from SMPS measurements – such as k-means, c-means, and hierarchical clustering algorithms; neural-network-based methods such as ART2-A; and the most recent algorithm of ordering points to identify the clustering structure (OPTICS) – to help analyse the data (Hinz et al., 1999; Murphy et al., 2003; Reitz et al., 2016; Zelenyuk et al., 2006b; Zhao et al., 2008). There also exist target (reference spectra/predefined clusters)-oriented methods (Hinz et al., 1999; Gleanta GmbH; LAAPTOF AnalysisPro, AeroMegt GmbH).

In this paper we have characterized our LAAPTOF instrument with respect to its ODE for PSL, NH_4NO_3, and

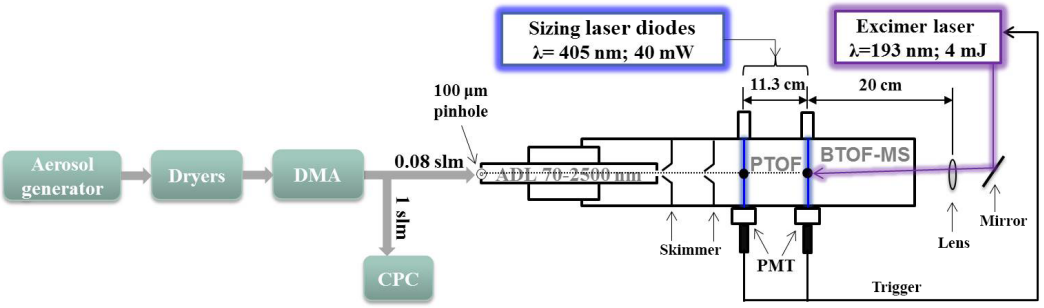

Figure 1. Schematic of the LAAPTOF instrument and the experimental setup for measuring standard samples (method A), e.g. PSL, NH_4NO_3, and K_2SO_4 particles, which were generated from a nebulizer, passed through two dryers, were size-selected by a differential mobility analyser (DMA), and were then measured by LAAPTOF.

sodium chloride (NaCl) particles for a wide size range (d_m: 200–2000 nm PSL; 300–1000 nm NH_4NO_3 and NaCl). We present laboratory-based reference spectra for aerosol particles containing atmospherically relevant components, which were grouped into three categories: (1) particles consisting of pure compounds, e.g. NH_4NO_3, K_2SO_4, and organic acids; (2) particles consisting of well-defined mixtures of pure salts and mixtures of organic compounds, e.g. α-pinene SOA, and PSL internally mixed with K_2SO_4, as well as other core–shell type of particles; and (3) particles consisting of complex mixtures, e.g. soot and dust particles. These reference spectra may also provide other users comprehensive references for comparison purposes and thus help better interpret ambient data. An example of field data analysis based on reference spectra as well as fuzzy c-means clustering will be given in Sect. 3.3.

2 Methods

2.1 The LAAPTOF instrument

The LAAPTOF has been described in several recent publications (Ahern et al., 2016; Gemayel et al., 2016; Marsden et al., 2016, 2018; Reitz et al., 2016; Wonaschuetz et al., 2017; Zawadowicz et al., 2017). Therefore, here we only briefly review the general operation steps that yield size and composition information of individual aerosol particles. The LAAPTOF instrument used in this study was delivered in April 2015 and may differ in a few technical aspects from earlier or later versions. A schematic of the main LAAPTOF components is given in Fig. 1. Particles with a vacuum aerodynamic diameter (d_{va}) between ∼ 70 nm and 2.5 µm are sampled with a sampling flow rate of ∼ 80 standard cubic centimetres per minute (SCCM); focused and accelerated by an ADL (LPL-2.5, AeroMegt GmbH) with close to 100 % transmission efficiency for particles with d_{va} 100 nm to 2 µm (http://www.aeromegt.com/#products?LPL-2.5_details, last access: 16 April 2018); and then pass through the particle time-of-flight (PTOF) chamber in which the individual particle can be detected by two sizing laser beams (405 nm continuous wave, 40 mW) separated by 11.3 cm. Based on the particle time of flight between the two laser beams, its d_{va} can be determined and recorded. After detection by the second sizing laser, a nanosecond excimer laser pulse (wavelength: 193 nm; pulse duration: 4 to 8 ns; maximum pulse energy: ∼ 8 mJ; beam diameter: ∼ 300 µm when it hits the particle (Ramisetty et al., 2017); power density: $\sim 10^9$ W cm^{-2}; ATLEX-S, ATL Lasertechnik GmbH) can be triggered to desorb and ionize particle compounds. A laser pulse energy of 4 mJ was used for all the measurements in this study. More details about the ionization region geometry are given by Ramisetty et al. (2017). The resulting ions are analysed by a bipolar time-of-flight mass spectrometer (BTOF-MS; TOFWERK AG; mass resolution of $m/\Delta m \sim 600$ to 800 at 184 Th, mass range $m/q = 1$ up to ∼ 2000 Th). The cations and anions are detected by corresponding microchannel plate arrays (MCPs), producing a pair of positive and negative spectra for each single particle.

2.2 Aerosol particle generation and experimental setup in the laboratory

The laboratory-based aerosol particles measured in this study (summarized in Table 1) were generated in four different ways (A, B1, B2, and S).

Method A: samples for pure particles and homogeneous and heterogeneous mixtures were dissolved/suspended in purified water and nebulized (ATM 221, Topas GmbH) with dry synthetic air, passed through two diffusion dryers (cylinder filled with Silica gel, Topas GmbH), and then size-selected by a differential mobility analyser (DMA 3080, TSI GmbH) before being sampled by LAAPTOF.

Method B1: particles were sampled from the 84.5 m^3 simulation chamber AIDA (Aerosol Interactions and Dynamics in the Atmosphere) of KIT (Saathoff et al., 2003). SOA particles were formed in the 3.7 m^3 stainless-steel Aerosol Preparation and Characterization (APC) chamber via ozonolysis (∼ 6 ppm ozone) of α-pinene (∼ 2.2 ppm) and then transferred into AIDA. Soil dust samples were dispersed by a ro-

Table 1. Overview of laboratory-generated aerosol particles for reference mass spectra.

Aerosol particle types	Size (nm) d_{va}	Width[a]	Morphology	Source	Generation method	No. of spectra
1. Particles consisting of pure compounds						
Ammonium nitrate, NH_4NO_3	1160	101	aspherical	$\geq 99.5\,\%$, Fluka	A	497
Ammonium sulfate[b], $(NH_4)_2SO_4$	611	79	aspherical	$\geq 99.5\,\%$, Merck	A	537
Potassium sulfate, K_2SO_4	1465	232	aspherical	$\geq 99\,\%$, Merck	A	300
Sodium chloride, NaCl	1202	133	cubic	$\geq 99.5\,\%$, Merck	A	250
Silica, SiO_2 (Glass beads)	2097	44	spherical	Palas GmbH	S	347
Oxalic acid, $C_2H_4O_2$	1081	322	spherical	Merck	A	736
Pinic acid, $C_9H_{14}O_4$	902	94	spherical	University of Mainz	A	683
Cis-pinonic acid, $C_{10}H_{16}O_3$	702	88	spherical	98 %, ACROS ORGANICS	A	600
Humic acid	1221	126	spherical	100 %, Alfa Aesar	A	773
Polystyrene latex (PSL)	818	3	spherical	Thermo scientific	A	235
2. Particles consisting of well-defined mixtures						
Ammonium nitrate & ammonium sulfate (mass ratio = 1 : 1)	1102	165	aspherical	Single-component samples are from the same source	A	454
Potassium sulfate & sodium chloride (mass ratio = 1 : 1)	1375	197	aspherical	as the corresponding pure compounds		259
Ammonium nitrate & potassium sulfate (mass ratio = 2 : 1)	854	112	aspherical			576
Hematite	1091	817	spherical	Karlsruhe Institute of Technology (KIT)	S	320
Pure sea salt	1205	218	cubic	Sigma Aldrich	B1	422
$\alpha-$Pinene secondary organic aerosols (SOA)	505	84	spherical	$(1S)-(-)-\alpha$-pinene (99 %) from Aldrich	B1[c]	1938
Potassium-sulfate-coated PSL	805	58	partially coated	Merck & Thermo scientific	A	609
Poly(allylamine hydrochloride)-coated gold	400[d]		300 nm core–50 nm shell	Nanopartz Inc.	Nebulized without sizing	417
3. Particles consisting of complex mixtures						
Soot 1 with low organic carbon	386[e]	275	agglomerates	incomplete combustion of propane, C / O = 0.29	B2	617
Soot 1 with high organic carbon	120[e]	58	agglomerates	incomplete combustion of propane, C / O = 0.54	B2	347
Soot 2, diesel particles	624 ± 980[f]		agglomerates	NIST (2975)	S	533
Soot 3, lignocellulosic char	828	766	agglomerates	lignocellulosic char from chestnut wood; University of Zurich, Switzerland	S	390
Arizona test dust	1169	874	aspherical	Powder Technology Inc.	S	261
Saharan dust 1 (Morocco)	890	1230	aspherical	Konrad Kandler, TU Darmstadt	S	338
Saharan dust 2 (Cairo)	1334 ± 1454[f]		aspherical	Khaled Megahed, KIT	S	396
Arable soil dust SDGe01 (Gottesgabe, Germany)	912	392	aspherical	Roger Funk[g]	B1[h]	583
Arable soil dust SDPA01 (Paulinenaue, Germany)	787	334	aspherical	Roger Funk[g]	B1[h]	385
Arable soil dust SDAr08 (Argentina)	910	407	aspherical	Roger Funk[g]	B1[h]	592
Arable soil dust SDWY01 (Wyoming, USA)	864	430	aspherical	Tom Hill[i]	B1[h]	623
Agricultural soil dust (northern Germany)	561	249	aspherical	Roger Funk[g]	B1[h]	286
Urban dust	1329	1266	aspherical	NIST(1649a)	S	375
Illite_NX	825	260	sheet	Arginotec	S	807
Sea salt with *Skeletonema marinoi*[j]	1212	338	cubic	Matt Salter[j]	B1	526

Note that for aerosol generation methods, "A" represents the method of using a nebulizer and a DMA (refer to the setup in Fig. 1) for sizing d_m =800 nm; "B1" and "B2" represent the methods in which particles were sampled from AIDA and a stainless-steel cylinder, respectively; "S" corresponds to particles mobilized by shaking in a reservoir. For particles size information, d_{va} values represent the expected values from Gaussian fitting to the particle sizes measured by LAAPTOF. Spectra number is the number of averaged spectra. [a] These values represent the standard deviation from Gaussian fitting to the measured particle sizes (d_{va}). [b] There is only one weak but reproducible peak m/z 30 NO^+ in the positive spectra. Therefore we do not give the reference spectra in this paper. [c] SOA particles were formed in the Aerosol Preparation and Characterization (APC) chamber and then transferred into the AIDA chamber. [d] The nominal geometric size given by the manufacture Nanopartz Inc. [e] Electrical mobility equivalent diameter, d_m, measured by a scanning mobility particle sizer (SMPS). [f] The sizes (d_{va}) of Diesel particles and Saharan dust 2 are average values with their standard deviation. [g] Institute of Soil Landscape Research, Leibniz Centre for Agricultural Landscape Research, Germany. [h] Soil dust samples were dispersed by a rotating brush generator and injected via cyclones into the AIDA chamber. [i] Department of Atmospheric Science, Colorado State University, Fort Collins, Colorado, USA. [j] Samples, provided by Elena Gorokhova and Matt Salter at Stockholm University, that were prepared by diluting a pure *Skeletonema marinoi* culture with artificial seawater (sigma sea salt) to conditions representative of a bloom in the ocean.

tating brush generator (RBG1000, PALAS) and injected via cyclones into the AIDA chamber. Sea salt particles were generated and injected into AIDA by ultrasonically nebulizing artificial seawater (Sigma Aldrich) and highly concentrated *Skeletonema marinoi* culture (in artificial seawater), respectively, via a droplet separator and two diffusion dryers (Wagner et al., 2018).

Method B2 was used only for soot particles, which were generated with a propane burner (RSG miniCAST; Jing Ltd.) and injected into and sampled from a stainless-steel cylinder of 0.2 m^3 volume.

Method S: silica, hematite, illite NX, Arizona test dust, desert and urban dust, black carbon from chestnut wood (University of Zurich, Switzerland), and diesel soot reference particles from NIST were suspended in their reservoir bottles by shaking them and sampled directly from the headspace (upper part) of these reservoirs through a tube connecting it with the LAAPTOF.

For all the measurements, except measuring the particles generated by method S, a condensation particle counter (CPC 3010, TSI GmbH) was used to record the particle number concentration in parallel with the LAAPTOF inlet. The setup in Fig. 1 was specific for particles generated from method A.

2.3 Field measurement

Unusually high particle number concentrations, similar to downtown Karlsruhe (a city in southwest Germany), were observed frequently northeast of Karlsruhe by particle counters on board a tram wagon (www.aero-tram.kit.edu, last access: 16 April 2018) intersecting the city (Hagemann et al., 2014). To study the nature and to identify possible sources of these particles, their number, size, chemical composition, associated trace gases, and meteorological conditions were measured from 15 July to 1 September 2016 at a rural location (49°6′10.54″ N, 8°24′26.07″ E), next to the tram line north of the village of Leopoldshafen, Germany. Ambient aerosol particles were sampled through a $PM_{2.5}$ inlet (SH 2.5–16, Comde-Derenda GmbH) with 1 $m^3\,h^{-1}$, a fraction of which was guided into the LAAPTOF, which was deployed for ∼ 5 weeks from 26 July to 31 August. LAAPTOF measurements provided information on size and mass spectral patterns for individual particles. In this paper we use data from 1 day as an example of the potential interpretation of LAAPTOF spectral data using reference spectra.

2.4 Efficiency calculations

In the literature, two definitions of detection efficiency (DE) of SPMS are used: one is equal to the scattering efficiency (SE) of the detection lasers (Brands et al., 2011; Gaie-Levrel et al., 2012; Su et al., 2004; Zelenyuk and Imre, 2005; Zelenyuk et al., 2009), which is the fraction of particles detected by the scattering optics in the detection region of the instrument; the other one is the product of SE and hit rate (HR) of the ablation/ionization laser (Su et al., 2004; Gemayel et al., 2016; Marsden et al., 2016). The hit rate is the fraction of particles detected actually leading to a useful mass spectrum. In this paper we use ODE, defined by the following equations:

$$\mathrm{ODE} = \mathrm{SE} \times \mathrm{HR} \times 100\,\% \quad (1)$$

$$\mathrm{SE} = N_d/N_0 \times 100\,\% \text{ (transmission efficiency of ADL is included)}, \quad (2)$$

$$\mathrm{HR} = N_s/N_d \times 100\,\% \text{ (ionization efficiency is included)}, \quad (3)$$

$$N_0 = C_n \times \text{flow rate} \times \text{time}, \quad (4)$$

where N_d is the number of particles detected by light scattering, N_0 is the number of particles in front of the ADL, N_s is the number of bipolar spectra, C_n is the particle number concentration (cm^{-3}) measured by a CPC in front of the ADL, and the flow rate is the LAAPTOF sample flow rate.

2.5 Spectral and size data analysis

For each type of laboratory-generated aerosol particles, we measured at least 300 mass spectra. Data analysis is done via the Igor LAAPTOF data analysis software (version 1.0.2, AeroMegt GmbH). There are five main steps for the basic analysis procedure: (a) removal of the excimer laser ringing signal from the raw mass spectra; (b) determination of the signal baseline; (c) filtering for empty spectra; (d) mass calibration; and (e) stick integration, that is, the integration of nominal masses for peaks. It should be noted that spectrum-to-spectrum differences in peak positions for the same ion fragments/clusters complicate the mass calibrations. This may be caused by differences in kinetic energy of the ions produced; however this effect is typically compensated in the TOFs with reflectron (Kulkarni et al., 2011). Spectrum-to-spectrum peak shifts, especially in the positive spectra in our study, are mainly because of variance in the position of particle–laser interaction, which cannot be corrected with the existing AeroMegt software or the LAAPTOF instrument (Ramisetty et al., 2017). Details can be found in "Procedure 1" in the Supplement. Spectra presented in this paper were typically normalized to the sum of ion signal before further aggregation.

For ambient data analysis, we used two different classification methods. The first one is fuzzy *c*-means clustering algorithm embedded in the Igor LAAPTOF data analysis software, commonly used to do classification based on the similarities of the individual spectra. The number of the classes is chosen manually; afterwards the particle spectra with a minimum distance between their data vectors and a cluster centre are grouped into a specific class (Hinz et al., 1999; Reitz et al., 2016). Since each spectrum can belong to multiple classes (Reitz et al., 2016), the resulting fraction/percentage for each class represents the information about the degree of

similarity between aerosol particles in one particular class, not a number percentage. The second method developed in this study is based on the correlation between each ambient spectrum and our reference spectra. The resulting Pearson's correlation coefficient (r) is used as the criterion to group particles into different types (here we use "types" instead of "classes" in order to differentiate these two classification methods). When r is higher than a threshold value of 0.6, the ambient spectrum is considered to have high correlation with the corresponding reference spectrum. For simplification we chose 10 positive and 7 negative reference spectra. For example, we only use German soil dust as the reference for arable soil dust, rather than using four arable soil dust samples from different places. More details about the procedure for this method as well as the corresponding equations and uncertainties estimation can be found in "Procedure 2" in the Supplement.

In addition, particle size (d_{va}) was recorded for individual particles. The corresponding size distribution can be plotted as d_{va} histogram, a Gaussian fit of which yields number mean d_{va} values and the standard deviation (width).

3 Results and discussion

3.1 LAAPTOF performance

3.1.1 Hit rate, scattering efficiency, and overall detection efficiency for standard samples

HR, SE, and ODE for spherical PSL particles as a function of electrical mobility equivalent diameter d_m are plotted in Fig. 2. It should be noted that the LAAPTOF detection behaviour may vary depending on the alignment of the ADL and the optical components (especially the detection laser diodes), which is difficult to reproduce. We therefore show results for PSL particles based on two repeated experiments after three alignments each and thus a total of six experiments for each data point. The uncertainty intervals in Fig. 2 are the difference between the maximum/minimum and the average values obtained from these six experiments. As shown in panel a of Fig. 2, for particle diameters from 200 to 400 nm, HR_{PSL} exhibits an increase from 69 to 94 %, decreases to 83 % for 700 nm particles, and then becomes stable at ∼ 85 % for particles with diameters up to 2 µm. The average HR_{PSL} ($\overline{HR}_{PSL}$) is ∼ 84 %. SE_{PSL} and ODE_{PSL} show an M-like shape with two peaks, at 500 nm (SE_{PSL} 3.0 %, ODE_{PSL} 2.7 %) and at 1000 nm (SE_{PSL} 4.8 %, ODE_{PSL} 4.2 %) (see panels b and c of Fig. 2). We attribute this behaviour to a combined effect of the spherical shape of PSL particles and the optical system of this instrument, e.g. Mie resonances related to particle size and laser wavelength (see Sect. 3.1.2 for details). As shown in panel c of Fig. 2, values and trends of ODE_{PSL} in the size range of 300–800 nm of our instrument are similar to those reported by Gemayel et al. (2016) and Marsden et al. (2016) for their LAAPTOF instruments. A recent LAAPTOF study by Zawadowicz et al. (2017) shows comparable results for PSL particles with $d_p \leq 500$ nm and an M-like shape of ODE in the size range of 200–2000 nm (after instrument modification).

We also measured mass spectra of non-spherical NH_4NO_3 ($\chi = 0.8$; Williams et al., 2013) and NaCl particles (cubic, $\chi = 1.06$ to 1.17; Zelenyuk et al., 2006a). Similar to PSL particles, NH_4NO_3 and NaCl particles show relatively high and stable HR with average values of 80 and 66 % (see panel d in Fig. 2); thus SE and ODE have a similar trend. No M-like shape of ODE as a function of particle size is observed due to the different light scattering properties of the non-spherical salt particles (Bohren and Huffman, 2007; see panels e and f in Fig. 2). Comparable results were shown for $(NH_4)_2SO_4$ particles ($\chi = 1.03$ to 1.07; Zelenyuk et al., 2006a) by Zawadowicz et al. (2017). As shown in Fig. 2e–f, SE and ODE decrease with increasing shape factor for salt particles of the same size. We will discuss this in more detail in the following section.

3.1.2 Factors influencing overall detection efficiency

There are various factors that can influence the ODE of LAAPTOF. One of these is particle size. For particles with diameters below 200 nm, the scattered light becomes too weak to be detected due to the strong dependence of the scattering intensity on particle size (Bohren and Huffman, 2007). For particles with diameters larger than 2 µm, focusing by the ADL is much less efficient, resulting in a higher divergence of the particle beam (Schreiner et al., 1999). This lowers the probability of larger particles being detected by the detection/scattering laser and/or being hit by the ionization laser. In addition, light scattering of spherical particles like PSL changes from Rayleigh to Mie to geometric scattering as the size parameter $\alpha = \pi d_p/\lambda$ increases from $\ll 1$ to ~ 1 to $\gg 1$ (Seinfeld and Pandis, 2006). The scattering efficiencies of PSL particles, based on Mie calculation at the particle sizes and detection laser wavelength relevant to our LAAPTOF measurement, validate the M-like shape of SE_{PSL} (refer to Fig. S1 in the Supplement). As long as the particle diameter (d_p) is smaller than the wavelength of the detection laser light, here 405 nm, the scattered-radiation intensity (proportional to d_p^6) will rapidly decrease with decreasing particle sizes, resulting in low ODE. ODE is e.g. 0.01 % for 200 nm PSL particles. For non-spherical particles like salts, their SE and ODE are also size dependent (panel f in Fig. 2), due to size-dependent light scattering ability and particle beam divergence. However, in the size range of 300 to 1000 nm studied here, they do not exhibit Mie resonance and thus do not show an M-like shape in their scattering efficiency.

Optical properties of the particles have a strong impact on how light is scattered and absorbed, and thus it should be noted that the optical properties influence not only scattering efficiency but also absorption and ionization efficiency (or hit

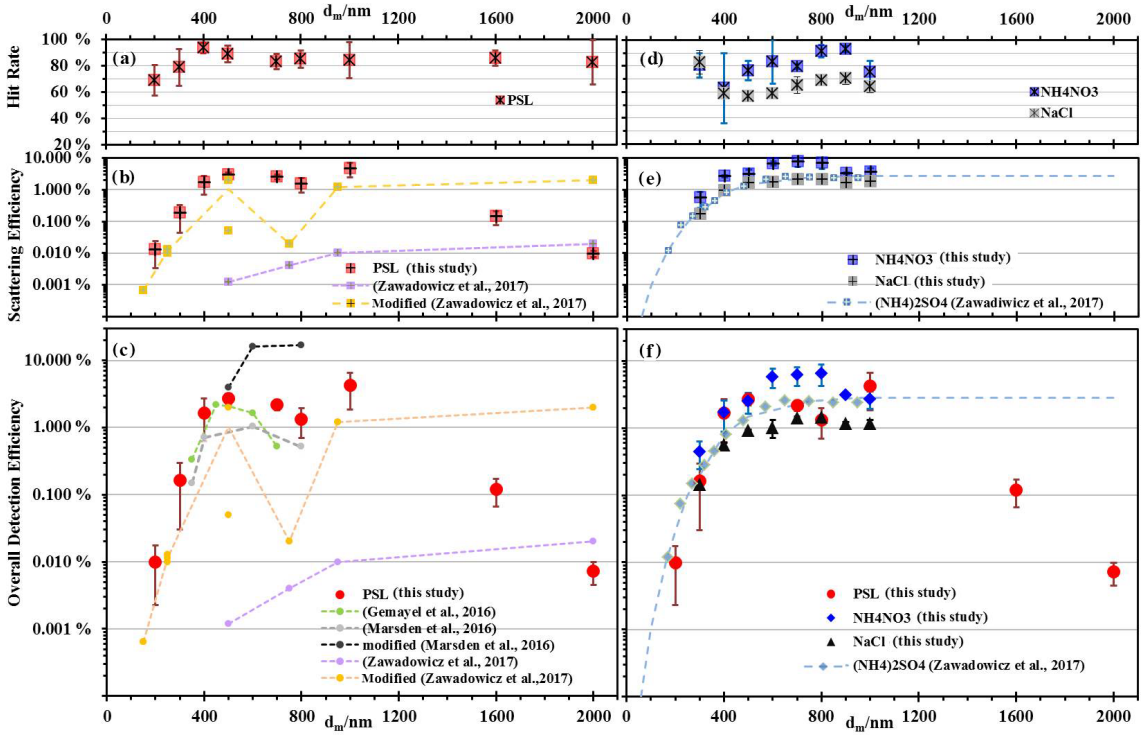

Figure 2. Hit rate (HR, **a** and **d**), scattering efficiency (SE, **b** and **e**), and overall detection efficiency (ODE, **c** and **f**) for PSL, ammonium nitrate (NH_4NO_3), and sodium chloride (NaCl) salt particles as a function of mobility diameter, d_m. Aerosol particles in this study were generated from a nebulizer and size-selected by DMA. In **(b)** and **(e)**, OCEs for PSL and ammonium sulfate ($(NH_4)_2SO_4$) at the detection beam from the study by Zawadowlcz et al. (2017), corresponding to the SE defined in this study, are plotted for comparison. In **(c)** and **(f)**, ODE for PSL and salt particles from other studies (Gemayel et al., 2016; Marsden et al., 2016; Zawadowicz et al., 2017) are plotted for comparison. In this figure, dashed lines are used only to guide the eyes.

rate). As shown in Fig. 2f, ODE for NH_4NO_3 is higher than that for NaCl at any size we studied. This is mainly caused by differences in their optical properties of scattering. Fresh soot particles scatter only little light due to their black colour and the small size (typically $\sim$20 nm) of the primary particles forming their agglomerates, and are thus hardly detected by the detection laser. However they are good light absorbers and thus relatively easy to ablate and ionize. The reference spectra of pure NH_4NO_3 and $(NH_4)_2SO_4$ particles showed intensive prominent peaks for pure NH_4NO_3 particles (refer to Fig. 3a) but only one weak peak of m/z 30 NO^+ for pure $(NH_4)_2SO_4$ particles. This indicates that NH_4NO_3 is a better absorber than $(NH_4)_2SO_4$ and thus easier to ablate and ionize. For homogeneous mixtures of these two ammonium salts, the sulfate species are ablated and ionized much more easily (refer to Sect. 3.2.2), due to increased UV light absorption by the nitrate component. Some small organic compounds with weak absorption properties are hard to ablate and ionize, e.g. oxalic acid ($C_2H_2O_4$), pinic acid, and *cis*-pinonic acid. They exhibited much weaker signals ($\sim$80 % lower) than macromolecular organic compounds in PSL or humic acid particles.

Particle morphology is another important factor. The scattering efficiency for non-spherical NH_4NO_3 is higher than for spherical PSL particles in the size range of 300–800 nm (Fig. 2b–e) (Ackerman et al., 2015). For larger particle sizes ($d_m > 800$ nm), beam divergence offsets the shape effect (Murphy, 2007). Apart from that, the increase of surface roughness and inhomogeneity can promote the scattering capability of particles (Ackerman et al., 2015).

The incident intensity of radiation, which is another parameter that influences the light scattered by particles (as well as background signal caused by stray light), is related to power and beam dimensions of the detection laser. Corresponding instrument modifications were done by Marsden et al. (2016) and Zawadowicz et al. (2017) (refer to Sect. 1). In addition, alignment of the excimer laser focus in the x, y, and z position influences optimum hit rates (Ramisetty et al., 2017).

There are further instrumental aspects that affect the detection efficiency. High number concentrations of the incoming particles influence the ODE, since there can be more than one particle present between the two detection lasers. The transmission efficiency of the ADL is included in the scattering efficiency and thus directly influences it. The size

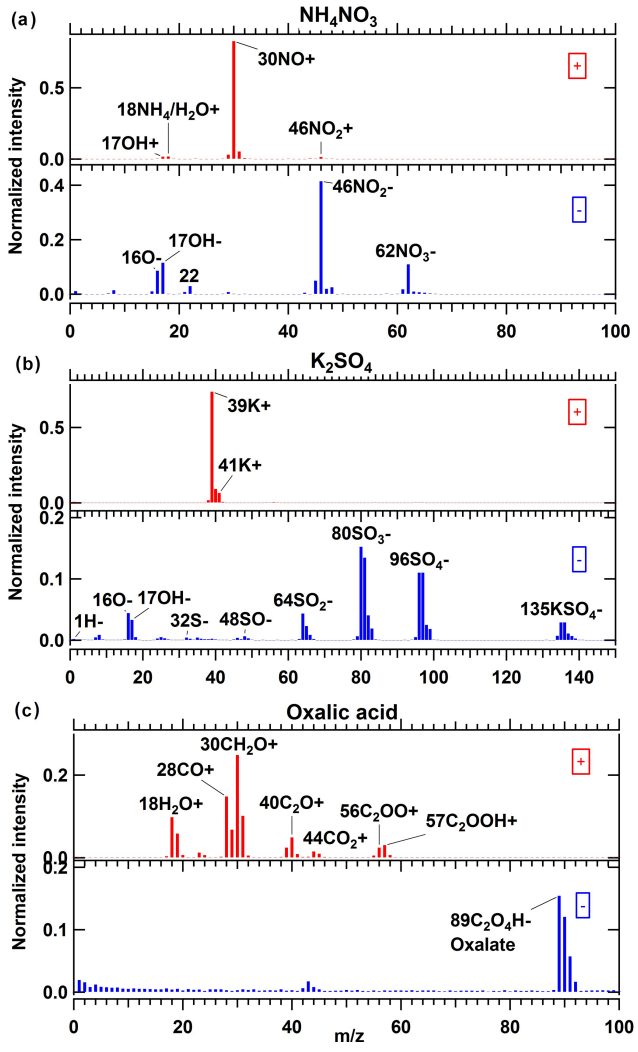

Figure 3. Average mass spectra for pure compound aerosol particles: **(a)** NH_4NO_3 ($d_{va} = 1160$ nm), 497 single spectra averaged; **(b)** K_2SO_4 ($d_{va} = 1465$ nm), 300 single spectra averaged; and **(c)** oxalic acid particles ($d_{va} = 1081$ nm), 736 single spectra averaged.

range of particles focused by the lens and the particle beam width strongly depend on the configuration of the ADL (Canagaratna et al., 2007; Johnston, 2000). Liu lenses and Schreiner lenses can focus the particles in the size range of 80–800 and 300–3000 nm, respectively (Kamphus et al., 2008; Liu et al., 1995; Schreiner et al., 1999). The ADL transmission efficiency of our instrument, as determined by the manufacturer (AeroMegt GmbH), is close to 100 % for particles with d_{va} 100–2000 nm.

3.2 LAAPTOF reference spectra of laboratory-generated particle types

Particles for which reference spectra are presented here are listed in Table 1. For each type of these aerosol particles, we present averaged spectra for typically 300 to 500 single particles. The relative standard deviations (RSDs, SD normalized to signal) for the characteristic peaks are in the range of 15–186 %, with a median value of 77 %.

Despite the lack of full quantitativeness of the LAAPTOF, mass spectral signal amplitudes show an increase with particle size (refer to Fig. S2). However, no systematic changes in the mass spectral signatures were observed for different particle sizes. Therefore, for the samples passing through the DMA, particles in the optimum size range of the LAAPTOF ($d_m = 800$ nm) and with good signal-to-noise ratio were chosen to generate reference spectra. For polydisperse particles generated in the AIDA chamber, the corresponding average spectra include particles of broader size distributions than those preselected by the DMA. Information on particle generation or source as well as the sizes is listed in Table 1.

A qualitative comparison between the relative peak intensity ratios within a single-particle spectrum and those in another spectrum can yield relative quantitation information, as suggested by Gross et al. (2000). We add information on typical peak ratios to some of our reference spectra to help identify specific species.

3.2.1 Pure compound particles

Although particles consisting of one single species only are rarely sampled in the atmosphere, interpretation of mass spectra of ambient samples is supported by the knowledge about the mass spectra of pure compounds. In the following, mass spectra for a few typical ambient aerosol constituents are discussed.

Figure 3 shows average spectra for pure compound aerosol particles. For NH_4NO_3 particles (panel a), we observed the positive ions m/z 18 NH_4^+ and m/z 30 NO^+, and the negative ions m/z 46 NO_2^- and m/z 62 NO_3^-, similar to Reitz et al. (2016). The LAAPTOF is much less sensitive to ammonium than nitrate fragments, leading to a weak NH_4^+ signal and prominent NO^+, NO_2^- and NO_3^- peaks. The ratio of NO^+ to NH_4^+ is ∼48, and the ratio of NO_2^- to NO_3^- is ∼4. The prominent peak of NO^+ arises not only from nitrate (majority), but also from ammonium (Murphy et al., 2006). In our ammonium nitrate spectra, there are weaker signatures of m/z 46 NO_2^+ and m/z 125 $HNO_3 \cdot NO_3^-$ (not shown here, but visible and reproducible), which were also observed in PALMS mass spectra (Zawadowicz et al., 2015). For K_2SO_4 particles, we observed the potassium signals at m/z 39 K^+ and m/z 41 K^+, and a sulfate signature with ion clusters grouped around m/z 32 S^-, m/z 64 SO_2^-, m/z 80 SO_3^-, and m/z 96 SO_4^-. Note that the extra peak at m/z 40^+ besides m/z 39 K^+ in Fig. 3b is likely due to the incorrect mass as-

signments as a result of peak shifts (refer to Sect. 2.5 and "Procedure 1" in the Supplement). For high-intensity peaks such as sodium chloride NaCl, extra peaks next to the main peak (Fig. S3) may have an additional cause: "ringing" due to partial saturation of the data acquisition system or signal reflections within the data acquisition circuitry (Gross et al., 2000). The real intensities of m/z 35 Cl^- should include its corresponding side ringing peak. The ratio of m/z 39 K^+ to m/z 41 K^+ is ∼ 13.2, close to the natural isotopic ratio of ∼ 13.9 for $^{39}K/^{41}K$. For pure NaCl particles, the ratio of m/z 35 Cl^- to m/z 37 Cl^- is ∼ 3.2, similar to the natural isotopic ratio of ∼ 3.1 for $^{35}Cl/^{37}Cl$. Therefore, these two isotopic ratios can be used as markers to identify K and Cl measured by LAAPTOF. Another inorganic compound measured here is silica (Fig. S4), and its typical peak ratio of (m/z 76 SiO_3^- + m/z 77 $HSiO_3^-$) to m/z 60 SiO_2^- is ∼ 1.0. The corresponding histograms of such ratios for different particle samples can be found in Fig. S5.

High signal intensities in oxalic acid spectra are observed at m/z 18 H_2O^+, 28 CO^+, and 30 CH_2O^+, as well as some weaker peaks at m/z 40$^+$, 44$^+$, 56$^+$, and 57$^+$. M/z 89 $C_2O_4H^-$ is used as a signature ion for oxalic acid in other SPMS studies (Roth et al., 2016). In our study, a distinct signal at around m/z 89$^-$ is observed as well, indicating oxalate fragment formation after laser ablation.

In order to identify humic-like substances in the ambient particles, we measured humic acid particles (Fig. S6) and found hydrocarbon and elemental carbon fragments, with very prominent peaks at m/z 24$^-$, 25$^-$, and 26$^-$ suggested to be organic ions (Silva et al., 2000), as well as peaks at m/z 25$^-$, 26$^-$, 49$^-$, and 73$^-$ for unsaturated organic compounds.

3.2.2 Particles consisting of well-defined internal mixtures

Figure 4 shows average spectra from homogeneously internally mixed particles. The spectrum from the mixture of NH_4NO_3 and $(NH_4)_2SO_4$ (panel a) contains the signature from pure NH_4NO_3 particles, but with lower relative intensities (each peak intensity is normalized to the sum of ion signal) for NO_2^- and NO_3^-, due to the formation of anion clusters at ∼ m/z = 80 SO_3^- and 97 HSO_4^-. Compared to the pure NH_4NO_3 particles, the ratio of NO^+ to NH_4^+ (∼ 34) is ∼ 30 % lower in the spectrum for the mixture, due to its lower molar ratio of nitrate to ammonium, whereas the ratio of NO_2^- to NO_3^- (∼ 7) is 80 % higher. In addition, as already discussed in Sect. 3.1.2, the better UV light absorber NH_4NO_3 assists in light absorbing for mixed particles, resulting in a sulfate signature that could not be observed for pure $(NH_4)_2SO_4$. This exemplifies potential effects of individual particle chemical composition on mass spectral performance of the LAAPTOF. For the mixture of K_2SO_4 and NaCl (panel b), similar signatures to those of the pure particles were observed. Compared to the pure NaCl particle spectra, the signal intensity of Na^+ is decreased. This can be explained by more cations formed from the mixed particles, including from potassium, which has a higher ionization potential and lower lattice energy than NaCl. For the mixed particles, expected clusters such as 113/115 K_2Cl^+, 109 KCl_2^-, and 119 $NaSO_4^-$ and a minor fragment 97 $KNaCl^+$ were observed, but not 81/83 Na_2Cl^+ as found in pure NaCl particles. These results show that, compared to pure compounds, mass spectra from aerosol particles consisting of mixtures can feature new ions, while some marker ions for the pure compounds may disappear. These spectra are thus not simply a combination of the spectra from single-component particles. Another example of an inorganic mixture of NH_4NO_3 and K_2SO_4 is provided in Fig. S7. The α-pinene SOA spectrum is shown in panel c of Fig. 4. Ablation of α-pinene SOA particles forms different types of organic fragments: (1) hydrocarbon and oxygenated organic fragments $C_xH_yO_z$ (x = 1–6, y = 0–9, z = 0–3; details about the peak assignments can be found in Table S1) – except for m/z 59$^+$, 83$^+$, 85$^+$, and 95$^+$ – are comparable to the combination mass spectral patterns for *cis*-pinonic and pinic acids (refer to Fig. S8), which are oxidation products from α-pinene ozonolysis (Saathoff et al., 2009; Yu et al., 1999); (2) carbon clusters 12 C^+, 24 C_2^+, 36 C_3^+, and 60 C_5^+, with the most prominent peak in 12 C^+, assigned to both soot and organic matter fragments in another LAAPTOF study (Ahern et al., 2016); and (3) carboxylic acid groups in the negative spectra, e.g. 45 $COOH^-$, 59 CH_2COOH^-, 73 $C_2H_4COOH^-$, 85 $C_3H_4COOH^-$, and 99 $C_4H_6COOH^-$.

Figure 5a shows the spectrum for heterogeneously internally mixed K_2SO_4 and PSL particles (PSL core, K_2SO_4 shell). All signatures for PSL particles – i.e. hydrocarbon fragments in positive spectra; intensive organic signature m/z 24$^-$, 25$^-$, and 26$^-$; carbon clusters $C_n^{+/-}$; and m/z 49$^-$ and 73$^-$ fragments arising from unsaturated structures such as aromatic structures – are retained in this spectra (grey labels), and the corresponding peak intensities are similar to the pure PSL particles (Fig. S9). However, the intensities of most of the K_2SO_4 fragments are weaker than pure K_2SO_4 particles, likely due to the quite thin or only partial coating layer of K_2SO_4 on the PSL core (the nominal geometric size of the PSL particles mixed with the aqueous solution of K_2SO_4 was 800 nm, which is the same size that was selected by the DMA prior to sampling by the mass spectrometer.). The most prominent peak at m/z 39$^+$ with a normalized intensity of ∼ 0.46, containing both K^+ and $C_3H_3^+$ fragments, is mainly attributed to K^+ (intensity ∼ 0.73 for pure K_2SO_4), since the intensity of $C_3H_3^+$ (∼ 0.06) for pure PSL is much lower (refer to Fig. S9). The still intensive signal from 39 K^+, despite the weaker sulfate peaks, corresponds to the high sensitivity of the instrument to potassium. Figure 5b shows the average spectrum for poly(allylamine hydrochloride)-coated gold particles. Prominent signatures of nitrogen-containing compounds (NOCs) are observed at m/z 58 C_2H_5–NH–CH_2^+, 15 NH^+, 26 CN^-, and 42 CNO^-,

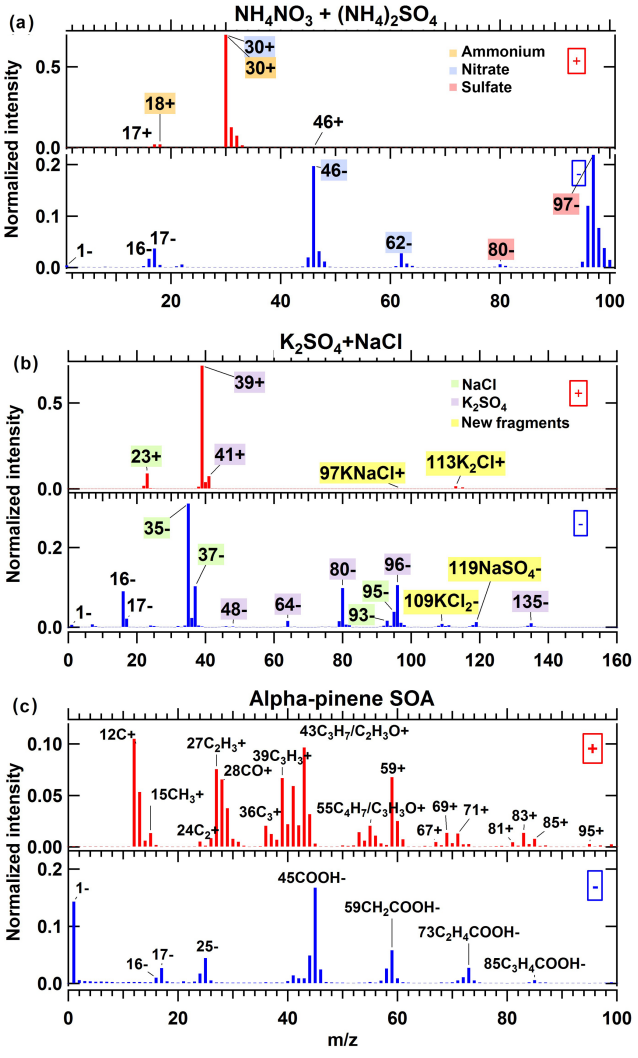

Figure 4. Average mass spectra for particles of internal mixtures of **(a)** NH_4NO_3 and $(NH_4)_2SO_4$ ($d_{va} = 1102$ nm), 454 single spectra averaged, and **(b)** NaCl and K_2SO_4 ($d_{va} = 1375$ nm), 259 single spectra averaged, as well as **(c)** secondary organic aerosol (SOA) particles from α-pinene ozonolysis, which was performed in the APC chamber, and then the resulting particles were transferred into the AIDA chamber at 263 K and 95 % RH, $d_{va} = 505$ nm, 1938 single spectra averaged. In **(a)**, red, blue, and orange label shadings represent fragments of sulfate, nitrate, and ammonium, respectively. In **(b)**, green and purple label shadings represent fragments from NaCl and K_2SO_4 components (see Sect. 3.2.1) in the mixed particles, respectively; yellow label shadings represent the fragments only in the internal mixture of NaCl and K_2SO_4.

as well as the signatures for unsaturated organic compounds at m/z 25^-, 26^-, 49^-, and 73^-. Strong intensities for m/z (35^- plus 36^-) and 37^- with a ratio of ~ 3.1 can be assigned to Cl isotopes derived from the hydrochloride. We also observed small gold peaks at m/z $197^{+/-}$ both in positive and negative spectra.

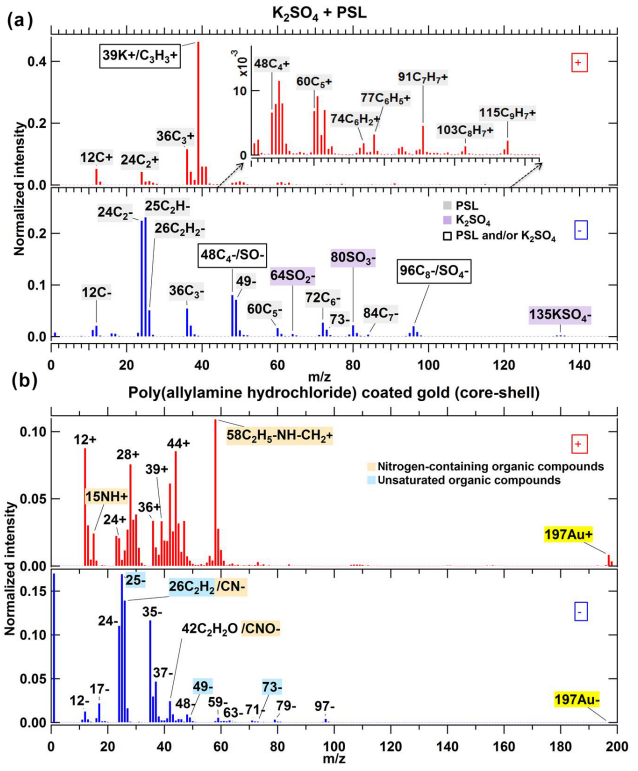

Figure 5. Average mass spectra for core–shell particles of **(a)** PSL coated with K_2SO_4, $d_{va} = 805$ nm, 609 single spectra averaged, and **(b)** poly(allylamine hydrochloride)-coated gold (Au) particles with geometric 300 nm gold core and 50 nm thick organic shell, 417 single spectra averaged. In **(a)**, grey and purple label shadings represent the fragments arising from pure PSL and pure K_2SO_4 components, respectively; box labels represent the fragments with contributions from core and shell compounds. In **(b)** orange and blue label shadings represent the fragments arising from nitrogen-containing and unsaturated organic compounds, respectively, and yellow label shadings represent gold.

Mass spectra for other well-defined compounds, i.e. synthetic hematite and pure sea salt particles, are also provided in the Supplement (Figs. S10 and S11).

3.2.3 Particles consisting of complex mixtures

Figure 6 shows the average spectra for different types of soot particles. All of them show characteristic patterns for elemental carbon (EC) $Cn^{+/-}$. For soot 1 with high organic carbon (OC) content from propane combustion in the laboratory (panel b), prominent peaks were observed at m/z 28 CO^+ and 27 $C_2H_3^+$, as well as some other organic carbon signatures at m/z 39^+, 40^+, 44^+, and 56^+. All the organic signatures in soot 1 with high OC were also observed for soot 3, lignocellulosic char from chestnut wood (panel d), indicating that biomass burning soot contains a significant fraction of OC. It should be noted that biomass burning will also form potassium; thus m/z 39^+ contains both K^+ and $C_3H_3^+$ frag-

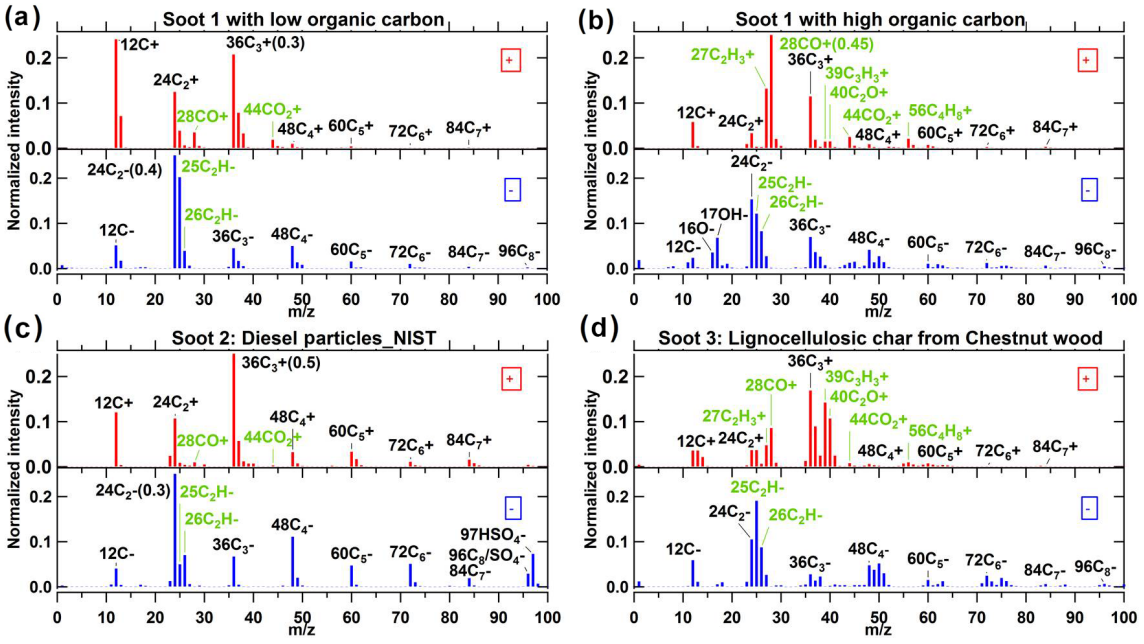

Figure 6. Average mass spectra for soot particles with **(a)** high elemental carbon (EC) and low organic carbon (OC) content, and **(b)** low EC and high OC from combustion of propane in a soot generator and transferred to a stainless-steel cylinder of $\sim 0.2\,m^3$ volume, as well as soot particles of **(c)** diesel particles (NIST) and **(d)** lignocellulosic char from chestnut wood. In **(a)** and **(c)**, the numbers in brackets beside peak 36^+ and 24^- are the exact intensity values for them. The OC signatures are labelled in green. The numbers of spectra averaged for each spectrum are 617 **(a)**, 347 **(b)**, 533 **(c)** and 390 **(d)**.

ments. $M/z\,24^-$, 25^-, and 26^- can be observed in all the soot types, but with slightly different patterns: (1) soot with high EC content shows very high $m/z\,24^-$ ($\sim$2 to 3 times that of $m/z\,25^-$), while (2) soot with high OC shows comparable or even higher $m/z\,25^-$ to/than $m/z\,24^-$. These patterns might help to distinguish EC and OC contributions in the spectra from ambient particles.

Figure 7 shows spectra for Arizona test dust (milled desert dust) (panel a), arable soil SDGe01 sampled from Gottesgabe in Germany (panel b), and agricultural soil dust collected from harvesting machines after rye and wheat harvest (panel c). For Arizona test dust, we observed high mineral signatures of aluminium- and silicon-containing clusters, namely 27 Al^+, 28 Si^+, 44 SiO^+, 43 AlO^-, 59 AlO_2^-, 60 SiO_2^-, 76 SiO_3^-, 119 $AlSiO_4^-$, 179 $AlSiO_4.SiO_2^-$, and 136 $(SiO_2)_2O^-$. It should be noted that high 16 O^- and 17 OH^- accompany the intensive mineral signatures, attributed to the adsorbed water on the active surface of mineral particles. In panel a, we also observed the following peaks: other mineral related metal clusters (e.g. 7 Li^+, 23 Na^+, 24 Mg^+, 40 Ca^+, 39/41 K^+, 55 Mn^+, 56 Fe^+, 58 Ni^+, and 64 Zn^+); metal oxides and hydroxides (e.g. 56 CaO^+, 57 $CaOH^+$, 96 Ca_2O^+, and 112 $(CaO)_2^+$, and 88 FeO_2^-); and weak anion clusters of organic signature ($m/z\,24$ C_2^-, 25 C_2H^-, 26 $C_2H_2^-$, and 42 $C_2H_2O^-$), NOCs ($m/z\,26$ CN^- and 42 CNO^-), chloride ($m/z\,35^-$ and 37^-), sulfate ($m/z\,32^-$, 48^-, 64^-, 80^-, and 97^-), phosphate (63 PO_2^- and 79 PO_3^-), diacids (oxalate 89 $(CO)_2OOH^-$ and 117$(CO)_3OOH^-$), and an unknown fragment $m/z\,148^-$. $M/z\,26^+$ in panels b and c is much higher than $m/z\,24^-$ and 25^-, due to the contribution of CN fragments from NOCs. Similar signatures can also be observed in the spectra for Saharan dust (Fig. S12).

Most of the mineral and organic fragments of soil dust are similar to those of desert dust; however with different intensities – e.g. $m/z\,24^-$, 25^-, 26^-, and 42^- (labelled in green) – they are more intensive than those in desert dust, indicating higher organic compound content. Some peak ratios of fragments are similar across the different dust types; e.g. 40 Ca^+ to 56 CaO^+ is 2.2, 1.1, and 2 for desert dust, arable soil dust and agricultural soil dust, respectively. Compared with desert dust, there are different fragments from soil dust particles, e.g. EC patterns (labelled in grey), organic acids signatures (blue), ammonium signatures (orange), unsaturated organic fragments ($m/z\,49^-$ and 73^-), and some other unknown fragments (red). For arable soil dust particles, we also measured samples from Paulinenaue in Germany (SDPA01), Argentina (SDAr08), and Wyoming in the USA (SDWY01) (refer to Fig. S13). Dominant mass spectral peak patterns are similar across all soil dust samples. They are located at around $m/z\,27^+$, 39^+, and 56^+ in the positive spectra, and 26^-, 42^-, 60^-, and 76^- in negative spectra. Less prominent but reproducibly detected are carboxylic acid groups (e.g. $COOH^-$) and EC patterns. The German soil dust, however, contains more organic species than soil dust

Table 2. Summary of mass spectral patterns.

Species	Signature peaks in positive spectra	Signature peaks in negative spectra	Typical peak ratios histogram x_0 (width)*
potassium	39 K^+, 41 K^+		$I39 : I41 = \sim 13.5$ (0.9)
calcium	40 Ca^+, 56 CaO^+		
aluminium	27 Al^+	43 AlO^-, 59 AlO_2^-	
silicon	28 Si^+, 44 SiO^+	60 SiO_2^-, 76 SiO_3^-, 77 $HSiO_3^-$	$(I76 + I77) : I60 = \sim 1.0$ (0.33)
silicon & aluminium	27 Al^+, 28 Si^+, 44 SiO^+	43 AlO^-, 59 AlO_2^-, 60 SiO_2^-, 76 SiO_3^-,	
	77 $HSiO_3^-$, 119 $AlSiO_4^-$, 179 $AlSiO_4.SiO_2^-$		
ammonium	18 NH_4 / H_2O^+, 30 NO^+		
nitrate	30 NO^+	46 NO_2^-, 62 NO_3^-	
sulfate		32 S^-, 48 SO^-, 64 SO_2^-, 80 SO_3^-, 81HSO_3^-, 96 SO_4^-, 97 HSO_4^-,	
chloride		35 Cl^-, 37 Cl^-	$(I35 + I36) : I37 = \sim 3.1$ (0.5)
elemental carbon	12_n C_n^+	$12_n C_n^-$	
organics		24 C_2^-, 25 C_2H^-, 26 C_2H_2 / CN^- 26 C_2H_2 / CN^-	
organic acids		45 $COOH^-$, 59 CH_2COOH^-, 71 CCH_2COOH^-, 73 $C_2H_4COOH^-$, 85 $C_3H_4COOH^-$, 99 $C_4H_6COOH^-$, 117 $(CO)_3OOH^-$	
nitrogen-containing organics		26 CN^-, 42 CNO^-	
unsaturated organics		25 C_2H^-, 26 $C_2H_2^-$, unknown fragments 49- and 73-	
aromatic compounds	77 $C_6H_5^+$, 91$C_7H_7^+$, 103 $C_8H_7^+$ / 105 $C_8H_9^+$, 115 $C_9H_7^+$	25 C_2H^-, 26 $C_2H_2^-$, unknown fragments 49- and 73-	

* We have made histograms for each of the three typical peak ratios (ref. Fig. S5). Histogram x_0 is the expected value that indicates the position of the peak resulting from Gaussian fit, and the width is the corresponding standard deviation. I is short for the intensity of the corresponding peak in LAAPTOF spectra; typical peak ratios for potassium and chloride are based on pure and mixed salt containing K and Cl; typical peak ratios for silicon are based on pure SiO_2.

from Argentina and the USA, reflected in higher intensities at m/z 24^-, 25^-, and 26^-. Argentinian soil dust contains far fewer mineral species, expressed in much lower intensities of mineral signatures, e.g. m/z 27^+, 28^+, 40^+, 44^+, and 56^+. The ratios of m/z 39 K^+ and 41 K^+ (3.6, 3.8, 3.5, and 5.3 for SDGe01, SDPA01, SDAr08, and SDWY01, respectively) are much lower than the typical peak ratio ($\sim$ 13.5) for potassium (Table 2), indicating that they are likely contributed to by both potassium isotopes and hydrocarbon fragments.

For agricultural soil dust particles, obviously ammonium (m/z 18 NH_4^+ and 30 NO^+), phosphate (m/z 63 PO_2^-, 79 PO_3^-, and 95 PO_5^-), and potassium signatures (m/z 39 K^+ and 41 K^+) can be found in the spectra, attributed to fertilization. Apart from that, typical biological signatures were observed: (1) the strong m/z 26^-, 42^-, and 39^+ pattern is similar to the potassium organo-nitrogen particle type observed by an ATOFMS at an urban site in Barcelona (Dall'Osto et al., 2016), which was assigned to carbohydrates arising from biogenic species (Schmidt et al., 2017; Silva et al., 2000). (2) 26^- and 42^- could also be contributed by CN^- and CNO^- derived from NOCs, i.e. amines, as well as m/z 30 CH_3NH^+, 58 $C_2H_5NHCH_2^+$, and 59 $(CH_3)_3N^+$. These biological signatures have also been observed by ALABAMA in the field (Schmidt et al., 2017). (3) Some weak but reproducibly detected fragment pattern at around m/z 77 $C_6H_5^+$, 91 $C_7H_7^+$, 103 $C_8H_7^+$, 105 $C_8H_9^+$, and 115 $C_9H_7^+$ might originate from aromatic compounds. Similar patterns can also be found for PSL particles.

Other examples for complex mixtures, i.e. illite and sea salt particles with biological components, are provided in the Supplement (Figs. S14 and S11).

All the peak assignments and mass spectral patterns, like signature peaks, as well as some stable peak ratios mentioned above have been summarized in Table S1 in the Supplement and Table 2, respectively. We consider these laboratory-based reference spectra as useful for the analysis of data obtained

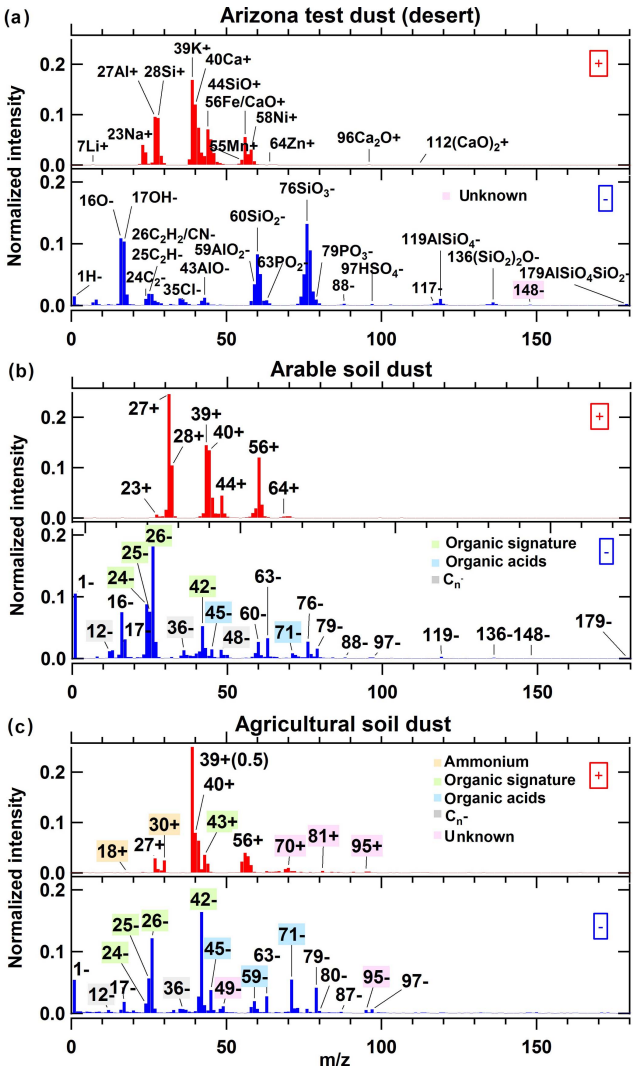

Figure 7. Average mass spectra for particles of complex mixtures: **(a)** Arizona test dust (desert dust), directly sampled into the LAAPTOF from a shaked bottle **(b)** arable soil dust, collected from Gottesgabe in Germany, was dispersed by a rotating brush generator and injected via cyclones into the AIDA chamber at 256 K and 80 % RH, and **(c)** agricultural soil dust, collected from harvesting machines after rye and wheat harvest, were generated by using the same method as **(b)**. For **(b)** and **(c)**, fragments labelled in green represent more intensive organic signatures in soil dust particles; grey labels represent EC patterns; blue labels represent organic acids; orange labels represent ammonium salts; red labels represent unknown fragments. The numbers of spectra averaged for each spectrum are 261 **(a)**, 583 **(b)**, and 286 **(c)**.

also by other LAAPTOF versions and to some extent even for other single-particle mass spectrometers. Similar mass spectra are to be expected as long as they use similar ablation and ionization laser pulses (4 mJ, 193 nm), inlet regions for the mass spectrometer, and mass spectrometer types. In the near future, we plan to make these laboratory-based reference spectra publicly available via the EUROCHAMP-2020 database (www.eurochamp.org, last access: 16 April 2018).

3.3 Interpretation of field data

Figure 8 shows an example of bipolar mass spectra for six different particle classes measured in the field campaign at a rural site near Leopoldshafen in southwest Germany. On 29 July 2016 within 24 h, 7314 particles were detected and successfully ablated, and mass spectra were generated by LAAPTOF. The 7314 pairs of spectra were then clustered by the fuzzy *c*-means algorithm, resulting in six classes. The resulting number of classes with clearly different features depends on the experience of the operating scientist to identify them (please refer to the details of fuzzy clustering in Procedure 1 in the Supplement). The fuzzy results are compared with the laboratory-based reference spectra by calculating their correlation coefficients (Fig. 9). All classes exhibit a sulfate signature with m/z 97 HSO_4^- and m/z 80 SO_3^-; a nitrate signature with m/z 46 NO_2^- and 62 NO_3^- ; an organic compound signature with m/z 24 C_2^-, 25 C_2H^-, and 26 C_2H_2/CN^-; and a NOC signature with m/z 26 CN^- and 42 CNO^- in the negative spectra. More characteristic signatures for each particle class can be observed in the positive spectra. All particles measured on this day show a 35 % similarity to class 5 with obvious signatures for potassium (K) and sulfate, with significant correlation with the reference particles containing potassium and sulfate (Fig. 9). Additionally, class 5 has a significant correlation with some other cations arising from ammonium, organic compounds, and dust. The ratio of m/z ($39^+ + 40^+$) to 41^+ is ∼ 11, close to the value for pure K_2SO_4 particles (∼ 13.5); thus we assigned them to K^+ rather than organic fragments. Further, there is a 15 % similarity to class 4 with prominent ammonium signatures at m/z 18 NH_4^+ and 30 NO^+, sulfate signatures, and a relatively weaker but reproducible nitrate signature. The corresponding spectrum is similar to the spectrum for the homogeneous mixtures of NH_4NO_3 and $(NH_4)_2SO_4$ (panel a in Fig. 4). This class also has strong correlation with both positive and negative reference spectra for the mixture of ammonium nitrate and ammonium sulfate particles. Ammonium, nitrate, and sulfate are the major secondary inorganic species in atmospheric aerosol particles (Seinfeld and Pandis, 2006); thus we name this class "secondary inorganic". It should be noted that this class has a significant correlation with ammonium and cations arising from oxalic acid; however class 4 has a weak correlation with the signature anion, i.e. m/z 89 $C_2O_4H^-$ (oxalate), of oxalic acid. Therefore, we can rule out a significant contribution of oxalic acid. There is also a 15 % similarity to class 2 (sodium rich), with a characteristic pattern of a strong signal at m/z 23 Na^+ accompanied by two weaker peaks at m/z 39 K^+ (with typical potassium peak ratio of ∼ 12) and 63^+ (might contain both Cu^+ and $C_5H_3^+$ fragments). Class 2 has a significant correlation with the cations (i.e. Na and K) arising from sea salt

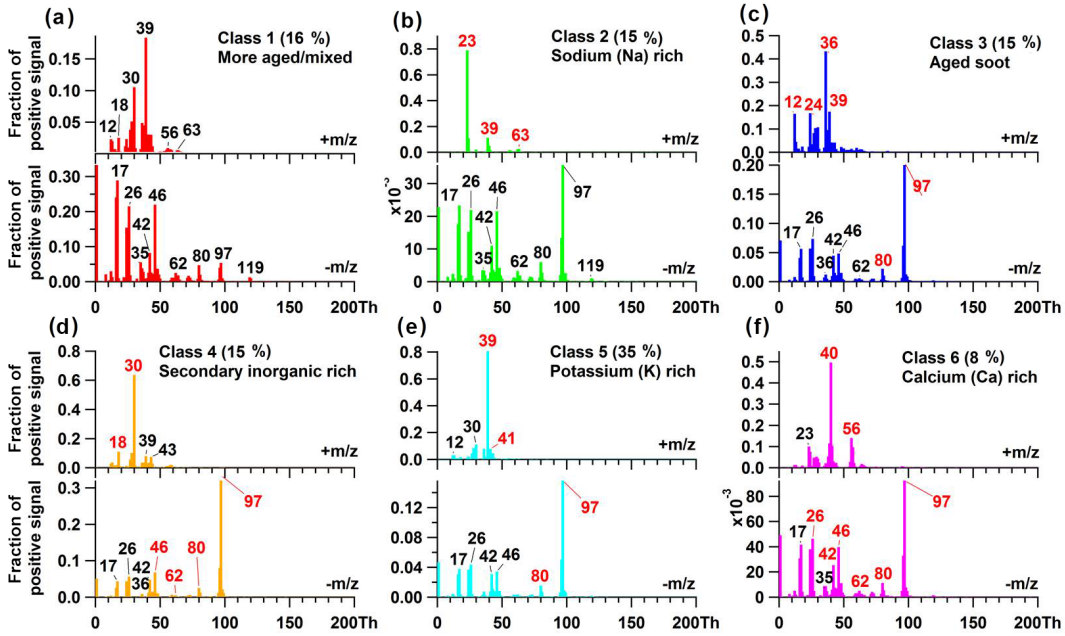

Figure 8. Mass spectra for six classes of particles measured on 29 July 2016 during the field campaign TRAM01, based on classification according to the fuzzy *c*-means algorithm. The percentage in each pair of spectra (**a** to **f**) gives us information about the similarity of the total aerosols to different classes. The red tags represent the signatures for each typical class, but there is no red tag in **(b)**, since this class consists of more aged particles containing signatures for different classes. Mean particle size: d_{va} (676 ± 165) nm.

but a weak correlation with its anions, such as m/z 35$^-$ and 37$^-$ chloride isotopes. A sea salt contribution can thus be ruled out. Its negative spectrum significantly correlates with nitrate, sulfate, and dust particles. Besides sodium-rich dust, aged sea salt may be an appropriate classification. Class 3 is named "aged soot", since it has a significant correlation with soot particles, especially diesel soot, and a prominent sulfate signal. This class has an EC pattern with m/z 12n C_n^+, similar to those in the reference spectra for soot particles (Fig. 6) as well as the reference spectra for PSL particles (Fig. S9). The patterns at m/z 27 $C_2H_3^+$ and 28 CO^+; m/z 36 C_3^+ and 39 $C_3H_3^+$; and the m/z 24$^-$, 25$^-$, and 26$^-$ with higher m/z 26$^-$ indicate an OC contribution. This is supported by the correlations, especially with PSL particles, as well as several other organic compounds, suggesting that this class of particles contains organic species. Class 6 is dominated by calcium (Ca) and sulfate with characteristic calcium signature peaks at m/z 40 Ca^+ and 56 CaO^-, also found in the spectra for dust particles (Figs. 7, S12, and S13). M/z 40$^+$ and 56$^+$ may also contain 40 C_2O^+ and 56 Fe/$C_4H_8^+$ fragments, respectively. Class 1 contains almost all fragments observed in other classes and is thus named "more aged/mixed particles". As shown in Fig. 9, class 6 is consequently correlated with almost all of the reference spectra (both positive and negative ones).

In order to further interpret the field data, we also classified the ambient mass spectra only based on correlation with 17 selected laboratory-based reference spectra (10 positive +7 negative spectra) listed in Table S2. This approach resulted in 13 particle types, 7 more than were distinguished by fuzzy clustering. It should be mentioned that at the beginning we were able to identify all but the Ca-rich particle class resulting from fuzzy clustering, since initially we did not have a reference for this type. We therefore used class 6 as an additional reference spectrum for this type of particles, which is among one of the 13 types (here we use "types" instead of "classes" in order to differentiate these two classification methods). Their corresponding spectra are shown in Fig. 10. All the types above the dashed line (panels a to i) exhibit more prominent secondary inorganic signatures (m/z 97 HSO_4^-) and higher number fractions than the ones below the dashed line. Although particle types A to I all exhibit a more prominent sulfate pattern with m/z 80 and 97 than nitrate pattern with m/z 46 and 62, they are more highly correlated with the mixture of nitrate and sulfate than either of them. Therefore, we assign the corresponding types to nitrate and sulfate. All the types in the lower panels (j to m) have significant correlation with arable soil dust in the negative spectra, which have organic signatures (e.g. m/z 24$^-$, 25$^-$, and 26$^-$) as well as some mineral signatures like m/z 119$^-$. Compared with the negative spectra, the positive spectra are more characteristic, which was also observed in the fuzzy results. Type A, B, C, D, and E are comparable with fuzzy class 5, 4, 2, 6, and 3, respectively (the correlation coefficients are 0.89 for type A and class 5, 0.95 for type B and class 4, 0.84 for type C and class 2, 0.76 for type D and

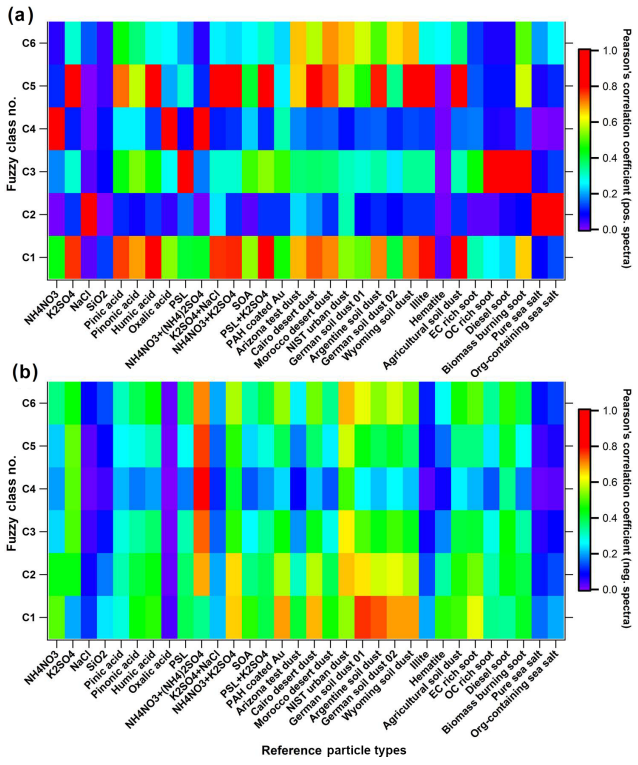

Figure 9. Correlation between fuzzy classification results (6 classes, C1 to C6) and laboratory-based reference spectra. **(a)** and **(b)** are the correlation results for the positive and negative spectra, respectively. PAH is short for poly(allylamine hydrochloride); biomass burning soot is the lignocellulosic char from chestnut wood.

class 6, and 0.81 for type E and class 3). Types F to I are more similar to aged/mixed particles, with more fragments than types A to E. Type H is comparable with fuzzy class 1. About 10 % of the particles cannot be grouped into any type. This is most likely because of an incorrect mass assignment for the stick spectra, resulting from too-large spectrum-to-spectrum peak shifts for the same ion fragments/clusters which cannot be corrected on a single-particle basis with the existing software (Ramisetty et al., 2017). As shown in the spectra in both Figs. 8 and 10, all organic species were internally mixed with inorganic species.

This reference-spectra-based classification can also be used for identification of particles with low number fractions among the huge amount of ambient data, and for selection of particles containing particular species, e.g. ones to which the instrument has a lower sensitivity. This can be achieved by e.g. excluding peaks with high signal, such as m/z 39 $K/C_3H_3^+$, or by selecting a certain particle size range or mass range. As an example, 55 lead-containing particles (Pb, with isotopes at m/z 206, 207, and 208) (details are given in the Procedure 3 in the Supplement) were identified among the 7314 ambient aerosol particles. The resulting spectra of particle classes/types in one field study can also be used as a reference for other studies. More applications of these procedures for field data interpretation will be presented in an upcoming paper.

In short, fuzzy and reference-spectra-based classifications have some comparable results with high correlations (r: 0.76–0.95) and also have different advantages: fuzzy classification can identify special ambient particle types without any existing reference if they have a significant abundance and signal strength, while reference-spectra-based methods can identify target particle types even with little abundance. They are complementary to some extent, and thus their combination has the potential to improve interpretation of field data.

4 Conclusions

In this study, the overall detection efficiency (ODE) of LAAPTOF was determined to range from $\sim(0.01 \pm 0.01)$ to $\sim(4.23 \pm 2.36)$ % for polystyrene latex (PSL), with the size of 200 to 2000 nm, $\sim(0.44 \pm 0.19)$ to $\sim(6.57 \pm 2.38)$ % for ammonium nitrate (NH_4NO_3) and $\sim(0.14 \pm 0.02)$ to $\sim(1.46 \pm 0.08)$ % for sodium chloride (NaCl) particles in the size range of 300 to 1000 nm. This is a relative good detection efficiency compared to earlier versions of the instruments, especially when considering the good reproducibility and stability even during field measurements. A comparison to other single-particle mass spectrometers is the subject of another study and will be discussed in a separate publication. Matrix effects from aerosol particles (e.g. size, morphology, and optical property) and certain instrument influences (e.g. aerodynamic lens, detection system) and their interaction must be taken into account to evaluate the LAAPTOF performance.

In order to facilitate the interpretation of single-particle mass spectra from field measurements, we have measured various well-defined atmospherically relevant aerosol particles in the laboratory and provide here laboratory-based reference spectra for aerosol particles of different complexity with comprehensive spectral information about the components (such as organic compounds, elemental carbon, sulfate, nitrate, ammonium, chloride, mineral compounds, and metals, as commonly observed in atmospheric aerosol particles). Our results show that the interpretation of spectra from unknown particle types is significantly supported by using known mass spectral patterns like signature peaks for ammonium, nitrate, sulfate, and organic compounds as well as typical peak ratios for e.g. potassium, silicon, and chlorides. Spectra for internally mixed particles may show new clusters of ions, rather than simply a combination of the ions from single-component particles. This may be a complication for data interpretation which can be overcome if suitable reference spectra for correspondingly mixed particles are available. Organic compounds generally have some ions in common but exhibit variations depending on the com-

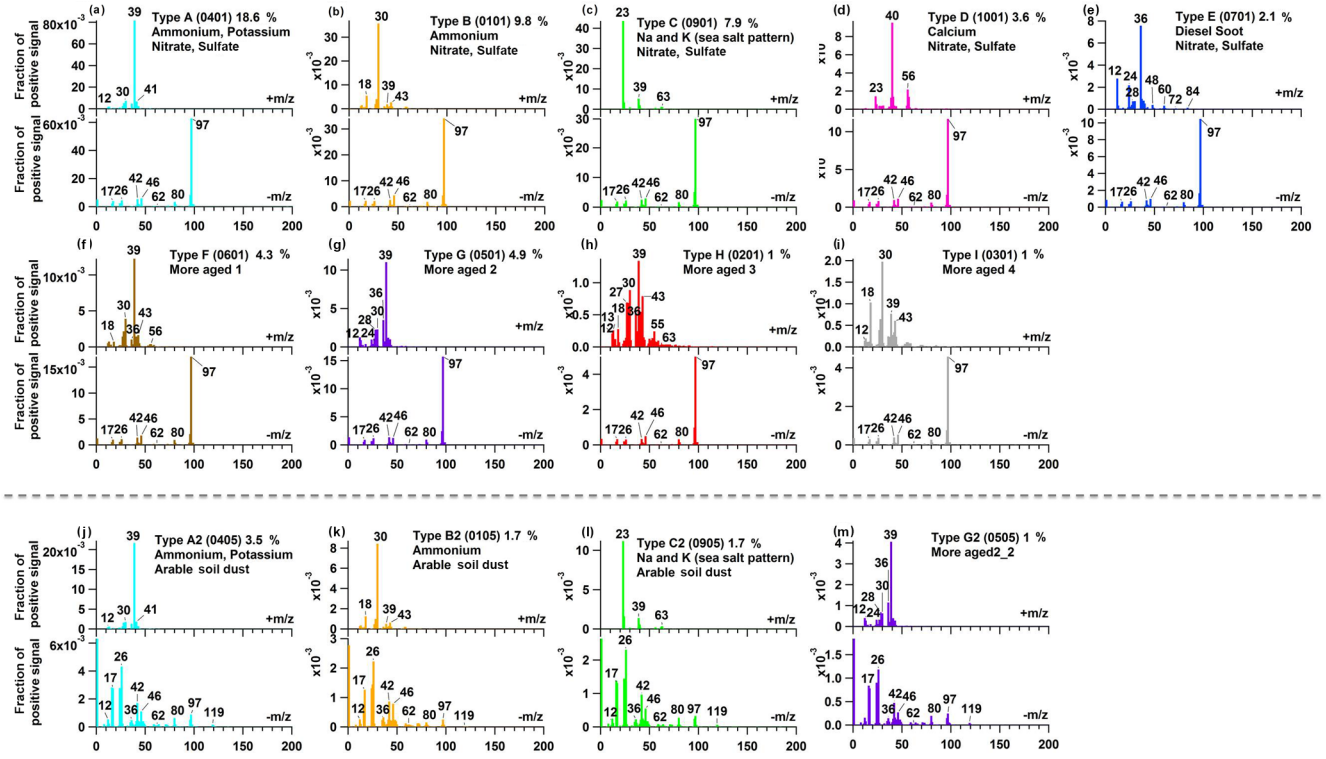

Figure 10. Mass spectra for 13 different types of particles measured on 29 July 2016 during the field campaign TRAM01, based on the classification according to laboratory-based reference spectra. The four-digit codes in the brackets represent particle types (refer to Table S2). The percent values are the particle number fractions. For **(a)** to **(e)** and **(j)** to **(l)**, there are two lines for the names; the first and second lines correspond to the highly correlated positive and negative references, respectively.

pound. Several peaks can originate from different fragments: for example, m/z 26$^-$ and 42$^-$ could be CN^- and CNO^- and/or $C_2H_2^-$ and $C_2H_2O^-$, m/z 39$^+$ and 41$^+$ could originate from K^+ isotopes and/or organic fragments, and organic matter can also be ionized to form the typical elemental carbon pattern with $C_n^{+/-}$ ions. Hence the interpretation is not always unambiguously possible for such particles but may require additional information (e.g. size, additional marker peaks, or even higher-resolution spectra) or comparison to data from other instruments like online aerosol mass spectrometers (e.g. AMS) or chemical ionization mass spectrometers (e.g. FIGAERO-CIMS).

A set of 7314 mass spectra obtained during 1 day of field measurements was used for particle type classification by both fuzzy clustering and reference spectra. Fuzzy clustering yielded six different classes, which could then be identified with the help of reference spectra. Classification of the mass spectra based on comparison with 17 reference spectra resulted in 13 different particle types, 6 of which exhibited high correlation with the fuzzy clusters (r: 0.76–0.95). Compared with the reference spectra, we found that each particle class/type has a sulfate signature at m/z 80 SO_3^- and 97 HSO_4^-; a nitrate signature at m/z 46 NO_2^- and 62 NO_3^-; an organic compound signature at m/z 24 C_2^-, 25 C_2H^-, and 26 C_2H_2/CN^-; and a nitrogen-containing organic signature at m/z 26 CN^- and 42 CNO^-. Furthermore, we performed a target-oriented classification by using selected reference spectra, allowing for the identification of particles with low number fraction in the ambient aerosol, e.g. lead-containing particles. Based on our results, we advise using a combination of both methods for the analysis of SPMS field data.

We conclude that the reference spectra presented in this paper are useful for interpretation of field measurements and for understanding the impact of mixing on typical mass spectral signatures. Furthermore, the reference spectra should be useful for interpretation of data obtained by other LAAPTOF versions or other single-particle mass spectrometers using a similar ionization method and comparable mass spectrometers. For future experiments using the LAAPTOF, systematic studies are still required on its sensitivity to different species, distinguishing the organic and inorganic contribution to the same peak in the spectra, and investigating peak ratios.

Data availability. The reference spectra are available upon request from the authors and are available in electronic format via the EUROCHAMP DATA CENTER – Library of Analytical Resources of the EU project EUROCHAMP-2020 (https://data.eurochamp.org/, EUROCHAMP, 2018).

The Supplement related to this article is available online at https://doi.org/10.5194/amt-11-2325-2018-supplement.

Author contributions. XS characterized the LAAPTOF, measured all the particles samples, did the data analysis, produced all figures, and wrote the manuscript. RR helped to characterize the LAAPTOF and to measure some of the particle samples. CM provided technical and scientific support for characterizing the LAAPTOF as well as data analysis, and for interpretation and discussion of the results. WH provided scientific support for interpretation and discussion of the results. TL gave general advices and comments for this paper. HS provided technical and scientific support for characterizing the LAAPTOF, as well as suggestions for the data analysis, interpretation, and discussion. All authors contributed to the final text.

Competing interests. The authors declare that they have no conflict of interest.

Acknowledgements. The authors gratefully thank the AIDA staff at KIT for helpful discussions and technical support, and the China Scholarship Council (CSC) for financial support of Xiaoli Shen and Wei Huang. Special thanks go to Robert Wagner for Mie calculation and discussion and comments on the sea salt samples; to Thea Schiebel, Kristina Höhler, and Ottmar Möhler for discussions about the soil dust samples; to Isabelle Steinke for discussions regarding the plant samples; to Konrad Kandler for providing the Morocco desert dust samples; to Roger Funk and Thomas Hill for providing the soil dust samples; to Elena Gorokhova and Matt Salter for providing the sea salt with *Skeletonema marinoi* culture; and to AeroMegt GmbH for discussions about the LAAPTOF performance and analysis software.

The article processing charges for this open-access publication were covered by a Research Centre of the Helmholtz Association.

Edited by: Joachim Curtius
Reviewed by: two anonymous referees

References

Ackerman, A. A., Adam, J. A., Cairns, B., Cho, H., Gritsevich, M., Jethva, H., Kacenelenbogen, M., Kandler, K., Knobelspiesse, K., Lanconelli, C., Lupi, A., Mazzola, M., Nousiainen, T., Peltoniemi, J. I., Platnick, S., Puttonen, E., Savenkov, S. N., Segal-Rosenheimer, M., Sharma, S., Tomasi, C., Torres, O., and Zhang, Z.: Light scattering reviews 9: Light scattering and radiative transfer, Springer-Praxis, 2015.

Ahern, A. T., Subramanian, R., Saliba, G., Lipsky, E. M., Donahue, N. M., and Sullivan, R. C.: Effect of secondary organic aerosol coating thickness on the real-time detection and characterization of biomass-burning soot by two particle mass spectrometers, Atmos. Meas. Tech., 9, 6117–6137, https://doi.org/10.5194/amt-9-6117-2016, 2016.

Arndt, J., Sciare, J., Mallet, M., Roberts, G. C., Marchand, N., Sartelet, K., Sellegri, K., Dulac, F., Healy, R. M., and Wenger, J. C.: Sources and mixing state of summertime background aerosol in the north-western Mediterranean basin, Atmos. Chem. Phys., 17, 6975–7001, https://doi.org/10.5194/acp-17-6975-2017, 2017.

Bohren, C. F. and Huffman, R. D.: Absorption and scattering of light by small particles, WILEY-VCH Verlag GmbH & Co. KGaA, 2007.

Brands, M., Kamphus, M., Böttger, T., Schneider, J., Drewnick, F., Roth, A., Curtius, J., Voigt, C., Borbon, A., Beekmann, M., Bourdon, A., Perrin, T., and Borrmann, S.: Characterization of a newly developed aircraft-based laser ablation aerosol mass spectrometer (ALABAMA) and first field deployment in urban pollution plumes over Paris during MEGAPOLI 2009, Aerosol Sci. Tech., 45, 46–64, 2011.

Burkholder, J. B., Abbatt, J. P. D., Barnes, I., Roberts, J. M., Melamed, M. L., Ammann, M., Bertram, A. K., Cappa, C. D., Carlton, A. G., Carpenter, L. J., Crowley, J. N., Dubowski, Y., George, C., Heard, D. E., Herrmann, H., Keutsch, F. N., Kroll, J. H., McNeill, V. F., Ng, N. L., Nizkorodov, S. A., Orlando, J. J., Percival, C. J., Picquet-Varrault, B., Rudich, Y., Seakins, P. W., Surratt, J. D., Tanimoto, H., Thornton, J. A., Tong, Z., S., T. G., Wahner, A., Weschler, C. J., Wilson, K. R., and Ziemann, P. J.: The essential role for laboratory studies in atmospheric chemistry, Environ. Sci. Technol., 51, 2519–2528, 2017.

Canagaratna, M. R., Jayne, J. T., Jimenez, J. L., Allan, J. D., Alfarra, M. R., Zhang, Q., Onasch, T. B., Drewnick, F., Coe, H., Middlebrook, A., Delia, A., Williams, L. R., Trimborn, A. M., Northway, M. J., DeCarlo, P. F., Kolb, C. E., Davidovits, P., and Worsnop, D. R.: Chemical and microphysical characterization of ambient aerosols with the aerodyne aerosol mass spectrometer, Mass Spectrom. Rev., 26, 185–222, 2007.

Dall'Osto, M., Beddows, D. C. S., McGillicuddy, E. J., Esser-Gietl, J. K., Harrison, R. M., and Wenger, J. C.: On the simultaneous deployment of two single-particle mass spectrometers at an urban background and a roadside site during SAPUSS, Atmos. Chem. Phys., 16, 9693–9710, https://doi.org/10.5194/acp-16-9693-2016, 2016.

EUROCHAMP: EUROCHAMP DATA CENTER – Library of Analytical Resources of the EU project EUROCHAMP-2020, available at: https://data.eurochamp.org/, last access: 16 April 2018.

Gaie-Levrel, F., Perrier, S., Perraudin, E., Stoll, C., Grand, N., and Schwell, M.: Development and characterization of a single particle laser ablation mass spectrometer (SPLAM) for organic aerosol studies, Atmos. Meas. Tech., 5, 225–241, https://doi.org/10.5194/amt-5-225-2012, 2012.

Gemayel, R., Hellebust, S., Temime-Roussel, B., Hayeck, N., Van Elteren, J. T., Wortham, H., and Gligorovski, S.: The performance and the characterization of laser ablation aerosol particle time-of-flight mass spectrometry (LAAP-ToF-MS), Atmos. Meas. Tech., 9, 1947–1959, https://doi.org/10.5194/amt-9-1947-2016, 2016.

Gross, D. S., Gälli, M. E., Silva, P. J., and Prather, K. A.: Relative sensitivity factors for alkali metal and ammonium cations in single particle aerosol time-of-flight mass spectra, Anal. Chem., 72, 416–422, 2000.

Hagemann, R., Corsmeier, U., Kottmeier, C., Rinke, R., Wieser, A., and Vogel, B.: Spatial variability of particle number concentra-

tions and NOx in the Karlsruhe (Germany) area obtained with the mobile laboratory "AERO-TRAM", Atmos. Environ., 94, 341–352, 2014.

Hinz, K. P., Greweling, M., Drews, F., and Spengler, B.: Data processing in on-line laser mass spectrometry of inorganic, organic, or biological airborne particles, J. Am. Soc. Mass Spectr., 10, 648–660, 1999.

Jimenez, J. L., Canagaratna, M. R., Donahue, N. M., Prevot, A. S. H., Zhang, Q., Kroll, J. H., DeCarlo, P. F., Allan, J. D., Coe, H., Ng, N. L., Aiken, A. C., Docherty, K. S., Ulbrich, I. M., Grieshop, A. P., Robinson, A. L., Duplissy, J., Smith, J. D., Wilson, K. R., Lanz, V. A., Hueglin, C., Sun, Y. L., Tian, J., Laaksonen, A., Raatikainen, T., Rautiainen, J., Vaattovaara, P., Ehn, M., Kulmala, M., Tomlinson, J. M., Collins, D. R., Cubison, M. J., Dunlea, E. J., Huffman, J. A., Onasch, T. B., Alfarra, M. R., Williams, P. I., Bower, K., Kondo, Y., Schneider, J., Drewnick, F., Borrmann, S., Weimer, S., Demerjian, K., Salcedo, D., Cottrell, L., Griffin, R., Takami, A., Miyoshi, T., Hatakeyama, S., Shimono, A., Sun, J. Y., Zhang, Y. M., Dzepina, K., Kimmel, J. R., Sueper, D., Jayne, J. T., Herndon, S. C., Trimborn, A. M., Williams, L. R., Wood, E. C., Middlebrook, A. M., Kolb, C. E., Baltensperger, U., and Worsnop, D. R.: Evolution of organic aerosols in the atmosphere, Science, 326, 1525–1529, 2009.

Johnston, M. V.: Sampling and analysis of individual particles by aerosol mass spectrometry, J. Mass Spectrom., 35, 585–595, 2000.

Kamphus, M., Ettner-Mahl, M., Brands, M., Curtius, J., Drewnick, F., and Borrmann, S.: Comparison of two aerodynamic lenses as an inlet for a single particle laser ablation mass spectrometer, Aerosol Sci. Tech., 42, 970–980, 2008.

Kulkarni, P., Baron, P. A., and Willeke, K.: Aerosol measurement: Principles,techniques, and applications, Wiley, J & Sons, Inc., 2011.

Li, L., Huang, Z. X., Dong, J. G., Li, M., Gao, W., Nian, H. Q., Fu, Z., Zhang, G. H., Bi, X. H., Cheng, P., and Zhou, Z.: Real time bipolar time-of-flight mass spectrometer for analyzing single aerosol particles, Int. J. Mass Spectrom., 303, 118–124, 2011.

Li, W., Sun, J., Xu, l., Shi, Z., Riemer, N., Sun, Y., Fu, P., Zhang, J., Lin, Y., Wang, X., Shao, L., Chen, J., Zhang, X., Wang, Z., and Wang, W.: A conceptual framework for mixing structures in individual aerosol particles, J. Geophys. Res.-Atmos., 121, 13784–13798, 2016.

Lin, Q., Zhang, G., Peng, L., Bi, X., Wang, X., Brechtel, F. J., Li, M., Chen, D., Peng, P., Sheng, G., and Zhou, Z.: In situ chemical composition measurement of individual cloud residue particles at a mountain site, southern China, Atmos. Chem. Phys., 17, 8473–8488, https://doi.org/10.5194/acp-17-8473-2017, 2017.

Liu, P., Ziemann, P. J., Kittelson, D. B., and McMurry, P. H.: Generating particle beams of controlled dimensions and divergence: II. Experimental evaluation of particle motion in aerodynamic lenses and nozzle expansions, Aerosol Sci. Tech., 22, 314–324, 1995.

Marsden, N., Flynn, M. J., Taylor, J. W., Allan, J. D., and Coe, H.: Evaluating the influence of laser wavelength and detection stage geometry on optical detection efficiency in a single-particle mass spectrometer, Atmos. Meas. Tech., 9, 6051–6068, https://doi.org/10.5194/amt-9-6051-2016, 2016.

Marsden, N. A., Flynn, M. J., Allan, J. D., and Coe, H.: Online differentiation of mineral phase in aerosol particles by ion formation mechanism using a LAAP-TOF single-particle mass spectrometer, Atmos. Meas. Tech., 11, 195–213, https://doi.org/10.5194/amt-11-195-2018, 2018.

Moffet, R. C., de Foy, B., Molina, L. T., Molina, M. J., and Prather, K. A.: Measurement of ambient aerosols in northern Mexico City by single particle mass spectrometry, Atmos. Chem. Phys., 8, 4499–4516, https://doi.org/10.5194/acp-8-4499-2008, 2008.

Murphy, D. M.: The design of single particle laser mass spectrometers, Mass Spectrom. Rev., 26, 150–165, 2007.

Murphy, D. M., Middlebrook, A. M., and Warshawsky, M.: Cluster analysis of data from the Particle Analysis by Laser Mass Spectrometry (PALMS) instrument, Aerosol Sci. Tech., 37, 382–391, 2003.

Murphy, D. M., Cziczo, D. J., Froyd, K. D., Hudson, P. K., Matthew, B. M., Middlebrook, A. M., Peltier, R. E., Sullivan, A., Thomson, D. S., and Weber, R. J.: Single-particle mass spectrometry of tropospheric aerosol particles, J. Geophys. Res.-Atmos., 111, D23S32, https://doi.org/10.1029/2006JD007340, 2006.

Noble, C. A. and Prather, K. A.: Real-time single particle mass spectrometry: a historical review of a quarter century of the chemical analysis of aerosols, Mass Spectrom. Rev., 19, 248–274, 2000.

Pöschl, U.: Atmospheric aerosols: Composition, transformation, climate and health effects, Angew. Chem. Int. Edit., 44, 7520–7540, 2005.

Pratt, K. A. and Prather, K. A.: Mass spectrometry of atmospheric aerosols-Recent developments and applications. Part II: On-line mass spectrometry techniques, Mass Spectrom. Rev., 31, 17–48, 2012.

Ramisetty, R., Abdelmonem, A., Shen, X., Saathoff, H., Leisner, T., and Mohr, C.: Exploring femtosecond laser ablation in single particle aerosol mass spectrometry, Atmos. Meas. Tech. Discuss., https://doi.org/10.5194/amt-2017-357, in review, 2017.

Reitz, P., Zorn, S. R., Trimborn, S. H., and Trimborn, A. M.: A new, powerful technique to analyze single particle aerosol mass spectra using a combination of OPTICS and the fuzzy c-means algorithm, J. Aerosol Sci., 98, 1–14, 2016.

Roth, A., Schneider, J., Klimach, T., Mertes, S., van Pinxteren, D., Herrmann, H., and Borrmann, S.: Aerosol properties, source identification, and cloud processing in orographic clouds measured by single particle mass spectrometry on a central European mountain site during HCCT-2010, Atmos. Chem. Phys., 16, 505–524, https://doi.org/10.5194/acp-16-505-2016, 2016.

Saathoff, H., Möhler, O., Schurath, U., Kamm, S., Dippel, B., and Mihelcic, D.: The AIDA soot aerosol characterisation campaign 1999, J. Aerosol Sci., 34, 1277–1296, 2003.

Saathoff, H., Naumann, K.-H., Möhler, O., Jonsson, Å. M., Hallquist, M., Kiendler-Scharr, A., Mentel, Th. F., Tillmann, R., and Schurath, U.: Temperature dependence of yields of secondary organic aerosols from the ozonolysis of α-pinene and limonene, Atmos. Chem. Phys., 9, 1551–1577, https://doi.org/10.5194/acp-9-1551-2009, 2009.

Schill, G. P. and Tolbert, M. A.: Heterogeneous ice nucleation on phase-separated organic-sulfate particles: effect of liquid vs. glassy coatings, Atmos. Chem. Phys., 13, 4681–4695, https://doi.org/10.5194/acp-13-4681-2013, 2013.

Schmidt, S., Schneider, J., Klimach, T., Mertes, S., Schenk, L. P., Kupiszewski, P., Curtius, J., and Borrmann, S.: Online single particle analysis of ice particle residuals from mountain-top mixed-

phase clouds using laboratory derived particle type assignment, Atmos. Chem. Phys., 17, 575–594, https://doi.org/10.5194/acp-17-575-2017, 2017.

Schreiner, J., Schild, U., Voigt, C., and Mauersberger, K.: Focusing of aerosols into a particle beam at pressures from 10 to 150 Torr, Aerosol Sci. Tech., 31, 373–382, 1999.

Seinfeld, J. H. and Pandis, S. N.: Atmospheric chemistry and physics: From air pollution to climate change, Wiley, J & Sons, Inc., Hoboken, New Jersey, 2006.

Silva, P. J., Carlin, R. A., and Prather, K. A.: Single particle analysis of suspended soil dust from Southern California, Atmos. Environ., 34, 1811–1820, 2000.

Su, Y. X., Sipin, M. F., Furutani, H., and Prather, K. A.: Development and characterization of an aerosol time-of-flight mass spectrometer with increased detection efficiency, Anal. Chem., 76, 712–719, 2004.

Tsigaridis, K., Krol, M., Dentener, F. J., Balkanski, Y., Lathière, J., Metzger, S., Hauglustaine, D. A., and Kanakidou, M.: Change in global aerosol composition since preindustrial times, Atmos. Chem. Phys., 6, 5143–5162, https://doi.org/10.5194/acp-6-5143-2006, 2006.

Usher, C. R., Michel, A. E., and Grassian, V. H.: Reactions on mineral dust, Chem. Rev., 103, 4883–4939, 2003.

Wagner, R., Kaufmann, J., Möhler, O., Saathoff, H., Schnaiter, M., Ullrich, R., and Leisner, T.: Heterogeneous ice nucleation ability of NaCl and sea salt aerosol particles at cirrus temperatures, J. Geophys. Res., 123, 2841–2860, https://doi.org/10.1002/2017JD027864, 2018.

Williams, L. R., Gonzalez, L. A., Peck, J., Trimborn, D., McInnis, J., Farrar, M. R., Moore, K. D., Jayne, J. T., Robinson, W. A., Lewis, D. K., Onasch, T. B., Canagaratna, M. R., Trimborn, A., Timko, M. T., Magoon, G., Deng, R., Tang, D., de la Rosa Blanco, E., Prévôt, A. S. H., Smith, K. A., and Worsnop, D. R.: Characterization of an aerodynamic lens for transmitting particles greater than 1 micrometer in diameter into the Aerodyne aerosol mass spectrometer, Atmos. Meas. Tech., 6, 3271–3280, https://doi.org/10.5194/amt-6-3271-2013, 2013.

Wonaschuetz, A., Kallinger, P., Szymanski, W., and Hitzenberger, R.: Chemical composition of radiolytically formed particles using single-particle mass spectrometry, J. Aerosol Sci., 113, 242–249, 2017.

Yu, J. Z., Cocker, D. R., Griffin, R. J., Flagan, R. C., and Seinfeld, J. H.: Gas-phase ozone oxidation of monoterpenes: Gaseous and particulate products, J. Atmos. Chem., 34, 207–258, 1999.

Zawadowicz, M. A., Abdelmonem, A., Mohr, C., Saathoff, H., Froyd, K. D., Murphy, D. M., LeisnerI, T., and Cziczo, D. J.: Single-particle time-of-flight mass spectrometry utilizing a femtosecond desorption and ionization laser, Anal. Chem., 87, 12221–12229, 2015.

Zawadowicz, M. A., Lance, S., Jayne, J. T., Croteau, P., Worsnop, D. R., Mahrt, F., Leisner, T., and Cziczo, D. J.: Quantifying and improving the performance of the Laser Ablation Aerosol Particle Time of Flight Mass Spectrometer (LAAPToF) instrument, Atmos. Meas. Tech. Discuss., https://doi.org/10.5194/amt-2017-1, 2017.

Zelenyuk, A. and Imre, D.: Single particle laser ablation time-of-flight mass spectrometer: An introduction to SPLAT, Aerosol Sci. Tech., 39, 554–568, 2005.

Zelenyuk, A., Cai, Y., and Imre, D.: From agglomerates of spheres to irregularly shaped particles: Determination of dynamic shape factors from measurements of mobility and vacuum aerodynamic diameters, Aerosol Sci. Tech., 40, 197–217, 2006a.

Zelenyuk, A., Imre, D., Cai, Y., Mueller, K., Han, Y. P., and Imrich, P.: SpectraMiner, an interactive data mining and visualization software for single particle mass spectroscopy: A laboratory test case, Int. J. Mass Spectrom., 258, 58–73, 2006b.

Zelenyuk, A., Yang, J., Choi, E., and Imre, D.: SPLAT II: An aircraft compatible, ultra-sensitive, high precision instrument for in-situ characterization of the size and composition of fine and ultrafine particles, Aerosol Sci. Tech., 43, 411–424, 2009.

Zhang, Q., Jimenez, J. L., Canagaratna, M. R., Allan, J. D., Coe, H., Ulbrich, I., Alfarra, M. R., Takami, A., Middlebrook, A. M., Sun, Y. L., Dzepina, K., Dunlea, E., Docherty, K., DeCarlo, P. F., Salcedo, D., Onasch, T., Jayne, J. T., Miyoshi, T., Shimono, A., Hatakeyama, S., Takegawa, N., Kondo, Y., Schneider, J., Drewnick, F., Borrmann, S., Weimer, S., Demerjian, K., Williams, P., Bower, K., Bahreini, R., Cottrell, L., Griffin, R. J., Rautiainen, J., Sun, J. Y., Zhang, Y. M., and Worsnop, D. R.: Ubiquity and dominance of oxygenated species in organic aerosols in anthropogenically-influenced Northern Hemisphere midlatitudes, Geophys. Res. Lett., 34, L13801, https://doi.org/10.1029/2007GL029979, 2007.

Zhao, W. X., Hopke, P. K., and Prather, K. A.: Comparison of two cluster analysis methods using single particle mass spectra, Atmos. Environ., 42, 881–892, 2008.

B.5 Understanding atmospheric aerosol particles with improved particle identification and quantification by single-particle mass spectrometry

Authors: Xiaoli Shen, Harald Saathoff, **Wei Huang**, Claudia Mohr, Ramakrishna Ramisetty, and Thomas Leisner

In: Atmospheric Measurement Techniques, 12, 2219–2240, 2019. DOI: 10.5194/amt-12-2219-2019.

Authorship statement

This peer-reviewed scientific journal article is based on the field data from a six-week campaign (TRAM01) during July–August 2016 in a rural area near Eggenstein-Leopoldshafen (southwest Germany), located ~12 km north of the city of Karlsruhe, with a focus on the aerosol particle types measured in the field and quantification method development for LAAPTOF data. In particular, I was responsible for the operation and calibrations of AMS, AMS data analysis, and data interpretation and discussion of this article.

Atmos. Meas. Tech., 12, 2219–2240, 2019
https://doi.org/10.5194/amt-12-2219-2019

Atmospheric Measurement Techniques
Open Access
EGU

Understanding atmospheric aerosol particles with improved particle identification and quantification by single-particle mass spectrometry

Xiaoli Shen[1,2], Harald Saathoff[1], Wei Huang[1,2], Claudia Mohr[1,3], Ramakrishna Ramisetty[1,a], and Thomas Leisner[1,4]

[1]Institute of Meteorology and Climate Research, Karlsruhe Institute of Technology, Hermann-von-Helmholtz-Platz 1, 76344 Eggenstein-Leopoldshafen, Germany
[2]Institute of Geography and Geoecology, Working Group for Environmental Mineralogy and Environmental System Analysis, Karlsruhe Institute of Technology, Kaiserstr.12, 76131 Karlsruhe, Germany
[3]Department of Environmental Science and Analytical Chemistry, Stockholm University, Stockholm, 11418, Sweden
[4]Institute of Environmental Physics, University of Heidelberg, In Neuenheimer Feld 229, 69120 Heidelberg, Germany
[a]now at: TSI Instruments India Private Limited, Bangalore, 560102, India

Correspondence: Harald Saathoff (harald.saathoff@kit.edu)

Received: 12 October 2018 – Discussion started: 17 October 2018
Revised: 18 March 2019 – Accepted: 22 March 2019 – Published: 10 April 2019

Abstract. Single-particle mass spectrometry (SPMS) is a widely used tool to determine chemical composition and mixing state of aerosol particles in the atmosphere. During a 6-week field campaign in summer 2016 at a rural site in the upper Rhine valley, near the city of Karlsruhe in southwest Germany, $\sim 3.7 \times 10^5$ single particles were analysed using a laser ablation aerosol particle time-of-flight mass spectrometer (LAAPTOF). Combining fuzzy classification, marker peaks, typical peak ratios, and laboratory-based reference spectra, seven major particle classes were identified. With the precise particle identification and well-characterized laboratory-derived overall detection efficiency (ODE) for this instrument, particle similarity can be transferred into corrected number and mass fractions without the need of a reference instrument in the field. Considering the entire measurement period, aged-biomass-burning and soil-dust-like particles dominated the particle number (45.0 % number fraction) and mass (31.8 % mass fraction); sodium-salt-like particles were the second lowest in number (3.4 %) but the second dominating class in terms of particle mass (30.1 %). This difference demonstrates the crucial role of particle number counts' correction for mass quantification using SPMS data. Using corrections for size-resolved and chemically resolved ODE, the total mass of the particles measured by LAAPTOF accounts for 23 %–68 % of the total mass measured by an aerosol mass spectrometer (AMS) depending on the measurement periods. These two mass spectrometers show a good correlation (Pearson's correlation coefficient $\gamma > 0.6$) regarding total mass for more than 85 % of the measurement time, indicating non-refractory species measured by AMS may originate from particles consisting of internally mixed non-refractory and refractory components. In addition, specific relationships of LAAPTOF ion intensities and AMS mass concentrations for non-refractory compounds were found for specific measurement periods, especially for the fraction of org / (org + nitrate). Furthermore, our approach allows the non-refractory compounds measured by AMS to be assigned to different particle classes. Overall AMS nitrate mainly arose from sodium-salt-like particles, while aged-biomass-burning particles were dominant during events with high organic aerosol particle concentrations.

1 Introduction

Lifetimes of ambient aerosol particles range from hours to several days, except for newly formed particles ($\sim$ 3 to 5 nm), which have a lifetime on the order of seconds (Pöschl, 2005). The atmospheric evolution of aerosol particles can alter their internal and external mixing states, as well as their chemical and physical properties on timescales of several hours; e.g.

they can acquire coatings of secondary inorganic (e.g. sulfates, nitrates, and ammonium) and secondary organic compounds (Fuzzi et al., 2015). Hence, most aerosol particles are relatively complex mixtures; they are not easy to distinguish and trace to their primary source and/or secondary formation pathway. Single-particle mass spectrometry (SPMS) has the capability of measuring most components of the particles in real time; thus it has been a widely used technique to investigate mixing state and aging of aerosol particles for many years (Murphy, 2007; Noble and Prather, 2000; Pratt and Prather, 2012). However, there are still challenging issues related to large amounts of SPMS data analysis.

Particle type identification, i.e. the assignment of every detected particle to one out of a set of particle types, which are either predefined or deduced from the experimental data, is perhaps one of the most critical issues. Different data classification methods, e.g. fuzzy *k*-means clustering algorithm, fuzzy *c*-means (modification of *k*-means), ART-2a neural network, hierarchical clustering algorithms, and machine learning algorithms, are applied to reduce the complexity and highlight the core information of mass spectrometric data (Reitz et al., 2016; Christopoulos et al., 2018). Reitz et al. (2016) reviewed commonly used data classification methods in SPMS studies and pointed out the advantage of the fuzzy *c*-means clustering approach, which allows individual particles to belong to different particle classes according to spectral similarities. One recent classification approach applied machine learning algorithms and successfully distinguished SOA, mineral dust, and soil dust, as well as biological aerosols based on a known a priori data set (Christopoulos et al., 2018). In this study we used the fuzzy *c*-means clustering approach which is embedded in the data analysis Igor software for our laser ablation aerosol particle time-of-flight mass spectrometer (LAAPTOF; AeroMegt GmbH). Based on the data classification, averaged or representative mass spectra of different particle classes can be obtained.

Due to the relatively complex laser desorption and ionization (LDI) mechanisms, including charge and proton transfer, as well as ion-molecule reactions that may occur in the plume with many collisions (Murphy, 2007; Reilly et al., 2000; Reinard and Johnston, 2008; Zenobi and Knochenmuss, 1998), some mass spectroscopic signature peaks do not necessarily reflect the primary composition of the particles. Gallavardin et al. (2008) used a pair of peak area ratios, such as Ca_2O^+/Ca^+ vs. CaO^+/Ca^+ and SiO^-/SiO_2^- vs. SiO_3^-/SiO_2^-, to differentiate calcium-/silicon-containing mineral dust. Normalized histograms of PO_3^-/PO_2^- and CN^-/CNO^- ratios were used to identify primary biological aerosol particles (Zawadowicz et al., 2017). Setting thresholds for marker peak signals can also help to classify and further identify specific particles (Köllner et al., 2017). Lu et al. (2018) used natural silicon isotopic signatures to study the sources of airborne fine particulate matter ($PM_{2.5}$), which shows how useful isotopic signatures can be for particle identification. A combination of peak area and peak shift ratio, based on subtle changes in ion arrival times in the mass spectrometer, was introduced by Marsden et al. (2018) for the differentiation of mineral phases in silicates. Ternary subcomposition systems, such as $(Al+Si)^+$–K^+–Na^+ and Cl^--$(CN+CNO)^-$–SO_4^-, were used to identify mineralogy and internal mixing state of ambient particles (Marsden et al., 2019). In our previous study (Shen et al., 2018), laboratory-based reference spectra were suggested to be a useful tool for particle identification. These methods guide the way for improving the techniques to identify particle type and further identify individual aerosol particles.

An even more challenging issue is the quantitative analysis of individual particles' mass and chemical composition, which cannot be directly provided by SPMS measurements because laser ablation only allows an a priori unknown fraction (neutral species) of the single particle to be vaporized/desorbed and then ionized (Murphy, 2007; Reinard and Johnston, 2008). In addition, matrix effects may obscure the particle composition (Gemayel et al., 2017; Gross et al., 2000; Hatch et al., 2014). Our previous laboratory SPMS study also verified the difficulty of particle quantification due to incomplete ionization, which could not be improved significantly by replacing the originally used nanosecond excimer laser with a femtosecond laser with higher laser power density and shorter laser pulse length (Ramisetty et al., 2018). In the last two decades, great effort has been put into solving such quantification issues by using specific scaling or normalization methods. Allen et al. (2006) developed an explicit scaling method to quantify SPMS data, based on comparison with co-located more quantitative particle measurement. This approach has been widely used to obtain continuous aerosol mass concentrations as a function of particle size (Allen et al., 2006; Bein et al., 2006; Fergenson et al., 2001) and has been improved by a hit rate correction (Qin et al., 2006; Wenzel et al., 2003). Recently, composition-dependent density corrections were applied to such scaling approaches to obtain chemically resolved mass concentrations (Gunsch et al., 2018; May et al., 2018; Qin et al., 2006, 2012). In these studies, the scaled SPMS data showed good agreement with the results from reference instruments, e.g. a micro-orifice uniform deposition impactor (MOUDI), a scanning mobility particle sizer (SMPS), an aerodynamic particle sizer (APS), and other independent quantitative aerosol particle measurements, e.g. by a high-resolution time-of-flight aerosol mass spectrometer (HR-ToF-AMS). With respect to particulate chemical compounds, Gross et al. (2000) reported relative sensitivity factors (RSFs) for ammonium and alkali metal cations in a single-particle mass spectrometer to corresponding bulk concentrations and accurately determined the relative amounts of Na^+ and K^+ in sea salt particles. Jeong et al. (2011) developed a method to quantify ambient particulate species from scaled single-particle analysis. Healy et al. (2013) quantitatively determined the mass contribution of different carbonaceous particle classes to total mass and estimated the mass fractions of different chemical species, i.e.

sulfate, nitrate, ammonium, organic carbon (OC), elemental carbon (EC), and potassium determined for each particle class, by using RSFs. The resulting SPMS-derived mass concentrations of these particulate species were comparable with the reference bulk data. Similar methodologies have been used in other SPMS studies (Gemayel et al., 2017; Zhou et al., 2016). It should be noted that these field-based scaling approaches (field-based overall detection efficiency, ODE) rely on the availability of a reference instrument, and their corrections are mainly class-independent.

Many previous studies have also compared single-particle classes and bulk species (Dall'Osto et al., 2009, 2012, 2013, 2016; Dall'Osto and Harrison, 2012; Decesari et al., 2011, 2014; Drewnick et al., 2008; Gunsch et al., 2018; Pratt et al., 2010, 2011; Pratt and Prather, 2012). Some studies compared ion intensities from single-particle data (Bhave et al., 2002) or specific ion ratios, such as nitrate / sulfate (Middlebrook et al., 2003), OC/EC (Spencer and Prather, 2006), and EC/(EC + OC) (Ferge et al., 2006), carbonaceous / (carbonaceous + sulfate) (Murphy et al., 2006) with the other bulk data. Hatch et al. (2014) used m/z 36 C_3^+ as a pseudo-internal standard to normalize the secondary inorganic and organic peak areas in organic-rich particles, resulting in good correlation with the independent AMS measurements. Similarly, Ahern et al. (2016) used the peak area ratio of organic matter marker at m/z 28 CO^+ to EC markers ($C_2-C_5^+$) to account for laser shot-to-shot variability and demonstrated a linear relationship between normalized organic intensity and secondary organic aerosol (SOA) coating thickness on soot particles. A normalized or relative peak area (RPA) method was suggested by Hatch et al. (2014) to account for shot-to-shot variability of laser intensities. Although the LDI matrix effects cannot be completely overcome by the aforementioned method, some examples for good comparisons between single-particle and bulk measurements were shown.

In this study we aim to quantify mass contributions of different particle classes based on single-particle measurements only by employing overall detection efficiencies determined in systematic laboratory studies. As a test case ambient aerosol particles were analysed in summer 2016 at a rural site in the upper Rhine valley of Germany, using a LAAPTOF and a HR-ToF-AMS. Seven major particle classes were identified by a fuzzy c-means analysis among a total of $\sim 3.7 \times 10^5$ measured single particles. Based on laboratory-determined size-dependent overall detection efficiencies (ODEs) of LAAPTOF for different reference particle types, mass contributions for individual aerosol particles could be estimated. Aerosol particle mass concentrations determined independently by LAAPTOF and AMS are compared, and potentially useful relationships of specific ion intensity ratios of LAAPTOF and AMS are discussed.

2 Methods

2.1 Measurement location and instrumentation

The measurements were made as part of the TRAM01 campaign at a rural site in the upper Rhine valley from 15 July to 1 September 2016 next to the tram line north of the village of Leopoldshafen, Germany (49°6′10.54″ N, 8°24′26.07″ E). This location is about 12 km north of the city of Karlsruhe, with 300 000 inhabitants and significant industry including a power plant and refineries (Hagemann et al., 2014). Ambient particles were sampled for mass spectroscopic analysis with a flow rate of $1\,m^3\,h^{-1}$ through a $PM_{2.5}$ inlet (SH 2.5 – 16, Comde-Derenda GmbH) and vertical stainless steel tubes. A total suspended particulate (TSP) inlet (Comde-Derenda GmbH) was used for instruments for particle physical characterization. Trace gases were sampled via an 8 mm PFA sampling tube. All sampling inlets were positioned 1.5 m above a measurement container and 3.7 m a.g.l. To study the nature and to identify possible sources of the particles in this area, their number, size, chemical composition, and associated trace gases, as well as meteorological conditions, were measured using the following instruments: condensation particle counters (CPC3022A, CPC3772, TSI Inc.), an optical particle counter (FIDAS, PALAS GmbH), an aethalometer (AE33-7, Magee Scientific), an ozone monitor (O341M, Environment SA), a SO_2 monitor (AF22M Environment SA), a NO_2 monitor (AS32M, Environment SA), a CO_2 monitor (NGA2000, Rosemont Inc.), and meteorology sensors (WS700 & WS300, Lufft GmbH). From 26 July to 31 August, the following mass spectrometers were in operation: a high-resolution time-of-flight aerosol mass spectrometer (HR-ToF-AMS; Aerodyne Inc.) and a laser ablation aerosol particle time-of-flight mass spectrometer (LAAPTOF; AeroMegt GmbH), providing real-time information on size and mass spectral patterns for bulk samples and individual particles, respectively.

The HR-ToF-AMS yields quantitative information (mass concentration) on size-resolved particle bulk chemical composition with high time resolution and high sensitivity (DeCarlo et al., 2006). Briefly, aerosols are sampled with a flow rate of $\sim 84\,cm^3\,min^{-1}$ via an aerodynamic lens, which focuses particles with sizes of 70 to 2500 nm (vacuum aerodynamic diameter, d_{va}) into a narrow beam. The particle beam passes through a sizing chamber where the particles' size is determined. Afterwards, particles encounter a 600 °C heater that vaporizes the non-refractory species. The vapours are ionized by electron impact (electron energy: 70 eV). The generated positive ions are analysed by a time-of-flight mass spectrometer. Particles can bounce off the heater/vaporizer, leading to an underestimation of ambient mass concentrations measured by AMS. Collection efficiencies (CEs) are used to correct for this (CE is the product of net particle transmission and detection efficiency) (Canagaratna et al., 2007). It is important to note that the CE can vary depending on

composition and phase of the particles (Bahreini et al., 2005). In this study, we applied a CE value of 0.5. This is in agreement with previous studies (Canagaratna et al., 2007; Middlebrook et al., 2012) and close to a composition-dependent CE calculated for this measurement campaign by Huang et al. (2019).

The LAAPTOF is a commercially available SPMS and has been described elsewhere (Ahern et al., 2016; Gemayel et al., 2016; Marsden et al., 2016; Ramisetty et al., 2018; Reitz et al., 2016; Shen et al., 2018; Wonaschuetz et al., 2017). In brief, aerosols are sampled with a flow rate of $\sim 80\,\mathrm{cm^3\,min^{-1}}$ via an aerodynamic lens, focusing and accelerating particles in a size range between 70 and 2500 nm d_{va}. Afterwards, they pass through the detection chamber with two diode laser beams ($\lambda = 405$ nm). Particles smaller than 200 nm and larger than 2 µm are difficult to detect, due to weak light scattering by the smaller particles and due to a larger particle beam divergence for the larger particles. Once a single particle is detected successively by both of the detection lasers, its aerodynamic size is determined and recorded based on its time of flight, and an excimer laser pulse ($\lambda = 193$ nm) is fired for a one-step desorption/ionization of the refractory and non-refractory species of the particle. The resulting cations and anions are analysed by a bipolar time-of-flight mass spectrometer, resulting in mass spectra with unit mass resolution. Thus, for each individual particle, its size and a pair of positive and negative mass spectra are measured.

2.2 Single-particle identification and quantification methods for LAAPTOF data

The general data analysis procedures for particle spectral and size information were described in full detail in our previous study (Shen et al., 2018). In brief, spectral data are classified by a fuzzy *c*-means clustering algorithm embedded in the LAAPTOF data analysis Igor software (Version 1.0.2, AeroMegt GmbH) to find the major particle classes. Afterwards, we can obtain particle-class-resolved size (d_{va}) distribution and the representative spectra, which will be correlated with laboratory-based reference spectra. The resulting correlations together with marker peaks (characteristic peaks arising from the corresponding species) and some typical peak ratios, e.g. isotopic ratio of potassium, are used to identify the particle classes. Here, we extend this approach to quantify particle class mass contributions using a large ambient sample as test case.

The fuzzy *c*-means clustering approach has the advantage of allowing particles to belong to multiple classes based on the similarity of the mass spectra (Reitz et al., 2016), namely attributing one spectrum (particle) to multiple clusters (particle classes). The similarity metric is Euclidian distance between the spectral data vectors and a cluster centre (Hinz et al., 1999; Reitz et al., 2016). In our study, the fuzzy-clustering-derived fraction for each particle class is the degree of similarity between aerosol particles in one particular class, rather than a number percentage. Thus, we can obtain similarity information for the whole data set rather than a single particle (Hinz et al., 1999; Reitz et al., 2016). One drawback is that the individual particles are not directly assigned to individual particle classes, which hinders a direct class-dependent quantification of particle mass. In order to quantify particle mass, we first need to assign a particle class to every individual particle, which is achieved by correlating the individual bipolar mass spectra with the representative fuzzy class spectra using Pearson's correlation coefficient (γ). Since the positive LAAPTOF spectra are more characteristic than the negative ones (Shen et al., 2018), the threshold value for the positive spectra correlation was set to $\gamma_{pos} \geq 0.6$, while for the negative spectra, γ_{neg} was tuned with values ranging from 0.3 to 0.8 (refer to Table S1). Individual particles are assigned to the class for which the corresponding correlation coefficients for both spectra exceed the threshold values. All corresponding correlation coefficients (γ_{pos} and γ_{neg}) are listed in Table S1. This way, we can obtain time series of particle counts, which have good ($\gamma > 0.6$) or strong correlation ($\gamma > 0.8$) with the fuzzy results. The corresponding correlation coefficients are also listed in Table S1, and typical examples are shown in Fig. S1. With this method, we were able to successfully classify 96 % of the measured particles. Once the class information for individual particles has been determined, we are able to calculate single-particle geometric size, volume, and mass as described in the following.

For simplicity, we assume the particles are spherical with a shape factor (χ) of 1; thus particle geometric diameter (d_p), volume (V_p), and mass (m_p) can be obtained from the following equations:

$$d_p = d_m = \frac{d_{va}}{\rho_{eff}} \times \rho_0 \left(\chi = 1; \rho_p = \rho_{eff}\right) \quad \text{(DeCarlo et al., 2004)} \tag{1}$$

$$V_p = \frac{1}{6} \times \pi \times {d_p}^3 \tag{2}$$

$$m_p = V_p \times \rho_{eff}, \tag{3}$$

where d_m is the electrical mobility diameter, d_{va} is the vacuum aerodynamic diameter measured by LAAPTOF, ρ_0 is the standard density ($1\,\mathrm{g\,cm^{-3}}$), ρ_p is the particle density, and ρ_{eff} is the effective density. It should be noted that in some previous studies, the particle shapes were also assumed to be spherical, and uniform particle densities ranging from ~ 1.2 to $1.9\,\mathrm{g\,cm^{-3}}$ were applied for total aerosol particle mass quantification (Allen et al., 2000, 2006; Ault et al., 2009; Gemayel et al., 2017; Healy et al., 2012, 2013; Jeong et al., 2011; Wenzel et al., 2003; Zhou et al., 2016). In our study, we have determined an average density of $1.5 \pm 0.3\,\mathrm{g\,cm^{-3}}$ for all ambient particles, based on a comparison between d_{va} measured by AMS and d_m measured by SMPS. However, the density for different types of ambient particles varies,

especially for fresh ones (Qin et al., 2006). Particle densities varied during the campaign (Fig. S2), and the representative mass spectra of different particle classes indicate chemical inhomogeneity. In order to reduce the uncertainty induced by the assumption of a uniform density, we assigned specific effective densities (derived from d_{va}/d_m) from literature data to each particle class. A density of 2.2 g cm^{-3} was used for calcium-nitrate-rich particles (Zelenyuk et al., 2005), 1.25 g cm^{-3} for aged soot rich in ECOC and sulfate (Moffet et al., 2008b; Spencer et al., 2007), 2.1 g cm^{-3} for sodium salts (Moffet et al., 2008b; Zelenyuk et al., 2005), 1.7 g cm^{-3} for secondary-inorganic-rich particles (Zelenyuk et al., 2005, 2008), 2.0 g cm^{-3} for aged-biomass-burning particles (Moffet et al., 2008b), and 2.6 g cm^{-3} for dust-like particles (Bergametti and Forêt, 2014; Hill et al., 2016). These densities were used for the individual particles of each class without size dependence. Similar chemically resolved densities have also been used in some previous studies (Gunsch et al., 2018; May et al., 2018; Qin et al., 2006, 2012).

Furthermore, the single-particle identification allows for correcting the particle number counts by using the overall detection efficiency (ODE), which depends strongly on particle size and type (Allen et al., 2000; Dall'Osto et al., 2006; Qin et al., 2006; Shen et al., 2018). In a previous publication, we defined ODE as the number of bipolar mass spectra obtained from the total number of particles in the sampled air, described how to generate the laboratory-derived ODE, and discussed the factors influencing ODE in detail (Shen et al., 2018). Our ODE accounts for both physical and chemical factors (e.g. particle size and types shown in Fig. 1). However, we did not determine relative sensitivity factors for individual chemical compounds. As shown in Fig. 1, we have determined ODEs for several particle types, from particles consisting of pure compounds to the more realistic ones including major ambient particles (refer to Fig. 1). For simplicity and in order to account for different types of ambient particles, we averaged the ODE determined for ammonium nitrate, sodium chloride, PSL particles, and some other particles, e.g. agricultural soil dust, sea salt, and organic acids, as well as secondary organic aerosol particles measured in the lab. The mean ODEs with uncertainties as a function of particle size (d_m) are shown in Fig. 1. However, using a mean ODE will obviously lead to some bias. For example, if we apply ODE mean values to all the ambient particles, the number of ammonium-nitrate-rich particles will be overestimated due to the higher ODE of ammonium nitrate, while the ammonium-sulfate-rich, sea salt particles, and some organic-rich particles will be underestimated. Therefore, we used reference particle ODE values to estimate the size-dependent ODE values for the particle classes observed in the field as follows. ODE values for ammonium nitrate and sodium chloride were used to fit ODE curves for secondary-inorganic-rich and sodium-salt-like particles, respectively. The mean ODE values from all reference particles were used for the class of aged soot particles since they showed best agreement with the reference soot particles (refer to Fig. 1). For the same reason, the minimum ODE curve from all reference particles was used for all dust-like particle classes. It should be noted that dust-like particles were often mixed with other species such as organics (e.g. biomass burning–soil particles; refer to Sect. 3.1) and that they likely have dust-core-shell structures (Goschnick et al., 1994). We assume that their detection is dominated by the dust core as it significantly influences the light scattering (size) and the particle beam divergence (shape).

The chemically resolved ODE could also bring some bias due to the complex particle matrix. For instance, if ammonium sulfate is internally mixed with ammonium nitrate, LAAPTOF can detect both of them with good efficiency. This has been verified in our laboratory, and the matrix effect has been discussed in our previous study (Shen et al., 2018). As shown in Fig. 1, ODEs for ammonium nitrate are at a higher level, while ODEs for sodium chloride are relatively low. This could lead to an underestimation and overestimation of secondary-inorganic-rich and sodium salt particles, respectively. ODEs from reference particles with low detection efficiency were applied to dust-like particles. This may lead to an overestimation of their concentration if they are mixed with better detectable species. Mean ODE values were applied to soot particles which may lead to an overestimation if they were, e.g. coated. This is because even non-absorbing species, e.g. organics, can refract light towards the absorbing black carbon core, increasing light absorption (Ackerman and Toon, 1981). Since most of the particle classes consist of mixtures of the poorly detectable types with better detectable types, this seems to partially compensate for the limitation of LAAPTOF to detect certain particle types as evident by comparison with the AMS mass concentrations (refer to Sect. 3.2).

As shown Fig. 1, we determined ODE values for mobility equivalent particle sizes (d_m) ranging from 300 to 1 µm. The ODE decreases significantly for larger particles because of increasing particle beam divergence. We assume ODEs for supermicron particles to follow the decreasing trend illustrated in Fig. 1. Please note that LAAPTOF cannot measure particles larger than a d_{va} of 2.5 µm, which corresponds to a d_m of 1.0 to 1.5 µm, assuming effective particle densities of 1.7 to 2.6 g cm^{-3} for different ambient particle classes, respectively. Hence, a large fraction of the ambient particles measured by LAAPTOF could be number-corrected by using our laboratory-derived ODEs.

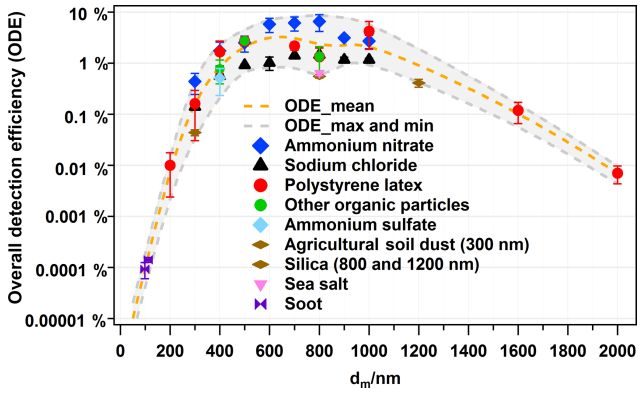

Figure 1. Overall detection efficiency of LAAPTOF for different types of particles as a function of the mobility diameter (d_m), adapted from Shen et al. (2018) and extended. Dashed lines are fitting curves for maximum, mean, and minimum values of ODE. For other organic particles (green), ODE at 400 nm is the data from secondary organic aerosol (SOA) particles from α-pinene ozonolysis, ODE at 500 nm is the data from humic acid, and ODE at 800 nm is the data from humic acid (1.9 ± 0.3 %), oxalic acid (0.3 ± 0.1 %), pinic acid (1.6 ± 0.1 %), and *cis*-pinonic acid (1.9 ± 0.7 %). SOA particles were formed in the Aerosol Preparation and Characterization (APC) chamber and then transferred into the AIDA chamber. Agricultural soil dust (brown symbol) was dispersed by a rotating brush generator and injected via cyclones into the AIDA chamber. Sea salt particles (purple) were also sampled from the AIDA chamber. Soot particles from incomplete combustion of propane were generated with a propane burner (RSG miniCAST; Jing Ltd.) and then injected into and sampled from a stainless steel cylinder of $\sim 0.2\,m^3$ volume. SiO_2 particles were directly sampled from the headspace of their reservoirs. The other aerosol particles shown in this figure were generated from a nebulizer and were size-selected by a DMA. Note that there is uncertainty with respect to particle size due to the particle generation method. The nebulized and DMA-sized samples have relative smaller standard deviation (SD) from Gaussian fitting to the measured particle sizes. PSL size has the smallest size SD (averaged value is 20 nm), and the corresponding relative SD (RSD = SD divided by the corresponding size) is ~ 6 %, since the original samples are with certain sizes. The other nebulized samples have standard deviations ranging from 70 to 120 nm SD and 3 % to 23 % RSD. Particles sampled from the AIDA chamber have a much bigger size SD: ~ 70 nm for SOA (17 % RSD), ~ 100 nm for agricultural soil dust (~ 83 % RSD), and ~ 180 nm for sea salt particles (~ 34 % RSD). Considering this uncertainty, we have chosen a size segment of 100 nm (± 50 nm) for correction; e.g. particles with sizes of 450 to 550 nm will use the ODE at 500 nm particle number correction.

The equations for correction and calculation of mass concentration are as follows:

$$\text{counts}_{\text{corrected}} = 1/\text{ODE}_{\text{size-resolved and chemically resolved}} \quad (4)$$

$$\text{mass}_{\text{corrected}} = \text{counts}_{\text{corrected}} \times m_p \quad (5)$$

$$\text{mass concentration} = \text{total mass}/(\text{sample flow rate} \times \text{time}), \quad (6)$$

where ODE_{d_m} is the mean ODE that depends on d_m, $\text{counts}_{\text{corrected}}$ and $\text{mass}_{\text{corrected}}$ are the corrected particle number counts and mass at each time point, and the sample flow rate is $\sim 80\,\text{cm}^{-3}\,\text{min}^{-1}$. Using Eqs. (4) to (6) we can calculate the corrected number and mass fractions.

The aforementioned assumptions and the related uncertainties in particle mass are summarized as follows: (1) ambient particles are spherical with a shape factor $\chi = 1$. However, several ambient particle types are non-spherical with a shape factor χ not equal to 1, e.g. $\chi_{NaCl} = 1.02$–1.26 (Wang et al., 2010) and $\chi_{NH_4NO_3} = 0.8$ (Williams et al., 2013). This can cause uncertainties of 26 % and 20 % for the particle diameter and 100 % and 50 % for the particle mass of sodium-chloride-like and ammonium-nitrate-like particles, respectively. For soot-like particles, the shape-caused uncertainty could be even larger, due to their aggregate structures. Such an uncertainty is difficult to reduce, since we do not have particle shape information for individual particles. However, using effective densities may at least partially compensate for some of the particle-shape-related uncertainties. (2) Particles in the same class have the same density, which is likely to vary and lead to an uncertainty hard to estimate. (3) The variability of the ODE values (refer to Fig. 1) depends on particle size and type. It reaches values ranging from ± 100 % for 200 nm particles to ± 170 % for 800 nm size particles.

Hence, the overall uncertainty in particle mass according to the assumptions is ~ 300 %, with the ODE-caused uncertainty being dominant. This is because (1) the aforementioned particle matrix effects may cause higher or lower ODEs than their surrogates generated in the laboratory. In addition, the more complex morphology and various optical properties of ambient particles can have a strong impact on their ODE (Shen et al., 2018). (2) Instrumental aspects such as alignment and variance in particle-laser interaction lead to uncertainty in ODE. They are included in the uncertainties given in Fig. 1, for which repeated measurements after various alignments were used. The fluctuations of particle-laser interactions can be reduced by using a homogeneous laser desorption and ionization beam (Wenzel and Prather, 2004) or delayed ion extraction (Li et al., 2018; Vera et al., 2005; Wiley and Mclaren, 1955). Note that we used the same sizing laser and desorption/ionization laser pulse energy (4 mJ) in the field as those used for generating ODE and aligned the instrument in the field with the similar procedures as we did in the lab. During our field measurements we did calibrations of the LAAPTOF with PSL particles of 400, 500, 700, and 800 nm d_m, resulting in ODE values with no significant difference compared to the ODE values determined in the laboratory. This finding reflects the good stability of the LAAPTOF performance in the temperature-controlled container. Actually, once the LAAPTOF adjustments were optimized after transport, no further adjustments were necessary during the 6 weeks of the campaign. Moreover, it is important to note that the ODE curve applied herein should not be extrapolated to other LAAPTOF or SPMS instruments without a standard check against, e.g. PSL particles. In order to evaluate our quantification approach, we will compare the particle

mass estimated based on single-particle measurements with AMS total mass in Sect. 3.2.

It is noteworthy that the major difference between our quantification method and previous SPMS studies is that our ODE is based on elaborate laboratory work, while previous studies typically used field-based scaling approaches (field-derived ODE).

3 Results and discussion

3.1 Identification of particle classes and the internal mixing

During the 6-week measurement campaign, we obtained $\sim 3.7 \times 10^5$ bipolar LAAPTOF spectra for single particles. Seven major particle classes were found using fuzzy *c*-means classification. The corresponding representative spectra with marker peaks' assignment are shown in Fig. 2. Considering some weak but characteristic peaks, we show the spectra with a logarithmic scale. The linearly scaled spectra (refer to Fig. S3 in the Supplement) are provided for comparison in the supporting information. Furthermore, Fig. 3 shows the size-resolved number fraction for the seven particle classes measured during the field campaign TRAM01, based on fuzzy classification according to the fuzzy *c*-means clustering algorithm as well as the overall size distribution for all particles measured by LAAPTOF during the campaign. Signatures for organic and secondary inorganic compounds can be observed in each class, i.e. for organics m/z 24 C_2^-, 25 C_2H^-, 26 C_2H_2/CN^-, and 42 C_2H_2O/CNO^-, for sulfate 32 S^-, 64 SO_2^-, 80 SO_3^-, 81 HSO_3^-, 97 HSO_4^-, 177 $SO_3HSO_4^-$, and 195 $HSO_4H_2SO_4^-$, for nitrate 30 NO^+, 46 NO_2^-, and 62 NO_3^-, and for ammonium 18 NH_4^+ and 30 NO^+. Similar species were previously identified offline in the same region (Faude and Goschnick, 1997; Goschnick et al., 1994). Note that 30 NO^+ can not only originate from nitrate (majority), but also from ammonium (Murphy et al., 2006; Shen et al., 2018). Besides, m/z 24 C_2^- could also be related to elemental carbon (EC). In this case, m/z 24^- should actually show a higher intensity than m/z 26^-, and further EC markers ($C_n^\pm$) should show up as well. Although different particle classes have similar fragments, they show characteristic patterns with several intensive marker peaks in the corresponding spectra, which can also be identified using reference spectra (Shen et al., 2018).

After fuzzy classification each particle was tested for its similarity to the different particle classes. Although a similarity is not equal to the number fraction, they are related. A higher similarity of the total aerosol particles to one class indicates that a bigger number fraction of this class may be expected once the individual particles are assigned to it. As shown in Fig. 4a, the highest similarity (43.5 % of all particles) is found to class 3, which is named sodium salts due to its strong correlation ($\gamma \geq 0.8$) with Na salts (refer to Fig. 5). The spectra of this class in our study feature marker peaks arising from $NaNO_3$ (m/z 115 $Na(NO_2)_2^-$, 131 $NaNO_2NO_3^-$, and 147 $Na(NO_3)_2^-$), Na_2SO_4 (m/z 165 $Na_3SO_4^+$), and NaCl (m/z 81/83 Na_2Cl^+, 139/141 $Na_3Cl_2^+$, 35/37 Cl^-, and 93/95 $NaCl_2^-$) (refer to Fig. 2). These signature peaks were also observed for Na-related particle types such as aged sea salt, Na-containing dust, and Na/K-sulfate-rich particles in the other SPMS studies (Gard et al., 1998; Gaston et al., 2011; Jeong et al., 2011; May et al., 2018; Middlebrook et al., 2003; Schmidt et al., 2017). In the positive spectra of class 3, there is a nitrogen-containing organic compound marker at m/z 129 $C_5H_7NO^+$, which could originate from the OH oxidation of volatile organic compounds (VOCs) in the presence of NO_x on the seed particles, since the same peak was observed during simulation chamber studies with OH radicals reacting with α-pinene and/or toluene in the presence of NO_x. Besides, peaks at m/z 149 $C_4H_7O_2NO_3^+$ and 181 $C_4H_7O_4NO_3^+$ are associated with organonitrates that can form from the oxidation of VOCs in the presence of NO_x (Perring et al., 2013) and are expected to increase the light absorbing capability of the particles (Canagaratna et al., 2007). Huang et al. (2019) showed that organonitrates contributed to particle growth during night-time at this location. This class accounts for the largest fraction in the size range from 1000 to 2500 nm d_{va} (refer to Fig. 3). The size distribution of class 3 particles was dominated by two modes centred at about 1400 and 2000 nm d_{va}, indicating two sub-particle populations in this class. Goschnick et al. (1994) did offline depth-resolved analysis of the aerosol particles collected north of Karlsruhe in the upper Rhine valley and observed sodium chloride in both fine and coarse particles, while sodium nitrate was mainly enriched in the coarse mode. This hints at possible sub-class assignments, which are likely to be fresh and aged sea salts. However, the measurement site is relatively far away from the sea (e.g. the North Atlantic Ocean is $\sim$ 800 km away). Therefore, we need more evidence, such as back trajectory analysis or other transport modelling, to prove that this class is really fresh and/or aged sea salt. This will be discussed in a separate study.

A total of 20.8 % of the total particle population belongs to class 4 (secondary inorganics–amine). This class has the most prominent secondary inorganic signature and strongest correlation with the reference spectra for homogeneous mixtures of NH_4NO_3 and $(NH_4)_2SO_4$. In addition, it features marker peaks for amines at m/z 58 $C_2H_5NHCH_2^+$, 59 $(CH_3)_3N^+$, 86 $(C_2H_5)_2NCH_2^+$, 88 $(C_2H_5)_2NO/C_3H_6NO_2^+$, and 118 $(C_2H_5)_2NCH_2^+$, which were also identified by SPMS in the other field and lab studies (Angelino et al., 2001; Dall'Osto et al., 2016; Healy et al., 2013; Jeong et al., 2011; Köllner et al., 2017; Lin et al., 2017; Pratt et al., 2009; Roth et al., 2016; Schmidt et al., 2017). Among all the representative mass spectra for the seven particle classes, class 4 is relatively "clean" with the fewest peaks (refer to Figs. 2 and S3), indicating that these particles did not have had the time

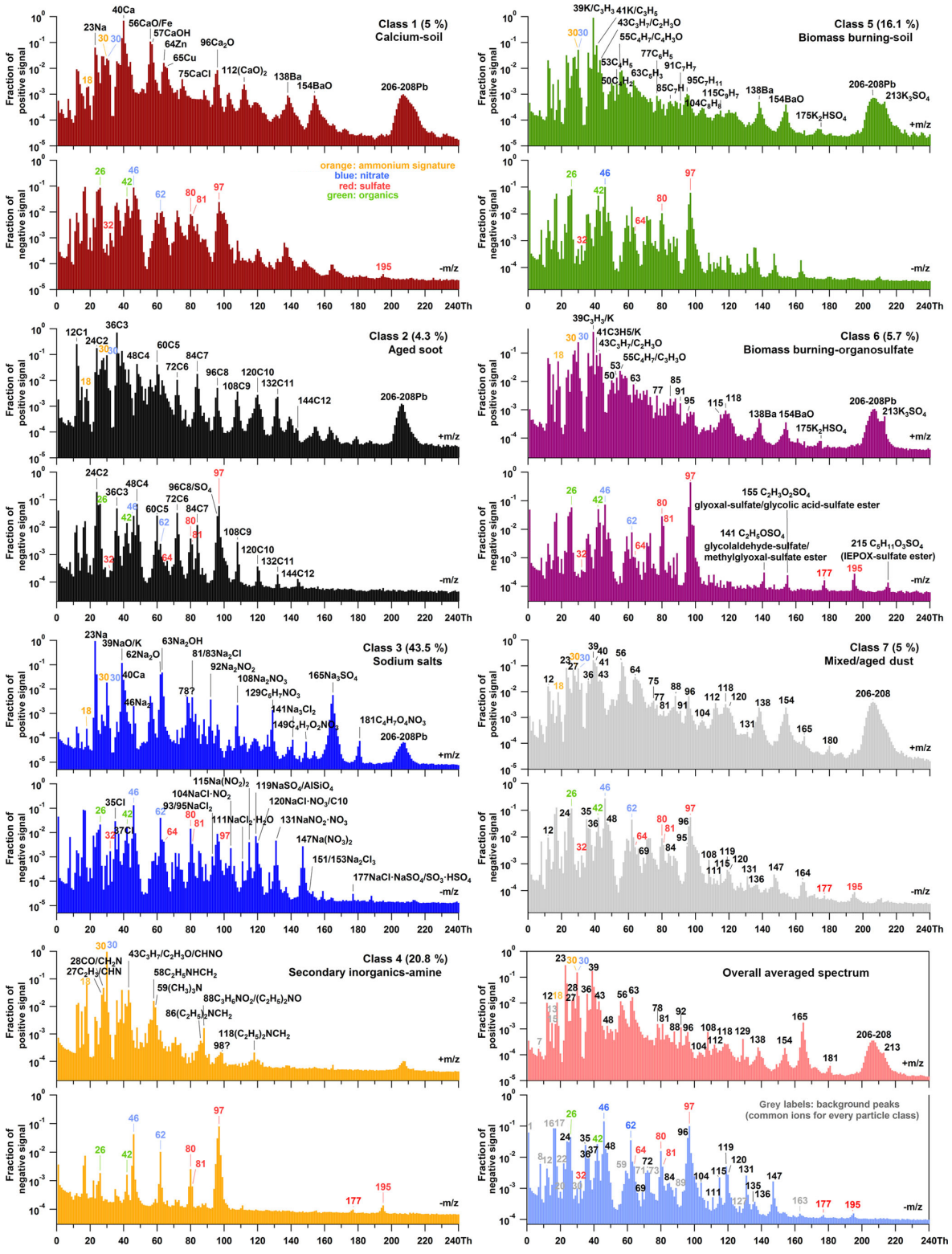

Figure 2. Representative mass spectra of seven particle classes measured during the field campaign TRAM01, based on fuzzy classification according to the fuzzy *c*-means clustering algorithm, and averaged spectrum of a total of $\sim 3.7 \times 10^5$ single particles measured. The percentage in each pair of spectra gives us information about the similarity of the total aerosol particles to different classes. Black labels represent the ions characteristic for different classes. The red, blue, and orange labels represent the signatures for sulfate (32 S^-, 64 SO_2^-, 80 SO_3^-, 81 HSO_3^-, 97 HSO_4^-, 177 $SO_3HSO_4^-$, and 195 $HSO_4H_2SO_4^-$), nitrate (30 NO^+, 46 NO_2^-, and 62 NO_3^-), and ammonium (18 NH_4^+ and 30 NO^+). The green labels represent the organic compounds (26 C_2H_2/CN^- and 42 C_2H_2O/CNO^-). In the overall averaged spectrum, grey labels represent the background fragments (common ions) that exist for every particle class.

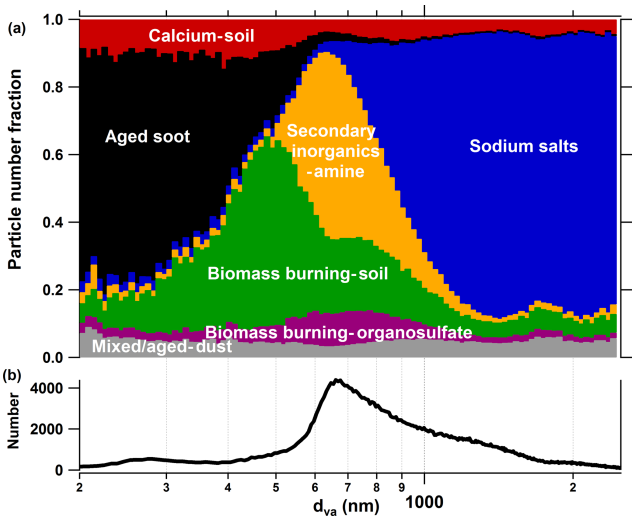

Figure 3. **(a)** Size-resolved number fraction for seven particle classes measured during the field campaign TRAM01, based on fuzzy classification according to the fuzzy *c*-means clustering algorithm. **(b)** Overall size distribution for the particles measured by LAAPTOF during the whole campaign.

to uptake other components. Hence, most likely they were formed not very long ago by conversion of their precursors. The secondary inorganic–amine particles have a rather narrow size distribution in the range between 500 and 1000 nm d_{va} (refer to Fig. 3).

Aged-biomass-burning and soil-dust-like particles (class 5: biomass burning–soil) comprise 16.1 % of all particles according to the similarity of the mass spectra. It has the most prominent peak at m/z 39 $K/C_3H_3^+$ and aromatic marker peaks at 50 $C_4H_2^+$, 63 $C_5H_3^+$, 77 $C_6H_5^+$, 85 C_7H^+, 91 $C_7H_7^+$, 95 $C_7H_{11}^+$, 104 $C_8H_8^+$, and 115 $C_9H_7^+$. The ratio of m/z 39$^+$/41$^+$ is $\sim$ 11.6, which is similar to the value of (13.5 $\pm$ 0.9) measured for pure potassium-containing inorganic particles (e.g. K_2SO_4) by our LAAPTOF in the laboratory. The contribution of organic fragments is likely the reason for the slightly lower value, as this ratio was determined to be $\sim$ 8 for humic acid and $\sim$ 1.1 for α-pinene SOA (Shen et al., 2018). Hence, we assign the signal at m/z 39$^+$ mainly to potassium. The aromatic signature was observed by the other SPMS (Dall'Osto and Harrison, 2012; Schmidt et al., 2017; Silva and Prather, 2000). As suggested by previous studies, such potassium-rich particles can originate from biomass burning and are often mixed with sulfate and/or nitrate (Gaston et al., 2013; Lin et al., 2017; Middlebrook et al., 2003; Moffet et al., 2008a; Pratt et al., 2010; Qin et al., 2012; Roth et al., 2016; Schmidt et al., 2017). This is also the case for class 5 particles that exhibit a characteristic peak at m/z 213 $K_3SO_4^+$. Note that we also denoted this class as soil-dust-like particles based on the correlation diagram (Fig. 5), although there are no obvious marker ions visible. It is correlated well ($\gamma \geq 0.6$) with reference spectra of dust particles, especially agricultural soil dust. The weak spectral signal might be due to the core-shell structure of the particles (Pratt and Prather, 2009). In fact, previous studies identified soil dust as the particle type dominating the coarse particles sampled in the same region (Faude and Goschnick, 1997; Goschnick et al., 1994). Goschnick et al. (1994) found a core-shell structure in both submicron and coarse particles collected north of the city of Karlsruhe in the upper Rhine valley. This supports our hypothesis. In addition, similar to class 3, class 5 also has two modes in its size distribution centred at about 500 and 800 nm d_{va}. Such potential sub-classes will be further analysed in the future.

Particle class 6 contains 5.7 % of all particles, and they have sizes ranging from 400 to 1000 nm d_{va}. This class is named biomass burning–organosulfate, short for aged-biomass-burning and organosulfate-containing particles. It also shows biomass burning markers such as m/z 213 $K_3SO_4^+$ and features organosulfates at m/z 141 $C_2H_5OSO_4^-$, 155 $C_2H_3O_2SO_4^-$, and 215 $C_5H_{11}OSO_4^-$, which are consistent with signals from sulfate esters of glycolaldehyde/methylglyoxal, glyoxal/glycolic acid, and isoprene epoxydiols (IEPOX), respectively, observed by other SPMS in field measurements (Froyd et al., 2010; Hatch et al., 2011a, b). Unfortunately, we do not have laboratory-based reference spectra for organosulfate particles. Such reference values could be very useful for a further analysis. The ratio of m/z 39$^+$/41$^+$ of $\sim$ 6.7 is closer to organics rather than to potassium. However, we cannot rule out a significant potassium contribution. In addition, this class features a specific pattern of m/z 39$^+$, 41$^+$, and 43$^+$ (which have much higher intensities than their interstitial peaks at m/z 40$^+$ and 42$^+$) and hydrocarbon and oxygenated organic fragments at m/z 53$^+$, 55$^+$, 63$^+$, 65$^+$, 67$^+$, 69$^+$, 71$^+$, 73$^+$, 81$^+$, 83$^+$, 85$^+$, 95$^+$, 97$^+$, and 99$^+$, likely from organic acids and biogenic SOA (Shen et al., 2018).

Class 1 (5.0 % of all particles) is identified as calcium–soil, short for calcium-rich and soil-dust-like particles. It contains calcium-related signatures at m/z 40 Ca^+, 56 CaO^+/Fe^+, 57 $CaOH^+$, 75 $CaCl^+$, 96 Ca_2O^+, and 112 $(CaO)_2^+$, as well as some other metal-related signatures including m/z 23 Na^+, 64/66 Zn^+, 65 Cu^+, 138 Ba^+, 154 BaO^+, and 206–208 Pb^+. Most of the signature peaks for calcium-related particles, such as Ca-rich soil dust, engine exhaust, and lake spray aerosols, were also identified by other SPMS studies (Dall'Osto et al., 2016; May et al., 2018; Roth et al., 2016). This class shows a strong correlation with nitrate and correlates well with all reference spectra of dust samples, especially soil dust (refer to Fig. 5). Class 2 (4.3 % of all particles), aged soot, is predominantly located in the small size range (200 to 600 nm d_{va}) and exhibits prominent EC patterns in mass spectra (characteristic $C_n^{\pm}$ progressions with up to $n = 12$) and is mixed with sulfate and nitrate. Such soot signatures are normally found in SMPS studies (Ault et al., 2010; Dall'Osto et al., 2016; Gaston et al., 2013; Middlebrook et al., 2003; Spencer and Prather, 2006). These mass

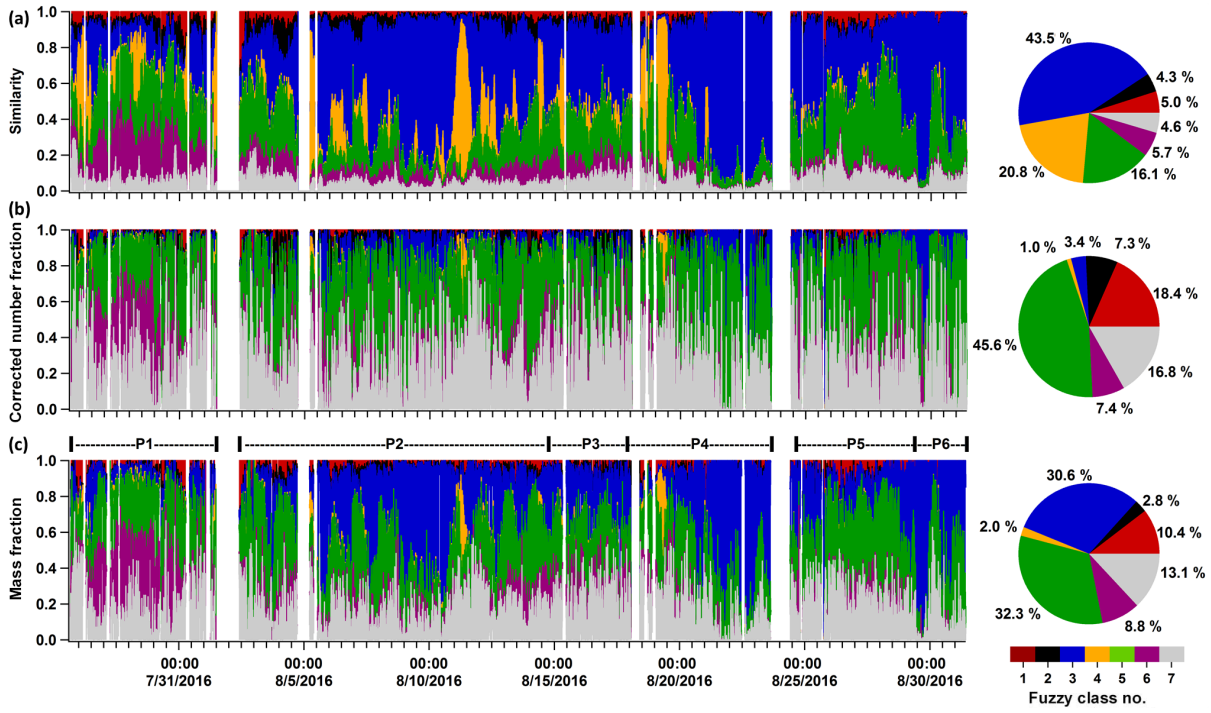

Figure 4. Time series of the similarity, corrected number fraction, and mass fraction of seven major particle classes and the corresponding pie charts for total fractions. Note that the correction shown here is based on a chemically resolved or particle-class-resolved ODE. The seven classes are class 1: calcium–soil; class 2: aged soot; class 3: sodium salts; class 4: secondary inorganics–amine; class 5: biomass burning–soil, class 6: biomass burning–organosulfate; and class 7: mixed/aged dust. In panel **(c)**, six periods have been marked: P1 is Period 1 from 26 July 2016 16:23 to 1 August 2016 11:43, P2 from 2 August 2016 09:43 to 14 August 2016 17:53, P3 from 14 August 2016 18:03 to 17 August 2016 21:03, P4 from 17 August 2016 21:13 to 23 August 2016 15:33, P5 from 24 August 2016 15:03 to 29 August 2016 08:33, and P6 from 29 August 2016 08:43 to 31 August 2016 09:13.

spectra show a strong correlation to the reference spectra of soot particles, especially diesel soot ($\gamma =\sim 1$). Class 7 (4.6 % of all particles) is identified as mixed/aged dust, which contains no obvious characteristic features and is correlated with most of the reference spectra. It has a relatively even and broad size distribution covering the whole size range that LAAPTOF is able to measure.

We observe intensive signals at m/z 138 Ba^+ and 154 BaO^+ in class 1, 5, 6, and 7, indicating a similar source of these particle types, which all have a good correlation with mineral and soil dust particles (Fig. 5). Prominent lead markers at m/z 206^+ to 208^+ can be found in each class, except class 4, which is further evidence for these particles being relatively young. The marker peaks for lead appear broader because at higher m/z, we observe larger peak shifts that cannot be completely corrected with the existing LAAPTOF software. Note that even though we did not obtain spectra for pure ammonium sulfate or pure biogenic SOA particles in ambient air, it is still possible for such particles to be present. However, laboratory measurements show a very low sensitivity of the LAAPTOF to these types of particles, potentially due to their low absorbance at 193 nm. Due to this low instrument sensitivity for these types of particles, it is very difficult to achieve reasonable quantitative estimates about their abundance based on LAAPTOF measurements alone.

The aforementioned full and short names for seven classes, as well as their signature ion peaks, are listed in Table 1. We emphasize here that the expression "rich" as used in this study only indicates a strong signal in the mass spectra rather than a large fraction in mass, since there is no well-defined relationship between LAAPTOF spectral signal and the corresponding quantity. The sensitivities of this instrument to different species have to be established in the future.

All the laboratory-based reference spectra used in this study are publicly available via the EUROCHAMP-2020 database (https://www.eurochamp.org/default.aspx, last access: 28 March 2019). Information on newly added reference spectra is given in Table S2.

3.2 Quantification of single-particle mass and the external mixing

In this section, we estimate mass concentrations of the particle classes observed in the field. This is based on the particle identification discussed above as well as the assignment of appropriate ODE values of surrogate reference particles and on several assumptions on particle density and shape (refer to

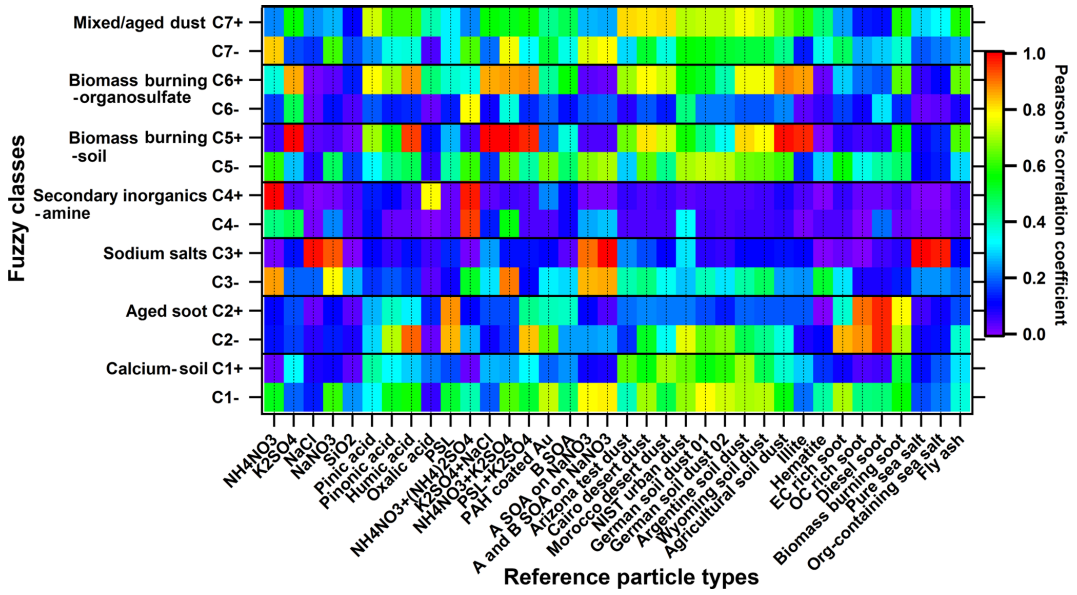

Figure 5. Correlation diagram of fuzzy classification results (seven classes, C1 to C7) and 36 laboratory-based reference spectra. Correlation results for the positive and negative spectra (e.g. for C1) are in the separated rows (e.g. C1+ and C1−). PAH is short for poly(allylamine hydrochloride), B SOA is short for biogenic SOA (α-pinene SOA in this study), A SOA is short for anthropogenic SOA (toluene SOA in this study), and biomass burning soot is the lignocellulosic char from chestnut wood. Note that the strong and good correlations mentioned in the paper stand for Pearson's correlation coefficient $\gamma \geq 0.8$ and $\gamma \geq 0.6$, respectively. The seven classes are class 1: calcium–soil; class 2: aged soot; class 3: sodium salts; class 4: secondary inorganics–amine; class 5: biomass burning–soil; class 6: biomass burning–organosulfate; and class 7: mixed/aged dust.

Sect. 2.2). Please note that both AMS and LAAPTOF cannot measure particles larger than 2.5 µm, which can be analysed by FIDAS. FIDAS data showed that $PM_{2.5}$ accounted for majority mass of the total aerosol particles sampled through the TSP inlet ($PM_{2.5} = 73\,\%$ of PM_{10} and 64 % of PM_{total}, respectively). In this study, we only focus on $PM_{2.5}$ particles. The fuzzy-classification-derived similarity (Fig. 4a) can be transferred into corrected number fractions using size-resolved and chemically resolved ODE (Fig. 4b) and further transferred into mass fractions (Fig. 4c) of the seven particle classes. The corresponding time series of chemically resolved number and mass concentrations can be found in Fig. S4. Please note that the aged soot particles (class 2), which dominate the number fraction for particles below 400 nm in the fuzzy c-means analysis, comprise only a minor fraction of the total number counts in Fig. 4 because the total particle number is dominated by particles larger than 500 nm (refer to Fig. 3b). Significant changes can be observed between the similarity number fraction, the corrected number fraction, and the resulting mass fractions (cf. Fig. 4a to b to c). Compared to the similarity fraction, the number fractions of class 3, sodium salts, and class 4, secondary inorganics–amine, decrease dramatically; sodium salt particles changed from 43.5 % (similarity) to 3.4 % (corrected number fraction), and secondary inorganics–amine dramatically decreased from 20.8 % to 2.4 %, while those of the other classes increase. This is because classes 3 and 4 comprise mainly larger particles (class 3: d_{va} peaks at ~ 1400 and 2000 nm corresponding to $d_p \sim 700$ and 1000 nm; class 4 peaks at ~ 680 nm d_{va} and 400 nm d_p), which have the highest ODE values. In contrast the other classes comprise mainly smaller particles ($d_{va} < 500$ nm; $d_p < 300$ nm) (refer to Fig. 3), which have a lower ODE (refer to Fig. 1). Class 5, biomass burning–soil, accounts for the second highest number fraction of the smaller particles and has a relatively high effective density. After correction, the number fraction of particles attributed to this class increased from 16.1 % to 45.0 %, corresponding to 31.8 % mass fraction, and it becomes the dominating class with respect to particle number and mass. Sodium salts are another dominating class with respect to mass (30.1 % mass fraction) due to their relatively large size. These observations demonstrate the crucial role of the corrections applied for particle mass quantification in SPMS data. Note that we can obtain similarly corrected number and mass fractions by using minimum, mean, and maximum ODE, respectively (Table S3). The observed external mixing of aerosol particles varied significantly with time, e.g. class 6, biomass burning-organosulfate, dominated both particle number and mass at the beginning of the measurements until 1 August, while class 3 dominated the mass for 5–10, 21–24, and 29–30 August, and class 4 particles peaked twice on 11–19 August (refer to Fig. 4).

As discussed above, raw LAAPTOF data overestimate the particles with higher ODE, while the ones with lower

Table 1. Particle class numbers, names, labels, and corresponding signature ion peaks.

Class number: name (label)	Signature ion peaks (anions are marked in italic)
Class 1: calcium-rich and soil-dust-like particles (calcium–soil)	23 Na^+, 40 Ca^+, 56 CaO/Fe^+, 57 $CaOH^+$, 64/66 Zn^+, 65 Cu^+, 75 $CaCl^+$, 96 Ca_2O^+, 112 $(CaO)_2^+$, 138 Ba^+, 154 BaO^+, 206–208 Pb^+
Class 2: aged-soot-like particles (aged soot)	12*n* Cn^+, 206–208 Pb^+; *12n* Cn^-, *sulfate* (*32* S^-, *64* SO_2^-, *80* SO_3^-, *81* HSO_3^-, *97* HSO_4^-, *177* $SO_3HSO_4^-$, *195* $HSO_4H_2SO_4^-$)
Class 3: sodium-salt-like particles (sodium salts)	23 Na^+, 39 NaO/K^+, 40 Ca^+, 46 Na_2^+, 62 Na_2O^+, 63 Na_2OH^+, 81/83 Na_2Cl^+, 92 $Na_2NO_2^+$, 108 $Na_2NO_3^+$, 129 $C_5H_7NO_3^+$, 141 $Na_3Cl_2^+$, 149 $C_4H_7O_2NO_3^+$, 165 $Na_3SO_4^+$, 181 $C_4H_7O_4NO_3^+$, 206–208 Pb^+; *35/37* Cl^-, *93/95* $NaCl_2^-$, *104* $NaClNO_2^-$, *111* $NaCl_2H_2O^-$, *115* $Na(NO_2)_2^-$, *119* $NaSO_4/AlSiO_4^-$, *120* $NaClNO_3^-$, *131* $NaNO_2NO_3^-$, *147* $Na(NO_3)_2^-$, *151/153* $Na_2Cl_3^-$, *177* $NaClNaSO_4^-/SO_3HSO_4^-$
Class 4: secondary- inorganics-rich and amine-containing particles (secondary inorganics–amine)	ammonium and amine (18 NH_4^+, 27 C_2H_3/CHN^+, 28 CO/CH_2N^+, 30 NO^+, 43 $C_3H_7/C_2H_3O/CHNO^+$, 58 $C_2H_5NHCH_2^+$, Amine 59 $(CH_3)_3N^+$, 86 $(C_2H_5)_2NCH_2^+$, 88 $(C_2H_5)_2NO/C_3H_6NO_2^+$, 118 $(C_2H_5)_2NCH_2^+$); *nitrate* (*46* NO_2^-, *62* NO_3^-), *sulfate*
Class 5: aged-biomass-burning and soil-dust-like particles (biomass burning–soil)	39 $K/C_3H_3^+$, 41 $K/C_3H_5^+$, 43 $C_3H_7/C_2H_3O^+$, 50 $C_4H_2^+$, 53 $C_4H_5^+$, 55 $C_4H_4/C_3H_3O^+$, 63 $C_5H_3^+$, 77 $C_6H_5^+$, 85 C_7H^+, 91 $C_7H_7^+$, 95 $C_7H_{11}^+$, 104 $C_8H_8^+$, 115 $C_9H_7^+$, 138 Ba^+, 154 BaO^+, 175 $K_2HSO_4^+$, 206–208 Pb^+, 213 $K_3SO_4^+$; *sulfate*
Class 6: aged-biomass-burning and organosulfate-containing particles (biomass burning– organosulfate)	positive signature peaks feature biomass burning very similar to those given for class 5 *organosulfate* (*141* $C_2H_5O_5O_4^-$, *155* $C_2H_3O_2SO_4^-$, *215* $C_5H_{11}O_3SO_4^-$)
Class 7: mixed/aged and dust-like particles (mixed/aged dust)	contains almost all the signature peaks from the other classes

Note that "rich" used in the names stands for the strong spectral signal rather than the real mass fraction.

ODE will be underestimated. After correction of the number counts and estimation of the mass concentrations, we can compare the LAAPTOF result with the quantitative instruments such as AMS in the overlapping size range of 200 to 2500 nm d_{va}. A correction for the particles in the size range between 70 and 200 nm considering mass concentrations may be negligible since they typically contribute only a minor mass fraction. It turns out that the total mass of the particles measured by LAAPTOF is 7 ± 3 % (with maximum ODE), 16 ± 6 % (mean ODE), 60 ± 24 % (minimum ODE), and 45 ± 16 % (23 %–68 % with chemically resolved ODE) of the total AMS mass depending on the measurement periods. Two criteria were used to select characteristic time periods: a period should have a stable correlation between LAAPTOF and AMS total mass; and a period should contain special events or dominating particle classes observed by LAAPTOF and/or AMS (refer to Figs. 4c and 6). Despite the relatively large differences in the average mass concentrations of LAAPTOF and AMS, they show much better agreement in total mass and also good correlations during specific periods (P), such as P1, 2, 4, and 5 (refer to Figs. 6 and S5), covering ~ 85 % of the measurement time. Hence, the large differences in the average mass concentrations are caused by larger deviations during some relatively short periods or events. Considering the fact that AMS can only measure non-refractory compounds, the good correlation between AMS and LAAPTOF gives us a hint that the species measured by AMS may mainly originate from the particles of complex mixtures of both refractory and non-refractory species. It is worth noting that the weakest correlation ($\gamma = -0.1$) is observed in P6 when LAAPTOF measured the highest fraction of sodium salt particles (especially sodium chloride) on 29 August, while AMS is unable to measure refractory species such as sodium chloride. Specifically, from 09:00 to 23:53 on 29 August, LAAPTOF and AMS tended to be slightly anti-correlated ($\gamma = -0.3$).

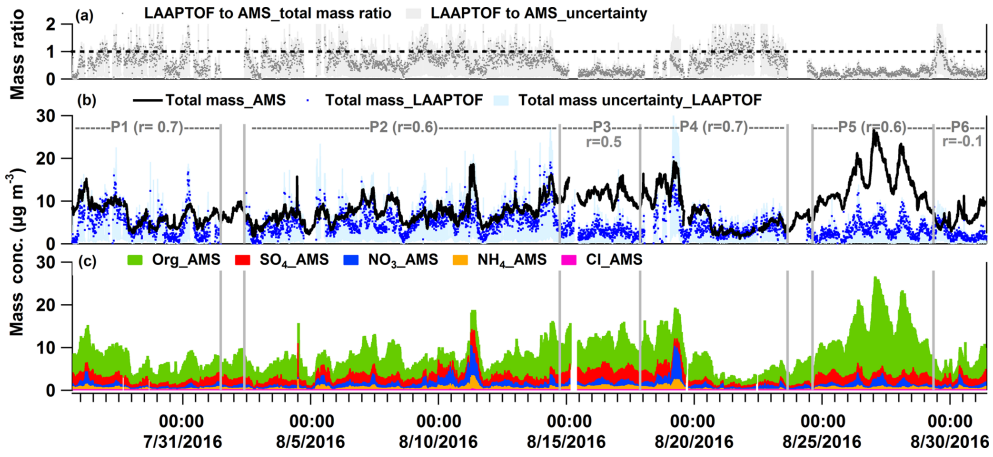

Figure 6. Time series of **(a)** total mass ratio of LAAPTOF to AMS data, **(b)** LAAPTOF total mass and AMS total mass, and **(c)** mass concentrations of organic, sulfate, nitrate, and ammonium compounds measured by AMS. In **(b)** r is Pearson's correlation coefficient between LAAPTOF and AMS results. P1 is Period 1 from 26 July 2016 16:23 to 1 August 2016 11:43, P2 from 2 August 2016 09:43 to 14 August 2016 17:53, P3 from 14 August 2016 18:03 to 17 August 2016 21:03, P4 from 17 August 2016 21:13 to 23 August 2016 15:33, P5 from 24 August 2016 15:03 to 29 August 2016 08:33, and P6 from 29 August 2016 08:43 to 31 August 2016 09:13. Close-up figures for P1, 2, 4, and 5 can be found in Fig. S5, as well as the corresponding scatter plots for LAAPTOF and AMS data comparison.

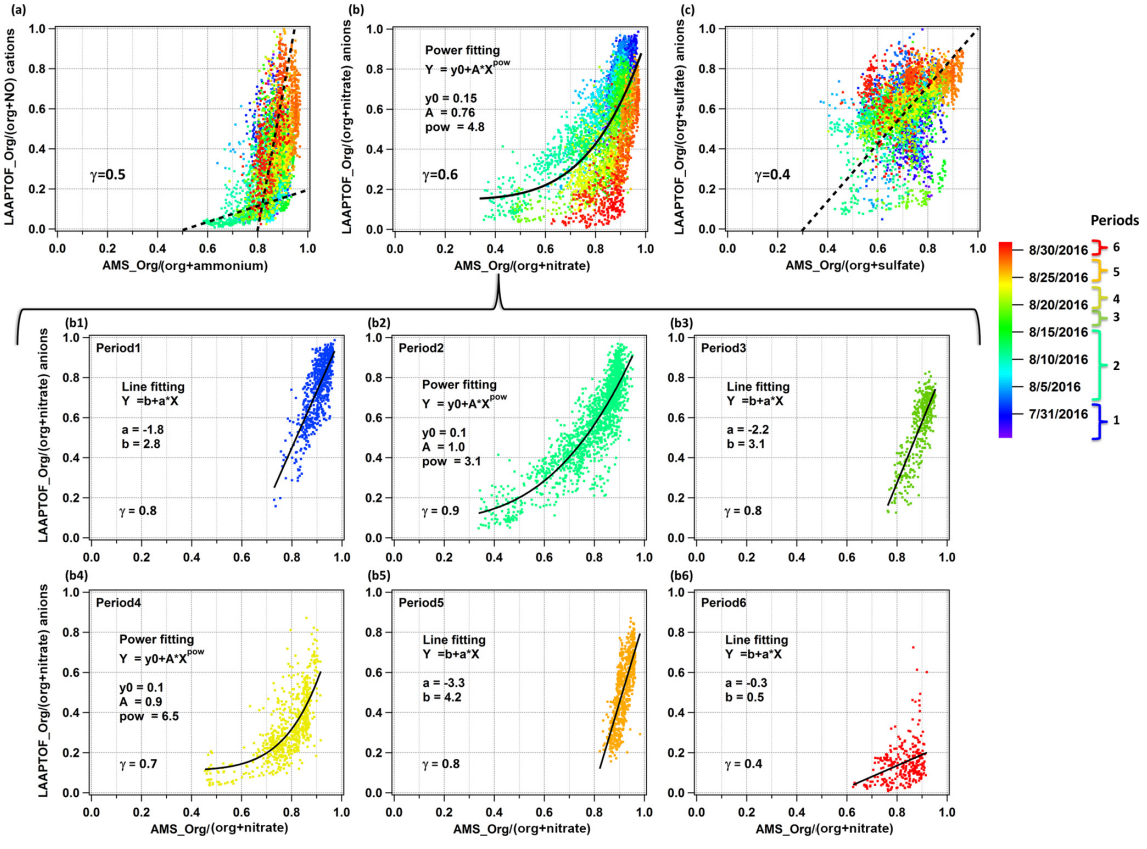

Figure 7. Comparison of non-refractory compounds measured by LAAPTOF and AMS: **(a)** LAAPTOF organic cations and NO^+ fractions org/(org + NO), **(b)** organic anions and nitrate fractions org / (org + nitrate), and **(c)** organic anions and sulfate fractions org / (org + sulfate) to the corresponding AMS mass fractions. Each point is 10 min averaged data, and there are 4483 points in each scatter plot. Dashed lines in **(a)** and **(c)** are used to guide the eyes, while the curve in **(b)** is from the fitting result. The colour scale is related to the timeline, including periods 1 to 6, the same as the ones in Fig. 6. Further comparison of org / (org + nitrate) during six periods are in the scatter plots (b1) to (b6).

As shown in Fig. 6a, the mass ratio of LAAPTOF to AMS has its lower values in P3 and P5 when the AMS organic mass concentration is higher than in most of the other periods. Although LAAPTOF data show a good correlation with the AMS data, e.g. for period P5, they obviously miss a large mass fraction of most likely smaller organic particles. The corresponding chemically resolved size distributions of particles measured by AMS are given in Fig. S6. This may be due to an insufficient representation of this kind of organic-rich particles in the particles classes identified initially. Even using reference spectra of organic particles, it was not possible to identify a number of those particles sufficient to close this gap. In addition, during the whole campaign the sulfate mass fraction measured by AMS is largest in P3 (refer to Fig. 6c). However, the LAAPTOF is not sensitive to some sulfate salts, e.g. pure ammonium sulfate (Shen et al., 2018); thus it is likely that such particles were dominating in P3, which resulted in a weaker correlation between these two instruments. Relatively pure ammonium sulfate was also suggested to be a "missing" particle type in the other SPMS field studies (Erisman et al., 2001; Stolzenburg and Hering, 2000; Wenzel et al., 2003), and Thomson et al. (1997) showed in a laboratory study that pure ammonium sulfate particles were difficult to measure using LDI at various wavelengths.

3.3 Correlation of AMS and LAAPTOF results for non-refractory compounds

Considering the different capabilities of LAAPTOF and AMS, we did not apply the relative sensitivity factor (RSF) method (Healy et al., 2013; Jeong et al., 2011). We analysed our LAAPTOF and AMS data independently and compared them thereafter. For LAAPTOF data, we used relative ion intensities (each ion peak intensity is normalized to the sum of all or selected ion signals; positive and negative ions were analysed separately), similar to the relative peak area (RPA) method suggested by Hatch et al. (2014). As shown in Fig. S7a, m/z 30 NO^+ measured by LAAPTOF has a good correlation ($\gamma = 0.6$) with ammonium measured by AMS, but LAAPTOF m/z 18 NH_4^+ does not show this ($\gamma = 0.3$, not shown in the figure). This was also found by Murphy et al. (2006) for another single-particle mass spectrometer, PALMS, which also uses an excimer laser with the same wavelength for ionization as that in the LAAPTOF. For nitrate (panel b: sum of the marker peaks at m/z 46 NO_2^- and 62 NO_3^-), sulfate (panel c: sum of m/z 32 S^-, 64 SO^-, 80 SO_3^-, 81 HSO_3^-, 96 SO_4^-, 97 HSO_4^-, 177 $SO_3HSO_4^-$, and 195 $H_2SO_4HSO_4^-$), and organics (cations in panel d: sum of m/z 43 $C_3H_7/C_2H_3O/CHNO^+$, 58 $C_2H_5NHCH_2^+$, 59 $(CH_3)_3N^+$, 88 $(C_2H_5)_2NO/C_3H_6NO_2^+$, 95 $C_7H_{11}^+$, 104 $C_8H_8^+$, 115 $C_9H_7^+$, and 129 $C_5H_7NO^+$; and anions in panel e: sum of m/z 24 C_2^-, 25 C_2H^-, 26 C_2H_2/CN^-, 42 C_2H_2O/CNO^-, 45 $COOH^-$, 59 CH_2COOH^-, 71 CCH_2COOH^-, 73 $C_2H_4COOH^-$, 85 $C_3H_4COO^-$, and 89 $(CO)_2OOH^-$), there is a poor correlation ($\gamma \leq 0.4$) between these two instruments if we consider the entire measurement period. However, the fraction of LAAPTOF organic cations to the sum of ammonium and organic cations, org / (org + ammonium), anion fraction of org / (org + sulfate), and org / (org + nitrate), shows better correlations between these two instruments (Fig. 7), especially for org / (org + nitrate). As shown in Fig. 7b, a scatter plot of org / (org + nitrate) measured by LAAPTOF and AMS shows an exponential trend. A similar trend for the ratio carbonaceous / (carbonaceous + sulfate) was observed by PALMS compared to AMS results for free tropospheric aerosol particles measured by Murphy et al. (2006).

Note that the aforementioned comparisons in this section are for the entire measurement period and demonstrate general correlations between these two instruments. Considering different time periods, the correlations vary (Fig. 7). All corresponding Pearson's correlation coefficient (γ) values for the comparisons of compounds measured by LAAPTOF and AMS are summarized in Table S4. During period 4, most of the γ values are above 0.6, suggesting good correlation, which is comparable with the mass comparison results discussed in Sect. 3.2.2. In particular, for the comparison of the org / (org + nitrate) ratio, LAAPTOF and AMS show good or strong correlations for almost the complete measurement time. The corresponding scatter plots are shown in Fig. 7b1–b6. Periods 2 and 4, covering more than 50 % of the measurement time, show similar exponential trends to the general fit in Fig. 7b, while periods 1, 3, and 5 show a linear correlation (especially in periods 3 and 5). This implies different dominant particle types. Consistent with the observations shown in Fig. 4c, period 2 and 4 are dominated by sodium salts, and there are two secondary inorganics–amine burst events, while period 3 and 5 are dominated by biomass burning–soil particles containing more organics, which can also be validated by AMS results as shown in Fig. 6. Therefore, we conclude that the relationship between LAAPTOF-org / (org + nitrate) and AMS-org / (org + nitrate) varies due to changing particle types.

Taken together, the correlations shown in Figs. 7 and S7 may be used to estimate the mass concentrations of non-refractory compounds for LAAPTOF measurements without AMS in rural locations: ammonium mass concentrations can be estimated from Fig. S7a, afterwards organic mass concentrations can be estimated by using Fig. 7a, and then nitrate can be estimated from Fig. 7b and/or Fig. 7b1–b6 once the dominating particle types are determined, and finally the sulfate mass can be estimated from Fig. 7c.

3.4 Particle sources of non-refractory components

The AMS can quantify the bulk particle mass of non-refractory species such as ammonium, nitrate, sulfate, and organics. LAAPTOF measurements suggest that ambient aerosol particles at this location are often internal mixtures of ammonium, nitrate, sulfate, organics, and other character-

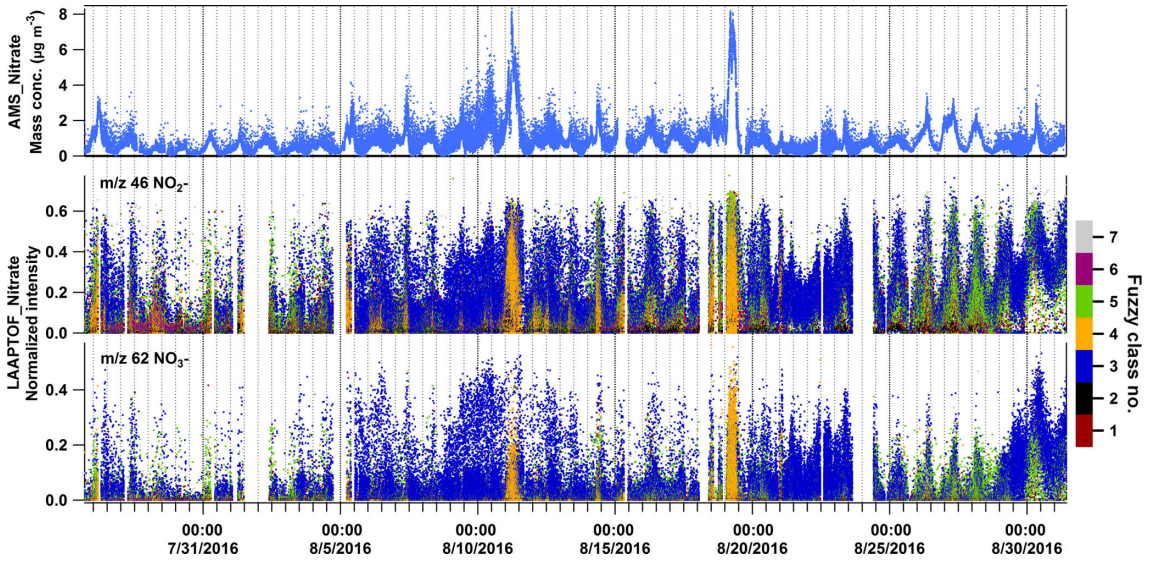

Figure 8. Time series of nitrates measured by AMS in mass concentration and LAAPTOF in normalized ion intensities, respectively. Normalized intensity refers to the fragment intensity divided by the sum of all the ion intensities. Marker peaks for nitrates are at m/z 46 NO_2^- and 62 NO_3^- in LAAPTOF spectra. The seven fuzzy classes are class 1: calcium–soil; class 2: aged soot; class 3: sodium salts; class 4: secondary inorganics–amine; class 5: biomass burning–soil; class 6: biomass burning–organosulfate; and class 7: mixed/aged dust.

istic species such as metals. In order to find out the dominant particle class/classes contributing to/donating a certain non-refractory compound measured by AMS (namely compound-donor particle class/classes), we also need the class information of the single particles, which can be achieved using the single-particle identification method described in Sect. 2.2, and assume that LAAPTOF has a similar sensitivity to the same components of different particle classes. For nitrate measured by AMS, the dominating nitrate-donor particles with marker peaks at m/z 46 NO_2^- and 62 NO_3^- in LAAPTOF varied in different periods (Fig. 8): sodium salts was the dominating class for the whole measurement campaign, but secondary inorganics–amine was dominant in its burst events (11 and 19 August), while biomass burning–soil was dominant from 25–29 August. For ammonium measured by AMS, we have observed a similar trend as for secondary inorganic–amine particles, indicating that the ammonium AMS measured mainly originated from this class. This can be reinforced by comparing marker peaks for ammonium and amine at m/z 18 NH_4^+, 30 NO^+, 58 $C_2H_5NHCH_2^+$, 59 $(CH_3)_3N^+$, and 88 $(C_2H_5)_2NO/C_3H_6NO_2^+$ with the time series of LAAPTOF (Fig. S8). For sulfate measured by AMS, we cannot infer the dominating donor class, since there is no comparable LAAPTOF class and fragments. This indicates again that this instrument has a low sensitivity to some sulfate-containing particles, such as pure ammonium sulfate. For organic compounds measured by AMS, it is also hard to find the comparable class and marker peaks in LAAPTOF data, probably due to two reasons: one is the same as that for sulfate-containing particles, and another one is that compared with AMS there are more fragments (cations and anions) arising from organics in LAAPTOF mass spectra. Nevertheless, we have found that peaks at m/z 129 $C_5H_7NO_3^+$ (arising from organonitrates) and 73 $C_2H_4COO^-$ (from organic acids) have a similar trend as the organics measured by AMS (Fig. 9b and c). At the beginning of the LAAPTOF measurements, the dominating organic-donor class is class 6, biomass burning–organosulfate (mainly contributing organic acids to be measured by AMS), while at the end of the measurement period this changed to sodium-salt-rich particles and biomass burning–soil (mainly contributing organonitrate and organic acids, respectively). Apart from that, aromatic compounds mainly in biomass burning–soil could also contribute to the organic mass fraction measured by AMS, especially for the strongest organic burst event towards the end of the measurement period (refer to Fig. 9d and e).

Although the LDI matrix effects cannot be completely overcome by using relative ion intensities, the time series of the corresponding maker peaks (Figs. 8, 9, and S8) can still be used for preliminary assignments of the bulk species to different particle types.

4 Conclusions and atmospheric implications

In this study, we used a combination of representative spectra obtained by fuzzy classification, laboratory-based reference spectra, marker peaks, and typical peak ratios for the improved single aerosol particle identification at a rural site in the upper Rhine valley near the city of Karlsruhe, Germany. Seven major particle classes were identified among a total of $\sim 3.7 \times 10^5$ single particles: calcium–soil, aged soot,

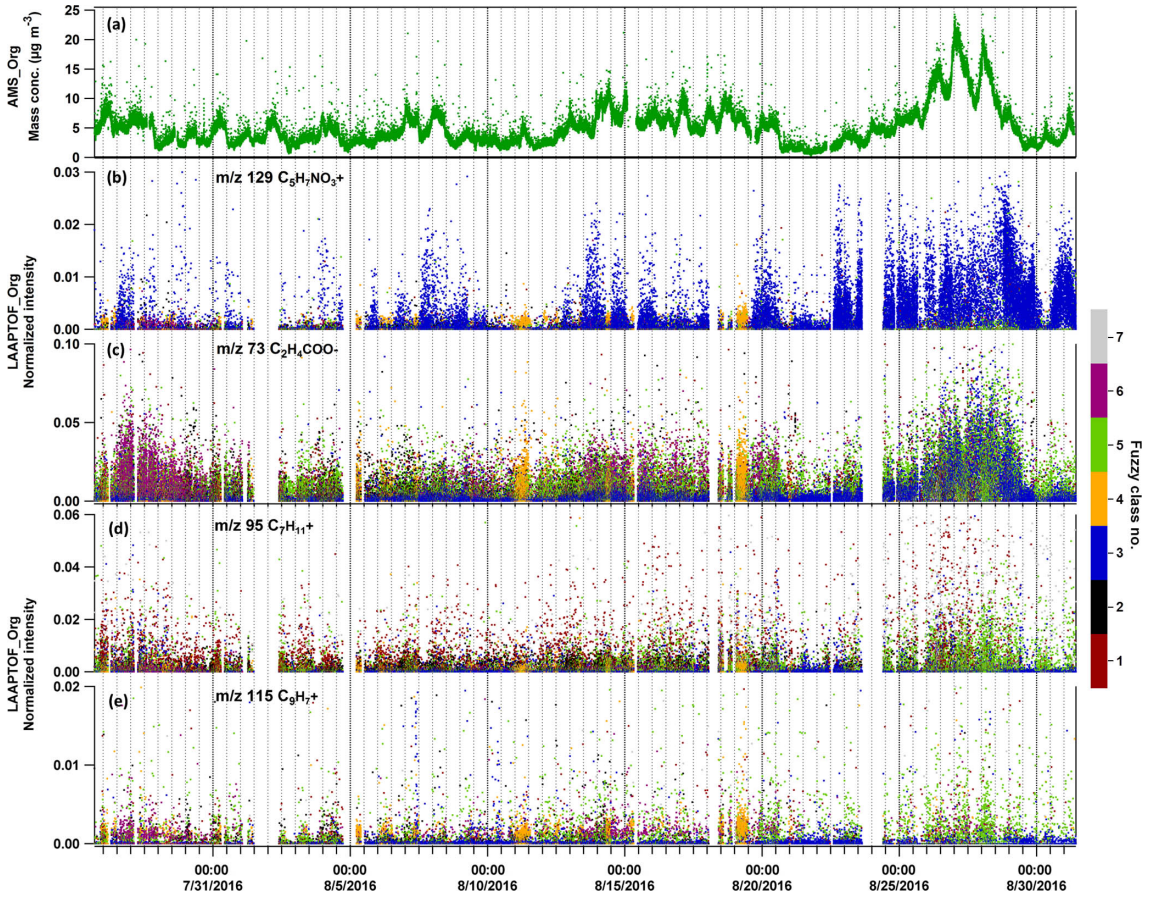

Figure 9. Time series of organic species measured by AMS in mass concentration and LAAPTOF in normalized ion intensities, respectively. Normalized intensity refers to the fragment intensity divided by the sum of all the ion intensities. In LAAPTOF spectra, the peak at m/z 129 $C_5H_7NO_3^+$ is arising from organonitrates, m/z 73 $C_2H_4COO^-$ from organic acids, and m/z 95 $C_7H_{11}^+$ as well as m/z 115 $C_9H_7^+$ from aromatic compounds. The seven classes are class 1: calcium–soil; class 2: aged soot; class 3: sodium salts; class 4: secondary inorganics–amine; class 5: biomass burning–soil; class 6: biomass burning–organosulfate; and class 7: mixed/aged dust.

sodium salts, secondary inorganics–amine, biomass burning–soil, biomass burning–organosulfate, and mixed/aged dust. All particles were internally mixed with organic and secondary inorganic compounds, i.e. ammonium, sulfate, and nitrate. According to our observations, these particles are expected to show a significant hygroscopicity due to their secondary inorganic contents (Fuzzi et al., 2015), as well as the presence of organosulfates (Thalman et al., 2017). The light absorption of soot particles is expected to be enhanced by mixing with non-absorbing species such as organic compounds (Bond et al., 2013). Organonitrate signatures found on sodium salt particles are also expected to increase their light absorbing capability (Canagaratna et al., 2007) and to assist nocturnal particle growth (Huang et al., 2019). The good correlation of most of the particle classes and dust signatures suggests that condensation processes and heterogeneous chemistry have modified the dust particles during their transportation. For example, organosulfate-coated dust could form from heterogeneous reactions of volatile organic compounds (VOCs), such as glyoxal, on mineral dust particles aged by reaction with, e.g. SO_2 (Shen et al., 2016). Since organosulfates can form by heterogeneous reactions of IEPOX on acidic particles at low NO_x level (Froyd et al., 2010; Surratt et al., 2010), it is likely that they form also on acidified dust particles under similar conditions. Our general observation of dominating aged and mixed aerosol particles is expected at a location about 2 h downwind of nearest major emission sources (12 km distance to Karlsruhe at an average daytime wind speed of 1.7 m s^{-1}).

Based on the precise identification for particle classes and individual particles, we applied a quantification method for single particles, employing size- and particle-class-resolved/chemically resolved overall detection efficiency (ODE) for this instrument. In contrast to methods used in previous SPMS studies, our approach is laboratory-based and does not rely on the availability of a reference instrument in the field. The corresponding "corrections" to the standard similarity classification result in substantial changes in

the particle class abundances: sodium salt particles changed from 43.5 % (similarity) to 3.4 % (corrected number fraction), corresponding to a mass fraction of 30.1 %, becoming the second dominating class in mass; secondary inorganics–amine dramatically decreased from 20.8 % to 2.4 %, corresponding to a mass fraction of 3.6 %, becoming the second least abundant class; biomass burning–soil changed from 16.1 % to 45.0 %, corresponding to a mass fraction of 31.8 %, becoming the dominating class in number and mass. The big difference between number-based and mass-based SPMS results has reinforced the importance of particle mass quantification. It is noteworthy that our quantification approach requires several assumptions mainly regarding particle shape and density, which results in potential uncertainties of up to $\sim 300\,\%$, with the dominant source still being the ODE values. Despite this large uncertainty, the resulting total particle mass shows good agreement with the total mass of non-refractory compounds measured by AMS in different periods, covering $\sim 85\,\%$ of the measurement time. However, some discrepancies still remain, most likely due to the low sensitivity of LAAPTOF for small particles as well as ammonium sulfate and organic-rich particles. Furthermore, we have found specific relationships of LAAPTOF ion intensity ratios and AMS mass concentration results for non-refractory compounds, especially for the fraction of org / (org + nitrate). This will be applied for source apportionment in an upcoming publication. The corresponding scatter plots may be used to estimate mass concentrations in future SPMS studies as well.

We have shown how particle size, density, morphology (shape), and chemical composition have impacted the ODE of the LAAPTOF. Therefore, these factors need to be taken into account for a reasonable quantitative interpretation of SPMS data. Considering reduced quantification uncertainties, systematic measurements on different types of standard samples, as well as real ambient samples (size-selected) under controlled environmental conditions (temperature and relative humidity), are still needed to obtain more comprehensive sensitivities for LAAPTOF.

Employing particle class information for individual particles and specific marker peaks with relative ion intensities, this study is able to assign non-refractory compounds measured by AMS to different classes of particles measured by SPMS. It turns out that nitrate measured by AMS was mainly from sodium-salt-like particles. Ammonium measured by AMS mainly arose from secondary inorganic–amine particles. However, the dominating donor particle classes varied in different time periods during the measurements. Organic compounds measured by AMS were from organic acids (mainly on aged-biomass-burning particles), organonitrates (from sodium salts), and aromatic compounds (from aged-biomass-burning particles). During the entire measurement campaign, the dominating particle classes changed with respect to particle number and mass, and the donor classes for non-refractory compounds also varied substantially, indicating changes of particles sources.

In spite of significant uncertainties stemming from several assumptions and instrumental aspects, our study provides a good example for the identification and quantitative interpretation of single-particle data. Together with the complimentary results from bulk measurements by AMS, we have shown how a better understanding of the internal and external mixing state of ambient aerosol particles can be achieved.

Data availability. LAAPTOF reference spectra are available upon request to the corresponding author and are available in electronic format via the EUROCHAMP Data Center – Library of Analytical Resources of the EU project EUROCHAMP-2020 at https://data.eurochamp.org/ (last access: 28 March 2019).

Supplement. The supplement related to this article is available online at: https://doi.org/10.5194/amt-12-2219-2019-supplement.

Author contributions. XS operated LAAPTOF and AMS during the whole field campaign, did the LAAPTOF data analysis, produced all figures, and wrote the paper. HS organized the campaign and provided suggestions for the data analysis, interpretation, and discussion. WH operated AMS during the whole campaign and did AMS data analysis. CM helped to operate the instruments and provided suggestions for the data analysis, interpretation, and discussion. RR helped to operate LAAPTOF. TL gave general advice and comments for this paper. All authors contributed to the final text.

Competing interests. The authors declare that they have no conflict of interest.

Acknowledgements. The authors gratefully thank the AIDA staff at KIT for helpful discussions and technical support and the China Scholarship Council (CSC) for the financial support of Xiaoli Shen and Wei Huang. Special thanks go to Daniel Cziczo for discussions about particle identification and quantification methods, to Nsikanabasi Umo for discussions about the coal fly ash sample, and to the Albtal-Verkehrs-Gesellschaft (AVG) for providing power and the measurement location near the tram line.

The article processing charges for this open-access publication were covered by a Research Centre of the Helmholtz Association.

Review statement. This paper was edited by Mingjin Tang and reviewed by four anonymous referees.

References

Ackerman, T. P. and Toon, O. B.: Absorption of visible radiation in atmosphere containing mixtures of absorbing and non-absorbing particles, Appl. Opt., 20, 3661–3668, 1981.

Ahern, A. T., Subramanian, R., Saliba, G., Lipsky, E. M., Donahue, N. M., and Sullivan, R. C.: Effect of secondary organic aerosol coating thickness on the real-time detection and characterization of biomass-burning soot by two particle mass spectrometers, Atmos. Meas. Tech., 9, 6117–6137, https://doi.org/10.5194/amt-9-6117-2016, 2016.

Allen, J. O., Fergenson, D. P., Gard, E. E., Hughes, L. S., Morrical, B. D., Kleeman, M. J., Gross, D. S., Galli, M. E., Prather, K. A., and Cass, G. R.: Particle detection efficiencies of aerosol time of flight mass spectrometers under ambient sampling conditions, Environ. Sci. Technol., 34, 211–217, 2000.

Allen, J. O., Bhave, P. V., Whiteaker, J. R., and Prather, K. A.: Instrument busy time and mass measurement using aerosol time-of-flight mass spectrometry, Aerosol Sci. Tech., 40, 615–626, 2006.

Angelino, S., Suess, D. T., and Prather, K. A.: Formation of aerosol particles from reactions of secondary and tertiary alkylamines: Characterization by aerosol time-of-flight mass spectrometry, Environ. Sci. Technol., 35, 3130–3138, 2001.

Ault, A. P., Moore, M. J., Furutani, H., and Prather, K. A.: Impact of emissions from the Los Angeles port region on San Diego air quality during regional transport events, Environ. Sci. Technol., 43, 3500–3506, 2009.

Ault, A. P., Gaston, C. J., Wang, Y., Dominguez, G., Thiemens, M. H., and Prather, K. A.: Characterization of the single particle mixing state of individual ship plume events measured at the port of Los Angeles, Environ. Sci. Technol., 44, 1954–1961, 2010.

Bahreini, R., Keywood, M. D., Ng, N. L., Varutbangkul, V., Gao, S., Flagan, R. C., Seinfeld, J. H., Worsnop, D. R., and Jimenez, J. L.: Measurements of secondary organic aerosol from oxidation of cycloalkenes, terpenes, and m-xylene using an Aerodyne aerosol mass spectrometer, Environ. Sci. Technol., 39, 5674–5688, 2005.

Bein, K. J., Zhao, Y. J., Pekney, N. J., Davidson, C. I., Johnston, M. V., and Wexler, A. S.: Identification of sources of atmospheric PM at the Pittsburgh Supersite – Part II: Quantitative comparisons of single particle, particle number, and particle mass measurements, Atmos. Environ., 40, 424–444, 2006.

Bergametti, G. and Forêt, G.: Mineral Dust: a key player in the earth system, Chapter 8, 183 pp., Springer, Dordrecht, 2014.

Bhave, P. V., Allen, J. O., Morrical, B. D., Fergenson, D. P., Cass, G. R., and Prather, K. A.: A field-based approach for determining ATOFMS instrument sensitivities to ammonium and nitrate, Environ. Sci. Technol., 36, 4868–4879, 2002.

Bond, T. C., Doherty, S. J., Fahey, D. W., Forster, P. M., Berntsen, T., DeAngelo, B. J., Flanner, M. G., Ghan, S., Karcher, B., Koch, D., Kinne, S., Kondo, Y., Quinn, P. K., Sarofim, M. C., Schultz, M. G., Schulz, M., Venkataraman, C., Zhang, H., Zhang, S., Bellouin, N., Guttikunda, S. K., Hopke, P. K., Jacobson, M. Z., Kaiser, J. W., Klimont, Z., Lohmann, U., Schwarz, J. P., Shindell, D., Storelvmo, T., Warren, S. G., and Zender, C. S.: Bounding the role of black carbon in the climate system: A scientific assessment, J. Geophys. Res.-Atmos., 118, 5380–5552, 2013.

Canagaratna, M. R., Jayne, J. T., Jimenez, J. L., Allan, J. D., Alfarra, M. R., Zhang, Q., Onasch, T. B., Drewnick, F., Coe, H., Middlebrook, A., Delia, A., Williams, L. R., Trimborn, A. M., Northway, M. J., DeCarlo, P. F., Kolb, C. E., Davidovits, P., and Worsnop, D. R.: Chemical and microphysical characterization of ambient aerosols with the aerodyne aerosol mass spectrometer, Mass Spectrom. Rev., 26, 185–222, 2007.

Christopoulos, C. D., Garimella, S., Zawadowicz, M. A., Möhler, O., and Cziczo, D. J.: A machine learning approach to aerosol classification for single-particle mass spectrometry, Atmos. Meas. Tech., 11, 5687–5699, https://doi.org/10.5194/amt-11-5687-2018, 2018.

Dall'Osto, M. and Harrison, R. M.: Urban organic aerosols measured by single particle mass spectrometry in the megacity of London, Atmos. Chem. Phys., 12, 4127–4142, https://doi.org/10.5194/acp-12-4127-2012, 2012.

Dall'Osto, M., Harrison, R. M., Beddows, D. C. S., Freney, E. J., Heal, M. R., and Donovan, R. J.: Single-particle detection efficiencies of aerosol time-of-flight mass spectrometry during the North Atlantic marine boundary layer experiment, Environ. Sci. Technol., 40, 5029–5035, 2006.

Dall'Osto, M., Harrison, R. M., Coe, H., and Williams, P.: Real-time secondary aerosol formation during a fog event in London, Atmos. Chem. Phys., 9, 2459–2469, https://doi.org/10.5194/acp-9-2459-2009, 2009.

Dall'Osto, M., Ceburnis, D., Monahan, C., Worsnop, D. R., Bialek, J., Kulmala, M., Kurten, T., Ehn, M., Wenger, J., Sodeau, J., Healy, R., and O'Dowd, C.: Nitrogenated and aliphatic organic vapors as possible drivers for marine secondary organic aerosol growth, J. Geophys. Res.-Atmos., 117, D12311, https://doi.org/10.1029/2012JD017522, 2012.

Dall'Osto, M., Querol, X., Alastuey, A., Minguillon, M. C., Alier, M., Amato, F., Brines, M., Cusack, M., Grimalt, J. O., Karanasiou, A., Moreno, T., Pandolfi, M., Pey, J., Reche, C., Ripoll, A., Tauler, R., Van Drooge, B. L., Viana, M., Harrison, R. M., Gietl, J., Beddows, D., Bloss, W., O'Dowd, C., Ceburnis, D., Martucci, G., Ng, N. L., Worsnop, D., Wenger, J., Mc Gillicuddy, E., Sodeau, J., Healy, R., Lucarelli, F., Nava, S., Jimenez, J. L., Gomez Moreno, F., Artinano, B., Prévôt, A. S. H., Pfaffenberger, L., Frey, S., Wilsenack, F., Casabona, D., Jiménez-Guerrero, P., Gross, D., and Cots, N.: Presenting SAPUSS: Solving Aerosol Problem by Using Synergistic Strategies in Barcelona, Spain, Atmos. Chem. Phys., 13, 8991–9019, https://doi.org/10.5194/acp-13-8991-2013, 2013.

Dall'Osto, M., Beddows, D. C. S., McGillicuddy, E. J., Esser-Gietl, J. K., Harrison, R. M., and Wenger, J. C.: On the simultaneous deployment of two single-particle mass spectrometers at an urban background and a roadside site during SAPUSS, Atmos. Chem. Phys., 16, 9693–9710, https://doi.org/10.5194/acp-16-9693-2016, 2016.

DeCarlo, P. F., Kimmel, J. R., Trimborn, A., Northway, M. J., Jayne, J. T., Aiken, A. C., Gonin, M., Fuhrer, K., Horvath, T., Docherty, K. S., Worsnop, D. R., and Jimenez, J. L.: Field-deployable, high-resolution, time-of-flight aerosol mass spectrometer, Anal. Chem., 78, 8281–8289, 2006.

DeCarlo, P. F., Slowik, J. G., Worsnop, D. R., Davidovits, P., and Jimenez, J. L.: Particle morphology and density characterization by combined mobility and aerodynamic diameter measurements, Part 1: Theory, Aerosol Sci. Tech., 38, 1185–1205, 2004.

Decesari, S., Finessi, E., Rinaldi, M., Paglione, M., Fuzzi, S., Stephanou, E. G., Tziaras, T., Spyros, A., Ceburnis, D., O'Dowd, C., Dall'Osto, M., Harrison, R. M., Allan, J., Coe,

H., and Facchini, M. C.: Primary and secondary marine organic aerosols over the North Atlantic Ocean during the MAP experiment, J. Geophys. Res.-Atmos., 116, D22210, https://doi.org/10.1029/2011jd016204, 2011.

Decesari, S., Allan, J., Plass-Duelmer, C., Williams, B. J., Paglione, M., Facchini, M. C., O'Dowd, C., Harrison, R. M., Gietl, J. K., Coe, H., Giulianelli, L., Gobbi, G. P., Lanconelli, C., Carbone, C., Worsnop, D., Lambe, A. T., Ahern, A. T., Moretti, F., Tagliavini, E., Elste, T., Gilge, S., Zhang, Y., and Dall'Osto, M.: Measurements of the aerosol chemical composition and mixing state in the Po Valley using multiple spectroscopic techniques, Atmos. Chem. Phys., 14, 12109–12132, https://doi.org/10.5194/acp-14-12109-2014, 2014.

Drewnick, F., Dall'Osto, M., and Harrison, R. M.: Characterization of aerosol particles from grass mowing by joint deployment of ToF-AMS and ATOFMS instruments, Atmos. Environ., 42, 3006–3017, 2008.

Erisman, J. W., Otjes, R., Hensen, A., Jongejan, P., van den Bulk, P., Khlystov, A., Mols, H., and Slanina, S.: Instrument development and application in studies and monitoring of ambient ammonia, Atmos. Environ., 35, 1913–1922, 2001.

Faude, F. and Goschnick, J.: XPS, SIMS and SNMS applied to a combined analysis of aerosol particles from a region of considerable air pollution in the upper Rhine valley, Fresen. J. Anal. Chem., 358, 67–72, 1997.

Ferge, T., Karg, E., Schroppel, A., Coffee, K. R., Tobias, H. J., Frank, M., Gard, E. E., and Zimmermann, R.: Fast determination of the relative elemental and organic carbon content of aerosol samples by on-line single-particle aerosol time-of-flight mass spectrometry, Environ. Sci. Technol., 40, 3327–3335, 2006.

Fergenson, D. P., Song, X. H., Ramadan, Z., Allen, J. O., Hughes, L. S., Cass, G. R., Hopke, P. K., and Prather, K. A.: Quantification of ATOFMS data by multivariate methods, Anal. Chem., 73, 3535–3541, 2001.

Froyd, K. D., Murphy, S. M., Murphy, D. M., de Gouw, J. A., Eddingsaas, N. C., and Wennberg, P. O.: Contribution of isoprene-derived organosulfates to free tropospheric aerosol mass, P. Natl. Acad. Sci. USA, 107, 21360–21365, 2010.

Fuzzi, S., Baltensperger, U., Carslaw, K., Decesari, S., Denier van der Gon, H., Facchini, M. C., Fowler, D., Koren, I., Langford, B., Lohmann, U., Nemitz, E., Pandis, S., Riipinen, I., Rudich, Y., Schaap, M., Slowik, J. G., Spracklen, D. V., Vignati, E., Wild, M., Williams, M., and Gilardoni, S.: Particulate matter, air quality and climate: lessons learned and future needs, Atmos. Chem. Phys., 15, 8217–8299, https://doi.org/10.5194/acp-15-8217-2015, 2015.

Gallavardin, S., Lohmann, U., and Cziczo, D.: Analysis and differentiation of mineral dust by single particle laser mass spectrometry, Int. J. Mass Spectrom., 274, 56–63, 2008.

Gard, E. E., Kleeman, M. J., Gross, D. S., Hughes, L. S., Allen, J. O., Morrical, B. D., Fergenson, D. P., Dienes, T., Galli, M. E., Johnson, R. J., Cass, G. R., and Prather, K. A.: Direct observation of heterogeneous chemistry in the atmosphere, Science, 279, 1184–1187, 1998.

Gaston, C. J., Furutani, H., Guazzotti, S. A., Coffee, K. R., Bates, T. S., Quinn, P. K., Aluwihare, L. I., Mitchell, B. G., and Prather, K. A.: Unique ocean-derived particles serve as a proxy for changes in ocean chemistry, J. Geophys. Res.-Atmos., 116, D18310, https://doi.org/10.1029/2010JD015289, 2011.

Gaston, C. J., Quinn, P. K., Bates, T. S., Gilman, J. B., Bon, D. M., Kuster, W. C., and Prather, K. A.: The impact of shipping, agricultural, and urban emissions on single particle chemistry observed aboard the R/V *Atlantis* during CalNex, J. Geophys. Res.-Atmos., 118, 5003–5017, 2013.

Gemayel, R., Hellebust, S., Temime-Roussel, B., Hayeck, N., Van Elteren, J. T., Wortham, H., and Gligorovski, S.: The performance and the characterization of laser ablation aerosol particle time-of-flight mass spectrometry (LAAP-ToF-MS), Atmos. Meas. Tech., 9, 1947–1959, https://doi.org/10.5194/amt-9-1947-2016, 2016.

Gemayel, R., Temime-Roussel, B., Hayeck, N., Gandolfo, A., Hellebust, S., Gligorovski, S., and Wortham, H.: Development of an analytical methodology for obtaining quantitative mass concentrations from LAAP-ToF-MS measurements, Talanta, 174, 715–724, 2017.

Goschnick, J., Schuricht, J., and Ache, H. J.: Depth-structure of airborne microparticles sampled downwind from the city of Karlsruhe in the river Rhine Valley, Fresen. J. Anal. Chem., 350, 426–430, 1994.

Gross, D. S., Gälli, M. E., Silva, P. J., and Prather, K. A.: Relative sensitivity factors for alkali metal and ammonium cations in single particle aerosol time-of-flight mass spectra, Anal. Chem., 72, 416–422, 2000.

Gunsch, M. J., May, N. W., Wen, M., Bottenus, C. L. H., Gardner, D. J., VanReken, T. M., Bertman, S. B., Hopke, P. K., Ault, A. P., and Pratt, K. A.: Ubiquitous influence of wildfire emissions and secondary organic aerosol on summertime atmospheric aerosol in the forested Great Lakes region, Atmos. Chem. Phys., 18, 3701–3715, https://doi.org/10.5194/acp-18-3701-2018, 2018.

Hagemann, R., Corsmeier, U., Kottmeier, C., Rinke, R., Wieser, A., and Vogel, B.: Spatial variability of particle number concentrations and NO_x in the Karlsruhe (Germany) area obtained with the mobile laboratory 'AERO-TRAM', Atmos Environ, 94, 341–352, 2014.

Hatch, L. E., Creamean, J. M., Ault, A. P., Surratt, J. D., Chan, M. N., Seinfeld, J. H., Edgerton, E. S., Su, Y. X., and Prather, K. A.: Measurements of isoprene-derived organosulfates in ambient aerosols by aerosol time-of-flight mass spectrometry – Part 2: temporal variability and formation mechanisms, Environ. Sci. Technol., 45, 8648–8655, 2011a.

Hatch, L. E., Creamean, J. M., Ault, A. P., Surratt, J. D., Chan, M. N., Seinfeld, J. H., Edgerton, E. S., Su, Y. X., and Prather, K. A.: Measurements of isoprene-derived organosulfates in ambient aerosols by aerosol time-of-flight mass spectrometry – Part 1: single particle atmospheric observations in Atlanta, Environ. Sci. Technol., 45, 5105–5111, 2011b.

Hatch, L. E., Pratt, K. A., Huffman, J. A., Jimenez, J. L., and Prather, K. A.: Impacts of aerosol aging on laser desorption/ionization in single-particle mass spectrometers, Aerosol Sci. Tech., 48, 1050–1058, 2014.

Healy, R. M., Sciare, J., Poulain, L., Kamili, K., Merkel, M., Müller, T., Wiedensohler, A., Eckhardt, S., Stohl, A., Sarda-Estève, R., McGillicuddy, E., O'Connor, I. P., Sodeau, J. R., and Wenger, J. C.: Sources and mixing state of size-resolved elemental carbon particles in a European megacity: Paris, Atmos. Chem. Phys., 12, 1681–1700, https://doi.org/10.5194/acp-12-1681-2012, 2012.

Healy, R. M., Sciare, J., Poulain, L., Crippa, M., Wiedensohler, A., Prévôt, A. S. H., Baltensperger, U., Sarda-Estève, R., McGuire,

M. L., Jeong, C.-H., McGillicuddy, E., O'Connor, I. P., Sodeau, J. R., Evans, G. J., and Wenger, J. C.: Quantitative determination of carbonaceous particle mixing state in Paris using single-particle mass spectrometer and aerosol mass spectrometer measurements, Atmos. Chem. Phys., 13, 9479–9496, https://doi.org/10.5194/acp-13-9479-2013, 2013.

Hill, T. C. J., DeMott, P. J., Tobo, Y., Fröhlich-Nowoisky, J., Moffett, B. F., Franc, G. D., and Kreidenweis, S. M.: Sources of organic ice nucleating particles in soils, Atmos. Chem. Phys., 16, 7195–7211, https://doi.org/10.5194/acp-16-7195-2016, 2016.

Hinz, K. P., Greweling, M., Drews, F., and Spengler, B.: Data processing in on-line laser mass spectrometry of inorganic, organic, or biological airborne particles, J. Am. Soc. Mass Spectr., 10, 648–660, 1999.

Huang, W., Saathoff, H., Shen, X. L., Ramakrishna, R., Leisner, T., and Mohr, C.: Chemical characterization of highly functionalized organonitrates contributing to high night-time organic aerosol mass loadings and particle growth, Environ. Sci. Technol., 53, 1165–1174, 2019.

Jeong, C.-H., McGuire, M. L., Godri, K. J., Slowik, J. G., Rehbein, P. J. G., and Evans, G. J.: Quantification of aerosol chemical composition using continuous single particle measurements, Atmos. Chem. Phys., 11, 7027–7044, https://doi.org/10.5194/acp-11-7027-2011, 2011.

Köllner, F., Schneider, J., Willis, M. D., Klimach, T., Helleis, F., Bozem, H., Kunkel, D., Hoor, P., Burkart, J., Leaitch, W. R., Aliabadi, A. A., Abbatt, J. P. D., Herber, A. B., and Borrmann, S.: Particulate trimethylamine in the summertime Canadian high Arctic lower troposphere, Atmos. Chem. Phys., 17, 13747–13766, https://doi.org/10.5194/acp-17-13747-2017, 2017.

Li, L., Liu, L., Xu, L., Li, M., Li, X., Gao, W., Huang, Z. X., and Cheng, P.: Improvement in the Mass Resolution of Single Particle Mass Spectrometry Using Delayed Ion Extraction, J. Am. Soc. Mass Spectr., 29, 2105–2109, 2018.

Lin, Q., Zhang, G., Peng, L., Bi, X., Wang, X., Brechtel, F. J., Li, M., Chen, D., Peng, P., Sheng, G., and Zhou, Z.: In situ chemical composition measurement of individual cloud residue particles at a mountain site, southern China, Atmos. Chem. Phys., 17, 8473–8488, https://doi.org/10.5194/acp-17-8473-2017, 2017.

Lu, D. W., Liu, Q., Yu, M., Yang, X. Z., Fu, Q., Zhang, X. S., Mu, Y. J., and Jiang, G. B.: Natural silicon isotopic signatures reveal the sources of airborne fine particulate matter, Environ. Sci. Technol., 52, 1088–1095, 2018.

Marsden, N. A., Flynn, M. J., Taylor, J. W., Allan, J. D., and Coe, H.: Evaluating the influence of laser wavelength and detection stage geometry on optical detection efficiency in a single-particle mass spectrometer, Atmos. Meas. Tech., 9, 6051–6068, https://doi.org/10.5194/amt-9-6051-2016, 2016.

Marsden, N. A., Flynn, M. J., Allan, J. D., and Coe, H.: Online differentiation of mineral phase in aerosol particles by ion formation mechanism using a LAAP-TOF single-particle mass spectrometer, Atmos. Meas. Tech., 11, 195–213, https://doi.org/10.5194/amt-11-195-2018, 2018.

Marsden, N. A., Ullrich, R., Möhler, O., Eriksen Hammer, S., Kandler, K., Cui, Z., Williams, P. I., Flynn, M. J., Liu, D., Allan, J. D., and Coe, H.: Mineralogy and mixing state of north African mineral dust by online single-particle mass spectrometry, Atmos. Chem. Phys., 19, 2259–2281, https://doi.org/10.5194/acp-19-2259-2019, 2019.

May, N. W., Gunsch, M. J., Olson, N. E., Bondy, A. L., Kirpes, R. M., Bertman, S. B., China, S., Laskin, A., Hopke, P. K., Ault, A. P., and Pratt, K. A.: Unexpected contributions of sea spray and lake spray aerosol to inland particulate matter, Environ. Sc. Tech. Lett., 5, 405–412, 2018.

Middlebrook, A. M., Murphy, D. M., Lee, S. H., Thomson, D. S., Prather, K. A., Wenzel, R. J., Liu, D. Y., Phares, D. J., Rhoads, K. P., Wexler, A. S., Johnston, M. V., Jimenez, J. L., Jayne, J. T., Worsnop, D. R., Yourshaw, I., Seinfeld, J. H., and Flagan, R. C.: A comparison of particle mass spectrometers during the 1999 Atlanta Supersite Project, J. Geophys. Res.-Atmos., 108, 8424, https://doi.org/10.1029/2001jd000660, 2003.

Middlebrook, A. M., Bahreini, R., Jimenez, J. L., and Canagaratna, M. R.: Evaluation of composition-dependent collection efficiencies for the aerodyne aerosol mass spectrometer using field data, Aerosol Sci. Tech., 46, 258–271, 2012.

Moffet, R. C., de Foy, B., Molina, L. T., Molina, M. J., and Prather, K. A.: Measurement of ambient aerosols in northern Mexico City by single particle mass spectrometry, Atmos. Chem. Phys., 8, 4499–4516, https://doi.org/10.5194/acp-8-4499-2008, 2008a.

Moffet, R. C., Qin, X. Y., Rebotier, T., Furutani, H., and Prather, K. A.: Chemically segregated optical and microphysical properties of ambient aerosols measured in a single-particle mass spectrometer, J. Geophys. Res.-Atmos., 113, D12213, https://doi.org/10.1029/2007jd009393, 2008b.

Murphy, D. M.: The design of single particle laser mass spectrometers, Mass Spectrom. Rev., 26, 150–165, 2007.

Murphy, D. M., Cziczo, D. J., Froyd, K. D., Hudson, P. K., Matthew, B. M., Middlebrook, A. M., Peltier, R. E., Sullivan, A., Thomson, D. S., and Weber, R. J.: Single-particle mass spectrometry of tropospheric aerosol particles, J. Geophys. Res.-Atmos., 111, D23S32, https://doi.org/10.1029/2006jd007340, 2006.

Noble, C. A. and Prather, K. A.: Real-time single particle mass spectrometry: a historical review of a quarter century of the chemical analysis of aerosols, Mass Spectrom. Rev., 19, 248–274, 2000.

Perring, A. E., Pusede, S. E., and Cohen, R. C.: An observational perspective on the atmospheric impacts of alkyl and multifunctional nitrates on ozone and secondary organic aerosol, Chem. Rev., 113, 5848–5870, 2013.

Pöschl, U.: Atmospheric aerosols: Composition, transformation, climate and health effects, Angew. Chem. Int. Edit, 44, 7520–7540, 2005.

Pratt, K. A., Hatch, L. E., and Prather, K. A.: Seasonal Volatility Dependence of Ambient Particle Phase Amines, Environ. Sci. Technol., 43, 5276–5281, 2009.

Pratt, K. A., Heymsfield, A. J., Twohy, C. H., Murphy, S. M., DeMott, P. J., Hudson, J. G., Subramanian, R., Wang, Z. E., Seinfeld, J. H., and Prather, K. A.: In situ chemical characterization of aged biomass-burning aerosols impacting cold wave clouds, J. Atmos. Sci., 67, 2451–2468, 2010.

Pratt, K. A., Murphy, S. M., Subramanian, R., DeMott, P. J., Kok, G. L., Campos, T., Rogers, D. C., Prenni, A. J., Heymsfield, A. J., Seinfeld, J. H., and Prather, K. A.: Flight-based chemical characterization of biomass burning aerosols within two prescribed burn smoke plumes, Atmos. Chem. Phys., 11, 12549–12565, https://doi.org/10.5194/acp-11-12549-2011, 2011.

Pratt, K. A. and Prather, K. A.: Real-time, single-particle volatility, size, and chemical composition measurements of aged urban aerosols, Environ. Sci. Technol., 43, 8276–8282, 2009.

Pratt, K. A. and Prather, K. A.: Mass spectrometry of atmospheric aerosols-Recent developments and applications, Part II: Online mass spectrometry techniques, Mass Spectrom. Rev., 31, 17–48, 2012.

Qin, X. Y., Bhave, P. V., and Prather, K. A.: Comparison of two methods for obtaining quantitative mass concentrations from aerosol time-of-flight mass spectrometry measurements, Anal. Chem., 78, 6169–6178, 2006.

Qin, X. Y., Pratt, K. A., Shields, L. G., Toner, S. M., and Prather, K. A.: Seasonal comparisons of single-particle chemical mixing state in Riverside, CA, Atmos. Environ., 59, 587–596, 2012.

Ramisetty, R., Abdelmonem, A., Shen, X., Saathoff, H., Leisner, T., and Mohr, C.: Exploring femtosecond laser ablation in single-particle aerosol mass spectrometry, Atmos. Meas. Tech., 11, 4345–4360, https://doi.org/10.5194/amt-11-4345-2018, 2018.

Reilly, P. T. A., Lazar, A. C., Gieray, R. A., Whitten, W. B., and Ramsey, J. M.: The elucidation of charge-transfer-induced matrix effects in environmental aerosols via real-time aerosol mass spectral analysis of individual airborne particles, Aerosol Sci. Tech., 33, 135–152, 2000.

Reinard, M. S. and Johnston, M. V.: Ion formation mechanism in laser desorption ionization of individual nanoparticles, J. Am. Soc. Mass Spectr., 19, 389–399, 2008.

Reitz, P., Zorn, S. R., Trimborn, S. H., and Trimborn, A. M.: A new, powerful technique to analyze single particle aerosol mass spectra using a combination of OPTICS and the fuzzy c-means algorithm, J. Aerosol Sci., 98, 1–14, 2016.

Roth, A., Schneider, J., Klimach, T., Mertes, S., van Pinxteren, D., Herrmann, H., and Borrmann, S.: Aerosol properties, source identification, and cloud processing in orographic clouds measured by single particle mass spectrometry on a central European mountain site during HCCT-2010, Atmos. Chem. Phys., 16, 505–524, https://doi.org/10.5194/acp-16-505-2016, 2016.

Schmidt, S., Schneider, J., Klimach, T., Mertes, S., Schenk, L. P., Kupiszewski, P., Curtius, J., and Borrmann, S.: Online single particle analysis of ice particle residuals from mountain-top mixed-phase clouds using laboratory derived particle type assignment, Atmos. Chem. Phys., 17, 575–594, https://doi.org/10.5194/acp-17-575-2017, 2017.

Shen, X., Ramisetty, R., Mohr, C., Huang, W., Leisner, T., and Saathoff, H.: Laser ablation aerosol particle time-of-flight mass spectrometer (LAAPTOF): performance, reference spectra and classification of atmospheric samples, Atmos. Meas. Tech., 11, 2325–2343, https://doi.org/10.5194/amt-11-2325-2018, 2018.

Shen, X. L., Wu, H. H., Zhao, Y., Huang, D., Huang, L. B., and Chen, Z. M.: Heterogeneous reactions of glyoxal on mineral particles: A new avenue for oligomers and organosulfate formation, Atmos. Environ., 131, 133–140, 2016.

Silva, P. J. and Prather, K. A.: Interpretation of mass spectra from organic compounds in aerosol time-of-flight mass spectrometry, Anal. Chem., 72, 3553–3562, 2000.

Spencer, M. T. and Prather, K. A.: Using ATOFMS to determine OC/EC mass fractions in particles, Aerosol Sci. Tech., 40, 585–594, 2006.

Spencer, M. T., Shields, L. G., and Prather, K. A.: Simultaneous measurement of the effective density and chemical composition of ambient aerosol particles, Environ. Sci. Technol., 41, 1303–1309, 2007.

Stolzenburg, M. R. and Hering, S. V.: Method for the automated measurement of fine particle nitrate in the atmosphere, Environ. Sci. Technol., 34, 907–914, 2000.

Surratt, J. D., Chan, A. W. H., Eddingsaas, N. C., Chan, M. N., Loza, C. L., Kwan, A. J., Hersey, S. P., Flagan, R. C., Wennberg, P. O., and Seinfeld, J. H.: Reactive intermediates revealed in secondary organic aerosol formation from isoprene, P. Natl. Acad. Sci. USA, 107, 6640–6645, 2010.

Thalman, R., de Sá, S. S., Palm, B. B., Barbosa, H. M. J., Pöhlker, M. L., Alexander, M. L., Brito, J., Carbone, S., Castillo, P., Day, D. A., Kuang, C., Manzi, A., Ng, N. L., Sedlacek III, A. J., Souza, R., Springston, S., Watson, T., Pöhlker, C., Pöschl, U., Andreae, M. O., Artaxo, P., Jimenez, J. L., Martin, S. T., and Wang, J.: CCN activity and organic hygroscopicity of aerosols downwind of an urban region in central Amazonia: seasonal and diel variations and impact of anthropogenic emissions, Atmos. Chem. Phys., 17, 11779–11801, https://doi.org/10.5194/acp-17-11779-2017, 2017.

Thomson, D. S., Middlebrook, A. M., and Murphy, D. M.: Thresholds for laser-induced ion formation from aerosols in a vacuum using ultraviolet and vacuum-ultraviolet laser wavelengths, Aerosol Sci. Tech., 26, 544–559, 1997.

Vera, C. C., Trimborn, A., Hinz, K. P., and Spengler, B.: Initial velocity distributions of ions generated by in-flight laser desorption/ionization of individual polystyrene latex microparticles as studied by the delayed ion extraction method, Rapid Commun. Mass Sp., 19, 133–146, 2005.

Wang, Z., King, S. M., Freney, E., Rosenoern, T., Smith, M. L., Chen, Q., Kuwata, M., Lewis, E. R., Poschl, U., Wang, W., Buseck, P. R., and Martin, S. T.: The dynamic shapefactor of sodium chloride nanoparticles as regulated by drying rate, Aerosol Sci. Tech., 44, 939–953, 2010.

Wenzel, R. J., Liu, D. Y., Edgerton, E. S., and Prather, K. A.: Aerosol time-of-flight mass spectrometry during the Atlanta Supersite Experiment: 2. Scaling procedures, J. Geophys. Res.-Atmos., 108, 8427, https://doi.org/10.1029/2001jd001563, 2003.

Wenzel, R. J. and Prather, K. A.: Improvements in ion signal reproducibility obtained using a homogeneous laser beam for on-line laser desorption/ionization of single particles, Rapid Commun. Mass Sp., 18, 1525–1533, 2004.

Wiley, W. C. and Mclaren, I. H.: Time-of-Flight Mass Spectrometer with Improved Resolution, Rev. Sci. Instrum., 26, 1150–1157, 1955.

Williams, L. R., Gonzalez, L. A., Peck, J., Trimborn, D., McInnis, J., Farrar, M. R., Moore, K. D., Jayne, J. T., Robinson, W. A., Lewis, D. K., Onasch, T. B., Canagaratna, M. R., Trimborn, A., Timko, M. T., Magoon, G., Deng, R., Tang, D., de la Rosa Blanco, E., Prévôt, A. S. H., Smith, K. A., and Worsnop, D. R.: Characterization of an aerodynamic lens for transmitting particles greater than 1 micrometer in diameter into the Aerodyne aerosol mass spectrometer, Atmos. Meas. Tech., 6, 3271–3280, https://doi.org/10.5194/amt-6-3271-2013, 2013.

Wonaschuetz, A., Kallinger, P., Szymanski, W., and Hitzenberger, R.: Chemical composition of radiolytically formed particles using single-particle mass spectrometry, J. Aerosol Sci., 113, 242–249, 2017.

Zawadowicz, M. A., Froyd, K. D., Murphy, D. M., and Cziczo, D. J.: Improved identification of primary biological aerosol particles using single-particle mass spectrometry, Atmos. Chem. Phys., 17, 7193–7212, https://doi.org/10.5194/acp-17-7193-2017, 2017.

Zelenyuk, A., Cai, Y., Chieffo, L., and Imre, D.: High precision density measurements of single particles: The density of metastable phases, Aerosol Sci. Tech., 39, 972–986, 2005.

Zelenyuk, A., Imre, D., Han, J. H., and Oatis, S.: Simultaneous measurements of individual ambient particle size, composition, effective density, and hygroscopicity, Anal. Chem., 80, 1401–1407, 2008.

Zenobi, R. and Knochenmuss, R.: Ion formation in MALDI mass spectrometry, Mass Spectrom. Rev., 17, 337–366, 1998.

Zhou, Y., Huang, X. H. H., Griffith, S. M., Li, M., Li, L., Zhou, Z., Wu, C., Meng, J. W., Chan, C. K., Louie, P. K. K., and Yu, J. Z.: A field measurement based scaling approach for quantification of major ions, organic carbon, and elemental carbon using a single particle aerosol mass spectrometer, Atmos. Environ., 143, 300–312, 2016.

B.6 Composition and origin of $PM_{2.5}$ aerosol particles in the upper Rhine valley in summer

Authors: Xiaoli Shen, Heike Vogel, Bernhard Vogel, **Wei Huang**, Claudia Mohr, Ramakrishna Ramisetty, Thomas Leisner, André S. H. Prévôt, and Harald Saathoff

In: Atmospheric Chemistry and Physics, 1–30, in review, 2019.

Authorship statement

This article is based on the field data from a six-week campaign (TRAM01) during July–August 2016 in a rural area of near Eggenstein-Leopoldshafen (southwest Germany), located ~12 km north of the city of Karlsruhe, with a focus on the comparison of field data with model simulation results and on the source apportionment for the aerosol particles in the upper Rhine valley. In particular, I was responsible for the operation and calibrations of AMS during this campaign, AMS data analysis, and data interpretation and discussion of this article. Currently this article is under review in *Atmospheric Chemistry and Physics*.

Composition and origin of $PM_{2.5}$ aerosol particles in the upper Rhine valley in summer

Xiaoli Shen[1,2], Heike Vogel[1], Bernhard Vogel[1], Wei Huang[1,2], Claudia Mohr[3], Ramakrishna Ramisetty[1,4], Thomas Leisner[1,5], André S. H. Prévôt[6], and Harald Saathoff[1,*]

[1]Institute of Meteorology and Climate Research, Karlsruhe Institute of Technology, Hermann-von-Helmholtz-Platz 1, 76344 Eggenstein-Leopoldshafen, Germany
[2]Institute of Geography and Geoecology, Working Group for Environmental Mineralogy and Environmental System Analysis, Karlsruhe Institute of Technology, Kaiserstr.12, 76131 Karlsruhe, Germany
[3]Department of Environmental Science and Analytical Chemistry, Stockholm University, Stockholm, 11418, Sweden
[4]Now at: TSI Instruments India Private Limited, Bangalore, 560102, India
[5]Institute of Environmental Physics, University Heidelberg, In Neuenheimer Feld 229, 69120 Heidelberg, Germany
[6]Laboratory of Atmospheric Chemistry, Paul Scherrer Institute (PSI), 5232 Villigen PSI, Switzerland

Correspondence to: Harald Saathoff (harald.saathoff@kit.edu)

Abstract. We conducted a six-week measurement campaign in summer 2016 at a rural site about 11 km north of the city of Karlsruhe in southwest Germany in order to study the chemical composition and origin of aerosols in the upper Rhine valley. In particular, we deployed a single particle mass spectrometer (LAAPTOF) and an aerosol mass spectrometer (AMS) to provide complementary chemical information of the aerosol particles smaller than 2.5 µm. For the entire measurement period, the total aerosol particle mass was dominated by sodium salts contributing on average (36 ± 27) % to the total single particles. The total particulate organic compounds, sulfate, nitrate, and ammonium contributed on average (58 ± 12) %, (22 ± 7) %, (10 ± 1) %, and (9 ± 3) % to the total non-refractory particle mass, respectively. The regional transport model COSMO-ART was applied for source apportionment and to achieve a better understanding of the impact of complex transport pattern on the field observations. Combining field observations and model simulations, we attributed high particle numbers and SO_2 concentrations observed at this rural site to industrial emissions from power plants and a refinery in Karlsruhe. In addition, two characteristic episodes with aerosol particle mass dominated by sodium salts particles compromising (70 ± 24) % of the total single particles and organic compounds comprising accounting for (77 ± 6) % of total non-refractory species, respectively, were investigated in detail. For the first episode, we identified relatively fresh and aged sea salt particles originating from the Atlantic Ocean more than 800 km away. These particles showed markers like m/z 129 $C_5H_7NO_3^+$ indicating the influence of anthropogenic emissions modifying their composition e.g., from chloride to nitrate salts during the long-range transport. For a 3-day episode including high organic mass concentrations, model simulations show that on average (74 ± 7) % of the particulate organics at this site were of biogenic origin. Detailed model analysis allowed us to find out that three subsequent peaks of high organic mass concentrations originated from different sources, including local emissions from the city and industrial area of Karlsruhe, regional transport from the city of Stuttgart (~64 km away), and potential local night-time formation and growths. Biogenic

(forest) and anthropogenic (urban) emissions were mixed during transport and contributed to the formation of organic particles. In addition, topography, temperature inversion, and stagnant meteorological conditions also played a role in the build-up of higher organic particle mass concentrations. Furthermore, the model was evaluated using the field observations and corresponding sensitivity tests. The model results show good agreement with trends and concentrations observed for several trace gases (e.g., O_3, NO_2, and SO_2) and aerosol particle compounds (e.g., ammonium and nitrate). However, the model underestimates the number of particles by an order of magnitude and underestimates the mass of organic particles by a factor of 2.3. The discrepancy was expected for particle number since the model does not include all nucleation processes. The missing organic mass indicates either an underestimated regional background, missing sources, and/or mechanisms in the model like night-time chemistry. This study demonstrates the potential of combining comprehensive field observations with dedicated transport modelling to understand the chemical composition and complex origin of aerosols.

1 Introduction

Aerosols are ubiquitous in the atmosphere and play a crucial role in air quality, human health, ecosystem and climate change. In particular, aerosol particles modify atmospheric radiative fluxes and can serve as cloud condensation nuclei (CCN) and/or be activated as ice nuclei (IN), which influences the cloud formation, properties (albedo) and precipitation, thus has further impact on weather and climate change (Fuzzi et al., 2015; Pöschl, 2005; Seinfeld and Pandis, 2006). Such indirect impacts of aerosols on climate are still related to large uncertainties and low confidence levels (IPCC, 2013). There are various types of atmospheric aerosol particles, such as mineral dust, sea salt, soot, and organic aerosol particles, originating from biogenic and/or anthropogenic emission sources, as well as secondary formation from precursors within the atmosphere (Tsigaridis et al., 2006). Aerosol particles are not typically purely inorganic or organic; instead, they are often composed of different inorganic and organic species. The diverse origins and atmospheric aging cause the complexity of the aerosol particle mixtures.

Real-time mass spectrometry is widely used to measure size and chemical composition of aerosol particles with high temporal resolution. Two major instrument types are single particle mass spectrometers (singe-particle MS) and aerosol mass spectrometers (AMS). The single-particle MS is sensitive to both non-refractory and refractory species and to the mixing state of individual particles, and thus identifies particle types (Murphy, 2007), while the AMS can quantify mass concentrations of non-refractory particulate compounds in bulk samples (Canagaratna et al., 2007). Complementary data from single-particle MS and AMS allows quantitative interpretation of the internal and external mixing state of the aerosol (Gemayel et al., 2017; Gunsch et al., 2018; Healy et al., 2013; Jeong et al., 2011; Shen et al., 2019; Zhou et al., 2016). The mixing state of the aerosol particles can reflect their evolution e.g. caused by chemical reactions leading to changing compositions or coatings (Reitz et al., 2016). A good example is the aging of sea salt particles: chloride replacement by nitrate on sea-salt particles can be well identified by single-particle MS (Gard et al., 1998).

B Appendix

The large diversity of aerosols, containing hundreds of gaseous and particulate components, makes it difficult to trace their sources. Therefore, several source apportionment methods have been developed with the common aim of reducing the complexity of the aerosol particle mixtures and thus helping to identify the major particle types in the atmosphere. Clustering algorithms have been used commonly for the single-particle MS data analysis (Reitz et al., 2016), while positive matrix factorization (PMF; Paatero, 1997; Paatero and Tapper, 1994) is commonly applied for AMS data analysis (Canonaco et al., 2013; Canonaco et al., 2015; Crippa et al., 2014; Zhang et al., 2011). However, these methods can only provide indirect source information. The application of a transport model gives additional information. It can predict the state of the atmosphere based on detailed meteorology, emission data, as well as conversions of reactive species and thus allows studying the aerosol evolution from the emissions to a site of interest.

There exists a variety of so-called online coupled chemical transport models. A recent review is given by (Baklanov et al., 2014). Such models are important tools to better understand aerosol particles' sources and aging processes, and their impact on particles' climate-relevant properties, such as cloud condensation nuclei (CCN) activity, optical properties, and hygroscopicity (Fierce et al., 2017). Models can be improved with a good process understanding, e.g., emissions, transport and deposition, and corresponding parameterisations obtained from dedicated laboratory studies (Burkholder et al., 2017). They are often used to predict the evolution of the atmospheric composition on different spatial scales, which can be evaluated by comparison with field measurements. Besides, comparisons between model simulations and field observations also help to validate the model or to identify weaknesses like poorly represented chemistry, missing sources or mechanisms.

For comparison with measurements at a single location, regional scale models with small grid sizes (down to a few kilometres) are required. In addition, phenomena such as mountain and valley winds, land-sea breezes or lee waves become important, which requires a non-hydrostatic formulation of the model equations. In this study we use the regional-scale model system COSMO-ART (Consortium for small-scale modelling - aerosols and reactive trace gases; Vogel et al., 2009). The part of the model describing aerosols and reactive trace gases was developed at the Karlsruhe Institute of Technology (http://www.imk-tro.kit.edu/english/3509.php). It extends the operational weather forecast model COSMO of the German Weather Service (DWD), and it allows studying the feedback processes between aerosol particles and the state of the atmosphere covering the continental to the regional scale.

Mobile particle measurements on a tram line intersecting the city of Karlsruhe in southwest Germany and in the upper Rhine valley, showed particle number concentrations in the rural area north of the city almost as high as in downtown (particle size > 4 nm; mean value = 1.2×10^4 cm^{-3}, maximum values 3×10^4 cm^{-3}) (Hagemann et al., 2014). The Rhine valley provides a well-known wind channel of large-scale flow. This results in faster transport of pollutants along the valley axis, e.g., NO_x, SO_2, volatile organic compounds (VOCs) and particles (Gross and Wippermann, 1987; Hagemann et al., 2014; Kalthoff and Vogel, 1992; Vogel et al., 1986).According to data from the local air quality monitoring administration (LUBW, https://www.lubw.baden-wuerttemberg.de/luft) from 2016 to 2018, the annual averaged mass concentrations of NO_2, SO_2, PM_{10}, and soot are 20, 2, 16, and 1.8 μg m^{-3}, respectively, measured at their Eggenstein monitoring station (3.3 km south of the

measurement site used in this study and about 9 km north of the city of Karlsruhe). Specifically, NO_2 concentrations are about half of the values measured in downtown Karlsruhe, but they exhibit comparable peak values (around 50–80 μg m^{-3}). SO_2 levels at Eggenstein are the second highest in the state of Baden-Württemberg (from the available data from 2016 to 2018), and maximum hourly values can reach up to~50 μg m^{-3}.

In order to understand the sources for high local particle concentrations as well as the chemical nature and mass concentrations of aerosol types prevailing in the upper Rhine valley in summer-time we combine comprehensive aerosol information from point measurements with a regional transport model. Besides a better understanding of the origin of the aerosol in that region, we want to validate the capabilities of our transport model to predict characteristic air quality parameters.

2 Methods

2.1 Measurement site and instrumentation

The measurement site (49°6'10.54" N, 8°24'26.07" E) is in the upper Rhine valley 175 m north of the village of Leopoldshafen and 10 m east of the tramline No S1/11 described by Hagemann et al., (2014) (marked with a star in Fig. 1). The Rhine valley often acts as a wind channel leading to wind directions mainly from southwest or northeast. As shown in Fig. 1, the measurement site is located ~11 km north of downtown Karlsruhe and ~5 to 15 km northeast of an industrial area, including a refinery with 15.5 Mt/yr capacity, a 1450 MW hard coal fired power plant, as well as a 365 MW gas fired power plant (Hagemann et al., 2014). Therefore, the measurement site is potentially subject to the urban and industrial emissions especially for southerly wind directions. Apart from that, there are several nearby biogenic emission sources, e.g., forests, sunflower fields, as well as other agricultural areas (Hagemann et al., 2014; Huang et al., 2019). Local traffic emissions from the minor road near the measurement site was identified by measurements with high time resolution. Its contributions to the aerosol load are small due to the generally weak traffic.

The instrumentation for this campaign has been described in detail in previous publications (Huang et al., 2019; Shen et al., 2019). Briefly, the data we use here are from the 6-week (26 July to 31 August 2016) deployment of a laser ablation aerosol particles time-of-flight mass spectrometer (LAAPTOF; AeroMegt GmbH) and a high-resolution time-of-flight aerosol mass spectrometer (HR-ToF-AMS; Aerodyne Inc.; hereafter AMS). These instruments were used to provide real time information on size and chemical composition for individual particles and bulk samples, respectively. The LAAPTOF is a commercially available single particle mass spectrometer and has been well described in recent publications (Ahern et al., 2016; Gemayel et al., 2016; Gemayel et al., 2017; Marsden et al., 2018; Marsden et al., 2016; Marsden et al., 2019; Ramisetty et al., 2018; Reitz et al., 2016; Shen et al., 2018; Shen et al., 2019). In brief, aerosol particles with a size range of 70 nm to 2.5 μm vacuum aerodynamic diameter (d_{va}) are sampled with a flowrate of ~80 cm^3 min^{-1}, focused and accelerated via an aerodynamic lens (ADL). Afterwards, the particles of ~200 nm to 2.5 μm d_{va} can be detected with two laser diodes (λ = 405 nm) mounted in the

particle time-of-flight (PTOF) chamber. Once a single particle is detected successively by both of the detection lasers, its d_{va} is calculated from the time of flight and an excimer laser (λ = 193 nm) is triggered to desorb and ionize the refractory and non-refractory species of the particle. The resulting cations and anions are analysed with a bipolar ToF mass spectrometer. The AMS measures the particle size-resolved bulk chemical composition, e.g., organic compounds, ammonium, nitrate, sulfate, and chloride, in mass concentrations with high time resolution and sensitivity (DeCarlo et al., 2006). Similarly as the LAAPTOF, aerosols are sampled with a flowrate of ~84 cm^3 min^{-1} via a similar ADL in the size range 70 nm to 2.5 µm d_{va} and then pass through a PTOF chamber. At the end of the PTOF chamber, particles encounter a 600 ºC heater that vaporises the non-refractory species. The corresponding vapours are ionized by electron impact with high energy of 70 eV, generating positive ions that are analysed with a ToF mass spectrometer. To account for a particle bouncing effect, a collection efficiency (CE, the product of net particle transmission and detection efficiency) is used (Canagaratna et al., 2007). The CE depends on composition and phase of the particles (Bahreini et al., 2005). Therefore, composition dependent CEs were used to correct the AMS data for this measurement campaign.

All sampling inlets (PM_{10}, $PM_{2.5}$, TSP) were positioned at the top of a measurement container (3.7 m above ground level, a.g.l.). Particle number (size>2.5 and >7 nm, CPC3776 and CPC 3022A, TSI Inc.), particle mass (total suspended particulates, PM_{10}, and $PM_{2.5}$; FIDAS, PALAS GmbH), black carbon (AE33-7 Aethalometer, Magee Scientific Co.), and trace gases O_3 (O341M, Environment SA), SO_2 (AF22M, Environment SA), NO_2 (AS32M, Environment SA) CO_2 (NGA2000, Rosemont Inc.) were measured. Meteorological parameters temperature, relative humidity, solar radiation, wind direction and speed (WS700, Lufft GmbH) were measured 10 m a.g.l. and complemented by meteorological data from a 200 m tower located at the KIT campus north, ~2 km east of the measurement site (49°5′43.0″N 8°25′46.0″E).

2.2 Regional transport model COSMO-ART

The regional transport model COSMO-ART is used in this study to simulate an episode with high mass concentration of organics (up to ~25 µg m^{-3} measured by AMS). Detailed model descriptions can be found in previous studies (Bangert et al., 2011; Knote et al., 2011; Stanelle et al., 2010; Vogel et al., 2009). Therefore, we will only give a brief review here. COSMO-ART is a fully online coupled model system, which uses the same spatial and temporal resolution for all scalars, such as temperature, gas and aerosol particle concentrations. The meteorological module is based on the operational weather forecast model COSMO of the German weather service (Deutscher Wetterdienst, DWD). When atmospheric chemistry and aerosol dynamics are coupled to COSMO, it allows the online calculation of the transport of reactive trace gases and aerosol particles as well as their interaction with the state of the atmosphere. Physical processes, e.g., nucleation, coagulation, condensation and sedimentation are included in the model. The aerosol particles are represented by five interactive log-normal modes representing particles consisting of internally mixed sulfate, ammonium, nitrate and organic compounds, pure soot, as well as internal mixtures of them all. The hourly biogenic emissions are calculated online according to the land use data, the simulated temperatures, and radiative fluxes (Vogel et al., 1995). The anthropogenic emissions, including traffic emissions, large point and area sources such as industrial

and households' areas, were pre-calculated by J. Bieser at Helmholtz Zentrum Geesthacht (Backes et al., 2016; Bieser et al., 2011). In our study, the simulation domain is covered by a 350×330 grid with a horizontal resolution of 1×1 km^2 and 50 vertical atmospheric layers (nonlinear increase up to 22 km a.g.l.). Most of the simulation results shown in this paper correspond to the lowest atmospheric level (10 m a.g.l.) and we indicate if results are from higher levels. The hourly emissions of SO_2, NO_x, CO, NH_3, anthropogenic volatile organic compounds (VOCs), and primary organic aerosols (POA) were pre-calculated. As shown in Fig S1, VOCs, NO_x and POA are mainly emitted at a lower atmospheric level in urban areas, such as the cities of Karlsruhe, Stuttgart, Mannheim, and Strasburg, as well as the corresponding highways. SO_2 hot spots typically correspond to the stack heights of the power plants emitting, such as the one in the western part of Karlsruhe.

3 Results and Discussion

In the first section, we give an overview of the meteorological conditions, the trace gases, and particles measured during the whole measurement campaign and will then give an example for source identification using the transport model. In the following two sections, we discuss two selected episodes in more detail, which are dominated by aged sea salt particles and relatively high organic particle mass concentrations, respectively.

3.1 Overview of the field observation

Table 1 and Fig. S2 give an overview of meteorological conditions, trace gases, and particle concentrations for the entire measurement campaign. In summer 2016, the major wind direction was southwest (174 ± 75°) and an average wind speed was (1.3 ± 0.9) m s^{-1} at the measurement site in the upper Rhine valley. This wind speed allows trace gases and particles to be transported over a distance of 10 km within 2 hours e.g. from the city of Karlsruhe to the measurement site. During the measurement time the sunrise and sunset were at around 06:30 and 20:30, respectively. Temperature and relative humidity (RH) were showing relatively stable anti-correlated diurnal patterns. Given the frequent clear nights, night-time temperature inversions occurred for 32 out of 37 nights during the entire measurement period (Fig. S3). Among the trace gases, CO_2 and O_3 were showing clear diurnal patterns with ozone peaking in the afternoon. NO_2 concentrations were higher in the morning hours and in the late evenings and generally behaved anti-correlated to O_3. NO_2 and particle number were showing spikes at similar times (more frequently during the day-time), mainly due to the local emissions from nearby road traffic. The averaged particle number concentration of (1.2 ± 0.8) × 10^4 cm^{-3} for particles larger than 2.5 nm measured in this study, is comparable with that observed at the same site in previous tram-based measurements (Hagemann et al., 2014). SO_2 concentrations showed peaks with low frequency (up to >10 ppb) but only when the wind was coming from the direction of the industrial area in the southwest. As shown in Fig. S2, these SO_2 peaks correspond to higher particle number concentrations at around noontime, when the wind speed is higher (~1.7 m s^{-1}) and vertical mixing intensified. This is in agreement with downward mixing of stack emissions from industrial sources, which can be validated by model calculations using COSMO-ART (refer to section 3.2).

In the entire measurement period, the total organic compounds, sulfate, nitrate, and ammonium were analysed to contribute on average (58 ± 12) %, (22 ± 7) %, (10 ± 1) %, and (9 ± 3) % to the total non-refractory $PM_{2.5}$ mass measured by AMS, respectively. In a previous publication (Shen et al., 2019), we could identify seven major particle classes at the measurement site among ~3.7×10^5 single particles with sizes between 200 nm and 2.5 µm d_{va}: Calcium-soil (class 1, C1); Aged soot (C2); Sodium salts (C3); Secondary inorganic–amine (C4); Biomass burning–soil (C5); Biomass burning–organosulfate (C6); and Mixed/aged dust (C7). These particle types were not always present in similar fractions but showed distinct periods with one or two types dominating the particle mass (Shen et al., 2019). Here, we will mainly discuss two particle classes that dominated the total particle mass, i.e., sodium salts and biomass burning–soil particles, contributing on average (36 ± 27) % and (30 ± 18) % to the $PM_{2.5}$ mass measured by the LAAPTOF, respectively. We will also discuss one characteristic particle class, i.e., secondary inorganic–amine particles, which showed relatively intensive and distinct peaks three times during this campaign (Fig. S2) as well as several weaker peaks.

As shown in Fig. 2 (a), total particle mass concentrations have clear diurnal pattern, showing higher night-time values and a peak during the morning rush hour (~9:00 local time). Higher particle mass values mainly correspond to southern wind directions, with one exception of extremely high masses associated with northwesterly winds (Fig. 2c). Specifically, sodium salt containing particles have higher fractions during day-time and correspond to southwesterly wind directions (Fig. 2b). Such wind was observed mainly during day-time and with higher wind speeds than at night. Biomass burning–soil particles enrich during night-time and mainly correspond to southeast wind (Fig. 2d). Secondary inorganic–amine particles typically rise in the morning and correspond to south and southwest wind directions (Fig. 2). When we compare weekdays (Monday to Friday) and weekends (Saturday and Sunday) in Fig. S4, the sodium salt particles were always correlated with southwest wind directions. Obvious differences can be found for secondary inorganic–amine and biomass burning–soil, respectively. For secondary inorganic–amine type particles, they were mainly advected by south and southwest wind during weekdays. However, they were much less abundant during weekends and did not show a clear relationship with wind directions (only a small peak for northwest). For biomass burning–soil particles the observations are a bit more complex.

The biomass burning–soil particles measured during weekdays were correlated with south and southwest wind as well, indicating potential sources from the city of Karlsruhe and its industrial area. Please note, that the representative spectra of these particles show aromatic ion peaks which may arise from aromatic compounds such as toluene and xylene due to motor vehicle emissions. Besides, this type of particles contains also some metals such as barium and lead that are related to coal combustion from industry. These features correspond to urban and industrial sources. During the weekends, biomass burning–soil particles had higher mass concentrations than during weekdays and were correlated with wind directions from east, southeast and northwest, where are mainly forests and agricultural areas. Therefore, we can infer that there were various sources for biomass burning–soil particles and these sources differed between weekdays and weekends. This could be e.g., barbeque fires during weekends while the weekdays' source is likely to be associated with that for secondary inorganic–amine particles.

In order to refine this type of particles, we compared them with black carbon particles measured by an Aethalometer (AE33-7). The equivalent black carbon concentration was calculated by the mass absorption cross sections value of 11.7 $m^2 g^{-1}$ (Herich et al., 2011). They seem to show a similar trend in the time series with a triplet of peaks from August 25th to 28th (refer to Fig. S2 and Fig. S5). We found that biomass burning-soil and black carbon concentrations are well correlated only for the weekends, with Pearson's correlation coefficients $\gamma \geq 0.6$ (Fig. S5 b), and poorly correlated for weekdays ($\gamma < 0.3$). This points to different major sources for weekdays and weekends. In addition, the black carbon instrument measuring the light absorption at different wavelengths (λ) can be used to determine the absorption Ångström exponent (α) (Drinovec et al., 2015). For the entire campaign, the average α was 0.96 ± 0.24, calculated by using a pair of wavelengths and their corresponding mass absorption cross sections (MAC=11.7 and 23.6 $m^2 g^{-1}$ for λ=950 and 470 nm, respectively, Herich et al., 2011). Herich et al. (2011) and Zotter et al. (2017) have assigned an α =~0.9 to BC from road traffic emissions, while the α values for wood burning BC were typically higher ~1.68 (Zotter et al., 2017). Our measurements indicate that traffic was the dominating source of BC. Considering the good correlation between BC and biomass burning–soil particles during the weekend, we could infer the corresponding traffic emissions that contributed to biomass burning–soil particles. All observations support the conclusion that this particle class has significant anthropogenic sources, which may vary between weekends and weekdays. However, it still needs some more analysis to identify the different sources contributing to this particle class.

As mentioned before, the dominating particle classes varied for different time periods (Shen et al., 2019). In the following we focus on an episode with particles rich in sodium salts, to find out if sea salt particles can significantly influence the aerosol particle composition at this central European location about 800 km inland. Furthermore, we discuss another episode with relatively high organic mass concentrations to find out how these mass loads could form and exist for a relatively long time period. Both episodes are easily recognized from the time series of particles measured by LAAPTOF and organic compounds measured by AMS (Fig. S2 and Fig. 3; see also Fig. 4 in Shen et al, 2019). Apart from the difference of dominating particle classes and particulate organics, the particle acidity, organonitrate fraction and organic carbon oxidation state, as well as meteorological conditions were quite different between these two episodes. For particle acidity, we used an acidity indicator, namely the ratio of NH_4^+ measured/predicted from AMS measurement (Zhang et al., 2007). The predicted NH_4^+ value is the mass concentration required to fully neutralize sulfate, nitrate, and chloride measured by AMS. The averaged value of NH_4^+ measured/predicted for the entire campaign is 0.82 ± 0.10. As shown in Fig. 3, this ratio reaches lowest value during sodium salts rich episode, corresponding to the highest acidity, while the value in the organic rich episode is at the averaged level. While the apparent high acidity for the sea salt may partially be due to sea salt sulfate included in the AMS measurement, the correlation between particle acidity and organics concentrations may be related to acid-catalysed organic particle formation. For the fraction of organonitrates, the AMS derived ratio of NO^+/NO_2^+ is commonly used as an indicator (Farmer et al., 2010; Kiendler-Scharr et al., 2016). In the episode rich in sodium salts, particles contain the highest organonitrate fraction while the particles in the organic rich episode contain the lowest fraction (refer to Fig. S6). Both, higher acidity and higher fraction of organonitrates are indicators for a stronger influence of anthropogenic emissions on the sodium rich aerosol. The averaged carbon oxidation state

($\overline{OS}_C$) of the organic compounds is a robust metric of its degree of oxidation or processing (Canagaratna et al., 2015; Kroll et al., 2011). It turns out that the organics were more oxidized in the organic rich episode (refer to Fig. S6). In addition, the major wind with higher speeds was from southwest in the episode rich in sodium salt particles, and we will show in section 3.3 that this is related to long-range transport of sea salt particles. For the organic rich episode, the wind speeds were lower for most of the time. The different features of these two episodes are also summarized in Table 2. We will discuss these two episodes in more detail in sections 3.3 and 3.4, but will first demonstrate the usefulness of the transport model to identify an industrial point source.

3.2 Identification of an industrial point source

As shown in Fig. 4, we have modelled O_3, NO_2, SO_2, and particle number for the organic rich episode with COSMO-ART. Model simulations show comparable results and/or trends with field observations. For SO_2, there is a modelled peak at 10:00 on August 26th. As mentioned above, in the upwind direction of our measurement site is a coal fired power plant, where SO_2 is emitted from a stack at 230 m a.g.l.. Therefore, we compared SO_2 concentrations in an area including the power plant and our measurement site (refer to Fig. 5 a1 and a2), as well as time series of their vertical profile at the measurement site (Fig. 5b). The model results show that SO_2 emissions were starting at 02:00 from the stack of the power plant, continuously transported by southwest wind (from 06:00, not shown here). Around noon, the SO_2 was transported downward due to enhanced vertical mixing. Similar to SO_2, we found corresponding vertical transport of NO_x and primary particles (refer to Fig. 5 c and d), as well as secondary inorganic particles which will be discussed in section 3.3.3. In addition to the power plant emissions, particle emissions from the Karlsruhe refinery (e.g., around 8:00 at 122 m a.g.l.) and downtown Karlsruhe (at 10 m a.g.l.) were observed in the model results, which are visualized via videos of the evolution of particle number at these two altitudes (refer to Data availability). Given these findings, we have verified industrial contributions to the particles measured at this rural site. However, the particle numbers calculated by the model are 10 times lower than the measured values. In this context, it should be noted that, the observations relate to particles larger than 2.5 nm and 7 nm, respectively. The modelled particles include Aitken and accumulation mode particles with median diameter at around 30−80 nm and 300−400 nm, respectively. The model does not represent the ultrafine particles to their full extend, especially e.g., the contribution of organic compounds or ammonia to nucleation.

3.3 Aged sea salt in central Europe

Sodium salt particles accounted on average for (35.6 ± 26.7) % of the particle mass measured by LAAPTOF during the whole campaign, and they dominated several time periods (refer to Fig. S2). However, not all the peak events were the same. We chose a unique episode when sodium chloride signatures, e.g., m/z 81 Na_2Cl^+, were showing the strongest signal, as plotted in Fig. 6 (a). In this episode, the sodium salts accounted for (70 ± 24) % of total mass of the single particles. To study the origin of these particles, we used the Hybrid Single-Particle Lagrangian Integrated Trajectory (HYSPLIT; Stein et al., 2015) on the READY

website (http://www.ready.noaa.gov; Rolph et al., 2017) for back-trajectory analysis. The corresponding result suggests that these particles were coming from the Atlantic Ocean, which is more than 800 km west of our measurement site (refer to Fig. S7 a). Therefore, we can constrain the type of sodium salts particles as sea salts with an age of about 1.5 to 3 days.

In this episode, sea salt particles retained strong chloride signatures in spite of the long-range transport, due to relatively high wind speeds (e.g., the average wind speed was ~6 m s^{-1} from the ocean to our measurement site at noontime on August 21st and 22nd, based on 72 h back-trajectory analysis). Therefore, we interpret them as relatively fresh sea salt, which is the 1st sub-class of sodium salts particles identified with the fuzzy clustering analysis of the single particle mass spectra. As shown in Fig. 6 (a), there is an obvious decrease of m/z 81 Na_2Cl^+ at the end of this episode, while the sodium nitrate signature at m/z 108 $Na_2NO_3^+$ increases. Such trends can also be found in similar but much less prominent sodium chloride rich episodes (see the red guiding arrows in Fig. 6a). This indicates the aging process of sea salt particles, namely heterogeneous replacement of chloride by nitrate on sea salt particles (Gard et al., 1998). We assigned the 2nd sub-class of sodium salts to more aged sea salt particles, which are bigger than the relatively young sea salt (Fig. 6b). 72 h back-trajectory analysis suggests that these particles were coming from the Atlantic Ocean and were carried with southwesterly wind of relatively lower speed (~3.5 m s^{-1}) to reach our measurement site on August 23rd, thus they spent more time (~3 days) over the continent and are more aged. The representative spectra of sodium salt particles and the averaged spectra of their sub-classes can be found in Fig. S8. The signal difference between aged and young sea salts spectra (aged - young) is shown in Fig. 6 (c), highlighting their signatures. Similar relationships as for m/z 81 Na_2Cl^+ and 108 $Na_2NO_3^+$ can also be found for the other signature peaks (refer to Fig. S9). It is worth noting that there are also nitrate related peaks in young sea salt, such as m/z 104 $NaClNO_2^-$, verifying that these young sea salts were not fresh. In addition, m/z 92 $Na_2NO_2^+$ and 131 $NaNO_2NO_3^-$ increase earlier than 108 $Na_2NO_3^+$ and 147 Na $(NO_3)_2^-$. Such that, we can infer the aging degree from a series of signature peaks in LAAPTOF spectra: 81 Na_2Cl^+ → 104 $NaClNO_2^-$ → 92 $Na_2NO_2^+$ and 131 $NaNO_2NO_3^-$ → 108 $Na_2NO_3^+$ and 147 Na $(NO_3)_2^-$ (from relatively fresh to more aged, corresponding to chloride to nitrite to nitrate salts). However, this requires further systematic studies to be validated.

For sodium salt particles, a weak but characteristic peak at m/z 129 $C_5H_7NO_3^+$ was assigned to organonitrate in LAAPTOF spectra in our previous study (Shen et al., 2019). As shown in Fig. S9, m/z 129 $C_5H_7NO_3^+$ has a similar trend as m/z 131 $NaNO_2NO_3^-$ and it is more pronounced in the LAAPTOF spectra of aged sea salt. In the sodium chloride rich episode, m/z 129 $C_5H_7NO_3^+$ has a similar trend as organonitrate mass concentrations estimated by AMS results. The method for organonitrate estimation can be referred to Farmer et al. (2010) and the parameters used here are the same as those used by Huang et al. (2019). We have briefly described this method in the supplement after the caption for Fig. S9. AMS derived organonitrate mass concentrations are comparable with the results of molecular analysis using FIGAERO-HR-ToF-CIMS (stands for a filter inlet for gases and aerosols coupled to a high-resolution time-of-flight chemical ionization mass spectrometer) in a companion study by (Huang et al., 2019). Therefore, we can confirm that the m/z 129 $C_5H_7NO_3^+$ signal is due to organonitrates, rather than the recombination of nitrate and organic fragments due to the laser desorption and ionization (LDI) matrix effect in single-particle MS (Murphy, 2007; Reilly et al., 2000; Reinard and Johnston, 2008; Zenobi and Knochenmuss, 1998). In addition, our

simulation chamber studies revealed that m/z 129 $C_5H_7NO_3^+$ in LAAPTOF spectra could be a signature for anthropogenic sources (refer to Fig. S10 and the corresponding detailed description in the supporting information). Therefore, m/z 129 $C_5H_7NO_3^+$ on sea salt particles indicates interactions between the natural sea salt and anthropogenic emissions. It is worth noting that another weak but characteristic peak was observed at m/z 165 $Na_3SO_4^+$. This signature peak for sea salt sulfate can be found with stronger signal in young sea salt than in aged sea salt (Gard et al., 1998).

3.4 Origin of the aerosol particles during the organics rich episode

At the end of the measurement period, we observed three subsequent organic peaks (see Fig. 3, Fig. S2, or Fig. S5): one peak during Friday August 26th day-time and two peaks during following two nights. Organics measured in this episode exhibited the highest mass concentrations of (12.9 ± 3.9) µg m^{-3}, which accounted for (77 ± 6) % of the total non-refractory particle mass and is almost 3 times more than organic masses measured in other periods of the entire AMS measurement period. Please note, some secondary inorganic components were also measured in this episode, showing some peaks at similar times as the high organic peaks. As for the sodium chloride rich episode, we have also done a HYSPLIT back-trajectory analysis for the organic rich episode. Fig. S7 (b) shows these results: the air mass was coming from the continent during this episode. In order to better interpret the measurements and to understand the impact of transport processes for the particles measured in the organics rich episode, we have done COSMO-ART simulations covering the time period from August 25th to 28th, 2016. Fig. 7 shows the particulate organic compounds, the secondary inorganics (ammonium, nitrate, and sulfate) measured by AMS, and the result calculated using COSMO-ART (panels d to g). The corresponding meteorological conditions measured are shown in panels (a) to (c) of Figure 7. In general, the trends and also the amplitudes of the model results compare quite well with the observations. In the following, we will combine field observation and transport model simulation results to address these questions: 1) were the organic rich aerosols due to local formation, regional transport, or vertical mixing; 2) were all three organic peaks caused by the same reasons; 3) were the secondary inorganics originating from the same sources as the organics. We will start the discussion with the inorganics, will then go to the organics, and will end up with a typical particle type in this episode.

3.4.1 Secondary inorganic compounds

As shown in Fig. 7 (e) to (g), observations and model results for secondary inorganic compounds show comparable diurnal cycles and even the concentration levels match quite well. While ammonium and nitrate have a similar trend for most of the time, the trend for sulfate seems to be somewhat different. The major peaks of ammonium and nitrate appear at similar times as the high organic peaks. As will be shown in the following section, these compounds originated from anthropogenic sources in the urban and industrial area of Karlsruhe and from the city of Stuttgart. There is only one instant when all the measured secondary inorganics are showing peaks together: the inorganics are peaking at ~10:00 on August 26th, when also high SO_2 concentrations were observed (c.f. Fig. 4) which were due to the emissions from a power plant located in upwind direction. To verify this, we can refer to the time series of vertical profiles for the simulated secondary inorganics (Fig. S11 b to d). Despite

similar spatial distributions of nitrate, ammonium, NO_2, and SO_2 from 02:00 to 12:00 (c.f. Fig. 5) the measured sulfate peak for that time is missing in the model output. The reason for this is still unclear. It should be noted that, compared to the sulfate peak observed, the companion ammonium and nitrate peaks are much broader, attributed to additional anthropogenic sources from the city and refineries rather than only the power plant.

Some of the differences between model result and observation, such as that on August 25th or e.g., for sharper peaks, may be explained by to missing (point) sources in the emission data and/or the limited spatial resolution. The general agreement is however quite well and also for some point sources like the largest power plant in Karlsruhe. Some of the differences in the trends of nitrate and sulfate may be caused by the different nature of the sources of their precursor gases SO_2 and NO_x. While SO_2 is emitted in this area mainly from a few point sources, NO_x is emitted from various sources over a larger area.

3.4.2 Organic compounds

For the organic compounds, the general temporal development is represented well by the model, showing similar trends as measured by AMS, but underestimates the mass concentrations by a factor of ~2.3; averaged model result is (5.5 ± 3.3) µg m^{-3}, while observed were (12.9 ± 3.9) µg m^{-3}. Potential reasons for this discrepancy will be discussed in the light of sensitivity tests at the end of this section.

As mentioned above, the organic particle fraction shows a peak on Friday August 26th during day-time (peak 1) and two more during the following nights of the weekend (peak 2 and 3) in the organics rich episode. Model result cover peak 1 and 2, as well as of the first part of peak 3. Analysis of the model results shows that the three peaks were caused by different reasons including meteorological conditions, regional transport, and local or in-situ new particle formation and growths (such as night-time new particle formation; Huang et al., 2019). As shown in Fig. 7a and d, peak 1 corresponds to south and southwest wind, indicating that the air masses came from the urban and industrial area of Karlsruhe. This is illustrated very well in a video showing the transmission of particulate organics leading to peak 1 (refer to Data availability). The most intensive peak in organic particle mass (peak 2), starts from August 26th 20:30 (Fig. 3 and Fig. S2) when the wind direction shifts from northwest to east (northeast, straight east, and southeast), the wind speed decreases to < 0.5 m s^{-1}, and the night-time temperature inversion starts. Such stagnant conditions limit aerosol mixing and support build up aerosols and their growth. During the entire campaign, the strongest temperature inversion was observed during this night from August 26th to 27th (peak inversion at 02:40 on August 27; Fig. S3). In spite of the stagnant conditions and rather low wind speeds, regional transport still plays an important role. The model results for this time show transport of organic aerosol particles from the city of Stuttgart (southeast to the measurement site) over forested areas into the Rhine valley. This is clearly visible in a corresponding video of the model results for particulate organics and wind directions (refer to Data availability). Furthermore, we investigate the relative contribution of biogenic and anthropogenic emissions and their interactions for this episode by comparing the model results with and without biogenic emissions. It turns out that the corresponding air masses originating from anthropogenic emissions in the Stuttgart area were transported to the measurement site by south-easterly winds via forested hills. During this transport, the organic particle mass

concentrations increased while being mixed with biogenic emissions from the forest. The resulting air mass finally reaching the measurement site consisted therefore of anthropogenic and biogenic organics. For peak 3, we can also find impact of transport as illustrated in another video of particulate organic mass evolution (refer to data availability). However, the origin of this peak is more complex and is most likely more influenced by local particle formation and growths. After the night-time peak 2, from 12:00 on August 27 the air mass were doing back and forth movements in west-east directions, showing a strong concentration gradient (west-east). Such a conditions lead to a high uncertainty of the model results for one point. Hence, although we observed quite similar particle compositions in these three subsequent peaks with high organic mass concentrations for similar meteorological conditions with low wind speeds, all three peaks were caused by air masses of different origin.

As mentioned above, the model underestimates the organic aerosol mass on average by a factor of 2.3. In order to better understand this discrepancy, we have done three sensitivity tests: with/without biogenic emissions (test 01), one with doubled biogenic emissions (test 02) and one with boundary values or regional background values (outside the model domain) of particulate organic compounds increased by a factor of 10 (test 03). The results of test 01 suggest that (80 ± 4) % of the organic mass calculated was resulting from biogenic sources for the peak 1 time period, corresponding to the air masses coming from Karlsruhe. Regarding the time period of peak 2, there was a sharp drop of the biogenic contribution from the 88% to 68% corresponding to August 26th 23:00 to August 27th 2:00 when the air mass was coming from direction of Stuttgart (see Fig. 8). Hence, we can infer that the anthropogenic contribution to the air mass that originated from Stuttgart was somewhat larger than that originated from Karlsruhe. Over the entire organic rich episode, on average (74 ± 7) % of the organics mass was contributed by biogenic sources. To test if missing emissions of biogenic precursors can explain the underestimated organic particulate masses we doubled this major (biogenic) source for organics (test 02). As shown in Fig. 9, doubling biogenic emissions makes some of the peaks of organic mass fit the observations better but the concentrations before and in between the peak values are still underestimated. Another potential reason for the discrepancy could be to low boundary values (regional background); therefore, we increased them by a factor of 10 (test 03). This elevates the overall simulated concentration levels, leading to an overestimation especially of the first peak. These tests demonstrate the potential role of precursor emissions and regional transport of organic aerosol particles on the model results. There seems to be evidence that the model underestimates the regional background of organic aerosol particles. However, we cannot rule out that also underestimated sources of VOC or weaknesses in the SOA formation mechanism may contribute to the underestimation of the organic aerosol particle mass. For example, night-time new particle formations mechanisms are not included in the current model version.

4 Conclusions and atmospheric implication

High particle number concentrations have been observed at a rural site in the upper Rhine valley by measurements on a tramline (Hagemann et al., 2014). In order to study the nature of the aerosols in the same region, we conducted a 6-week stationary field measurement campaign at a rural site next to the tramline in summer 2016, and applied a regional transport model COSMO-

ART to analyse the origin of the aerosols. Comparing the field observations and model calculations, we have verified that industrial emissions contribute to the high particle number concentrations at this rural site.

For the whole measurement period, the particles that dominate the mass are sodium salts, which contributed (36 ± 27) % to the $PM_{2.5}$ mass measured by the LAAPTOF. According to the AMS measurements, organics, sulfate, nitrate, and ammonium contributed (58 ± 12) %, (22 ± 7) %, (10 ± 1) %, and (9 ± 3) % to the total non-refractory $PM_{2.5}$ mass, respectively. Furthermore, we have investigated two episodes, which were dominated by aged sea salt and organics, which show characteristic features such as higher particle acidities and carbon oxidation states, respectively. Both episodes selected, were dominated by particles formed from the interaction of natural/biogenic and anthropogenic emissions.

For the sodium chloride rich episode, sodium salt particles accounted for (70 ± 24) % of total mass of the single particles. We could show that the dominating particles were originally sea salt, from the Atlantic Ocean (~800 km away from the measurement site). These particles consisted of two classes with different aging stages. After 1.5−3 days of transport, the original sea salt particles retained strong chloride signatures while after 3.5−4 days of transport over the continent aged sea salt with stronger nitrate signatures and larger size arrived at the measurement location. In addition, the organonitrate signature peaks at m/z 129 $C_5H_7NO_3^+$ were stronger for the aged sea salt particles. According to chamber experiments on OH oxidation of α-pinene and/ or toluene in the presence of NO_x on sodium nitrate seed particles, we have evidence that m/z 129 $C_5H_7NO_3^+$ is a signature peak for anthropogenic organics in single particle mass spectra. Hence, the m/z 129 $C_5H_7NO_3^+$ observed on sea salt particles in this study is another indicator for the interaction of anthropogenic emissions with the sea salt particles. Besides, the observed signature peak at m/z 165 $Na_3SO_4^+$ for sea salt sulfate may indirectly explain apparently higher particle acidity in this episode. Some other signature peaks such as 81 Na_2Cl^+, 92 $Na_2NO_2^+$, 108 $Na_2NO_3^+$, 104 $NaClNO_2^-$, 131 $NaNO_2NO_3^-$, and 147 Na $(NO_3)_2^-$ have the potential to indicate degree of aging of sea salt particles.

For the organics rich episode, the particulate organic compounds accounted for (77 ± 6) % of total non-refractory particle mass. We identified potential sources of the elevated organic particle concentrations and of secondary inorganic compounds. Transport model results suggest that (74 ± 7) % of the particulate organic mass calculated was related to biogenic emissions. With the combination of mass spectrometry and COSMO-ART modelling, we can confirm that during Friday, August 26th , air masses came from an industrial area and the city of Karlsruhe, leading to high particle numbers (including all the particles with size >2.5 nm), high particulate organics and secondary inorganics, as well as high fractions of aged-biomass-burning and soil-dust like particles. During night-time on August 26th, south-easterly winds transported air masses from Stuttgart via forested areas to the measurement site, resulting in particles formed by the interaction of anthropogenic and biogenic precursors. Such air masses flowed into the Rhine valley and contributed also to the high organic aerosol mass concentrations during the night from August 27th to 28th. In addition, low wind speeds and temperature inversion limited mixing and supported new particle formation and growth, partially contributing to higher organic particle masses.

Comparing comprehensive field observations with the COSMO-ART model results showed quite good agreement for trends and most concentration levels for several aerosol particle compounds and trace gases even if not all details could be reproduced

by the model. However, the simulated particle numbers are 10 times less than the observed values. This is mainly due to the fact that not all new particle formation processes (nucleation mode) are included in the model (e.g. night time chemistry as well as the role of organics or ammonia). Furthermore, the model underestimates particulate organics by a factor of 2.3. This discrepancy may be partly explained by an underestimated regional background, missing sources, or incomplete SOA formation and growths mechanisms, in the current model version.

As discussed above, we can conclude that factors related to topography, metrological conditions, local emissions, in-situ formation and growths, regional transport, as well as the interaction of biogenic and anthropogenic compounds need to be considered for a comprehensive understanding of aerosol composition and processing in this region. This study provides a good insight into the chemical nature and complex origin of aerosols in the upper Rhine valley, achieved by combining complimentary mass spectrometry and transport modelling.

Data availability

Video data will be available at KIT open data (https://publikationen.bibliothek.kit.edu/1000094401).

Author contributions

X.S. operated LAAPTOF and AMS during the whole field campaign, did the LAAPTOF data analysis, did COSMO-ART model runs and model output data analysis, did HYSPLIT back-trajectory analysis, produced all figures, and wrote the manuscript. H.S. organized the campaign, provided trace gas, meteorology, and particle measurements as well as suggestions for the data analysis, interpretation, and discussion. H.V. and B.V. provided the input data for COSMO-ART model, provided suggestions for the model simulation, the model data analysis, interpretation, and discussion. W.H. operated AMS during the whole campaign and did AMS data analysis. C.M. helped to operate the instruments, did black carbon data analysis, and provided suggestions for the data analysis, interpretation, and discussion. R.R. helped to operate LAAPTOF. A.S.H.P. gave comments for interpretation of black carbon data. T.L. gave general advices and comments for this paper. All authors contributed to the final text.

Competing interests

The authors declare no conflict of interest.

Acknowledgements

The authors gratefully thank the IMK-AAF AIDA staff and IMK-TRO modellers at KIT for helpful discussions and technical support, and the China Scholarship Council (CSC) for financial support of Xiaoli Shen and Wei Huang. Special thanks go to the Albtal-Verkehrs-Gesellschaft (AVG) for providing power and the measurement location near the tramline, to Norbert Kalthoff's group for providing tower data. Besides, the authors gratefully acknowledge the NOAA Air Resources Laboratory (ARL) for provision of the HYSPLIT transport and dispersion model and the READY website (http://www.ready.noaa.gov).

References

Ahern, A. T., Subramanian, R., Saliba, G., Lipsky, E. M., Donahue, N. M., and Sullivan, R. C.: Effect of secondary organic aerosol coating thickness on the real-time detection and characterization of biomass-burning soot by two particle mass spectrometers, Atmos Meas Tech, 9, 6117–6137, 2016.

Backes, A., Aulinger, A., Bieser, J., Matthias, V., and Quante, M.: Ammonia emissions in Europe, part I: Development of a dynamical ammonia emission inventory, Atmos Environ, 131, 55–66, 2016.

Bahreini, R., Keywood, M. D., Ng, N. L., Varutbangkul, V., Gao, S., Flagan, R. C., Seinfeld, J. H., Worsnop, D. R., and Jimenez, J. L.: Measurements of secondary organic aerosol from oxidation of cycloalkenes, terpenes, and m-xylene using an Aerodyne aerosol mass spectrometer, Environ Sci Technol, 39, 5674–5688, 2005.

Baklanov, A., Schlunzen, K., Suppan, P., Baldasano, J., Brunner, D., Aksoyoglu, S., Carmichael, G., Douros, J., Flemming, J., Forkel, R., Galmarini, S., Gauss, M., Grell, G., Hirtl, M., Joffre, S., Jorba, O., Kaas, E., Kaasik, M., Kallos, G., Kong, X., Korsholm, U., Kurganskiy, A., Kushta, J., Lohmann, U., Mahura, A., Manders-Groot, A., Maurizi, A., Moussiopoulos, N., Rao, S. T., Savage, N., Seigneur, C., Sokhi, R. S., Solazzo, E., Solomos, S., Sorensen, B., Tsegas, G., Vignati, E., Vogel, B., and Zhang, Y.: Online coupled regional meteorology chemistry models in Europe: current status and prospects, Atmos Chem Phys, 14, 317–398, 2014.

Bangert, M., Kottmeier, C., Vogel, B., and Vogel, H.: Regional scale effects of the aerosol cloud interaction simulated with an online coupled comprehensive chemistry model, Atmos Chem Phys, 11, 4411–4423, 2011.

Bieser, J., Aulinger, A., Matthias, V., Quante, M., and Builtjes, P.: SMOKE for Europe - adaptation, modification and evaluation of a comprehensive emission model for Europe, Geosci Model Dev, 4, 47–68, 2011.

Burkholder, J. B., Abbate, J. P. D., Barnes, I., Roberts, J. M., Melamed, M. L., Ammann, M., Bertram, A. K., Cappa, C. D., Carlton, A. G., Carpenter, L. J., Crowley, J. N., Dubowski, Y., Georges, C., Heard, D. E., Herrmann, H., Keutsch, F. N., Kroll, J. H., McNeill, V. F., Ng, N. L., Nizkorodov, S. A., Orlando, J. J., Percival, C. J., Picquet-Varrault, B., Rudich, Y., Seakins, P. W., Surratt, J. D., Tanimoto, H., Thornton, J. A., Tong, Z., Tyndall, G. S., Wahner, A., Weschler,

C. J., Wilson, K. R., and Ziemann, P. J.: The Essential Role for Laboratory Studies in Atmospheric Chemistry, Environ Sci Technol, 51, 2519–2528, 2017.

Canagaratna, M. R., Jayne, J. T., Jimenez, J. L., Allan, J. D., Alfarra, M. R., Zhang, Q., Onasch, T. B., Drewnick, F., Coe, H., Middlebrook, A., Delia, A., Williams, L. R., Trimborn, A. M., Northway, M. J., DeCarlo, P. F., Kolb, C. E., Davidovits, P., and Worsnop, D. R.: Chemical and microphysical characterization of ambient aerosols with the aerodyne aerosol mass spectrometer, Mass Spectrom Rev, 26, 185–222, 2007.

Canagaratna, M. R., Jimenez, J. L., Kroll, J. H., Chen, Q., Kessler, S. H., Massoli, P., Hildebrandt Ruiz, L., Fortner, E., Williams, L. R., Wilson, K. R., Surratt, J. D., Donahue, N. M., Jayne, J. T., and Worsnop, D. R.: Elemental ratio measurements of organic compounds using aerosol mass spectrometry: characterization, improved calibration, and implications, Atmos Chem Phys, 15, 253–272, 2015.

Canonaco, F., Crippa, M., Slowik, J. G., Baltensperger, U., and Prevot, A. S. H.: SoFi, an IGOR-based interface for the efficient use of the generalized multilinear engine (ME-2) for the source apportionment: ME-2 application to aerosol mass spectrometer data, Atmos Meas Tech, 6, 3649–3661, 2013.

Canonaco, F., Slowik, J. G., Baltensperger, U., and Prevot, A. S. H.: Seasonal differences in oxygenated organic aerosol composition: implications for emissions sources and factor analysis, Atmos Chem Phys, 15, 6993–7002, 2015.

Crippa, M., Canonaco, F., Lanz, V. A., Aijala, M., Allan, J. D., Carbone, S., Capes, G., Ceburnis, D., Dall'Osto, M., Day, D. A., DeCarlo, P. F., Ehn, M., Eriksson, A., Freney, E., Hildebrandt Ruiz, L., Hillamo, R., Jimenez, J. L., Junninen, H., Kiendler-Scharr, A., Kortelainen, A. M., Kulmala, M., Laaksonen, A., Mensah, A., Mohr, C., Nemitz, E., O'Dowd, C., Ovadnevaite, J., Pandis, S. N., Petaja, T., Poulain, L., Saarikoski, S., Sellegri, K., Swietlicki, E., Tiitta, P., Worsnop, D. R., Baltensperger, U., and Prevot, A. S. H.: Organic aerosol components derived from 25 AMS data sets across Europe using a consistent ME-2 based source apportionment approach, Atmos Chem Phys, 14, 6159–6176, 2014.

DeCarlo, P. F., Kimmel, J. R., Trimborn, A., Northway, M. J., Jayne, J. T., Aiken, A. C., Gonin, M., Fuhrer, K., Horvath, T., Docherty, K. S., Worsnop, D. R., and Jimenez, J. L.: Field-deployable, high-resolution, time-of-flight aerosol mass spectrometer, Anal Chem, 78, 8281–8289, 2006.

Drinovec, L., Mocnik, G., Zotter, P., Prevot, A. S. H., Ruckstuhl, C., Coz, E., Rupakheti, M., Sciare, J., Muller, T., Wiedensohler, A., and Hansen, A. D. A.: The "dual-spot" Aethalometer: an improved measurement of aerosol black carbon with real-time loading compensation, Atmos Meas Tech, 8, 1965–1979, 2015.

Farmer, D. K., Matsunaga, A., Docherty, K. S., Surratt, J. D., Seinfeld, J. H., Ziemann, P. J., and Jimenez, J. L.: Response of an aerosol mass spectrometer to organonitrates and organosulfates and implications for atmospheric chemistry, P Natl Acad Sci USA, 107, 6670–6675, 2010.

Fierce, L., Riemer, N., and Bond, T. C.: Toward reduced representation of mixing state for simulating aerosol effects on climate, B Am Meteorol Soc, 98, 971–980, 2017.

Fuzzi, S., Baltensperger, U., Carslaw, K., Decesari, S., van Der Gon, H. D., Facchini, M. C., Fowler, D., Koren, I., Langford, B., Lohmann, U., Nemitz, E., Pandis, S., Riipinen, I., Rudich, Y., Schaap, M., Slowik, J. G., Spracklen, D. V., Vignati, E., Wild, M., Williams, M., and Gilardoni, S.: Particulate matter, air quality and climate: lessons learned and future needs, Atmos Chem Phys, 15, 8217–8299, 2015.

Gard, E. E., Kleeman, M. J., Gross, D. S., Hughes, L. S., Allen, J. O., Morrical, B. D., Fergenson, D. P., Dienes, T., Galli, M. E., Johnson, R. J., Cass, G. R., and Prather, K. A.: Direct observation of heterogeneous chemistry in the atmosphere, Science, 279, 1184–1187, 1998.

Gemayel, R., Hellebust, S., Temime-Roussel, B., Hayeck, N., Van Elteren, J. T., Wortham, H., and Gligorovski, S.: The performance and the characterization of laser ablation aerosol particle time-of-flight mass spectrometry (LAAP-ToF-MS), Atmos Meas Tech, 9, 1947–1959, 2016.

Gemayel, R., Temime-Roussel, B., Hayeck, N., Gandolfo, A., Hellebust, S., Gligorovski, S., and Wortham, H.: Development of an analytical methodology for obtaining quantitative mass concentrations from LAAP-ToF-MS measurements, Talanta, 174, 715–724, 2017.

Gross, G. and Wippermann, F.: Channeling and Countercurrent in the Upper Rhine Valley - Numerical Simulations, J Clim Appl Meteorol, 26, 1293–1304, 1987.

Gunsch, M. J., May, N. W., Wen, M., Bottenus, C. L. H., Gardner, D. J., VanReken, T. M., Bertman, S. B., Hopke, P. K., Ault, A. P., and Pratt, K. A.: Ubiquitous influence of wildfire emissions and secondary organic aerosol on summertime atmospheric aerosol in the forested Great Lakes region, Atmos Chem Phys, 18, 3701–3715, 2018.

Hagemann, R., Corsmeier, U., Kottmeier, C., Rinke, R., Wieser, A., and Vogel, B.: Spatial variability of particle number concentrations and NOx in the Karlsruhe (Germany) area obtained with the. mobile laboratory 'AERO-TRAM', Atmos Environ, 94, 341–352, 2014.

Healy, R. M., Sciare, J., Poulain, L., Crippa, M., Wiedensohler, A., Prevot, A. S. H., Baltensperger, U., Sarda-Esteve, R., McGuire, M. L., Jeong, C. H., McGillicuddy, E., O'Connor, I. P., Sodeau, J. R., Evans, G. J., and Wenger, J. C.: Quantitative determination of carbonaceous particle mixing state in Paris using single-particle mass spectrometer and aerosol mass spectrometer measurements, Atmos Chem Phys, 13, 9479–9496, 2013.

Herich, H., Hueglin, C., and Buchmann, B.: A 2.5 year's source apportionment study of black carbon from wood burning and fossil fuel combustion at urban and rural sites in Switzerland, Atmos Meas Tech, 4, 1409–1420, 2011.

Huang, W., Saathoff, H., Shen, X. L., Ramakrishna, R., Leisner, T., and Mohr, C.: Chemical characterization of highly functionalized organonitrates contributing to high night-time organic aerosol mass loadings and particle growth, Environ Sci Technol, 53, 1165–1174, 2019.

IPCC: Climate Change 2013: The Physical Science Basis. Contribution of Working Group I to the Fifth Assessment Report of the Intergovernmental Panel on Climate Change. Cambridge Univ. Press.

Jeong, C. H., McGuire, M. L., Godri, K. J., Slowik, J. G., Rehbein, P. J. G., and Evans, G. J.: Quantification of aerosol chemical composition using continuous single particle measurements, Atmos Chem Phys, 11, 7027–7044, 2011.

Kalthoff, N. and Vogel, B.: Countercurrent and Channeling Effect under Stable Stratification in the Area of Karlsruhe, Theor Appl Climatol, 45, 113–126, 1992.

Kiendler-Scharr, A., Mensah, A. A., Friese, E., Topping, D., Nemitz, E., Prevot, A. S. H., Aijala, M., Allan, J., Canonaco, F., Canagaratna, M., Carbone, S., Crippa, M., Dall Osto, M., Day, D. A., De Carlo, P., Di Marco, C. F., Elbern, H., Eriksson, A., Freney, E., Hao, L., Herrmann, H., Hildebrandt, L., Hillamo, R., Jimenez, J. L., Laaksonen, A., McFiggans, G., Mohr, C., O'Dowd, C., Otjes, R., Ovadnevaite, J., Pandis, S. N., Poulain, L., Schlag, P., Sellegri, K., Swietlicki, E., Tiitta, P., Vermeulen, A., Wahner, A., Worsnop, D., and Wu, H. C.: Ubiquity of organic nitrates from nighttime chemistry in the European submicron aerosol, Geophys Res Lett, 43, 7735–7744, 2016.

Knote, C., Brunner, D., Vogel, H., Allan, J., Asmi, A., Aijala, M., Carbone, S., van der Gon, H. D., Jimenez, J. L., Kiendler-Scharr, A., Mohr, C., Poulain, L., Prevot, A. S. H., Swietlicki, E., and Vogel, B.: Towards an online-coupled chemistry-climate model: evaluation of trace gases and aerosols in COSMO-ART, Geosci Model Dev, 4, 1077–1102, 2011.

Kroll, J. H., Donahue, N. M., Jimenez, J. L., Kessler, S. H., Canagaratna, M. R., Wilson, K. R., Altieri, K. E., Mazzoleni, L. R., Wozniak, A. S., Bluhm, H., Mysak, E. R., Smith, J. D., Kolb, C. E., and Worsnop, D. R.: Carbon oxidation state as a metric for describing the chemistry of atmospheric organic aerosol, Nat Chem, 3, 133–139, 2011.

Marsden, N. A., Flynn, M. J., Allan, J. D., and Coe, H.: Online dfferentiation of mineral phase in aerosol particles by ion formation mechanism using a LAAP-TOF single-particle mass spectrometer, Atmospheric Measurement Techniques Discussions, 11, 195–213, 2018.

Marsden, N. A., Flynn, M. J., Taylor, J. W., Allan, J. D., and Coe, H.: Evaluating the influence of laser wavelength and detection stage geometry on optical detection efficiency in a single-particle mass spectrometer, Atmos Meas Tech, 9, 6051–6068, 2016.

Marsden, N. A., Ullrich, R., Möhler, O., Hammer, S. E., Kandler, K., Cui, Z., Williams, P. I., Flynn, M. J., Liu, D., Allan, J. D., and Coe, H.: Mineralogy and mixing state of north African mineral dust by online single-particle mass spectrometry, Atmos Chem Phys, 19, 2259–2281, 2019.

Murphy, D. M.: The design of single particle laser mass spectrometers, Mass Spectrom Rev, 26, 150–165, 2007.

Paatero, P.: Least squares formulation of robust non-negative factor analysis, Chemometr Intell Lab, 37, 23–35, 1997.

Paatero, P. and Tapper, U.: Positive Matrix Factorization - a Nonnegative Factor Model with Optimal Utilization of Error-Estimates of Data Values, Environmetrics, 5, 111–126, 1994.

Pöschl, U.: Atmospheric aerosols: Composition, transformation, climate and health effects, Angew Chem Int Edit, 44, 7520–7540, 2005.

Ramisetty, R., Abdelmonem, A., Shen, X. L., Saathoff, H., Leisner, T., and Mohr, C.: Exploring femtosecond laser ablation in single-particle aerosol mass spectrometry, Atmos Meas Tech, 11, 4345–4360, 2018.

Reitz, P., Zorn, S. R., Trimborn, S. H., and Trimborn, A. M.: A new, powerful technique to analyze single particle aerosol mass spectra using a combination of OPTICS and the fuzzy c-means algorithm, J Aerosol Sci, 98, 1–14, 2016.

Rolph, G., Stein, A., and Stunder, B.: Real-time Environmental Applications and Display sYstem: READY, Environ Modell Softw, 95, 210–228, 2017.

Seinfeld, J. H. and Pandis, S. N.: Atmospheric chemistry and physics: From air pollution to climate change, Wiley, J & Sons, Inc., Hoboken, New Jersey, 2006.

Shen, X. L., Ramisetty, R., Mohr, C., Huang, W., Leisner, T., and Saathoff, H.: Laser ablation aerosol particle time-of-flight mass spectrometer (LAAPTOF): performance, reference spectra and classification of atmospheric samples, Atmos Meas Tech, 11, 2325–2343, 2018.

Shen, X. L., Saathoff, H., Huang, W., Mohr, C., Ramisetty, R., and Leisner, T.: Understanding of atmospheric aerosol particles with improved particle identification and quantification by single particle mass spectrometry, Atmos. Meas. Tech. , 12, 2219–2240, 2019.

Stanelle, T., Vogel, B., Vogel, H., Baumer, D., and Kottmeier, C.: Feedback between dust particles and atmospheric processes over West Africa during dust episodes in March 2006 and June 2007, Atmos Chem Phys, 10, 10771–10788, 2010.

Stein, A. F., Draxler, R. R., Rolph, G. D., Stunder, B. J. B., Cohen, M. D., and Ngan, F.: Noaa's Hysplit Atmospheric Transport and Dispersion Modeling System, B Am Meteorol Soc, 96, 2059–2077, 2015.

Tsigaridis, K., Krol, M., Dentener, F. J., Balkanski, Y., Lathière, J., Metzger, S., Hauglustaine, D. A., and Kanakidou, M.: Change in global aerosol composition since preindustrial times, Atmos Chem Phys, 6, 5143–5162, 2006.

Vogel, B., Fiedler, F., and Vogel, H.: Influence of Topography and Biogenic Volatile Organic-Compounds Emission in the State of Baden-Wurttemberg on Ozone Concentrations during Episodes of High Air Temperatures, J Geophys Res-Atmos, 100, 22907–22928, 1995.

Vogel, B., Gross, B., and Wippermann, F.: Mesoklip (1st Special Observation Period) - Observations and Numerical-Simulation - a Comparison, Bound-Lay Meteorol, 35, 83–102, 1986.

Vogel, B., Vogel, H., Baumer, D., Bangert, M., Lundgren, K., Rinke, R., and Stanelle, T.: The comprehensive model system COSMO-ART - Radiative impact of aerosol on the state of the atmosphere on the regional scale, Atmos Chem Phys, 9, 8661–8680, 2009.

Zhang, Q., Jimenez, J. L., Canagaratna, M. R., Ulbrich, I. M., Ng, N. L., Worsnop, D. R., and Sun, Y. L.: Understanding atmospheric organic aerosols via factor analysis of aerosol mass spectrometry: a review, Anal Bioanal Chem, 401, 3045–3067, 2011.

Zhang, Q., Jimenez, J. L., Worsnop, D. R., and Canagaratna, M.: A case study of urban particle acidity and its influence on secondary organic aerosol, Environ Sci Technol, 41, 3213–3219, 2007.

Zhou, Y., Huang, X. H. H., Griffith, S. M., Li, M., Li, L., Zhou, Z., Wu, C., Meng, J. W., Chan, C. K., Louie, P. K. K., and Yu, J. Z.: A field measurement based scaling approach for quantification of major ions, organic carbon, and elemental carbon using a single particle aerosol mass spectrometer, Atmos Environ, 143, 300–312, 2016.

Zotter, P., Herich, H., Gysel, M., El-Haddad, I., Zhang, Y. L., Mocnik, G., Huglin, C., Baltensperger, U., Szidat, S., and Prevot, A. H.: Evaluation of the absorption angstrom ngstrom exponents for traffic and wood burning in the Aethalometer-based source apportionment using radiocarbon measurements of ambient aerosol, Atmos Chem Phys, 17, 4229–4249, 2017.

B Appendix

Table 1: Mean values (±sdev) of characteristic parameters for the entire measurement period.

Parameter	Mean value ± sdev	Parameter	Mean value ± sdev
Wind Direction (°)	174.0 ± 75.0	**Particulate compounds measured by AMS**	
Wind Speed (m s^{-1})	1.3 ± 0.9	Organics (µg m^{-3})	5.1 ± 3.3
Temperature (K)	294.4 ± 4.5	Ammonium (µg m^{-3})	0.7 ± 0.4
Relative Humidity (%)	70.0 ± 17.0	Nitrate (µg m^{-3})	0.8 ± 0.8
O_3 (ppb)	26.5 ± 15.8	Sulfate (µg m^{-3})	1.7 ± 0.8
NO_2 (ppb)	11.4 ± 6.9	**Seven particle classes measured by LAAPTOF**	
SO_2 (ppb)	1.2 ± 2.7	C1: Calcium-soil (µg m^{-3})	0.4 ± 0.5
CO_2 (ppm)	446.0 ± 32.0	C2: Aged soot (µg m^{-3})	0.1 ± 0.4
Particle Number (10^4 cm^{-3}) (size >2.5 nm)	1.2 ± 0.8	C3: Sodium salts (µg m^{-3})	1.2 ± 1.2
Particle Number (10^3 cm^{-3}) (size: 2.5 to7 nm)	4.7 ± 4.9	C4: Secondary inorganics-amine (µg m^{-3})	0.1 ± 0.6
BC (µg m^{-3})	0.8 ± 0.7	C5: Biomass burning–soil (µg m^{-3})	1.2 ± 1.3
$PM_{2.5}$ (µg m^{-3})	6.3 ± 3.2	C6: Biomass burning–organosulfate (µg m^{-3})	0.4 ± 0.6
PM_{10} (µg m^{-3})	8.6 ± 4.2	C7: Mixed/aged dust (µg m^{-3})	0.5 ± 0.7

Note that the full names of seven particle classes are C1: calcium-rich and soil-dust-like particles; C2: aged-soot-like particles; C3: sodium-salt-like particles; C4: secondary- inorganics-rich and amine containing particles; C5: aged-biomass-burning and soil-dust like particles; C6: aged-biomass-burning and organosulfate-containing particles; C7: mixed/aged and dust-like particles

Table 2: Features and mean values (±sdev) of characteristic parameters for the two selected episodes

	Sodium chloride rich episode	Organics rich episode	Instrument
Date and time	0820 noon to 0823 noon	0825 midnight to 0828 midnight	
Sodium salts (µg m^{-3})	2.2 ± 1.0 Higher	0.6 ± 0.4 Lower	LAAPTOF
Biomass burning–soil (µg m^{-3})	0.7 ± 0.7 Lower	1.7 ± 1.1 Higher	LAAPTOF
Organics (µg m^{-3})	2.0±1.2 Lowest	12.9±3.9 Highest	HR-Tof-AMS
Particle acidity indicator NH_4^+ measured/predicted	0.67±0.10 Highest acidity	0.83 ± 0.06 Average acidity Anti-correlated with org	HR-Tof-AMS
Organonitrate fraction indicator NO^+/NO_2^+	11.0 ± 6.1 Highest	6.1 ± 0.9 Lowest	HR-Tof-AMS
Oxidation state (Osc) (Anti-correlated with org)	-0.24 ± 0.34 Less oxidized Strongest variability	-0.10 ± 0.20 More oxidized Least variability	HR-Tof-AMS
Wind Direction (°)	Southwest	Varying	Meteorology sensor (WS700, Lufft GmbH)
Wind Speed (m s^{-1})	1.6 ± 1.0	1.2 ± 1.0	

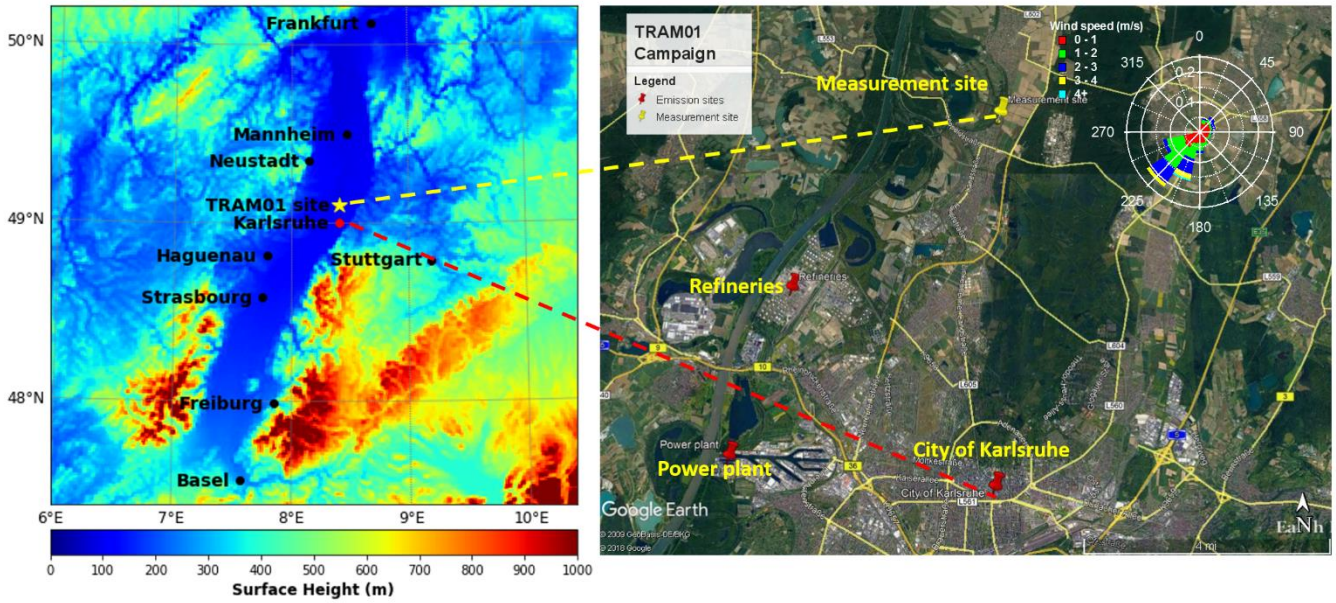

Figure 1: Measurement location and topography (left), nearby peak emission sites and wind rose for the complete measurement campaign in summer 2016 (right).

645

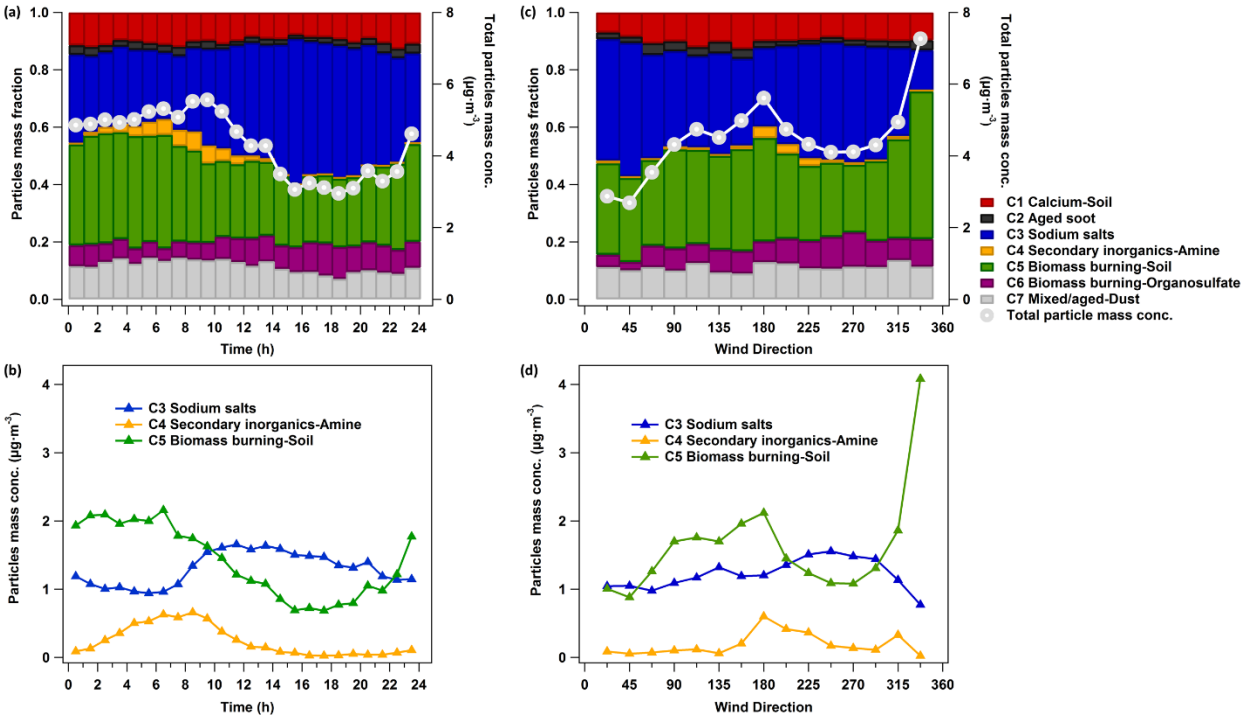

Figure 2: Diurnal pattern (a and b) and wind direction resolved particle class masses (c and d) measured by LAAPTOF. Please note that the uncertainties of the particle class mass concentrations are relatively large (Shen et al., 2019).

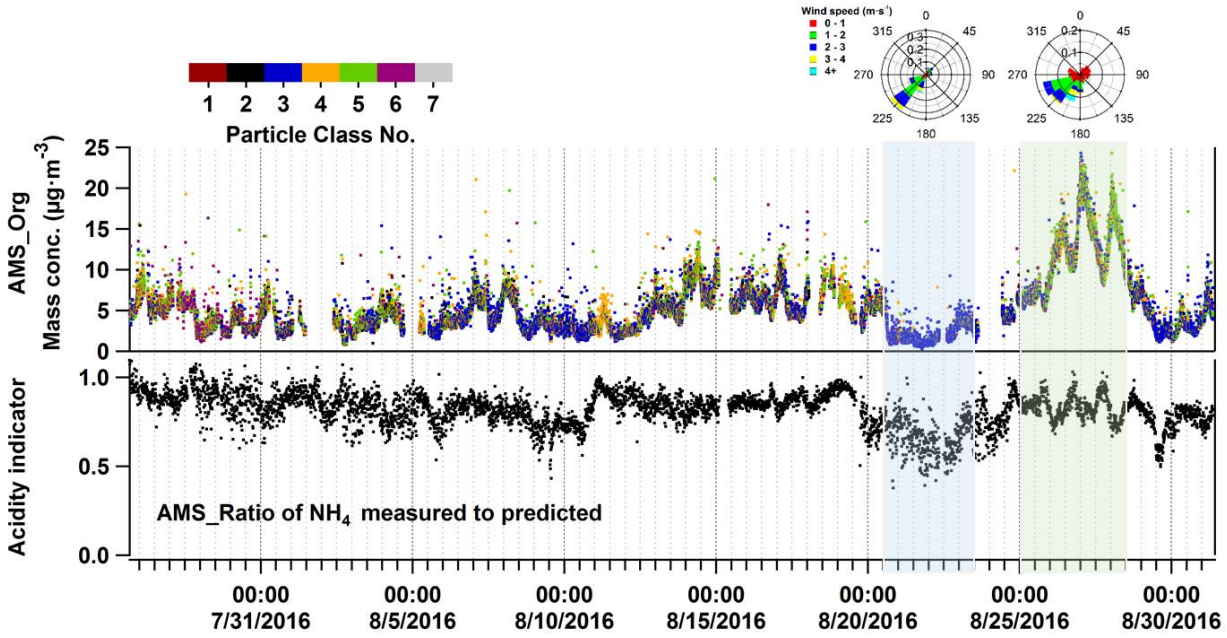

Figure 3: Time series of particulate organic mass measured by the AMS (AMS org in the upper panel), the particle acidity indicator (the lower the value the more acidic, lower panel), and the particle class number classified by LAAPTOF (colour code, upper panel). The seven classes are class 1: calcium-Soil; class 2: aged soot; class3: sodium salts; class 4: secondary inorganics-amine; class 5: biomass burning-soil; class 6: biomass burning-organosulfate; and class 7: mixed/aged-dust. The first (blue) and second (green) shaded areas mark the sodium chloride rich and organic rich episodes, respectively.

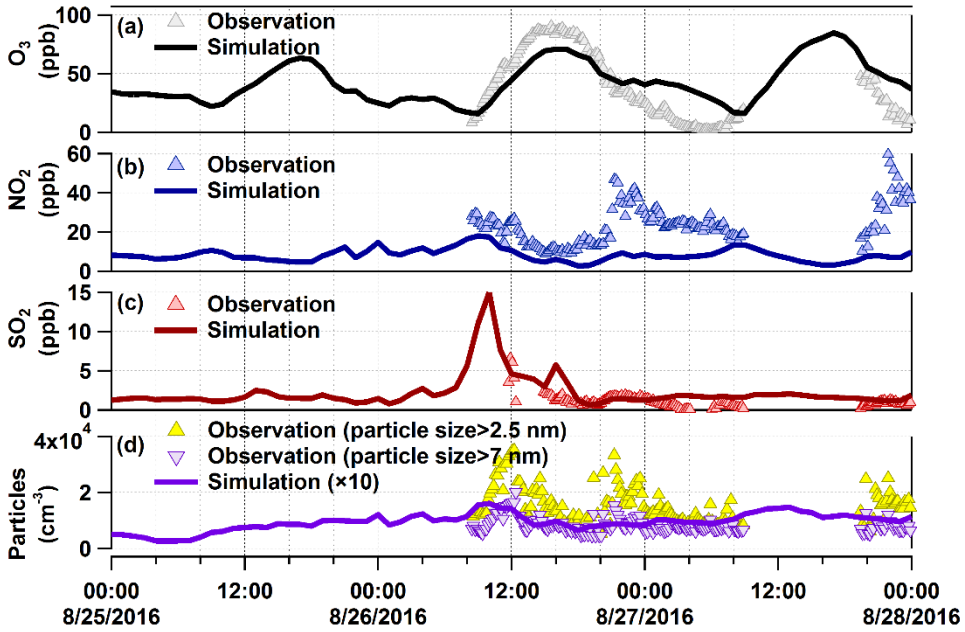

Figure 4: Comparison between observations and model results for O_3, NO_2, SO_2, and particle number in organic-rich episode. The modelled particles do not represent the ultrafine particles to their full extend, especially for the particles in the nucleation mode.

660

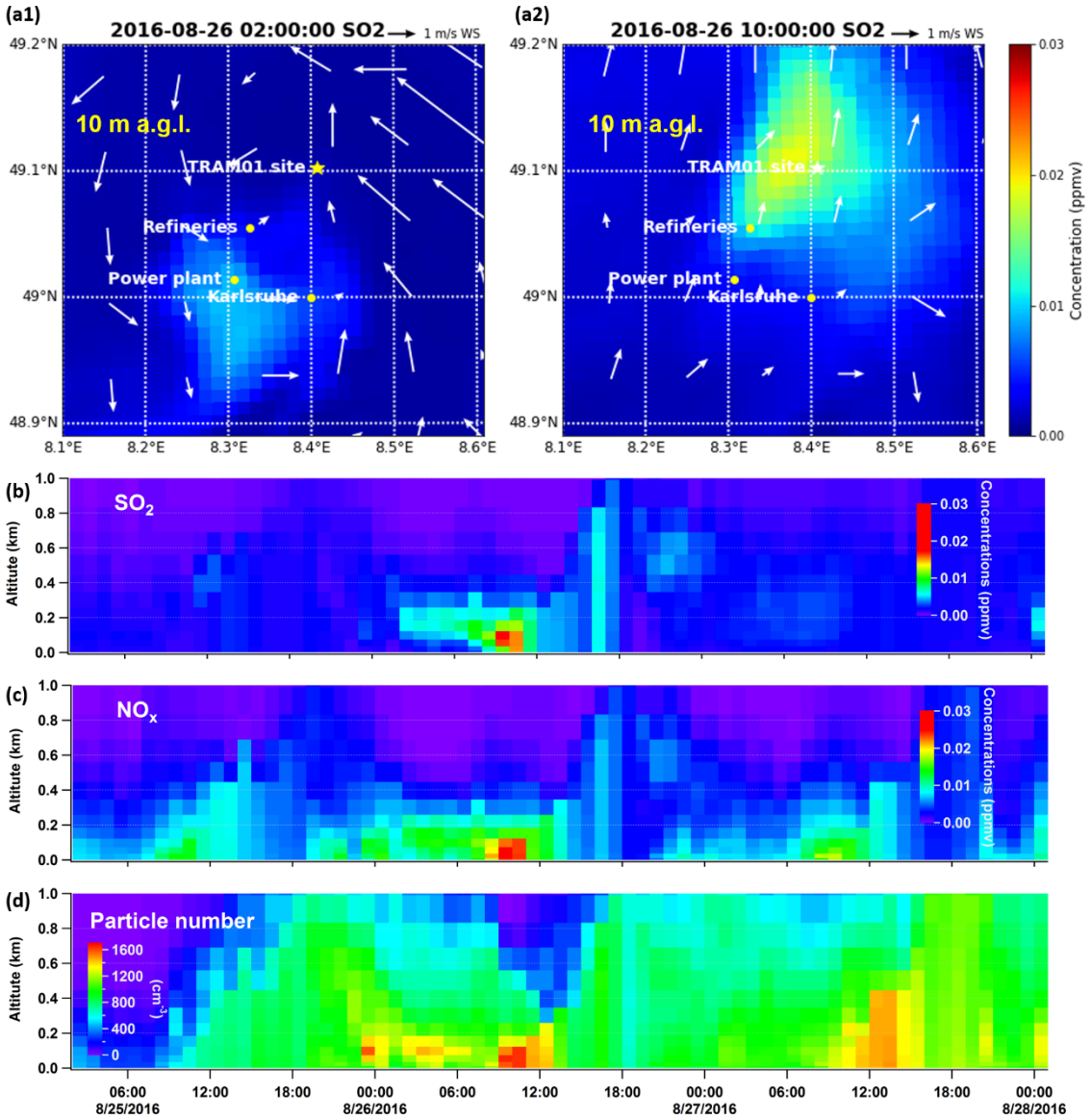

Figure 5: Modelled SO_2 concentrations at 2:00 (a1) and 10:00 (a2) on August 26th at 10 m a.g.l.. Panels (b) to (d) are time series of vertical profiles above the measurement site for simulated SO_2, NO_x and total particle number.

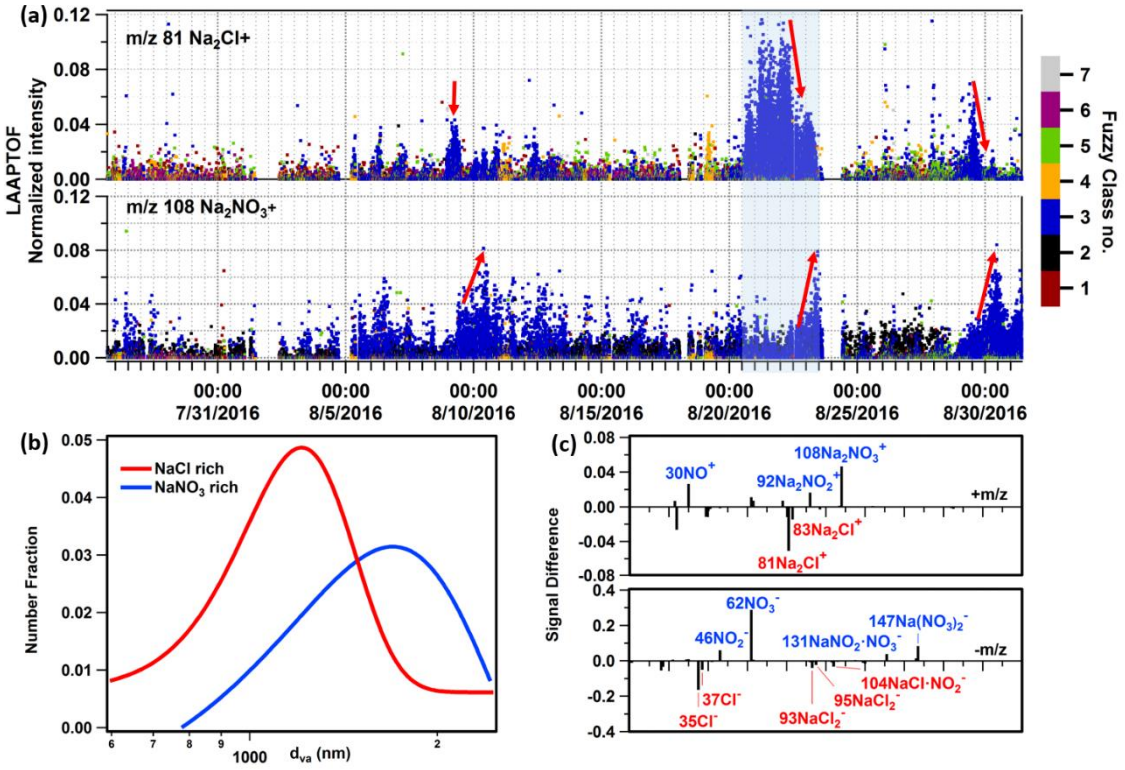

Figure 6: (a) Time series of sodium chloride and nitrate signatures in seven particle classes. Y-axis is the normalized ion intensity (each ion peak intensity is normalized to the sum of all ion signals; positive and negative ions were analysed separately). The seven classes are class 1: calcium-Soil; class 2: aged soot; class3: sodium salts; class 4: secondary inorganics-amine; class 5: biomass burning-soil; class 6: biomass burning-organosulfate; and class 7: mixed/aged-dust. Obvious sodium chloride and nitrate signatures are mainly found in class 3 labelled in blue colour. (b) Size distributions of NaCl rich (young sea salt) and $NaNO_3$ rich (aged sea salt) particles. Gaussian fit NaCl dva (±σ) = 1211(±352) nm; $NaNO_3$ 1697(±946) nm. (c) Spectra difference between aged and young sea salt particles (aged-young). The blue band marks the sodium chloride rich episode.

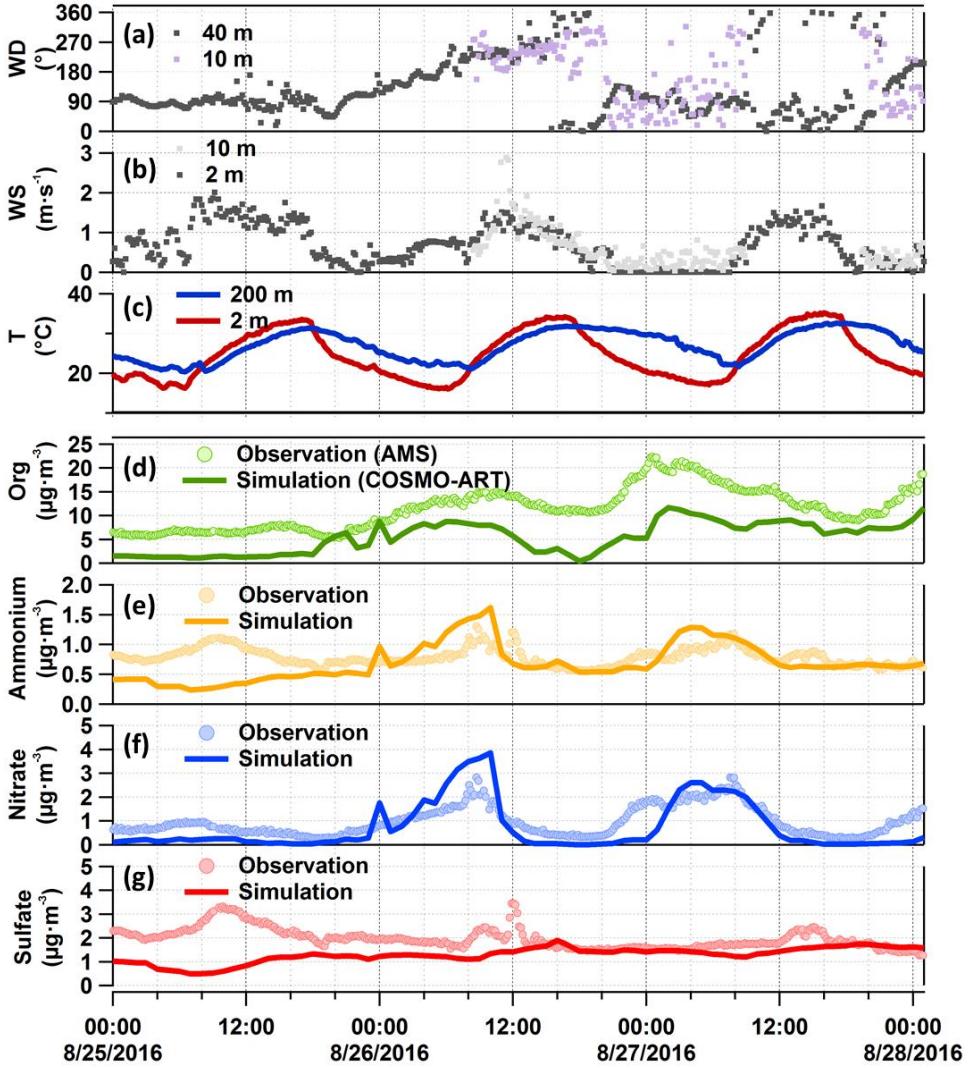

Figure 7: Comparison between observations and model simulations for organic-rich episode. Panel (a) and (b) are wind conditions measured 10 m a.g.l. at our measurement site (purple and light grey dots for wind direction and speed, respectively), as well as the complementary KIT-tower data (dark grey dots). Panel (c) is the temperature data from the KIT-tower. Panel (d) to (g) are the particulate organic compounds, ammonium, nitrate, and sulfate measured by AMS and simulated by COSMO-ART. The simulation results are at the lowest atmospheric level in the model, namely 10 m a.g.l.

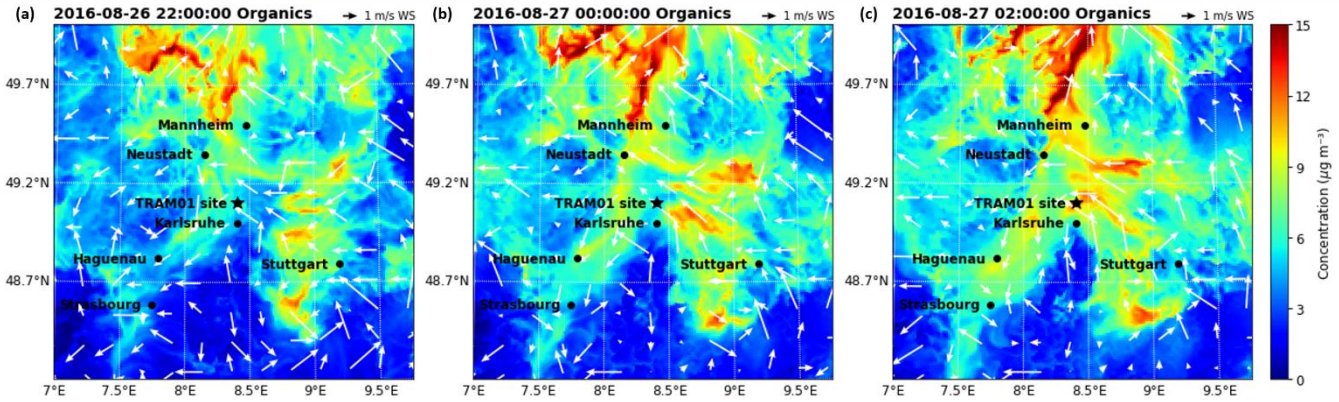

Figure 8: Particulate organics concentrations calculated by COSMO-ART for three different time points (a) to (c) during the night from August 26th to 27th for 10 m a.g.l..

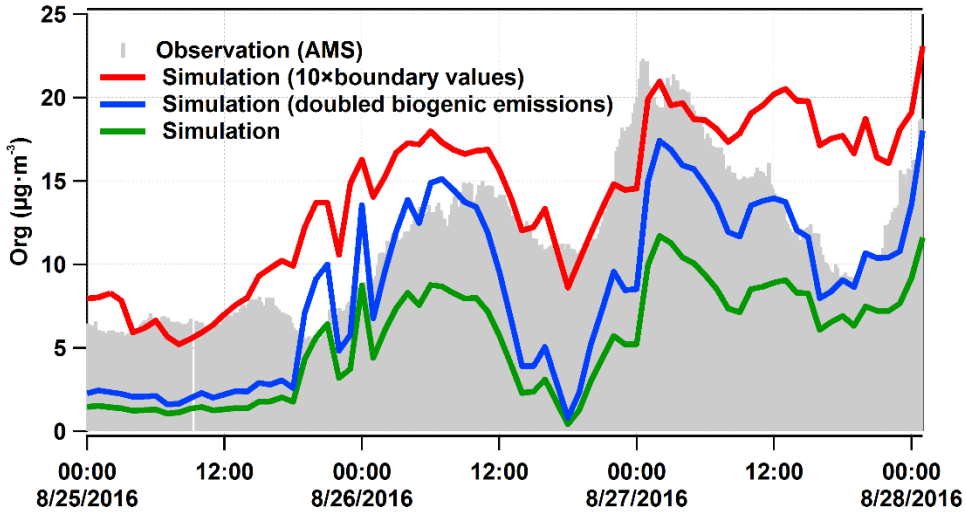

Figure 9: Modelled organic mass concentrations (lines) compared to measured values (grey area). The green line is the same as in Figure 7, the red line was calculated for a tenfold-enhanced regional background in organics, and the blue was calculated for doubles biogenic emissions in COSMO-ART.